

A High-Resolution Reconstruction of Palaeoceanographic Conditions in the Glacial Southern Ocean (Scotia Sea and Adélie Land Coast)



A thesis submitted for the degree of
Doctor of Philosophy
by

Lewis G. Collins

Submitted to
Cardiff University
School of Earth and Ocean Sciences

UMI Number: U585298

All rights reserved

INFORMATION TO ALL USERS

The quality of this reproduction is dependent upon the quality of the copy submitted.

In the unlikely event that the author did not send a complete manuscript and there are missing pages, these will be noted. Also, if material had to be removed, a note will indicate the deletion.



UMI U585298

Published by ProQuest LLC 2013. Copyright in the Dissertation held by the Author.
Microform Edition © ProQuest LLC.

All rights reserved. This work is protected against
unauthorized copying under Title 17, United States Code.



ProQuest LLC
789 East Eisenhower Parkway
P.O. Box 1346
Ann Arbor, MI 48106-1346

Declaration

This work has not previously been accepted for any degree and is not concurrently submitted in candidature for any degree.

Signed.......... LEWIS COLLINS

Date.....23-02-10.....

This thesis is being submitted in partial fulfilment for the degree of PhD.

Signed.......... LEWIS COLLINS

Date.....23-02-10.....

This thesis is the result of my own investigations, except where otherwise stated. Other sources are acknowledged by footnotes giving explicit references. A bibliography is appended.

Signed.......... LEWIS COLLINS

Date.....23-02-10.....

I hereby give consent for my thesis, if accepted, to be available for photocopying and for inter-library loan, and for the title and summary to be made available to outside organisations.

Signed.......... LEWIS COLLINS

Date.....23-02-10.....

Summary

Antarctic sea-ice is a critical component of the climate system, an enhancer of glacial climate and, as recently hypothesised by modelling studies, a potential driver of the millennial scale climate variability that dominated the last glacial cycle (LGC). Unfortunately a severe lack of glacial sea-ice records from the Southern Ocean has so far prevented the testing of this hypothesis with field data. In this thesis, I present detailed reconstructions of Antarctic sea-ice and ocean conditions derived from diatom assemblages and the first application of highly branched isoprenoid biomarkers to glacial sediments. These sea-ice sensitive proxies were measured in high-resolution, glacial sediment cores from the Scotia Sea (Southwest Atlantic, West Antarctica) and the Adélie Land Coast (Australia – Antarctica Basin, East Antarctica). Good chronological control for the past 50 kyrs was achieved through the correlation of geochemical tracers with an oxygen isotope stack, a combination of biostratigraphic datums and relative geomagnetic palaeointensity data, and the identification of the Laschamp geomagnetic excursion at its most southerly site to date. These records permit a critical assessment of the contemporaneous nature of the regional extent, duration and seasonality of summer and winter sea-ice in West and East Antarctica during the LGC, and further afford an opportunity to determine validity of the proposed role played by Antarctic sea-ice in millennial-scale climate change through its influence on oceanography and climate. Results show that the environmental response to climate perturbations in West and East Antarctica was heterogeneous between 46.9 cal ka B.P. and ~25 cal ka B.P. and broadly homogenous between ~25 cal ka B.P. and deglaciation. This study builds on existing Last Glacial Maximum (LGM) sea-ice reconstructions and shows greater summer sea-ice expansion in the Scotia Sea than previously recognised, a reduced maximum winter sea-ice extent along the Adélie Land Coast, a circum-Antarctic sea-ice maximum earlier than the LGM, decreased sea-ice seasonality in the Scotia Sea prior to maximum conditions, and an extensive period of extended sea-ice seasonality after maximum conditions. Further, this investigation has revealed close relationships between these new glacial reconstructions of Antarctic sea-ice and Antarctic Isotope Maxima, Dansgaard/Oeschger events, atmospheric CO₂ variability and deep-water formation, confirming the likely importance of Antarctic sea-ice in the propagation of global millennial-scale climate change during the LGC.

Acknowledgements

I would like to take this opportunity to express my undying thanks and sincere gratitude towards those people who have helped during the course of this project. First and foremost I would like to thank my supervisors; Dr Claire Allen, Dr Jennifer Pike, and Dr Dominic Hodgson for their unwavering support and encouragement over the past few years. Claire's commitment and enthusiasm has been contagious and truly inspiring and without her open-door policy and the many 'quick' chats, this thesis would not have been possible, I feel privileged to have been Claire's first Ph.D. student. Jenny's critical eye, attention to detail and help in facilitating the often difficult link between Cambridge and Cardiff was also very much appreciated. Dom's experience and guidance throughout the closing stages of the thesis was invaluable.

I would also like to thank Dr. Guillaume Massé for providing the facilities of the Petroleum and environmental Geochemistry group at the University of Plymouth, and later of LOCEAN-CNRS at Universite Paris, for the processing of unsaturated hydrocarbon compounds, and for useful discussion of these data. Thanks also to Dr. Mark Hounslow at the Lancaster Environment Centre at Lancaster University for relative palaeointensity data generation and discussion. I am also indebted to my many colleagues at the British Antarctic Survey, thanks in particular goes to Dr. C-D Hillenbrand for his leadership aboard British Antarctic Survey cruise JR179 and for the many papers from his seemingly endless library! Thanks also to Xavier Crosta and Massimo Presti for the supply of materials and data pertaining to sediment core MD03-2603.

Thanks to my friends for providing encouragement and distractions when needed, particularly Stig, Jazzy, Pico, Smithy, Ali, the members of City Life FC and Spud, my comrade in arms. Thanks to my family for setting me on this journey and to the many inspiring teachers and tutors along the way. Finally, thank you Julie, my rock, my love, my life, for your endless patience and understanding, this is for you.

This project was supported by NERC grant NER/S/A/2005/13647 and the British Antarctic Survey CACHE-PEP project.

List of Abbreviations

AABW	Antarctic Bottom Water
AAIW	Antarctic Intermediate Water
AASW	Antarctic Surface Water
ACC	Antarctic Circumpolar Current
AIM	Antarctic Isotope Maxima
AIS	Antarctic Ice Sheet
ALBW	Adélie Land Bottom Water
AMOC	Atlantic Meridional Overturning Circulation
APF	Antarctic Polar Front
APFZ	Antarctic Polar Frontal Zone
ARM	Anhysteretic Remnant Magnetisation
ASF	Antarctic Slope Front
CDW	Circumpolar Deep Water
ChRM	Characteristic Remnant Magnetisation
CLIMAP	Climate Long Range Investigation Mapping and Prediction
EAIS	East Antarctic Ice Sheet
EDML	EPICA Dronning Maud Land
EPILOG	Environmental Processes of the Ice Age: Land, Oceans, Glaciers
EPICA	European Project for Ice Coring in Antarctica
GCM	General Circulation Models
HSSW	High Salinity Surface Water
HBI	Highly Branched Isoprenoids
HNLC	High Nutrient Low Chlorophyll
HNLSLC	High Nutrient Low Silica Low Chlorophyll
HRW	High Resolution Window
IPCC	Intergovernmental Panel on Climate Change
IRM	Isothermal Remnant Magnetisation
ISW	Ice Shelf Waters
LCDW	Lower Circumpolar Deep Water
LGC	Last Glacial Cycle
LGM	Last Glacial Maximum
MCDW	Modified Circumpolar Deep Water
MIS	Marine Isotope Stages
MIZ	Marginal Ice Zone
MS	Magnetic Susceptibility
mT	Millitesla
NADW	North Atlantic Deep Water
NGRIP	North Greenland Ice-core Project
NRM	Natural Remnant Magnetisation
PCA	Principal Component Analysis
POOZ	Permanently Open Ocean Zone

RPI	Relative Palaeointensity
rs	Resting Spores
SACCF	Southern Antarctic Circumpolar Front Current
SAF	Sub-Antarctic Front
SAPIS	South Atlantic Palaeointensity Stack
SAZ	Sub-Antarctic Zone
SF	Scotia Front
SIZ	Sea-ice Zone
SOIREE	Southern Ocean Iron Release Experiment
SPDW	South Pacific Deep Water
SSI	Summer Sea-Ice
SST	Sea Surface Temperature
THC	Thermohaline Circulation
v/gds	Valves/gram of dried sediment
UCDW	Upper Circumpolar Deep Water
WAIS	West Antarctic Ice Sheet
WDW	Warm Deep Water
WSBW	Weddell Sea Bottom Water
WSDW	Weddell Sea Deep Water
WSC	Weddell-Scotia Confluence
WSI	Winter Sea-Ice

1. BACKGROUND READING	1-48
1.1. The Geological Setting	1
1.1.1. Formation of Antarctica	1
1.1.1.1. Formation of the Scotia Sea	5
1.1.1.2. Formation of the Adélie Land Coast	8
1.1.1.3. Development of the Antarctic Circumpolar Current	9
1.1.1.3.1. The Tasmanian Gateway	9
1.1.1.3.2. Drake Passage	10
1.2. The Oceanographic Setting	11
1.2.1. Thermohaline Circulation	11
1.2.2. The Southern Ocean	14
1.2.2.1. The Antarctic Circumpolar Current	15
1.2.2.2. Water Masses	16
1.2.2.2.1. North Atlantic Deep Water	16
1.2.2.2.2. Circumpolar Deep Water	17
1.2.2.2.3. Antarctic Bottom Water	17
1.2.3. The Scotia Sea	19
1.2.3.1. Circulation	19
1.2.3.2. Frontal Systems	19
1.2.3.2.1. The Sub-Antarctic Front	19
1.2.3.2.2. The Antarctic Polar Front	20
1.2.3.2.3. The South Antarctic Circumpolar Current Front	20
1.2.3.2.4. The Southern Boundary/Scotia Front	21
1.2.3.2.5. The Weddell-Scotia Confluence	21
1.2.4. The Australia – Antarctic Basin and the Adélie Land Coast	21
1.2.4.1. Circulation	23
1.2.5. Sedimentology	23
1.2.5.1. Sediments of the Scotia Sea	24
1.2.5.2. Sediments along the Adélie Land Coast	25
1.3. Antarctic Sea-Ice	26
1.3.1. Formation and Extent	26
1.3.2. Climatic Influence	29
1.3.2.1. Albedo	30
1.3.2.2. Deep-water Formation	30
1.3.2.3. Heat and Gas Transfer	31
1.3.2.4. Sensitivity	31
1.3.2.5. Biota	32
1.3.3. Palaeoreconstructions	32
1.3.4. Antarctic Sea-Ice: A Glacial Climate Driver?	35
1.4. Palaeoenvironments and Palaeoclimate	36
1.4.1. Modern-day Antarctica	36
1.4.2. Glaciations During the Cenozoic	38

1.4.3.	The Last Glacial Cycle	40
1.4.3.1.	Millennial Oscillations in the Northern Hemisphere	41
1.4.3.2.	Millennial Oscillations in the Southern Hemisphere	42
1.4.4.	The Last Glacial Maximum	44
1.4.4.1.	The LGM Time-slice	45
1.5.	Summary	46
1.6.	The Project	47
1.6.1.1.	Aims and Objectives	48
2.	MAJOR PROXIES EMPLOYED IN THIS STUDY	49-70
2.1.	Diatoms as Palaeo-indicators of Climate Change	49
2.1.1.	Environmental Controls on Diatom Distribution	50
2.1.1.1.	Diatoms of the Sea-Ice Zone	50
2.1.1.2.	Diatoms of the Marginal Ice Zone	51
2.1.1.3.	Diatoms of the Permanently Open Ocean Zone	52
2.1.1.4.	Diatoms of the Antarctic Polar Frontal Zone	53
2.1.2.	Diatom Preservation Controls	54
2.1.2.1.	Dissolution	54
2.1.2.2.	Advection	57
2.1.2.3.	Aggregation	58
2.1.2.4.	Winnowing and Scouring	58
2.1.3.	Diatom Species Ecological Associations	59
2.1.3.1.	<i>Actinocyclus actinochilus</i> (Ehrenberg) Simonsen	59
2.1.3.2.	<i>Azpeitia tabularis</i> (Grunow) G. Fryxell and P.A. Sims	59
2.1.3.3.	<i>Eucampia antarctica</i> (Castracane) Mangin	60
2.1.3.4.	<i>Fragilariopsis curta</i> (Van Heurck) Hustedt	60
2.1.3.5.	<i>Fragilariopsis cylindrus</i> (Grunow) Krieger	61
2.1.3.6.	<i>Fragilariopsis kerguelensis</i> (O'Meara) Hustedt	61
2.1.3.7.	<i>Fragilariopsis obliquecostata</i> (Van Heurck) Heiden in Heiden et Kolbe	62
2.1.3.8.	<i>Fragilariopsis ritscheri</i> Hustedt	62
2.1.3.9.	<i>Fragilariopsis separanda</i> Hustedt	63
2.1.3.10.	<i>Hyalochaete Chaetoceros</i> resting spores (<i>Chaetoceros</i> rs)	63
2.1.3.11.	<i>Porosira glacialis</i> (Grunow) Jørgensen	64
2.1.3.12.	<i>Rhizosolenia</i> spp.	65
2.1.3.13.	<i>Thalassiosira antarctica</i> Comber	65
2.1.3.14.	<i>Thalassiosira gracilis</i> group (Karsten) Hustedt	66
2.1.3.15.	<i>Thalassiosira lentiginosa</i> (Janisch) Fryxell	67
2.1.3.16.	<i>Thalassiosira scotia</i> Fryxell and Hoban	67
2.1.3.17.	<i>Thalassiothrix antarctica</i> Schimper ex Karsten	67
2.2.	Highly Branched Isoprenoids as Palaeoindicators of Climate Change	68

3. MATERIALS AND METHODS	71-98
3.1. Core Material	71
3.1.1. TPC063	72
3.1.2. TPC286	75
3.1.3. MD03-2603	78
3.1.4. Quantitative Diatom Assemblage Data	81
3.1.4.1. Sample Preparation	81
3.1.4.2. Assemblage Data	81
3.1.4.2.1. Valve Counts	81
3.1.4.2.2. Diatom Counting Methods	82
3.1.4.2.2.1. Conventional Counting Method	82
3.1.4.2.2.2. Area Counting Method	82
3.1.5. Data Analysis	84
3.1.5.1. Assemblage Data	84
3.1.5.2. Principle Components Analysis	84
3.2. Chronostratigraphy Methods	88
3.2.1. Radiometric Dating Techniques	88
3.2.1.1. Radiocarbon Dating	88
3.2.1.1.1. Sample Preparation	89
3.2.2. Magnetic Susceptibility Correlation Dating	90
3.2.2.1. Sample Preparation	91
3.2.3. Relative Palaeointensity Dating	91
3.2.3.1. The Laschamp Event	93
3.2.3.2. Sample Preparation	94
3.2.4. Biostratigraphic Dating	95
3.2.4.1. Sample Preparation	96
3.2.5. Highly Branched Isoprenoids	97
3.2.5.1. Sample Preparation	97
4. RESULTS: ENVIRONMENTAL PROXIES	99-132
4.1. TPC063 – Results	99
4.1.1. Core Description – Sedimentology	99
4.1.2. Magnetic Susceptibility	101
4.1.3. Diatom Assemblage Data	101
4.1.3.1. MIS 3	102
4.1.3.2. MIS 2	103
4.1.3.3. MIS 1	104
4.1.4. Principle Components Analysis – Relative Abundance Data	104
4.1.5. Highly Branched Isoprenoids	108
4.2. TPC286 – Results	110
4.2.1. Core Description – Sedimentology	110
4.2.2. Magnetic Susceptibility	111
4.2.3. Diatom Assemblage Data	113

4.2.3.1.	MIS 5 – MIS 3	113
4.2.3.2.	MIS 3	114
4.2.3.3.	MIS 3 – MIS 2	114
4.2.3.4.	MIS 2 – MIS 1	115
4.2.4.	Principle Components Analysis – Relative Abundance Data	116
4.2.5.	Highly Branched Isoprenoids	121
4.3.	MD03-2603 – Results	123
4.3.1.	Core description – Sedimentology	123
4.3.2.	Magnetic Susceptibility	123
4.3.3.	Diatom Assemblage Data	123
4.3.3.1.	MIS 3	123
4.3.3.2.	MIS 2	126
4.3.3.3.	MIS 1	126
4.3.4.	Principle Components Analysis – Relative Abundance Data	127
5.	RESULTS: CHRONOSTRATIGRAPHY	133-154
5.1.	Cores TPC063 and TPC286	133
5.1.1.	Chronostratigraphic Data	133
5.1.1.1.	Radiocarbon Dates	133
5.1.1.1.1.	TPC063	133
5.1.1.1.2.	TPC286	134
5.1.1.2.	Magnetic Susceptibility	135
5.1.1.2.1.	TPC063	135
5.1.1.2.2.	TPC286	135
5.1.1.3.	Biostratigraphy – <i>Eucampia antarctica</i> Abundance Curve	136
5.1.1.3.1.	TPC063	136
5.1.1.3.2.	TPC286	137
5.1.1.4.	Biostratigraphy – Total Diatom Concentration Curve	138
5.1.1.4.1.	TPC063	138
5.1.1.4.2.	TPC286	138
5.1.1.5.	Palaeomagnetic Data	139
5.1.1.5.1.	TPC063	139
5.1.1.5.2.	TPC286	140
5.1.2.	Core Correlation	141
5.1.3.	Core Chronologies	141
5.1.4.	Age-Depth Models	145
5.1.4.1.	TPC063	145
5.1.4.2.	TPC286	146
5.1.4.3.	Age-Depth Model Evaluation	147
5.1.4.3.1.	TPC063	147
5.1.4.3.2.	TPC286	148
5.2.	Core MD03-2603	150
5.2.1.	Magnetic Susceptibility	150

5.2.2. Thorium-excess Dating	151
5.2.3. Geochemical Tracers	152
5.2.4. Oxygen Isotope Correlation	152
5.3 Summary	153
6. INTERPRETATION AND DISCUSSION	155-214
6.1. TPC063	155
6.1.1. Summary of Interpretations	155
6.1.1.1. The Glacial, 44.7 cal ka B.P. to 17.3 cal ka B.P.	156
6.1.1.2. Deglaciation, 17.3 cal ka B.P. to 11.5 cal ka B.P.	158
6.1.1.3. The Holocene, 11.5 cal ka B.P. to 0 cal ka B.P.	158
6.1.2. Glacial Maximum (HRW)	158
6.1.2.1. Diatom Species Relationships	158
6.1.2.1.1. PCA Axis 1	159
6.1.2.1.2. PCA Axis 2	160
6.1.2.1.3. PCA Axis 3	160
6.1.2.2. Palaeoenvironment Reconstruction Across the Glacial Maximum	161
6.1.2.2.1. HRW Zone 1: Unique Productivity Event, 34.2 cal ka B.P. to 30.7 cal ka B.P.	161
6.1.2.2.2. HRW Zone 2: Cooling Open Ocean, 30.7 cal ka B.P. to 24.7 cal ka B.P.	161
6.1.2.2.3. HRW Zone 3: Glacial Sea-ice Maximum, 24.7 cal ka B.P. to 23.2 cal ka B.P.	162
6.1.2.2.4. HRW Zone 4: Enhanced Sea-ice Seasonality, 23.2 cal ka B.P. to 21.9 cal ka B.P.	163
6.2. TPC286	164
6.2.1. Summary of Interpretations	164
6.2.1.1. The Glacial, 47.9 cal ka B.P. to 17.3 cal ka B.P.	165
6.2.1.2. Deglaciation, 17.3 cal ka B.P. to 12.9 cal ka B.P.	167
6.2.1.3. The Holocene, 12.9 cal ka B.P. to 0 cal ka B.P.	167
6.2.2. Glacial Maximum (HRW)	167
6.2.2.1. Diatom Species Relationships	167
6.2.2.1.1. PCA Axis 1	167
6.2.2.1.2. PCA Axis 2	168
6.2.2.1.3. PCA Axis 3	169
6.2.2.1.4. PCA Axis 4	169
6.2.2.2. Palaeoenvironment Reconstruction Across the Glacial Maximum	170
6.2.2.2.1. HRW Zone 2: Temperature Minima, 29.7 cal ka B.P. to 22.9 cal ka B.P.	170
6.2.2.2.2. HRW Zone 2: Temperature Minima, 29.7 cal ka B.P. to 22.9 cal ka B.P.	171
6.2.2.2.3. HRW Zone 3: Seasonal Shift in Sea-ice Dynamics, 22.9 cal ka B.P. to 22.2 cal ka B.P.	172

6.3. Regional Reconstruction: The Scotia Sea	173
6.3.1. 48.6 cal ka B.P. to 34.4 cal ka B.P.	173
6.3.2. 34.4 cal ka B.P. to 30.4 cal ka B.P.	174
6.3.3. 30.4 cal ka B.P. to 25 cal ka B.P.	175
6.3.4. 25 cal ka B.P. to 23.5 cal ka B.P.	176
6.3.5. 22.9 cal ka B.P. to 22.8 cal ka B.P.	177
6.3.6. 22.8 cal ka B.P. to 19.7 cal ka B.P.	178
6.3.7. 19.7 cal ka B.P. to 17.8 cal ka B.P.	179
6.3.8. 17.8 cal ka B.P. to the modern-day	180
6.3.9. Scotia Sea Reconstruction: Discussion	181
6.3.9.1. Sea-ice	181
6.3.9.2. Antarctic Polar Front	187
6.3.9.3. <i>Hyalochaete Chaetoceros</i> Resting Spore Peak	188
6.4. MD03-2603	190
6.4.1. Summary of interpretations	190
6.4.1.1. The Glacial, 46.9 cal ka B.P. to 20 cal ka B.P.	191
6.4.1.2. Deglaciation, 20 cal ka B.P. to 12.8 cal ka B.P.	193
6.4.1.3. The Holocene, 12.8 cal ka B.P. to ~0 cal ka B.P.	193
6.4.2. Glacial Maximum (HRW)	194
6.4.2.1. Diatom Species Relationships	194
6.4.2.1.1. PCA Axis 1	194
6.4.2.1.2. PCA Axis 2	195
6.4.2.1.3. PCA Axis 3	196
6.4.2.1.4. PCA Axis 4	196
6.4.2.2. Palaeoenvironment Reconstruction Across the Glacial Maximum	197
6.4.2.2.1. HRW Zone 1: Open Water Frontal Upwelling, 34.4 cal ka B.P. to 31 cal ka B.P.	197
6.4.2.2.2. HRW Zone 2: Cold Water Environment, 31 cal ka B.P. to 20.5 cal ka B.P.	198
6.4.2.2.3. HRW Zone 3: Enhanced Sea-ice Seasonality, 20.5 cal ka B.P. to 16.5 cal ka B.P.	199
6.5. Regional Reconstruction: The Adélie Land Coast	199
6.5.1. Sea-ice	199
6.5.2. The Southern Boundary	201
6.5.3. Influence of the Australia – Antarctic Basin Gyre	202
6.6. Circum-Antarctic Comparison	203
6.6.1. Circum-Antarctic Sea-ice	204
6.6.1.1. 59.1 cal ka B.P. to 31.6 cal ka B.P.	204
6.6.1.2. 32.2 cal ka B.P. to 17.7 cal ka B.P.	205
6.6.1.3. Circum-Antarctic Sea-ice: Discussion	205
6.6.2. Circum-Antarctic Frontal Dynamics	210
6.6.2.1. 44.7 cal ka B.P. to 34.3 cal ka B.P.	211
6.6.2.2. 32.2 cal ka B.P. to 24 cal ka B.P.	211
6.6.2.3. 24 cal ka B.P. to 17.8 cal ka B.P.	211

6.6.2.4.	Circum-Antarctic Fronts: Discussion	211
6.7.	Summary	213
7.	ADDRESSING THE AIMS	215-229
7.1.	Was West Antarctica as sensitive to perturbations in climate during the last glacial cycle as it is today?	215
7.2.	Was East Antarctica's climate stable in comparison to West Antarctica during the last glacial cycle as it appears today?	217
7.3.	When was the Last Glacial Maximum?	219
7.4.	What was the role of the Southern Ocean in global forcings and feedbacks during MIS 2 and 3?	220
7.5.	Future Work	227
7.5.1.	Scotia Sea Low-resolution Sections	227
7.5.2.	Additional Core Sites	227
7.5.3.	Highly Branched Isoprenoids	228
7.5.4.	<i>Hyalochaete Chaetoceros</i> Resting Spore Productivity Peak	229
7.5.5.	Relative Palaeointensity versus Beryllium-10	229
	REFERENCES	230-254
	APPENDICIES	255-302

List of Figures

1.1a.	Southern hemisphere tectonic configuration at 180 Ma.	3
1.1b.	Southern hemisphere tectonic configuration at 150 Ma.	3
1.1c.	Southern hemisphere tectonic configuration at 110 Ma.	4
1.1d.	Southern hemisphere tectonic configuration at 80 Ma.	4
1.1e.	Southern hemisphere tectonic configuration (0 Ma).	5
1.2.	Topography of the Scotia Sea.	6
1.3.	Andean continental link.	7
1.4.	A schematic of the global Meridional Overturning Circulation.	13
1.5.	Primary current systems and sea-floor topography of the southern hemisphere.	14
1.6.	Schematic illustrating the vertical distribution of water masses of the Southern Ocean.	18
1.7.	Southern Ocean bottom water potential temperatures.	18
1.8.	Sea-ice distribution and frontal structure of the ACC throughout the Scotia Sea Basin.	20
1.9.	The primary oceanographic features along the Adélie Land Coast.	22
1.10.	Lithology of modern sediments in the Southern Ocean.	25
1.11.	Average seasonal Antarctic sea-ice extent at present.	28
1.12.	Schematic illustrating the primary physical processes related to polynya formation.	29
1.13.	Impacts of Antarctic sea-ice on oceanography and climate.	30
1.14.	Comparison of last glacial maximum summer sea-ice extents.	33
1.15.	Comparison of last glacial maximum winter sea-ice extents.	33
1.16.	Comparison of Ph.D. core sites with the EPILOG-LGM dataset.	35
1.17.	$\delta^{18}\text{O}$ trend for the past 70 Ma.	39
1.18.	Marine isotope stages of the last glacial cycle.	40
1.19.	$\delta^{18}\text{O}$ oscillations identified in the Greenland ice-cores.	41
1.20.	Conceptual model of the bi-polar seesaw.	42
1.21.	$\delta^{18}\text{O}$ oscillations identified in the Antarctic.	43
1.22.	Methane synchronization of EDML and NGRIP $\delta^{18}\text{O}$ records.	44
1.23.	Figure illustrating the large degree of variation in the timings of local LGM.	45
2.1.	Zonation of the Southern Ocean with respect to productivity.	50
2.2.	Light microscope images of lightly silicified diatoms.	55
2.3.	Light microscope images of common heavily silicified diatoms.	56
3.1.	Map of Antarctica illustrating circum-Antarctic distribution of core sites.	71
3.2.	Map of the Scotia Sea, illustrating core site locations (TPC063 and TPC286).	72
3.3.	Core TPC063: Sediment logs and magnetic susceptibility records for trigger and piston components.	74

3.4.	Core TPC063: Effects of dissolution on the downcore diatom assemblage.	75
3.5.	Core TPC286: Sediment logs and magnetic susceptibility records for trigger and piston components.	77
3.6.	Core TPC286: Effects of dissolution on the downcore diatom assemblage.	78
3.7.	Map of the Adélie Land Coast illustrating core site location (MD03-2603).	79
3.8.	Core MD03-2603: Effects of dissolution on the downcore diatom assemblage.	80
3.9a.	Core TPC286: down core total diatom concentration.	82
3.9b.	Core TPC286: down core relative abundance of <i>Chaetoceros</i> rs excluding the dummy variable.	82
3.9c.	Core TPC286: down core relative abundance of <i>Chaetoceros</i> rs including the dummy variable.	82
3.10.	Core TPC063: PCA comparison, absolute abundance vs relative abundance.	87
3.11.	Core TPC286: PCA comparison, absolute abundance vs relative abundance.	88
3.12.	Burckle and Cooke (1983) <i>Eucampia antarctica</i> abundance stratigraphy.	96
4.1.	Core TPC063: Sediment log, MIS stratigraphy, magnetic susceptibility and diatom species assemblage data.	100
4.2.	Core TPC063 (HRW): PCA Scree plot.	106
4.3.	Core TPC063 (HRW): PCA variable loadings, axis 2 versus axis 1.	106
4.4.	Core TPC063 (HRW): PCA variable loadings, axis 3 versus axis 1.	107
4.5.	Core TPC063 (HRW): PCA component scores, axes 1 to 3.	107
4.6.	Core TPC063: HBI concentrations versus <i>Fragilariopsis</i> sea-ice group relative abundance.	110
4.7.	Core TPC286: Sediment log. MIS stratigraphy, magnetic susceptibility and diatom species assemblage data.	112
4.8.	Core TPC286 (HRW): PCA Scree plot.	117
4.9.	Core TPC286 (HRW): PCA variable loadings, axis 2 versus axis 1.	117
4.10.	Core TPC286 (HRW): PCA variable loadings, axis 3 versus axis 1.	118
4.11.	Core TPC286 (HRW): PCA variable loadings, axis 4 versus axis 1.	118
4.12.	Core TPC286 (HRW): PCA component scores, axes 1 to 4.	119
4.13.	Core TPC286: HBI concentrations versus <i>Fragilariopsis</i> sea-ice group relative abundance.	122
4.14.	Core MD03-2603: Sediment log. MIS stratigraphy, magnetic susceptibility and diatom species assemblage data.	125
4.15.	Core MD03-2603 (HRW): PCA Scree plot .	128
4.16.	Core MD03-2603 (HRW): PCA variable loadings, axis 2 versus axis 1.	129

4.17.	Core MD03-2603 (HRW): PCA variable loadings, axis 3 versus axis 1.	129
4.18.	Core MD03-2603 (HRW): PCA variable loadings, axis 4 versus axis 1.	130
4.19.	Core MD03-2603 (HRW): PCA component scores, axes 1 to 3.	130
5.1.	Cores TPC063, TPC286 and GC027: Uncorrected radiocarbon dates sampled from cores.	134
5.2.	Cores TPC063 and TPC286: Magnetic susceptibility curves and proposed MIS stratigraphy.	136
5.3.	Cores TPC063 and TPC286: <i>E. antarctica</i> relative abundance curves and proposed 2Ea ₁ datum for deglaciation.	137
5.4.	Cores TPC063 and TPC286: Total diatom concentration versus <i>Hyalochaete Chaetoceros</i> resting spores (absolute abundance).	139
5.5.	Cores TPC063 and TPC286: Magnetic parameters.	140
5.6.	Cores TPC063 and TPC286: Core correlation.	142
5.7.	SAPIS Stack core locations.	144
5.8.	Scotia Sea relative palaeointensity stack.	145
5.9.	Scotia Sea RPI stack – SAPIS RPI reference stack correlation.	145
5.10.	Cores TPC063 and TPC286: Age-depth models.	147
5.11.	Cores TPC063 and TPC286: Age-depth models, evaluation.	149
5.12.	Core MD03-2603: Magnetic susceptibility curve.	150
5.13.	Core MD03-2603: ²³⁰ Thorium-excess inferred Sedimentation rate.	151
5.14.	Core MD03-2603: Age model.	152
5.15.	Cores TPC063, TPC286 and MD03-2603: MIS time lines based on refined age-models.	153
6.1.	Core TPC063: Environmental log	157
6.2.	Core TPC063 (HRW): PCA component scores versus <i>Fragilariopsis</i> sea-ice group and <i>Fragilariopsis obliquecostata</i> relative abundance.	159
6.3.	Core TPC286: Environmental log	166
6.4.	Core TPC286 (HRW): PCA component scores versus <i>Fragilariopsis</i> sea-ice group and <i>Fragilariopsis obliquecostata</i> relative abundance.	168
6.5.	Reconstructed Scotia Sea oceanography between 48.6 cal ka B.P. and 34.4 cal ka B.P.	174
6.6.	Reconstructed Scotia Sea oceanography between 34.4 cal ka B.P. and 30.4 cal ka B.P.	175
6.7.	Reconstructed Scotia Sea oceanography between 30.4 cal ka B.P. and 25 cal ka B.P.	176
6.8.	Reconstructed Scotia Sea oceanography between 25 cal ka B.P. and 23.5 cal ka B.P.	177
6.9.	Reconstructed Scotia Sea oceanography between 22.9 cal ka B.P. and 22.8 cal ka B.P.	178
6.10.	Reconstructed Scotia Sea oceanography between 22.4 cal ka B.P. and 19.7 cal ka B.P.	179
6.11.	Reconstructed Scotia Sea oceanography between 19.7 cal ka B.P. and 17.8 cal ka B.P.	180

6.12.	Reconstructed Scotia Sea oceanography between 17.8 cal ka B.P. and the modern-day.	181
6.13.	Scotia Sea sea-ice reconstruction: Regional comparison.	185
6.14.	<i>Hyalochaete Chaetoceros</i> Resting Spore Peak: Record comparison.	190
6.15.	Core MD03-2603: Environmental log	192
6.16.	Core MD03-2603 (HRW): PCA component scores versus <i>Fragilariopsis</i> sea-ice group and <i>Fragilariopsis obliquecostata</i> relative abundance.	195
6.17.	Map of the Adélie Land Coast, showing core location (MD03-2603) and primary oceanographic features.	200
6.18.	Primary circulation features of the Australia – Antarctic Basin.	203
6.19.	Cores TPC063, TPC286 and MD03-2603: Environmental log comparison (50 cal ka B.P.).	206
6.20.	PhD estimated winter and summer sea-ice edges at their maximum extent during the last glacial cycle and at the E-LGM time-slice.	209
7.1.	Figure illustrating the large degree of variation in the timings of local LGM.	220
7.2.	Comparison of Ph.D. Antarctic sea-ice records with global records of millennial scale climate change during the LGC.	224

List of Tables

1.1.	Potential temperature and salinity characteristics of Southern Ocean water masses.	16
3.1.	Cores TPC063, TPC286 and MD03-2603: Location.	72
3.2.	Core TPC063: Core components.	74
3.3.	Core TPC296: Core components.	78
3.4.	Diatom species and species groups identified in this study.	85
3.5.	Cores TPC063, TPC286 and GC027: Depths sampled for radiocarbon analysis.	90
3.6.	Geomagnetic excursions known to have interrupted the Brunhes Chron.	93
4.1.	Core TPC063 (HRW): Diatom species and species groups identified (>0.5%).	105
4.2.	Core TPC063 (HRW): PCA axes eigenvalues.	105
4.3.	Core TPC286 (HRW): Diatom species and species groups identified (>0.5%).	116
4.4.	Core TPC286 (HRW): PCA axes eigenvalues.	116
4.5.	Core MD03-2603 (HRW): Diatom species and species groups identified (>0.5%).	127
4.6.	Core MD03-2604 (HRW): PCA axes eigenvalues.	128
5.1.	Cores TPC063, TPC286 and GC027: Uncorrected radiocarbon dates.	135
5.2.	SAPIS relative palaeointensity stack marine core components.	143
5.3.	Core MD03-2603: Thorium age-model.	151

1. Background Reading

This chapter first reviews the geological settings relevant to the project, second details the physical oceanography and dynamics of Antarctic Sea-ice, thirdly describes the climatological context and palaeoenvironments and lastly introduces the project rationale, aims and objectives.

1.1. The Geological Setting

Through geological time tectonic processes have continually influenced the Earth's climate. Redistribution of landmasses, ocean basins and the opening and closing of oceanic seaways changes the Earth's energy budget (Brown *et al.*, 2006). One of the most significant events triggered by tectonic behaviour is the development of the Antarctic Ice Sheet (AIS) and formation of the Antarctic Circumpolar Current (ACC) ~34 Ma (Barker *et al.*, 2007), which have played a key role in the development of Earth's modern climate (Section 1.4.), its evolution beginning with the break-up of the Gondwana supercontinent ~182 Ma (Anderson, 1999).

1.1.1. Formation of Antarctica

Antarctica is divided into East Antarctica and West Antarctica by the trans-Antarctic mountains, which span nearly 3500 km (Anderson, 1999). East Antarctica and West Antarctica differ in size, shape and dynamics, due to differences in geology, including tectonics and evolution. East Antarctica is mainly comprised of the East Antarctic craton, a relic from the supercontinent Nena, some 1.8 billion years ago (for a full review of its geological evolution see Tingey, 1991). Conversely, West Antarctica is composed of several islands; the West Antarctic archipelago, dissected by the Weddell, Bellingshausen, Amundsen and Ross seas. These islands include a number of discrete, or semi-discrete crustal blocks belonging to individual microplates, which evolved during the Mesozoic.

The Antarctic continent formed during the Jurassic with the break-up of Gondwana (~182 Ma) (Figure 1.1a). This coincided with a major outpouring of continental flood basalts from mantle plumes beneath the Karoo basin of South Africa, Dronning Maud Land of Antarctica and the Tasman province of Australia (King *et al.*, 1996; Lawver *et al.*, 2003). At this time the East Antarctic craton existed as a central component of the Gondwana landmass, with the West Antarctic microplates composing its western margin along with the North and South

New Zealand Blocks (King *et al.*, 1996). Researchers have proposed that the West Antarctic margin is in fact a montage of several independent microplates that moved relative to each other and East Antarctica during Gondwana break-up (Lawver *et al.*, 1992). However, there is still considerable uncertainty concerning the exact number and position of these microplates. According to Lawver *et al.* (1992) the West Antarctic margin was composed of four individual microplates, the Ellsworth-Whitmore Mountains, the Antarctic Peninsula, Thurston Island and Marie Byrd Land (MBL). The Weddell Sea area is cited as the location of microplate translation, with block rotation proposed as the primary mechanism (Storey, 1996) accomplished prior to ~165 Ma (Figure 1.1.b), with their present day location attained by ~110 Ma (Fitzgerald, 2002) (Figure 1.1c). Fragmentation around Antarctica occurred throughout the Cretaceous, at several localities, beginning south of Africa in the Ruser – Larsen Sea (~155 Ma), and proceeding in a clockwise direction around the supercontinent to the Weddell Sea in the west (145 Ma) (Jokat *et al.*, 2003). This was followed by the separation of the craton from India and Australia during the early Cretaceous at ~135 Ma and ~125 Ma respectively (Lawver *et al.*, 2003). However, seafloor spreading between Australia and Antarctica did not commence until ~95 Ma. By the Late Cretaceous (~80 Ma) both West Antarctica and East Antarctica had reached their present polar location and configuration, forming the modern-day Antarctic continent (Figures 1.1d and 1.1e). The northward migration of Antarctica's adjacent Gondwana fragments, combined with the continents' own rotation south resulted in its physical isolation. However, shallow submarine barriers continued to connect the East Antarctic craton with Australia and West Antarctica with South America, well into the Cenozoic (Anderson, 1999; Fitzgerald, 2002), and the onset of deep-water flow and the ACC was yet to be established.

During the Cretaceous the Earth experienced a greenhouse climate, with global temperatures some 12° C higher than those of today (Skelton *et al.*, 2003). This warmth was also present at high-latitudes where temperatures were 20° C to 30° C higher than today, supporting lush vegetation and preventing the formation of polar ice (Francis and Poole, 2002). According to the $\delta^{18}\text{O}$ record in the ocean, this warmth extended into the Cenozoic era from 65 Ma to 50 Ma. Post ~50 Ma the Earth experienced a gradual deterioration in temperature, which was followed by a rapid cooling event at the Eocene/Oligocene boundary (Livermore *et al.*, 2005). This Eocene/Oligocene transition (Oi1) represents one of the most significant evolutions of the Earth's climate, when the extreme global warmth of the early Eocene's greenhouse climate was replaced by the glacial icehouse conditions of the early Oligocene,

during which extensive ice caps coalesced on East Antarctica (Flower, 1999; Ruddiman, 1999).



Figure 1.1a. Tectonic configuration of the southern hemisphere at 180 Ma. Abbreviations in the figure: AP = Antarctic Peninsula, EWM = Ellsworth-Whitmore Mountains, MBL = Marie Bird Land, TI = Thurston Island (Winterton and Livermore, 2004).

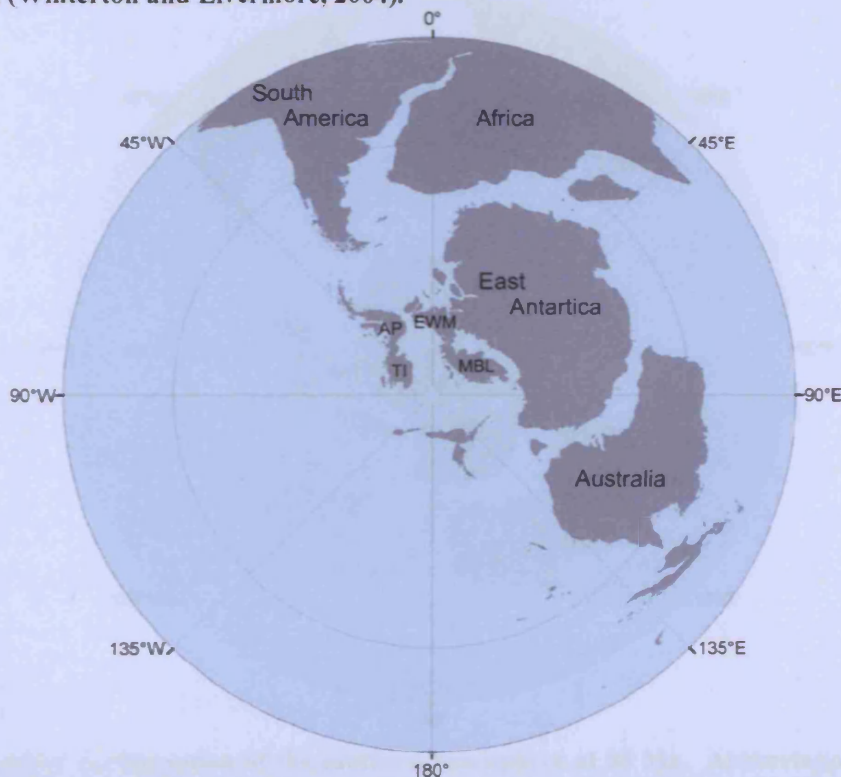


Figure 1.1b. Tectonic configuration of the southern hemisphere at 150 Ma. Abbreviations in the figure: AP = Antarctic Peninsula, EWM = Ellsworth-Whitmore Mountains, MBL = Marie Bird Land, TI = Thurston Island (Winterton and Livermore, 2004).

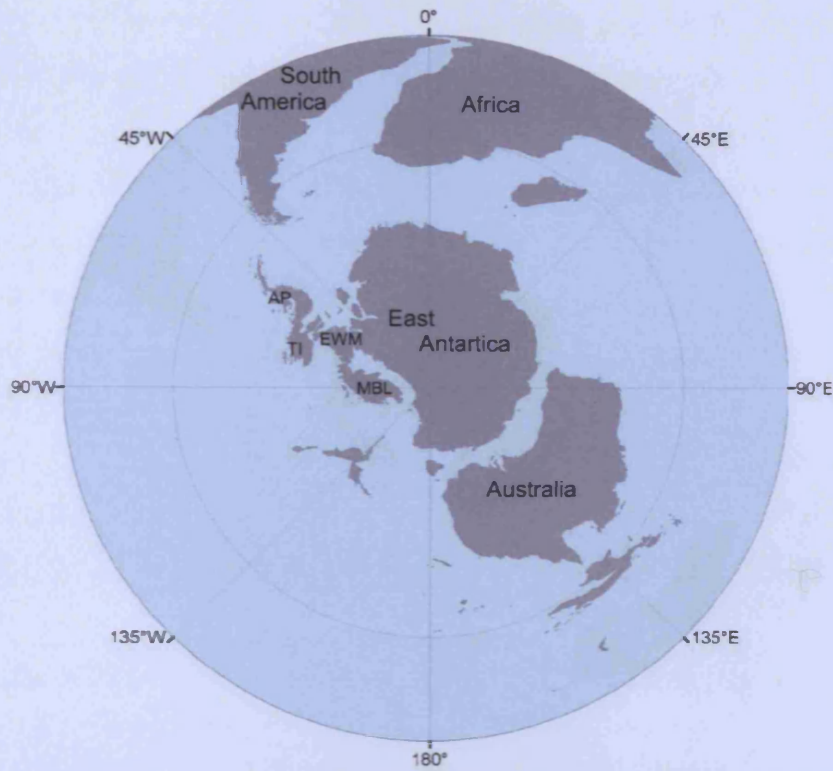


Figure 1.1c. Tectonic configuration of the southern hemisphere at 110 Ma. Abbreviations in the figure: AP = Antarctic Peninsula, EWM = Ellsworth-Whitmore Mountains, MBL = Marie Bird Land, TI = Thurston Island (Winterton and Livermore, 2004).



Figure 1.1d. Tectonic configuration of the southern hemisphere at 80 Ma. Abbreviations in the figure: AP = Antarctic Peninsula, EWM = Ellsworth-Whitmore Mountains, MBL = Marie Bird Land, TI = Thurston Island (Winterton and Livermore, 2004).

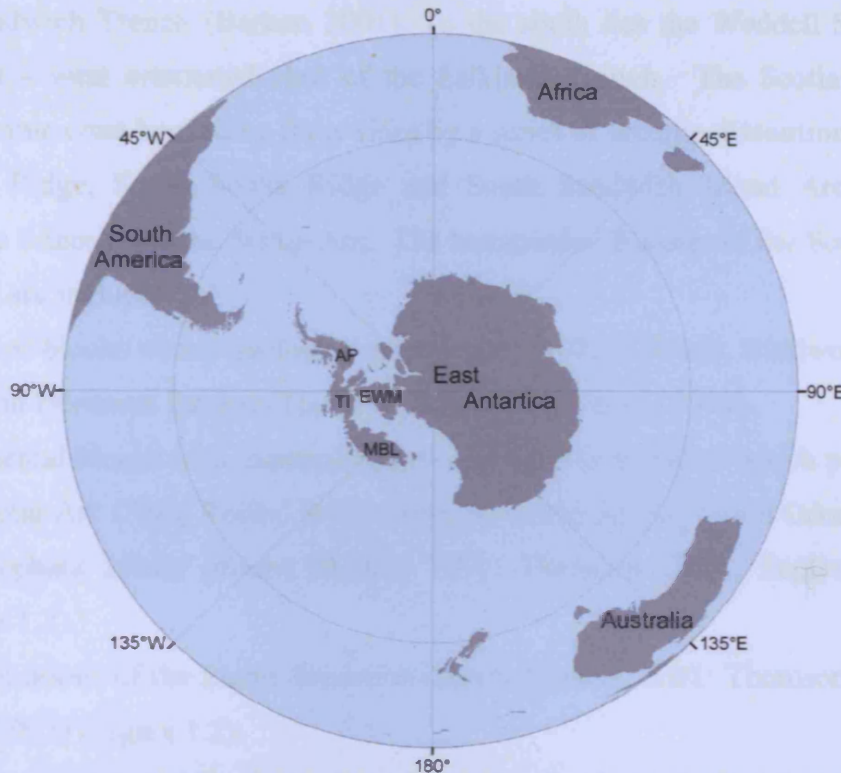


Figure 1.1e. Present day tectonic configuration of the southern hemisphere. Abbreviations in the figure: AP = Antarctic Peninsula, EWM = Ellsworth-Whitmore Mountains, MBL = Marie Bird Land, TI = Thurston Island (0 Ma) (Winterton and Livermore, 2004).

The first appearance of ice sheets on the East Antarctic landmass occurred at the Eocene/Oligocene boundary (~34 Ma) (Barker and Burrell 1977; Kennett, 1977; Kennett and Hodell, 1995; Exon *et al.*, 2001; Barker and Thomas, 2004). Glaciation of the West Antarctic and Antarctic Peninsula is proposed to have occurred much later, around ~26 Ma and ~15 Ma respectively (Barker *et al.*, 2007). What triggered this widespread global cooling? Numerous theories have been proposed over the years, including tectonic uplift (Raymo and Ruddiman, 1992), a decline in atmospheric CO₂ (DeConto and Pollard, 2003; Huber *et al.*, 2004) and the closure of the Tethys seaway (Lawver and Gahagan 03). The development of key deep-water seaways at the South Tasman Rise (Between Antarctica and Australia) and Drake Passage (between Antarctica and South America) prompted the initiation of a circumpolar current (Fitzgerald, 2002) (Section 1.1.1.3.), and a reduction in the meridional heat transfer from low latitudes (Kennett, 1977), thus initiating the thermal isolation of Antarctica and encouraging the formation of ice (Livermore *et al.*, 2005).

1.1.1.1. Formation of the Scotia Sea

The Scotia Sea is located in the South Atlantic sector of the Southern Ocean (75° W to 25° W, 61° S to 53° S), immediately downstream of Drake Passage and extending eastwards to

the South Sandwich Trench (Barker, 2001). To the south lies the Weddell Sea, and to the north the east – west orientated cleft of the Falkland Trough. The Scotia Sea primarily comprises oceanic crust banded on three sides by a series of seismic discontinuous ridges, the North Scotia Ridge, South Scotia Ridge and South Sandwich Island Arc (Figure 1.2). Together these ridges form the Scotia Arc. The topographic features of the Scotia Sea and its encompassing arc include:

- Subsided blocks whose geology is poorly known (Pirie, Bruce, Burdwood, Discovery, Jane and Herdman Banks) (Thomson, 2004; Eagles *et al.*, 2005).
- Continental blocks with exposed islands and submarine highs, which partly constitute the Scotia Arc (Shag Rocks, South Georgia, Clarke Rocks, South Orkney Islands and the Elephant Island group) (Barker, 2001; Thomson, 2004; Eagles *et al.*, 2005) (Figure 1.2).
- Arc volcanoes of the South Sandwich Islands (Barker, 2001; Thomson, 2004; Eagles *et al.*, 2005) (Figure 1.2).

Together the Scotia Arc and the Scotia Sea are a rather young geological feature, having only evolved since 40 Ma (Thomas, 2004). The marine basin itself is a complex collage of marginal basins, submerged blocks, relict continental fragments and ancient spreading centres (Brown *et al.*, 2006), a legacy of its complex tectonic history.

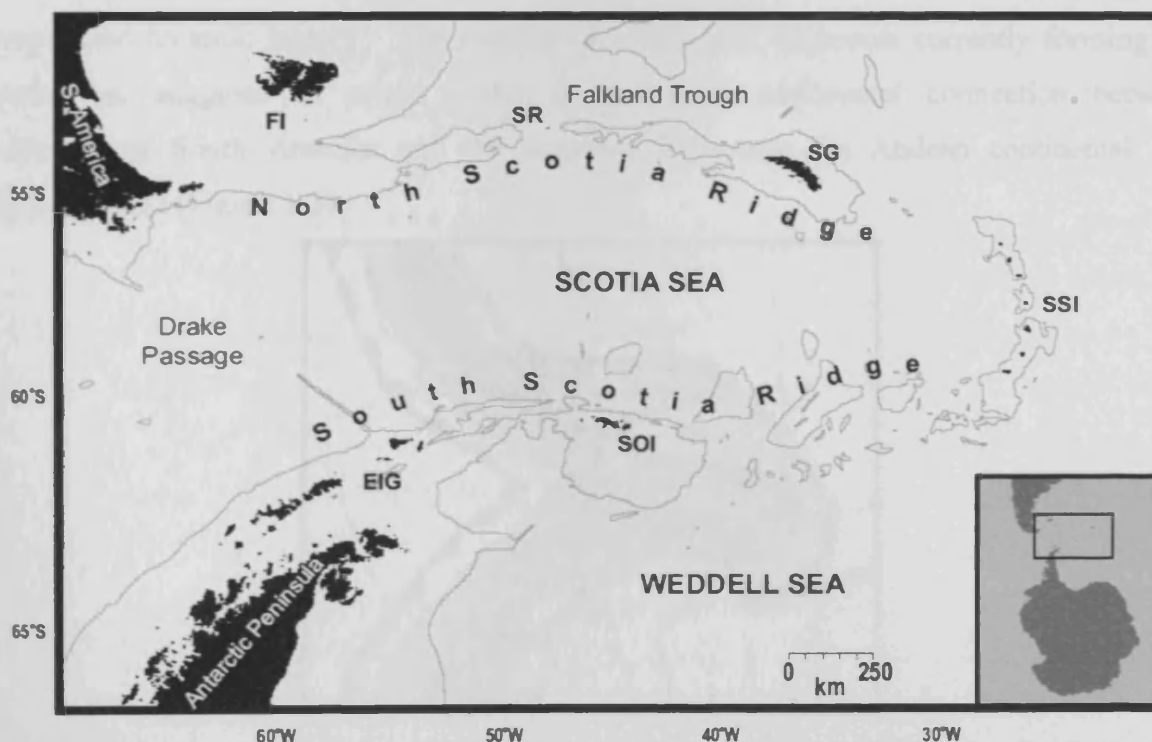


Figure 1.2. Topography of the Scotia Sea. Map showing the Scotia Sea and the encompassing North Scotia Ridge, South Sandwich Island Arc and South Scotia Ridge in relation to the Falkland Islands (FI),

southern South America and the Antarctic Peninsula. The main topographic features are Shags Rocks (SR), South Georgia (SG), the South Sandwich Islands (SSI), the South Orkney Islands and the Elephant Island Group (EIG), the 2000 m depth contour is also marked. This map is based on data from the Australian Antarctic Data Centre (2000) and Arhan *et al.* (2002).

The Scotia Sea is composed of two microplates; the Scotia plate and the Sandwich plate. The Scotia plate is situated between the major South American and Antarctic plates to the north and south respectively, with which it primarily shares strike/slip boundaries (Thomas *et al.*, 2004). Its northern boundary is the Falkland Trough, a deep trench separating the North Scotia Ridge from the Falkland Plateau on the South American plate (Eagles *et al.*, 2005). The complex South Scotia Ridge, an area of dramatic relief, represents the southern boundary of the Scotia Sea, with highs separated by steep slopes from elongated deep basins that reach more than 6000 m in depth (Galindo-Zaldivar *et al.*, 2002). To the east lies the divergent boundary separating the Scotia plate from the Sandwich plate. The Sandwich plate overthrusts the South America plate in the east, developing a subduction zone at the eastern extent of the Scotia Sea. In comparison to the slow absolute and relative motions of the Scotia, South American and Antarctic plates, the Sandwich plate is moving rapidly eastwards, forming the eastern flank of the East Scotia Sea spreading system (Barker, 1995; Barker, 2001; Thomas *et al.*, 2003). Together, the microplates of the Scotia Sea act to accommodate the sinistral transcurrent motion between the major South American and Antarctic plates (Galindo-Zaldivar *et al.*, 2002). Features within the Scotia Sea suggest a complicated tectonic history. The geology of continental fragments currently forming the Scotia Arc suggests an origin within a continuous continental connection between southernmost South America and the Antarctic Peninsula; the Andean continental link (Barker, 2001) (Figure 1.3).

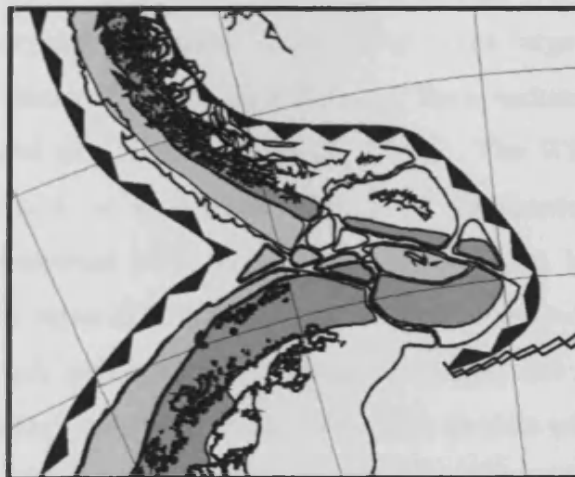


Figure 1.3. Reconstructed continental link between the Antarctic Peninsula and southern South America. In dark grey is the Pacific margin batholith and associated arc volcanics, in light grey a non-magnetic

fore-arc and palaeo-forearc. Also shown are Pacific margin and Atlantic-directed subduction zones (Barker, 2001).

The Scotia Arc evolved from this collection of continental fragments. Through back-arc extension the Scotia Arc unfolded behind an eastward migrating arc and trench (Barker, 2001). It is thought that as the continental blocks (namely South Georgia) migrated into the newly founded gap, seafloor began to accrete in the central Scotia Sea, although speculation still surrounds the tectonic evolution of this central portion of the marine basin (Eagles *et al.*, 2005). Magnetic dating indicates the onset of the Drake Passage spreading regime at the now extinct West Scotia Ridge, north of the Shackleton Fracture Zone (~28 Ma) (Thomson, 2004), although the timing of Drake Passage opening is debated (section 1.1.1.3.2.). This spreading regime resulted in the formation of the west Scotia basin, the largest area of seafloor in the Scotia Sea. Spreading rates at the West Scotia Ridge (Drake Passage), and within the central Scotia Sea, began to slow and eventually ceased ~7 Ma and the respective regions were fused into a single Scotia Plate north of the Shackleton Fracture Zone (Barker, 2001; Eagles, 2003). The spreading regimes of the west and central Scotia Sea basins are thought to have overlapped that of the east Scotia Sea, which is believed to have commenced ~21 Ma (Barker, 1995).

1.1.1.2. Formation of the Adélie Land Coast

The Wilkes Land Margin of East Antarctica, which features the George V and Adélie Land Coasts, is believed to have formed during the mid Jurassic/Cretaceous, as a consequence of extensional tectonics as the Antarctic and Australian continents separated (Escutia *et al.*, 2005; Caburlotto *et al.*, 2006). The underlying geology consists of block faulted continental crust, thinned and intruded transitional crust and oceanic crust, which is generally characterised by deep marginal rift basins. Subsequent to the large scale tectonic rifting its evolution has been characterised by the deposition of thick sedimentary sequences on the continental shelf, slope and rise (Caburlotto *et al.*, 2006). The Wilkes Land Margin has a mean width of 125 km and, as with most sections of continental shelf surrounding the Antarctic, has an over-deepened (450 m to 500 m on average) landward sloping profile (Escutia *et al.*, 2005). The inner shelf has deep, glacially eroded troughs, flanked by shallow banks, which shoal seaward, terminating in prograding wedges and glacial flutes (Escutia *et al.*, 2005; Presti *et al.*, 2005; Caburlotto *et al.*, 2006) with mouths of the glaciers also eroded by deeper basins (>1000 m).

Located between 136° E and 140° E, the Wilkes Land Margin represents the seaward termination of the largest subglacial basin in East Antarctica (Presti *et al.*, 2005; Caburlotto *et al.*, 2006). This stretch of Antarctic coast is characterised by ice shelves and glaciers, which protrude onto the peripheral continental shelf (Escutia *et al.*, 2005). The drainage of the EAIS in this region is characterised primarily by a divergent flow, except where ice is focused into the Mertz and Ninnis glaciers. Presently, part of this fringe of the EAIS is grounded below sea-level, making it exceptionally vulnerable to climate change and sea-level rise. Although data are scarce, evidence, from glacially scoured troughs, striations, unconformities and till deposits (Eittrheim *et al.*, 1995; Escutia *et al.*, 1997, 2000; DeSantis *et al.*, 2003; Donda *et al.*, 2003. Caburlotto *et al.*, 2006), suggests that this sector of the EAIS extended to at least the mid – continental shelf during the Last Glacial Maximum (LGM) (Anderson *et al.*, 2002).

1.1.1.3. Development of the Antarctic Circumpolar Current

Significant debate surrounds the exact timing of the establishment of the ACC and the precise role played by the development of deep-water gateways in the thermal isolation and glaciation of Antarctica. This debate has intensified in recent years due to a climate modelling study conducted by DeConto and Pollard (2003), which proposed that a decline in atmospheric CO₂ alone – without the thermal isolation of Antarctica – would be sufficient to trigger the accumulation of ice on the continent. Prior to this it was thought that a deep-water circumpolar pathway existed ~34 Ma, coinciding with the onset of Antarctic glaciation. Two primary gateways were involved in establishing the ACC; Drake Passage and the Tasmanian Gateway. However, the number of continental fragments, microplates and spreading centres involved in the opening of Drake Passage has caused complications in its dating (Lawver *et al.*, 2003; Brown *et al.*, 2006), whereas the tectonic processes and timing of the opening of the Tasmanian Gateway is generally accepted as being reasonably well constrained (Kennett, 1977; Thomas, 2003; Lawver *et al.*, 2003; Pfuhl and McCave, 2005; Brown *et al.*, 2006).

1.1.1.3.1. The Tasmanian Gateway

It is speculated that a narrow passageway through the South Tasman Saddle may have evolved by ~50 Ma. However, its small size precluded major circulation, thus, the South Tasman Rise still remained a barrier to circumpolar flow (Lawver *et al.*, 2003). Seafloor spreading rates between Australia and the Antarctic began to rapidly accelerate ~43 Ma, further expanding the Australia-Antarctic Basin (Brown *et al.*, 2006). The final detachment

of the west South Tasman Rise (~40 Ma) resulted in the opening of the first shallow through-flowing Southern Ocean gateway between the South Indian and Pacific Oceans (Kennett, 1977; Brown *et al.*, 2006). Development of a deep-water circulation and the onset of full marine conditions has been dated at ~34 Ma (Lawver *et al.*, 1992; You, 2002; Barker and Thomas, 2004). Further deepening to bathyal depths (>2000 m) and the establishment of stable, open ocean free flowing current is thought to have occurred ~33.5 Ma to <30.2 Ma (Stickley *et al.*, 2004).

1.1.1.3.2. Drake Passage

Establishing the timing of the opening of Drake Passage is much more circumstantial as the geostrophic deep-water jets of the ACC flowing through Drake Passage scour sediment from the ocean floor of the passage, leaving only sparse, incomplete sedimentary records within the Scotia Basin. Core recovery is also impaired by high seas (Pfuhl and McCave 2005). In addition, micro-continents (South Georgia and South Orkney) and a significant amount of continental debris crowd the passage – the geological histories and palaeomotion of which are unknown (Lawver *et al.*, 2003). Dates for the timing of Drake Passage opening range from the Late Eocene to the Early Miocene (34 Ma to 5 Ma) (Lawver *et al.*, 1992; Barker, 2001; Thomas, 2003; Pfuhl and McCave, 2005). Barker and Burrell (1977) originally showed that the opening of Drake Passage removed the final impediment to deep circumpolar flow, much later than the Tasmanian Gateway and north of the Kerguelen Plateau (Macquarie Ridge) and argued (Barker *et al.*, 1991) that deep-water flow would have been prevented by the presence of continental fragments, subducted volcanic relicts (Barker and Burrell, 1977) and prominent ridges extending along the Shackleton Fracture Zone until they cleared 22 ± 2 Ma (Barker and Thomas 2004). Conversely, Lawver and Gahagan (2003) argue that plate motion between South America and Antarctica necessitates a deep-water seaway to have existed at Drake Passage prior to 28 Ma, probably by 31 ± 2 Ma. Geophysical and geochemical data presented by Livermore *et al.*, (2004) suggest that the Shackleton Fracture Zone is a relatively young feature, formed by uplift since 8 Ma. If true, the barrier proposed by Barker *et al.*, (1977, 1982, 1991) did not exist, and deep-water circulation probably evolved soon after spreading in Drake Passage commenced (~29 Ma). This hypothesis is supported further by Scher and Martin (2004), whose Southern Ocean (South Atlantic) neodymium isotope record (and the consequent identification of Pacific seawater) suggests that a shallow opening of Drake Passage existed by 39 Ma, and the establishment of a deep-water flow at 28.5 Ma. A new plate tectonic model presented by Livermore *et al.* (2007)

suggests that an effective ocean gateway may have developed as early as the Middle Eocene (~44 Ma), developing into a deep-water cleft through seafloor spreading at the West Scotia Ridge by 34 Ma to 30 Ma (Livermore *et al.*, 2005), substantiated by a number of palaeo-productivity studies identifying reorganisations of the ocean circulation and establishment of Southern Ocean upwelling during the Eocene (Diester-Hass and Zahn 1996; Diekmann *et al.*, 2004). Further, studies employing neodymium isotopes as a seawater tracer have identified the presence of Pacific seawater at the Agulhas Ridge at ~41 Ma, indicating the opening of Drake Passage prior to the Tasmanian Gateway and the establishment of a complete deep-water ACC by the Late Eocene (Scher *et al.*, 2006; Scher and Martin, 2006).

1.2. The Oceanographic Setting

This section reviews the major ocean circulatory patterns of the globe, focusing on the deep ocean circulation and water mass formation of the Southern Ocean and particularly the Scotia and Australia – Antarctic Basins.

The atmosphere-ocean system is fundamentally a giant heat engine. Today, this heat redistribution system attempts to compensate for the net radiative gain at low latitudes and net radiative loss at high latitudes. The system is composed of three components: winds driven by the atmospheric circulation; surface currents driven by wind shear from above; and deep flow, initiated in polar regions at present through the formation and transportation of dense water masses (Brown *et al.*, 1989). Surface currents are broadly categorised into western boundary currents and open ocean gyres, which operate together to transfer excess heat from the tropics toward the poles. Deep ocean circulation influences the Earth's climate through the transport of heat around the globe but is limited by its inherent inertia. The sinking of dense surface waters at the poles provides the link between the atmosphere and the deep ocean and the strong upwelling in the Southern Ocean driven by Ekman transport provides a link between the deep ocean and the atmosphere.

1.2.1. Thermohaline Circulation

The term thermohaline circulation (THC) refers to a conceptual driving mechanism where fluxes of heat and freshwater across the sea-surface and subsequent interior mixing of heat and salt result in a large-scale deep overturning motion of the ocean where masses of water are transferred around the globe, this circulation is sometimes likened to an ocean 'conveyor' (Rahmstorf, 2006). The THC is not a wind-driven current, an observational concept or a measurable quantity but instead refers to a physical driving mechanism. The THC is a

mechanically driven fluid engine driven by downward mass flux at high latitudes. This downward flux is associated with severe heat loss to the atmosphere in the Northern North Atlantic Ocean and Southern Ocean. In these regions fluid becomes dense and convectively unstable resulting in a downward flux, the generation of deep waters and their subsequent lateral flow (Wunsch, 2002). In the Northern North Atlantic, specifically the Greenland-Norwegian Sea and the Labrador Sea, during winter, surface waters are strongly cooled, increasing their density (Bigg, 2001). When sea-ice forms over the continental shelf – rejecting brine into the surface ocean – the density of the surface waters is increased sufficiently to destabilise the water column and initiate over-turning, resulting in the formation of NADW (Brown *et al.*, 1989). In the Southern Ocean, primarily the Weddell Sea and Adélie Land Coast, this downward flux is manifest as Antarctic Bottom Water (AABW), which is primarily generated along the Antarctic continental margin. Negative buoyancy is caused by the cooling and salinization of partially-ventilated surface and shelf waters and through subsequent mixing with warmer and saltier deep-waters (Jacobs, 2004). Several interrelated mechanisms are also involved to a lesser degree including the generation of high salinity surface water, meltwater from continental ice shelves, supercooling below ice-shelves and sea-ice and polynya formation (Jacobs, 2004). However, despite the prevalence of the term THC throughout the literature recent research has shown that it is in fact misleading and that the ocean flow is a much more complicated beast (Wunsch, 2002; Kerr, 2005). Laboratory experiments suggest that surface thermohaline forcing alone (as implied in the THC mechanism) may not be able to sustain the THC overturning and that wind forcing plays an essential role (Wunsch 2002; Kuhlbrodt *et al.*, 2007; Guan and Huan, 2008). It is postulated that the strong westerly circumpolar winds over the Southern Ocean provide the primary forcing mechanism through vigorous Ekman transport and upwelling from depth (Toggweiler and Samuels, 1995; 1998). In this scenario it would be the strength of these winds that govern the strength of the overturning circulation rather than diapycnal mixing as suggested by the term THC (Kuhlbrodt *et al.*, 2007). Kuhlbrodt *et al.*, (2007) show that both vertical mixing and wind-driven upwelling play important roles in the generation of two overturning cells within the Atlantic Ocean. A more appropriate term for the circulation, and one being increasingly used throughout the literature, is the Atlantic meridional overturning circulation (AMOC), which simply refers to a circulation in the meridional/vertical plane and does not refer to any forcing mechanism (unlike THC). There are four main components of the AMOC (Figure 1.4):

- Deep water formation at high latitudes where, through a variety of processes, waters become dense and sink (see above).
- Deep currents generated by the lateral movement of deep waters.
- Upwelling processes, both wind-driven and mixing-driven, transporting water volume from depth to the surface.
- Surface currents that transport relatively light water to high latitudes, closing the loop, or conveyor.

Although wind and thermohaline mixing have been shown to each play an important role in the forcing of this circulation more work is needed to quantify their respective contributions. In addition to these drivers variations in the quantity and rate of formation of deepwaters (NADW and AABW) can also exert a significant impact on the AMOCs spatial pattern, which can in turn have a drastic impact on global climate. Definitions of the THC vary throughout the literature, where the term is often mistakenly used interchangeably with the term AMOC, this ambiguity causes problems when using either term. When discussing the palaeorecords presented in this study any reference to the AMOC is purely in a conceptual context, relating to the generation and flow of deepwaters and their potential impact on the circulation system.

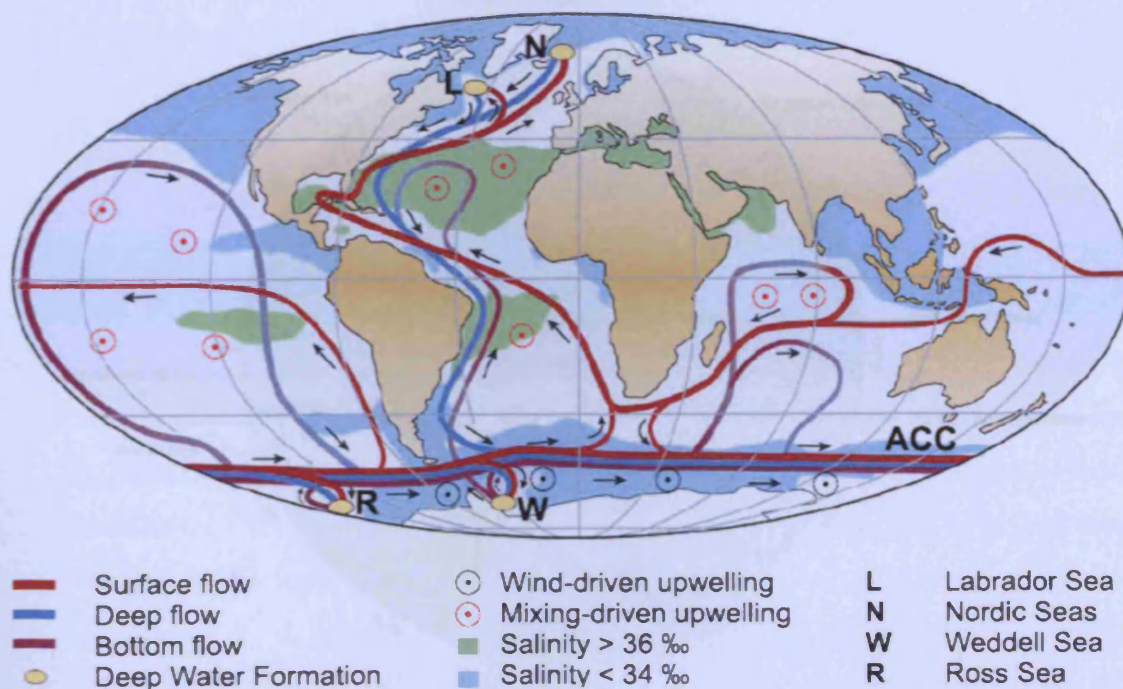


Figure 1.4. Strongly simplified sketch of the global overturning circulation system. In the Atlantic, warm and saline waters flow northward all the way from the Southern Ocean into the Labrador and Nordic Seas. By contrast, there is no deepwater formation in the North Pacific, and its surface waters are fresher.

Deep waters formed in the Southern Ocean become denser and thus spread in deeper levels than those from the North Atlantic. Note the small, localized deepwater formation areas in comparison with the widespread zones of mixing-driven upwelling. Wind-driven upwelling occurs along the Antarctic Circumpolar Current (ACC). After Rahmstorf [2002].

1.2.2. The Southern Ocean

The Southern Ocean exerts a significant influence over the global climate. Its oceanography is primarily influenced by the atmospheric circulation, the glaciated Antarctic continent, exchanges with neighbouring oceans and interactions with seafloor topography. Unimpeded by land the unique geography of the circumpolar Southern Ocean is an important regulator of the AMOC, allowing circumpolar upwelling and providing the only deep ocean connection between the major ocean basins. The predominant flow throughout the Southern Ocean is the eastward flowing ACC, however, easterly winds blowing off the continent drive the Antarctic Coastal Current; a fast, shallow, discontinuous west-flowing current that occupies a narrow zone over the continental shelf around most of Antarctica. The ASF defines the boundary between the cold relatively fresh waters associated with the Antarctic Coastal Current and the warmer, more saline waters associated with the ACC. In addition to these large current systems are the cyclonic Weddell and Ross Sea Gyres, which are fed by the Antarctic Coastal Current (Figure 1.5).

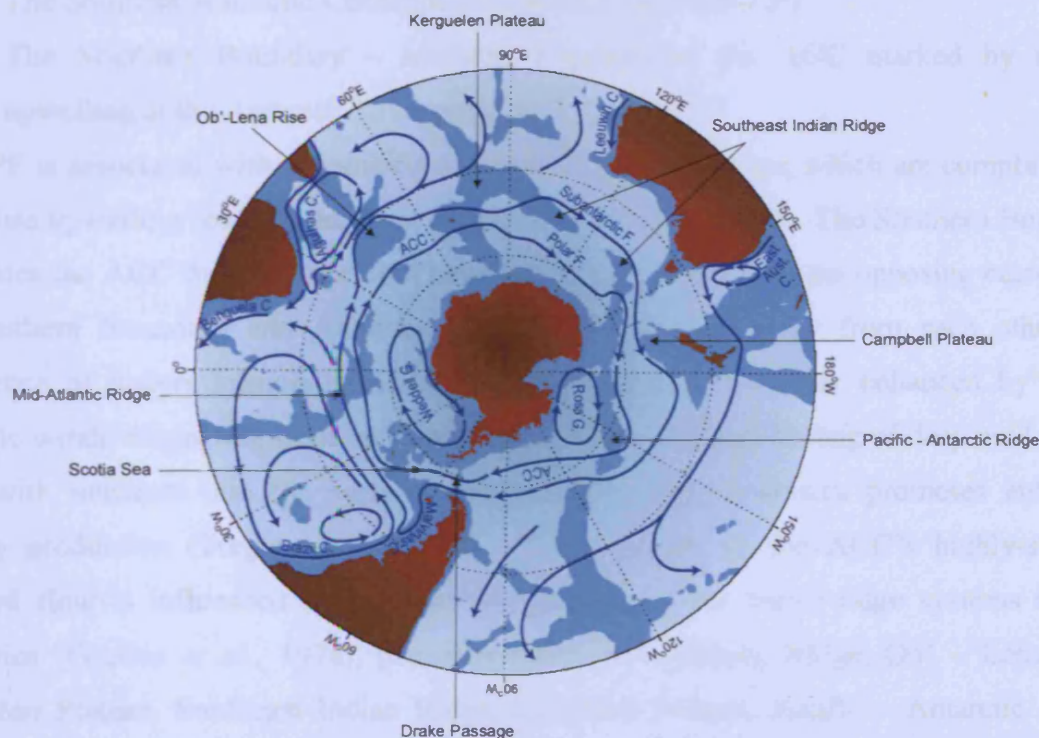


Figure 1.5. Primary frontal systems, gyre circulations and sea-floor topography of the southern hemisphere. The pathways of the primary frontal systems of the major current system in the Southern Ocean, the ACC, are constrained by the major topographic features of the Southern Ocean's bathymetry. This is most explicit at Drake Passage (modified from Rintoul *et al.*, 2001)

1.2.2.1. The Antarctic Circumpolar Current

The ACC is the largest ocean current system in the world. It extends from the ocean surface to the sea floor and transports 130 Sv through Drake Passage (Barker and Thomas, 2004), with a zonal flow directly related to the mean intensity and position of the atmospheric westerlies. Ekman transport pushes waters to the north, which forms a series of circumpolar convergences or *fronts* representing large horizontal density gradients superimposed onto the southward rise of isopycnals associated with the eastward flow of the ACC (Orsi *et al.*, 1995). These frontal systems generally mark transition zones between water masses of different densities and exist in the vertical as well as the horizontal plane with a surface expression of a sharp southward drop in temperature (Orsi *et al.*, 1995; Pudsey and Howe, 1998; Garabato *et al.*, 2002). The steeping of isopycnal surfaces generates increased flow velocity and strong, narrow, deep-reaching zonal jets (Barker and Thomas, 2003) into which the bulk transport of the ACC is focused. The four ACC fronts are:

- The Sub-Antarctic Front (SAF) – northern boundary of the ACC, segregating subtropical surface waters from sub-Antarctic surface waters.
- The Antarctic Polar Front (APF) – primary axis of ACC flow, segregating warm sub-Antarctic surface waters from cool Antarctic surface waters.
- The Southern Antarctic Circumpolar Current Front (SACCF).
- The Southern Boundary – southern boundary of the ACC marked by intense upwelling at the Antarctic Divergence.

The APF is associated with the sinking of Antarctic surface waters, which are complimented by diffuse upwelling south of the front (Barker and Thomas, 2004). The Southern Boundary segregates the ACC from the northern boundary of the ACC. As the opposing currents of the Southern Boundary and Antarctic Coastal Current flow away from each other, the divergence of waters initiates upwelling. This upwelling is further enhanced by strong katabatic winds originating from the continental interior. This upwelling of deep cold waters laden with nutrients into the surface waters surrounding Antarctica promotes enhanced primary production (Treguer *et al.*, 1995). The trajectory of the ACC's highly-sheared eastward flow is influenced by seafloor topography and the major ridge systems around Antarctica (Gordon *et al.*, 1978), primarily the Mid – Atlantic Ridge, Ob' – Lena Rise, Kerguelen Plateau, Southeast Indian Ridge, Campbell Plateau, Pacific – Antarctic Ridge, Drake Passage and the Scotia Arc (Figure 1.6). The interaction of the flow of the ACC with abyssal bathymetry means expansive migrations are restrained and the fast flowing fronts of

the ACC are restricted in a number of locations (Moore *et al.*, 1999; Rintoul *et al.*, 2001; Carter and Cortese, 2009). At such locations the ACC fronts become focused and intensified. Typical characteristics of this intensification include increased width and temperature changes, enhanced velocity and the generation of eddies and warm and cold core rings (Moore *et al.*, 1999). In contrast, over the deep ocean basins within the Southern Ocean, which lack large topographic obstructions, the surface expressions of the ACC fronts weaken and the fronts meander over wider latitudinal ranges (Emery, 1977; Moore *et al.*, 1999).

1.2.2.2. Water Masses

Southern Ocean water masses are juxtaposed and, in some cases, weak stratification is the only barrier preventing vigorous diapycnal mixing. NADW infiltrates from the South Atlantic, AABW forms and descends the Antarctic continental slope, and numerous deep, intermediate and surface waters are produced (Table 1.1, Figure 1.6).

Table 1.1. Potential temperature and salinity characteristics of Southern Ocean water masses important for this study.

Water Mass	Potential Temperature (°C)	Salinity (PSU)
North Atlantic Deep Water (NADW)	2.0	>34.9
Antarctic Bottom Water (AABW)	-0.4	34.66
Warm Deep Water (WDW)	0 to 0.8	>34.6 to 34.72
Upper Circumpolar Deep Water (UCDW)	1.6 to 3.2	34 to 34.71
Lower Circumpolar Deep Water (LCDW)	0.2 to 1.9	>34.7
Antarctic Intermediate Water (AAIW)	3.8 to 4.8	34.2
High Salinity Surface Water (HSSW)	-1.95 to -1.75	34.75 to 35
Ice Shelf Water (ISW)	>-1.95	~34.62
Weddell Sea Deep Water (WSDW)	-0.7 to 0.0	34.64 to 34.7
Weddell Sea Bottom Water (WSBW)	<-0.7	34.62 to 34.66
Antarctic Surface Water (AASW)	-1.7 to 2	<34.3

1.2.2.2.1. North Atlantic Deep Water

On its transit south through the Atlantic Ocean the once extremely dense NADW entrains such large volumes of less dense waters that it eventually resembles an intermediate water mass. As the NADW enters the ACC via the South Atlantic it is upwelled and entrained into the ACC south of the APF providing the main source of heat to the Antarctic continent. Upwelled NADW aids in the formation of Antarctic Intermediate Water (AAIW), whereas the rest of the NADW is swept into the eastward flow of the ACC as Circumpolar Deep Water (CDW) (Figure 1.6).

1.2.2.2.2. Circumpolar Deep Water

The primary constituent of the ACC is CDW, which represents the core of the ACC. The intrusion of warm NADW from the South Atlantic sector of the Southern Ocean acts to divide CDW into Upper CDW (UCDW) and Lower CDW (LCDW) (Orsi *et al.*, 1999). The UCDW is characterised by low concentrations of oxygen and high concentrations of nutrients, whereas LCDW is defined by higher salinity (Orsi *et al.*, 1995) (Figure 1.6, Table 1.1). UCDW upwells to the surface of the ACC at the Southern Boundary. Heat is released into the atmosphere and a part of the cooled water flows north towards the convergence at the APF and descends again to form AAIW. The remainder of the ventilated UCDW flows poleward and interacts with cold, fresh Antarctic Ice Shelf Water (ISW). This UCDW will eventually descend the continental slope and flow into AABW. A branch of UCDW enters the Weddell Sea and is entrained into the Weddell Gyre, where it is freshened by coastal shelf waters altering its physical properties to form Warm Deep Water (WDW). WDW circulates within the Weddell Gyre and is observed on the continental shelf and infiltrating sub-ice shelf cavities (Foldvik *et al.*, 2004).

1.2.2.2.3. Antarctic Bottom Water

AABW formation is initiated as a result of the interaction between the cold, fresh, High Salinity Surface Water (HSSW) and the underlying warmer deep-waters (Figure 1.6). AABW formation processes vary around the margin and are influenced by differences in continental slope geomorphology. The Weddell and Ross Seas are traditionally cited as the primary formation centres, with the Weddell Sea estimated to generate more than half of all AABW (Deacon, 1937; Jacob *et al.*, 1970; Carmack and Foster, 1975; Jacobs *et al.*, 1985). However, some recent studies have suggested that the Ross Sea is a minor source of AABW as the majority of the deepest water masses generated along its margin are as warm as 0.0° C and markedly saltier than those formed in the Weddell Sea (Jacobs, 2004). A number of recent studies further cite the formation of Adélie Land Bottom Water (ALBW) along the Adélie Land Coast as being representing up to 25% of all AABW (Rintoul *et al.*, 1998) (Figure 1.7).

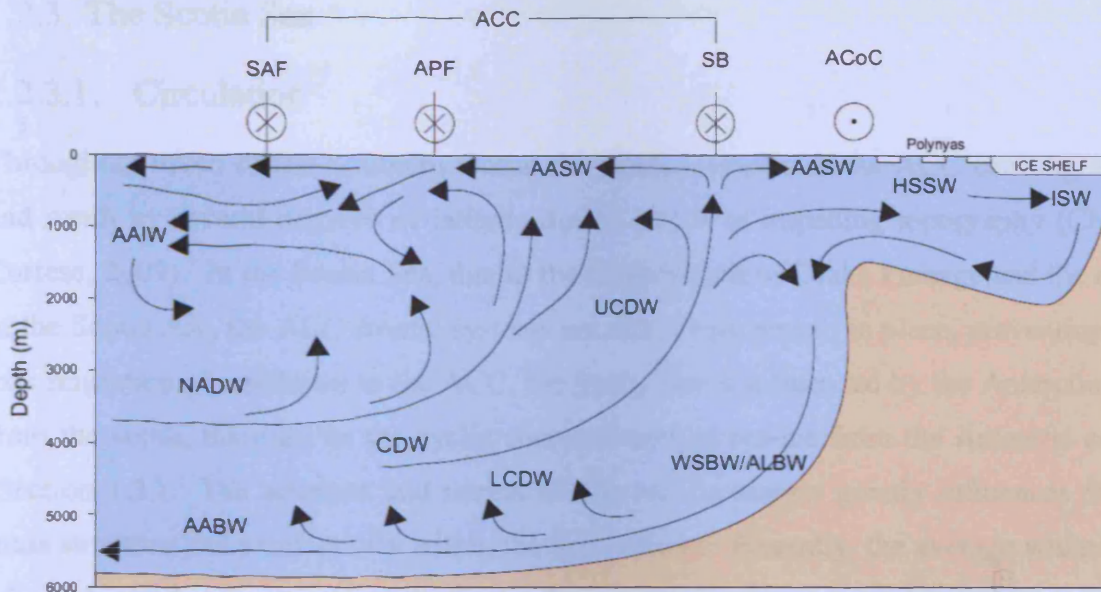


Figure 1.6. Schematic illustrating the vertical distribution of water masses of the Southern Ocean. Abbreviations: NADW = North Atlantic Deep Water; AABW = Antarctic Bottom Water; CDW = Circumpolar Deep Water; LCDW = Lower Circumpolar Deep Water; UCDW = Upper Circumpolar Deep Water; WSBW = Weddell Sea Bottom Water; ALBW = Adélie Land Bottom Water; AAIW = Antarctic Intermediate Water; AASW = Antarctic Surface Water; HSSW = High Salinity Surface Water; ISW = Ice Shelf Water; SAF = Sub-Antarctic Front; APF = Antarctic Polar Front; SB = Southern Boundary; ACC = Antarctic Circumpolar Current; Antarctic Coastal Current = Antarctic Coastal Current (Modified from Pickard and Emery, 1990).

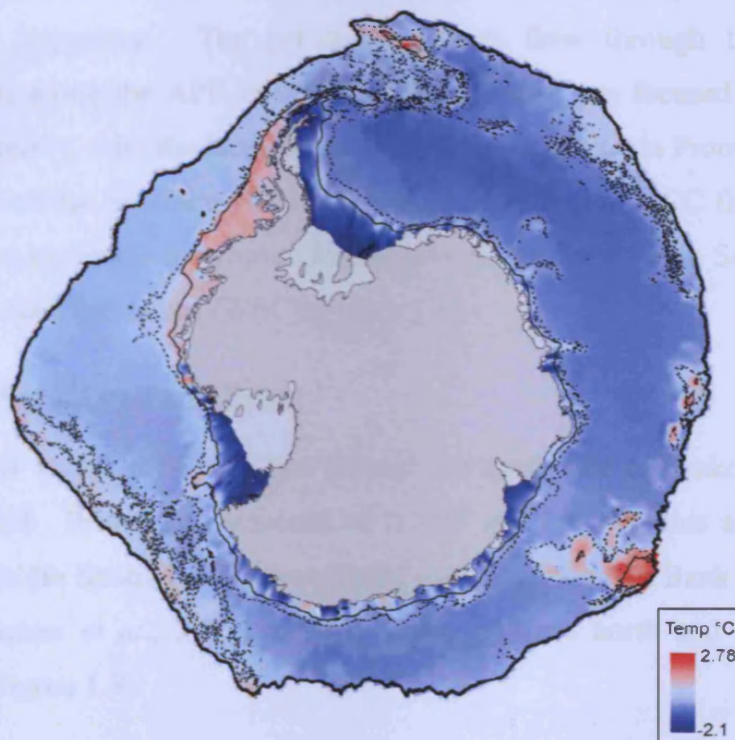


Figure 1.7. Southern Ocean bottom water potential temperatures around Antarctica. Important areas of deep and bottom water formation around the Antarctic continental margin, such as the Weddell Sea, Ross Sea and Adélie Land Coast are represented by dark blue shading (Clark *et al.*, 2009).

1.2.3. The Scotia Sea

1.2.3.1. Circulation

Throughout much of the Southern Ocean the frontal systems of the ACC can migrate north and south by several degrees of latitude due to a lack of impeding topography (Carter and Cortese, 2009). In the Scotia Sea, due to the constrictions of Drake Passage and the confines of the Scotia Arc, the ACC frontal systems are effectively pinned in place, preventing current axis migration. In addition to the ACC, the Scotia Sea is influenced by the Antarctic climate from the south, manifest in the cyclic encroachment of sea-ice from the Antarctic continent (Section 1.3.). The advance and retreat of this sea-ice margin greatly influences the water mass structure and productivity within the Scotia basin. Presently, the average winter sea-ice edge is located in the centre of the Scotia Basin, with summer sea-ice located far to the south and west, extending from the deep Weddell Basin to skirt the continental shelf around the Antarctic Peninsula (Figure 1.8). Weddell Sea deep and bottom waters also influx from the south, via the South Scotia Ridge and South Sandwich Island Arc, further complicating the oceanography within the Scotia Sea.

1.2.3.2. Frontal Systems

The ACC enters the Scotia basin via Drake Passage and flows through the Scotia Sea on an east to northeast trajectory. The primary eastward flow through the Scotia Sea is concentrated in jets along the APF and SAF, with additional jets focused along the SACCF and Southern Boundary, with the latter often referred to as the Scotia Front in the Scotia Sea. Immediately south of the Southern Boundary, the juxtaposition of ACC flow and outflow of Weddell Sea waters generates a complex frontal system along the South Scotia Ridge known as the Weddell-Scotia Confluence (WSC) (Figure 1.8).

1.2.3.2.1. The Sub-Antarctic Front

Flow along the SAF enters the Scotia Sea through the north side of Drake Passage, hugging the continental shelf. Primarily composed of AAIW and UCDW, this shallow, less dense mass is able to exit the Scotia basin immediately east of Burdwood Bank through a 2000 m cleft at 55° W (Arhan *et al.*, 2002), beyond which it flows north and passes east of the Falkland Islands (Figure 1.8).

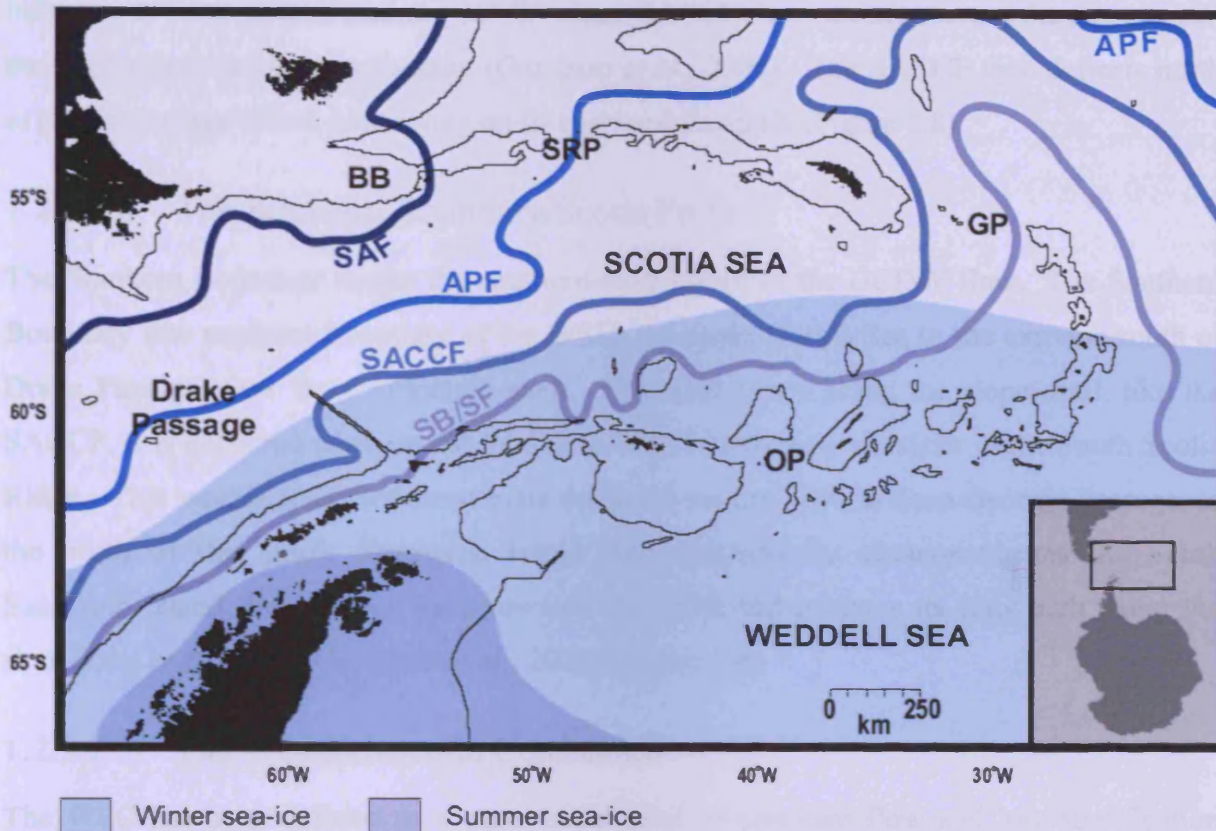


Figure 1.8. The frontal structure of the ACC and summer and winter sea-ice extents throughout the Scotia Sea Basin. Abbreviations: SAF = Sub-Antarctic Front; APF = Antarctic Polar Front; SACCF = Southern Antarctic Circumpolar Current Front; SB = Southern Boundary; SF = Scotia Front; BB = Burdwood Bank; SRP = Shag Rocks Passage; GP = Georgia Passage; OP = Orkney Passage.

1.2.3.2.2. The Antarctic Polar Front

Flow along the APF enters the basin through the centre of Drake Passage on a northeast trajectory and turns north at $\sim 50^\circ$ W via a 'S-shaped' meander (Garabato *et al.*, 2002). The APF crosses the North Scotia Ridge through Shag Rocks Passage (48° W) at approximately 3000 m (Garabato *et al.*, 2002). This sill is the deepest in the North Scotia Ridge and acts as a pinning point for the strong polar jet of the APF. The APF sweeps through this gorge carrying all but the densest ACC water masses with it. Most of the APF water masses that flow through Shag Rocks Passage are subsequently deflected by the Falkland Trough toward the western Georgia Basin (Allen *et al.*, 2005) (Figure 1.8).

1.2.3.2.3. The South Antarctic Circumpolar Current Front

Flow along the SAACF enters the Scotia Sea towards the south of Drake Passage having flowed through the Shackleton Fracture Zone and crosses the Scotia Sea south of the APF. Characteristics of the SACCF flow are continually modified along its route by WSDW emerging from the Weddell Sea via submarine passages in the South Scotia Ridge. This

influence is most pronounced at $\sim 35^\circ$ W where SACCF flow strongly forces the front to exit the Scotia Sea via Georgia Passage (Garabato *et al.*, 2002). The SACCF then deflects north of South Georgia before continuing on its eastward flowpath (Figure 1.8).

1.2.3.2.4. The Southern Boundary/Scotia Front

The Southern Boundary marks the southern-most extent of the UCDW flow. The Southern Boundary (the northern boundary of the WSC) enters the Scotia Sea to the extreme south of Drake Passage, over the continental shelf. The front flows along the slope until, like the SACCF, it is deflected north at 30° W due to WSDW intrusion via clefts in the South Scotia Ridge. This weakly stratified front exits the basin via the 3200 m deep Georgia Passage, to the north of the South Sandwich Island Arc, immediately circumnavigates the South Sandwich Island Arc, swings back towards the south and resumes its flow path along the shelf (Orsi *et al.*, 1995; Garabato *et al.*, 2002) (Figure 1.8).

1.2.3.2.5. The Weddell-Scotia Confluence

The WSC has been defined as a quasi-zonal band of eastward flow and low stratification containing a high proportion of shelf water mixtures from the northwest Weddell Sea (Whitworth *et al.*, 1994). The WSC is thought to form through the injection of Antarctic continental shelf waters along the northern limb of the Weddell Gyre (Heywood *et al.*, 2004). This zone of unusual stratification is bound to the south by the Weddell Front, segregating the more stratified Weddell Sea water from the weak stratification of the WSC, and to the north by the Southern Boundary (SF).

1.2.4. The Australia-Antarctic Basin and the Adélie Land Coast

The Adélie Land Coast is located between 136° E and 140° E along the Wilkes Land continental margin, poleward of the South Indian Ocean sector of the Southern Ocean and the Australia-Antarctic Basin (AAB). The coastline is dominated by rock cliffs, ice walls and two protruding glacial tongues (Mertz and Ninnis) (Escutia *et al.*, 2005; Presti *et al.*, 2005). The large glacial outflow system that terminates with the Mertz Glacier Tongue is located at $\sim 145^\circ$ E and is presently orientated southwest to northeast (although bedrock morphology suggests that outflow during the LGM was east-southeast to west-northwest). The Mertz Glacier Tongue exerts a strong influence on the oceanography of the Adélie Land Coast; its presence focuses katabatic winds towards the coast to the west, which forces pack ice off shore and enables the development of coastal polynya systems (Escutia *et al.*, 2005; Presti *et*

al., 2005) (Figure 1.9.). The largest polynya in the region is the Mertz Glacier Polynya, that persists throughout the year, extending between 20,000 km² and 60,000 km² at the time of maximum pack ice extent (Massom *et al.*, 1998) and is believed to have the greatest ice production and thus salt production in East Antarctica (Cavalieri and Martin 1985). It is due to these polynya systems that the Adélie Land Coast has been cited as one of the most important sites of bottom water production in East Antarctica (Rintoul, 1998). At present summer sea-ice (SSI) is restricted to small pockets skirting the continental margin and rarely extends beyond the continental shelf. Winter sea-ice (WSI) is thought to extend beyond the continental shelf out to latitudes of ~62° S (Comiso, 2003; Gersonde *et al.*, 2005) (Figure 1.9.).

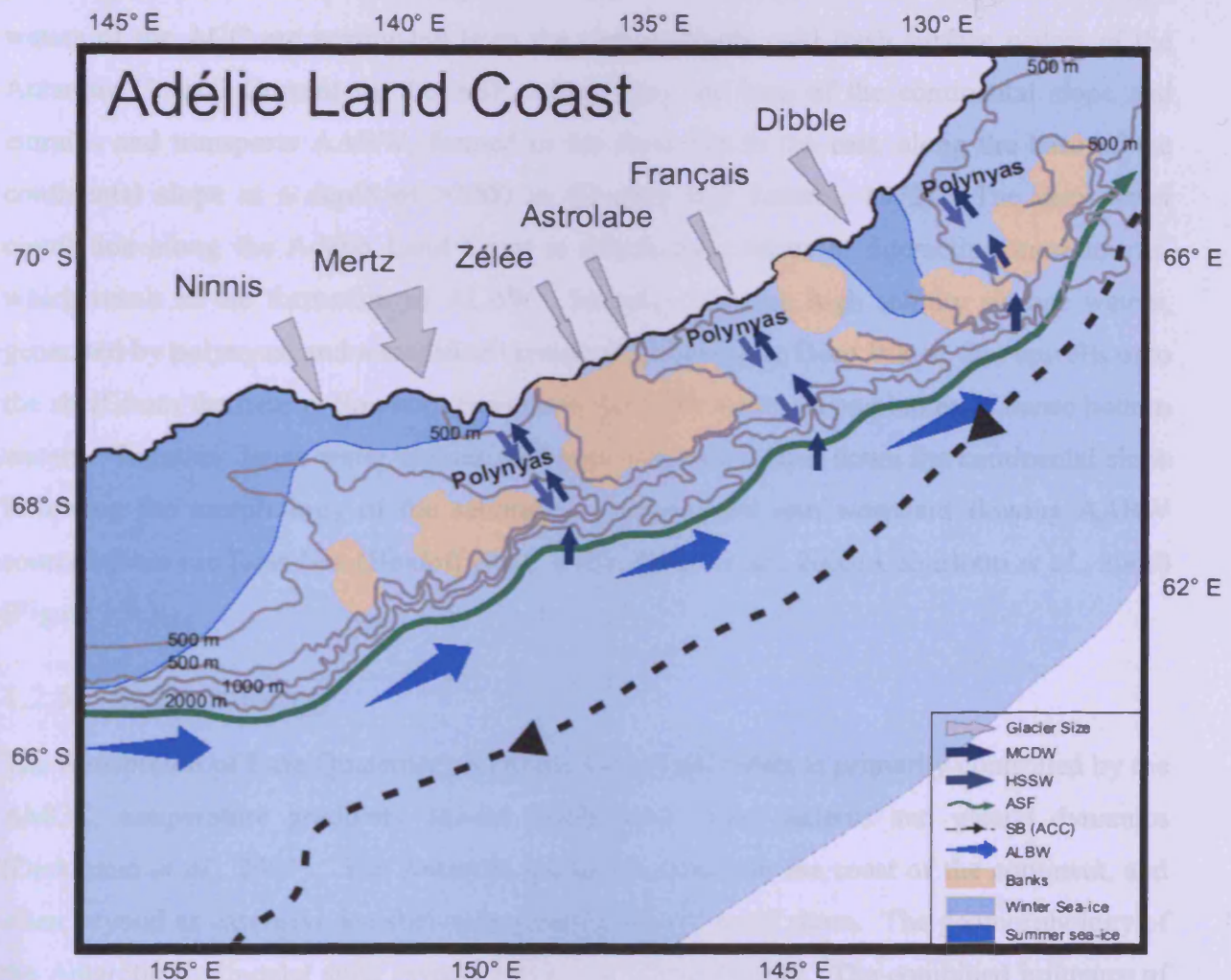


Figure 1.9. The primary oceanographic features along the Adélie Land Coast. Several major outlet glaciers and polynya systems dominate the coastline resulting in the downslope exchange of High Salinity Surface Water (HSSW) and Modified Circumpolar Deep Water (MCDW) encouraging the generation of deep and bottom waters. Deep waters formed along the coast flow down the slope to 2000 m to join bottom water flowing west from the Ross Sea. The Antarctic Slope Front (ASF) flows west, hugging the base of the continental slope and the Southern Boundary (SB) of the ACC flows west to east further off-

shore. Summer sea-ice is restricted to small pockets along the coastline whereas winter sea-ice extends to ~62°E.

1.2.4.1. Circulation

The most important ocean current system in the region is the east to west flowing Antarctic Coastal Current, which flows along the continental shelf at the surface. This current system is primarily composed of relatively cold, fresh Antarctic surface waters. Beyond the continental rise are the eastern margins of the AAB, which are dominated by the west to east flow of the ACC. In the Australia-Antarctica Basin the ACC and its frontal systems are relatively diffuse in comparison to their intensified configuration in the Drake Passage and Scotia Sea. A particular feature of ACC flow in the Australia-Antarctica Basin is the close proximity of the Southern Boundary to the Antarctic continent. The relatively warm saline waters of the ACC are segregated from the comparatively cold fresh surface waters of the Antarctic Coastal Current by the ASF, which hugs the base of the continental slope and entrains and transports AABW, formed in the Ross Sea in the east, along the base of the continental slope at a depth of >2000 m (Gordon and Tcherni, 1972). The deep-water circulation along the Adélie Land Coast is driven by a series of interacting mechanisms, which result in the formation of ALBW. Interplay between high salinity surface waters, generated by polynyas, and a modified version of Circumpolar Deep Water, that upwells onto the shelf from the nearby Southern Boundary, generates down-slope plumes of dense bottom waters. Together dense water masses spill over shelf edge, flow down the continental slope following the morphology of the submarine canyons, and join westward flowing AABW sourced from the Ross Sea (Bindoff *et al.*, 2001; Presti *et al.*, 2005; Caburlotto *et al.*, 2006) (Figure 1.9.).

1.2.5. Sedimentology

The distribution of Late Quaternary Southern Ocean sediments is primarily controlled by the AMOC, temperature gradients, sea-ice distribution, wind patterns and glacial dynamics (Diekmann *et al.*, 2007). The Antarctic ice sheets extend to the coast of the continent, and often beyond as extensive ice shelves expanding for miles off shore. The geomorphology of the Antarctic continental shelf reveals a dynamic glacial history. The combined influence of isostatic downwarping and glacial erosion has resulted in an over-deepened continental shelf profile, typically 1200 m on the inner shelf and 500 m on the outer shelf; seismic profiles have revealed repeated glacial advances and retreats across the shelf that resulted in irregular topography and the unique landward sloping profile (Anderson *et al.*, 1999). The

geomorphology and sedimentology of the continental margin is dependent upon the relative influence of glacial and marine processes, thus is very variable around the continent (Figure 1.10). The shelf is characterised by unusual depth, rugged topography, often annual sea-ice coverage and is buttressed by monolithic ice sheets. Consequently the sedimentary environment is dominated by glacial processes, sedimentary gravity flows and ice sheet and iceberg ploughing. Relict tills, evidence of past ice sheet advance are common on the shelf, contributing to its undulating topography. Composite glacial-marine deposits of Ice Rafted Debris and diatomaceous muds dominate the proglacial shelf, most prevalent at depths greater than 300 m. Draping units of siliceous mud and ooze often blanket these sediments, with biogenic silica concentrations at times up to 40% (Anderson, 1999).

Oceanographic currents exert a larger influence over sedimentation on the continental slope, primarily circumpolar currents impinging the upper slope and weak bottom currents on the lower slope. The continental slope features submarine canyons and channels, progressing from steep gradients of $\sim 25^\circ$ on the upper slope to shallower gradients towards the broad, relatively smooth continental rise. Much of the debris eroded from the continental shelf is deposited on the slope and rise, delivered by sedimentary gravity flows, resulting in an unsorted hummocky relief (Anderson, 1999).

Over the abyssal plains of the Southern Ocean, influences on sedimentation are predominantly marine, being more structured than the continental shelf and determined by oceanographic fronts, water depth, topography and distance from the continent. A broad belt of terrigenous silts and clays, sourced from turbidity currents, encompass the near-continent boundary of the plains, thicker in the west than the east, with sediments gradually becoming finer offshore. The northern limit of this belt is marked by the highly productive APF, where sediments are characterised by siliceous ooze, primarily composed of diatom frustules. Toward the Antarctic convergence, siliceous material is gradually replaced by calcareous material, resulting in a mixed zone 200 km to 300 km wide on the northern margins of the Abyssal plain (Anderson, 1999).

1.2.5.1. Sediments of the Scotia Sea

The lithofacies of the Scotia Sea are predominantly governed by surface productivity, seasonal sea-ice cover, offshore flux of fine-grain terrigenous sediment, Ice Rafted Debris, dissolution and reworking (Diekmann, 2007). High levels of primary production are associated with the APF, a region characterised by intense upwelling of cold, silica and nutrient-rich intermediate waters, which is reflected in the sediments by a wide belt of

diatomaceous mud and ooze (Moore *et al.*, 1999). South of this zone, seasonal sea-ice cover acts to constrain surface diatom productivity, resulting in their diminution or absence from the sediments. Instead, the lithofacies are primarily composed of fine-grained terrigenous material sourced from the Antarctic continent (Goodell, 1973; Diekmann *et al.*, 2000; Diekmann, 2007). The fast-flowing bottom currents of the ACC play a key role in the deposition of sediments within the Scotia Sea, resulting in both drift deposits and scoured seafloor with condensed or missing sedimentary sequences. The sheltering effects of the Scotia Arc encourages the formation of drift deposits, which in the southern Scotia Sea, and northwest Weddell Sea can also be related to the outflow of AABW. Glacial periods are characterised by the increased outflow of terrigenous material, extended sea-ice cover and reduced rates of surface productivity. Close proximity to expanded ice volumes on the Antarctic Peninsula and Patagonian ice fields, a more vigorous ACC and stronger winds generally result in expanded glacial sequences with respect to interglacials in the Scotia Sea (Diekmann, 2000).

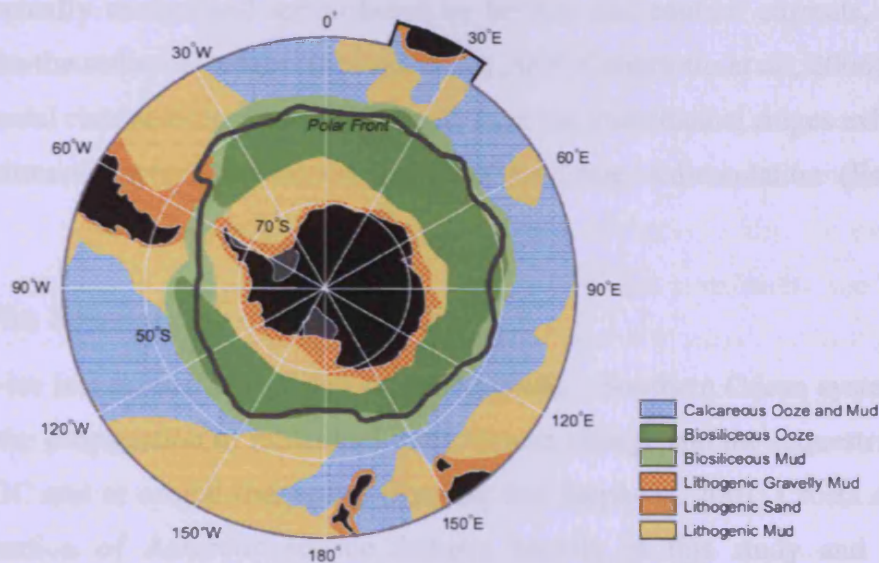


Figure 1.10. Lithology of modern sediments in the Southern Ocean. A clear banding of sediment types extends from the Antarctic continent toward the mid-latitudes, with siliceous ooze dominating south of the Polar Front and Calcareous ooze and mud to the north (Diekmann, 2007).

1.2.5.2. Sediments along the Adélie Land Coast

Sediments on the Adélie Land Coast shelf typically comprise a sequence progressing from basal till, to glacial – marine diamicton and graded sands, which is overlain by rich biosiliceous ooze (Presti *et al.*, 2005). The continental slope is relatively steep, and narrow, incised by numerous sub-marine canyons, believed to represent an extension of the troughs on the shelf above (Escutia *et al.*, 2005; Caburlotto *et al.*, 2006). The major sediments on the

slope are gravity flows (turbidity and debris flows), which were very active during glacial periods. Downslope the sediments exhibit a crude stratification, as deposits alternate between debris flows and turbidity flows, whereas the base of the slope and upper rise are characterised by finer-grained deposits, alternating with massive intervals containing high quantities of Ice Rafted Debris (Escutia *et al.*, 2003, 2005; Presti *et al.*, 2005; Caburlotto *et al.*, 2006).

The continental rise is also characterised by relative steepness and rugged topography. Tributary-like channels, which appear to stem from the submarine canyons, are accompanied by high relief ridges and are orientated north – south, with long gentle eastern flanks and short, steep western flanks (Escutia *et al.*, 2000, 2002, 2005; DeSantis *et al.*, 2003; Donda *et al.*, 2003; Caburlotto *et al.*, 2006). Gravity flow deposits originating from the slope, and hemi-pelagic deposits from the overriding water column, primarily control sedimentation on the rise. Facies range from silty muds to massive deposits with a high abundance of Ice Rafted Debris to bioturbated, well-preserved diatom assemblages. The finer fraction of these deposits is typically eroded and redistributed by bottom and contour currents, which focus deposition onto the sediment ridges (Escutia *et al.*, 2005; Caburlotto *et al.*, 2006). Elsewhere on the continental rise, sediment cores recovered from the interchannel ridges exhibit massive laminated sediments, which record continuous Pleistocene sedimentation (Escutia *et al.*, 2003).

1.3. Antarctic Sea-ice

Antarctic sea-ice is a critical component of the Antarctic - Southern Ocean system and plays a key role in the propagation of millennial-scale climate change and the sequestration of CO₂ during the LGC and at orbital timescales (Keeling and Stephens, 2001; Crosta *et al.*, 2004). The reconstruction of Antarctic sea-ice features heavily in this study and is therefore described in detail here.

1.3.1. Formation and extent

Sea-ice is formed in ocean surface waters exposed to surface air temperatures below -1.8°C , forming an effective boundary between the cool atmosphere above and the relatively warm ocean below and exerting an important impact on local and global climate (Crosta *et al.*, 1998; Gersonde and Zielinski, 2000; Gersonde *et al.*, 2003; Gersonde *et al.*, 2005). In the Southern Ocean sea-ice growth is supported by the cold ocean encompassing the Antarctic continent, limited only by the equatorward increase in ocean surface temperatures (Figure

1.11). Extending from a minimum of $4 \times 10^6 \text{ km}^2$ in March to a maximum of $20 \times 10^6 \text{ km}^2$ in September, the annual growth of Antarctic sea-ice is one of the greatest seasonal surface changes on Earth (Arrigo *et al.*, 1997). It more than doubles the areal expanse of the Antarctic continent; the equivalent of more than 82 times the size of the UK. Sea-ice extent, thickness and distribution vary with location. Permanent, summer sea-ice (SSI) is predominantly confined to the Weddell and Ross Seas and the West Antarctic coast, and is much less extensive along the coast of East Antarctica; this is especially true for the Adélie Land Coast where polynyas dominate the coastline. Winter sea-ice (WSI) formation occurs along the margins of the entire continent, however, the primary sea-ice production centres are again located within the Ross and Weddell Seas (Thomas and Dieckman, 2003). Sea-ice originating within the Weddell Sea has been tracked as far north as 2200 km from the coast, compared with only a few hundred kilometres in the East Antarctic (Comiso *et al.*, 2003).

Sea-ice can be broadly categorised as land-fast ice and pack ice. Land-fast ice is pinned to the Antarctic coast and represents only a small fraction of the total even during winter. Alternatively pack-ice represents the majority of Antarctic sea-ice, occurs in the ocean surrounding the continent and varies spatially in size, concentration, thickness and modes of formation (Eicken, 2003). The formation and decay of pack-ice off shore is subjected to the dynamics of the open ocean. Differing intensities of wind and wave action result in irregular formation and melt-back pathways with direct ramifications for sea-ice thickness, distribution, drift and biota (Eicken, 2003). In calm ocean conditions the freezing air temperatures promote the formation of *frazil* or *grease* ice. Prolonged cooling results in the coagulation of this *frazil* ice into *nilas*, further ice growth is achieved through the freezing of water molecules to the base of the sheet known as *congelation* growth, yielding first year ice up to 2 m thick (Eicken, 2003). Under calm conditions the melt-back of sea-ice is generally gradual, with stratification of the water column through freshwater supporting high surface primary production (Arrigo, 2003).

In turbulent ocean conditions frazil ice crystals eventually establish a mushy layer of *grease* ice, which accumulate into spongy pieces several centimetres in size known as *shuga*. Further compression induced by wind and wave action produces large plates of *pancake* ice up to several meters in diameter. The plates of *pancake* ice collide and raft together to form a more consolidated layer, which can further increase in thickness through ridging (Eicker, 2003), which is clearly visible on the surface. In addition, sea-ice can thicken further through snow ice, which forces ice floes below the surface, saturating the floe and resulting in freezing (Eicker, 2003). Melt mainly occurs at the bottom and sides of sea-ice, in contact

with the warm water, which can be enhanced in stormy conditions (Cunningham and Leventer, 1998). In these conditions sea-ice melt can be extremely rapid and does not create surface water production through stratification (Arrigo, 2003).

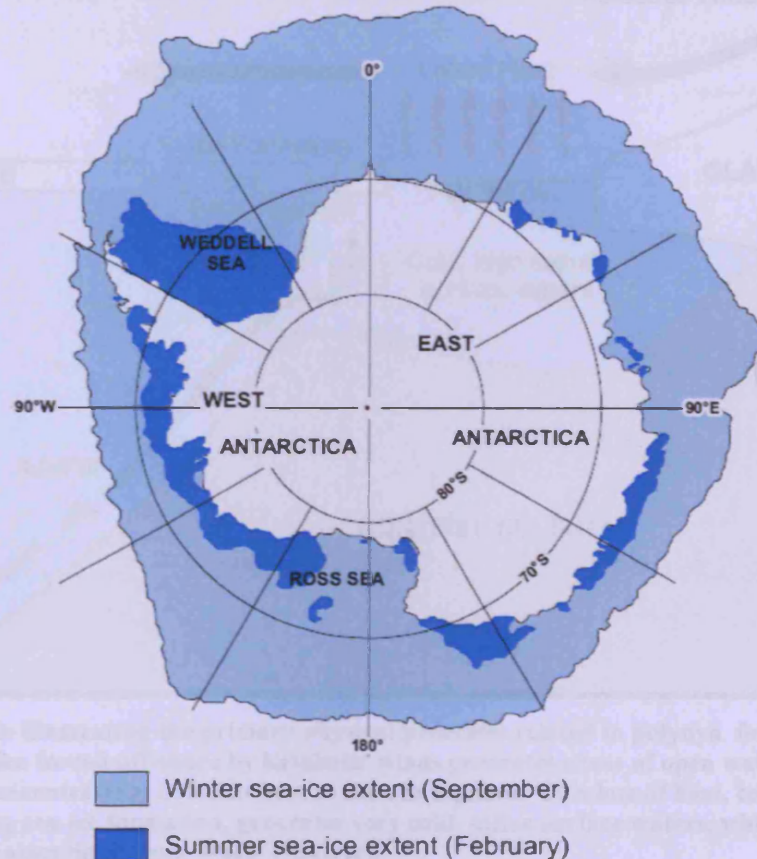


Figure 1.11. Average seasonal Antarctic sea-ice extent at present. Summer sea-ice expansion is primarily restricted to the Weddell and Ross Sea with very little expansion around the East Antarctic coast. Winter sea-ice expands around the whole of the continent, although again primarily from the Weddell and Ross Seas. The expansion of winter sea-ice is most restricted along the Wilkes Land Margin in East Antarctica (modified from Parkinson, 2004)

Pack ice is also highly mobile; its distribution determined by prevailing winds and currents. North of the Antarctic Divergence (Southern Boundary), sea-ice is subjected to the west-east flow of the ACC, with a northward component of drift, resulting in both sea-ice convergence and divergence. Convergence promotes sea-ice thickening through rafting and ridging, where as divergence exposes pockets of open water resulting in further sea-ice formation (Eicker, 2003). South of the Antarctic Divergence, and closer to the continent, the net sea-ice drift is northward. Katabatic winds blowing off the continent promote divergence, driving pack ice off-shore generating polynyas within the pack-ice along the coast (Figure 1.12). The most extensive polynya in East Antarctica, the Mertz Glacier Polynya grows to between 20,000 km² and 60,000 km² at its greatest extent. Polynyas therefore make a

disproportionately large contribution to the total ice mass and are important in the formation of AABW.

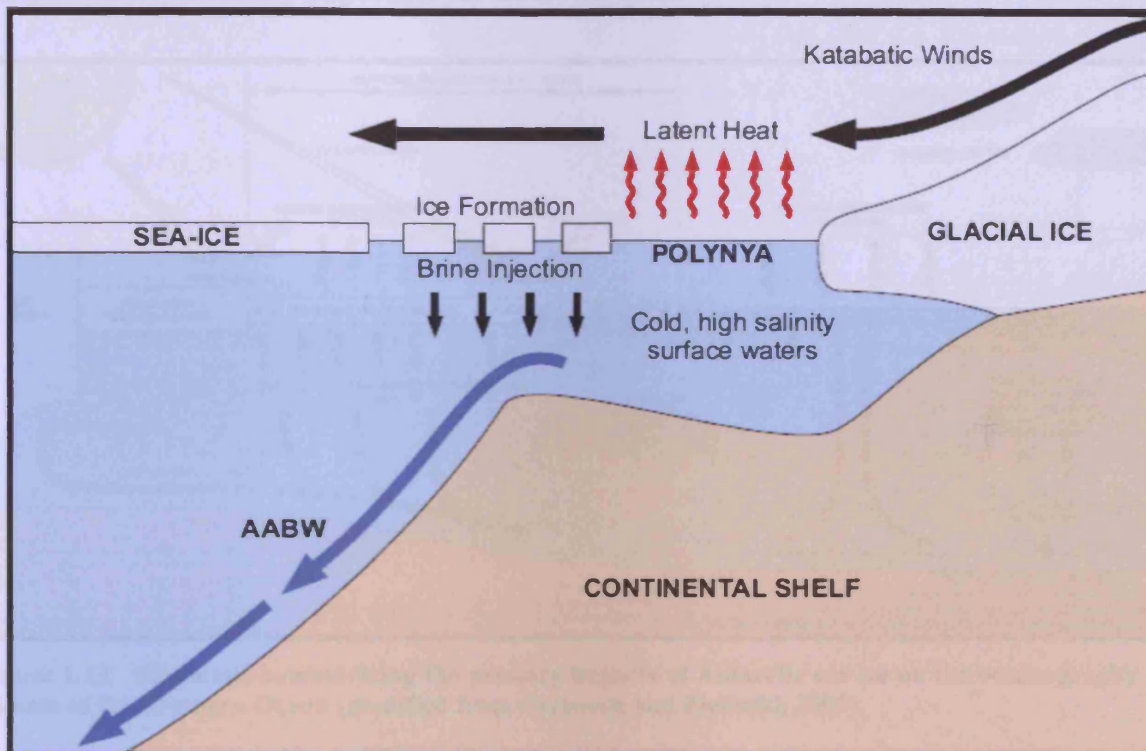


Figure 1.12. Schematic illustrating the primary physical processes related to polynya formation along the Antarctic coast. Sea-ice forced off-shore by katabatic winds generates areas of open water (polynyas), which release large concentrations of latent heat to the atmosphere. This loss of heat, combined with the rejection of salt during sea-ice formation, generates very cold, saline surface waters, which descend the continental slope as Antarctic Bottom Water (AABW).

1.3.2. Climatic Influence

Antarctic sea-ice represents one of, if not the most, important element of the climate system. It causes enhanced climate variability through positive feedbacks related to albedo and sea surface temperatures (SSTs). Due to its extreme seasonal variability Antarctic sea-ice exerts a significant impact on the physical and biological processes within the global climate system (Crosta *et al.*, 1998; Gersonde and Zielinski, 2000; Thomas and Dieckmann, 2003; Gersonde *et al.*, 2003; Gersonde *et al.*, 2005; Crosta *et al.*, 2005). The seasonal advance and retreat of sea-ice drastically modifies the transfer of heat, mass and momentum between the atmosphere and ocean, and growth and decay radically transforms the underlying water column (Stephens and Keeling, 2000). Sea-ice also acts as a thermal barrier, restricting the transfer of energy, gas and water vapour (Crosta *et al.*, 2005). These mechanisms have important implications for the efficiency of the Southern Oceans biological pump and its sequestration of CO₂. Expanded ice cover also dramatically reduces the amount of incoming

radiation absorbed at the ocean surface (Figure 1.13). The positive feedbacks associated with this albedo process can lead to the further expansion of sea-ice. Sea-ice seasonality during the LGC is an extremely important yet unknown quantity.

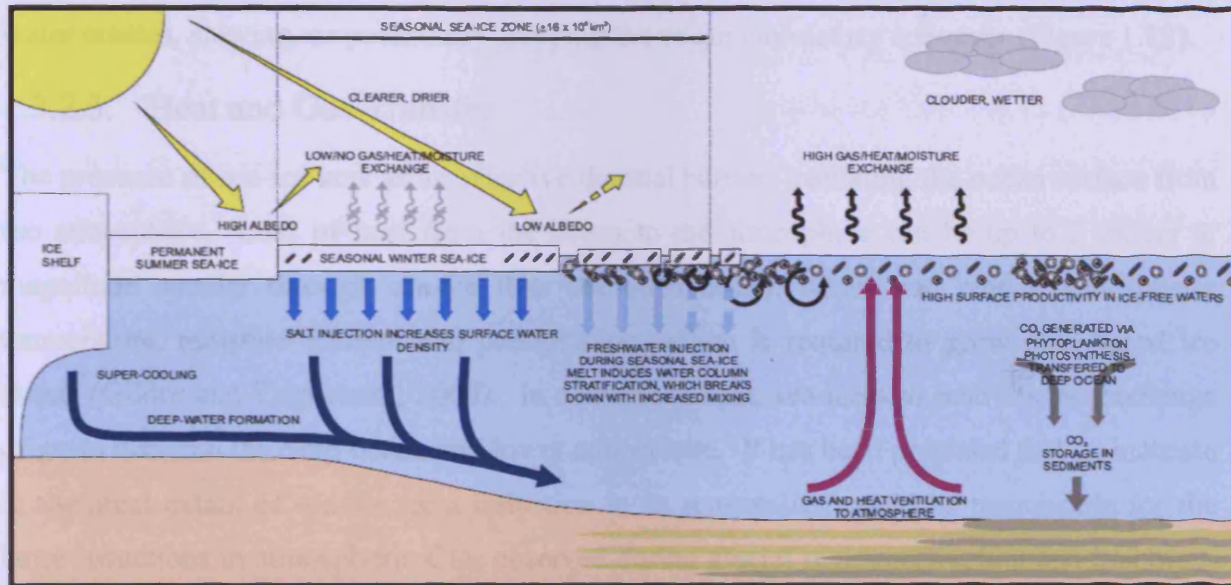


Figure 1.13. Schematic summarizing the primary impacts of Antarctic sea-ice on the oceanography and climate of the Southern Ocean (modified from Gersonde and Zielinski, 2000).

1.3.2.1. Albedo

Seawater reflects less than 5% of the incident radiation, decreasing with roughness. Sea-ice on the other hand reflects 80-90% of short-wave radiation (Warr and Smith, 2001) and, in austral winter, more than doubles the reflective capabilities of the Antarctic continent, enhancing latitudinal thermal gradients and strengthening the polar circulatory systems (Broecker, 2001). An increase in albedo also reduces surface temperatures, which in turn leads to the formation of more sea-ice and a further imbalance of the global thermal gradient. This positive feedback exemplifies the fast response and importance of sea-ice in the global climate system (Greenfell, 1983; Gersonde and Zielinski, 2000) (Figure 1.13).

1.3.2.2. Deep-water Formation

The seasonal advance and retreat of Antarctic sea-ice exerts a major influence on the AMOC, through deep-water formation and water column stratification (Gersonde *et al.*, 2005). AABW is an important component of the AMOC, and bathes 2/3 of the global ocean floor (Jacobs, 2004). The majority of AABW begins life as HSSW, generated as a bi-product of the masses of sea-ice continually formed along the margins of the Antarctic, primarily the Weddell Sea and Amery Basin (Gordon, 2001). As sea-ice forms, brine rejection

dramatically increases the surface water salinity and density resulting in the formation of HSSW, which sinks, eventually becoming AABW. Sea-ice melt-back also impacts the functioning of the AMOC through the release of large quantities of freshwater, which stratify the water column, preventing the ventilation of the deep ocean and the formation of dense water masses, slowing, or potentially stopping the ocean circulatory conveyor (Figure 1.13).

1.3.2.3. Heat and Gas Transfer

The presence of sea-ice acts as an effective thermal barrier, insulating the ocean surface from the atmosphere. Loss of heat from the ocean to the atmosphere can be up to 2 orders of magnitude smaller through sea-ice than the open ocean, which can reduce atmospheric temperature, moisture content and precipitation, which is required to grow land based ice sheets (Gildor and Tziperman, 2000). In addition to heat, sea-ice also restricts the exchange of gases between the deep ocean and lower atmosphere. It has been proposed that an increase in the areal extent of sea-ice, or a reduction in its seasonality, could be responsible for the large reductions in atmospheric CO₂ observed during glacial regimes (Keeling and Stephens, 2001). Ice core records indicate that atmospheric CO₂ concentrations during glacial periods were some 80 ppm lower relative to interglacials (Stephens and Keeling, 2000). Several modelling studies have proposed that up to 80% of this dramatic reduction in CO₂ could be driven by variations in Southern Ocean sea-ice extent (Stephens and Keeling, 2000). This suggestion is supported by geological evidence, which indicates close association between sea-ice extent and CO₂ fluctuations over the past 200 kyrs (Shemesh *et al.*, 2002; Crosta *et al.*, 2004).

1.3.2.4. Sensitivity

Sea-ice is sensitive to climatic change making it an important moderator of the global climate system. Sea-ice is exposed to forcings from the lower atmosphere and the ocean surface. Both atmospheric and oceanic circulations oscillate on a variety of timescales, manipulating global climate. Unlike the sluggish response of the terrestrial ice sheets sea-ice response to temperature perturbations in either the ocean or the atmosphere is extremely rapid (Crosta *et al.*, 2005). This sensitivity to variability in the climate system makes sea-ice an ideal gauge and driver of climate change and has led to the proposition that it could force orbital and millennial-scale changes in ocean circulation (Gildor and Tziperman, 2001; Gildor *et al.*, 2002; Shin *et al.*, 2003).

1.3.2.5. Biota

The sea-ice zone represents an important Antarctic biological habitat. Macro-fauna, such as penguins and seals utilise the sea-ice platforms as resting and breeding sites and predator refuge. On the micro-scale, sea-ice influences both primary and export production in the Southern Ocean (Arrigo, 2003) (Figure 1.13). It dramatically reduces the penetration of sunlight, effectively limiting photosynthesis and thus primary production and CO₂ drawdown (Anderson *et al.*, 2002). However, sea-ice also provides a substrate for many communities of phytoplankton (Crosta *et al.*, 2005) (Chapter 3). In addition, the gradual retreat of seasonal sea-ice cover stratifies the water column inducing highly productive spring blooms of phytoplankton in the Marginal Ice Zone (MIZ) (Arrigo, 2003).

1.3.3. Palaeoreconstructions

Despite its potential as a regulator of millennial climate change, few attempts have been made to reconstruct sea-ice variability throughout geological time. Studies have mainly focused on a LGM time-slice. Early studies used lithological boundaries and sediment facies of the seafloor as indicators of past sea-ice (Hays *et al.*, 1976; Cooke and Hays, 1982; CLIMAP, 1976, 1981) and using this method, CLIMAP Members (1976, 1981) generated the first circum-Antarctic SSI distribution map for the LGM (~18 ¹⁴C ka).

This placed the maximum SSI limit at the present day WSI edge and placed the WSI extent halfway between the reconstructed SSI limit and the modern APF, indicating much reduced sea-ice seasonality in comparison to present (Figures 1.14. and 1.15.). However, several problems with this method have been exposed (Burckle *et al.*, 1982; Burckle, 1983; Burckle, 1984a; Burckle and Cirilli, 1987). An alternative method for the reconstruction of past sea-ice extent, generally preferred in more recent studies, is based on the presence of sea-ice related subfossil diatoms preserved within the sediment record. A number of taxa have been associated with sea-ice and its surrounding waters including; *Amphiprora* spp., *Chaetoceros gracile*, *Chaetoceros socialis*, *Cylindrotheca closterium*, *Fragilariopsis curta*, *Fragilariopsis cylindrus*, *Fragilariopsis obliquecostata*, *Fragilariopsis sublinearis*, *Nitzschia lecontei*, and *Tropidoneis vanheurckii* (Garrison *et al.*, 1986; Gersonde, 1986; Burckle *et al.*, 1987; Tanimura *et al.*, 1990; Kang *et al.*, 1993; Gleitz *et al.*, 1998; Gersonde and Zielinski, 2000; Armand *et al.*, 2005).

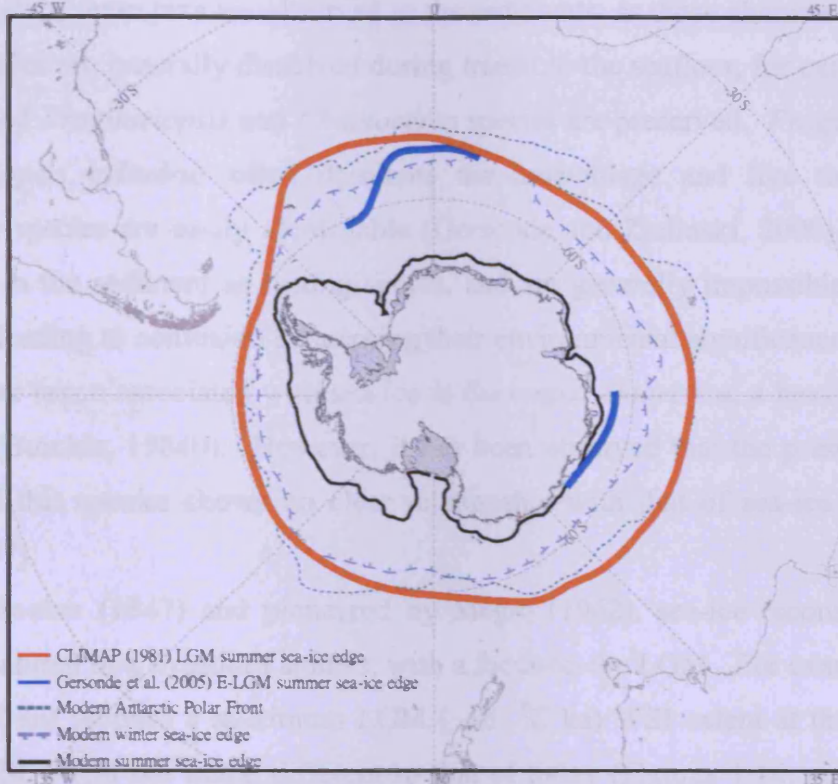


Figure 1.14. Comparison of Last Glacial Maximum (LGM) summer sea-ice (SSI) extents reconstructed by CLIMAP (1981) and Gersonde *et al.* (2005) and the modern-day winter and summer sea-ice limits and Antarctic Polar Front (modified from Gersonde *et al.*, 2005).

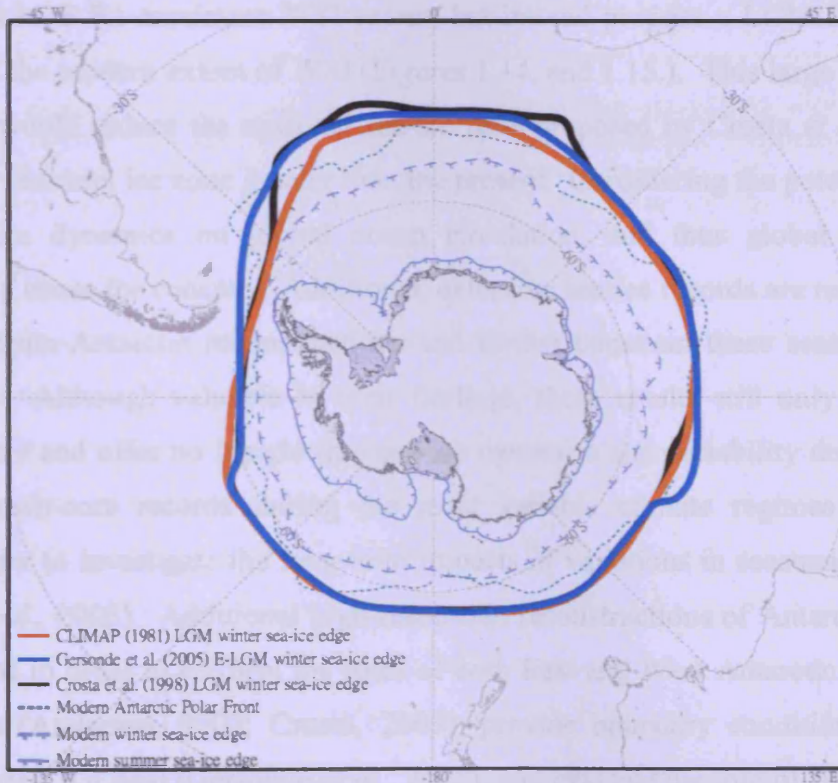


Figure 1.15. Comparison LGM winter sea-ice (WSI) extents reconstructed by CLIMAP (1981), Crosta *et al.* (1998) and Gersonde *et al.* (2005) and the modern-day winter and summer sea-ice limits and Antarctic Polar Front (modified from Gersonde *et al.*, 2005).

However, not all of these taxa are observed in the sediments, as those characterised by lightly silicified frustules are generally dissolved during transit to the seafloor, for example, only the heavily silicified *Fragilariopsis* and *Chaetoceros* species are preserved. *Fragilariopsis curta* and *Fragilariopsis cylindrus* often dominate the assemblage and like the majority of *Fragilariopsis* species are easily identifiable (Gersonde and Zielinski, 2000). *Chaetoceros* are preserved in the sediment as resting spores, and are generally impossible to identify to species level, leading to confusion concerning their environmental significance (Crosta *et al.*, 1997). Another taxon associated with sea-ice is *Eucampia antarctica*, a heavily silicified bipolar diatom (Burckle, 1984b). However, it has been observed that the present day spatial distribution of this species shows no clear relationship with that of sea-ice (Zielinski and Gersonde, 1997).

Founded by Hooker (1847) and pioneered by Megro (1962), sea-ice reconstruction using diatoms has featured in a wealth of studies, with a focus on the LGM. For example, Crosta *et al.* (1998a, 1998b) propose a maximum LGM (~ 18 ^{14}C ka) WSI extent at the modern APF and a LGM SSI extent not much different to that of today (Figures 1.14. and 1.15.). This implies the presence of an extensive seasonal sea-ice zone, which would have a considerable impact on the global climate. Gersonde *et al.* (2005) support these conclusions regarding the LGM (~ 21 cal ka B.P.) maximum WSI extent, but instead propose a LGM SSI extent near the margins of the modern extent of WSI (Figures 1.14. and 1.15.). This large increase in the extent of SSI would reduce the seasonal sea-ice zone proposed by Crosta *et al.* (1998), but still result in a seasonal ice zone greater than the present. Considering the potential impact of seasonal sea-ice dynamics on global ocean circulation, and thus global climate, such disparities are a cause for concern. Additional, extensive sea-ice records are required to build upon these circum-Antarctic reconstructions and further constrain these seasonal estimates (Figure 1.16.). Although valuable in their findings, these results still only represent one snapshot in time and offer no insight into sea-ice dynamics and variability during the LGC. Continuous down-core records during the most variable climate regimes are therefore required in order to investigate the long-term impacts of variations in seasonal sea-ice cover (e.g. Crosta *et al.*, 2005). Additional high-resolution reconstructions of Antarctic sea-ice are urgently needed in order to confirm the roles of both East and West Antarctic sea-ice on the global climate (Anderson, 2002; Crosta, 2005), provide boundary conditions for general circulation models (GCMs) (Gersonde *et al.*, 2005), and evaluate the role of Antarctic sea-ice as a potential regulator of orbital and millennial-scale climate change.

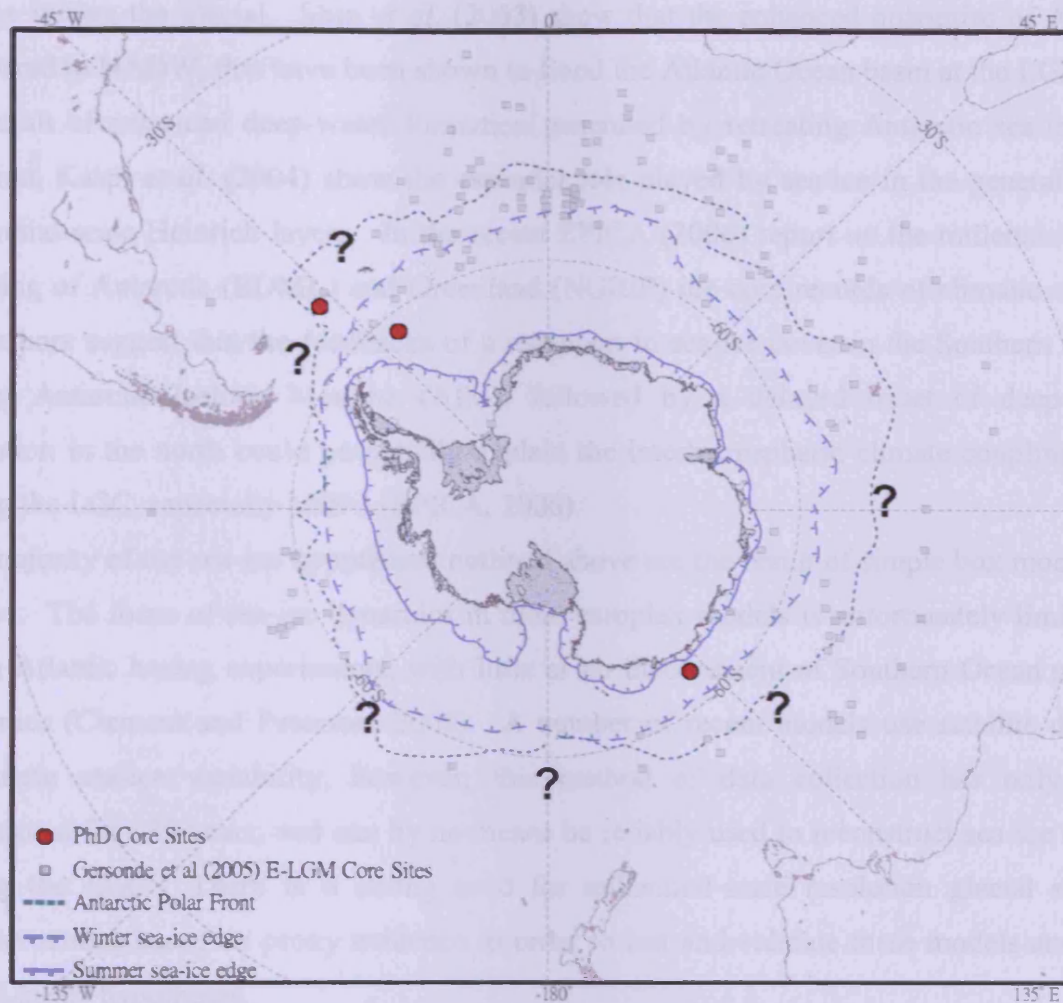


Figure 1.16. Comparison of PhD core sites TPC063, TPC286 and MD03-2603 with the most recent (Gersonde *et al.*, 2005) circum-Antarctic timeslice (EPILOG-LGM) dataset. Question marks indicate areas identified by Gersonde *et al.* (2005) as requiring additional data points. The modern-day extent of the winter sea-ice and summer sea-ice fields and the Antarctic Polar Front are also shown.

1.3.4. Antarctic Sea-ice: A Glacial Climate Driver?

Several simple box model studies have shown that variability in the Southern Ocean salinity budget, related to fluctuations in Antarctic sea-ice, have the potential to play a significant role in modulating oceanic overturning changes during periods of glacial – interglacial transition, possibly overriding freshwater fluxes in the North Atlantic (Goosse and Fichefet, 1999; Seidov *et al.*, 2001). Gildor and Tziperman (2001, 2003) propose that a sensitive sea-ice switch is in fact responsible for the mid-Pleistocene climatic mode switch from 41 kyr to 100 kyr cycles. Knorr and Lohman (2003) supported this proposal by using a more sophisticated three dimensional ocean circulation model and showing that Southern Ocean warming and associated sea-ice retreat force the abrupt resumption of a strong AMOC during periods of deglaciation via mass transport into the Atlantic Ocean via the Indian Ocean. The variability of Antarctic sea-ice extent could have also played a major role in the propagation of climatic

change during the glacial. Shin *et al.* (2003) show that the enhanced quantities of AABW compared to NADW, that have been shown to flood the Atlantic Ocean basin at the LGM, are the result of enhanced deep-water formation generated by retreating Antarctic sea-ice. In addition, Kaspi *et al.* (2004) show the essential role played by sea-ice in the generation of millennial-scale Heinrich layers. In the recent EPICA (2006) report on the millennial-scale coupling of Antarctic (EDML) and Greenland (NGRIP) ice core records of climatic change the authors suggest that the feedbacks of a reduction in sea-ice cover in the Southern Ocean during Antarctic Isotope Maxima (AIM), followed by a delayed onset of deep-water formation in the north could potentially explain the interhemispheric climate coupling seen during the LGC, especially MIS 3 (EPICA, 2006).

The majority of the sea-ice hypotheses outlined above are the result of simple box modelling studies. The focus of sea-ice dynamics in more complex models is unfortunately limited to North Atlantic hosing experiments, with little or no involvement of Southern Ocean sea-ice dynamics (Clement and Peterson, 2008). A number of recent models use satellite data to assimilate sea-ice variability, however, this method of data collection has only been operational for ~30 years, and can by no means be reliably used to reconstruct sea-ice extent during the LGC. There is a strong need for millennial-scale resolution glacial sea-ice reconstructions based on proxy evidence in order to test and validate these models and thus model-based hypotheses.

1.4. Palaeoenvironments and Palaeoclimate

1.4.1. Modern-day Antarctica

Together the ice sheets of Antarctica cover more than 98% of the continents surface (Ingólfsson, 2002), an area of $13.6 \times 10^6 \text{ km}^2$, and contain approximately $30 \times 10^6 \text{ km}^3$ of ice (Denton *et al.*, 1991). From a global perspective this accounts for 90% of the planets total ice volume, and if melted would result in eustatic sea-level rise somewhere in the region of ~66 m (Ingólfsson, 2002). However, in reality, the trans-Antarctic mountains divide the Antarctic ice-cap into two very different ice sheets. West Antarctica is composed of several individual islands that form the West Antarctic archipelago, the West Antarctic Ice Sheet (WAIS) amalgamates these land-masses, consequently obstructing exchange between the Weddell, Bellingshausen, Amundsen and Ross seas. As a result, the WAIS is predominantly marine based, with the majority of ice grounded >1 km below sea-level (Anderson, 1999), up to 2 km in places and holds the equivalent of 6 m of global sea-level rise (Anderson, 1999). Due

to a combination of converging drainage patterns and an easily deformable underlying bed, the WAIS is characterised by flow rates an order of magnitude greater than the EAIS. The WAIS drains into, and is potentially buttressed by, extensive ‘continent-sized’ ($>530 \times 10^3 \text{ km}^2$) ice shelves that extend hundreds of kilometres off shore and are grounded at water depths of up to 1300 m (Anderson, 1999), making them, along with the WAIS, highly susceptible to perturbations in climate and sea-level rise. The glacial dynamics of the WAIS and its northerly location relative to the EAIS have led to the consideration that the WAIS is less stable than the EAIS (Barker *et al.*, 2007). The WAIS has been shown to be one of the most rapidly warming regions on the planet, with temperatures rising more than 0.1° C per decade for the past 50 years (Steig *et al.*, 2009) and in response a number of glaciers and ice shelves that litter the West Antarctic coast have recently shown signs of retreat, thinning and collapse. The Pine Island, Thwaites and Smith glaciers and related ice shelves in the Amundsen Sea region have sped up and progressively thinned during at least the last 15 years (Shepherd *et al.*, 2004; Bamber *et al.*, 2007). In addition, the Larsen A ice shelf collapsed in 1995 followed by Larsen B in 2002 and most recently the Wilkins ice shelf in 2008. In order to help understand the modern-day response of West Antarctica to the changing climate it is important to determine how West Antarctica has responded in the past, for example during the LGC when rapid millennial-scale change was a standard feature of the climate system. A key question for palaeoclimate studies is: was West Antarctica as sensitive to perturbations in climate during the LGC as it is today?

In contrast to West Antarctica, the isostatically compensated sub-ice topography of East Antarctica is mostly above sea-level (Barker *et al.*, 2007), thus, the EAIS is primarily land based and grounded predominantly above sea-level. The EAIS averages just over 3 km in thickness, up to 4.5 km in places, and is characterised by flow rates of only tens of meters per year (Anderson, 1999), with primary drainage along the Wilkes Land Margin and Adélie Land Coast. The EAIS comprises the majority of modern-day Antarctica, covering $7.7 \times 10^6 \text{ km}^2$ and has been shown to vary mainly in accordance with accumulation fluctuations (Huybrechts, 2002). The EAIS drains into outlet glaciers that protrude from the towering ice cliffs that characterise much of the East Antarctic coast, which for the most part lacks the extensive ice shelves characteristic of West Antarctica (Anderson, 1999). In contrast to the rapidly warming West Antarctica, East Antarctica has been shown to exhibit slight cooling over the past 50 years (Steig *et al.*, 2009) and the large-scale collapses witnessed in West Antarctica have thus far been absent in the East, although a number of East Antarctic glaciers in the sector $\sim 100^\circ \text{ E}$ to 160° E do appear to be thinning slightly near their grounding lines

(Bamber *et al.*, 2007). Due to its sheer size, being grounded mainly above sea-level and the lack of sensitive ice shelves, the EAIS is thought to have been relatively stable for the past 14 million years (Denton *et al.*, 1993; Sugden *et al.*, 1993; Ingólfsson, 2005) and recent satellite altimetry data indicates that the EAIS is presently gaining mass in response to elevated precipitation (Davis *et al.*, 2005). Due to the severe implications for global climate that a melting of the EAIS would have, it is important to determine whether the present changes occurring in West Antarctica are a precursor for future change in East Antarctica, or whether the stability of the East Antarctic will prevail over modern climate changes. In order to determine this it is key to understand the variability of the WAIS and EAIS during the LGC, the most recent period of rapid millennial-scale climate change. One of the most pressing questions confronting today's palaeoclimate studies is: was East Antarctica's climate stable in comparison to West Antarctica during the LGC as it appears today?

1.4.2. Glaciation During the Cenozoic

One of the most significant evolutions of global climate occurred with the conception of the cryosphere (~34 Ma) and the transition from the global warmth of the early Eocene greenhouse climate to the glacial, icehouse conditions of the early Oligocene (Flower, 1999; Ruddiman, 1999). Since this period global climate has been influenced by the growth and decay of the polar ice sheets. Scientific consensus holds that the first appearance of ice occurred on the East Antarctic landmass at the Eocene/Oligocene boundary (~34 Ma). The mechanism that triggered this ice formation is thought to be the declining levels of atmospheric CO₂ (Mackensen and Ehrmann, 1992; Barrett, 2003; Zachos *et al.*, 1996, 2001; Deconto and Pollard, 2003), induced through plate tectonics, beginning with the break-up of the super-continent Gondwana (Section 1.1.1.). The growth of ice was further encouraged through the subsequent evolution of a deep-water circum-Antarctic circulation (Section 1.1.1.3.) (Barker and Burrell 1977; Kennett, 1977; Kennett and Hodell, 1995; Exxon *et al.*, 2001; Barker and Thomas, 2004) and the consequent strengthening of the equator-pole thermal gradient. This transition period continued throughout the Late Oligocene/Early Miocene with a stuttering warming trend interrupted several times by orbitally forced (400 kyr) East Antarctic glaciations (Figure 1.17) (Flower, 1999). By the Middle – Late Miocene (16 Ma to 12 Ma) a semi-permanent EAIS had been established, the most pronounced cooling stage occurred during this period (14 Ma) resulting in a 50 m lowering of sea level (Flower, 1999). There is a degree of uncertainty regarding the evolution of the EAIS throughout the Late Miocene – Early Pliocene. Two theories stand, both tried and tested, the

conventional, 'stablists' theory proposes that the EAIS has remained largely unchanged throughout the past ~14 Ma. This is supported by a wealth of terrestrial and marine evidence (Kennett and Hodell, 1995, Sugden, *et al.*, 1993) whilst the opposing theory, that of the 'dynamists', is based solely on an outcrop of terrestrial evidence known as the 'Sirius Group'. This second theory proposes that the EAIS has been fluctuating throughout its existence and that it last disappeared, completely, as recently as ~3 Ma (Abelmann, *et al.*, 1990; Dowsett and Cronin, 1990; Sugden, *et al.*, 1993). The WAIS

also developed during the Late Miocene and since its development the marine-based ice sheet has been characterised by instability, as a result of its sensitivity to changes in sea level and thermal convection (Bart and Anderson, 2000), although there is no evidence of a complete collapse.

Permanent northern hemisphere ice caps also developed during the Late Miocene and with it the modern-day bi-polar Earth. It has been suggested that ice growth in the northern hemisphere was triggered by the closing of the Panama seaway (Driscoll and Haug, 1998) and a decrease in solar insolation receipts due to volcanic eruptions (Kennett and Thunell, 1977). As declining atmospheric CO₂ levels breached a critical threshold during the Late Pliocene (~3 Ma to 2.75 Ma) the northern hemisphere ice caps evolved into large, orbitally forced (41 kyr and 23 kyr) ice sheets (Ruddiman, 2001), creating a cyclic trend of glacial and interglacial conditions. The majority of climate records tend to agree that this major cooling event, which persisted through to the Pleistocene, heralded the conclusion of the uni-polar world of the Tertiary and the dawn of the bi-polar Quaternary (Anderson, 1999). The northern hemisphere ice sheets continued to wax and wane at the orbital tilt and precession frequencies throughout the Late Pliocene and into the Pleistocene. Until, at approximately 0.9 Ma the northern hemisphere ice sheets grew to vast proportions and the marine oxygen isotope record indicates that the previous cycles of 41 kyr and 23 kyr had been overwritten by a larger amplitude, 100 kyr cycle, relating to orbital eccentricity (Imbrie *et al.*, 1984; Ruddiman, 2001). This modified pacing established larger and longer glaciations, which were terminated rapidly every 100 kyr, the last 100 kyr glacial cycle culminated 10 ka.

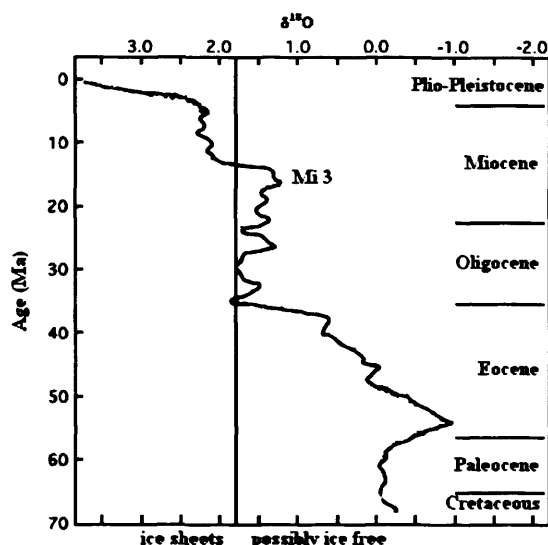


Figure 1.17. $\delta^{18}\text{O}$ trend for the past 70 Ma, illustrating the transition from greenhouse to icehouse from the Cretaceous to the modern-day (Flower, 1999).

Southern Ocean marine sediment cores and the Vostock ice core of Antarctica have confirmed that the EAIS also subscribed to this 100 kyr forcing (Jouzel *et al.*, 1987). The causal mechanism for this sudden switch in the pacing of global climate is unknown, several potential mechanisms have been proposed, with Antarctic sea-ice among them (Gildor and Tziperman, 2001; Gildor *et al.*, 2002).

Throughout the entire Cenozoic global climate has been forced by ice sheet fluctuations, driven through a combination of tectonic activity and orbital forcing. Originating in the southern hemisphere, with the conception and progressive evolution of the Antarctic ice sheets, and expanding to the northern hemisphere as atmospheric CO₂ levels declined. The conception of the polar ice sheets, and a bi-polar world, has established a principal component of the climate system and forged a permanent bond between cryosphere, hydrosphere and atmosphere.

1.4.3. The Last Glacial Cycle

The LGC occurred between ~130 ka and 10 ka (Figure 1.18), paced by the 100 kyr Milankovitch forcing. The drilling and analysis of marine sediment cores during the 1950's, '60s and '70s resulted in the development of the marine stable isotope record (Emiliani, 1955, Shackleton, 1967, Hays *et al.*, 1976, and Imbrie *et al.*, 1984). This revealed the superimposition of lower amplitude ice volume fluctuations onto a long term 100 kyr cooling trend, confirming that the tilt and precession orbital periodicities play a fundamental role in ice volume manipulation. The LGC commenced with the termination of the last interglacial regime at MIS 5e (~130 ka), reached glacial maxima at MIS 2 (Section 1.4.4.) and culminated with the onset of MIS 1 (~10 ka) (Figure 1.18).

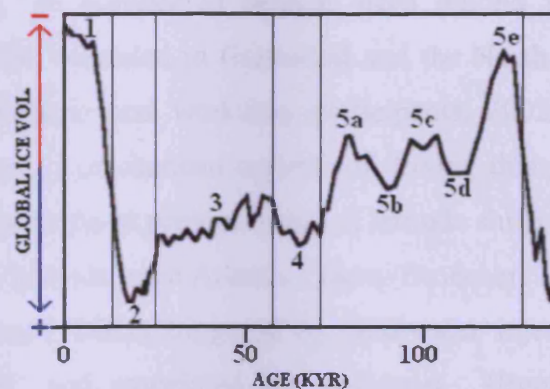


Figure 1.18. SPECMAP oxygen isotope curve derived from benthic foraminifera detailing the marine isotope stages of the last glacial cycle and current interglacial. Warm stages are assigned odd numbers and cold stages even numbers. The present interglacial is coded stage 1 and the last glacial maximum stage 2 (~130 yrs) (Martinson, 1989).

1.4.3.1. Millennial Oscillations in the Northern Hemisphere

Ice core studies, extending back further than 110 ka, revealed the existence of rapid millennial-scale oscillations (Dansgaard *et al.*, 1993). These oscillations in dust concentrations represented rapid temperature fluctuations of between 8° C and 16° C over periods as short as 1500 yrs over Greenland (Huber *et al.*, 2006). These events, termed Dansgaard/Oeschger (D/O) events, appear on 23 individual occasions through the Greenland ice cores (Dansgaard *et al.*, 1993), each characterised by an initial rapid warming (5° C to 10° C) followed by gradual cooling and terminated by a more rapid drop back to cold stadial conditions (Ruddiman, 2001) (Figure 1.19).

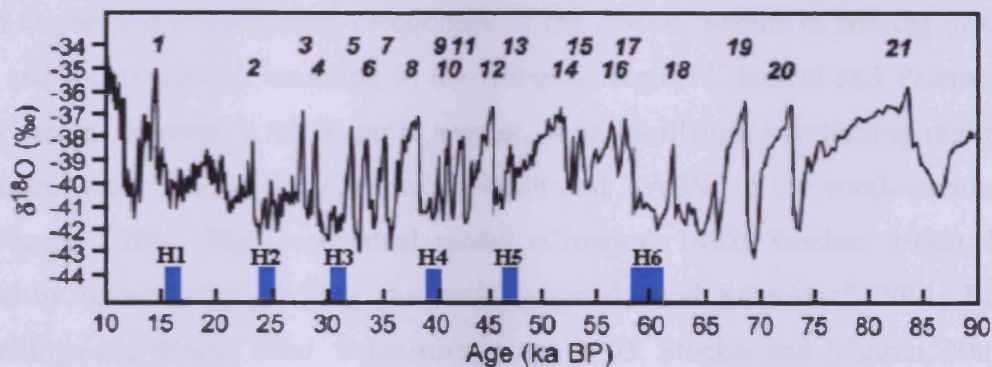


Figure 1.19. $\delta^{18}\text{O}$ oscillations identified in the GISP2 Greenland ice-cores. The saw-tooth pattern of 21 rapid Dansgaard/Oeschger events are identified over the past 90 kyrs (black line), with the culmination of several of the longer events coinciding with Heinrich layers (blue blocks) observed in North Atlantic Ocean sediments (modified from Blunier and Brook, 2001).

Similar oscillations have been identified within North Atlantic deep-sea sediment core records of SSTs, Ice Rafted Debris, and NADW formation (Heinrich, 1988; Bond *et al.*, 1992, 1993; Bond and Lotti, 1995; Bond *et al.*, 1997; Raymo *et al.*, 1998; Bianchi and McCave, 1999; Chapman and Shackleton, 2000), indicating a link in this region between the ocean and atmosphere. A number of records from around the world show temporal behaviour similar with that recorded in Greenland and the North Atlantic Ocean (Broecker and Hemming, 2001; Voelker and workshop participants, 2002; Hemming *et al.*, 2004), indicating the existence of a mechanism capable of driving this globally pervasive climate change. The leading hypothesis at present is that of latitude shifts of convection between the Nordic Seas and the mid-latitude open Atlantic Ocean (Broecker, 1991; Broecker *et al.*, 1992; Ganopolski and Rahmstorf, 2001) triggered by freshwater injections, which results in a disruption of the AMOC and associated heat transport. (Bond, 1993; Broecker, 1994; Rahmstorf, 1995; Manabe and Stouffer, 1997; Alley *et al.*, 2001; Ganopolski and Rahmstorf, 2001, 2002; Knutti, 2004; Rahmstorf *et al.*, 2005).

1.4.3.2. Millennial Oscillations in the Southern Hemisphere

Millennial-scale oscillations have also been identified in Antarctic ice cores, suggesting a globally linked pattern of climate change during the LGC. However, slower accumulation rates mean that these records cannot be directly compared with the abrupt temperature fluctuations identified in the North Atlantic. Nevertheless, Bender *et al.* (1994) identified several Antarctic warming events between 10 ka and 105 ka, characterised by gradual warming and cooling, that showed anti-phased behaviour with their northern counterparts D/O 8 to 12 (Dansgaard *et al.*, 1993). It was argued that this anti-phased interhemispheric coupling was the result of AMOC changes, whereby a vigorous AMOC draws heat from the Southern Ocean and a weakening or collapse of the AMOC results in cooling of the North Atlantic and a concomitant warming in the Antarctic region (Clement and Peterson, 2008). This mechanism, known as the bi-polar seesaw, is an oscillating overturning regime driven by two deep-water sources; NADW in the north and AABW in the south (Seidov, *et al.*, 2001) (Figure 1.20). This conceptual model (Crowley, 1992; Stocker, 1992), has been supported by numerical modelling studies (Ganopolski and Rahmstorf, 2001; Rahmstorf, 2002; Vellinga and Wood, 2002; Schmittner, *et al.*, 2003; Stocker and Johnsen, 2003; Knutti *et al.*, 2004). The operation of the seesaw hinges on the relative amounts of deep-water produced at each source. In its current mode of operation the formation of NADW dominates the Atlantic Ocean basin and serves to transfer heat from the southern hemisphere to the north (Figure 1.20). In the event of a freshwater pulse into the North Atlantic the formation of NADW slows/ceases, the northern hemisphere cools and the southern hemisphere gradually warms as the drainage of heat from the Southern Ocean reservoir slows/ceases and warmth is transferred to the Antarctic ice sheets. Based on the precise correlation of the methane records of the Byrd and GISP ice cores, Blunier and Brook (2001) concluded that at least 7 Antarctic warming events were asynchronous with, and possibly

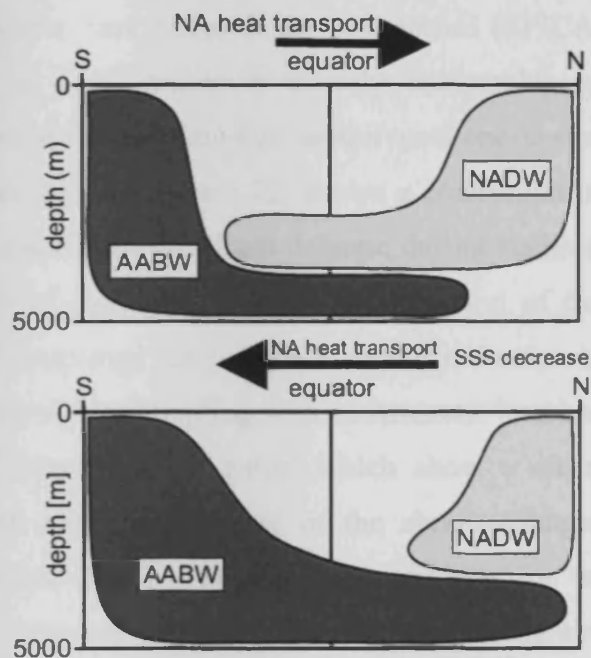


Figure 1.20. Conceptual model of the bi-polar seesaw. Enhanced concentrations of the NADW (AABW) generated in the North Atlantic Ocean (Southern Ocean) increases heat transport from (traps heat in) the Southern Ocean (Seidov *et al.*, 2001).

led, exceptionally strong Greenland coolings (D/O events) (Brook *et al.*, 2005), further supporting the bi-polar seesaw mechanism but with a trigger in the south (Figure 1.21).

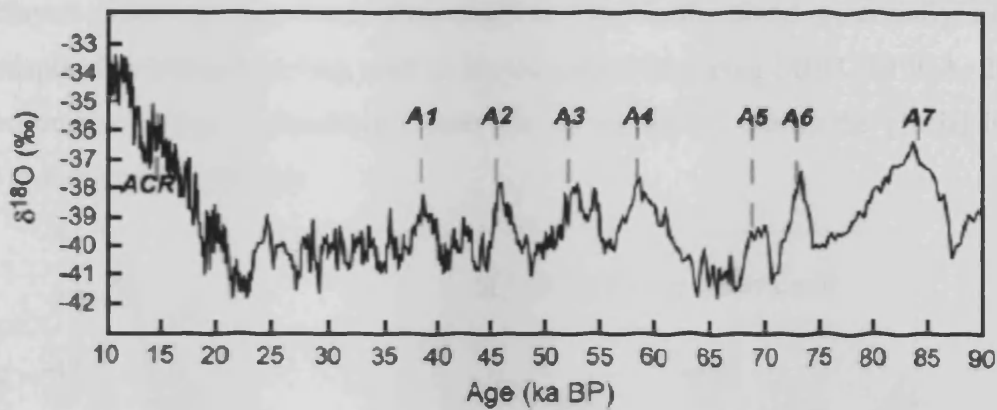


Figure 1.21. $\delta^{18}\text{O}$ oscillations identified in the Byrd ice core (Antarctic). Well-defined isotope maxima indicate Antarctic warm events (A1 to A7). The brief respite in the warming trend of the past ~20 kys around 14.5 kys is known as the Antarctic cold reversal (ACR) (Blunier and Brook, 2001).

The most conclusive evidence for a direct relationship between Antarctica and Greenland through the bi-polar seesaw mechanism was revealed in the ice core record at Dronning Maud Land. The EPICA Dronning Maud Land (EDML) ice core was recovered from the Atlantic section of the EAIS (75° S, 0° E) at the southern end of the bi-polar seesaw and has accumulation rates 2-3 times higher than any other East Antarctic ice core record (EPICA, 2006). Millennial-scale resolution during the LGC makes it directly comparable to Greenland ice core records and through methane synchronization an unequivocal one-to-one coupling of all AIM and D/O events, during the LGC (Figure 1.22) shows a connection of southern warming to reduced oceanic heat transport into the North Atlantic during stadials. The linear relationship between the amplitude of Antarctic warming and duration of the concurrent stadial in the north implies that all couplings result from a similar reduction in AMOC (EPICA, 2006). Further evidence of this bipolar coupling with an Antarctic lead has been revealed in the dust records from the Greenland ice cores, which show a clear, previously unrecognised, Antarctic style signal after the removal of the abrupt changes associated with D/O events (Barker and Knorr, 2007). Despite this evidence for an interhemispheric relationship propagated by variations in the strength of overturning the question of the trigger, forcing this interstadial – stadial switch, remains. The hypothesis of freshwater pulses into the North Atlantic, thereby slowing the conveyor, is complicated by inconsistencies between individual palaeoclimate models, an unknown freshwater source for all events and discrepancies between the timing of the events for those that are known.

Recently a case has been made for the Southern Ocean sea-ice variability being a potential means for reinstating an interglacial AMOC (Knorr *et al.*, 2003). It is proposed that the intrinsic feedback of a reduced sea-ice cover in the Southern Ocean during AIMs, followed by a delayed onset of deep-water formation in the North, could potentially explain the interhemispheric climate coupling seen in ice core records during MIS3 (EPICA, 2006). An improved understanding of Southern Ocean sea-ice variability during the glacial is required in order to test such hypotheses.

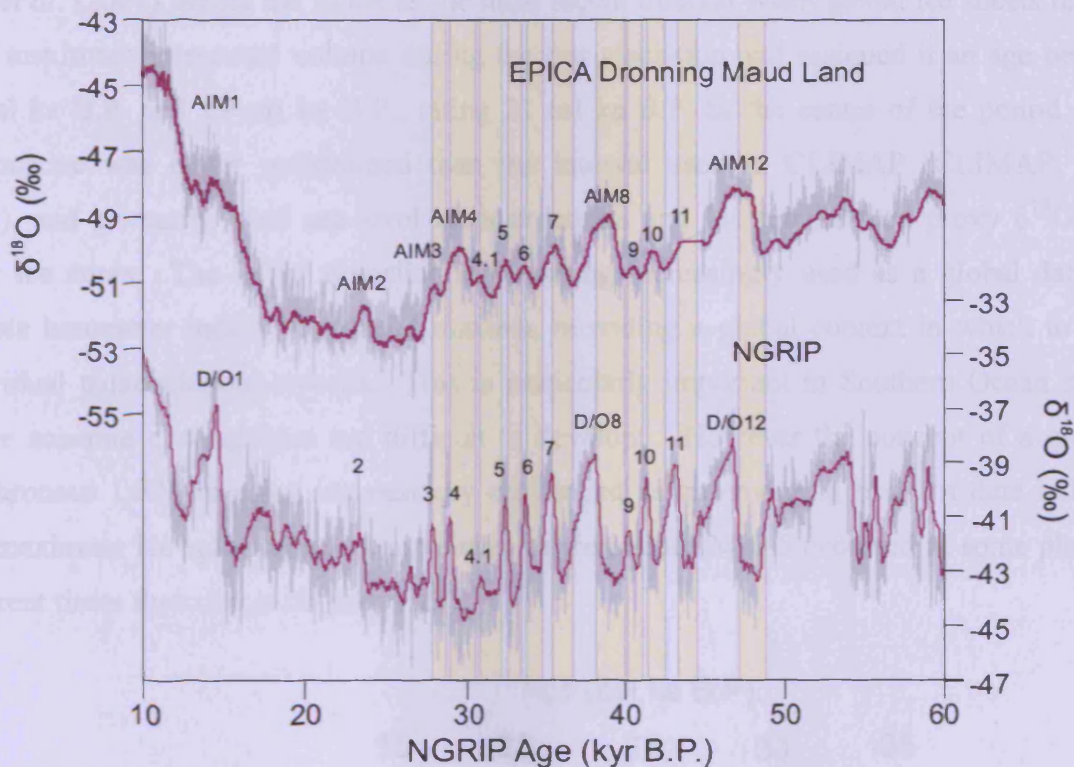


Figure 1.22. Methane synchronization of EDML and NGRIP $\delta^{18}\text{O}$ records reveals one-to-one coupling of each Antarctic warming with a corresponding stadial in Greenland. Displayed are 100-yr averages in the EDML for the time interval 10–60 kyr BP in comparison with the NGRIP $\delta^{18}\text{O}$ record from Northern Greenland. All records are CH_4 synchronized and given on the new GICC05 age scale for the NGRIP ice core. Yellow bars indicate the Greenland stadial periods that are related to respective Antarctic temperature increases. Abbreviations: AIM = Antarctic Isotope Maxima, D/O = Dansgaard/Oeschger events (EPICA, 2006).

1.4.4. The Last Glacial Maximum

The LGM refers to the period of maximum global ice volume during the LGC and is often used synonymously with the term MIS 2 (Suggate and Almond, 2005). The LGM is a global climate state dramatically different from today's, providing a critical test of climate model sensitivity, enabling validation of model geological reconstructions and future predictions. The LGM was also a relatively stable period, certainly in comparison to the rapid, millennial-scale variability characteristic of MIS 3 and primary boundary conditions for this period are

well known. The exact definition of the LGM has continued to evolve, with the definitions of its onset and culmination varying both temporally and spatially. The period is generally associated directly with MIS 2, dated to between 24 ka and 14 ka and characterised by a deep trough in the ice-volume/temperature proxy $\delta^{18}\text{O}$ (Shackleton, 1967; Chappell and Shackleton, 1986; Martinson *et al.*, 1987; Shackleton, 2000).

1.4.4.1. The LGM Time-slice

Mix *et al.* (2001) define the LGM as the most recent interval when global ice sheets reached their maximum integrated volume during the last glaciation and assigned it an age between 23 cal ka B.P. and 19 cal ka B.P., citing 21 cal ka B.P. as the centre of the period. This chronozone was better constrained than the interval used in CLIMAP (CLIMAP, 1976, 1981), and primarily used sea-level reconstructions and the temperature proxy $\delta^{18}\text{O}$ from polar ice cores. The LGM timeslice is becoming increasingly used as a global datum, a climate barometer indicating glacial maxima, providing a global context in which to place individual palaeoclimate records. This is particularly important in Southern Ocean studies where accurate chronologies are difficult to develop. However the concept of a globally synchronous LGM is being increasingly challenged as an emerging body of data indicates that maximum ice volumes and temperature minima since MIS 5 occurred in some places at different times than others (Figure 1.23).

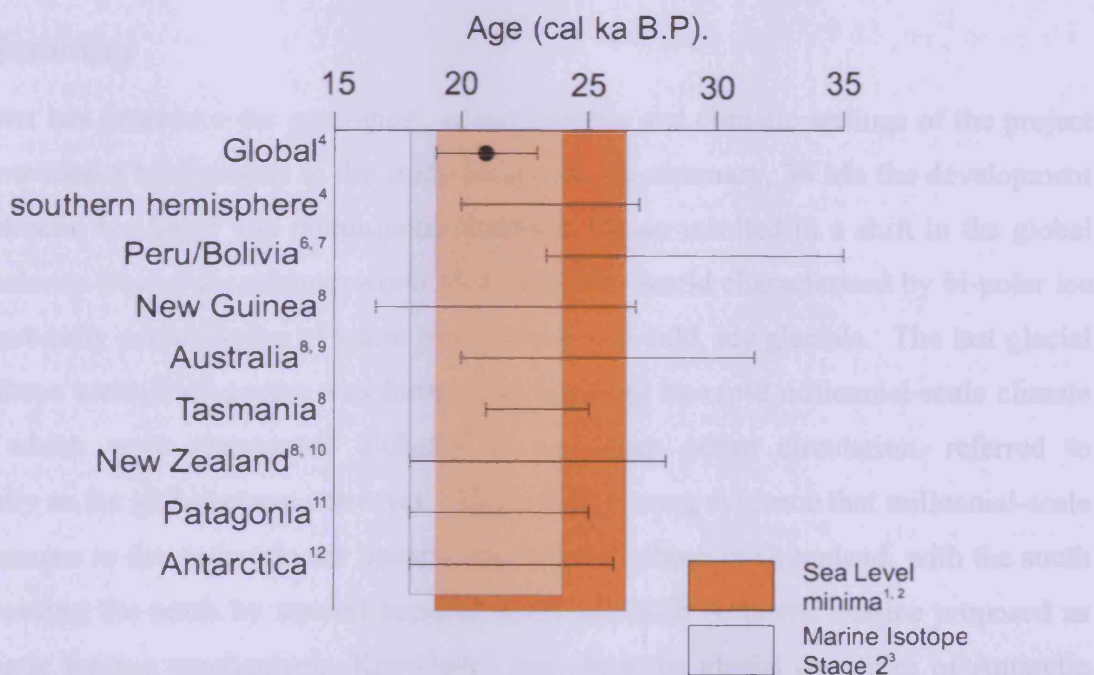


Figure 1.23. Figure illustrating the large degree of variation in the timings of local LGMs in comparison to global and hemispheric LGM windows. Dark band indicates the LGM as derived from sea-level lowstands. Light band indicates the duration of Marine Isotope Stage 2, as derived from oxygen isotopes.

References: 1. Peltier and Fairbanks (2006), 2. Hanebuth *et al.* (2009), 3. Martinson *et al.* (1987), 4. Mix *et al.* (2001), 5. Suggate and Almond (2005), 6. Bromley *et al.* (2009), 7. Smith *et al.* (2005), 8. Barrows *et al.* (2002), 9. Petherick *et al.* (2008), 10. Denton *et al.* (1999), 11. Kaplan *et al.* (2008), 12. Petit *et al.* (1999).

A synthesis of several southern hemisphere results from New Zealand, Australia and Chile led Suggate and Almond (2005) to propose an optimal LGM window for the southern hemisphere between 27 cal ka B.P. and 20 cal ka B.P. This interval appears to closely coincide with global sea-level low stands at Bonaparte Gulf, New Guinea (Lambeck *et al.*, 2002) and Barbados (Peltier and Fairbanks, 2006) and the Vostok ice core cold maxima (Petit *et al.*, 1999). However, there are still numerous southern hemisphere regional studies that identify glacial maximum outside of this window (Rodhell, 1991; Heine, 1996; Smith *et al.*, 2001; Dornbusch, 2002). It is becoming increasingly apparent that local glacial maximum can differ significantly from the widely accepted global LGM and these inconsistencies between both regional and hemispheric palaeorecords emphasise the necessity for caution when using the term global LGM and using the LGM as a datum. There is a need for further high resolution, well-dated, regional palaeoenvironmental records from both hemispheres in order to determine local glacial maximum in order to place your palaeorecord in the correct context. Determining the onset, duration and culmination of the LGM climate regime around the globe is essential in order to decipher the phasing of climate change and to determine whether the tropics, North Atlantic Ocean or Southern Ocean force abrupt regional and/or global climate changes (Kaplan *et al.*, 2008).

1.5. Summary

This chapter has described the geological, oceanographic and climatic settings of the project and has provided a background to the study locations. In summary, 34 Ma the development of the Antarctic Ice Sheet and circumpolar Southern Ocean resulted in a shift in the global climatic balance from a greenhouse world to an icehouse world characterised by bi-polar ice caps and orbitally paced cycles of warm interglacials and cold, icy glacials. The last glacial phase of these warm/cold cycles was further characterised by rapid millennial-scale climate changes, which were propagated globally via the deep ocean circulation, referred to conceptually as the global ocean conveyor. There is increasing evidence that millennial-scale climate changes in the Antarctic are linearly coupled with those in Greenland, with the south possibly leading the north by several hundred years and with Antarctic sea-ice proposed as the enigmatic forcing mechanism. Knowledge regarding the glacial dynamics of Antarctic sea-ice is poor and reconstructions extremely sparse, with those that do exist focusing on the

LGM timeslice, which itself is poorly constrained. Further, the West and East Antarctic are two very different systems, and it is unconfirmed whether these components and their associated sea-ice flux operated as a cohesive whole during the LGC or responded to local regimes. In the context of modern-day climate change the highest rates of warming have been observed in Antarctica (Steig *et al.*, 2009). The volume of water contained within the Antarctic Ice Sheet is equivalent to 66 m of sea-level rise and hence is of immense climatic significance. Studying the climate variability of the Antarctic and Southern Ocean through the LGC is fundamental to improving our understanding of global climate dynamics and to providing improved boundary conditions for climate models predicting the future of anthropogenic warming.

1.6. The Project

This project aims to improve our understanding of glacial Antarctic sea-ice dynamics through the high-resolution reconstruction of palaeoceanographic conditions across the Scotia Sea (southwest Atlantic Ocean sector) and along the Adelie Land Coast (southern Indian Ocean sector) of the Southern Ocean during the LGC. These reconstructions will subsequently be compared with global climate records in an attempt to identify a consistent relationship between Antarctic sea-ice, deep-water formation and millennial-scale variations in atmospheric temperature during the most recent glacial.

Diatom assemblages from a total of 3 cores from the Scotia Sea (2 cores) and along the Adélie Land Coast (1 core), which date back to Marine Isotope Stage (MIS) 3, will be used to reconstruct sea-ice dynamics and frontal migrations since approximately 60 cal ka B.P., with a primary focus on MIS 3 and MIS 2. In the case of the Scotia Sea cores these diatom reconstructions will be further supported by use of the emerging sea-ice proxy, highly branched isoprenoids. The chronologies of these climate archives are based on radiocarbon dating, diatom stratigraphy, relative magnetic palaeointensity correlations and thorium excess dating. The combination of these novel dating techniques and diatom assemblages preserved in the glacial sediments of the Scotia Sea and Adélie Land Coast provides the first accurately dated, high-resolution reconstructions of glacial conditions in these regions and affords the unique opportunity to compare the characteristics, timing and magnitude of glacial events in West and East Antarctica.

1.6.1. Aims and Objectives

The aim of this project is to provide the first detailed reconstruction of oceanographic conditions in the Scotia Sea and along the Adélie Land Coast from the diatom assemblages preserved in glacial marine sediments. The project also aims to provide the first demonstration that highly branched isoprenoids are a robust proxy for sea-ice variability during the late Pleistocene. We particularly intend to reconstruct the extent, duration and seasonality of summer sea-ice (SSI) and winter sea-ice (WSI) during the LGC in the Scotia Sea and along the Adélie Land Coast and to determine whether the frontal regimes (Antarctic Polar Front, Southern Boundary) of the Scotia Sea and Adélie Land Coast migrated during the glacial and to what extent they reflect or influenced the local/regional palaeoceanographic conditions. Based on these reconstructions I will address four important questions in palaeoclimate science:

- Was West Antarctica as sensitive to perturbations in climate during the LGC as it is today?
- Was East Antarctica's climate stable in comparison to West Antarctica during the LGC as it appears today?
- When was the Last Glacial Maximum?
- What was the role of the Southern Ocean in global forcings and feedbacks during MIS 2 and 3?

2. Major Proxies Employed in this Study

2.1. Diatoms as Palaeo-indicators of Climate Change

The growth of individual diatom species is regulated by a number of environmental parameters, including light levels, nutrient availability, salinity, temperature, predatory grazing and water column stratification; all of which are strongly influenced by seasonal sea-ice variability (Dunbar *et al.*, 1985; Zielinski and Gersonde, 1997; Cunningham and Leventer, 1998). Small changes in any of these parameters can result in significant changes in the diatom species assemblage, which makes diatoms a useful proxy for the reconstruction of past environmental conditions (Leventer, 1996; Crosta *et al.*, 1998; Cunningham, 1999; Taylor, 2001; Taylor and Leventer, 2003). This is especially true for the Southern Ocean, where diatom frustules are well preserved (Leventer and Dunbar, 1996; Cunningham and Leventer, 1998; Armand *et al.*, 2005; Crosta *et al.*, 2005). The use of diatoms as proxies assumes that fossil diatom assemblages directly reflect surface water hydrography, which has been well established (Crosta *et al.*, 2005; Armand *et al.*, 2005), hence many studies have employed diatoms as proxies for reconstructing parameters such as Southern Ocean sea surface temperatures (SSTs), Antarctic sea-ice limits, surface water primary productivity, the migration of oceanographic fronts and as water mass tracers (Defelice and Wise, 1981; Burckle *et al.*, 1982; Burckle and Cooke, 1983; Burckle, 1984; Jacques and Panouse, 1991; Pichon *et al.*, 1992a; Leventer, 1992; Leventer *et al.*, 1993, 1996, 2002; Leventer and Dunbar, 1996; Labeyrie *et al.*, 1996; Zielinski and Gersonde, 1997, 1998, 2000; Armand, 1997, 2000; Crosta *et al.*, 1998a, b; Moore and Abbott, 2000; Mengelt *et al.*, 2001; Moore and Abbott, 2002; Armand and Leventer, 2003; Allen *et al.*, 2005; Gersonde *et al.*, 2005). In order to relate changes in diatom assemblages to palaeoclimatic change it is essential that we first understand the contemporary environmental parameters influencing the modern species, and factors influencing their production and transport to the sediments (Cunningham and Leventer, 1998; Pike *et al.*, 2008). At present the best way to measure contemporary diatom production is by employing a variety of surface water, sediment trap, sediment surface and satellite data, a number of studies have revealed some of the factors influencing productivity (Truesdale and Kellogg, 1979; Horner, 1985; Burckle, 1987; Pichon *et al.*, 1987; Garrison and Buck, 1989; Kang and Fryxell, 1991; Gleitz *et al.*, 1996; Armand, 1997, 2000; Gersonde and Zielinski, 1997, 2000; Crosta *et al.*, 1998; Leventer, 1998, Crosta *et al.*, 2005; Armand *et al.*, 2005; Romero *et al.*, 2005). These studies have shown large regional differences in

Southern Ocean diatom productivity, from the Sea Ice Zone (SIZ), through the Marginal Ice Zone (MIZ) and Permanently Open Ocean Zone (POOZ) to the Antarctic Polar Frontal Zone (APFZ) (Figure 2.1).

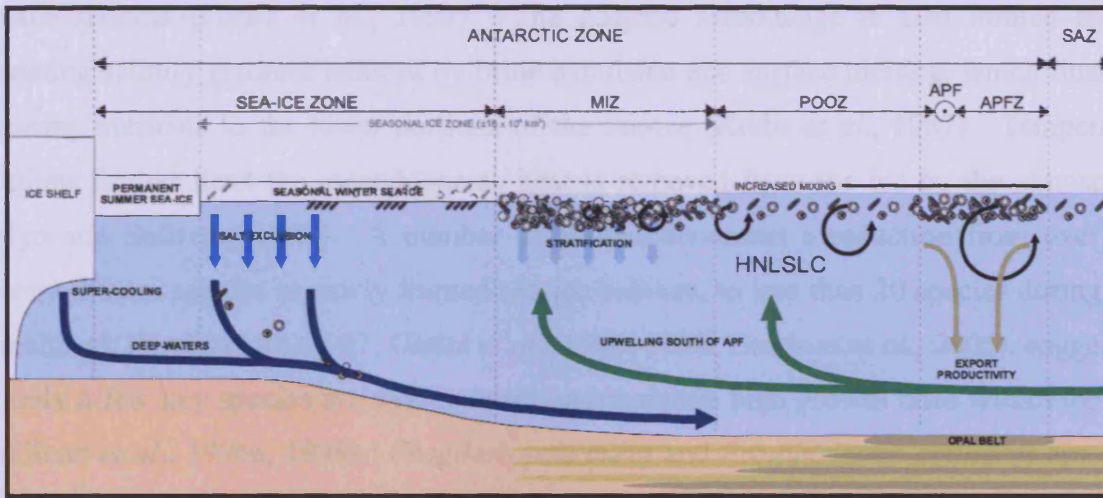


Figure 2.1. Schematic illustrating zonation of the Southern Ocean with respect to productivity. Abbreviations: MIZ = Marginal Ice Zone; POOZ = Permanently Open Ocean Zone; APF = Antarctic Polar Front; APFZ = Antarctic Polar Frontal Zone; SAZ = Sub-Antarctic Zone; HNLSLC = High Nutrient Low Silica Low Chlorophyll.

2.1.1. Environmental Controls on Diatom Distribution

2.1.1.1. Diatoms of the Sea-Ice Zone

The SIZ extends from the Antarctic continental shelf into the Southern Ocean to a latitude of between 55° S and 75° S, depending on local current regimes and heat fluxes (Thomas and Dieckmann, 2003).

The species composition of diatom assemblages within sea-ice is influenced by a number of factors including sea ice formation, type, duration and destruction as well as biological processes of colonization, growth and succession (Garrison *et al.*, 1986, 1989; Cunningham and Leventer, 1998; Gleitz *et al.*, 1998; Lizotte, 2001; Arrigo and Thomas, 2004). Different sea-ice formation processes result in different diatom assemblages. Fast-ice is restricted to near shore regions and its associated diatom assemblage is rarely preserved within the sediments. As such, the fast ice ecosystem will not be discussed here. Pack ice, or drift ice, is more abundant, comprising 90% of the ice within the Antarctic SIZ. Under turbulent conditions frazil ice crystals float to the ocean surface and phytoplankton are scavenged from the water column and incorporated into pore spaces within the ice. This initial assemblage closely resembles that of the adjacent water column (Gleitz *et al.*, 1998). As the season advances physical transformations within the ice occur, exerting selective pressures upon the assemblage. Snow cover in excess of 0.3 m limits light infiltration through the sea-ice

(Arrigo *et al.*, 1991, 2003) and compaction of the ice matrix results in compression of the pore spaces, excluding larger diatoms from the assemblage and reducing nutrient delivery. This process also excludes grazers, encouraging high standing stocks of the remaining small pennate diatoms (Gleitz *et al.*, 1998). The adapted assemblage is also limited by the fluctuating salinity gradient induced by brine expulsion and surface melting, which flush the remaining nutrients to the lower portions of the sea-ice (Krebs *et al.*, 1987). Temperature variations further limit the assemblage as heat is removed from the ice by the atmosphere (Arrigo and Sullivan, 1992). A number of studies document a reduction from over 100 different diatom species in newly formed sea-ice habitats, to less than 20 species during sea-ice meltback (Krebs *et al.*, 1987; Gleitz *et al.*, 1996; 1998; Garrison *et al.*, 2005), suggesting that only a few key species are able to adapt and maintain high growth rates within the sea-ice (Gleitz *et al.*, 1996a; 1998). *Fragilariopsis curta* and *Fragilariopsis cylindrus* are often the most abundant diatom species in the pack-ice (Garrison *et al.*, 1983, 1987; Gersonde, 1984; Horner, 1985; Krebs *et al.*, 1987; Garrison and Buck, 1989; Tanimura *et al.*, 1990; Garrison, 1991; Garrison and Close, 1993; Scott *et al.*, 1994; Leventer and Dunbar, 1996), and are observed in exceptionally high abundances in the water column at the melting sea-ice edge (Garrison *et al.*, 1983; Fryxell, 1989; Tanimura *et al.*, 1990; Kang and Fryxell, 1992, 1993; Andreoli *et al.*, 1995). Gleitz *et al.* (1996) found *Fragilariopsis curta*, *Fragilariopsis cylindrus* and *Thalassiosira antarctica* were the dominant phytoplankton throughout the entire length of the sea-ice season, despite variations in day length, light levels, temperature, salinity, nutrient concentrations and ratios. They propose that competition between species as conditions deteriorate and species-specific acclimatization are the most influential factors on diatom succession (Gleitz *et al.*, 1998). Although sub-dominant, a number of species of *Hyalochoete Chaetoceros* have also been observed within sea-ice (Gleitz *et al.*, 1998).

2.1.1.2. Diatoms of the Marginal Ice Zone

The MIZ represents the transition between the northern limits of permanent summer sea-ice (SSI) and maximum winter sea-ice (WSI) and the extent of this zone is continually modified by the advance and retreat of the sea-ice edge. The MIZ is considered an important region for phytoplankton growth, due to the melt-out of pack-ice in the spring and summer months releasing low-salinity meltwater that produces a vertically stable lens stratifying the upper water column (Smith and Nelson, 1985; Cunningham and Leventer, 1998; Lancelot *et al.*, 2000; Kang *et al.*, 2001; Fischer *et al.*, 2002; Buffen *et al.*, 2007). The receding ice-edge delivers micronutrients such as iron to the surface waters (Fischer *et al.*, 2002) that triggers

spring and summer diatom blooms seeded by the melt out of species such as *Fragilariopsis curta*, *Fragilariopsis cylindrus* and *Chaetoceros* (Garrison and Buck, 1985; Garrison *et al.*, 1987; Sedwick and Ditullio, 1997). The *Chaetoceros* subgenus *Hyalochaete* form resting spores when conditions become limiting to growth (Hargraves and French, 1983), which can remain viable for up to two years. Armand *et al.* (2005) speculate that these dormant resting spores may constitute a seed population, blooming when released during ice melt. This is supported by observations of their widespread abundance in the MIZ (Cunningham and Leventer, 1998; Kang *et al.*, 2001). Such blooms trail the ice-edge as a narrow band 50 km to 200 km wide, dominated by diatoms such as *Hyalochaete Chaetoceros* spp., *Fragilariopsis curta*, *Fragilariopsis cylindrus*, *Fragilariopsis sublinearis*, *Fragilariopsis obliquecostata* and *Fragilariopsis vanheurckii* (Smith and Nelson, 1985; Lancelot *et al.*, 1993; Kang *et al.*, 2001; Leventer *et al.*, 2002; de Baar *et al.*, 2005). It has been estimated that up to 60% of annual primary productivity within the Southern Ocean is the result of diatom blooms associated with the MIZ (Nelson and Smith, 1985; Legendre *et al.*, 1992; Arrigo *et al.*, 1998). The mode of ice breakout also influences the resulting diatom assemblage. Ice break out associated with wind stress produces a more diverse assemblage with higher concentrations of *Fragilariopsis cylindrus*, *Fragilariopsis kerguelensis*, *Fragilariopsis obliquecostata* and *Fragilariopsis ritscheri*, and a reduced abundance of *Fragilariopsis curta*, than that produced as a result of gradual melt-back of sea-ice (Cunningham and Leventer, 1998). The initiation, duration and breakdown of large diatom blooms associated with the MIZ are controlled largely by physical water column properties, with vertical stability of the water column being the most important (Park *et al.*, 1999; Kang *et al.*, 2001).

2.1.1.3. Diatoms of the Permanently Open Ocean Zone

The POOZ represents the broad swath of open water stretching from the WSI edge to the Antarctic Polar Front (APF). The zone is characterized by year-round ice-free waters where temperature and salinity exhibit little variation, excepting some seasonal change and occasional pockets of cold, low-density waters produced during iceberg melt (Allen *et al.*, 2005). As a whole, phytoplankton biomass is low within the POOZ, however, pockets of high diatom production still occur. During the winter season, nutrients are continuously pumped into the mixed surface layer, which results in a large diatom bloom when the light returns in spring, followed by constant primary production during the summer (Priddle *et al.*, 1998; Stramski *et al.*, 1999; Fischer *et al.*, 2002; van der Loeff *et al.*, 2002) although strong, wind-induced, wave action can still transfer cells to light-limited depths (Priddle *et al.*, 1998).

The combination of surface sediment and surface water studies has suggested that diatom assemblages differ both temporally and spatially during the productive seasons. Spring blooms have high concentrations of *Fragilariopsis kerguelensis*, with subordinate contributions from *Hyalochaete Chaetoceros* spp., *Pseudonitzschia* spp. and *Thalassionema* spp. (Froneman *et al.*, 1995; Burckle *et al.*, 1997; Fischer *et al.*, 2002; Crosta *et al.*, 2005). The summer community is more diverse with *Thalassiothrix* spp., *Rhizosolenia* spp., *Corethron* spp., and *Pseudonitzschia lineola*, and with less dominant *Fragilariopsis kerguelensis* (Froneman *et al.*, 1995; Tremblay *et al.*, 2002; Crosta *et al.*, 2005). Sediment studies have revealed that the diatom assemblage also varies spatially, south to north across the POOZ. A cold open ocean group has been identified toward the southerly extent of the POOZ, featuring *Rhizosolenia* ‘pointed’ group, *Thalassiosira gracilis* group and *Thalassionema reinboldii*, which appear to have a tolerance of autumn sea-ice formation (Crosta *et al.*, 2005). Sediments below the POOZ are dominated by *Fragilariopsis kerguelensis*, *Thalassiosira lentiginosa*, *Thalassiosira oliverana* and *Thalassiothrix* spp. group, with their concentrations increasing toward the APFZ (Crosta *et al.*, 2005). Toward the northern limits of the POOZ *Rhizosolenia* ‘rounded’ group, *T. nitzschoides* var. *lanceolata* group and *T. nitzschoides* group reach maximum abundances below the APFZ (Crosta *et al.*, 2005).

2.1.1.4. Diatoms of the Antarctic Polar Frontal Zone

The APFZ is bounded to the south by the APF and to the north by the Sub-Antarctic Front (SAF) and marks the transition between the sea-ice-influenced, colder, fresher waters of the Antarctic Zone (AZ) to the south (-1.9° C to 4° C) and the warmer surface waters of the Sub-Antarctic Zone (SAZ) to the north (4° C to 11° C) (Gordon, 1967; Pickard and Emery, 1990; Orsi *et al.*, 1995; Green *et al.*, 2006).

Diatom blooms associated with the stratified conditions of the APF occur during austral spring and summer during favourable light conditions and when the APF is furthest south (Allen *et al.*, 2005). Although generally dominated by large species, the diatom assemblage characterising these blooms differs depending on the study location, season, grazing pressures and degree of local macronutrient and micronutrient fertilization (Boyd *et al.*, 2000; Moore and Abbott, 2002). *Pseudo-nitzschia*, *Chaetoceros* spp (*Phaeoceros* and *Hyalochaete* subgenera), *Thalassiothrix antarctica*, *Thalassiosira lentiginosa*, *Corethron* spp. and *Fragilariopsis kerguelensis* are important diatoms at the APF, the latter dominating diatom

blooms following the SOIREE iron fertilization experiments (de Baar *et al.*, 1995; Bathmann *et al.*, 1997a; Smetacek *et al.*, 1997, 2002; Boyd *et al.*, 2000; Selph *et al.*, 2001).

2.1.2. Diatom Preservation Controls

Taphonomic processes complicate the relationship between the living diatom assemblage growing in the surface waters and the fossil assemblage preserved within the sediments, resulting in a modified and biased sedimentary assemblage. Dissolution, aggregation advection and winnowing are the most common of these processes.

2.1.2.1. Dissolution

Diatoms account for 75% of total primary production in Southern Ocean surface waters. However, within the Permanently Open Ocean Zone (POOZ) and Antarctic Polar Front Zone (APFZ) 18-58% of this production is remineralised by dissolution in the upper 100 m (Zelinski and Gersonde, 1997), this increases to between 30% and 60% in the SAZ and can be >60% in the Sea-Ice Zone (SIZ) (Pichon *et al.*, 1992), with further dissolution also occurring at the sediment/water interface (Van Bennekom *et al.*, 1988). Despite this apparent alteration of the phytoplankton assemblage, during transit between the water column and sediment record, a plethora of earlier studies have shown that the preserved fossil assemblage in surface sediments beneath all environmental zones is well diversified and their composition well related to the surface water hydrology (Kozlova, 1964; Jouse *et al.*, 1971; DeFelice and Wise, 1981; Pokras and Molfino, 1986; Truesdale and Kellogg, 1979; Gersonde, 1986; Kellogg and Kellog, 1987; Leventer and Dunbar, 1988; Leventer, 1992; Tanimura, 1992; Pichon, 1987, 1992; Pike *et al.*, 2008). Small, fragile and lightly silicified diatoms and those with higher surface area to volume ratios are most at risk regarding dissolution. The diatoms most susceptible to dissolution vary between different oceanographic environments. In the Sub-Antarctic Zone (SAZ) the diatoms *A. tabularis* and *Thalassionema* sp. are most at risk. In the APFZ and POOZ the diatoms *Thalassiothrix* sp., *Thalassiosira tumida*, *Fragilariopsis separanda*, *Rhizosolenia styliformis* and *Asteromphalus parvulus* are most susceptible to dissolution. And in the SIZ the diatoms *Thalassiosira antarctica*, *Actinocyclus actinochilus*, *Fragilariopsis cylindrus*, *Odontella weisflogii*, *Porosira glacialis*, *Thalassiosira gracilis* and *Fragilariopsis curta* are most likely to dissolve (Pichon *et al.*, 1992). A number of these weakly silicified species are present and well preserved throughout the diatom assemblages counted in cores employed in this study (Figure 2.2.).

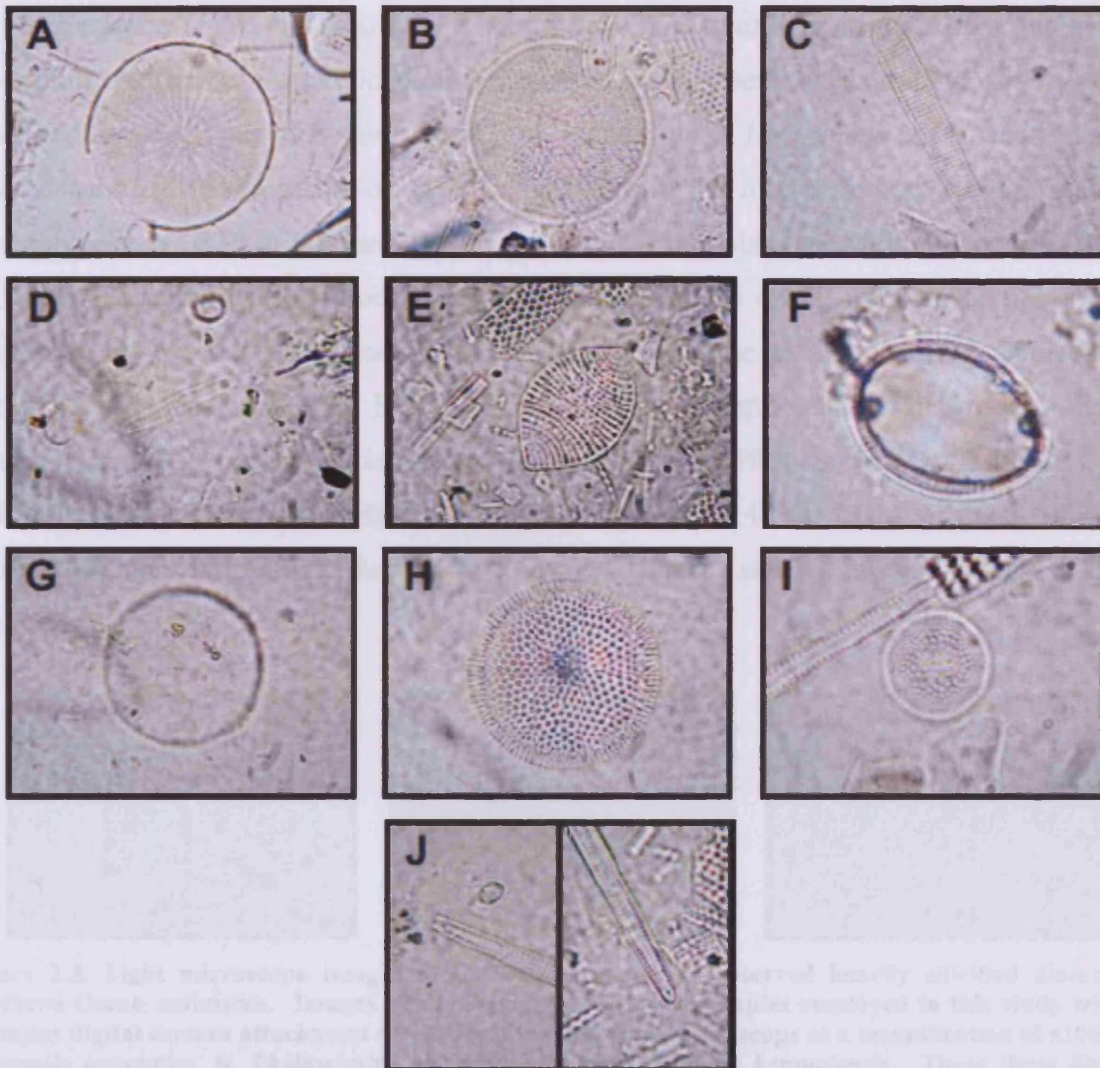


Figure 2.2. Light microscope images of lightly silicified diatoms consistently identified and well preserved in marine sediment cores MD03-2603, TPC063 and TPC286. Images were taken with an Olympus digital camera attachment on an Olympus BH2 light microscope at a magnification of x1000. A. *Actinocyclus actinocylus*, B. *Azpeitia tabularis*, C. *Fragilariopsis curta*, D. *Fragilariopsis cylindrus*, E. *Fragilariopsis separanda*, F. *Odontella weisflogii*, G. *Porosira glacialis*, H. *Thalassiosira antarctica*, I. *Thalassiosira gracilis* var. *gracilis*, J. *Thalassiothrix antarctica*.

The presence of these ‘at risk’ diatoms, in the sediment record, suggests that dissolution has had a negligible impact on the assemblage and allows increased confidence in palaeo-reconstructions. Preferential dissolution of lightly silicified diatoms can result in a sedimentary assemblage biased towards large, heavily silicified diatoms (DeMaster *et al.*, 1996; Nelson *et al.*, 1996; Cunningham and Leventer, 1998), with sediments often enriched in *F. kerguelensis*, *T. lentiginosa* and to a lesser extent *E. antarctica* (Shemesh *et al.*, 1989) (Figure 2.3). For the POOZ and APFZ, where diatom preservation is at its best, Shemesh *et al.* (1989) developed a preservation index (PI) based on the relationship between the relative abundance of *F. kerguelensis*, *T. lentiginosa* and the fraction of total initial opal dissolved after a particular time interval in controlled laboratory experiments. Based on the equation

(*F. kerguelensis*/(*F. kerguelensis* + *T. lentiginosa*)) the authors suggest that the typical dissolution pattern of Antarctic diatom assemblages in these oceanographic zones can be described as a decrease in *F. kerguelensis*, an increase in *T. lentiginosa* and a small increase in *E. antarctica*. Shemesh *et al.* (1989) show that in the modern ocean average seawater assemblages have a PI of 0.96 and that in Holocene sediments preservation increases towards high latitudes, although their core coverage is insufficient to reveal whether the preservation is affected by winter sea-ice cover and does not penetrate at all into areas subjected to summer sea-ice cover. For the SAZ, a region exposed to higher rates of dissolution than the Antarctic Zone (AZ) in the modern ocean, Shemesh *et al.* (1989) record PI of 0.55, 0.33, 0.61 and 0.61 for Holocene sediments and 0.52, 0.32, 0.19 and 0.49 for LGM sediments from the South Atlantic, Southeast Pacific, Southwest Indian and Southeast Indian Oceans respectively.

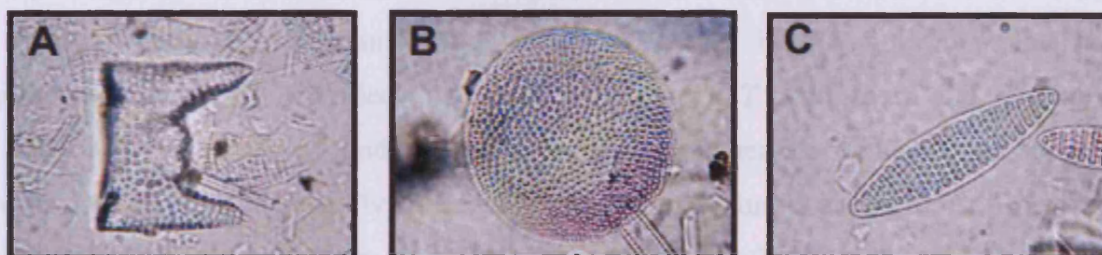


Figure 2.3. Light microscope images of the most commonly preserved heavily silicified diatoms in Southern Ocean sediments. Images were taken from sediment samples employed in this study with an Olympus digital camera attachment on an Olympus BH2 light microscope at a magnification of x1000. A. *Eucampia antarctica*, B. *Thalassiosira lentiginosa*, C. *Fragilariopsis kerguelensis*. These three diatoms feature heavily in the dissolution experiments conducted by Shemesh *et al.* (1989) and Pichon *et al.* (1992).

Results regarding the degree of dissolution during glacial periods compared to interglacial periods are inconclusive. In the controlled dissolution experiments by Shemesh *et al.* (1989) the authors show that in some cases diatom valves were better preserved in LGM sediments than samples from the Holocene. In a similar series of experiments, Pichon *et al.* (1992) indicate that during the glacial dissolution is enhanced relative to the Holocene in the Indian and Pacific Basins but not so in the South Atlantic Basin. This uncertainty is potentially due to differing accumulation rates, which have also been shown to have an impact on the severity of dissolution (DeMaster, 1996), with enhanced sedimentation rates reducing exposure of valves to dissolution at the sediment/water interface.

Parameterising dissolution in glacial sediments is often complicated by the preparation of quantitative microscope slides (Chapter 3). Subsequent to chemical preparation and prior to the settling stage, the samples are exposed, for a few seconds, to an ultra-sound bath, which aids in disaggregating the sample. This is necessary due to the high clay content of glacial

sediments, which acts to glue the diatom valves together, making counting difficult. Unfortunately, exposure to the ultra-sound bath can also fragment weakly silicified and small diatoms. Therefore any attempt to parameterise the effects of dissolution, based on for example a fragmentation index, would not accurately represent the sedimentation environment.

Dissolution of diatoms in the Southern Ocean is further encouraged by low opal export production, this is especially common in areas affected by sea-ice coverage (Gersonde and Zielinski, 2000; Gersonde *et al.*, 2003; Gersonde *et al.*, 2005). Dissolution is strongest in the deep Weddell Basin due to the combination of low opal export rates from the euphotic zone – due to heavy sea-ice cover – and strong dissolution at the sediment/water interface – due to abyssal bathing by more corrosive Antarctic Bottom Waters (Abelmann and Gersonde, 1991), unfortunately the study of Shemesh *et al.* (1989) did not extend this far south. Poorly preserved diatom assemblages have been reported in sediments from the Weddell Basin for the past 3 million years (Zielinski and Gersonde, 1997). However, even in this hostile environment the heavily silicified diatoms *F. kerguelensis*, *T. lentiginosa* and *E. antarctica* are still observed (Zielinski and Gersonde, 1997). Sediments completely devoid of any diatoms, lacking even the heavily silicified forms, are found under areas exposed to perennial sea-ice cover or extensive ice shelves (Gersonde *et al.*, 2003; Gersonde *et al.*, 2005; O'Cofaigh *et al.*, 2005). The presence of a permanent ice barrier results in almost no export production and thus can leave the sediments completely barren of biogenic silica, (Gersonde *et al.*, 2003; Gersonde *et al.*, 2005; O'Cofaigh *et al.*, 2005).

2.1.2.2. Advection

Diatom valves are susceptible to lateral advection (Kim *et al.*, 2009) by surface and bottom currents, which can alter the assemblage as well as increasing valve exposure to dissolution. Two modes of advection influence the diatom assemblage that reaches the sediment; (1) permanent, steady advection that results in the consistent removal of the same size/degree of silicification range; and (2) intermittent advection that results in the episodic removal of different size/degree of silicification ranges. Advection can transport frustules large distances during their water column descent (Burckle and Stanton, 1975; Semina, 1979; Burckle, 1981; Leventer and Dunbar, 1987; Leventer, 1991) and diatoms most at risk are generally more buoyant, small and lightly silicified.

2.1.2.3. Aggregation

The formation of diatom aggregates in the surface waters of the Southern Ocean can lead to the rapid removal of diatom cells from the euphotic zone and rapid transport through the water column, reducing valve exposure to both dissolution and advection (Jaeger *et al.*, 1996). Nelson *et al.* (1995) demonstrated that aggregation could lead to the fast burial of approximately one quarter of biogenic opal production within the POOZ. The formation of diatom aggregates within the surface waters is generally the result of cell entanglement, faecal pellet production and the formation of diatom mats (Grigorov, 2002; Thornton, 2002; Sarthou *et al.*, 2005). The rate of aggregate formation is dependent on a variety of factors including biomass concentration, the size and shape of individual cells - including presence of setae, the abundance of chain forming species and 'stickiness' (Sarthou *et al.*, 2005). Certain diatoms exhibit morphologies and colony structures suited to entanglement and mat formation, including *Nitzschia* spp., *Chaetoceros socialis*, *Rhizosolenia* spp., *Thalassiothrix* spp., *Thalassionema* spp., and *Corethron* spp. (Kemp *et al.*, 1999; Kemp *et al.*, 2000; Selph *et al.*, 2001; Thornton, 2002). The sedimentation of *Thalassiothrix* mats has been widely observed in the sediments of the APFZ and have been observed to aggregate in tangled masses along density discontinuities associated with oceanic fronts (Grigorov *et al.*, 2002). Further, some diatoms, particularly sea-ice communities, are inherently 'sticky' due to the production of an extracellular polysaccharide mucilage, which aids in their rapid aggregation (Riebesell *et al.*, 1991). Diatom frustules are also incorporated into faecal pellets by a variety of pelagic grazers, the sinking of which results in rapid rates of sedimentation.

2.1.2.4. Winnowing and Scouring

Strong bottom currents, such as those associated with the primary flow-paths of the ACC, can exert a strong influence over diatom assemblages through winnowing and scouring. Scouring by intense bottom currents can prevent the accumulation of any sediment, as is the case in Drake Passage (Robinson and Van der Flierdt, 2009). In addition to scouring, high-energy environments can also result in the winnowing of sediments, preferentially removing small, less robust diatom frustules from the assemblage (Allen *et al.*, 2005). A further, potential effect of current winnowing is the introduction of extinct diatoms to the assemblage as a result of reworking downstream (Crosta *et al.*, 2004).

2.1.3. Diatom Species Ecological Associations

Diatoms are widely employed in reconstructions of palaeoceanographic conditions through comparison of fossil assemblages with modern analogues. The following section reviews the ecological associations of the dominant diatom species identified in this study. It is based primarily on a suite of recently published papers (Armand *et al.*, 2005; Crosta *et al.*, 2005; Romero *et al.*, 2005).

2.1.3.1. *Actinocyclus actinochilus* (Ehrenberg) Simonsen

Actinocyclus actinochilus is generally classified as a cool water species (0° C to 1.8° C) associated with newly formed pack and fast-ice, and to a lesser extent the adjacent water column (Garrison *et al.*, 1983, 1987; Gersonde, 1984; Horner, 1985; Krebs *et al.*, 1987; Garrison and Buck, 1989; Tanimura *et al.*, 1990; Garrison, 1991; Garrison and Close, 1993). It is commonly identified in Southern Ocean sediments in association with other sea-ice taxa. *A. actinochilus* is often confined to the Antarctic Divergence, limited to the north by the APF, and possibly the maximum WSI edge (Donahue, 1973; DeFelice and Wise, 1981; Zielinski and Gersonde, 1997; Semina, 2003). Armand *et al.* (2005) observe that an abundance of 2% or more in the sediments is associated with sea-ice duration in excess of 7 months per year, with a maximum relative abundance of 2.9% related to an optimum of 8-9 months per year. In the South Atlantic sector of the Southern Ocean, Zielinski and Gersonde (1997) report a maximum abundance of 4.7% related to summer SSTs in the range of -2° C to 2.8° C.

2.1.3.2. *Azpeitia tabularis* (Grunow) G. Fryxell and P.A. Sims

Morphological variation within this species has led to the proposal of cold and warm water varieties *Azpeitia tabularis* var. *tabularis* and *A. tabularis* var. *egregious* (Fryxell *et al.*, 1986). However, the separation has not been proven (Fenner *et al.*, 1976; Armand, 1997), therefore, I group the varieties. *A. tabularis* is typically a tropical/subtropical diatom, presently observed in all oceans, including sub-Antarctic areas (Hasle and Syvertsen, 1996; Romero *et al.*, 2005). Within the Southern Ocean, highest abundances are observed north of the APF. Optimal SSTs for growth are 13° C to 11° C, beneath which maximum abundances of up to 24% have been observed in surface sediments (Romero *et al.*, 2005). The maximum WSI edge represents the southern boundary of this species, although *A. tabularis* is generally confined to SAZ (Zielinski and Gersonde, 1997) low levels have been observed along the Antarctic coast (Truesdale and Kellogg, 1979; Stockwell *et al.*, 1991; Tanimura, 1992;

Leventer, 1992; Cunningham and Leventer, 1998). Increases in the abundance of *A. tabularis* are indicative of the increasing proximity of SAZ surface waters and the APF.

2.1.3.3. *Eucampia antarctica* (Castracane) Mangin

Prasad and Fryxell identified two varieties of *Eucampia antarctica*; *Eucampia antarctica* var. *antarctica* and *Eucampia antarctica* var. *recta*. Each of the varieties produces a resting stage that is more resistant to dissolution and preferentially preserved in the sediments (Zielinski and Gersonde, 1997). *E. antarctica* is ubiquitous and not assigned to any particular Antarctic ecotone (Zielinski and Gersonde, 1997; Armand, 1997; Crosta *et al.*, 1998a, Armand *et al.*, 2005). Zielinski and Gersonde (1997) observed few *E. antarctica* valves in the water column, and those exhibited maximum abundances between -2°C and 0°C , and 2.5°C and 5.5°C in the POOZ and APFZ respectively. In the sediment record, *E. antarctica* occurs at high abundances during the glacial periods of the Late Pleistocene and its abundance curve is often employed as a stratigraphic tool (Burckle and Cooke, 1983; Abelman and Gersonde, 1988) (Chapters 3 and 5). During the last glacial maximum (LGM), relative abundances in excess of 40% were common across much of the Southern Ocean (Allen *et al.*, 2005) and *E. antarctica* abundance has been used as an indicator for past sea-ice extent (Burckle, 1984; Burckle *et al.*, 1990). However, mapping of modern Southern Ocean surface sediments demonstrates that maximum abundances of the species rarely exceed 20% and are generally in the range of 8% to 12% (Gersonde and Zielinski, 2000) and even in regions associated with sea-ice and icebergs, concentrations do not reach Late Pleistocene glacial abundance maxima. Therefore, *E. antarctica* is a non-analogue species and is often excluded from reconstructions and transfer functions (Crosta *et al.*, 1998a).

2.1.3.4. *Fragilariopsis curta* (Van Heurck) Hustedt

Fragilariopsis curta is strongly associated with Antarctic sea-ice. The species has been observed dominating both fast-ice and pack-ice with high quantities in the water column adjacent to the sea-ice edge (Garrison *et al.*, 1983; Gersonde, 1984; Horner, 1985; Krebs *et al.*, 1987; Garrison *et al.*, 1983, 1987; Garrison and Buck, 1989; Fryxell, 1989; Tanimura *et al.*, 1990; Garrison, 1991; Kang and Fryxell, 1992, 1993; Andreoli *et al.*, 1995; Leventer and Dunbar, 1996). Maximum abundances (60-90%) are associated with highly consolidated WSI cover of 9-11 months per year. *F. curta* prefers temperatures in the range of -1.3°C to 2.5°C , with a narrow optimal temperature range between 0.5°C and 1°C (Armand *et al.*, 2005). Highest concentrations within the sediment have been reported in coastal regions,

with the northward distribution of *F. curta* limited by the maximum WSI edge, except in the South Atlantic sector of the Southern Ocean, where sporadic trace excursions are reportedly linked to ice-berg discharge from the Peninsula (Kozlova, 1966; Truesdale and Kellogg, 1979; DeFelice and Wise, 1981; Gersonde, 1984; Gersonde and Wefer, 1987; Kellogg and Kellogg, 1987; Stockwell *et al.*, 1991; Leventer, 1992; Tanimura, 1992; Taylor *et al.*, 1997; Zielinski and Gersonde, 1997; Semina, 2003; Armand *et al.*, 2005).

2.1.3.5. *Fragilariopsis cylindrus* (Grunow) Krieger

Fragilariopsis cylindrus occupies sea-ice covered environments, is found in both fast and pack-ice and is considered to dominate the marginal sea-ice edge assemblage (Fryxell, 1989; Kang and Fryxell, 1992, 1993; Andreoli *et al.*, 1995; Leventer and Dunbar, 1996; Kang and Fryxell, 1992, 1993; Kang *et al.*, 1993). Armand *et al.* (2005) report a maximum abundance of 2.9% from surface samples, which they associate with a SST range of 0.5° C to 1° C and 8.5 months of annual sea-ice coverage. The species distribution is the same as that of *F. curta*, with highest abundances in the near-coast environment (Gersonde, 1984; Horner, 1985; Krebs *et al.*, 1987; Garrison and Buck, 1989; Tanimura *et al.*, 1990; Garrison and Close, 1993; Scott *et al.*, 1994). Within the South Atlantic Sector, Zielinski and Gersonde (1997) document a maximum abundance peak of 29% in the sediments occurring beneath SSTs of -0.5° C to 1° C.

Gersonde and Zielinski (2000) propose a sea-ice proxy based on the combined relative abundance of *Fragilariopsis curta* and *Fragilariopsis cylindrus*. They demonstrate that the average maximum WSI limit can be robustly reconstructed where a combined (*F. curta* and *F. cylindrus*) relative abundance value $\geq 3\%$ is preserved in the sediment.

2.1.3.6. *Fragilariopsis kerguelensis* (O'Meara) Hustedt

Fragilariopsis kerguelensis is considered endemic to Southern Ocean waters, dominating surface water assemblages of the POOZ south of the APF (Froneman *et al.*, 1995; Armand *et al.*, 2005), with its distribution extending as far north as the Subtropical Front (Hasle, 1976; Semina, 2003). It is most prevalent in waters with SSTs between 1° C and 8° C, with concentrations slowly declining toward temperatures of 19° C and dropping sharply beyond the extremes of 0° C and 20° C (Crosta *et al.*, 2005). *F. kerguelensis* is prevalent in the majority of Southern Ocean sediments, contributing up to 70% and 80% between the SSI edge and the APF (Abbott, 1973; Fenner *et al.*, 1976; DeFelice and Wise, 1981; Zielinski and Gersonde, 1997; Crosta *et al.*, 1998a; Crosta *et al.*, 2005) and is the primary component of

the diatom ooze belt underlying the ACC (Burckle and Cirilli, 1987). Highest abundances occur where summer open ocean conditions exist and little, if any, sea-ice occurs (Crosta *et al.*, 2005). Abundance within the phytoplankton is generally low around the Antarctic Coast, despite high concentrations in the sediments (Jouse' *et al.*, 1962; Kozlova, 1966; Truesdale and Kellogg, 1979; Gersonde, 1984; Gersonde and Wefer, 1987; Kellogg and Kellogg, 1987; Stockwell *et al.*, 1991; Leventer, 1992; Tanimura, 1992; Taylor *et al.*, 1997; Zielinski and Gersonde, 1997; Cunningham and Leventer, 1998). The *F. kerguelensis* frustule is heavily silicified, this characteristic has been used to explain concentrations of ~20% close to and north of the Subtropical Front, where it is preferentially preserved and protected from dissolution (Zielinski and Gersonde, 1997).

2.1.3.7. *Fragilariopsis obliquecostata* (Van Heurck) Heiden in Heiden et Kolbe

Fragilariopsis obliquecostata has been observed in both fast and pack-ice, is associated with perennial, SSI cover and high abundances have also been observed in surface melt pools and in the water column beneath sea-ice (Garrison *et al.*, 1983; 1987; Gersonde, 1984; Horner, 1985; Garrison and Buck, 1989; Tanimura *et al.*, 1990; Garrison, 1991). High abundances (10.2% in the surface sediments of the Ross Sea region) are linked to the SIZ, with a maximum abundance just north of the maximum SSI extent (Armand *et al.*, 2005). *F. obliquecostata* occupies waters with a SST range of -2°C to 0.5°C , with optimal growth at -1.5°C (Leventer, 1998; Cunningham and Leventer, 1998; Gersonde and Zielinski, 2000). Gersonde and Zielinski (2000) propose that the combination of a drop in the rate of biogenic sedimentation and the presence of *F. obliquecostata* at relative abundances in excess of 3% can be employed as a proxy for perennial SSI cover.

2.1.3.8. *Fragilariopsis ritscheri* Hustedt

Fragilariopsis ritscheri is observed at low abundances (~3%) within the sea-ice environment, identified in surface melt pools and fast and pack-ice samples. Highest abundances are associated with consolidated sea-ice conditions during winter, with the highest reported abundance (3.28%) from the Ross Sea (Cunningham and Leventer, 1998). High abundances are associated with SSTs of 0°C to 3°C and a widely varying annual sea-ice duration of 2 to 10.5 months (Zielinski and Gersonde, 1997; Armand *et al.*, 2005). Higher abundances have been identified in the adjacent water column than in the ice (Gersonde, 1984; Garrison *et al.*, 1983, 1987), leading to speculation that the species prefers melt water conditions (Armand *et*

al., 2005). Low sedimentary concentrations have been observed in all regions of the Southern Ocean, from near-shore coastal environments to beyond the SAF (47° S to 77° S), however, beyond the SIZ, occurrences are linked to ice rafting and bottom water transport (Armand, 1997).

2.1.3.9. *Fragilariopsis separanda* Hustedt

Fragilariopsis separanda has been described as a sea-ice species, although never identified within sea-ice samples (Armand *et al.*, 2005). Maximum abundances are generally associated with the Antarctic coast, with a relative abundance of 6.9% from surface sediment samples (Armand *et al.*, 2005). However, it has been observed throughout the Southern Ocean, beyond the WSI limit and occasionally north of the APF (DeFelice and Wise, 1981; Gersonde and Wefer, 1987; Stockwell *et al.*, 1991; Leventer, 1992; Zielinski and Gersonde, 1997; Armand *et al.*, 2005) and may be easily transported by bottom water currents. Highest abundances are reported in surface sediments beneath SSTs of -0.5° C to 0° C, although abundances in the region of ~2% have been identified within the broad range of -18° C to 8° C. This wide temperature range is presumably related to the observed wide dispersion of the species. Sea-ice conditions in regions of maximum abundance are generally highly consolidated during the winter, with coverage lasting 4.5 to 9 months per year (Armand *et al.*, 2005).

2.1.3.10. *Hyalochaete Chaetoceros* resting spores (*Chaetoceros* rs)

The *Chaetoceros* genus is divided into two subgenera; *Phaeceros* and *Hyalochaete*. One of the primary differences between these subgenera is the ability to produce resting spores; whereas most species of the subgenus *Hyalochaete* produce resting spores, only one species of the subgenus *Phaeceros* has the ability (*Chaetoceros eibonii* Grunow in Van Heurck) (Stockwell and Hargraves, 1984; Tomas, 1997). These resting spores dominate many diatom assemblages in sediments, posing a variety of problems for diatom taxonomy and statistical approaches (Crosta *et al.*, 1997). The association of resting spores with their parent vegetative cells employing Scanning Electron Microscope identification has been attempted but with little success (Hargraves, 1979; Stockwell and Hargraves, 1984; Leventer *et al.*, 1993). *Chaetoceros* resting spores (*Chaetoceros* rs) reach very high abundances in near-shore environments and have been related to high productivity events, with highest abundances noted in the sediments of Bransfield Strait in the Antarctic Peninsula, the South Orkney Plateau region and the Ross Sea (Leventer, 1991; Crosta *et al.*, 1997).

Armand *et al.* (2005) observed maximum *Chaetoceros* rs abundances of 91.8% in association with SSTs between -0.5°C and 1.5°C , and with sea-ice, with abundances of 80% coeval with consolidated WSI and an optimum coverage of 7 months per year (Armand *et al.*, 2005). *Chaetoceros* rs exhibit a circumpolar distribution in the sediments, with highest abundances (~20%) in the Antarctic Peninsula and the Ross Sea. Beyond the coastal zone, *Chaetoceros* rs abundance in the sediments is generally low. Abundances between 0 and 20% have been observed north of the WSI edge, decreasing to between 0% and 5% in the POOZ, with the exception of the Crozet-Kerguelen islands where concentrations reach ~20%. North of the APF *Chaetoceros* rs abundance varies between 0% and 10% (Zielinski, 1993; Armand *et al.*, 2005). *Chaetoceros* rs are generally present at quantities of less than 5% in the SAZ, apart from the Argentine Basin and Falkland Plateau where higher abundances have been observed (Zielinski and Gersonde, 1997; Allen *et al.*, 2005). Bottom water entrainment and eastward displacement by the ACC are thought to be the primary mechanisms responsible for producing concentrations north of the WSI limit (Armand *et al.*, 2005). Although *Chaetoceros* rs ecological associations are poorly understood, the influence of nutrient-rich waters is important to their distribution (Leventer, 1991; Sancetta *et al.*, 1992; Karpuz and Jansen, 1992; Zielinski and Gersonde, 1997). They are also abundant in the MIZ and its characteristic highly fertile stratified surface waters (Leventer *et al.*, 1993; Leventer *et al.*, 1996). *Chaetoceros* resting spore formation has also been associated with nutrient exhaustion in the water column following upwelling events (Bao *et al.*, 1997; Ettwein *et al.*, 2001; Giunta *et al.*, 2006) and as a result *Chaetoceros* resting spores have been shown to provide a record of palaeoupwelling regimes (Leventer, 1991; Rathburn *et al.*, 1997).

2.1.3.11. *Porosira glacialis* (Grunow) Jørgensen

Porosira glacialis has been observed at low relative abundances (~2%) within waters adjacent to sea-ice, characterized by SSTs of -1.3°C to 2°C , and with an optimal temperature range of 0°C to 0.5°C . *P. glacialis* has been identified in sediments at concentrations of <1 to ~6% (Prasad and Nienow, 1986; Kellogg and Kellogg, 1987; Stockwell *et al.*, 1991; Leventer, 1992; Taylor *et al.*, 1997; Cunningham and Leventer, 1998; Armand *et al.*, 2005). *P. glacialis* is found in sediments that are generally associated with at least 7.5 months per year of sea-ice cover overhead, ranging between MIZ to ice-free in summer and highly compacted during the winter (Armand *et al.*, 2005).

2.1.3.12. *Rhizosolenia* spp.

Rhizosolenia spp. are often difficult to accurately identify within the sediments as remains are usually fragmented. Crosta *et al.* (2005) separated *Rhizosolenia* into two groups based on the morphology of the valve apices. (1) The ‘pointed group’ consists of those species with pointed otaria, including *R. styliformis*, *R. antennata* var. *antennata* and *R. antennata* var. *semispina*, with the latter being the most common variety in the Southern Ocean. Crosta *et al.* (2005) observed the highest abundances of the pointed group just north of the WSI edge, with SSTs of 1° C to 2° C. Occurrence within the sediments is associated with unconsolidated sea-ice conditions during winter and open ocean conditions in the summer. In the Atlantic sector of the Southern Ocean the genus has been interpreted as an indicator of increased out-flow of ice-free Weddell Sea waters (Allen *et al.*, 2005). (2) The ‘rounded group’ consists of those species with rounded otaria, including *R. curvata*, *R. crassa* and *R. polydactyla* var. *polydactyla* with the latter being the most widely distributed. This group is closely associated with the POOZ and APFZ. Crosta *et al.* (2005) observe maximum abundances within the POOZ, between the temperatures 9.5° C to 14.5° C.

In my study, individual *Rhizosolenia* species and species groups do not appear in quantities significant enough to include in the statistical analyses (i.e. >0.5%), however, as common factors in their ecologies reflect frontal stability and freshwater intrusions all identified valves have been combined into the group *Rhizosolenia* spp., which is included in the analysis. The group *Rhizosolenia* spp. represents an ecological association ranging from the WSI edge to the APF.

2.1.3.13. *Thalassiosira antarctica* Comber

Thalassiosira antarctica is observed in both fast and pack-ice, as well as in the water column below and adjacent to the ice (Cassei, 1963; Krebs *et al.*, 1987; Garrison *et al.*, 1987; Garrison, 1991). It is observed in areas of unconsolidated sea-ice during the summer and consolidated sea-ice during the winter. Relative abundances of more than 10% (in surface sediments) have been linked to sea-ice duration in excess of 6 months per year (Armand *et al.*, 2005). *T. antarctica* occurs almost exclusively south of the maximum WSI edge, although sporadic occurrences have been observed in the South Atlantic and Indian sectors (Ligowski, 1993; Zielinski and Gersonde, 1997) and observations within the SAZ have been related to AABW transport (Zielinski and Gersonde, 1997). Armand *et al.* (2005) report a maximum relative abundance of 31.8% from surface sediments associated with SSTs between 0° C and 0.5° C. High sediment abundances within the sediments have been

documented in the coastal sections of the Weddell (32%) and Ross (31%) Seas (Zielinski and Gersonde, 1997; Cunningham and Leventer, 1998).

T. antarctica has been noted to include both a warm and cold water form, which are morphologically distinct (Villareal and Fryxell, 1983) in terms of process size and valve diameter (Bak *et al.*, 2007). The cold water form is considered indicative of cooler environments that experience greater sea-ice influence, at times demonstrating a coincident distribution with *Fragilariopsis curta* (Taylor *et al.*, 2001; Taylor and Sjunneskog, 2002; Buffen *et al.*, 2007). In contrast, the warmer water form shows a distribution coincident with *Chaetoceros* subgenus *Hyalochaete* spp., suggesting the indication of more open water productivity and reduced sea-ice influence (Taylor *et al.*, 2001; Taylor and Sjunneskog, 2002; Buffen *et al.*, 2007).

2.1.3.14. *Thalassiosira gracilis* group (Karsten) Hustedt

Thalassiosira gracilis var. *gracilis* and *Thalassiosira gracilis* var. *expecta* are growth stages of the same species and individual identification can be ambiguous (Fryxell, 1994). I have therefore combined the two varieties into a single *Thalassiosira gracilis* group. Although it has been shown to be widespread, the *Thalassiosira gracilis* group is considered an indicator of cooler temperatures and sea-ice presence (Armand *et al.*, 2005), however, Zielinski and Gersonde (1997) believe the group exhibits no environmental preference. Crosta *et al.* (2005) noted increasing abundances of the group approaching the region of maximum WSI extent and the Antarctic coast. The group has been observed north of the APF, albeit at low levels (Crosta *et al.*, 2005). Optimal growth conditions are related to SSTs between 1° C and 2° C, with decreasing abundance observed as temperatures climb towards ~8° C. Increasing occurrence is also related to increasing sea-ice duration, to a maximum of 8.5 months per year, however, prolonged duration results in reduced abundance (Crosta *et al.*, 2005). During the summer months the group favours open ocean conditions, although a slight increase in abundance, associated with fully consolidated sea-ice during winter, is noted (Crosta *et al.*, 2005). The *T. gracilis* group appears in low abundances in the sediments, reaching a maximum of 3% in the study by Crosta *et al.* (2005) and is generally reported as low abundance in the region of the ACC (Jouse' *et al.*, 1962; Kozlova, 1966; Abbott, 1973; Donahue, 1973; DeFelice and Wise, 1981). Abundances are less than 2% at the coast (Truesdale and Kellogg, 1979; Prasad and Nienow, 1986; Gersonde, 1984; Gersonde and Wefer, 1987; Kellogg and Kellogg, 1987; Stockwell *et al.*, 1991; Tanimura, 1992; Leventer, 1992; Taylor *et al.*, 1997; Cunningham and Leventer, 1998).

2.1.3.15. *Thalassiosira lentiginosa* (Janisch) Fryxell

Thalassiosira lentiginosa is widespread throughout the Southern Ocean with high abundances observed from the maximum WSI limit to the SAF, and low abundances reported from the Antarctic continental shelf. This widespread occurrence has led to uncertainty about its true distribution and ecological association. Maximum abundance of 30% occurs in surface sediments associated with SSTs of 1° C to 8° C, with levels steadily declining to very low abundance above 18° C and below 1° C. It exhibits an inverse relationship with sea-ice cover, preferring open ocean conditions during the summer, although appearing in regions associated with reasonably consolidated sea-ice in the winter (Crosta *et al.*, 2005). *T. lentiginosa* is well-preserved and abundant in sediments due to its resistance to dissolution. It is most commonly found in sediments under the POOZ and APFZ (Jouse' *et al.*, 1962; Kozlova, 1966; Kozlova and Mukhina, 1967; Abbott, 1973; Donahue, 1973; Fenner *et al.*, 1976; DeFelice and Wise, 1981; Zielinski and Gersonde, 1997; Crosta *et al.*, 1998a; Armand *et al.*, 2005) and abundances between 10% and 17% have also been reported north of the APFZ (Jouse' *et al.*, 1962; Kozlova, 1966; Abbott, 1973; Schuette and Schrader, 1981).

2.1.3.16. *Thalassiosira scotia* Fryxell and Hoban

Thalassiosira scotia vegetative cells exhibit similar characteristics to the *Thalassiosira antarctica* warm form resting cells and cannot be distinguished from one another based on light microscopy. This close affinity has introduced problems associated with taxonomic identification and consequently many authors have combined the two taxon under *T. antarctica*, citing *T. scotia* as a local warm water variety of *T. antarctica* (Zielinski, 1993; Armand *et al.*, 1997; Zielinski and Gersonde, 1997; Armand *et al.*, 2005). *T. scotia* has only been identified in the South Atlantic, primarily the Scotia Sea and Argentine Basin (Ligowski, 1993; Zielinski and Gersonde, 1997).

2.1.3.17. *Thalassiothrix antarctica* Schimper ex Karsten

Thalassiothrix antarctica is primarily associated with the POOZ and the APFZ. Maximum abundances occur in surface waters south of the APF (Eynaud *et al.*, 1999). The WSI edge generally represents the southern limit of occurrence and the SAF the northern limit, although occasional *Thalassiothrix antarctica* have been noted beyond both of these boundaries (Crosta *et al.*, 2005). Presently, optimal temperatures for maximum growth are cited between 1° C and 3° C, with abundance declining toward warmer temperatures (Crosta *et al.*, 2005). Zielinski and Gersonde (1997) observed a maximum sediment abundance of 9%, beneath a

SST range 2.5° C to 6° C, in the South Atlantic sector. *Thalassiothrix antarctica* exhibits an inverse relationship with sea-ice cover, consistently decreasing in abundance with increasing proximity to both the SSI and WSI edge (Crosta *et al.*, 2005). Although typical of the POOZ and APFZ, the distribution of *Thalassiothrix antarctica* in surface sediments is widespread. This indicates preferential preservation and transport by ocean currents (DeFelice and Wise, 1981; van Iperen *et al.*, 1987; Zielinski, 1993; Zielinski and Gersonde, 1997; Crosta *et al.*, 1998a).

2.2. Highly Branched Isoprenoids as Palaeoindicators of Climate Change

To date, the majority of Antarctic glacial sea-ice reconstructions employ the identification of preserved frustules of diatoms and sediment facies as the primary proxies (Crosta *et al.*, 1998; Gersonde and Zielinski *et al.*, 2000; Gersonde *et al.*, 2003; Gersonde *et al.*, 2005). However, many of the diatom taxa associated with sea-ice are often characterized by light silicification and are subject to dissolution in the water column during transit to the sediments of the sea floor. This results in poor preservation and makes unambiguous identification of the fossil diatoms difficult, which can in turn lead to inconclusive reconstructions of the sea-ice edge. It is therefore widely agreed that additional, complimentary sea-ice proxies are desirable (Crosta *et al.*, 2005; Gersonde *et al.*, 2005).

Recent studies have demonstrated that some unsaturated hydrocarbon compounds, also called Highly Branched Isoprenoids (HBIs), identified in ocean floor sediments are biosynthesised by a limited number of diatom genera, including *Haslea*, *Rhizosolenia*, *Pleurosigma* and *Navicula* (Rowland and Robson, 1994; Volkmann *et al.*, 1994; Belt *et al.*, 2000) and most likely produced in diatom chloroplasts (Massé *et al.*, 2004). Laboratory culture experiments have demonstrated that, for the diatom *Haslea ostrearia* (Gaillon) Simonsen, the extent of the HBI unsaturation co-varies with temperature. This co-variation results in a divergent production of the major isomers, with triene preferentially produced at temperatures of 25° C and 15° C and the production of diene at lower temperatures of 5° C (Rowland *et al.*, 2001).

A comprehensive study in the Candian High Arctic has demonstrated that a mono-unsaturated HBI isomer (IP₂₅) can be used as a stable and sensitive proxy for past sea-ice presence (Belt *et al.*, 2007). The unique isometric nature of the compound, its presence within the sea-ice, absence from the open water phytoplankton assemblages (Belt *et al.*, 2007) and its enriched $\delta^{13}\text{C}$ values (Belt *et al.*, 2008) supports the specificity of the biomarker to the sea-ice environment. This proxy has recently been measured in a sediment core recovered

from the North Icelandic Shelf, in the successful reconstruction of an uninterrupted high-resolution record of sea-ice during the last millennium (Massé *et al.*, 2008). Massé *et al.* (2008) demonstrate strong correlations between the HBI proxy and up to three complimentary proxies, demonstrating both its robustness and usefulness in reconstructing past sea-ice extent.

Although tried and to some degree tested in the Arctic, Antarctic studies are very much in their infancy. A number of studies have reported di-unsaturated HBI isomers within Antarctic sediments and sea-ice diatoms (Nichols *et al.*, 1993; Venkatesan, 1988), but have failed to fully identify them. More recently, through the use of and NRM analyses, Johns *et al.* (1999) have confirmed the identity of a diene, extracted from sedimentary samples from McMurdo Sound (East Antarctica), as the same as that produced in laboratory cultures of the diatom *Haslea ostrearia*. The authors were however unable to confirm the identity of the diene extracted from the sea-ice diatom matrix. A more recent study of Ellis Fjord (East Antarctica) identified the genus *Navicula* as the most likely phytoplankton source of the HBI diene found in the sediments (Sinninghe-Damsté *et al.*, 2007). This is supported by DNA data from a parallel study (Coolen *et al.*, 2007). However, *Navicula glacei* is the most abundant taxa in this genus associated with the sea-ice matrix, and other authors have failed to reproduce the sea-ice HBI diene from laboratory cultures of this diatom (G. Massé Pers. Com.).

Most recently, having analysed the hydrocarbon composition of sea-ice, phytoplankton and sediment samples collected from a wide range of Antarctic locations, Massé *et al.* (in prep.) report the presence of a unique di-unsaturated HBI isomer in all the sea-ice samples. By comparison of its retention time and mass spectral characteristics with authentic standards, they confirmed that this isomer was identical to the one reported in previous studies (Nichols *et al.*, 1993; Venkatesan, 1988; Johns *et al.*, 1999; Sinninghe-Damsté *et al.*, 2007). They also reported that this diene was absent in the phytoplankton assemblages and replaced by a suite of more un-saturated isomers previously observed in *Rhizosolenia* and *Pleurosigma* species. In addition GC-IRMS analyses have confirmed that as for IP₂₅ in the Arctic, the sea-ice diene is also heavily enriched in ¹³C ($-15\text{‰} < \delta^{13}\text{C} < -5\text{‰}$) compared to the isomers synthesised in open water conditions ($-30\text{‰} < \delta^{13}\text{C} < -40\text{‰}$). Analysis of the surface sediments revealed the presence of HBI isomers including the sea-ice diene, thus supporting its potential as a circum-Antarctic proxy for sea-ice reconstruction.

Presently the few studies that have employed this new proxy, at either pole, have been restricted to the Holocene. No study has attempted to use this proxy on Late Quaternary

Chapter 2. Major Proxies Employed in this Study

sediments and some potential caveats are to be considered when using this proxy for such studies. Like all organic matter these HBI hydrocarbon compounds are subject to diagenesis and can degrade over time. Although these dienes are known to undergo little diagenetic reaction in comparison to the more unsaturated HBIs (Belt *et al.*, 2001) this degradation potential must still be taken into consideration. In addition, although Johns *et al.* (1999) reported large concentrations of the diene in laboratory cultures of the diatom *Haslea otrearia*, the origin of this HBI isomer has yet to be confirmed.

3. Materials and Methods

3.1. Core Material

This study focuses on three deep-sea sediment piston cores, chosen for their locations and sedimentation rates to provide a high-resolution representation of the last glacial cycle (LGC) in Antarctica. Two of these cores, TPC063 and TPC286, were recovered from the Scotia Sea. The third core, MD03-2603, was recovered adjacent to the Adélie Land Coast (Figure 3.1, Table 3.1). This study examines these marine records for proxies of climate variability, reconstructs glacial palaeoceanographic conditions, compares and contrasts the glacial environments of West and East Antarctica, and relates these to palaeorecords of global climate.

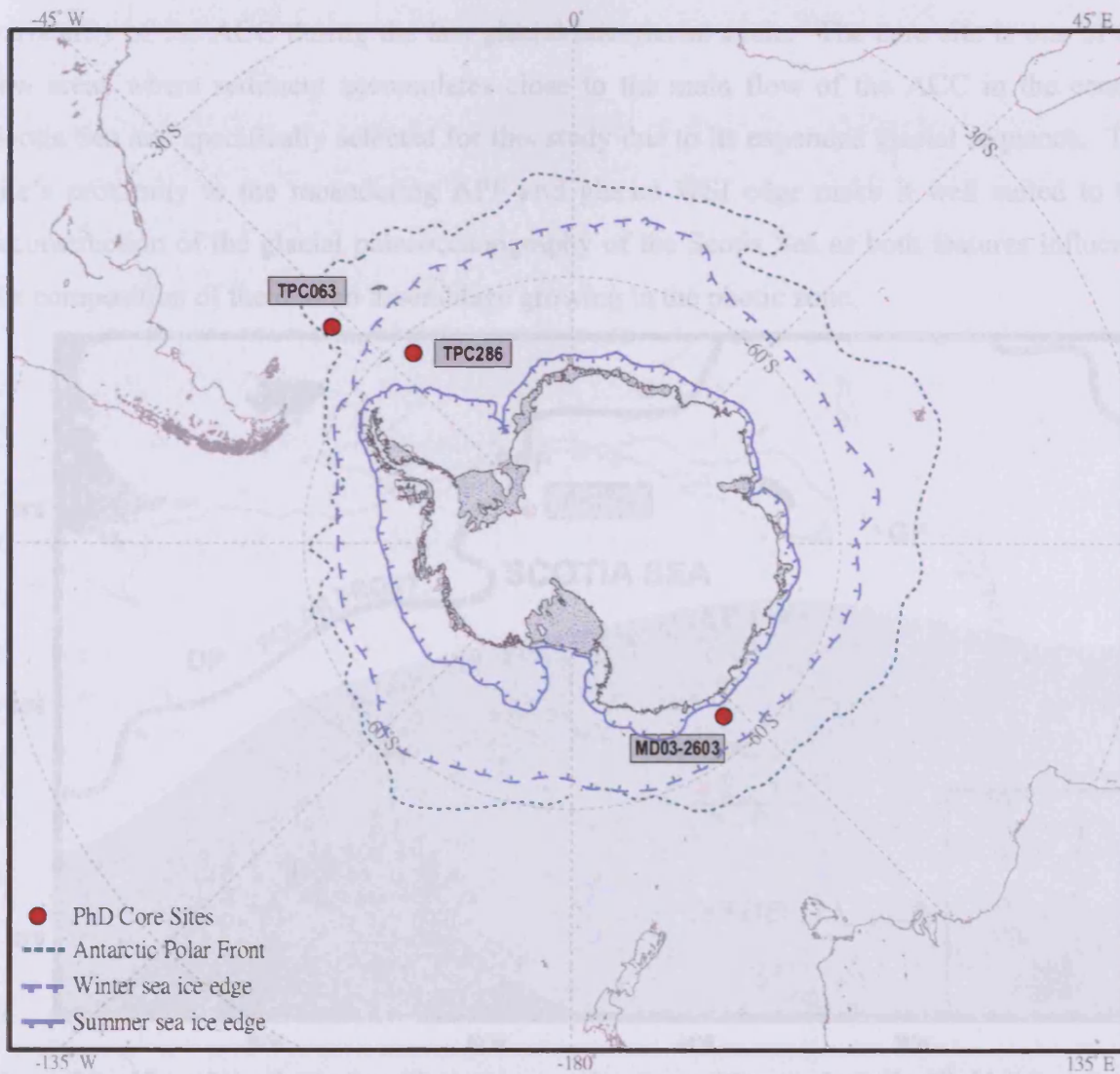


Figure 3.1. Map illustrating the locations of core sites employed in this study with regards to the Antarctic continent, Antarctic Polar Front (APF) and seasonal sea-ice limits. Cores TPC063 and TPC286

were recovered from within the Scotia Sea basin, south of the modern-day Antarctic polar front and either-side of the modern-day winter sea-ice limit, whereas core MD02-2603 was cored off the Adélie Land Coast, south of both the modern-day APF and winter sea-ice edge.

Table 3.1. Cores TPC063, TPC286 and MD03-2603: Location of cores.

Core	Latitude	Longitude	Water depth (m)	Core length (m)
TPC063	53° 56' 0" S	48° 02' 6" W	3956	7.7
TPC286	61° 47' 3" S	40° 08' 3" W	3467	9.35
MD03-2603	64° 17' 12" S	139° 22' 51" E	3290	32

3.1.1. TPC063

TPC063 was recovered in 1993 on cruise JR04 aboard the RRS *James Clark Ross* from the northern Scotia Sea, just south of the North Scotia Ridge and Shag Rocks Passage (56° 56' 0" S, 48° 02' 6" W) (Figure 3.2). The core site is presently in close proximity to the primary axis of the Antarctic Circumpolar Current (ACC), the Antarctic Polar Front (APF) and lies to the north of the modern winter sea-ice (WSI) limit. TPC063 was recovered to examine the variability of the ACC during the last glacial/interglacial cycle. The core site is one of the few areas where sediment accumulates close to the main flow of the ACC in the central Scotia Sea and specifically selected for this study due to its expanded glacial sequence. The site's proximity to the meandering APF and glacial WSI edge make it well suited to the reconstruction of the glacial palaeoceanography of the Scotia Sea as both features influence the composition of the diatom assemblage growing in the photic zone.

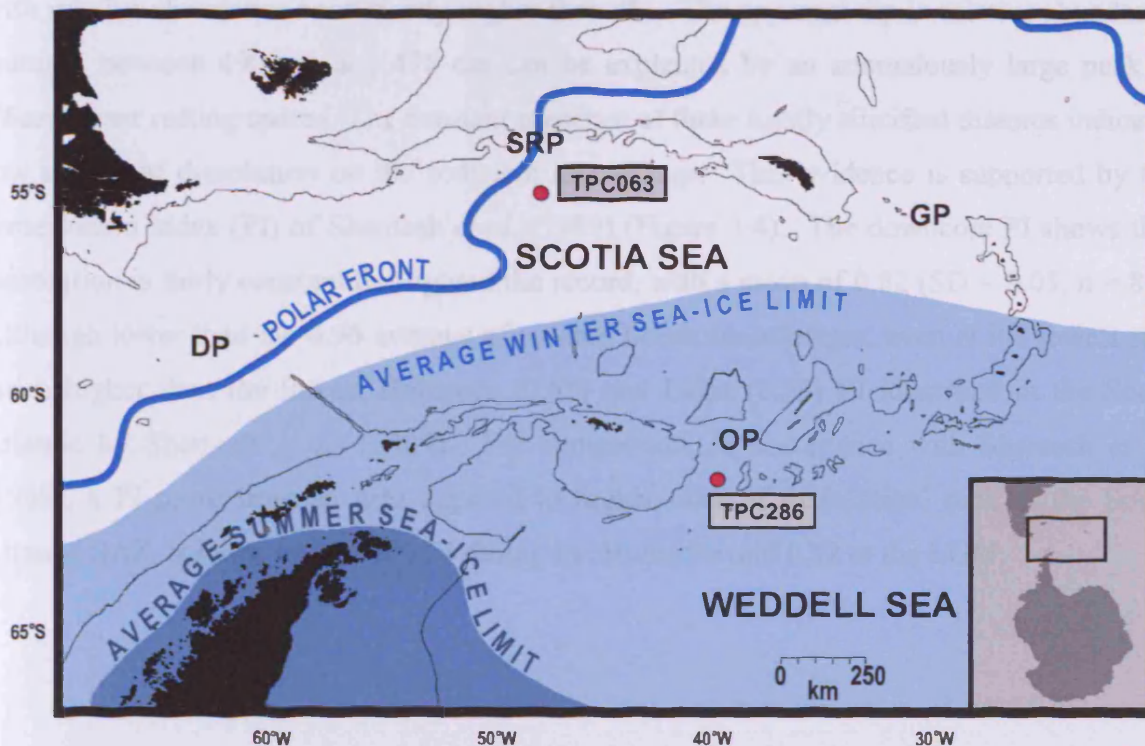


Figure 3.2. Map of the Scotia Sea, illustrating core locations with regards to the Weddell Sea, Scotia Ridge, Antarctic Polar Front, and seasonal sea-ice limits. The 2000 m contour is also shown to provide an impression of the main bathymetric features of the region.

TPC063 was recovered using a piston corer composed of trigger core barrel and piston core barrel. The trigger corer is deployed first and its contact with the seafloor triggers the release of the much larger piston corer. The greater mass and impact velocity of the piston core barrel can often result in the false expansion/compaction of surface sediments due to changes in sediment densities. In contrast, the much smaller and lighter trigger core generally maintains a more complete surface sediment record, with compaction or expansion minimal, however, the trigger core barrel can occasionally ‘bounce’ and repenetrate the seafloor, resulting in the recovery of duplicate surface sediments.

The piston core (PC063) and trigger core (TC063) recovered 656 cm and 151 cm of sediment, respectively (Table 3.2). Based on sediment logs and MS curves (Figure 3.3), ~50 cm of sediment has been lost from the surface of PC063. In order to examine as complete a sediment record as possible, TC063 and PC063 were aligned via changes evident in the sediment lithology and MS curves, resulting in a composite record (TPC063) 707 cm in length (Table 3.2, Figure 3.3).

The following section summarises the potential impact of dissolution on the diatom assemblages identified in the sediments of core TPC063. The combined relative abundance of diatoms most susceptible to complete dissolution (Chapter 2) (Pichon *et al.*, 1992) is plotted in Figure 3.4. The trend does not show a great deal of variation throughout the record with relative abundance consistently higher than 4%. The apparent dip in relative abundance featured between 490 cm and 478 cm can be explained by an anomalously large peak in *Chaetoceros* resting spores. The constant presence of these lightly silicified diatoms indicates low effects of dissolution on the sediment assemblage. This evidence is supported by the preservation index (PI) of Shemesh *et al.* (1989) (Figure 3.4). The downcore PI shows that dissolution is fairly constant throughout the record, with a mean of 0.82 (SD = 0.05, n = 85). Although lower than the 0.96 average of modern ocean assemblages, even at its lowest it is much higher than the lowest Holocene (0.55) and LGM (0.33) PI identified in the South Atlantic by Shemesh *et al.* (1989). For comparison, in accordance with Shemesh *et al.* (1989), a PI score from an area exposed to higher rates of dissolution, such as the South Atlantic SAZ, is in the region of 0.55 during the Holocene and 0.52 at the LGM.

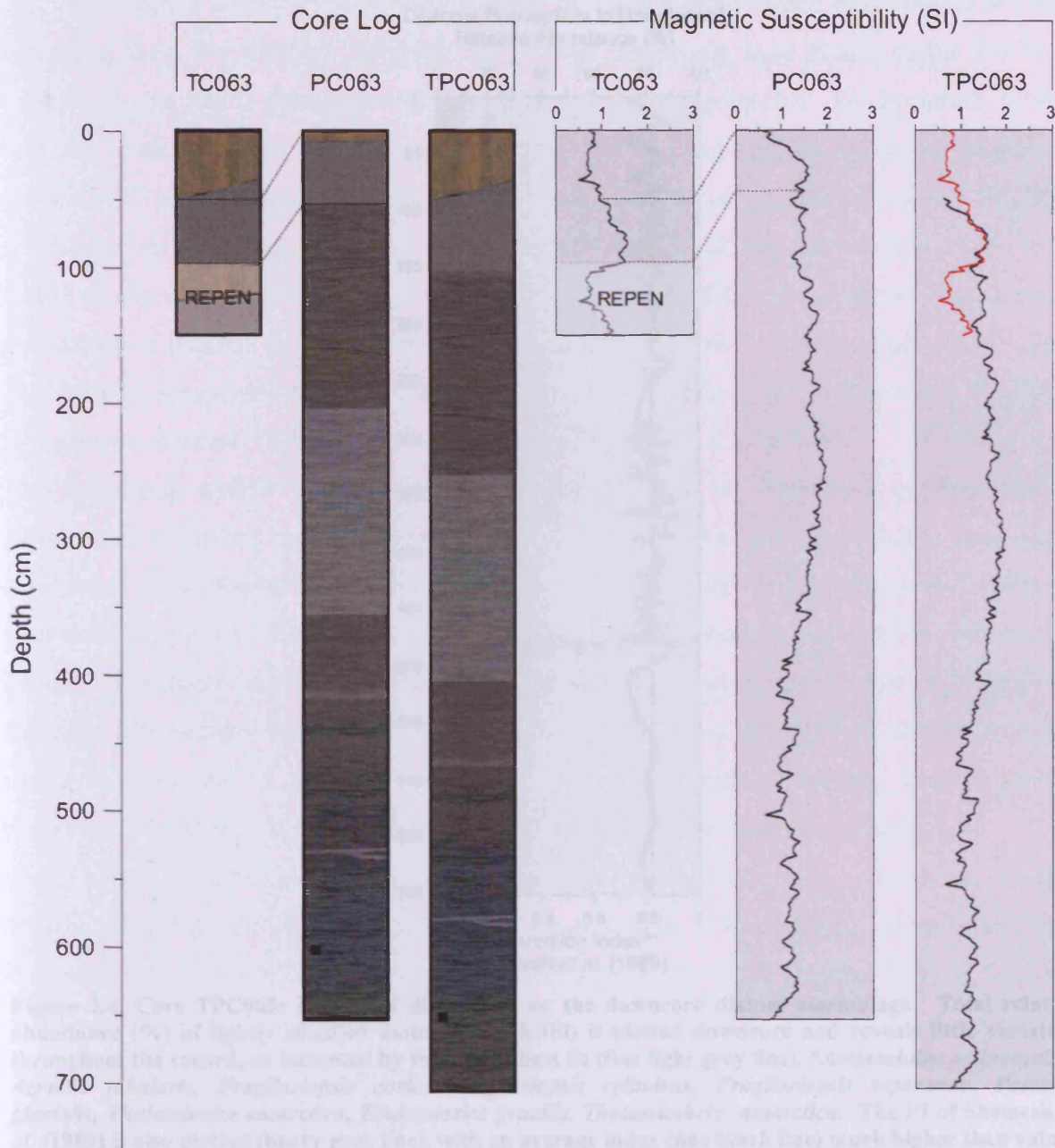


Figure 3.3. Core TPC063: Sediment logs and magnetic susceptibility records for trigger and piston core components. Trigger (TC) and piston core (PC) records were spliced (TPC) based on correlative features. Original ship-board core logs were recreated in a graphics package and Munsell colours were converted into a RGB format. The faded portion of the TC063 records labelled 'REPEN' indicate repenetration of the sediments. The TPC063 MS plot shows the TC record (red line) spliced with the PC record (black line).

Table 3.2. Core TPC063: Core components.

Core	Number of sections	Length (cm)
TC063 (Trigger Core)	1	151
PC063 (Piston Core)	5	656
TPC063 (Core composite)	6	707

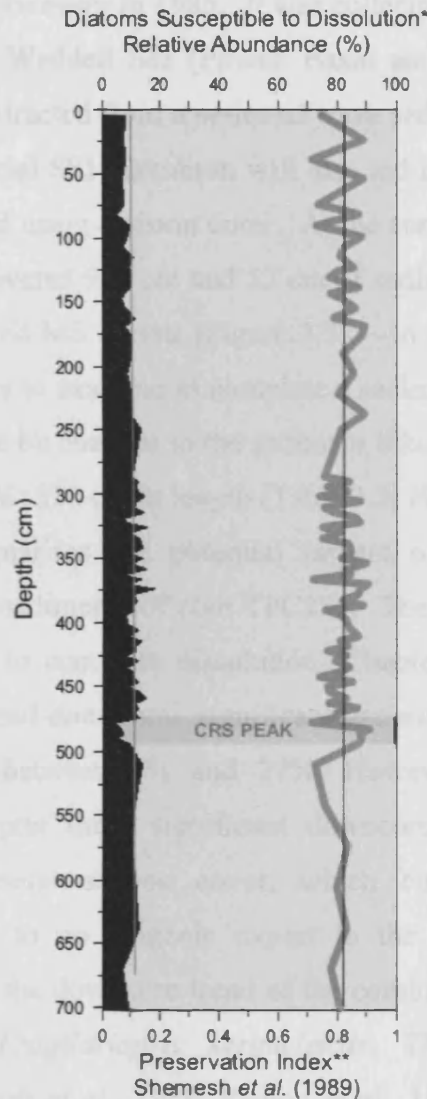


Figure 3.4. Core TPC063: Effects of dissolution on the downcore diatom assemblage. Total relative abundance (%) of lightly silicified diatoms (black fill) is plotted downcore and reveals little variation throughout the record, as indicated by the line of best fit (fine light grey line). **Actinocyclus actinocylus*, *Azpeitia tabularis*, *Fragilariopsis curta*, *Fragilariopsis cylindrus*, *Fragilariopsis separanda*, *Porosira glacialis*, *Thalassiosira antarctica*, *Thalassiosira gracilis*, *Thalassiothrix antarctica*. The PI of Shemesh *et al.* (1989) is also plotted (heavy grey line), with an average index (fine black line) much higher than values found in areas of high dissolution such as the SubAntarctic Zone (SAZ). ***Fragilariopsis kerguelensis*/ (*Fragilariopsis kerguelensis* + *Thalassiosira lentiginosa*).

3.1.2. TPC286

Sediment core TPC286 was recovered in 2002 on cruise JR48 aboard the RRS *James Clarke Ross* from a sediment drift on the southern flank of the South Scotia Ridge (SSR) (61° 47' 3" S, 40° 08' 3" W), a series of discontinuous ridges that segregates the Weddell and Scotia Seas. This core site is, at present, exposed to the seasonal encroachment of WSI, with the summer sea-ice (SSI) limit stationed to the south and is positioned beneath a region of complex oceanography where the eastern limb of the Weddell Gyre reaches the Weddell – Scotia Confluence (WSC) (Figure 3.2). Core TPC286 was a repeat of core GC027, originally

recovered aboard the vessel *Discovery* in 1985. It was collected as part of a transect of cores extending from the northern Weddell Sea (Powell Basin and Jane Basin) to the Falkland Trough, via the Scotia Sea, extracted from a series of wave sediments. The proximity of this core site to the estimated glacial SSI maximum will also aid in the glacial reconstruction of sea-ice. TPC286 was recovered using a piston corer. At the core site, the piston core (PC286) and trigger core (TC286) recovered 914 cm and 53 cm of sediment, respectively (Table 3.3). Based on the sediment logs and MS curves (Figure 3.5), ~16 cm of sediment was lost from the surface of PC286. In order to examine as complete a sediment record as possible, TC286 and PC286 were aligned based on changes in the sediment lithology and MS curves, resulting in a composite record (TPC286) 930 cm in length (Table 3.3, Figure 3.5).

The following section summarises the potential impact of dissolution on the diatom assemblages identified in the sediments of core TPC286. The combined relative abundance of diatoms most susceptible to complete dissolution (Chapter 2) (Pichon *et al.*, 1992) is plotted in Figure 3.6. The trend does show significant variation throughout the record with relative abundance varying between 0% and 27%. However, rather than evidence of enhanced dissolution I interpret these significant downcore changes as the product of repetitive episodes of perennial sea-ice cover, which curtail surface water primary production, resulting in low to no biogenic export to the underlying sediments. This interpretation is supported by the downcore trend of the combined relative abundance of the heavily silicified diatoms *Fragilariopsis kerguelensis*, *Thalassiosira lentiginosa* and *Eucampia antarctica* (Shemesh *et al.*, 1989; Pichon *et al.*, 1992) (Figure 3.6). If the low relative abundance of the diatoms susceptible to dissolution is indeed a product of enhanced dissolution we would expect the trends of the heavily and lightly silicified diatoms to mirror each other. However, in the samples where the relative abundance of the lightly silicified diatoms is anonymously low, the relative abundance of the heavily silicified diatoms are also low or 0%, indicating absence from the sediments.

The complete lack of these robustly silicified valves either indicates a dissolution environment significantly more corrosive than anything previously identified in Southern Ocean sediments, or it is evidence of an overlying ice barrier prohibiting primary production, for which there is president (Gersonde *et al.*, 2003, 2005; O'Cofaigh *et al.*, 2005). High relative abundance of lightly silicified valves outside of these low production periods and the enhanced relative abundance of the summer sea-ice proxy *Fragilariopsis obliquecostata*, at the culmination of these barren samples (Chapter 4), further supports the interpretation that perennial sea-ice cover is the primary control on the diatom assemblage and not dissolution.

The core coverage in the Shemesh *et al.* (1989) dissolution study did not penetrate as far south as 61°S in the South Atlantic Ocean, and has since been shown not to work in areas impacted by winter and summer sea-ice cover and thus cannot be applied to this core site.

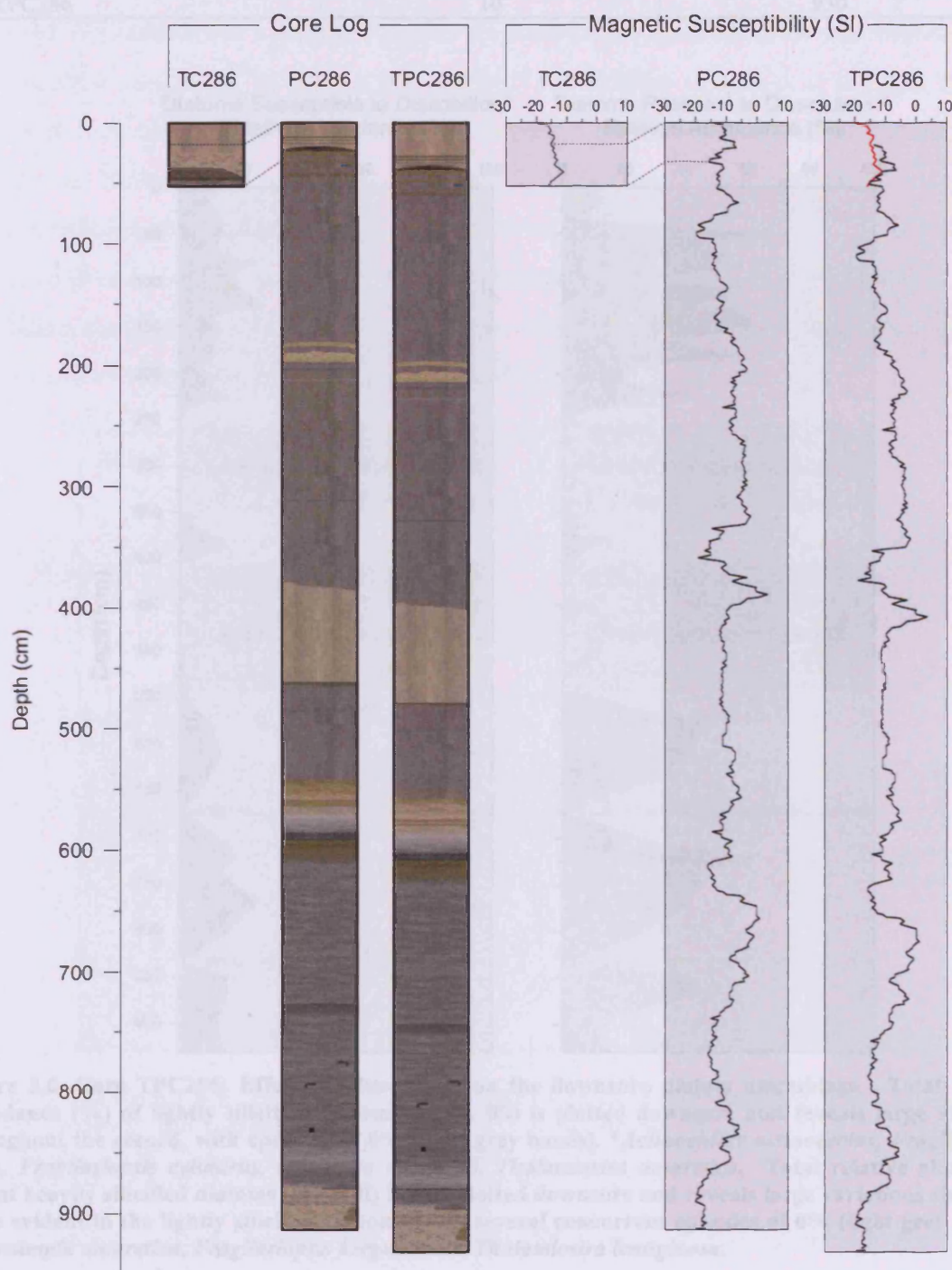


Figure 3.5. Core TPC286: Sediment logs and magnetic susceptibility records for trigger and piston components. Trigger (TC) and piston core (PC) records were spliced (TPC) based on correlative features. Original ship-board core logs were recreated in a graphics package and Munsell colours were converted into a RGB format. The TPC286 MS plot shows the TC record (red line) spliced with the PC record (black line).

Table 3.3. Core TPC286: Core components.

Core	Number of sections	Length (cm)
TC286	1	53
PC286	9	914
TPC286	10	930

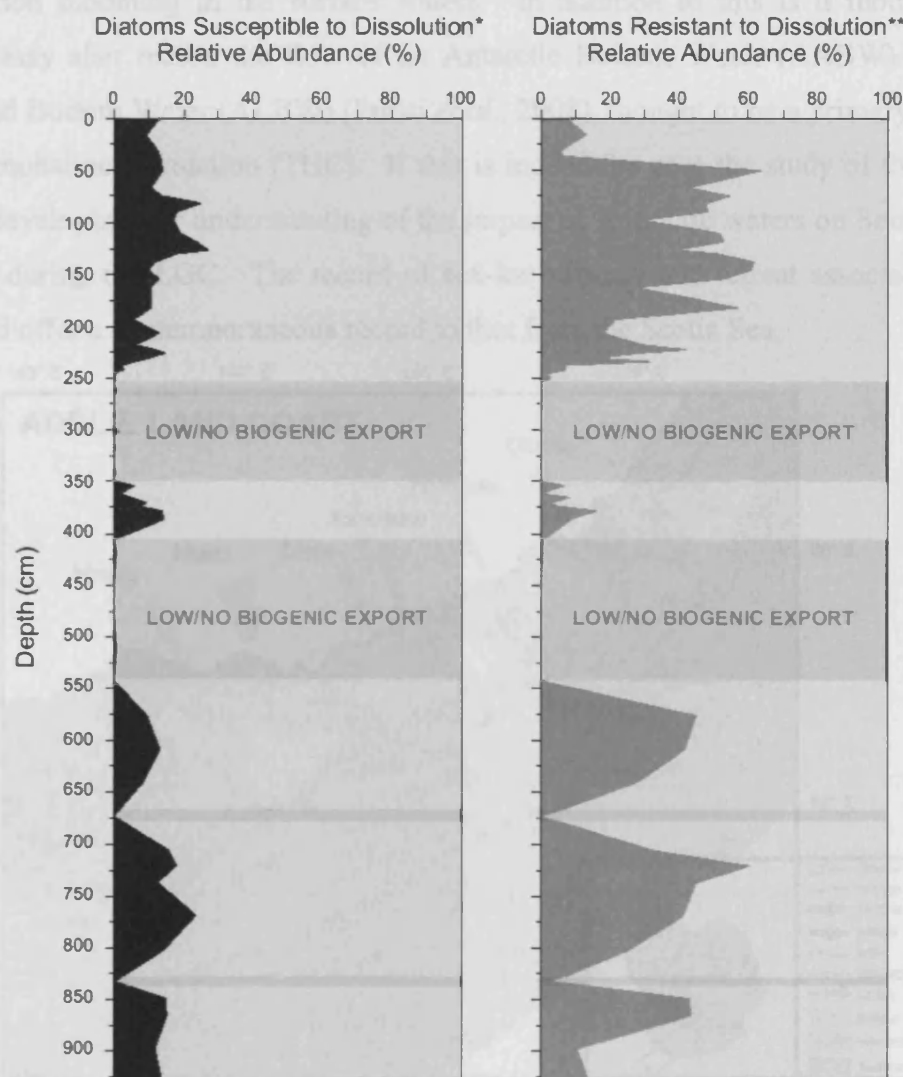


Figure 3.6. Core TPC286: Effects of dissolution on the downcore diatom assemblage. Total relative abundance (%) of lightly silicified diatoms (black fill) is plotted downcore and reveals large variation throughout the record, with episodes of 0% (light grey bands). **Actinochilus actinocyclus*, *Fragilariopsis curta*, *Fragilariopsis cylindrus*, *Odontella weisflogii*, *Thalassiosira antarctica*. Total relative abundance (%) of heavily silicified diatoms (grey fill) is also plotted downcore and reveals large variations similar to those evident in the lightly silicified diatoms, with several concurrent episodes of 0% (light grey bands). ***Eucampia antarctica*, *Fragilariopsis kerguelensis*, *Thalassiosira lentiginosa*.

3.1.3. MD03-2603

Sediment core MD03-2603 was recovered using the Calypso piston corer in 2003 during the IMAGES X-CADO research cruise aboard the *Marion Dufrense* from the continental margin of the Adélie Land Coast, East Antarctica (64° 17' 12" S, 139° 22' 51" E) (Figure 3.7), at a

site characterized by a series of canyons and mounds. The site was targeted due to its position at the seaward termination of the largest, marine-based sector (Wilkes Basin) of the East Antarctic Ice Sheet (EAIS). The site is at present influenced by the annual growth and retreat of WSI associated with the marginal ice zone (MIZ), and the associated deposition of phytoplankton blooming in the surface waters. In addition to this is it thought that the sediments may also record the flow of an Antarctic Bottom Water (AABW) component, Adélie Land Bottom Water (ALBW) (Presti *et al.*, 2008), thought to be a primary contributor to the thermohaline circulation (THC). If this is indeed the case the study of this margin is critical in developing our understanding of the impact of Antarctic waters on Southern Ocean circulation during the LGC. The record of sea-ice advance and retreat associated with the MIZ should offer a contemporaneous record to that from the Scotia Sea.

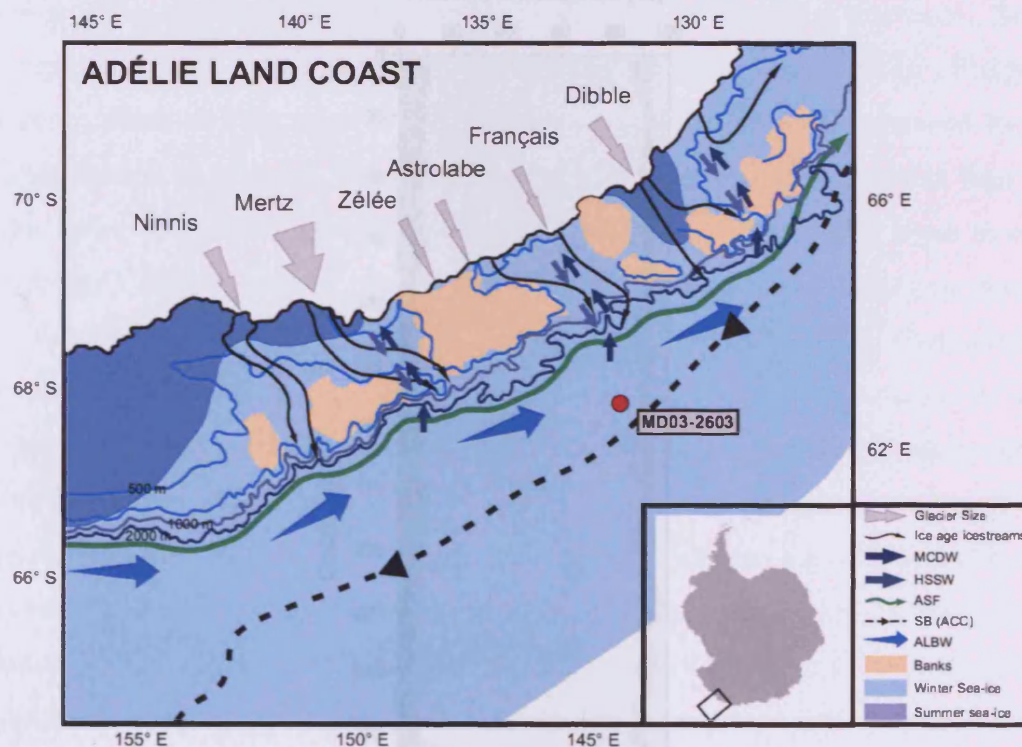


Figure 3.7. Map of the Adélie Land Coast illustrating the location of core site MD03-2603 with regards to primary glaciology and oceanography. Abbreviations in the legend: MCDW = Modified Circumpolar Deep Water, HSSW = High Salinity Surface Water, ASF = Antarctic Slope Front, SB = Southern Boundard, ACC = Antarctic Circumpolar Current, ALBW = Adélie Land Bottom Water.

The following section summarises the potential impact of dissolution on the diatom assemblages identified in the sediments of core MD03-2603. The combined relative abundance of diatoms most susceptible to complete dissolution (Chapter 2) (Pichon *et al.*, 1992) is plotted in Figure 3.8. The trend shows very little variation throughout the record with no significant difference between the glacial and Holocene. Relative abundance is consistently higher than 4.5% throughout the record, showing no evidence of complete

dissolution. The constant presence of these diatoms indicates consistent effects of dissolution on the sediment assemblage. This evidence is supported by the PI of Shemesh *et al.* (1989) (Figure 3.7). PI scores show that the effects of dissolution show very little variation throughout the record (SD = 0.02), with a mean of 0.92 (n = 65). This is only slightly lower than the 0.96 average of modern ocean assemblages, and is much higher than the lowest Holocene (0.61) and LGM (0.33) PI scores identified in the Southeast Indian Ocean by the Shemesh *et al.* (1989) study. For comparison, in the study by Shemesh *et al.*, (1989), according to the authors, the Southeast Indian Ocean SAZ, which has been shown to have higher rates of dissolution than the Antarctic Zone (AZ) (Zielinski and Gersonde, 1997), has a PI of 0.61 during the Holocene and 0.49 during the LGM.

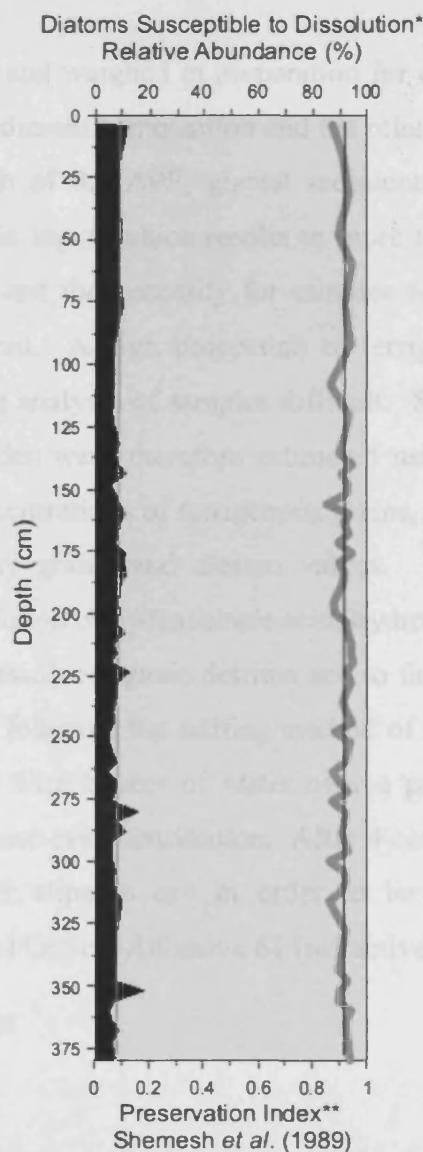


Figure 3.8. Core MD03-2603: Effects of dissolution on the downcore diatom assemblage. Total relative abundance (%) of lightly silicified diatoms (black fill) is plotted downcore and reveals little variation throughout the record, as indicated by the line of best fit (fine light grey line). **Actinochilus actinocyclus*, *Azpeitia tabularis*, *Fragilariopsis curta*, *Fragilariopsis cylindrus*, *Fragilariopsis separanda*, *Porosira*

glacialis, *Thalassiosira antarctica*, *Thalassiosira gracilis*, *Thalassiothrix antarctica*. The PI of Shemesh *et al.* (1989) is also plotted (heavy grey line), also revealing little variation downcore, with an average index (fine black line) similar to values found in the modern ocean. ***Fragilariopsis kerguelensis*/(*Fragilariopsis kerguelensis*+*Thalassiosira lentiginosa*).

3.1.4. Quantitative Diatom Assemblage Data

3.1.4.1. Sample Preparation

Scotia Sea cores TPC063 and TPC286 were initially sampled at intervals of 32 cm, and at higher resolution (4 cm) in specific portions of interest referred to as the high resolution windows (HRWs). The upper 380 cm of core MD03-2603 was sampled at a resolution of 12 cm, with a HRW, contemporaneous with those in the Scotia Sea cores, sampled at higher resolution intervals of 4 cm.

Sediment samples were dried and weighed in preparation for chemical treatment. Sediment mass is dependent upon the sediment composition and the relative contribution of terrigenous and biogenic material. South of the APF, glacial sediments are characterised by higher terrigenous input than biogenic input, which results in more terrigenous grains than diatom valves per gram of sediment and the necessity for samples with a higher mass in order to achieve suitable diatom content. A high proportion of terrigenous grains can overwhelm diatom valve presence making analysis of samples difficult. Samples of a mass adequate to produce clear quantitative slides were therefore estimated using a combination of the MS record, to infer the likely concentrations of terrigenous grains, and smear slides to assess the respective proportions of clay grains and diatom valves. Subsequent to weighing, the sediment was digested in a solution of hydrochloric acid, hydrogen peroxide and Calgon™ in order to remove carbonates, dissolve organic detritus and to further disaggregate the sample. Quantitative slide preparation followed the settling method of Scherer (1994), whereby each sample is settled through a 1 litre beaker of water over a period of 4 hours to minimise sediment clumping and maximise even distribution. After 4 hours the water was drip-drained overnight, allowing the cover slips to dry in order to be mounted upon a permanent microscope slide using Norland Optical Adhesive 61 (refractive index 1.56).

3.1.4.2. Assemblage Data

3.1.4.2.1. Valve Counts

Glacial sediments are often characterised by reduced concentrations of diatoms and enhanced quantities of terrigenous detritus. In addition to this, the diatoms that are preserved within the sediments can often be lightly silicified and heavily fragmented. Fragmentation creates a risk

of counting duplicate valves and thus over-estimating species abundance within an individual sample. This was avoided by following the strategy employed by Armand (1997), Cunningham and Leventer (1998) and Allen (2003). In all samples diatoms were identified to species level. Where detailed identification to species level was not possible valves were assigned to genus or included as an unidentified species. The original count sheets of diatom species assemblages can be viewed in Appendix 1.

Valve counts were converted into both relative and absolute abundances (as described by Scherer (1994), which allows the calculation of absolute diatom concentration per gram of sediment), reducing the species bias problems that can sometimes affect relative abundance datasets and eradicating the ‘closure issue’ also associated with relative abundance data. Absolute abundances, for both total diatom valve concentration and individual species were calculated using the following equation (Scherer, 1994):

$$T = \frac{(NB)/(AF)}{M}$$

N = Number of diatoms counted

B = Area of beaker bottom (7854 mm²)

A = Area of transect

F = Number of transects

M = Mass of sediment (g)

3.1.4.2.2. Diatom Counting Methods

Two microscope-based diatom valve counting methods were employed.

3.1.4.2.2.1. Conventional Counting Method

Where possible, between 300 and 450 valves (in accordance with the literature) were counted along slide transects using an Olympus BH-2 microscope at x1000 magnification (Zielinski and Gersonde, 1997; Cunningham and Leventer, 1998; Gersonde and Zielinski, 2000; Sjunneskog and Taylor, 2002; Allen *et al.*, 2005; Buffen *et al.*, 2007).

3.1.4.2.2.2. Area Counting Method

In addition to the conventional counting method a second method, more widely employed in macro-ecology quadrat counting (Fortin and Dale, 2008) was also used. This is based on the quantification of species within a statistically significant *area* of the quadrat/slide coverslip. Taxonomic identification was undertaken using an Olympus BH-2 microscope x1000

magnification for a statistically significant portion (10 transects) of the 22 x 22 mm² coverslip (Buffen *et al.*, 2007). This area-based method was necessary as a number of the samples from core TPC286 were barren of diatom valves and precluded use of the conventional counting method as counts of between 300 and 450 valves were not possible. These samples, in core TPC286, are primarily located between 406 cm and 543 cm, and 350 and 238 cm representing a major portion of the record (Figure 3.9a). Alternative attempts made to amplify the quantity of diatom valves per cover slip through increasing the sediment mass of each sample obscured the frustules with terrigenous grains.

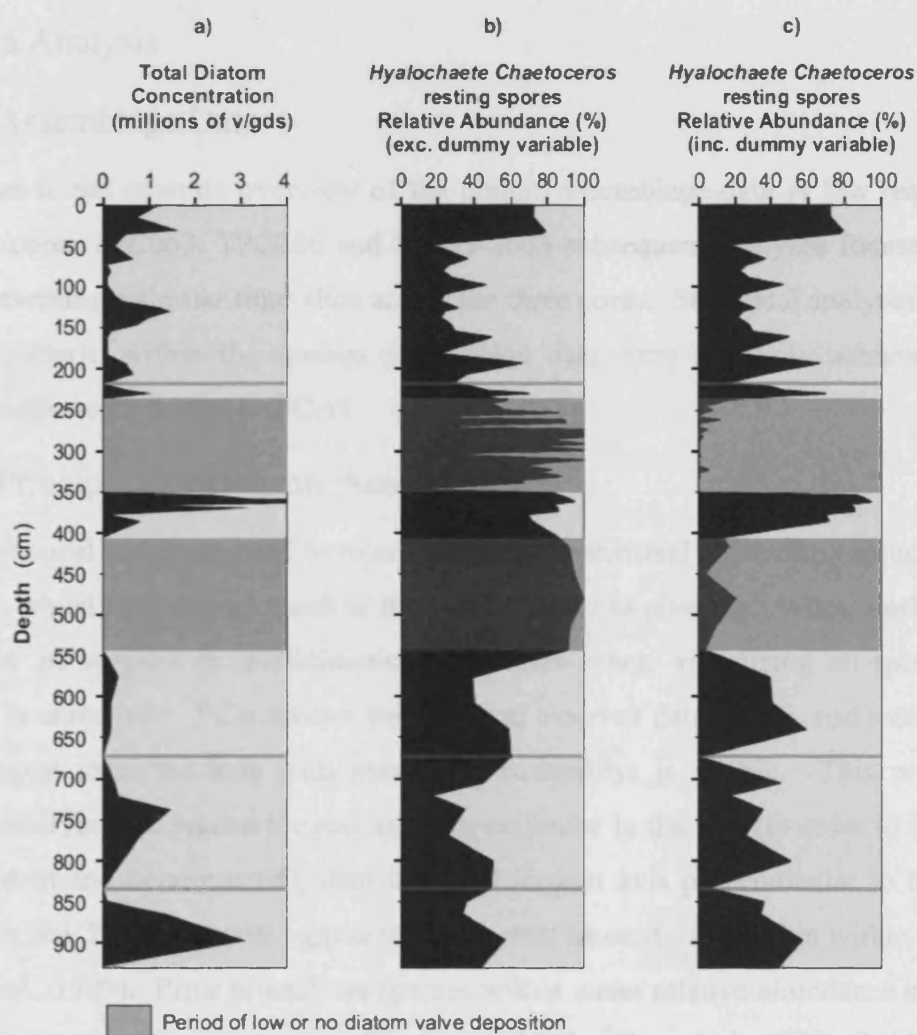


Figure 3.9. a) Core TPC286: down core total diatom concentration highlighting periods of low or no diatom deposition. b) Core TPC286: down core relative abundance of *Chaetoceros* rs calculated without the benefit of the dummy variable. c) Core TPC286: down core relative abundance of *Chaetoceros* rs calculated with the benefit of the dummy variable. Grey bands indicate periods of low or no diatom valve deposition.

The use of this area counting method requires caution when calculating relative abundance due to the exceptionally small sample sizes (in some cases as few as one solitary diatom valve) (Figure 3.9b). In order to compensate for this bias a measure of diatom absence was

introduced to the data in the form of a ‘dummy variable’. For any sample showing diatom depletion, where a tally of 300 to 450 values was impossible, the ‘dummy variable’ was used to make up the difference, and was given the value required to reach a significant tally of 400 valves, i.e. for a sample that only identifies 10 diatom valves, the ‘dummy variable’ was allocated a value of 390. This variable essentially represents the portion of the coverslip that is *not* diatoms, giving us a means to measure low rates of diatom deposition within the relative abundance statistics, which increases the comparability of relative abundance data throughout the core and with other cores (Figure 3.9c).

3.1.5. Data Analysis

3.1.5.1. Assemblage Data

Following an initial analysis overview of the diatom assemblage data at low resolution for each of the cores TPC063, TPC286 and MD03-2603 subsequent analyses focused on three HRWs representing a similar time-slice across the three cores. Statistical analyses to identify underlying patterns within the species assemblage data were primarily achieved through Principle Components Analysis (PCA).

3.1.5.2. Principle Components Analysis

PCA is a statistical technique used to represent multidimensional data with a reduced number of variables, whilst retaining as much of the data variance as possible. When working with a large number of samples in multidimensional species space, visualizing all species, in all dimensions is unrealistic. PCA takes a hypothetical cloud of data points, and rotates it, such that the longest axis (the axis with maximum variability) is visible. This procedure is repeated, identifying the second longest axis perpendicular to the first (in order to ensure axes are independent and uncorrelated), then the third longest axis perpendicular to the second, etc. The first few PCA axes will represent the greatest amount of variation within the dataset (Kovach *et al.*, 1999). Prior to analysis species with a mean relative abundance of less than $\geq 0.5\%$ were removed (Cunningham and Leventer, 1998; Allen *et al.*, 2005) (Table 3.4). To avoid biases in the sections of the core sampled at a lower resolution, the removal of species was based on the mean relative abundance in the high-resolution intervals of each respective core.

Prior to the execution of the PCA both the relative and absolute abundance data required several transformations to minimise inherent biases. These transformations included *centring*, *standardizing*, *square-rooting* (relative abundance) and *log* transformation (absolute

abundance). *Centring* is a normalising method, designed to reduce non-normal distributions by centring everything about the mean and is a standard in the majority of microfossil-applied PCA (Patel, 2002). *Standardizing* removes the variability component specific to each species, and creates a correlation matrix in place of a covariance matrix. It has been argued that the exclusion of individual species variability can negatively impact analyses, often resulting in the oversight of variability within minor species (Patel, 2002). However, minor species can often exhibit high coefficients of variability as a result of low means and appear to exert much more influence over an assemblage than is necessarily the case (Harris *et al.*, 1999). The application of a *square-root* transformation was used to confine relative abundance data with a large range of values. Relative abundance datasets can contain many species with widely varying values. Major species can often represent >50% of the assemblage, whereas the minor species, although possibly as important as the major in their environmental significance, can represent much less of the assemblage (0.5% in my study). By square-rooting the data the potential for major species abundance changes to mask or drive those changes in the minor species is minimised. A *log* transformation was applied to the absolute abundance data in order to down-weight the influence of dominant taxa acting in much the same way as the use of the *square-root* transformation on the relative abundance data. PCA on both the relative and absolute abundance data for each core was carried out in order to identify the dataset least dominated by its primary axis and that most representative of environmental changes within the assemblage, which was then used as the basis for the interpretation (Chapter 6).

Table 3.4. Diatom species and species groups identified in this study. Species with mean relative abundance in excess of a 0.5% (gray highlight). Species identified in all three cores (white text).

<i>Actinocyclus actinocylus</i>	<i>Fragilariopsis curta</i>	<i>Thalassiosira antarctica</i> (cold)
<i>Actinocyclus curvalatus</i>	<i>Fragilariopsis cylindrica</i>	<i>Thalassiosira antarctica</i> (warm)
<i>Actinocyclus igens</i>	<i>Fragilariopsis kerguelensis</i>	<i>Thalassiosira eccentrica</i>
<i>Asteromphalus hookeri</i>	<i>Fragilariopsis obliquecostata</i>	<i>Thalassiosira gracilis</i> var. <i>expecta</i>
<i>Asteromphalus hyalinus</i>	<i>Fragilariopsis rhombica</i>	<i>Thalassiosira gracilis</i> var. <i>gracilis</i>
<i>Aspeirina tabularis</i>	<i>Fragilariopsis ritscheri</i>	<i>Thalassiosira lentiginosa</i>
<i>Cocceneis</i> spp.	<i>Fragilariopsis separanda</i>	<i>Thalassiosira oestrupii</i>
<i>Corethron</i> spp.	<i>Fragilariopsis sublinearis</i>	<i>Thalassiosira oliverana</i>
<i>Coscinodiscus bouvet</i>	<i>Fragilariopsis vanheurckii</i>	<i>Thalassiosira perpusilla</i>
<i>Coscinodiscus</i> spp.	<i>Melosira sol.</i>	<i>Thalassiosira trifurcata</i>
<i>Hyalochaete Chaetoceros</i> resting spores (<i>Chaetoceros</i> rs)	<i>Odontella weissflogii</i>	<i>Thalassiosira tumida</i>
<i>Cyclotella</i> sp.	<i>Porosira glacialis</i>	<i>Thalassiosira</i> spp.
<i>Dactyliosolen</i> girdle bands	<i>Porosira pseudodenticulata</i>	<i>Thalassionema</i> spp.
<i>Denticulopsis</i> sp.	<i>Paralia</i> spp.	Trichotoxen
Dummy Variable	<i>Rhizosolenia</i> spp.	<i>Thalassiothrix antarctica</i>
<i>Eucampia antarctica</i>	<i>Stellaramis microtrias</i> rs	Unidentified centrics
Extinct reworked spp.	<i>Stephinopyxis</i>	Unidentified pennates

In the case of core TPC063 the PCA results indicate that the relative abundance data is less dominated by its primary axis and appears more representative of the changing environment system, and less dominated by extreme events, than the absolute abundance data. Whereas one event appears to dominate the primary axis in the absolute abundance data, this is less evident in the relative abundance data (Figure 3.10). In the case of TPC286, the results showed that both relative abundance (including the dummy variable) and absolute abundance data resulted in a very similar primary PCA output, validating the use of relative abundance data and the inclusion of the dummy variable (Figure 3.11). Further, the PCA primary axis relating to the relative abundance data (69.1%) showed less dominance than the absolute abundance data (74%), suggesting a better representation of the changing environment system. The PCA output of the relative abundance data was therefore chosen in preference to the absolute abundance data in the analysis of both TPC063 and TPC286. In the case of MD03-2603 the PCA output of both relative abundance and absolute abundance was similar and to be consistent with the Scotia Sea cores PCA and with the wider literature, which strongly favours the use of relative abundance data, the PCA was based on the relative abundance data.

The primary outputs of PCA are the principle component axes, which are the primary axes of variance within the data cloud. The degree of variance captured by each respective axis is represented by the *eigenvalue*, with the largest eigenvalue attributed to the first axis, the second largest for the second axis, etc. In addition to the eigenvalues the percentage of total variance portrayed by each axis is also calculated. Identifying the number of interpretable axes most representative of the dataset can be achieved in a number of ways. Kaiser's rule states that the minimum eigenvalue for consideration should be the average of all eigenvalues. Kaiser's rule is often considered a good rule of thumb for determining whether a component is interpretable (Legendre and Legendre, 1983; Kovach 1999). A scree plot also provides a means of assessing how well the variability in the data is represented by the first few axes of the ordinations (Kovach 1999). In addition to the eigenvalues, the variables associated with the data are each attributed a component loading known as an *eigenvector*. The eigenvectors represent the relative importance of each respective variable (species) in relation to each extracted PCA axis. The sign of the value (positive or negative) indicates which end of the PCA axis the variable is associated with and the value (which ranges from 0 to 1) provides a measure of the strength of correlation between the species and the PCA axis,

the significance of this correlation can be calculated via a simple students t-test. In this study I refer to significance at the 90% level.

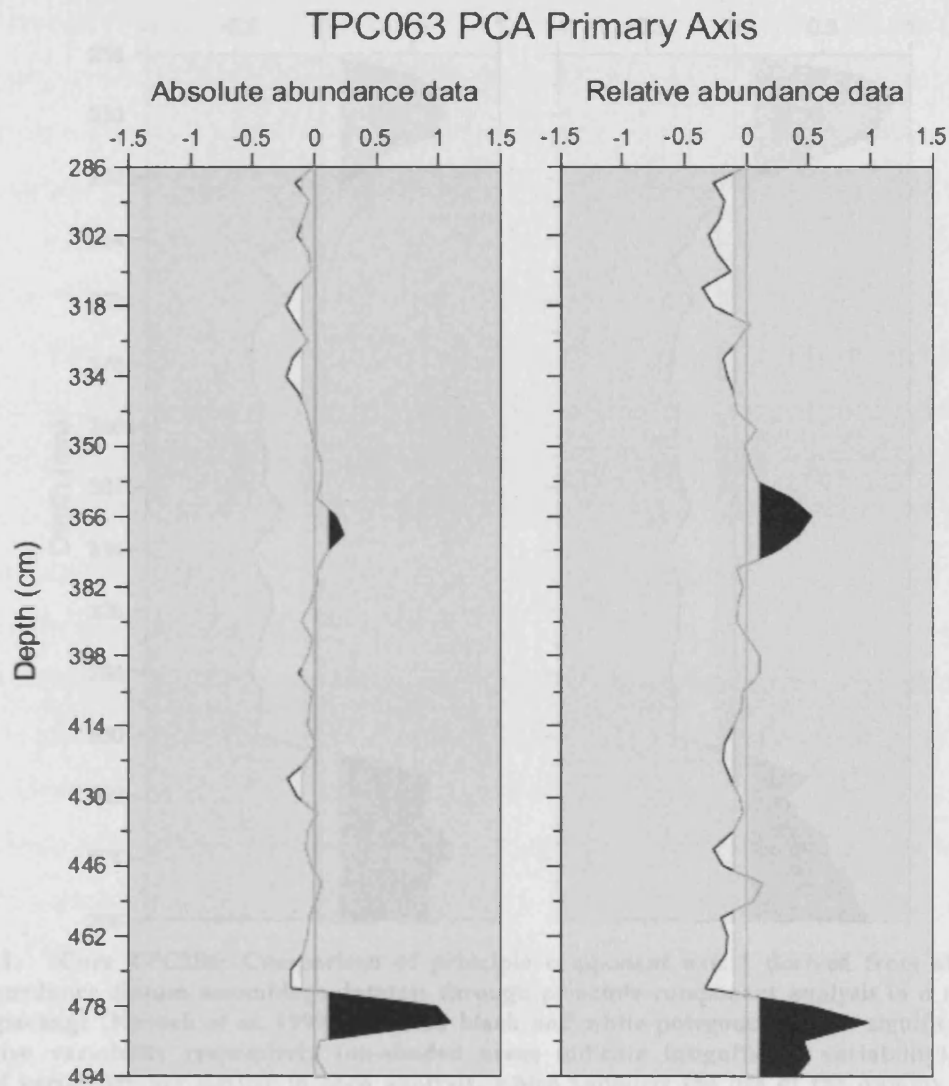


Figure 3.10. Core TPC063: Comparison of principle component axis 1 derived from absolute and relative abundance diatom assemblage datasets through principle component analysis in a multivariate statistical package (Kovach *et al.* 1999). Shaded black and white polygons indicate significant positive and negative variability respectively (un-shaded areas indicate insignificant variability). Primary patterns of variability are similar in each analysis, however the primary axis (PCA 1) derived from the absolute abundance dataset dominated the variability more so than that derived from the relative abundance dataset. In addition, in the absolute abundance data this axis was more dominated by an extreme productivity event at ~478 cm.

The third output from the PCA is the *matrix of component scores*, which are the component loadings multiplied by the original data. Scores are attributed to each sample (depth) and describe the strength of each axis to describe the cores variability in diatom assemblage composition. All principle component analyses were conducted using Multivariate Statistical Package developed by Kovach *et al.* (1999).

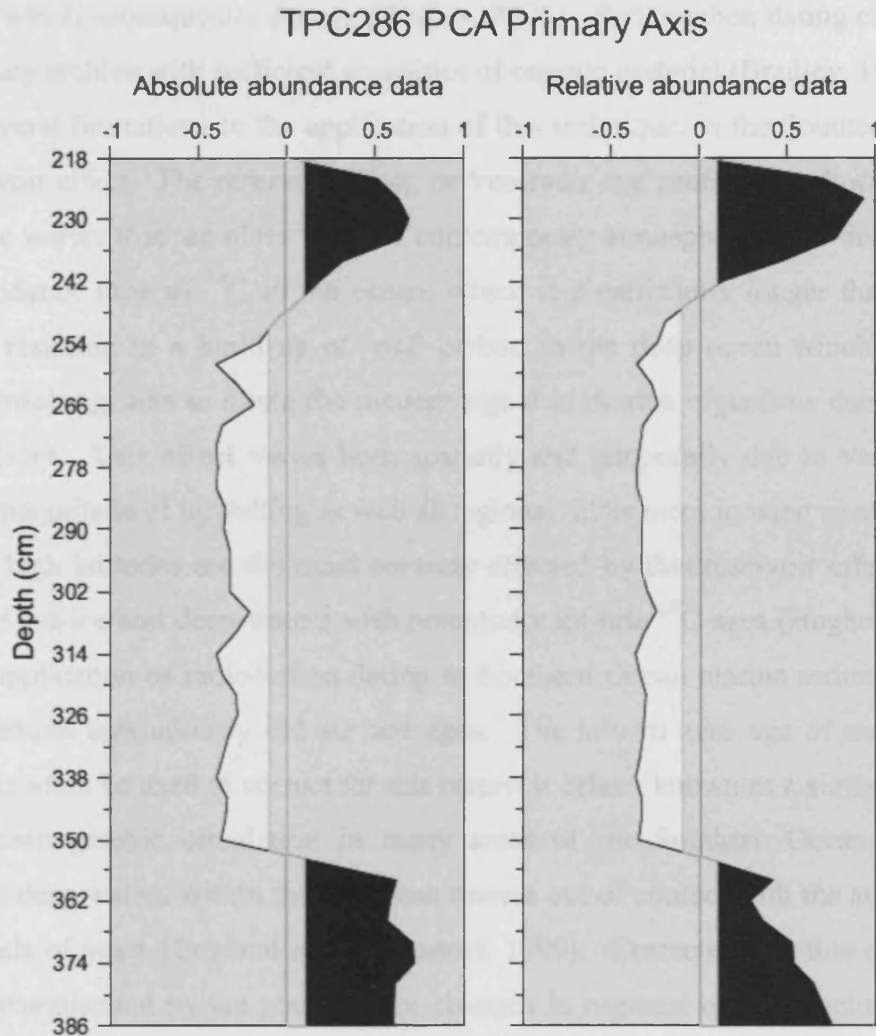


Figure 3.11. Core TPC286: Comparison of principle component axis 1 derived from absolute and relative abundance diatom assemblage datasets through principle component analysis in a multivariate statistical package (Kovach *et al.* 1999). Shaded black and white polygons indicate significant positive and negative variability respectively (un-shaded areas indicate insignificant variability). Primary patterns of variability are similar in each analysis, which supports the use of the dummy variable in conjunction with the relative abundance data. In addition, the primary axis (PCA 1) derived from the absolute abundance dataset dominated the variability more so than that derived from the relative abundance dataset. The relative abundance data is therefore less dominated by abundance and more representative of the changing environment as a whole.

3.2. Chronostratigraphy Methods

3.2.1. Radiometric Dating Techniques

3.2.1.1. Radiocarbon Dating

Radiocarbon dating is one of the most useful Late Quaternary dating techniques with the capacity for accurate dating over the past 50 ka (Hughen, 2007). It is based on the instability of the carbon isotope ^{14}C , which forms in the upper atmosphere through the interaction of cosmic ray neutrons and nitrogen atoms. The newly formed isotope combines with oxygen to

form $^{14}\text{CO}_2$, which subsequently decays (Walker, 2005). Radiocarbon dating can be applied globally, to any archive with sufficient quantities of organic material (Bradley, 1999).

There are several limitations to the application of this technique, in the Southern Ocean, the carbon reservoir effect. The reservoir effect, or ‘reservoir age’, refers to radiocarbon ages of ocean surface waters that are older than the contemporary atmosphere. The disparity results from the residence time of ^{14}C in the ocean, which is significantly longer than that in the atmosphere, resulting in a build up of ‘old’ carbon in the deep ocean which, through the process of upwelling, acts to dilute the modern signal in marine organisms due to growth in the surface layer. This effect varies both spatially and temporally due to variation in the position and magnitude of upwelling as well as regional differences in wind speed and sea-ice extent. The high latitudes are the most severely effected by this reservoir effect due to the prevalence of sea-ice and deep-waters with potentially infinite ^{14}C ages (Hughen, 2007). As a result the application of radiocarbon dating to Southern Ocean marine sediment core tops commonly returns anomalously old surface ages. The known zero age of modern marine organisms can often be used to correct for this reservoir effect; known as a surface correction. However, oceanographic circulation in many areas of the Southern Ocean hinders this correction, as deep waters within the ACC can remain out of contact with the atmosphere for many hundreds of years (England and Rahmstorf, 1999). Correcting for this effect back in time is also complicated by the potential for changes in regional oceanographic circulation, surface conditions, atmospheric ^{14}C concentrations and sea-ice variability over time, all of which limit the ability for surface water equilibrium (Hughen, 2007). Nevertheless radiocarbon dating is presently the most widely applied dating method in Southern Ocean Late Quaternary sediments (Hughen, 2007).

3.2.1.1.1. Sample Preparation

To establish age models and sedimentation rates, sediment cores TPC063 and TPC286 were sampled at various depths for radiocarbon dating (Table 3.5). In addition, the dating of TPC286 was complimented by several dates previously acquired from core GC027 (Pudsey *et al.*, 1992), recovered from the same sediment drift. Due to a near absence of biogenic calcium carbonate, accelerator mass spectrometry was employed to analyze the bulk organic carbon fraction. Each of the 18 samples were prepared to graphite and subsequently analyzed at the NERC Radiocarbon Laboratory, East Kilbride.

Table 3.5. Core TPC063, TPC286 and GC027: Depths sampled for radiocarbon analysis.

Core Code	Sample Depth (cm)
TC063	0
TC063	0
TC063	25
TC063	33
TC063	85
PC063	140
GC027	0
GC027	5
GC027	24.5
GC027	44.5
GC027	65
GC027	105
GC027	127
GC027	151.5
GC027	203
GC027	342
TC286	50
PC286	50

3.2.2. Magnetic Susceptibility Correlation Dating

MS is a measure of how magnetizable a material is in the presence of a magnetic field, and can be used to crudely differentiate various classes of magnetic substances (Hillaire-Marcel & Vernal 2007). MS curves can be employed as a proxy for changes in the relative contributions of terrigenous material versus biogenic material in Southern Ocean sediment cores, characteristic of glacial and interglacial regimes and associated marine isotope stages (Pudsey and Howe, 1998; Howe and Pudsey, 1999); providing a first approximation of core chronology. However, it can be strongly influenced by the local sedimentation regime (Pirrung *et al.*, 2002), with topography, current intensity, and sea-ice presence all potentially affecting local rates of sedimentation. A number of recent studies have also identified a strong correlation between Southern Ocean marine MS records and dust concentrations in East Antarctic ice-cores. This characteristic MS trend has been observed in marine records from the South Indian Ocean (Dezileau *et al.*, 2000; Thamban *et al.*, 2005; Mazaud *et al.*, 2002, 2007) and Southwest Pacific Ocean, as well as a large area of the Scotia Sea (Hofmann, 1999; Pugh *et al.*, 2009). Thought to originate from enhanced glacial dust transport from Patagonia (Grousset *et al.*, 1992; Basile *et al.*, 1997; Delmonte *et al.*, 2004; Fischer *et al.*, 2007), the correlation of these records could potentially offer a high-resolution age-model with which to correlate marine sediments of the high-latitude Southern Ocean. However, marine sediment records, from the Weddell Sea, southwest Scotia Sea and Pacific continental rise of the Antarctic Peninsula (Ó Cofaigh *et al.*, 2001; Pudsey, 2000; Lucchi *et al.*, 2002; Yoon *et al.*, 2007) exhibit either no, or little resemblance to the characteristic MS

trend identified by Hofmann, (1999), Dezileau *et al.* (2000), Thamban *et al.* (2005) Mazaud *et al.* (2002, 2007) and Pugh *et al.* (2009), as a result of differences in local sedimentation regimes.

3.2.2.1. Sample Preparation

MS was recorded at a resolution of 2 cm for the entire length of cores TPC063 and TPC286 using a Bartington MS2 MS meter with a Bartington MS2F probe. This instrument measures volume MS (κ) in dimensionless units (SI). Air readings were taken before and after each sample reading to correct for instrumental drift (Dearing, 1994). In core MD03-2603 MS data were acquired in a multi sensor core logger aboard the cruise vessel the *Marion Dufrense*, by M. Presti.

3.2.3. Relative Palaeointensity Dating

Records of geomagnetic RPI acquired from sedimentary sequences theoretically document the globally synchronous record of millennial-scale variability within the Earth's geomagnetic field (Stoner *et al.*, 1998, 2002; Channell *et al.*, 2000; Laj *et al.*, 2000) providing a powerful tool for stratigraphic correlation of sedimentary sequences (Guyodo and Valet, 1996, 1999; Stoner *et al.*, 1998, 2002; Laj *et al.*, 2000; Channell *et al.*, 2000). Correlations are based on the alignment of geomagnetic excursions and lows in RPI, characterised by anomalous, positive spikes in inclination values. Such excursions have been shown to occur periodically throughout the palaeosecular variation record (Channell *et al.*, 2002, 2008; Lund *et al.*, 2006b) such as the Laschamp excursion.

Inclination is defined as the angle between the vector representative of the geomagnetic field and the horizontal plane. This value ranges from 90° at the north magnetic pole to 0° at the magnetic equator to -90° at the South magnetic pole (Merrill and McFadden, 2005). Another potential palaeomagnetic correlation parameter is declination. Declination is defined as the angle between magnetic north and geographic north, recording positive values when magnetic north is east of true north, and negative values when north is west of true north (Merrill and McFadden, 2005). Declination data is often disregarded in palaeomagnetic correlation, as it is difficult to ensure that the sedimentary sequences are azimuthally orientated, often making the data unreliable when attempting to correlate records from different parts of the globe. However, the proximity of sedimentary sequences TPC063 and TPC286, employed in this study, is such that the secular variability within the declination data is comparable.

A chronological framework is generally achieved via correlation with RPI reference curves. Such reference curves are a compilation of records with independent dating control, stacked to form a regionalized, hemispheric or global record (Guyodo and Valet, 1996, 1999, Laj *et al.*, 2000, Channell *et al.*, 2000). The application of these global RPI reference stacks to the development of high-resolution age models for sedimentary sequences (Stoner *et al.*, 1998, 2002; Brachfeld *et al.*, 2000; Channell *et al.*, 2000; Laj *et al.*, 2000; Sagnotti *et al.*, 2001; Macri *et al.*, 2005, 2006; Willmott *et al.*, 2006) could prove vital in regions such as the Antarctic, where the use of traditional chronostratigraphic tools is often severely restricted.

There is some unreliability associated with the use of geomagnetic excursions as a stratigraphic tool. Excursions are characteristically short events, occurring over a few hundred to a few thousand years. Due to the short nature of excursions it is possible that the excursion is not recorded due to low frequency sampling of the sedimentary archive. Sedimentary processes such as a low sedimentation rates, bioturbation, loss of sediment during recovery, a hiatus, or erosion can also remove the signal. Magnetic processes too, such as lock-in depths, i.e. the depth to which particles settle before their magnetic signal is locked in the sediment archive and cannot change, or remagnetization of the sediment can cause problems (Merrill and McFadden, 2005).

There is some debate that geomagnetic excursions should be employed with caution as a stratigraphic tool. A fundamental assumption of palaeomagnetism is that if averaged during a period of stable polarity, the mean geomagnetic field will be that of a geocentric axial dipole (GAD). This implies that the dipole field is centred on the centre of the Earth and is aligned along and symmetrical about the rotation axis (Merrill and McFadden, 2005). However, in reality the geomagnetic field is much more complex than this and is constantly changing. Dynamo models, along with observations, suggest that during a geomagnetic excursion the ratio of dipole to non-dipole field energy decreases significantly, in favour of the non-dipole component (Whitney *et al.*, 1971; Guyodo and Valet, 1996, 1999; Channell *et al.*, 2002). This non-dipole field could potentially be characterized by a degree-6 harmonic, where the geomagnetic field is divided into six lobes, approximately 30° across. This could result in the regional occurrence of an excursion, which would not be echoed globally (Merrill and McFadden, 2005). This issue of global synchronicity has resulted in the conservative recommendation that correlated records be separated by angular distances of no more than 45° on the Earth's surface (Merrill and McFadden, 2005), the correlations of Scotia Sea cores TPC063 and TPC286 and the SAPIS RPI stack (Stoner *et al.*, 2002) are within this conservative distance.

3.2.3.1. The Laschamp Event

The palaeomagnetic excursion relevant to the timescale of this study is the Laschamp Event. Palaeomagnetic excursions are defined as short-term (a few thousand years) directional anomalies outside the normal range of secular variation of the geocentric axial dipole (Lund *et al.*, 2006b; Cassata *et al.*, 2008). Characterized by anomalously low inclinations and quasi-reversed magnetization, excursions possibly represent aborted palaeomagnetic reversals (Opdyke, 1972). Bonhommet and Babkine (1967) first introduced the concept of partially reversed excursions of the Earth's geomagnetic field with the discovery of nearly reversed magnetization in the Laschamp and Olby lavas (Chaîne des Puys, France). The excursion, known as the Laschamp Event, is one of the most recent of the many geomagnetic polarity excursions that interrupted the Brunhes Chron (780 ka to 0 ka) (Table 3.6) (Lund *et al.*, 2006b; Laj and Channell, 2007; Singer, 2007; Singer *et al.*, 08).

Table 3.6. Geomagnetic excursions known to have interrupted the Brunhes Chron (Guilou *et al.*, 2004).

Excursion	MIS	Age (ka)
Mono Lake	3	33±1
Laschamp	3	41±1
Norway-Greenland Sea	4	61±2
<i>Fram Strait I</i>	5.2/5.3	~100
Blake	5.5	123±3
<i>Baffin Bay/Fram Strait II</i>	6.2/6.3	~160
Iceland Basin	6.6/7.1	~190
Pringle Falls/Summer Lake II	7.5	~220
<i>CR0</i>	8	~260
<i>9α</i>	8/9	~290 – 310
<i>CR1</i>	9	~330
<i>11α</i>	11	~400
<i>CR2</i>	13	480 – 510
<i>14α</i>	14	~535
Big Lost	15	~575
La Palma	15	~605
<i>17α</i>	17	~665

The Laschamp Event was one of the first recognised geomagnetic excursions, which are now widely accepted as global expressions of geodynamo behaviour, and is one of the best documented and dated (Cassata *et al.*, 2008). Bonhommet and Zähringer (1969) were the first to attempt to accurately date the event and acquired a window of between 20 ka and 8 ka using K-Ar dating. Gillot *et al.* (1979) later improved upon this estimate, citing an age of between 40 ka and 50 ka, using the same technique.

Since its original identification, due mainly to the exploits of the Off-shore Drilling Project, the Laschamp excursion has been identified and independently dated in a number of palaeomagnetic records recovered from marine sedimentary sequences across the northern

hemisphere. Further, the Laschamp Event is one of the few excursions that have been directly correlated to lows in palaeointensity (RPI) (Laj *et al.*, 2000). These records consistently yield an age of ~41 ka for the occurrence of the Laschamp Event (Kristjansson and Gudmunsson, 1980; Levi *et al.*, 1990; Channell *et al.*, 2000; Laj *et al.*, 2000). The Laschamp geomagnetic excursion has also been revealed as abrupt intervals of enhanced cosmogenic nuclide flux in both polar ice (Baumgartner *et al.*, 1997, 1998; Wagner *et al.*, 2000) and sediment archives (Frank *et al.*, 1997; Carcaillet *et al.*, 2004). The correlation of RPI and cosmogenic nuclide records has helped to further constrain the age of the Laschamp Event. Correlation of the NAPIS RPI stacked record (Laj *et al.*, 2000) with ^{36}Cl GRIP record (Wagner *et al.*, 2000) resulted in an age of ~41 ka. This estimate was reproduced by the correlation of a RPI low and ^{10}Be high in Portuguese margin sediments (Carcaillet *et al.*, 2004). These estimates concur with the latest precise Ar/Ar dating of the Laschamp and Obly lavas: 40.4 ± 1 ka (Guillou *et al.*, 2004). However, despite the identification of the Laschamp Event in a wide range of records and in numerous locations across the northern hemisphere, observations in the southern hemisphere are limited to only a few studies in the South Atlantic and Indian Oceans, the Chilean coast and the Auckland volcanic field lava flows, New Zealand (Channell *et al.*, 2000; Mazaud *et al.*, 2002; Lund *et al.*, 2006b; Cassata *et al.*, 2008) and the identification of the Laschamp Event in Antarctic sediments is even more elusive. Recently, high-resolution RPI records have been based on Holocene sediments from the Palmer Deep (Brachfeld *et al.*, 2000) and northern Antarctic Peninsula (Willmott *et al.*, 2006), and more extensive records recovered from the western Antarctic Peninsula (160 ka, Sagnotti *et al.*, 2001 and 270 ka, Macri *et al.*, 2006) and the Wilkes Land Basin (780 ka, Macri *et al.*, 2005). However, each of these studies consistently report inclination values of normal polarity and fail to identify the positive inclination signatures characteristic of geomagnetic excursions, including the Laschamp Event. A number of geomagnetic excursions were however identified in a study by O'Brien (1989) of a suite of sediment cores from the northern Weddell and southern Scotia Seas. However, an imprecise chronology prevented an unequivocal assignment of the individual palaeomagnetic events.

3.2.3.2. Sample Preparation

Samples for RPI analyses were extracted from sections of sediment cores TPC063 and TPC286 based on prior diatom assemblage analyses. Core TPC063 was sampled between 252 cm and 702 cm and core TPC286 was sampled between 144 cm and 500 cm, both at a resolution of 4 cm. Discrete samples were extracted from the centre of the working half of

each respective core into 20 mm³ plastic cubes, with care taken not to disturb the surrounding material. Each individual pot was subsequently sealed air tight and cleaned of any excess material prior to labelling. Magnetic data for each sample was acquired at the Centre for Environmental Magnetism and Palaeomagnetism within the Geography Department of the Lancaster Environment Centre at Lancaster University under the supervision of Dr M. Hounslow. Discrete samples were measured using an AGICO JR6 magnetometer with a MolSpin alternating field demagnetiser with reverse tumbling attachment for demagnetisation of natural remanent magnetization (NRM), anhysteretic remanent magnetization (ARM) or isothermal remanent magnetization (IRM) and an IRM pulse magnetiser.

For several samples the NRM was progressively demagnetized by alternating field generally with peak values of 10–15–30–40–50–60 mT. An ARM was then imparted by translating each sample in a constant symmetric AF of 100 mT with a superimposed direct current bias field of 0.1 mT, with subsequently stepwise demagnetization using the same sequence of alternating field peaks applied to the NRM. Alternating field demagnetization ensured that any possible viscous component or magnetic overprint was completely removed at low fields, isolating the Characteristic Remanent Magnetization (ChRM) as a single, stable and well defined component at a field of 15 mT and above (Appendix 2). Subsequent to this finding, NRM was demagnetized by alternating field (AF) at a peak value of 15 mT for all samples. The ChRM orientation for each sample was then computed by PCA for demagnetization step 15 mT. RPI records were obtained by dividing the NRM intensity, demagnetized at 15 mT (NRM_{15 mT}) by the ARM intensity after demagnetization at 15 mT (ARM_{15 mT}).

3.2.4. Biostratigraphic Dating

Biostratigraphy uses fossils to establish the relative stratigraphic position of sedimentary sequences between different geographic localities, and has been employed since the dawn of geology (McGowran, 2005). In the oceans the biostratigraphic framework of the Quaternary is dominated by microfossils, including diatoms (McGowran, 2005). A number of biostratigraphic datums have been derived, including several in the Late Quaternary; *Actinocyclus ingens* (Abbott, 1974), *Hemidiscus karstenii*, *Rouxia constricta* and *Rouxia leventerae* (Zielinski and Gersonde, 2002; McGowran, 2005). However, the first and last occurrence datums of these species occurred during MIS 11, 7, 6 and 5 respectively and represent a period of time beyond the scope of this study. As a result, rather than implementing the conventional biozonation framework, this study employs variations in diatom abundance curves as a means of biostratigraphic dating.

In core MD03-2603 40 samples were analysed for diatom biostratigraphic control at the EPOC – University of Bordeaux I by X. Crosta. A number of diatoms were identified including the specific biostratigraphic markers *Rouxia leventerae* (~0.14 Ma to 0.13 Ma), *Rouxia constricta* (~0.3 Ma to 0.28 Ma) and *Hemidiscus karstenii* (MIS 7) (Presti *et al.*, 2007). Although, these datums are beyond the chronological scope of this study, identification acted as an independent age control in support of the previously applied uranium-series dating (Chapter 5). Sample preparation of the *E. antarctica* samples in cores TPC063 and TP286, followed the procedures described in Section 3.1.4.1.

3.2.5. Highly Branched Isoprenoids

I conduct the first application of HBIs to Late Quaternary Southern Ocean sediments in order to test their potential as an accurate proxy for the reconstruction of past sea-ice extent.

3.2.5.1. Sample Preparation

In order to reconstruct past sea-ice presence the concentrations of two HBI isomers (the sea ice diene and a tri-unsaturated isomer believed to be synthesised exclusively in open water conditions), have been reconstructed for sediment core TPC063 between 8 cm and 498 cm. Due to the pilot nature of this study, sampling resolution varied down core. The top 60 cm of the core, believed to mark the transition from the LGC into the Holocene, was sampled at a resolution of ~8 cm. Sampling resolution was then reduced to ~32 cm over the following 225 cm increasing to ~8 cm between 297 cm and 498 cm. The same compounds were measured in core TPC286, between the depths of 1 cm and 917 cm, at a resolution of ~16 cm. Sediment samples were initially freeze-dried and an internal standard (7 hexylnonadecane) was added. This standard enables quantification when performing the Gas-Chromatography Mass-Spectrometry analyses. The sediment material was then extracted using a mixture of CH₂Cl₂/CH₂OH (50/50; 5 ml) in order to yield a total organic extract and hydrocarbon fractions were obtained using open column chromatography (SiO₂/Hexane). HBI concentrations are relative to the internal standard added with the mass of the sample also considered, and as such are measured in units yg (internal standard)/g (mass of the sediment sample). These fractions were analysed using Gas Chromatography – Mass Spectrometry and HBIs were identified by comparison of their retention time and mass spectral characteristics with authentic standards. Sample processing was carried out by G. Massé at the University of Plymouth.

No study has attempted to use this proxy on Late Quaternary sediments and some potential caveats are to be considered when using this proxy for such studies. Like all organic matter these HBI hydrocarbon compounds are subject to diagenesis and can degrade over time. Although these dienes are known to undergo little diagenetic reaction in comparison to the more unsaturated HBIs (Belt *et al.*, 2001) this degradation potential must still be taken into consideration. In addition, although Johns *et al.* (1999) reported large concentrations of the diene in laboratory cultures of the diatom *Haslea otrearia*, the origin of this HBI isomer has yet to be confirmed.

4. Results: Environmental Proxies

The chapter presents brief descriptions of cores TPC063, TPC286 and MD03-2603, a detailed account of stratigraphic variability in total diatom concentration and species assemblages, and an analysis of the diatom assemblage data using Principle Components Analysis (PCA). The diatom results are also compared with the magnetic susceptibility (MS) data and, in the case of cores TPC063 and TPC286, the HBI data.

4.1. TPC063 – Results

4.1.1. Core Description – Sedimentology

The lithological composition of TPC063 (Figure 4.1) is primarily characterised by fine slit clay/mud and biogenic silica, with little evidence of carbonate test preservation. The lower 302 cm of the core (707 cm to 405 cm) is generally characterised by a homogenous dark-grey diatom-bearing mud, which features varying degrees of lamination. A basaltic drop stone is evident at 652 cm. Between 593 cm and 553 cm, the sediment is characterised by very faintly laminated greeny muds, which are silty in places, with a darker band of sediment present at ~580 cm, characterised by higher diatom content. The sediment becomes faintly laminated and more-silty again between 495 cm and 520 cm, with the degree of lamination gradually increasing up core. Between 495 cm and 468 cm, the colour and texture of the sediment becomes less grey and less-silty up-core. The upper 63 cm (468 cm to 405 cm) of the diatom-bearing grey mud is characterised by high water content. A unit of homogenous grey mud of lighter colour and reduced diatom content characterises the core between 252 cm and 405 cm. Above this material, between 105 cm and 252 cm, the core is characterised by a diatom-bearing clayey-mud similar to the sediment described between 707 cm and 405 cm, with sharp-based laminae evident at 210 cm and 150 cm. Between 105 cm and 60 cm the core is characterised homogenous mud, significantly lighter than the material below, with faint laminations in evidence throughout, which terminates in a stiff layer of bentonite clay (60 cm). The upper 60 cm of the core (60 cm to 0 cm) is composed of a greyish – brown organic-rich sediment. A combination of biostratigraphy and relative palaeointensity (RPI) correlation has determined that the 707 cm of core TPC063 covers the past ~45 kys (Chapter 5), representing the majority of MIS 1 to 3 (Figure 4.1). The majority of the core (707 cm to 90 cm) is glacial in age and defined by higher concentrations of terrestrial derived material and reduced concentrations of biogenic silica.

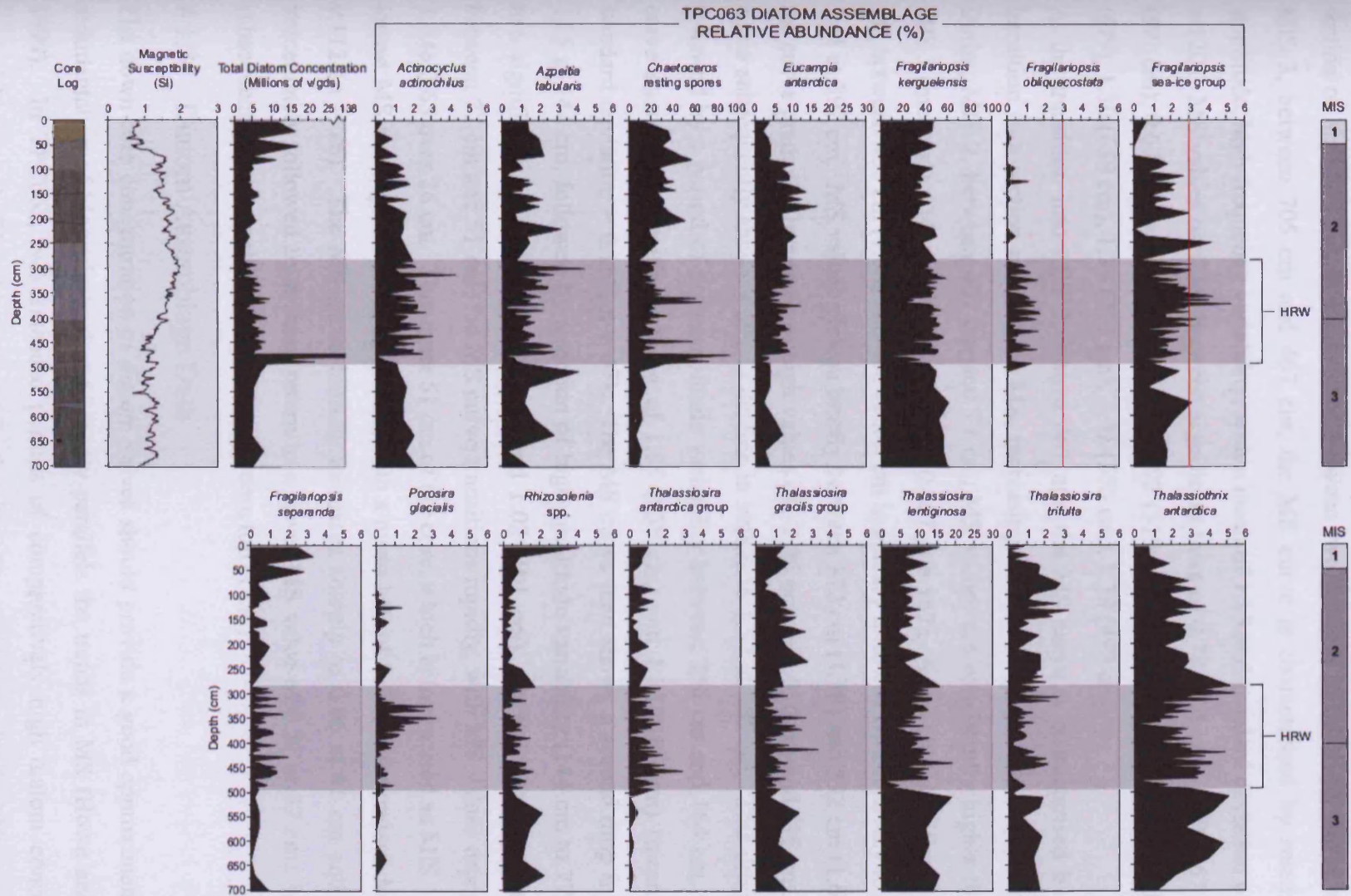


Figure 4.1. Core log (prepared digitally in a graphic package with RGB conversions of Munsell colours), MIS stratigraphy (based on magnetic susceptibility), magnetic susceptibility (recorded with probe and sensor) and diatom species assemblage data for core TPC063. Total diatom concentrations presented in absolute numbers (calculated using the equation of Scherer, 1994). Relative percentages for species comprising $>0.5\%$ of the assemblage data. The dark rectangle indicates the high-resolution window (HRW). Red lines indicate the sea-ice 3% threshold.

4.1.2. Magnetic Susceptibility

The Magnetic susceptibility (MS) curve for core TPC063 (Figure 4.1) is characterised by a section of high MS values sandwiched between two sections of relatively lower values. In MIS 3, between 705 cm and 467 cm, the MS curve is characterised by relatively high amplitude, high frequency variability, with a mean of 1.15 and standard deviation of 0.142 ($n = 120$). MS values oscillate between significant lows of 0.78 (705 cm), 0.99 (667 cm), 0.98 (591 cm), 0.67 (555 cm), 0.90 (533 cm), 0.92 (519 cm) and 0.89 (467 cm) and highs of 1.37 (679), 1.30 (659 cm), 1.38 (613 cm), 1.41 (575 cm), 1.38 (493 cm).

At the transition into MIS 2, Above 467 cm, the MS curve is characterised by a steady transition to a section of elevated MS, increasing from 0.89 at 467 cm to 1.66 at 407 cm. During MIS 2, between 407 cm and 77 cm, MS values are consistently higher than during MIS 3 (mean = 1.634, standard deviation = 0.167, $n = 167$). A brief but significant decline in MS between 407 cm (1.66) and 400 (1.34) cm is quickly followed by a recovery to a value of 1.61 at 392 cm. MS values plateau briefly between 372 cm (1.58) and 392 cm (1.61), before the curve gradually increases to high values of ~1.95 between 310 cm and 298 cm. The MS curve subsequently shows a steady decline in values to 1.57 at 265 cm. This drop in MS is followed by a period of high amplitude variability between 256 cm and 164 cm, where the curve shows two significant highs of 1.85 (238 cm) and 1.83 (186 cm) (mean = 1.634, standard deviation = 0.167, $n = 47$). The MS curve then shows a second drop in values to 1.25 at 144 cm, followed by a section of high amplitude variability (144 cm to 77 cm) with two significant lows of 1.25 (144 cm) and 1.02 (101 cm). At the transition into MIS 1, between 77 cm and 51 cm, the MS curve transitions rapidly, with MS values dropping from 1.6 to 0.65 over 26 cm. The upper 51 cm of the core, which is interpreted as MIS 1, have the lowest MS readings of the entire record, with a mean MS of 0.773 and standard deviation of 0.112 ($n = 26$). The MS curve initially increases sharply to 0.96 at 41 cm and is almost immediately followed by a sharp return to a lower MS value of 0.51 at 37 cm. MS values subsequently increase slightly to 0.74 at the core top (1 cm).

4.1.3. Diatom Assemblage Data

The down-core concentration of diatom valves should provide a good approximation of the sedimentation of biogenic opal and broadly parallels the trends in MS (Howe and Pudsey, 1999). In TPC063, two extended periods of comparatively high diatom concentrations sandwich a period of low biogenic production, roughly consistent with the MS curve (section 4.1.2.). The variability in total diatom concentrations and the associated diatom species

assemblages will now be described from the base of the core to the core top with reference to the age-depth model (Figure 4.1.)

4.1.3.1. MIS 3

The lower portion of the total diatom absolute abundance record, between 702 cm and 542 cm, has a mean diatom concentration of 5.43×10^6 v/gds, with a standard deviation of 1.22×10^6 v/gds ($n = 6$). Concentrations at the base (702 cm) and top of the section (542 cm) are 4.87×10^6 v/gds and 5.09×10^6 v/gds respectively, with the only significant variation in between being a peak in concentrations of 7.92×10^6 v/gds at 670 cm. The high, stable relative abundances of *F. kerguelensis* (mean = 55.3%, standard deviation = 5.08%, $n = 6$) and *T. lentiginosa* (mean = 13.4%, standard deviation = 1.73%, $n = 6$) and low relative abundance of *Hyalochaete Chaetoceros* resting spores (*Chaetoceros* rs) (mean = 10.4%, standard deviation = 3.13%, $n = 6$) are most evident over this lower portion (702 cm to 542 cm) of the species assemblage data. A significant degree of variability is observed in *A. tabularis* and *Rhizosolenia* spp., with relative abundances shifting between maxima of 2.8% and ~2.2% and minima of 0.2%, and ~0.88%, respectively. Furthermore, relative abundance of the *Fragilariopsis* sea-ice group (*Fragilariopsis curta* and *Fragilariopsis cylindrus*) breach the 3% threshold for the first time in the record, recording a value of 3.09% at 574 cm (Figure 4.1). Between 542 cm and 494 cm valve concentrations exhibit a gradual increase from 5.09×10^6 v/gds to 8.85×10^6 v/gds. This portion of the record also has distinct peaks (510 cm) in the relative abundances of the *Fragilariopsis* sea-ice group (2.4%), *Thalassiothrix antarctica* (5.1%), and *A. tabularis* (4.1%) (Figure 4.1).

The gradual rise in absolute abundance between 542 cm and 494 cm, is followed by a rapid increase to 21.8×10^6 v/gds at 490 cm. Valve concentrations then drop to 13.4×10^6 v/gds followed by a second rapid increase to a peak concentration of 138×10^6 v/gds at 478 cm. These peak concentrations are brief because total diatom absolute abundance drops back to 5.04×10^6 v/gds at 474 cm. Despite the magnitude of these peaks a signature is not observed in the MS record (Figure 4.1). The large, double peak in total diatom concentration at 494 cm and 474 cm, is exclusively dominated by *Chaetoceros* rs, which has relative abundances of 72.7% and 92% at 490 cm and 478 cm, respectively. The rapid ending of this peak (478 cm to 474 cm) results in enhanced relative abundances across the diatom assemblage, most notably in *F. kerguelensis*, *T. lentiginosa*, *Thalassiothrix antarctica* and *E. antarctica*, which increase from 1%, 0.4%, 0.1% and 0% to 49.4%, 12.3%, 3.4% and 6.6%, respectively (Figure 4.1).

4.1.3.2. MIS 2

Between 474 cm and 286 cm, the total diatom absolute abundance curve is characterised by high-frequency variability, with a succession of peaks and troughs of varying amplitude. Initially, during the transition into MIS 2, between 474 cm and 382 cm, the record shows a gradual decline in values to 2.55×10^6 v/gds (382 cm), where concentrations oscillate between peaks of $\sim 8.43 \times 10^6$ v/gds and troughs of $\sim 4.39 \times 10^6$ v/gds. Above this decline, valve concentrations recover to a peak of 9.06×10^6 v/gds at 362 cm, prior to a second decline culminating in low of 1.66×10^6 v/gds at a depth of 314 cm. Above this low, between 314 and 286 cm, the total diatom concentration curve describes two small peaks in valve concentration at 310 cm and 294 cm, with values of 5.20×10^6 v/gds and 5.95×10^6 v/gds respectively, before returning to a lower concentration of 2.55×10^6 v/gds at 286 cm (Figure 4.1). The high-frequency variability in total diatom absolute abundance, between 474 cm and 286 cm is even more pronounced in the diatom species assemblage relative abundance plots. The variability is characterised by elevated relative abundances of the *Fragilariopsis* sea-ice group, *F. obliquecostata*, and *Chaetoceros* rs, which increase between the depths of 474 cm and 366 cm, peak around 366 cm and steadily decrease thereafter to 286 cm. The *Fragilariopsis* sea-ice group relative abundance increases from 2.5% at 474 cm and peaks between 374 cm and 356 cm, where values vary between $\sim 4.6\%$ and $\sim 1.7\%$, and subsequently declines to 0.25% at 286 cm. *Chaetoceros* rs relative abundance increases from 14.2% at 474 cm to a double peak of 65.8% and 60.2% at 370 cm and 362 cm, respectively. *Chaetoceros* rs concentrations subsequently decline to a minimum of 8.6% at 286 cm. *F. obliquecostata* relative abundance varies dramatically between maxima of $\sim 1.6\%$ and minima of 0% between 374 cm and 314 cm and decline to trace values beyond 286 cm. The opposite of the *Fragilariopsis* sea-ice group and *Chaetoceros* rs relative abundance pattern is exhibited by *T. lentiginosa*, *Thalassiothrix antarctica* and *A. tabularis*. Their relative abundance curves show a gradual reduction from 12.3%, 3.4% and 2.8% at 474 cm, 474 cm and 458 cm, to minima of 1.8%, 0% and 0.24% at 370 cm, 362 cm and 378 cm, and subsequently increase to peaks of 15.8%, 5.2% and 4.5% at 286 cm, 286 and 302 cm, respectively. The *Thalassiosira antarctica* group (*T. antarctica* (cold) and *T. antarctica* (warm)) increases to maximum relative abundances of 2.9% at 458 cm, declining thereafter to 0.49% at 286 cm. *P. glacialis* relative abundance gradually climbs from 0% at 474 cm to peak abundance of 3.2% at 350 cm and declines to trace values above 314 cm. The major taxon *F. kerguelensis* shows a fairly constant relative abundance throughout the period (474 cm to 286 cm), with a mean

relative abundance of 44.8% (standard deviation = 8.67%, $n = 48$), with the exception of a decline to 1% and 17.2% at 450 cm and ~366 cm, respectively. The drops in *F. kerguelensis* relative abundance at 450 cm and ~366 cm are coeval with peaks in the *Chaetoceros* rs relative abundance curve (Figure 4.1). The high-frequency variability characteristic of the previous 188 cm (474 cm to 286 cm) is absent over the next 198 cm (286 cm to 90 cm) with the diatom absolute abundance curve increasing gradually from 2.55×10^6 v/gds at 286 cm to 4.54×10^6 v/gds at 90 cm. Between these depths (286 cm and 90 cm) the species assemblage shows elevated relative abundances in *E. antarctica*, *T. trifulta*, and *Chaetoceros* rs, with means of 9.6% (standard deviation = 2.86, $n = 20$), 1.59% (standard deviation = 0.82, $n = 20$) and 30.9% (standard deviation = 9.26, $n = 20$), respectively. Over the same period the *T. lentiginosa* and *Thalassiothrix antarctica* relative abundance curves show a gradual reduction, declining from 15.8% and 5.2% to 9.8% and 3.3% between 286 cm and 90 cm, respectively (Figure 4.1).

4.1.3.3. MIS 1

The remaining 86 cm (90 cm to 4 cm) of the total diatom absolute abundance curve, during MIS 1, is characterised by rapid fluctuations in valve concentrations, between low values (4.54×10^6 v/gds (90 cm), 4.56×10^6 v/gds (74 cm), 5.13×10^6 v/gds (38 cm)) and higher values (11.3×10^6 v/gds (82 cm), 17.2×10^6 v/gds (54 cm), 16.6×10^6 v/gds (24 cm), 12.0×10^6 v/gds (4 cm)). The transition observed in the diatom absolute abundance data is consistent with transition between MIS 2 and MIS 1 in the MS curve (Figure 4.1). Total diatom concentrations at the core top (4 cm) are 12.0×10^6 v/gds. This section of the core is characterised by a large increase in the relative abundance curves of *Rhizosolenia* spp. (0.69% to 4.1%), *F. separanda* (0.67% to 2.6%), *T. lentiginosa* (9.8% to 15.7%) and *A. tabularis* (0.92% to 1.38%) and a coeval decline in the relative abundance curves of *Chaetoceros* rs (57.1% to 14.5%), *E. antarctica* (10.5% to 3.6%), *Thalassiothrix antarctica* (3.3% to 0.76%) and the *Fragilariopsis* sea-ice group (1.8% to 0.69%) (Figure 4.1).

4.1.4. Principle Components Analysis – Relative Abundance Data

Prior to PCA analysis, species present at quantities $\geq 0.5\%$ were removed (Chapter 3). In core TPC063, the number of analysed species (and species groups) were reduced from 46 to 16 (Table 4.1). The subsequent analysis was conducted on the 16 species and species groups for the high-resolution portion of the record between 286 cm and 494 cm.

Table 4.1. Core TPC063 (HRW): Diatom species and species groups representing >0.5% of the assemblage (Appendix 1) identified during light microscope analysis.

<i>Actinochilus actinocyclus</i>	<i>Porosira glacialis</i>
<i>Azpeitia tabularis</i>	<i>Rhizosolenia</i> spp.*
<i>Hyalochaete Chaetoceros</i> rs	<i>Thalassiosira antarctica</i> group*
<i>Eucampia antarctica</i>	<i>Thalassiosira gracilis</i> var <i>gracilis</i>
<i>Fragilariopsis</i> sea-ice group*	<i>Thalassiosira gracilis</i> group*
<i>Fragilariopsis kerguelensis</i>	<i>Thalassiosira lentiginosa</i>
<i>Fragilariopsis obliquecostata</i>	<i>Thalassiosira trifulta</i>
<i>Fragilariopsis separanda</i>	<i>Thalassiothrix antarctica</i>

Species groups:Fragilariopsis* sea-ice group – *F. curta*, *F. cylindrus**Rhizosolenia* spp. – *Rhizosolenia antennata antennata*, *Rhizosolenia antennata semispina*, *Rhizosolenia crassa*, *Rhizosolenia polydactyla polydactyla*, *Rhizosolenia polydactyla squamosa*, *Rhizosolenia simplex*, *Rhizosolenia styliformis**Thalassiosira antarctica* group – varieties cold and warm.*Thalassiosira gracilis* group – varieties *gracilis* and *expecta*.

The PCA accounted for more than 78% of the variance within the first 6 axes (Table 4.2). Based on Kaiser's rule, the scree plot (Figure 4.2) and current understanding regarding diatom ecological associations (Chapter 3), it was decided that the most representative and interpretable modes of variability were explained by the first three PCA axes, which capture ~57 % of the variability and hence the highest eigenvalues (Table 4.2).

Table 4.2. Core TPC063 (HRW): PCA axes eigenvalues (shading indicates those PCA axes included in the interpretation based on the scree plot and knowledge of diatom ecologies).

	Axis 1	Axis 2	Axis 3	Axis 4	Axis 5	Axis 6
Eigenvalues	5.721	3.058	2.099	1.476	1.336	1.149
Percentage	30.109	16.097	11.048	7.769	7.032	6.045
Cum. Percentage	30.109	46.207	57.254	65.024	72.055	78.101

Figures 5.3 and 5.4 show the diatom assemblages associated with each PCA axis and Figure 4.5 shows the PCA axes plotted against the component scores associated with each depth.

Axis 1 is characterised by significant positive loadings for one species only; *Chaetoceros* rs (0.39), and significant negative loadings for *T. lentiginosa* (-0.361), *Thalassiothrix antarctica* (-0.353) and *F. kerguelensis* (-0.351), *E. antarctica* (-0.312), *A. actinochilus* (-0.275), *T. trifulta* (-0.269), and *A. tabularis* (-0.261) (Figure 4.3). Samples associated with high positive loadings occur at two intervals of the record, between 492 cm and 476 cm and again between 378 cm and 344 cm, whilst negatively loaded samples dominate the record between 476 cm and 405 cm and 344 cm and 284 cm (Figure 4.5).

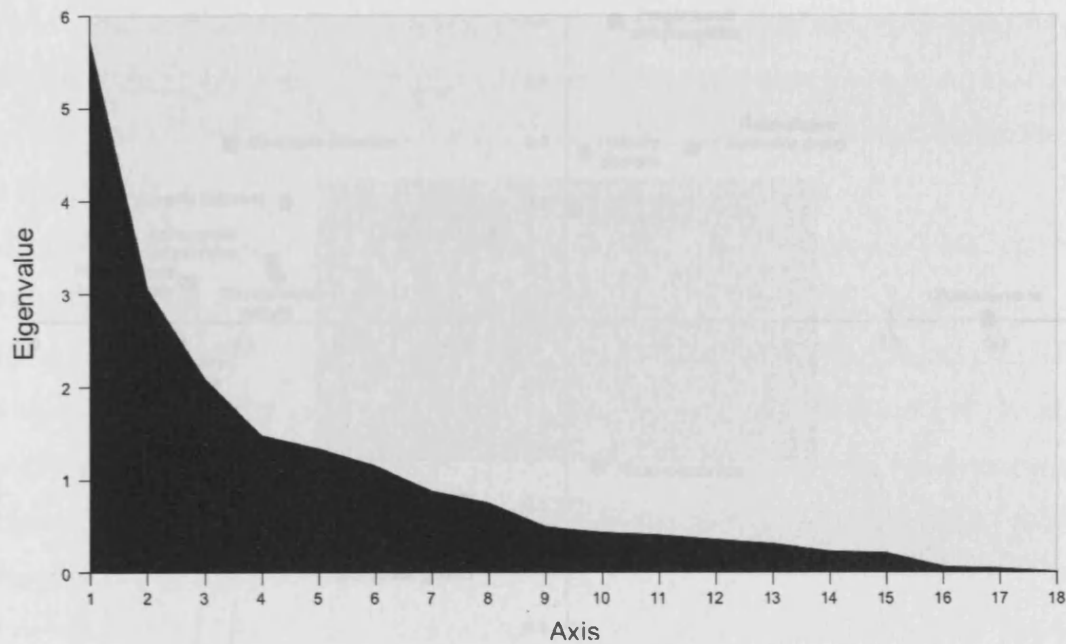


Figure 4.2. Core TPC063 (HRW): PCA Scree plot generated from the analysis of diatom assemblage relative abundance data in the Multivariate Statistical Package (MVSP) developed by Kovach *et al.* (1999).

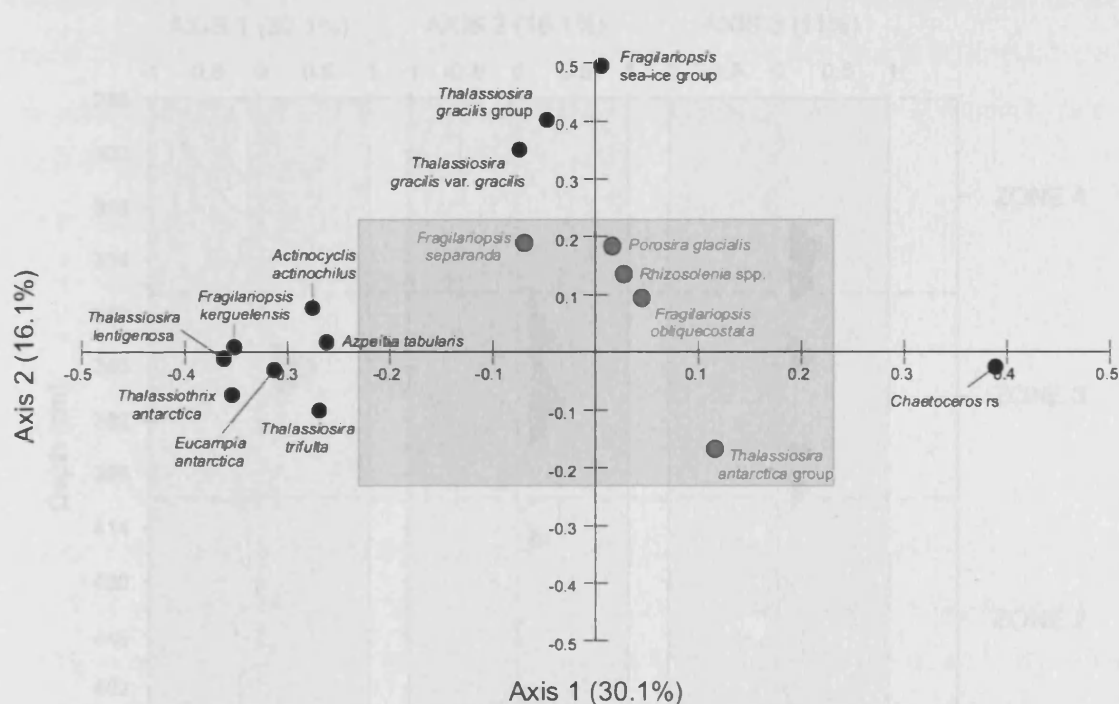


Figure 4.3. Core TPC063 (HRW): PCA variable loadings, axis 2 versus axis 1, generated from the analysis of diatom assemblage relative abundance data in the Multivariate Statistical Package (MVSP) developed by Kovach *et al.* (1999). Black circles indicate diatom species and species groups significant at the 90% level (Shaded region and gray circles indicate species and species groups not significant at the 90% level).

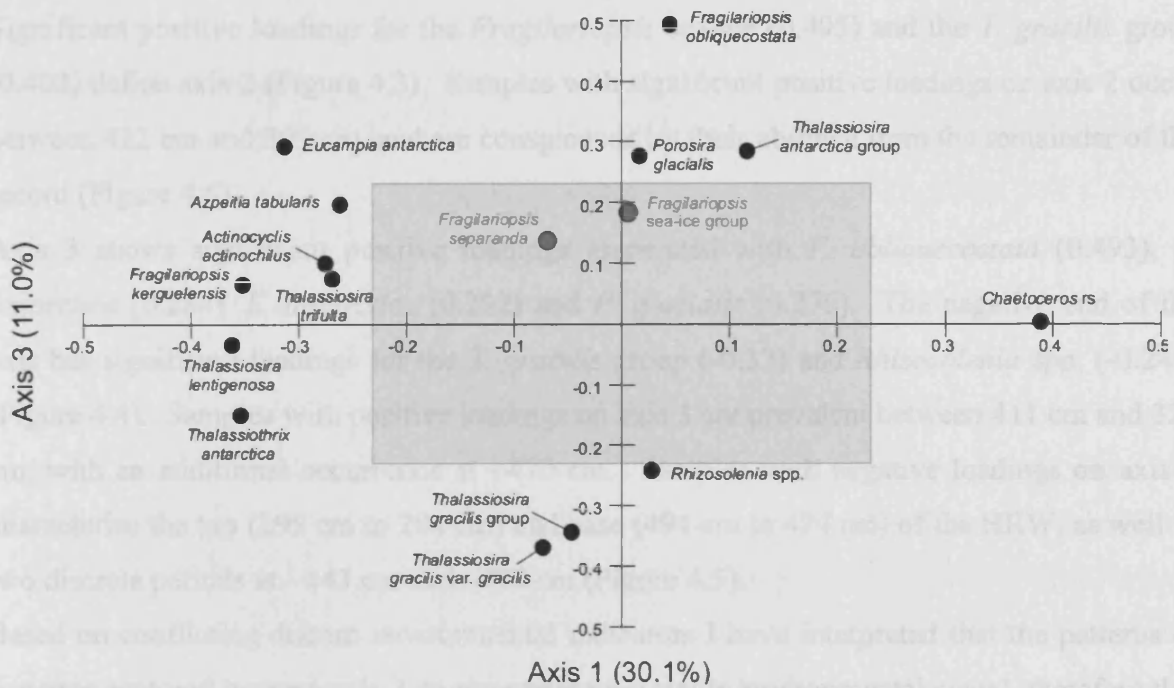


Figure 4.4. Core TPC063 (HRW): PCA variable loadings, axis 3 versus axis 1, generated from the analysis of relative abundance data in a MVSP (Kovach *et al.* 1999). Black circles indicate diatom species and species groups significant at the 90% level (Shaded region and gray circles indicate species and species groups not significant at the 90% level).

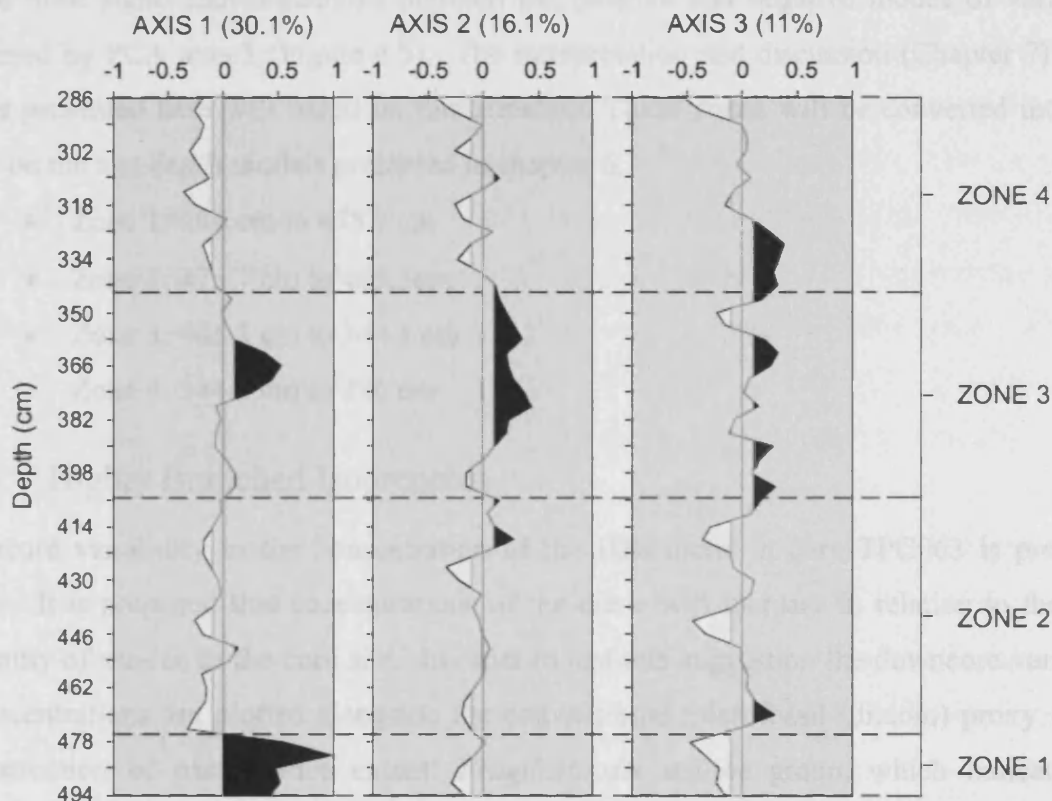


Figure 4.5. Core TPC063 (HRW): PCA component scores, axes 1 to 3, generated from the analysis of relative abundance data in a MVSP (Kovach *et al.* 1999). Shaded black and white polygons indicate significant positive and negative variability respectively (un-shaded areas indicate insignificant variability). Zones are primarily based on significant mode shifts on axis 1, the primary principle component.

Significant positive loadings for the *Fragilariopsis* sea-ice (0.495) and the *T. gracilis* group (0.402) define axis 2 (Figure 4.3). Samples with significant positive loadings on axis 2 occur between 422 cm and 399 cm, and are conspicuous by their absence from the remainder of the record (Figure 4.5).

Axis 3 shows significant positive loadings associated with *F. obliquecostata* (0.493), *T. antarctica* (0.284), *E. antarctica* (0.292) and *P. glacialis* (0.276). The negative end of the axis has significant loadings for the *T. gracilis* group (-0.37) and *Rhizosolenia* spp. (-0.243) (Figure 4.4). Samples with positive loadings on axis 3 are prevalent between 411 cm and 322 cm, with an additional occurrence at ~470 cm. Samples with negative loadings on axis 3 characterise the top (295 cm to 284 cm) and base (494 cm to 474 cm) of the HRW, as well as two discrete periods at ~443 cm and ~417 cm (Figure 4.5).

Based on conflicting diatom environmental indicators I have interpreted that the patterns of variance captured beyond axis 3 do not represent a single environmental signal, therefore this analysis focuses only on the first 3 PCA axes.

The HRW of core TPC063, which occurs during MIS 2, is divided into zones primarily based on the most significant transitions between the positive and negative modes of variability explained by PCA axis 1 (Figure 4.5). The interpretation and discussion (Chapter 7) of the results presented here will be based on this zonation. These zones will be converted into ages based on the age-depth models presented in chapter 6.

- Zone 1: 494 cm to 475.7 cm
- Zone 2: 475.7 cm to 405.3cm
- Zone 3: 405.3 cm to 344.1 cm
- Zone 4: 344.1 cm to 286 cm

4.1.5. Highly Branched Isoprenoids

Downcore variability in the concentration of the HBI diene in core TPC063 is presented below. It is proposed that concentrations of the diene will increase in relation to the close proximity of sea-ice to the core site. In order to test this suggestion the downcore variations in concentrations are plotted alongside the conventional microfossil (diatom) proxy for the reconstruction of past sea-ice extent: *Fragilariopsis* sea-ice group, which indicates the presence of the sea-ice edge when observed at relative abundances >3% (Figure 4.6).

At the base of the HBI record, between 498 cm and 432 cm, diene concentrations are relatively low, varying between 0.22 yg/g and 0.46 yg/g and coincide with *Fragilariopsis* sea-ice group relative abundance lower than 3%. The diene trend subsequently shows three

small peaks in values at 416 cm (1.02 yg/g), 400 cm (1.32 yg/g) and 319 cm (0.96 yg/g), coincident with the first breach of the 3% threshold by the *Fragilariopsis* sea-ice group relative abundance curve. Diene values decline from 0.96 at 319 cm to 0.52 at 384 cm before steadily increasing to a value of 1.5 at 353 cm, concurrent with a sharp drop in the relative abundance of the *Fragilariopsis* sea-ice group from values greater than 3%. Diene values decline between 353 cm and 285 cm to a value of 0.33 yg/g, showing low values while relative abundance of the *Fragilariopsis* sea-ice group exceeds 3% at 306 cm and 294 cm. Diene values increase between 294 cm and 182 cm to a peak of 2.78 yg/g. This peak coincides with relative abundances of the *Fragilariopsis* sea-ice group less than 3%. Subsequent to this peak diene values decline to 0 yg/g at the top of the record (8 cm), concurrent with marked drop in *Fragilariopsis* sea-ice group relative abundance (Figure 4.6). From the results it is clear that the diene trend shares a number of similarities with the *Fragilariopsis* sea-ice group relative abundance curve, consistently increasing in concentration with relative abundance greater than 3% during the HRW. The close relationship between the diene and diatom trends during the HRW shows that high-resolution changes in the HBI proxy can be used to indicate fluctuations in the extent of Antarctic sea-ice. The apparent divergence between the trends in the upper portion of the record could potentially relate to a lower sampling resolution or a shift in sea-ice seasonality (chapter 7) higher resolution sampling in the future could help to further constrain this. There appears to be a small lag between the two trends, with peaks in the concentration of the diene occurring just after major peaks in the relative abundance of sea-ice diatoms. This apparent lag has also been identified in the latest analysis of modern Antarctic sediments. Although the source of this offset is presently unknown it could be related to different rate of sedimentation. On going studies are presently comparing satellite imagery of chlorophyll production with the preservation of diatoms and HBI's in rapidly accumulating sediments in an attempt to improve our understanding of bloom dynamics and transferral of the diatom and HBI signal to the sediments Massé *et al.*, unpublished).

These results further support previous indications that a mechanism similar to that observed in the Arctic operates in the Antarctic, confirming the HBI's covariance with temperature and the diene's specificity to the sea-ice environment and, for the first time, extend the temporal influence of this mechanism into the last glacial, back as far as at least MIS 3. I show that variations in the concentration of the HBI diene can be used to reconstruct high-resolution records of Antarctic sea-ice variability during the last glacial cycle and confirm that HBI's have enormous potential as a much-needed complimentary sea-ice proxy. This proxy is still

very much in its early stages and ongoing research is continuously attempting to improve its robustness. The data presented here represents an important facet in this proxy's development and indicates that it has a very exciting future.

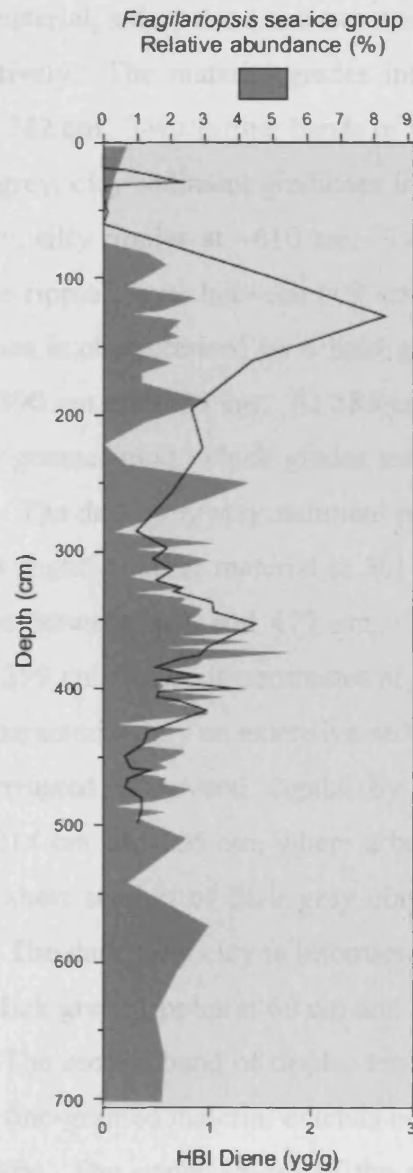


Figure 4.6. Core TPC063: HBI diene concentration in yg/g (black line) plotted alongside *Fragilariopsis* sea-ice group relative abundance (gray block).

4.2. TPC286 – Results

4.2.1. Core Description – Sedimentology

The lithological composition of TPC286 shows a higher degree of variability than core TPC063 (Figure 4.7). The lower 39 cm (929 cm to ~890 cm) of the core sediments are characterised by a diatom-rich clay material. The lower half of the sediment is characterised by fine ripples and a patch of discoloured material. The upper half of the sediment shows

intermittent bands of heavy ripples. The sediment terminates at a sharp boundary, defined by a speckled, dark colouring. The sediment facies is characterised by a considerably greyer clay material at 890 cm with a lower diatom content, which persists up-core for ~195 cm (~890 cm to 625 cm). Within this material, a dropstone and two small lenses are evident at 883 cm, 848 cm and 830 cm, respectively. The material grades into a band of heavy, more-silty, rippling between 751 cm and 742 cm. Two further bands of lighter ripples are evident at 703 cm and 632 cm. At 625 cm the grey, clay sediment graduates into a richer, greener mud, which terminates in a band of heavy, silty ripples at ~610 cm. Two fine-grained bands of darker material are evident above the rippled layer between 609 cm and 603 cm. Between 603 cm and 586 cm the sediment facies is characterised by a light grey clay material, similar to the sediment described between 890 cm and 625 cm. At 586 cm the light grey clay once more graduates into a considerably greener mud, which grades into a dark grey homogenous clay between 558 cm and 549 cm. The dark grey clay sediment persists between 549 cm and 480 cm, features a jagged band of slightly darker material at 501 cm and terminates in a band of darker, fine grained sediment between 481 cm and 477 cm. Sediment of pale green clay is present between 477 cm and 399 cm, where it terminates at a sharp, sloped contact. Above this contact the sediment is characterised by an extensive sediment of dark grey homogenous clay. This material is interrupted at several depths by bands of rippling. The first interruption occurs between 214 cm and 206 cm, where a band of fine green ripples grades into heavier rippling. After short section of dark grey clay, a second band of fine green ripples is evident at 200 cm. The dark grey clay is interrupted several more times at the top of the sediment by moderate dark green ripples at 60 cm and two sections of moderate brown ripples at 49 cm and 42 cm. The second band of ripples terminated in a sharp horizon at 40 cm. Sediment of dark brown fine-grained material extends between 40 cm and 36 cm, which terminate in a curved boundary. The upper 35 cm of the core is characterised by a fine-grained brown – green ‘organic-rich’ material. (Chapter 5), back to the last interglacial, MIS 5 (Figure 4.7). Glacial sediments dominate the sequence, with Holocene sediments restricted to the upper 50 cm of the core.

4.2.2. Magnetic Susceptibility

The MS curve from core TPC286 (Figure 4.7) is characterized by extreme variability that, potentially, is a consequence of extensive periods of perennial sea-ice over the core site (Chapter 4).

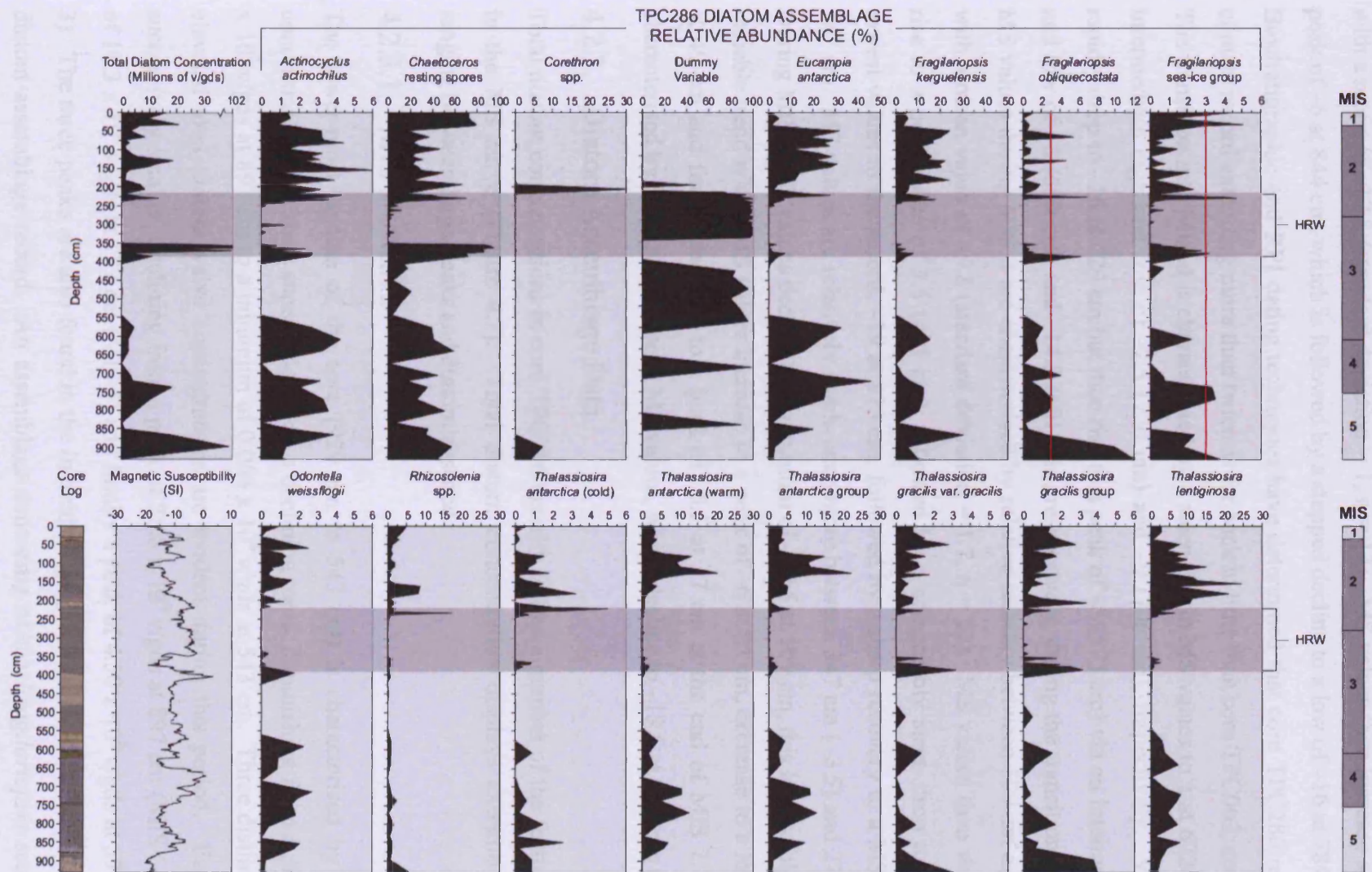


Figure 4.7. Core log (prepared digitally in a graphic package with RGB conversions of Munsell colours), MIS stratigraphy (based on magnetic susceptibility), magnetic susceptibility (recorded with Bartington probe) and diatom species assemblage data for core TPC286. Total diatom concentrations presented in absolute numbers (calculated using the equation of Scherer, 1994). Relative percentages for species comprising >0.5% of the assemblage data. The dark rectangle indicates the high-resolution window (HRW). Red lines indicate sea-ice 3% threshold.

During MIS 5, at the base of the core (930 cm to 906 cm), MS shows consistently low values, with a mean of -17.8 (standard deviation = 1, $n = 13$). MS values then increase sharply to a peak of -6 at 844 cm, which is followed by a stepped decline to a low of -16 at 784 cm.

Biostratigraphic and RPI dating techniques have determined that core TPC286 represents a climate record extending more than twice as far back in time than core TPC063, covering ~96 ka. The transition into MIS 4 is characterised by a steep rise in MS values to 1 at 672 cm, via an intermediate high and low of -2.5 (720 cm) and -9 (706 cm), respectively. Values then rapidly drop to -16 at 629 cm but then rise to a peak of -5 (573 cm) via an intermediate peak and low of -8 (609 cm) and -14.5 (601 cm), respectively, during the transition into MIS 3. MS values during MIS 3 are characterised by relative stability between 599 cm and 419 cm, with a mean value of -9.8 (standard deviation = 1.7, $n = 92$). MS values then show a steep rise to a peak value of 3.5 (405 cm), followed by a comparably steep drop to one of the lowest values in the record, -19 at 375 cm, followed by a sharp recovery to a MS of -3.5 at 347 cm. MS values are relatively stable once more between 347 cm (-3.5) and 279 cm (-4). During MIS 2 MS values decline to a minimum of -19.5 at 109 cm, this low is followed by a variable trend where MS values increase to a peak of -6 at 83 cm, decrease to a low of -15.5 at 49 cm and finally increase to a peak of -6.5 at 37 cm at the end of MIS 2. MIS 1 is characterised by a sharp decrease in MS values, which decline to -19.5 at the core top (1 cm).

4.2.3. Diatom Assemblage Data

Total diatom concentrations in core TPC286 broadly follow a number of the features evident in the MS curve (Figure 4.7). Total diatom concentration displays extreme variability ranging between large peaks and diatom absence.

4.2.3.1. MIS 5 – MIS 3

The lower-most portion of the core (929 cm to 543 cm) is characterised by oscillating concentrations of valves superimposed on a declining trend, diminishing from a peak of 38.8×10^6 v/gds at 897 cm to a minimum of 0.066×10^6 v/gds at 543 cm. Three distinct peaks of elevated total diatom valve concentrations are evident during this period. Each peak is successively smaller, declining from a peak of 38.8×10^6 v/gds at 897 cm (MIS 5), to a peak of 18.3×10^6 v/gds at 737 cm (MIS 5) and finally a peak of 4.50×10^6 v/gds at 576 cm (MIS 3). The three peaks are also found in the individual species relative abundance curves of the diatom assemblage record. An assemblage consisting of the *Fragilariopsis* sea-ice group (*Fragilariopsis curta* and *Fragilariopsis cylindrus*) (1.8%), *F. obliquecostata* (9.9%),

Chaetoceros rs (56.9%), *T. gracilis* group (*T. gracilis* var. *gracilis* and *T. gracilis* var. *expecta*) (3.8%) and *Corethron* spp. (7.4%) dominates the lowermost peak at 897 cm. The middle peak in the sequence (737 cm) is defined by elevated relative abundances in the *Fragilariopsis* sea-ice group (3.3%), *A. actinochilus* (2.1%), *F. kerguelensis* (12.3%), *Rhizosolenia* spp. (2.3%), *T. lentiginosa* (7.1%), *E. antarctica* (45.9%), *T. antarctica* (warm) (~9.9%) and *O. weissflogii* (2%). The third peak (576 cm) is primarily characterised by marked peaks evident in the relative abundance of *Fragilariopsis* sea-ice group (2.2%), *A. actinochilus* (4.3%), *T. gracilis* group (1.6%), and *F. kerguelensis* (15.2%) (Figure 4.7).

4.2.3.2. MIS 3

Above the third peak in absolute abundance, valve concentrations decline to an extremely low concentration of 0.066×10^6 v/gds at 543 cm. Low absolute abundances are maintained for the following 137 cm (543 cm to 406 cm), with valve concentrations attaining values no higher than 0.38×10^6 v/gds. Between 543 cm and 406 cm the species assemblage is characterised by very low relative abundance. *Chaetoceros* rs are the only species to achieve quantities >1% for this entire section, varying between values of 4% and 20.5%. In contrast, values for the dummy variable vary between 70% and 95.6% during this section of the core, indicating low rates of valve deposition. The following 144 cm of the core (406 cm to 362 cm) is then characterised by three successively higher peaks in total diatom concentration, culminating in a peak of 102×10^6 v/gds. The first, relatively small, peak reaches values of 11.1×10^6 v/gds at 386 cm and then shows a steep increase to a value of 39.6×10^6 v/gds at 370 cm. Concentrations fall to 17.1×10^6 v/gds at 366 cm, before a sharp rise to 102×10^6 v/gds at 362 cm (Figure 4.7). Following the third peak at 362 cm, valve concentrations drop to 0.028×10^6 v/gds at 350 cm.

The sharp pulse in deposition evident at 362 cm is seen in the individual species relative abundance curves. Several species and groups within the diatom assemblage exhibit an increase in relative abundance centred about a depth of 378 cm, however, despite relative abundances >3% evident in the curves of the *Fragilariopsis* sea-ice group, *F. obliquecostata*, *T. gracilis* group, *F. kerguelensis* and *E. antarctica*, *Chaetoceros* rs clearly dominate the interval, with relative abundances >90% (Figure 4.7).

4.2.3.3. MIS 3 – MIS 2

The transition from MIS 3 to MIS 2 is characterised by an extensive section of low valve concentrations, extending upwards from 350 cm (MIS 3) to 238 cm (MIS 2) when valve

concentrations vary between values of 0 v/gds and 0.30×10^6 v/gds. This period of low valve deposition is also shown in the species relative abundance curves. During this section, the only diatom present above concentrations of 0.5% is *Chaetoceros* rs, with a mean value of 2.9% (Standard deviation = 3.8, n = 29) (Figure 4.7).

4.2.3.4. MIS 2 – MIS 1

The uppermost portion of the record (238 cm to 0 cm) shows an increase in total diatom concentrations with peaks of 13.5×10^6 v/gds, 8.61×10^6 v/gds and 18.6×10^6 v/gds at 230 cm, 206 cm and 130 cm respectively. Subsequent to the third peak, valve concentrations decline, to 1.27×10^6 v/gds at 90 cm. The transition from MIS 2 to MIS 1, during the remaining 90 cm of sediment, is characterised by a gradual increase in valve concentrations to 15.0×10^6 v/gds at the core top (Figure 4.7). The increase in total diatom valve concentrations observed above 238 cm includes enhanced relative abundances across the entire species assemblage. Between 238 cm and 50 cm, the diatom assemblage is characterised by a series of high frequency, high amplitude shifts in relative abundance, most evident in the curves of *F. obliquecostata*, *Rhizosolenia* spp., *Corethron* spp., *F. kerguelensis*, *E. antarctica*, *Chaetoceros* rs and the *Fragilariopsis* sea-ice group. The individual peaks in total diatom absolute abundance observed at 230 cm, 206 cm, and 130 cm are also reflected in the species relative abundance curves. An assemblage primarily composed of the *Fragilariopsis* sea-ice group (4.7%), *F. kerguelensis* (~13.7%), and *Chaetoceros* rs (69.9%) dominate the peak at 230 cm.

The peak in absolute abundance observed at 206 cm is primarily the result of a major increase in the relative abundance of *Corethron* spp. (30.4%), with contributions from the *Fragilariopsis* sea-ice (2.4%) and *T. gracilis* groups (3.4%). The third and last peak in the sequence (130 cm) occurs during a section (146 cm to 50 cm) of elevated relative abundances of *A. actinochilus* (mean = 2.9%, standard deviation = 0.8, n = 12), *F. kerguelensis* (mean = 17%, standard deviation = 4, n = 12), *E. antarctica* (mean = 24.3%, standard deviation = 5.9, n = 12) and *Chaetoceros* rs (mean = 27.1%, standard deviation 7.8, n = 12). The peak (130 cm) itself is characterised by *F. obliquecostata* (4.7%), *T. antarctica* (warm) (20.4%), *F. kerguelensis* (~20.7%) and *E. antarctica* (~26.1%). The remaining 50 cm of sediment (50 cm to 0 cm) is defined by a marked increase in the relative abundance of *Rhizosolenia* spp. (1.3% to 4.9%), *Chaetoceros* rs (16.8% to 72.5%), and the *Fragilariopsis* sea-ice group (1.1% to 4.3%), and a contemporaneous decrease in the relative abundance of *E. antarctica* (31.8% to 1.3%) (Figure 4.7).

4.2.4. Principle Components Analysis – Relative Abundance Data

Periods of extremely low diatom abundance necessitated the use of the macro-ecological counting technique for a number of samples in core TPC286 employing a dummy variable to enable the calculation of relative abundance data (Chapter 4).

Diatom assemblage counts of TPC286 identified 52 species and species groups. Of these 52, 15 have a mean relative abundance $\geq 0.5\%$ (Table 4.3). Following the format used for TPC063 mean relative abundance was investigated for the high-resolution portion of the record only (386 cm to 218 cm). This further reduced the number of species/species groups from 15 to 12 (Table 4.3).

Table 4.3. Core TPC286 (HRW): Diatom species and species groups representing $>0.5\%$ of the assemblage (Appendix 1) identified during light microscope analysis.

<i>Actinocyclus anctinophilus</i>	<i>Rhizosolenia</i> spp.*
<i>Chaetoceros</i> rs	<i>Thalassiosira antarctica</i> (cold)
<i>Eucampia antarctica</i>	<i>Thalassiosira antarctica</i> (warm)
<i>Fragilariopsis kerguelensis</i>	<i>Thalassiosira gracilis</i> group*
<i>Fragilariopsis obliquecostata</i>	<i>Thalassiosira lentiginosa</i>
<i>Fragilariopsis</i> sea-ice group*	Dummy variable

*Species groups:

Fragilariopsis sea-ice group – *F. curta*, *F. cylindrus*

Rhizosolenia spp. – *Rhizosolenia antennata*, *semispina*, *Rhizosolenia crassa*, *Rhizosolenia polydactyla polydactyla*, *Rhizosolenia polydactyla squamosa*, *Rhizosolenia sima sima*, *Rhizosolenia simplex*, *Rhizosolenia styliformis*

Thalassiosira gracilis group – varieties *gracilis* and *expecta*.

The PCA accounted for 91.6% of the dataset's variance within the first 4 Axes (Table 4.4). Kaiser's rule and the scree plot (Figure 4.8) imply that the most significant modes of variability have been identified within the initial 2 Axes, with axis 1 dominating the data. However, upon closer inspection, it is evident that the primary pattern of variability, discerned by PCA axis 1, is purely one of diatom presence versus diatom absence. When taking this into account, the relatively minor third and fourth Axes become more important in terms of the environmental gradients they represent; their significance merely subdued by the dominance of axis 1.

Table 4.4. Core TPC286 (HRW): PCA axes eigenvalues (shading indicates those PCA Axes included in the interpretation based on the scree plot and knowledge of diatom ecologies).

	Axis 1	Axis 2	Axis 3	Axis 4
Eigenvalues	8.292	1.465	0.702	0.528
Percentage	69.103	12.211	5.853	4.402
Cum. Percentage	69.103	81.314	87.167	91.57

The species assemblages associated with each axis are described below and illustrated in Figures 5.9, 5.10 and 5.11 and component scores reflecting down core PCA variability are

shown in Figure 4.12. When a variable loading is described as 'significant' in the following discussion this refers to significance at the 90% level.

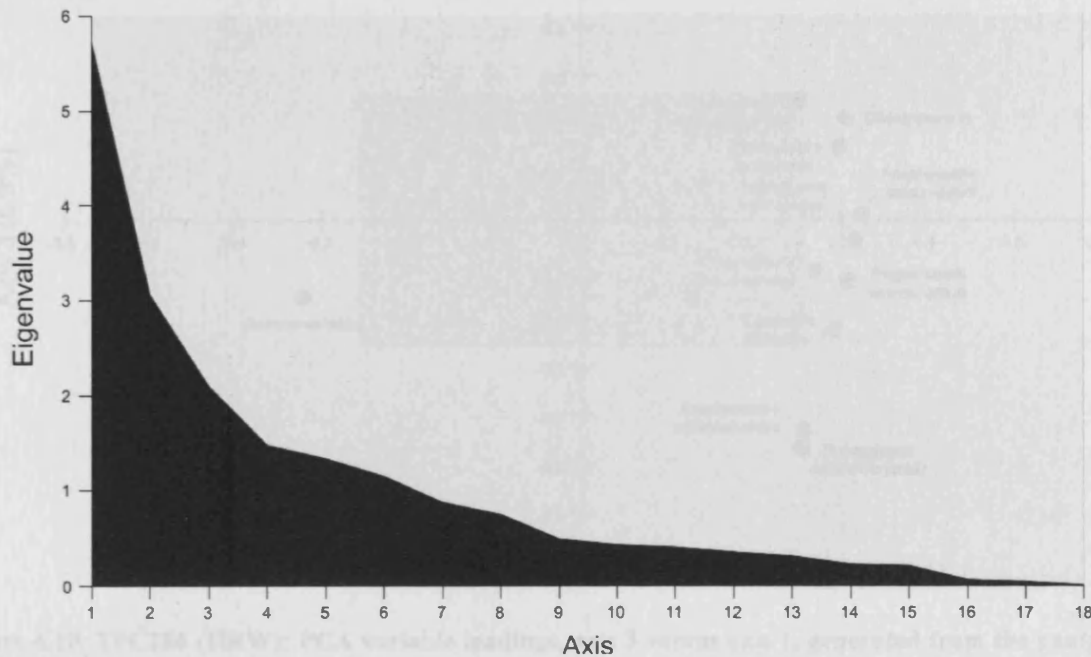


Figure 4.8. Core TPC286 (HRW): PCA Scree plot generated from the analysis of relative abundance data in a MVSP (Kovach *et al.* 1999).

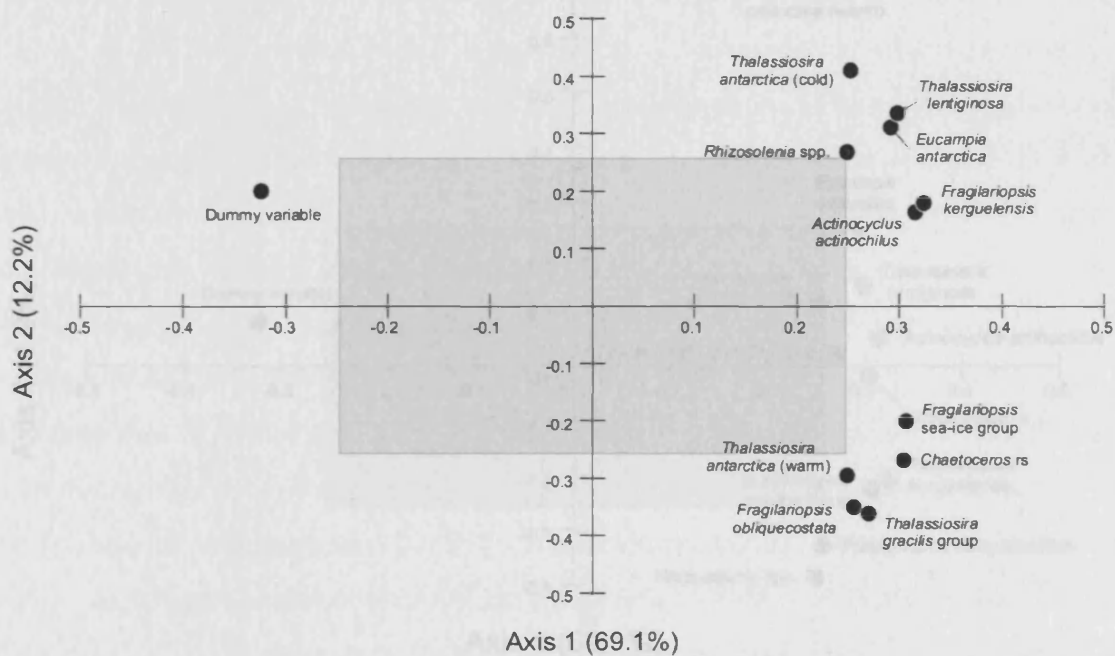


Figure 4.9. Core TPC286 (HRW): PCA variable loadings, axis 2 versus axis 1, generated from the analysis of diatom assemblage relative abundance data in a MVSP (Kovach *et al.* 1999). Black circles indicate diatom species and species groups significant at the 90% level (Shaded region and gray circles indicate species and species groups not significant at the 90% level).

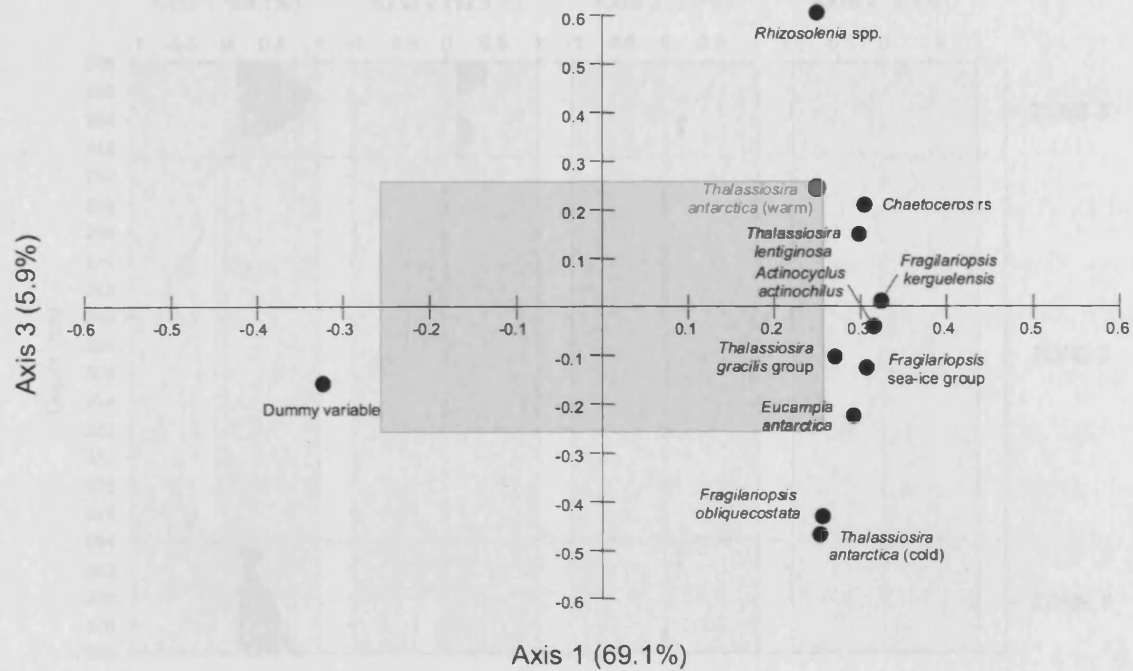


Figure 4.10. TPC286 (HRW): PCA variable loadings, axis 3 versus axis 1, generated from the analysis of relative abundance data in a MVSP (Kovach *et al.* 1999). Black circles indicate diatom species and species groups significant at the 90% level (Shaded region and gray circles indicate species and species groups not significant at the 90% level).

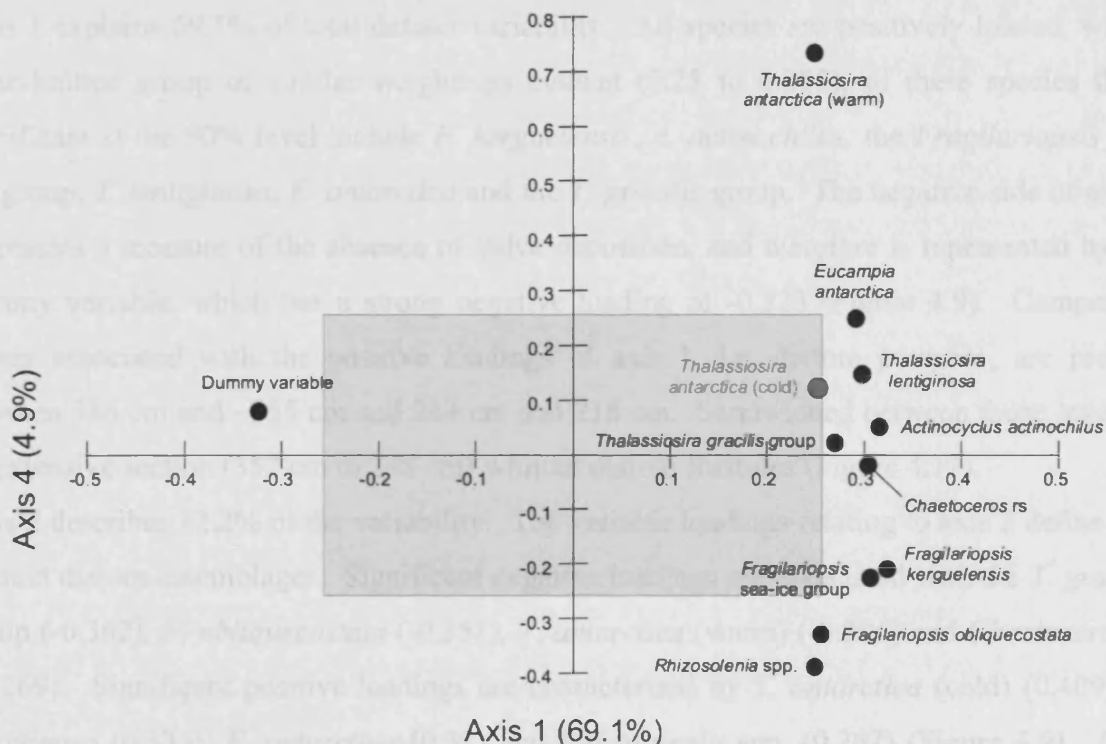


Figure 4.11. TPC286 (HRW): PCA variable loadings, axis 4 versus axis 1, generated from the analysis of relative abundance data in a MVSP (Kovach *et al.* 1999). Black circles indicate diatom species and species groups significant at the 90% level (Shaded region and gray circles indicate species and species groups not significant at the 90% level).

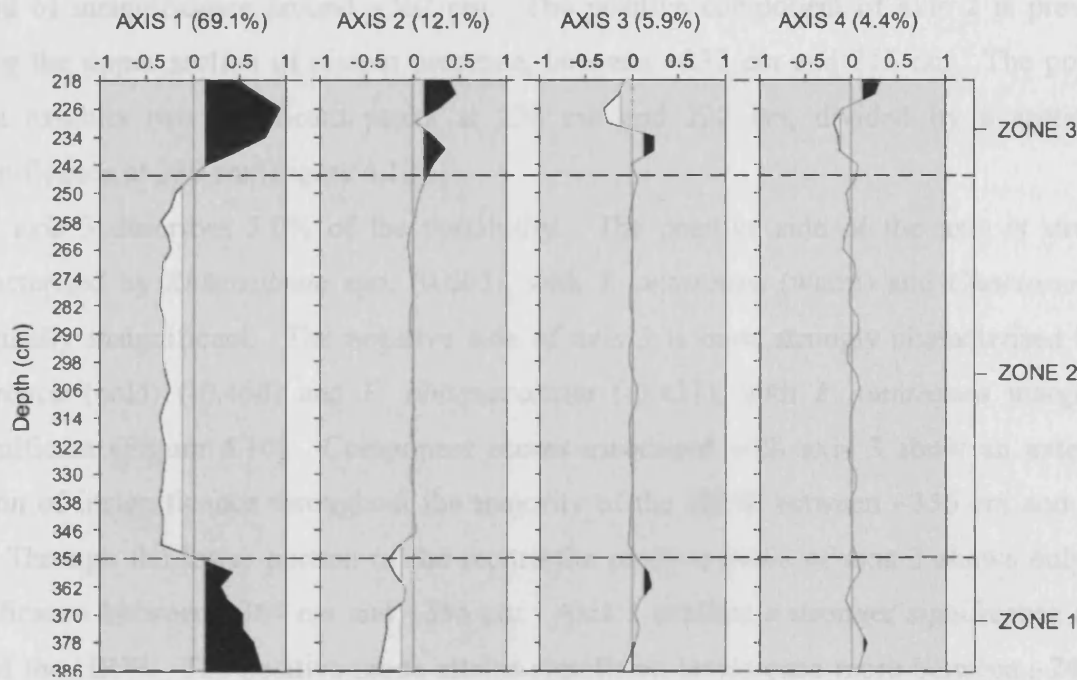


Figure 4.12. Core TPC286 (HRW): PCA component scores, axes 1 to 4, generated from the analysis of relative abundance data in a MVSP (Kovach *et al.* 1999). Shaded black and white polygons indicate significant positive and negative variability respectively (un-shaded areas indicate insignificant variability). Zones are primarily based on significant mode shifts on axis 1, the primary principle component.

Axis 1 explains 69.1% of total dataset variability. All species are positively loaded, with a close-knitted group of similar weightings evident (0.25 to 0.325), of these species those significant at the 90% level include *F. kerguelensis*, *A. actinochilus*, the *Fragilariopsis* sea-ice group, *T. lentiginosa*, *E. antarctica* and the *T. gracilis* group. The negative side of axis 1 represents a measure of the absence of valve deposition, and therefore is represented by the dummy variable, which has a strong negative loading of -0.323 (Figure 4.9). Component scores associated with the positive loadings of axis 1, i.e. diatom presence, are present between 386 cm and ~355 cm and 244 cm and 218 cm. Sandwiched between those levels is an extensive section (352 cm to 248 cm) without diatom frustules (Figure 4.12).

Axis 2 describes 12.2% of the variability. The variable loadings relating to axis 2 define two distinct diatom assemblages. Significant negative loadings are associated with the *T. gracilis* group (-0.362), *F. obliquecostata* (-0.351), *T. antarctica* (warm) (-0.296) and *Chaetoceros* rs (-0.269). Significant positive loadings are characterised by *T. antarctica* (cold) (0.409), *T. lentiginosa* (0.335), *E. antarctica* (0.31) and *Rhizosolenia* spp. (0.267) (Figure 4.9). Case components show that ecological association with axis 2 is restricted to the portions of the HRW defined by diatom presence on axis 1. The negative component of axis 2 dominates the lower portion of the record, significant between 386 cm and 350 cm and exhibiting a

period of insignificance around ~362 cm. The positive component of axis 2 is prevalent during the upper section of diatom presence, between ~232 cm and 218 cm. The positive mode exhibits two significant peaks at 238 cm and 222 cm, divided by a section of insignificance at 230 cm (Figure 4.12).

PCA axis 3 describes 5.9% of the variability. The positive side of the axis is strongly characterised by *Rhizosolenia* spp. (0.605), with *T. antarctica* (warm) and *Chaetoceros* rs marginally insignificant. The negative side of axis 3 is most strongly characterised by *T. antarctica* (cold) (-0.468) and *F. obliquecostata* (-0.431), with *E. antarctica* marginally insignificant (Figure 4.10). Component scores associated with axis 3 show an extensive section of insignificance throughout the majority of the HRW between ~356 cm and ~240 cm. Through the lower portion of the record the positive mode of axis 3 shows only low significance between ~364 cm and ~356 cm. Axis 3 exhibits a stronger significance at the top of the HRW. The positive mode attains significant levels once more between ~240 cm and ~233 cm before the axis switches to its negative mode between ~231 cm and ~221 cm (Figure 4.12).

Axis 4 describes 4.4% of the variability. The variable loadings associated with axis 4 show a relatively narrow spread. The significant positive loadings on the axis are strongly characterised by *T. antarctica* (warm) (0.733), with *E. antarctica* marginally insignificant. Significant negative loadings on axis 4 are characterised by *Rhizosolenia* spp. (-0.39) and *F. obliquecostata* (-0.33), with the *Fragilariopsis* sea-ice group marginally insignificant (Figure 4.11). The environmental gradient represented by axis 4 is significant at the bottom and top of the HRW. The positive mode of axis 4 shows a low significant peak at ~378 cm near the base of the HRW and once more between ~222 cm and 218 cm. The negative mode of axis 4 exhibits a period of significance in the upper portion of the HRW, between 338 cm and 228 cm (Figure 4.12).

The HRW of core TPC286 is divided into zones based on the most significant transitions between the positive and negative modes of variability explained by PCA axis 1 (Figure 4.12). The interpretation and discussion (Chapter 7) of the results presented in this Chapter will be based on this zonation. These zones will be converted into ages based on the age-depth models presented in chapter 6.

- Zone 1: 386 cm to 353.4 cm
- Zone 2: 353.4 cm to 245 cm
- Zone 3: 245 cm to 218 cm

4.2.5. Highly Branched Isoprenoids

Results from the extraction of the sea-ice tracer HBI compound (diene) and their comparison with the *Fragilariopsis* sea-ice group relative abundance curve is shown in Figure 4.13. The results show three peaks in values at 917 cm (1.62 yg/g), 801 cm (1.33 yg/g) and 749 cm (0.88 yg/g), each separated by 0 yg/g values. The diene peaks coincide with periods of the record where the *Fragilariopsis* sea-ice group relative abundance is greater than 3%. Between 733 cm and 414 cm diene values remain low, varying between 0 yg/g and 0.38 yg/g. During this period the *Fragilariopsis* sea-ice group relative abundance is consistently lower than 3%. Between 414 cm and 350 cm values increase to a peak of 9.7 yg/g, which is immediately followed by a decline back to 0 yg/g, coinciding with a peak in the relative abundance of the *Fragilariopsis* sea-ice group in excess of 3%. Between 350 cm and 246 cm diene values remain low, varying between 0 yg/g and 0.75 yg/g, coinciding with extremely low *Fragilariopsis* sea-ice group relative abundance. Diene values show two small peaks at 230 cm (1.89 yg/g) and 198 cm (1.35 yg/g), concurrent with elevated relative abundances of the *Fragilariopsis* sea-ice group greater than 3%. Between 182 cm and 50 cm the diene trend returns to low values, varying between 0 yg/g and 0.75 yg/g. During this period the *Fragilariopsis* sea-ice group relative abundance is consistently less than 3%. The diene trend shows two large peaks at 48 cm (6.14 yg/g) and 16 cm (4.78 yg/g), each followed by a return to a value of 0 at 32 cm and 1 cm. A similar pattern is shown in the *Fragilariopsis* sea-ice group relative abundance curve, with two peaks of 5.1% and 4.3% (Figure 4.13).

From the results it is clear that the diene trend shares a number of similarities with the *Fragilariopsis* sea-ice group relative abundance curve, consistently increasing in values with relative abundance greater than 3%. The close relationship between the diene and diatom trends shows that high-resolution changes in the HBI proxy are in sync with variations in the diatom sediment assemblage throughout the record and can be used to reconstruct Antarctic sea-ice. At times there appears to be a small lag between the two trends, this could be a result of sampling offsets and difference in sampling resolution, although this apparent lag has also been identified in the latest analysis of modern Antarctic sediments and could in fact be related to different rates of sedimentation. One of the most important observations from Figure 4.13 is that when diatom relative abundance is anonymously low, or when diatoms are absent from the record, the HBI diene is also absent. This result is logical as if the production of diatoms in the surface water is constrained by the presence of permanent sea-ice cover then the production of HBI's by the diatoms will too be constrained. None-the-less it was

hoped that the production of HBI's by diatoms living within the sea-ice would still be preserved in the sediments, providing a much needed, unambiguous proxy for the presence of perennial sea-ice. The results presented here show, for the first time, that this is not the case, and that although the diene trend supports and compliments the diatom sediment assemblage, and associated interpretations, it too is constrained by the presence of perennial sea-ice cover. On a positive note the absence of the HBI compounds as well as diatom valves in certain portions of the record supports the interpretation of low surface water production (associated with perennial sea-ice cover) rather than enhanced dissolution. The results from core TPC286 are consistent with those from core TPC063 and thus support the conclusions made above (chapter 7) and confirm the viability and exciting prospects of HBI's as a sea-ice proxy during the last glacial cycle. This study provides the first steps towards a circum-Antarctic suite of high-resolution HBI reconstructions during the last glacial cycle, extending both the temporal and spatial resolution of this emerging sea-ice proxy.

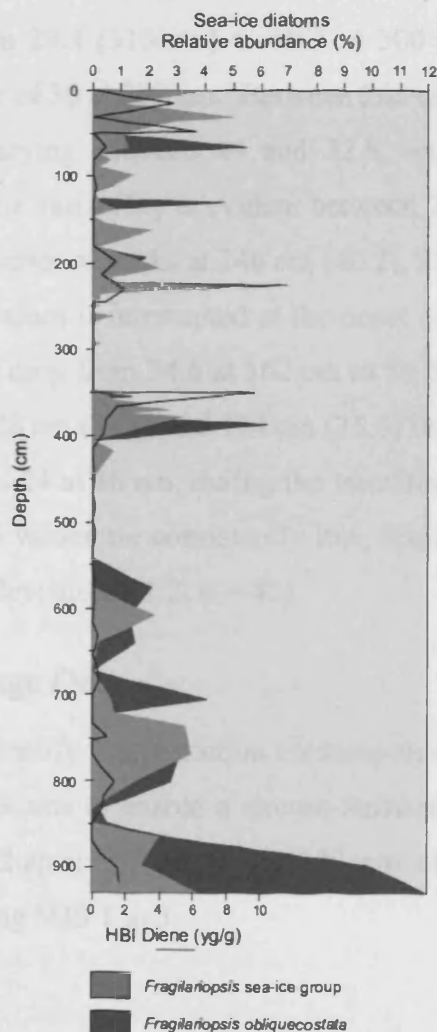


Figure 4.13. Core TP286: HBI diene concentration in yg/g (black line) plotted alongside *Fragilariopsis* sea-ice group (light gray block) and *Fragilariopsis obliquecostata* relative abundance (dark gray block).

4.3. MD03-2603 – Results

4.3.1. Core description – Sedimentology

In this study, I have analysed the upper 380 cm of the 3200 cm of core MD03-2603 (Figure 4.14). The sediment is characterised by brown silty clay with occasional, dark, fine-grained laminae between 400 cm and 150 cm. In addition a section of darker, mottled silty clay is evident between 375 cm and 380 cm. The upper 150 cm of the core are characterised by homogenous brown clay – silty clay and the sparse occurrence of small pebbles. A narrow band of light brown flocs of diatom ooze is evident between 100 cm and 75 cm (Figure 4.14).

4.3.2. Magnetic Susceptibility

The MS curve for core MD03-2603 is shown in Figure 4.14. During MIS 3, between 380 cm and 310 cm, MS values are relatively consistent, with relatively low values of 25.8 and 32.2 and a mean MS value of 28 (standard deviation = 1.8, $n = 36$). Between 310 cm and 282 cm MS values drop sharply from 29.4 (310 cm) to 18.5 at 300 cm, which is followed by an equally sharp climb to a value of 36 at 282 cm. Between 282 cm and 162 cm the MS curve is characterised by a period varying between 44 and 32.8, with a mean of 37.4 (standard deviation = 2.8, $n = 61$). Some variability is evident between 260 cm and 184 cm during the transition into MIS 2, with a series of peaks at 246 cm (40.2), 214 cm (42.6) and 196 cm (44). This period of elevated MS values is interrupted at the onset of MIS 2, between 162 cm and 128 cm, where values rapidly drop from 34.6 at 162 cm to 16.5 at 146 cm. MS values return to high MS values between 128 cm (34.8) and 104 cm (35.6) followed by a gradual decline in values from 35.6 at 104 cm to 24 at 86 cm, during the transition into MIS 1. During MIS 1, between 86 cm and 2 cm, MS values are consistently low, displaying little variation with and a mean MS of ~24 (standard deviation = 1.2, $n = 43$).

4.3.3. Diatom Assemblage Data

MD03-2603 was studied to identify a core section contemporaneous with the high-resolution windows of the Scotia Sea records to enable a circum-Antarctic comparison. Based on the ^{230}Th -derived stratigraphy (Chapter 5), the upper 380 cm of the 35 m long record was therefore analysed, representing MIS 1 to 3.

4.3.3.1. MIS 3

Total diatom concentrations (Figure 4.14) at the base of the record (380 cm to 372 cm) show a small decrease in values from 7.66×10^6 v/gds to 4.76×10^6 v/gds, then increase to a

relatively large peak of 16.7×10^6 v/gds at 356 cm. This peak is followed by a return to a low of 5.99×10^6 v/gds at 348 cm. Coeval peaks in the relative abundance curves of *F. ritscheri* (1.3%), *P. glacialis* (10%) and the *T. gracilis* group (*T. gracilis* var. *gracilis* and *T. gracilis* var. *expecta*) (1.9%) reflect the peak in valve concentrations at ~356 cm, with an increase in relative abundance also noted in *T. lentiginosa* (8.1%). In contrast, the *Fragilariopsis* sea-ice group (*Fragilariopsis curta* and *Fragilariopsis cylindrus*) (0%), *Thalassiothrix antarctica* (0.2%) and *F. separanda* (1.1%) show a distinct trough in relative abundance (Figure 4.14). The following 140 cm (348 cm to 288 cm) of the total diatom absolute abundance curve is characterised by a mean of 6.83×10^6 v/gds (standard deviation = 0.77×10^6 v/gds, $n = 11$) and low amplitude high frequency variability. Total diatom concentrations fluctuate between significant lows of 5.99×10^6 v/gds (348 cm), 5.87×10^6 v/gds (308), 6.03×10^6 v/gds (292 cm) and highs of 7.71×10^6 v/gds (344 cm), 7.76×10^6 v/gds (316 cm) and 7.95×10^6 v/gds (304 cm). This mode of variability is reflected across the species assemblage relative abundance curves, with enhanced contributions of the *Fragilariopsis* sea-ice group (~0.89%), *A. actinochilus* (~1%), *E. antarctica* (~4.6%), *Chaetoceros* rs (~9.9%) and *Thalassiothrix antarctica* (~1%) (Figure 4.14). Over the following 80 cm (284 cm to 204 cm) total diatom concentrations retain the high frequency variability but with a drop in mean valve concentrations to 5.61×10^6 v/gds. The absolute abundance curve shows several excursions, of varying amplitude, primary peaks of 8.82×10^6 v/gds, 13.1×10^6 v/gds and 9.05×10^6 v/gds occur at 280 cm, 228 cm and 216 cm respectively. This variability is also shown in components of the diatom species assemblage, with the three peaks in absolute abundance evident at 280 cm, 228 cm and 216 cm expressed differently within the species assemblage data (Figure 4.14). The peak at 280 cm is only reflected in the relative abundance curves of *P. glacialis* (10.6%) and the *T. gracilis* group (2.2%), with coeval marked lows shown by *Chaetoceros* rs (2.2%), *F. separanda* (0%) and *Thalassiothrix antarctica* (0%). The peak at 228 cm appears to be primarily linked to *F. ritscheri* (2%) and to a lesser extent the *Fragilariopsis* sea-ice group (1.5%) and *Thalassiothrix antarctica* (1.3%). The only distinct increases in relative abundance associated with the absolute abundance peak at 216 cm are the *T. gracilis* group (1.5%), *F. ritscheri* (0.9%) and *Rhizosolenia* spp. (1.1%) (Figure 4.14). Valve concentrations drop to a low value of 3.05×10^6 v/gds at 200 cm, which is driven in the species assemblage by decreased relative abundances of *F. separanda* (1%), the *T. gracilis* group (1.3%), the *Fragilariopsis* sea-ice group (0.8%) and *E. antarctica* (3.2%) (Figure 4.14).

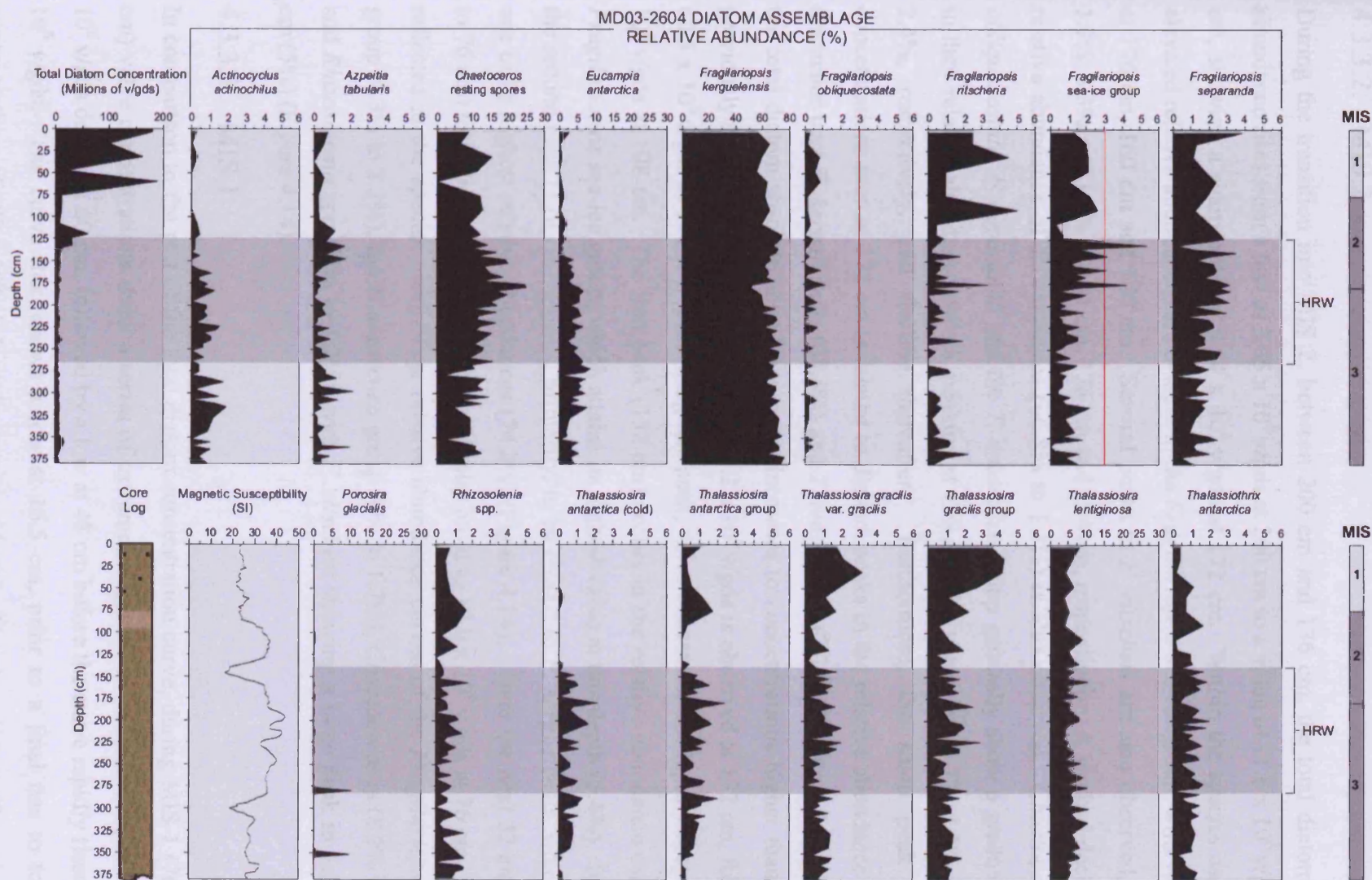


Figure 4.14. Core log (prepared digitally in a graphic package with RGB conversions of Munsell colours), MIS stratigraphy (based on magnetic susceptibility), magnetic susceptibility (recorded on a shipboard logger (Presti *et al.*, 2008)) and diatom species assemblage data for core MD03-2603. Total diatom concentrations presented in absolute numbers (calculated using the equation of Scherer, 1994). Relative percentages for species comprising >0.5% of the assemblage data. The dark rectangle indicates the high-resolution window (HRW). Red lines indicate sea-ice 3% threshold.

4.3.3.2. MIS 2

During the transition into MIS 2, between 200 cm and 136 cm, the total diatom absolute abundance rises from a low of 3.05×10^6 v/gds at 200 cm to a value of 11.6×10^6 v/gds at 136 cm, showing a sharp peak of 9.54×10^6 v/gds at 172 cm. Within the species assemblage, elevated relative abundances are evident in the *Fragilariopsis* sea-ice group, with values >3% at 176 cm, 160 cm and 144 cm. Several peaks in *F. ritscheri* are also observed, reaching 1.7%, 3.3% and 1.8% at 184 cm, 176 cm and 144 cm, respectively. A gradual decline in the relative abundance of *E. antarctica* (~6.8% to 1.1%) is also observed. *Chaetoceros* rs, *F. obliquecostata*, *F. separanda* and the *T. antarctica* group generally show a gradual increase in their relative abundance curves, peaking at 176 cm with values of 24.7%, 1.1%, 3.2% and 2.4%, respectively, and decline thereafter. Furthermore, the sharp peak in valve concentrations seen at 172 cm is related to distinct peaks in the relative abundance curves of the major taxa *F. kerguelensis* (68.4%) and *T. lentiginosa* (7.7%) (Figure 4.14). At 136 cm the total diatom absolute abundance curve increases to concentrations higher than anything previously in the core. An initial peak of 31.2×10^6 v/gds is observed at 132 cm, followed by 60.5×10^6 v/gds at 120 cm. Following this peak, valve concentrations rapidly drop to 7.02×10^6 v/gds at 108 cm. The first peak (132 cm) occurs in the relative abundance curve of the *Fragilariopsis* sea-ice group, which attains its highest value at this depth (5.4%). In contrast, the second peak (120 cm) appears, primarily, to be related to *F. kerguelensis*, which reaches one of its highest relative abundances (74.2%) (Figure 4.14). Over the next 32 cm (108 cm to 76 cm) total diatom concentrations gradually build to 12.0×10^6 v/gds at 76 cm. This trend reflected in the species assemblage relative abundance curves of the *Fragilariopsis* sea-ice group (0.3% to 2.2%), the *T. antarctica* group (0% to 1.7%), *Chaetoceros* rs (8.9% to 12.1%) and *Rhizosolenia* spp. (0% to 1.2%), with *F. ritscheri* showing a large peak in values at 92 cm (5%) (Figure 4.14).

4.3.3.3. MIS 1

In comparison to the rest of the total diatom concentration curve, during MIS 1 (76 cm to 0 cm) valve concentrations show a series of extremely high values. An initial peak of 188×10^6 v/gds occurs at 60 cm, followed by a low at 48 cm before the curve rapidly rises to 161×10^6 v/gds. The curve then shows a low at 16.5 cm, prior to a final rise to total valve concentrations of 180×10^6 v/gds at the core top (4 cm). The steep rise at 60 cm is reflected by a mixed signal in the diatom species assemblage. Although elevated relative abundances are observed in *F. kerguelensis* (63.4%) and *F. separanda* (2.4%), the species *F. ritscheri*

(1%), the *Fragilariopsis* sea-ice group (0.9%) and *Chaetoceros* rs (0%) show marked lows in relative abundance. The peak-low-peak morphology observed in the upper 48 cm of the absolute abundance curve is reflected in the relative abundance curves of *F. obliquecostata*, *F. ritscheri* and *Chaetoceros* rs, which show peaks of 0.8%, 15.3% and 4.5% at 32 cm, followed by a decrease to 0.13%, 6.4% and 2.5% at 16.5 cm respectively. The section of the core is also characterised by stable relative abundances of *F. kerguelensis* (mean = 58.9%, standard deviation = 2.2, n = 4), a marked increase in the relative abundance of the *T. gracilis* group (mean = 3.7%, standard deviation = 0.67, n = 4) and decreased relative abundances in *Rhizosolenia* spp. (mean = 0.69%, standard deviation = 0.12, n = 4) and *Thalassiothrix antarctica* (mean = 0.51%, standard deviation = 0.41, n = 4). *F. separanda* has a decrease in relative abundance for the majority of this section, however, it increases to a peak (3.9%) at the core top (Figure 4.14).

4.3.4. Principle Components Analysis – Relative Abundance Data

Species and species groups in the MD03-2603 dataset were limited to those with a mean relative abundance $\geq 0.5\%$. This reduced the number of species and species groups from 46 to 15 (Table 4.5), and removes the impact of rare species that are likely to obscure the environmental signature.

Table 4.5. Core MD03-2603 (HRW): Diatom species and species groups representing $>0.5\%$ of the assemblage (Appendix 1) identified during light microscope analysis.

<i>Actinocyclus actinochilus</i>	<i>Porosira glacialis</i>
<i>Azpeitia tabularis</i>	<i>Rhizosolenia</i> spp.*
<i>Chaetoceros</i> rs	<i>Thalassiosira antarctica</i> (cold)
<i>Eucampia antarctica</i>	<i>Thalassiosira antarctica</i> group*
<i>Fragilariopsis</i> sea-ice group*	<i>Thalassiosira gracilis</i> var <i>gracilis</i>
<i>Fragilariopsis kerguelensis</i>	<i>Thalassiosira gracilis</i> group*
<i>Fragilariopsis obliquecostata</i>	<i>Thalassiosira lentiginosa</i>
<i>Fragilariopsis ritscheri</i>	<i>Thalassiothrix antarctica</i>
<i>Fragilariopsis separanda</i>	

***Species groups:**

Fragilariopsis sea-ice group – *F. curta*, *F. cylindrus*

Rhizosolenia spp. – *Rhizosolenia antennata antennata*, *Rhizosolenia antennata semispina*, *Rhizosolenia crassa*, *Rhizosolenia polydactyla polydactyla*, *Rhizosolenia simplex*, *Rhizosolenia styliformis*.

Thalassiosira antarctica group – varieties cold and warm.

Thalassiosira gracilis group – varieties *gracilis* and *expecta*.

PCA of these 15 species and species groups was applied between the depths of 124 cm to 264 cm; a section of the record broadly contemporaneous to the HRWs of Scotia Sea cores TPC063 and TPC286.

The PCA captured more than 60% of the variance within the assemblage (Table 4.6). Kaiser's rule and the scree plot (Figure 4.15) suggest that the first 4 axes are important. The specific diatom assemblages associated with each of the four axes are described below and illustrated in Figures 5.16, 5.17, and 5.18. Component scores, illustrating PCA variation down core are shown in Figure 4.19. When a variable loading is described as 'significant' in the following discussion this refers to significance at the 90% level.

Table 4.6. Core MD03-2604 (HRW): PCA axes eigenvalues (shading indicates those PCA Axes included in the interpretation based on the scree plot and knowledge of diatom ecologies).

	Axis 1	Axis 2	Axis 3	Axis 4
Eigenvalues	4.430	2.241	1.918	1.722
Percentage	26.061	13.180	11.283	10.127
Cum. Percentage	26.061	39.241	50.524	60.651

PCA axis 1 explains 26.1% of the variance and is characterised by significant positive loadings for the diatoms *T. antarctica* (cold) (0.384), *T. gracilis* var. *gracilis* (0.355), with *E. antarctica* (0.273) marginally insignificant. Significant negative loadings on axis 1 are characterised by *F. kerguelensis* (-0.379), with *A. tabularis* (-0.26) marginally insignificant (Figure 4.16).

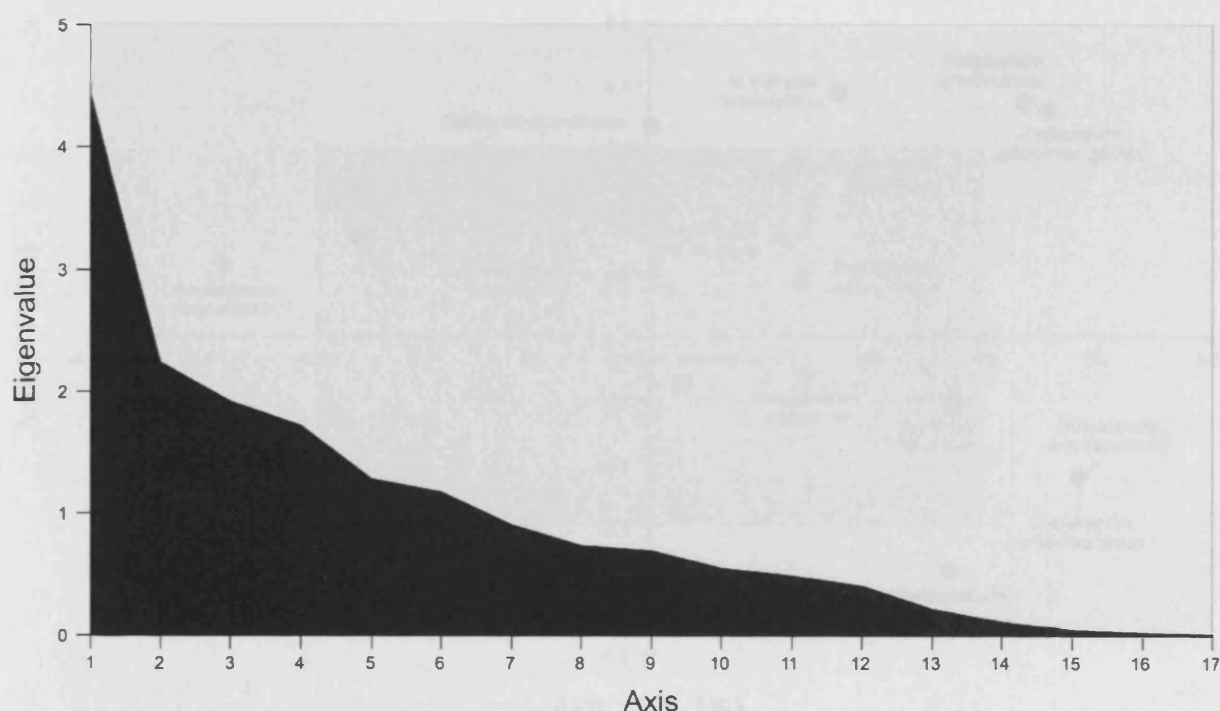


Figure 4.15. Core MD03-2603 (HRW): PCA Scree plot generated from the analysis of diatom assemblage relative abundance data in the Multivariate Statistical Package (MVSP) developed by Kovach *et al.* (1999).

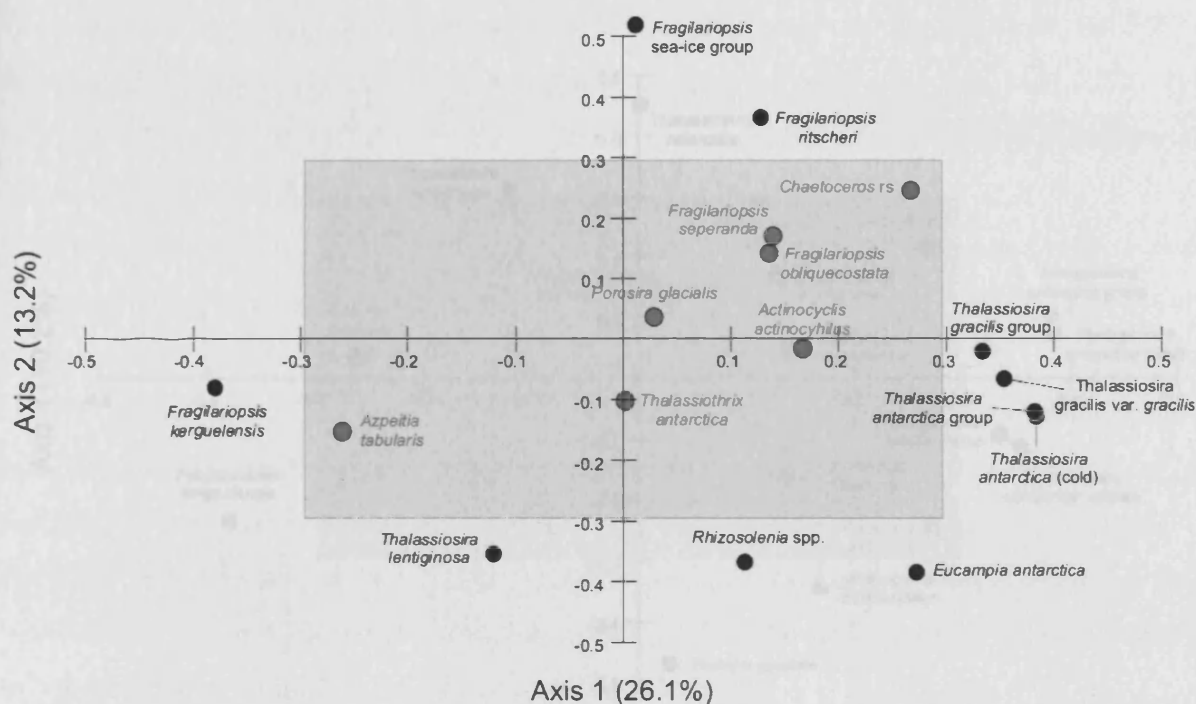


Figure 4.16. Core MD03-2603 (HRW): PCA variable loadings, axis 2 versus axis 1, generated from the analysis of relative abundance data in a MVSP (Kovach *et al.* 1999). Black circles indicate diatom species and species groups significant at the 90% level (Shaded region and gray circles indicate species and species groups not significant at the 90% level).

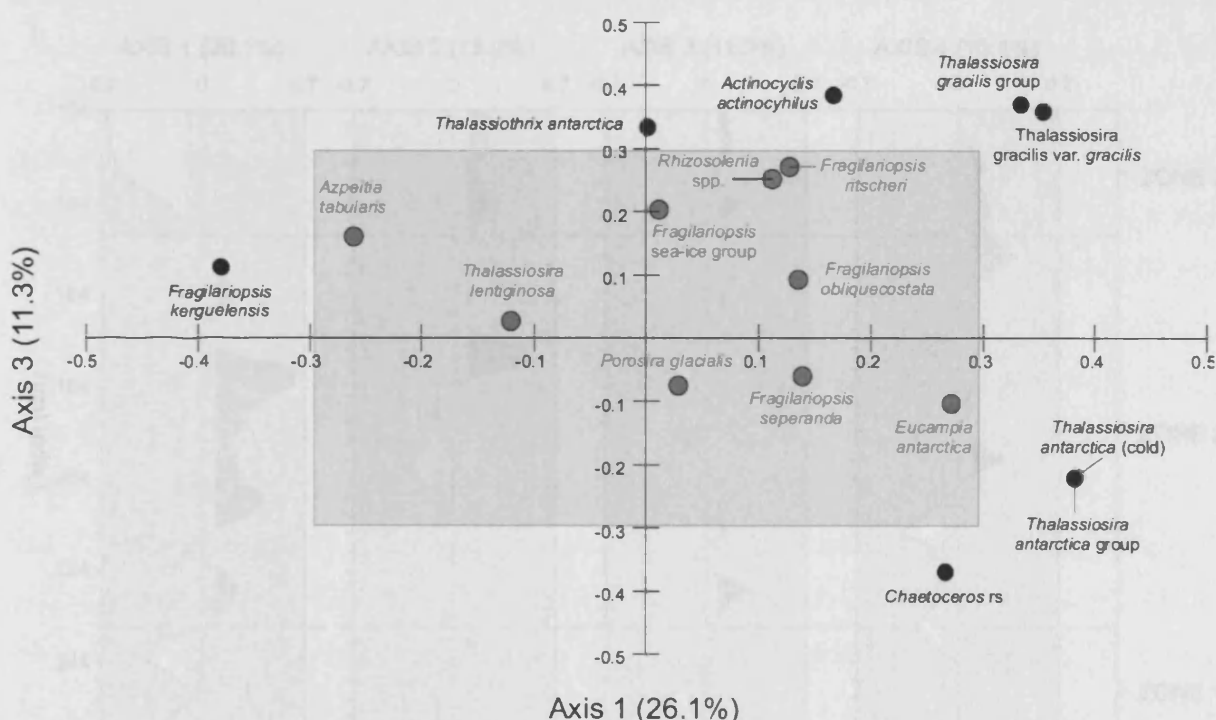


Figure 4.17. Core MD03-2603 (HRW): PCA variable loadings, axis 3 versus axis 1, generated from the analysis of relative abundance data in a MVSP (Kovach *et al.* 1999). Black circles indicate diatom species and species groups significant at the 90% level (Shaded region and gray circles indicate species and species groups not significant at the 90% level).

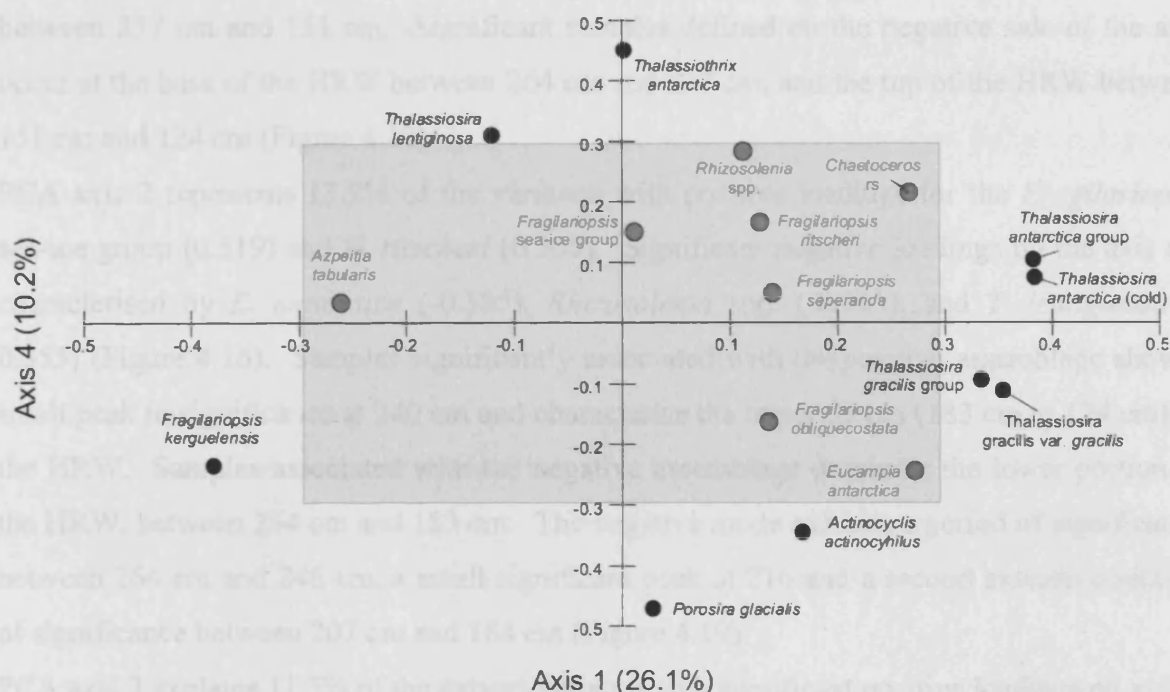


Figure 4.18. Core MD03-2603 (HRW): PCA variable loadings, axis 4 versus axis 1, generated from the analysis of relative abundance data in a MVSP (Kovach *et al.* 1999). Black circles indicate diatom species and species groups significant at the 90% level (Shaded region and gray circles indicate species and species groups not significant at the 90% level).

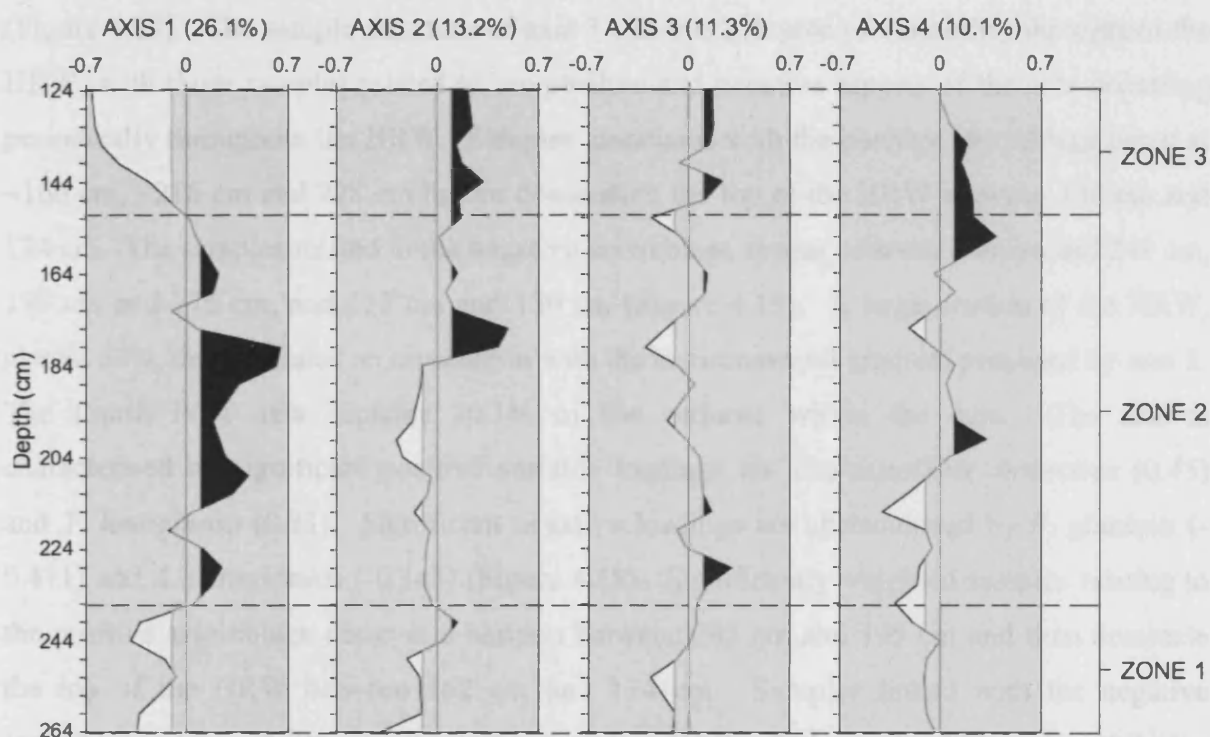


Figure 4.19. Core MD03-2603 (HRW): PCA component scores, axes 1 to 4, generated from the analysis of relative abundance data in a MVSP (Kovach *et al.* 1999). Shaded black and white polygons indicate significant positive and negative variability respectively (un-shaded areas indicate insignificant variability). Zones are primarily based on significant mode shifts on axis 1, the primary principle component.

Core samples on the positive side of axis 1 primarily occur in the centre of the HRW, between 237 cm and 151 cm. Significant samples defined on the negative side of the axis occur at the base of the HRW between 264 cm and 237 cm, and the top of the HRW between 151 cm and 124 cm (Figure 4.19).

PCA axis 2 represents 13.2% of the variance with positive loadings for the *Fragilariopsis* sea-ice group (0.519) and *F. ritscheri* (0.365). Significant negative loadings on the axis are characterised by *E. antarctica* (-0.385), *Rhizosolenia* spp. (-0.369), and *T. lentiginosa* (-0.355) (Figure 4.16). Samples significantly associated with the positive assemblage show a small peak in significance at 240 cm and characterise the upper 59 cm (183 cm to 124 cm) of the HRW. Samples associated with the negative assemblage dominate the lower portion of the HRW, between 264 cm and 183 cm. The negative mode exhibits a period of significance between 264 cm and 246 cm, a small significant peak at 216 and a second extensive section of significance between 207 cm and 184 cm (Figure 4.19).

PCA axis 3 explains 11.3% of the dataset variance with significant positive loadings on axis 3 characterised by *A. actinochilus* (0.384), *T. gracilis* var. *gracilis* (0.358), *Thalassiothrix antarctica* (0.333) with *F. ritscheri* (0.27) marginally insignificant. Significant negative loadings on this axis are characterised by *Chaetoceros* spp. (-0.371) and *T. antarctica* (cold) (Figure 4.17). The sample structure of axis 3 exhibits a degree of variability throughout the HRW, with those samples related to the positive and negative aspects of the axis occurring periodically throughout the HRW. Samples associated with the positive assemblage occur at ~166 cm, ~216 cm and 228 cm before dominating the top of the HRW between 148 cm and 124 cm. The samples related to the negative assemblage appear between 260 cm and 249 cm, 198 cm and 175 cm, and 155 cm and 150 cm (Figure 4.19). A large portion of the HRW, almost 50%, demonstrates no association with the environmental gradient proposed by axis 3. The fourth PCA axis explains 10.1% of the variance within the data. The axis is characterised by significant positive variable loadings for *Thalassiothrix antarctica* (0.45) and *T. lentiginosa* (0.31). Significant negative loadings are characterised by *P. glacialis* (-0.471) and *A. actinochilus* (-0.345) (Figure 4.18). Significantly weighted samples relating to the positive assemblage occur at a horizon between 203 cm and 195 cm and then dominate the top of the HRW between 162 cm and 124 cm. Samples linked with the negative assemblage dominate the lower portion of the HRW (264 cm to 208 cm), exhibiting significant levels between 242 cm and 226 cm, and between 220 cm and 209 cm and again at 176 cm (Figure 4.19).

The HRW of core MD03-2603 is divided into Zones based on the most significant transitions between the positive and negative modes of variability explained by PCA axis 1 (Figure 4.19). The interpretation and discussion (Chapter 7) of the results presented in this Chapter will be based on this zonation. These zones will be converted into ages based on the age-depth models presented in chapter 6.

- Zone 1: 364 cm to 236.5 cm
- Zone 2: 236.5 cm to 151.4 cm
- Zone 3: 151.4 cm to 124 cm

5. Results: Chronostratigraphy

This chapter presents results of the chronostratigraphic analysis of cores TPC063, TPC286 and MD03-2603. An accurate age-model was developed for cores TPC063 and TPC286 based on a combination of geomagnetic palaeointensity and biostratigraphic data (section 5.1.), whereas the chronology for core MD03-2603, developed by M. Presti (2008), is based on the correlation of geochemical tracers and an independently dated oxygen isotope stack (section 5.2.).

5.1. Cores TPC063 and TPC286

Based on the first resolute identification of the Laschamp geomagnetic excursion in the Antarctic Southern Ocean, this study presents a novel approach, combining geomagnetic intensity data with several chronostratigraphical markers to generate the first reliable, high-resolution age-model for glacial sediments from the Scotia Sea. Sedimentary sequences TPC063 and TPC286 were correlated and interpolated on to a common depth-scale and subsequently tuned to a published, independently dated, relative palaeomagnetic stack (SAPIS), resulting in the generation of an accurate age model between 43.7 cal ka B.P. and 25.3 cal ka B.P. The age-model is further extended to 17.3 cal ka B.P. through the identification of the biostratigraphic *Eucampia antarctica* 2Ea₁ datum.

The steps taken in the construction of this age-model are detailed in the following sections. The chronostratigraphic data for each core is presented in section 5.1.1, the identification of chronostratigraphic markers and core correlation is presented in section 5.1.2, the development of the respective core chronologies are presented in section 5.1.3 and finally, the core age-models are presented and evaluated in section 5.1.4.

5.1.1. Chronostratigraphic Data

5.1.1.1. Radiocarbon Dates

5.1.1.1.1. TPC063

Core TPC063 was sampled at six depths for radiocarbon dating. Five samples were extracted from the trigger core TC063 and a sixth from the piston core PC063 (Figure 5.1, Table 5.1). As is common in Southern Ocean sediments, the core top samples from core TPC063 show anomalously old ages (3250 ± 65 ¹⁴C years B.P. and 5680 ± 80 ¹⁴C years B.P.). Further, the two samples retrieved from the core top (0 cm) give dates differing by more than 2000 years.

A discrepancy of this magnitude significantly hinders the ability to apply a surface reservoir correction to the down-core profile. As a result the radiocarbon dates cannot be used to construct a reliable absolute age model. However, the down-core profile of the remaining four dates (13575 ^{14}C years B.P., 16010 ^{14}C years B.P., 18140 ^{14}C years B.P., and 16530 ^{14}C years B.P.) shows no inversions (Figure 5.1) and if a line of best fit is applied, it implies a stable sedimentation rate for this portion of the record. Although these results cannot provide an absolute age model, the four older dates provide one estimate of the potential sedimentation rate during this section of the core.

5.1.1.1.2. TPC286

Core TPC286 included two radiocarbon samples, one from the trigger (TC286) and one from the piston core (PC286). These were supplemented by 10 samples from gravity core GC027 (Pudsey *et al.*, 1992), recovered from the same sediment drift as TPC286, only slightly closer to the apex of the drift ($61^\circ 48' 63''$, $40^\circ 10' 12''$) (Figure 5.1, Table 5.1). The core top age of core GC027 gives an exceptionally old date of 16530 ± 130 ^{14}C years B.P. The ages given by the remainder of the samples are not in stratigraphic order, with one of the deepest samples (207 cm) giving the youngest age (2720 ± 120 ^{14}C years B.P.). As a result these dates were not used in the construction of an age-model.

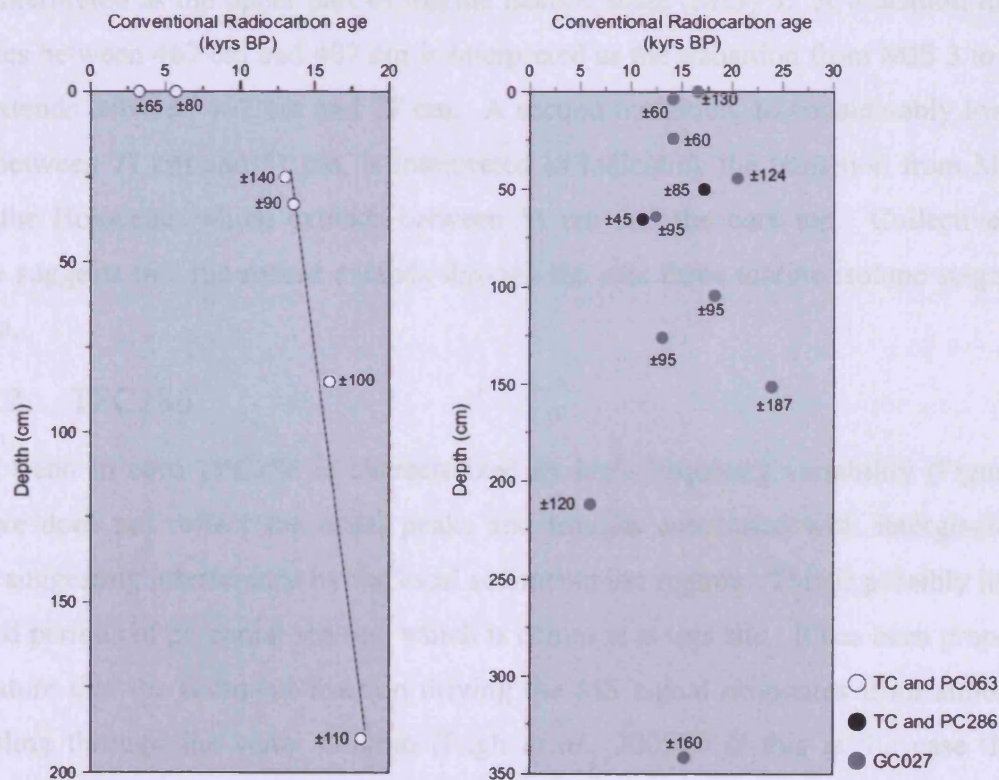


Figure 5.1. Cores TPC063, TPC286 and GC027: Uncorrected radiocarbon dates plotted against depth, details listed in Table 5.1.

Table 5.1. Cores TPC063, TPC286 and GC027: Uncorrected radiocarbon dates.

NERC Publication Code	Core Code	Core depth (m)	Conventional ^{14}C age (years BP $\pm\sigma$)
AA-22653	TC063	0	3250 \pm 65
AA-22655	TC063	0	5680 \pm 80
AA-22656	TC063	0.25	13010 \pm 140
AA-23442	TC063	0.33	13575 \pm 90
AA-22657	TC063	0.85	16010 \pm 100
AA-22658	PC063	1.4	18140 \pm 110
AA-11610	GC027	0	16530 \pm 130
AA-11610	GC027	5	14134 \pm 60
AA-11610	GC027	0.245	14119 \pm 60
AA-11610	GC027	0.445	20461 \pm 124
AA-11610	GC027	0.50	17170 \pm 85
AA-11610	GC027	0.50	11131 \pm 45
AA-11611	TC286	0.65	12380 \pm 95
AA-11611	PC286	1.05	18217 \pm 95
AA-11612	GC027	1.27	13070 \pm 95
AA-11612	GC027	1.515	23833 \pm 187
AA-11613	GC027	2.03	2720 \pm 120
AA-11614	GC027	3.42	15270 \pm 160

5.1.1.2. Magnetic Susceptibility

5.1.1.2.1. TPC063

The magnetic susceptibility (MS) trend in core TPC063 appears to show a succession of three marine isotope stages (1-3) (Figure 5.2). Relatively low MS values between 705 cm and 467 cm are interpreted as the upper part of marine isotope stage (MIS) 3. A transition to higher MS values between 467 cm and 407 cm is interpreted as the transition from MIS 3 to MIS 2, which extends between 407 cm and 77 cm. A second transition, to considerably lower MS values, between 77 cm and 51 cm, is interpreted as indicating the transition from MIS 2 to MIS 1, the Holocene, which extends between 51 cm and the core top. Collectively, this evidence suggests that the record extends through the past three marine isotope stages, back to ~60 ka.

5.1.1.2.2. TPC286

The MS trend in core TPC286 is characterized by high-frequency variability (Figure 5.2). The curve does not reflect the usual peaks and troughs associated with interglacials and glacials, suggesting interference by the local sedimentation regime. This is possibly linked to prolonged periods of perennial sea-ice, which is common at this site. It has been proposed in the literature that the sediment fraction driving the MS signal originates from atmospheric dust settling through the water column (Pugh *et al.*, 2009). If this is the case then the presence of permanent sea-ice would interrupt the transfer of this signal to the sediment. Based on these results the MS curve, for the majority of core TPC286, cannot be used to

provide even a crude chronology, although the transition to lower values between 37 cm and 0 cm could indicate the transition to Holocene conditions and MIS 1.

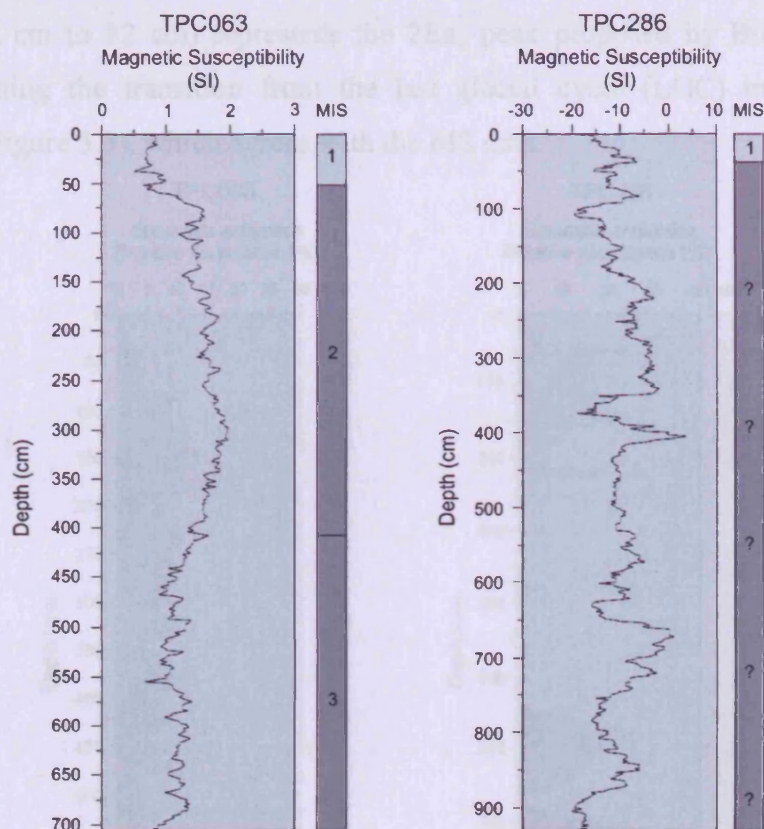


Figure 5.2. Cores TPC063 and TPC286: Magnetic susceptibility curves and proposed MIS stratigraphy based on the relative contribution of terrigenous and biogenic derived material, which varies during warm and cold stages.

5.1.1.3. Biostratigraphy – *Eucampia antarctica* abundance curve

5.1.1.3.1. TPC063

E. antarctica relative abundance shows relatively low values for the lower-most portion of core TPC063, with a mean of 3.5% between 702 cm and 478 cm. Relative abundance then shows a sharp increase to a value 9.3% at 470 cm, leading into a section of core (470 cm to 374 cm) characterized by high variability. Between 470 cm and 374 cm relative abundance varies between high values averaging 9.3% and low values averaging 4.6%. Following this section, relative abundance drops to lower values between 374 cm and 342 cm, averaging 5%. Subsequently, relative abundance increases to a higher mean of 8.2% between 338 cm and 190 cm, before showing a sharp increase to a peak of 16.8% at 177 cm. The succeeding record is characterized by four peaks in relative abundance, giving values of 12.6%, 13.8%, 9.3% and 10.5% at 162 cm, 147 cm, 115 cm and 90 cm, respectively. Following these peaks in relative abundance, values show a sharp drop to 3.6% at 82 cm, coinciding with a proposed

transition into the Holocene. Between 82 cm and the core top, *E. antarctica* relative abundance shows a low mean of 3.4%. I propose that the final two-pronged peak in relative abundance (126 cm to 82 cm) represents the 2Ea₁ peak proposed by Burckle and Cooke (1983) representing the transition from the last glacial cycle (LGC) into the Holocene (deglaciation) (Figure 5.3), which agrees with the MS data.

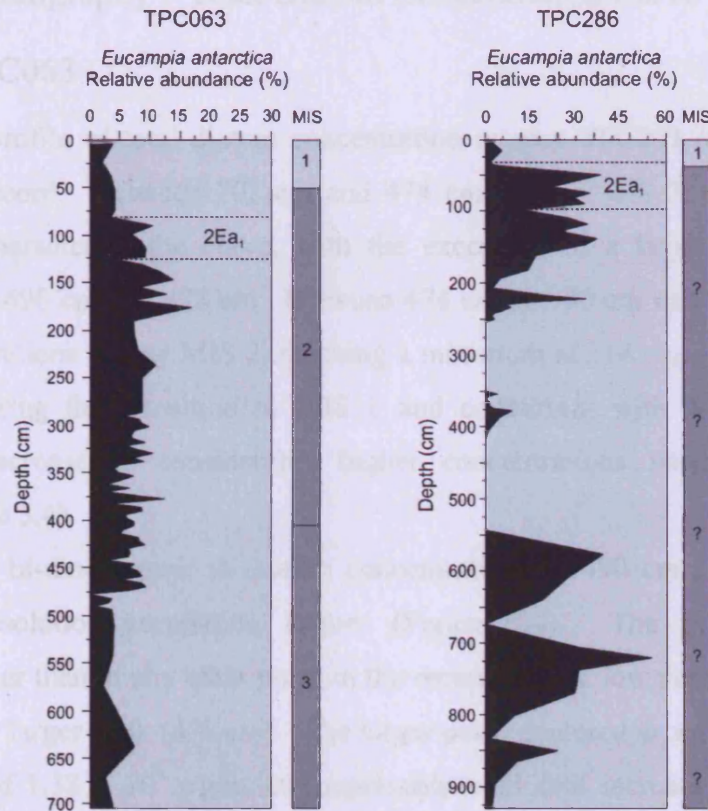


Figure 5.3. Cores TPC063 and TPC286: *E. antarctica* relative abundance curves calculated from raw counts (section 3.1.4.) and identified 2Ea₁ datums based on the chronostratigraphy proposed by Burckle and Cooke, 1983. Peak 2Ea₁ indicates the culmination of the LGC and onset of deglaciation. MIS stratigraphy is based on magnetic susceptibility data (Figure 5.2).

5.1.1.3.2. TPC286

Core TPC286 demonstrates a much larger variability in its *E. antarctica* relative abundance curve than TPC063 (Figure 5.3). The lower 386 cm of the record (929 cm to 543 cm) has three peaks in relative abundance, reaching values of 20%, 46% and 32.3 % at 849 cm, 721 cm, and 576 cm, respectively. This section is succeeded by a relatively barren period between 543 cm and 418 cm, which has a mean relative abundance of just 0.52 %. A sharp, increase in relative abundance to a value of 27.6% occurs at 222 cm, before dropping to a low of 1.9% at 206 cm. Relative abundance subsequently increases once more, reaching a peak of 30.7% at 138 cm. The next 88 cm (138 cm to 50 cm) of record show a succession of high relative abundances, with a mean of 29.4%. Following the final peak in this sequence (50

cm), relative abundance shows a sharp decrease to 1%. The remainder of the record (50 cm to 0 cm) is characterized by low values, with a mean of 3% (Figure 5.3). The final peak (50 cm), prior to the potential Holocene transition, is interpreted as the 2Ea₁ peak proposed by Burckle and Cooke (1983) representing the onset of deglaciation.

5.1.1.4. Biostratigraphy – Total Diatom Concentration Curve

5.1.1.4.1. TPC063

The down-core profile of total diatom concentration in core TPC063 roughly parallels the respective MS record. Between 702 cm and 474 cm, during MIS 3, relatively low valve concentrations characterize the curve, with the exception of a large twin-peak in valve concentrations at 490 cm and 478 cm. Between 474 cm and 90 cm valve concentrations fall to lower concentrations during MIS 2, reaching a minimum at 314 cm. Between 90 cm and the core top, during the transition to MIS 1 and concurrent with the 2Ea₁ peak, valve concentrations increase to considerably higher concentrations indicative of Holocene conditions (Figure 5.4).

The conspicuous bi-modal peak in diatom concentrations at 490 cm and 478 cm offers a potential high-resolution correlation feature (Figure 5.4). The peaks exhibit values significantly higher than at any other point in the record, with a low peak (490 cm) followed by a significantly larger peak (478 cm). The larger peak, centered at a depth of 478 cm, is a core maximum of 1.38×10^8 v/gds, this represents a 23 fold increase on the mean valve concentration (5.87×10^6 v/gds). The event occurs over 20 cm of the record, suggesting a relatively prolonged event. The resting spores of the diatom subgenus *Hyalochaete Chaetoceros* (*Chaetoceros* rs) dominate the event, representing 72.7% during the peak featured at 490 cm and 92% during the larger peak at 478 cm (Figure 5.4). The overwhelming dominance of *Chaetoceros* rs is somewhat surprising considering a record mean relative abundance, outside the double peak, of just 18%. This event is possibly related to a prolonged period of surface water productivity.

5.1.1.4.2. TPC286

The down-core profile of total diatom concentration in core TPC286 roughly parallels the MS record, although there are a number of differences, possibly relating to the sea-ice environment. The most consistent feature between the two records is the increase in valve concentrations between 50 cm and 0 cm, which coincides with the transition into MIS 1 and

also the 2Ea₁ peak evident in the *E. antarctica* relative abundance curve (Figure 5.4). The curve also exhibits a conspicuous double peak in diatom concentrations between 379 cm and 351 cm, which offers a potential, high-resolution correlation feature. The second, larger peak of 1.02×10^8 v/gds, represents a 22 fold increase over mean valve concentrations (4.55×10^6 v/gds). The entire event extends over 28 cm and is dominated by *Chaetoceros* rs (Figure 5.4).

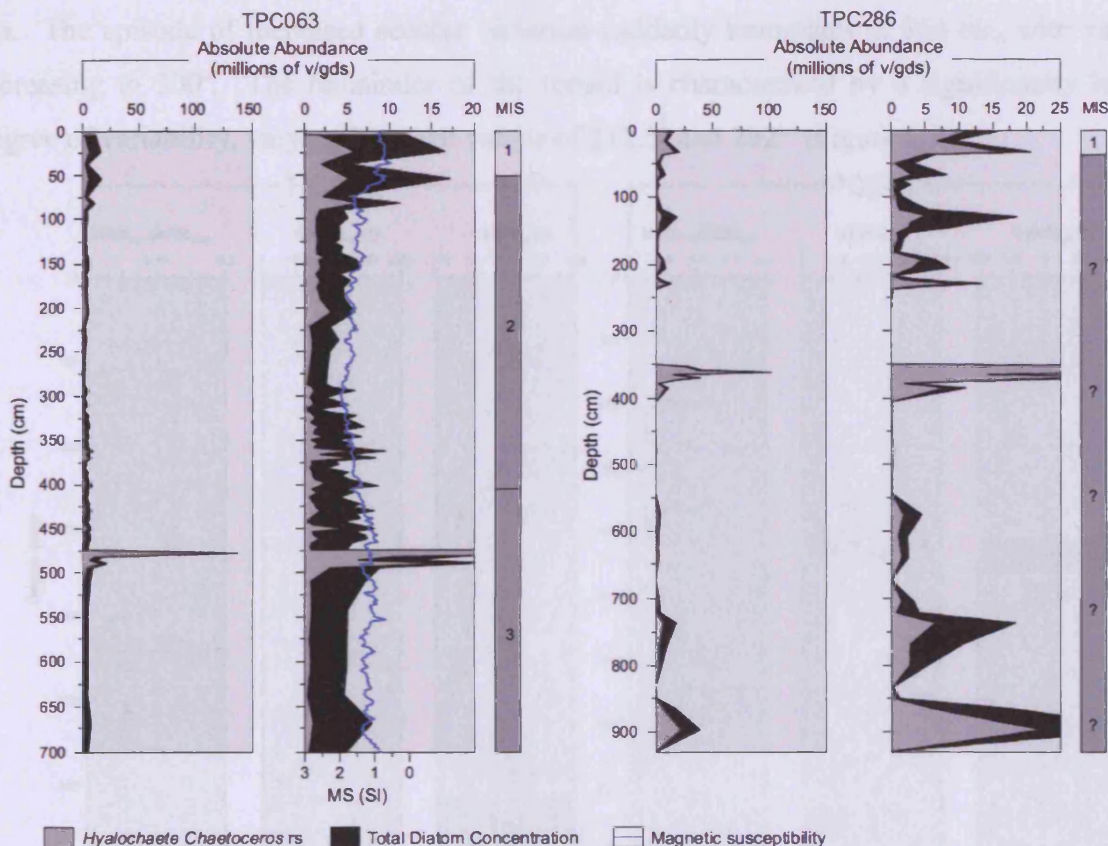


Figure 5.4. Cores TPC063 and TPC286: Total diatom concentration in absolute abundance (black), calculated from raw counts using the Scherer (1994) equation, compared with *Hyalochaete Chaetoceros* resting spores (also absolute abundance) (gray), and magnetic susceptibility (blue line) in the case of core TPC063. MIS stratigraphy is based on magnetic susceptibility data (Figure 5.2).

5.1.1.5. Palaeomagnetic Data

5.1.1.5.1. TPC063

Relative palaeointensity (RPI) ($\text{NRM}_{15 \text{ mT}}/\text{ARM}_{15 \text{ mT}}$) was analysed between 252 and 702 cm. Complete removal of any possible viscous component or magnetic overprint was generally achieved at low demagnetisation fields (10-15 mT). At higher fields the characteristic remanent magnetisation (ChRM) of the sediment was identified as a single stable and well-defined remanence component. Following comparison of a number of potential normalisers and the down core variability in magnetic grain size, the magnetic parameter anhysteretic

remanent magnetisation (ARM) was deemed an appropriate normaliser (Figure 5.5). TPC063 exhibits mean inclination values close to those expected for this latitude (-62.379°), with the bulk of the record dominated by normal (negative) inclination values. However, between 666 cm and 618 cm, the trend climbs to shallow, and eventually positive values (peaking at 77.6° at 638 cm) before returning to normal (Figure 5.5). The base of core TPC063 is characterized by low declination values, prior to entering a period of enhanced variability at a depth of 674 cm. The episode of increased secular variation suddenly terminates at 562 cm, with values increasing to 300° . The remainder of the record is characterized by a significantly lower degree of variability, varying between values of 212.5° and 292° (Figure 5.5).

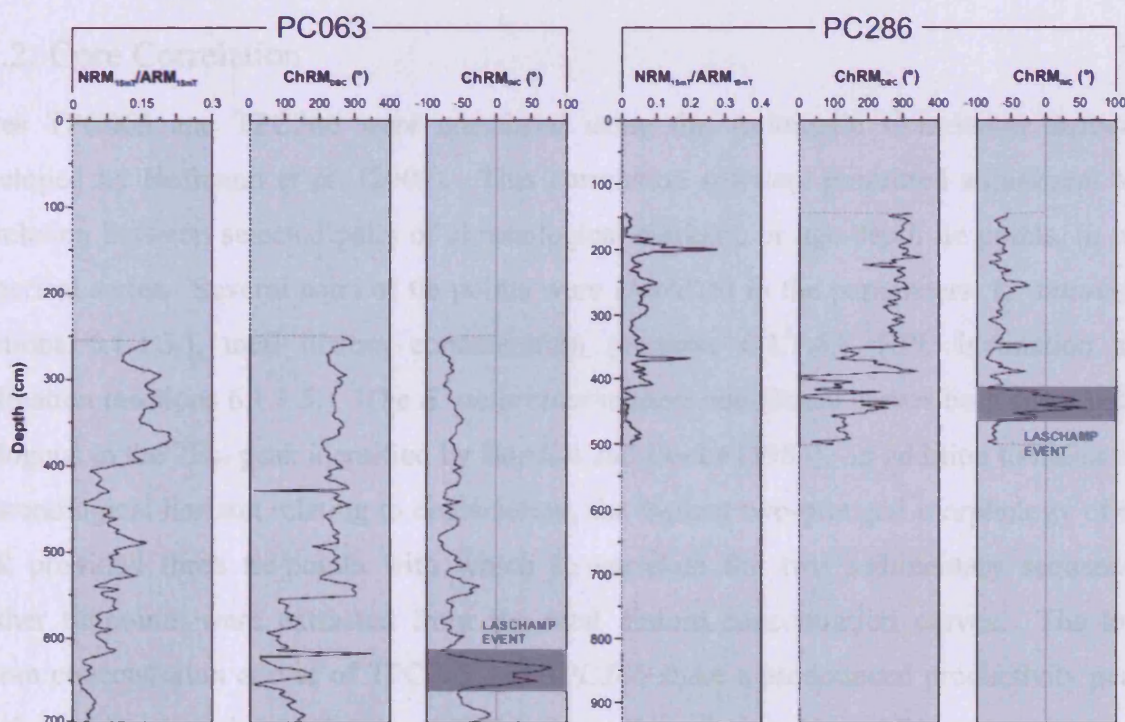


Figure 5.5. Cores TPC063 and TPC286: Magnetic parameters, left to right: Relative palaeointensity (RPI) (measured in milliTesla), declination and inclination (measured in degrees). MIS stratigraphy based on magnetic susceptibility data (Figure 5.2).

5.1.1.5.2. TPC286

RPI ($\text{NRM}_{15 \text{ mT}}/\text{ARM}_{15 \text{ mT}}$) was measured between 144 cm and 500 cm. Complete removal of any possible viscous component or magnetic overprint was generally achieved at low demagnetisation fields (10-15 mT). At higher fields the ChRM of the sediment was identified as a single stable and well-defined remanence component. Following the comparison of a number of potential normalisers and the down core variability in magnetic grain size, the magnetic parameter ARM was deemed an appropriate normaliser (Figure 5.5). The inclination record of TPC286 has mean inclination in close agreement with the expected

values for this latitude (-61.71°). Normal (negative) inclinations are in evidence for the majority of the record apart from a period between the depths of 464 cm to 412 cm. During this episode, inclinations begin to shallow, progressing into anomalously positive values before returning back to normal values (Figure 5.5). The declination record of core TPC286 is initially characterized by low declination values, before entering a period of rapid secular variability at a depth of 456 cm, which then abruptly terminates at a depth of 348 cm as declination climbs to higher values of $\sim 286^\circ$. The trend then has a second, brief descent to low values before recovering, with the remainder of the record showing high values (Figure 5.5).

5.1.2. Core Correlation

Cores TPC063 and TPC286 were correlated using the Automatic Correlation Software developed by Hofmann *et al.* (2005). This correlation software permitted adjustment and correlation between selected pairs of chronological markers, or age-depth tie points, in two numerical series. Several pairs of tie-points were identified in the parameters; *E. antarctica* (sections 6.1.1.3.), total diatom concentration (sections 6.1.1.4.), RPI, inclination and declination (sections 6.1.1.5.). The *E. antarctica* relative abundance curves both show peaks analogous to the 2Ea₁ peak identified by Burckle and Cooke (1983). In addition to indicating a chronological horizon relating to deglaciation, the distinct two-pronged morphology of the peak provided three tie-points with which to correlate the two sedimentary sequences. Further tie-points were extracted from the total diatom concentration curves. The total diatom concentration curves of TPC063 and TPC286 share a pronounced productivity peak, which has a two-peak morphology and the same diatom assemblage (*Chaetoceros* sp.) and shows a 23 and 22 fold increase on background total diatom concentrations. These similarities suggest a coeval causal mechanism, providing two additional tie-points. Supplementary tie-points were extracted from the palaeomagnetic intensity data. A distinctive, robust, positive inclination anomaly, indicating a geomagnetic excursion (section 5.1.1.5, Figure 5.5.) has been identified in both cores, between 666 cm and 626 cm in core TPC063 and 460 cm and 408 cm in core TPC286. The onset and culmination of this event provided two tie-points. The comparative declination records also exhibited strikingly similar characteristics. A period of high secular variability observed in each record, between 658 cm and 551 cm in TPC063 and 464 cm and 384 cm in TPC286, can be matched peak for peak for the duration of the period, providing four features that can also be used as tie-points.

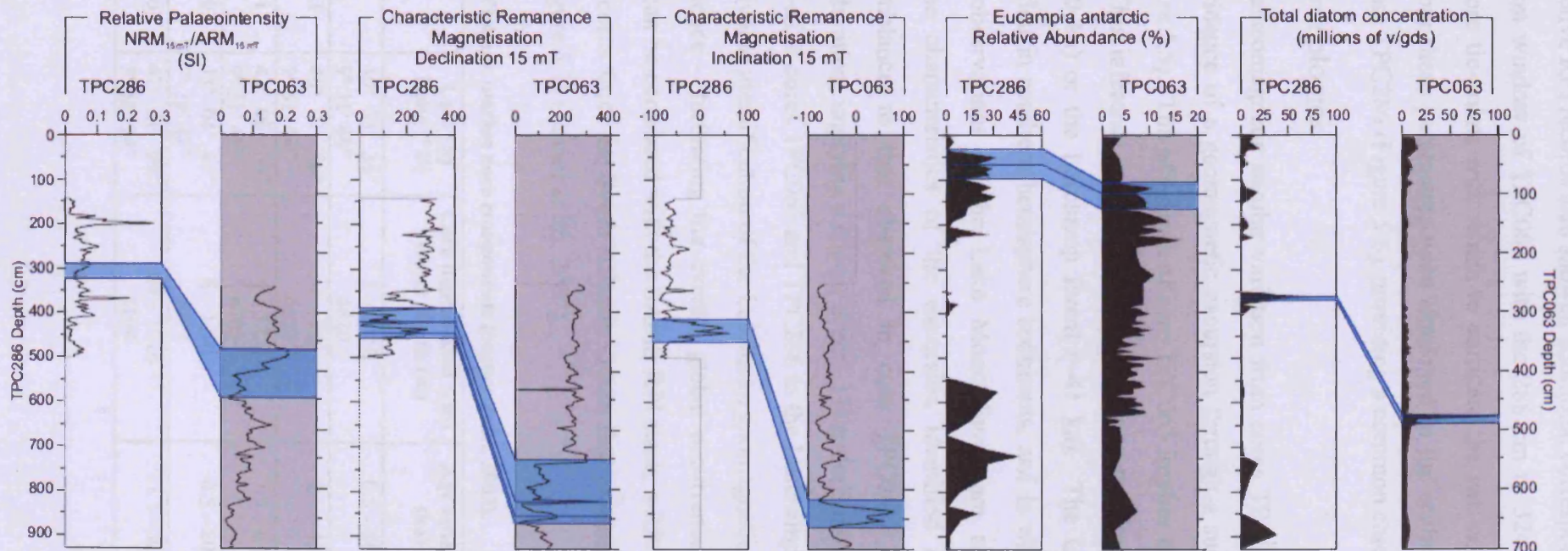


Figure 5.6. Core correlation of TPC063 (Grey blocks) and TPC286 (white blocks) based on 13 depth tie-points from five chronostratigraphic parameters, blue banding indicates tie-point correlation. Left to right: Relative palaeointensity, declination, inclination, *Eucampia antarctica* abundance curve, Total diatom concentration curve.

Finally, the respective RPI records also showed additional corresponding features, linking the 373 cm to 449 cm window of TPC063 with the 288 cm to 324 cm window of TPC286, providing two more tie-points with which to correlate the two cores. The 13 pairs of tie-points derived from these parameters were employed in the scaling of core TPC063 to the depth model of core TPC286 (Figure 5.6), providing a common chronological framework.

5.1.3. Core Chronologies

The records of palaeomagnetic secular variation from cores TPC063 and TPC286 (sections 5.1.1.5.) show evidence of a geomagnetic excursion through a sustained period of positive inclinations (Figure 5.5). The MS curve of core TPC063 implies that the excursion occurred during MIS 3. This inference restricts the assignment to two known excursions: the Lake Mono Event (~30 ka) or the Laschamp Event (~41 ka). The Laschamp Event has been repeatedly identified in southern hemisphere sediments, and is widely accepted as a global event, whereas observations of the Lake Mono Event are restricted to the northern hemisphere. The characteristics of the excursion identified in core TPC286 bear a remarkable resemblance to that observed in core TPC063, showing the same peak morphology and duration, implying a coeval event. I therefore assign the robust geomagnetic excursions observed in cores TPC063 and TPC286 to the Laschamp Event and cite this result as the first unequivocal identification of the Laschamp geomagnetic excursion in an Antarctic sedimentary sequence – furthering the event’s global occurrence. Both the TPC063 and TPC286 records can be correlated with the SAPIS RPI stack, a RPI stack compiled from five marine sediment cores from the South Atlantic Ocean that extends back to ~80 cal ka B.P. (Table 5.2 and Figure 5.7) (Stoner *et al.*, 2002).

Table 5.2. SAPIS RPI stack marine core components (Stoner *et al.*, 2002).

Core	Lat (° S) Long (° E)	Core depths used (cm) Water depth (m)	Age estimate (ka)	Average Sedimentation rate (cm/kyr)
Site 1089	40° 33' 36" 9° 31' 48"	1 – 1450 4620	0.5 – 80.7	18
TTN-057-4-PC03	40° 33' 36" 9° 31' 48"	4 – 858 4622	9.6 – 43.8	25
TTN-057-5-PC01	41° 00' 00" 9° 31' 48"	4 – 1258 4702	7.5 – 63.7	22.3
TTN-057-21-PC03	41° 04' 48" 7° 28' 48"	6 – 1201 4977	0.5 – 80.7	14.9
TTN-057-10-PC03	47° 21' 60" 5° 32' 24"	64 – 1016 4109	21.1 – 80.7	16

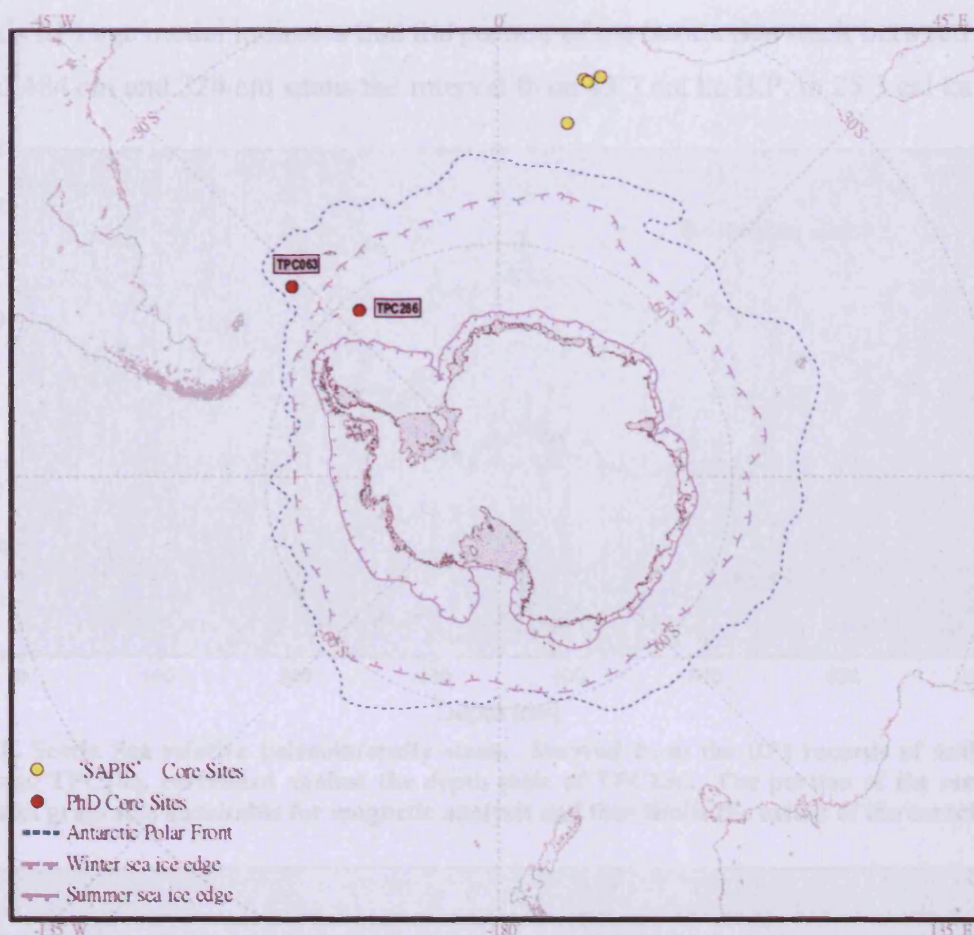


Figure 5.7. Locations of the sediment cores TTN-057-4-PC03, TTN-057-5-PC01, TTN-057-21-PC03, TTN-057-10-PC03 and ODP site 1089 (yellow circles), which contributed to the South Atlantic Paleointensity Stack (SAPIS) in relation to the location of sediment cores TPC063 and TPC286 (red circles) presented in this study.

By combining the RPI data from TPC063 and TPC286 I have compiled a Scotia Sea RPI stack independently correlated (section 5.1.2) to the TPC286 depth scale. To achieve this the two RPI records were interpolated to a common sampling interval of 0.02 mm, in order to give an equal weighting to both records and retain the high-resolution features, and the arithmetic mean was subsequently calculated for each interpolated interval, resulting in the first average, stacked record of RPI for the Scotia Sea (Figure 5.8).

This normalized Scotia Sea RPI ($\text{NRM}_{15\text{mT}}/\text{ARM}_{15\text{mT}}$) stacked record was correlated with the SAPIS reference palaeointensity curve (Stoner *et al.*, 2002), in order to derive an age model for at least a portion of the Scotia Sea sedimentary sequences. Employing the Automatic Correlation Software (Hofmann *et al.*, 2005), I transferred the SAPIS RPI ages – originally derived from oxygen isotope and radiocarbon dates – to the newly stacked Scotia Sea RPI record. The RPI curves were thus matched on the basis of the visual correlation of the main palaeointensity features: RPI lows occur at ~41 cal ka B.P. (Laschamp Event), and ~25 cal ka B.P. and RPI highs occur at ~44 cal ka B.P., ~37 cal ka B.P., and at ~32 cal ka B.P. (Figure

5.9). This RPI age model indicates that the portion of the Scotia Sea stack between the scaled depths of 484 cm and 324 cm spans the interval from 43.7 cal ka B.P. to 25.3 cal ka B.P.

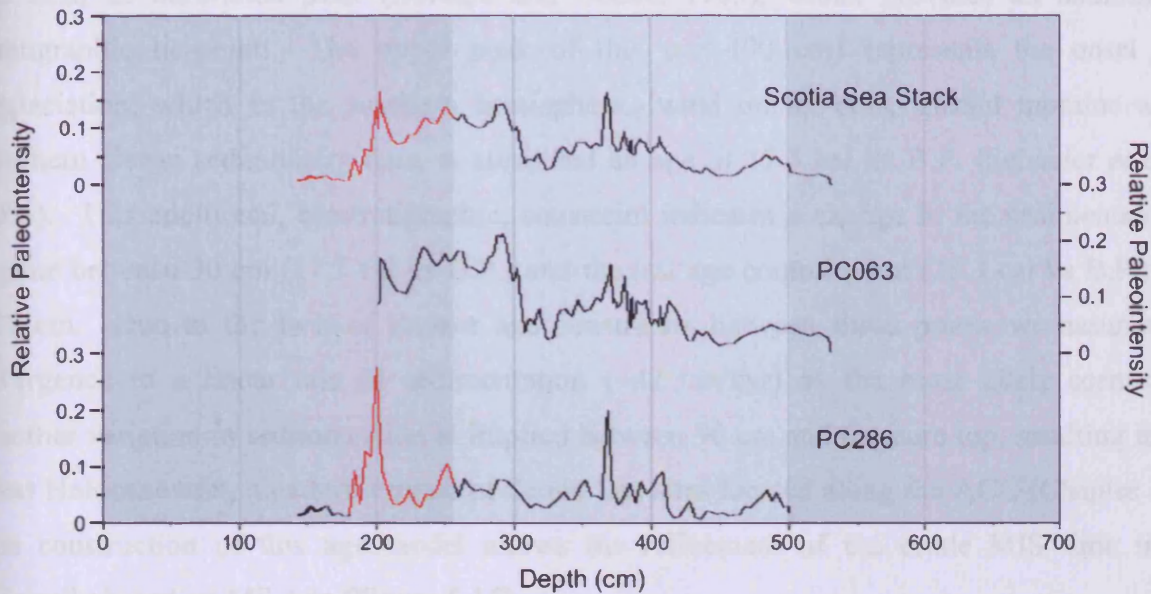


Figure 5.8. Scotia Sea relative palaeointensity stack. Derived from the RPI records of sediment cores TPC063 and TPC286, correlated against the depth scale of TPC286. The portion of the record shaded red indicates grain size unsuitable for magnetic analysis and thus limits the extent of the correlation.

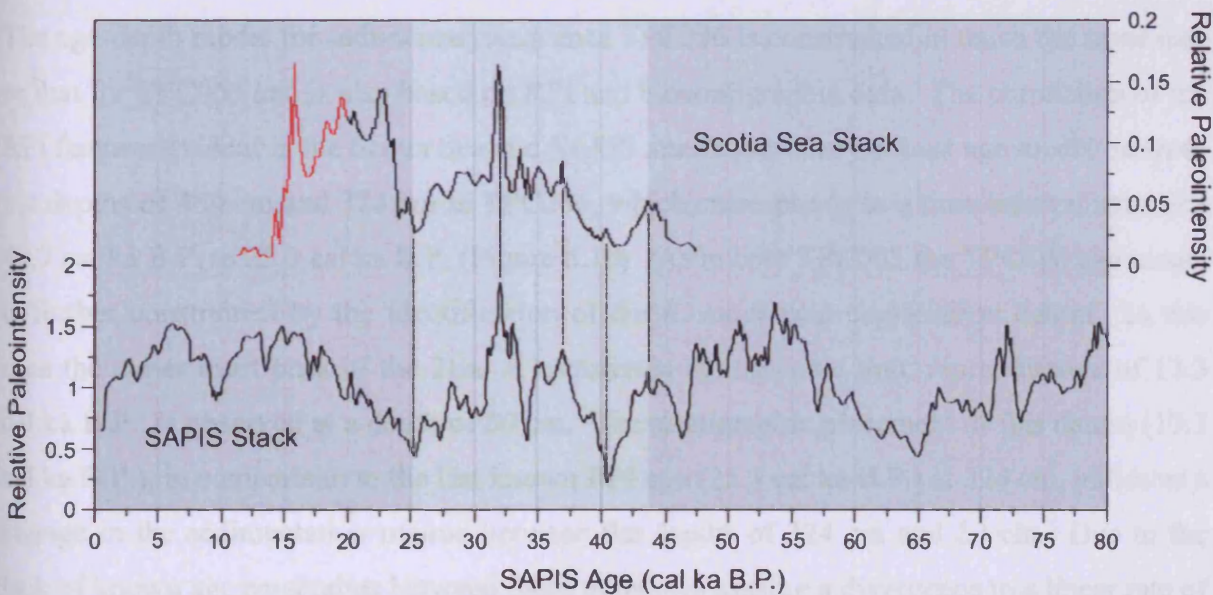


Figure 5.9. Correlation of Scotia Sea RPI stack and the SAPIS RPI reference stack. The portion of the record shaded red indicates grain size unsuitable for magnetic analysis. As a result this portion of the Scotia Sea Stack was not included in the correlation.

5.1.4. Age – Depth Models

5.1.4.1. TPC063

The age-depth model for sedimentary sequence TPC063 is constructed based on RPI and biostratigraphic data. The correlation of the RPI features evident in the Scotia Sea and SAPIS stacks provides a robust age model between the depths of 677 cm and 427 cm, which

corresponds to a time interval spanning 43.7 cal ka B.P. to 25.3 cal ka B.P. (Figure 5.10). Beyond 427 cm (25.3 cal ka B.P.), the model is further constrained by the identification of the 2Ea₁ *E. antarctica* peak (Burckle and Cooke, 1983), which provides an additional stratigraphic tie-point. The upper peak of this unit (90 cm) represents the onset of deglaciation, which in the southern hemisphere, based on ice-core, glacial moraine and Southern Ocean sedimentary data, is attributed an age of 17.3 cal ka B.P. (Schaefer *et al.*, 2006). This additional, biostratigraphic, constraint indicates a change in the sedimentation regime between 90 cm (17.3 cal ka B.P.) and the last age control point (25.3 cal ka B.P.) at 427 cm. Due to the lack of known age constraints between these points we assume a divergence to a linear rate of sedimentation (~42 cm/kyr) as the most likely scenario. Another variation in sedimentation is implied between 90 cm and the core top, resulting in a short Holocene unit, a pattern typical of Scotia Sea sites located along the ACC (Chapter 1). The construction of this age model allows the refinement of the crude MIS time line originally based on MS data (Figure 5.15).

5.1.4.2. TPC286

The age-depth model for sedimentary sequence TPC286 is constructed in much the same way as that for TPC063 and is also based on RPI and biostratigraphic data. The correlation of the RPI features evident in the Scotia Sea and SAPIS stacks provides a robust age model between the depths of 484 cm and 324 cm in TPC286, which corresponds to a time interval spanning 43.7 cal ka B.P. to 25.3 cal ka B.P. (Figure 5.10). As in core TPC063 the TPC286 age model is further constrained by the identification of the *E. antarctica* deglaciation datum. In this case the upper most peak of the 2Ea₁ *E. antarctica* stratigraphic unit, representative of 17.3 cal ka B.P., is observed at a depth of 50 cm. The stratigraphic placement of this datum (17.3 cal ka B.P.), in comparison to the last known RPI age (25.3 cal ka B.P.) at 324 cm, indicates a change in the sedimentation regime between the depths of 324 cm and 50 cm. Due to the lack of known age constraints between these points we assume a divergence to a linear rate of sedimentation of ~34 cm/kyr as the most likely scenario. This record also exhibits an extremely compact Holocene unit in comparison to the glacial in the upper ~50 cm. Extended glacial sedimentary units relative to the interglacial are common at sites in close proximity to the sediment source, i.e. the Antarctic continent (Chapter 1). Further, the construction of this age model enables the development of an improved MIS time line (Figure 5.15).

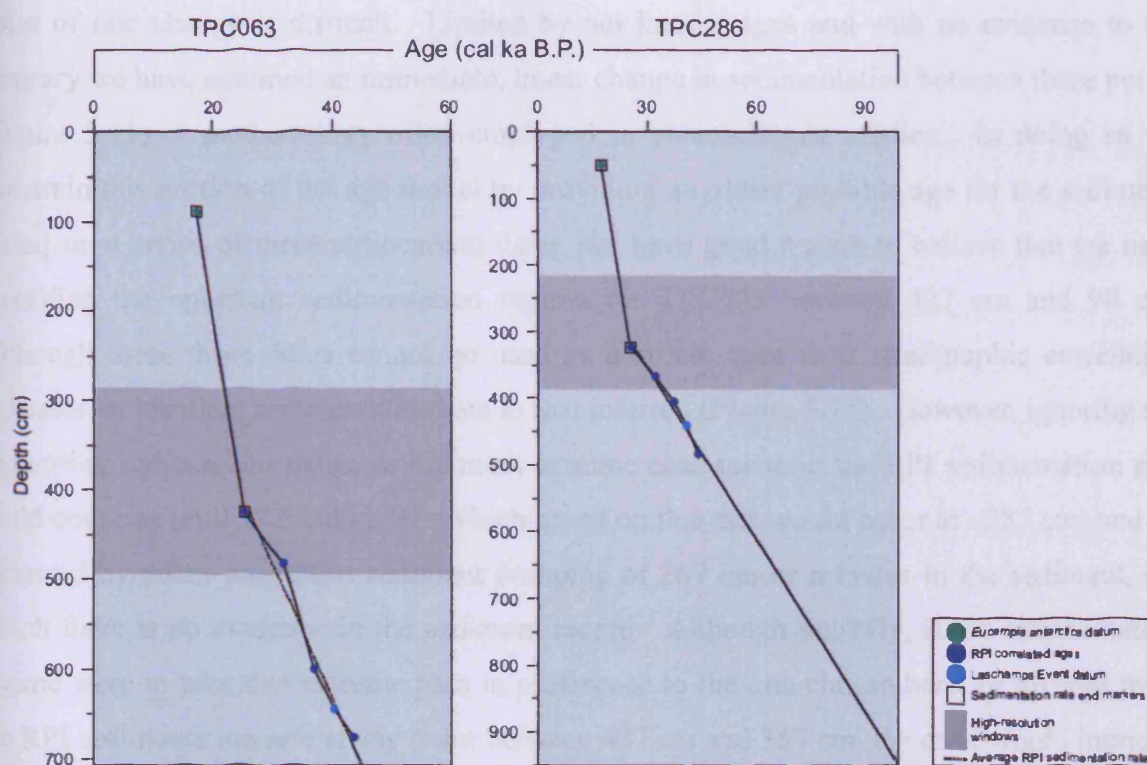


Figure 5.10. Age – depth models for cores TPC063 and TPC286 based on tie-point and RPI correlations. Correlation with the SAPIS chronology is represented by the blue circles, ages between the base of the sediment records and the onset of the SAPIS correlation is based on the extrapolation of the average sedimentation rate as inferred by the RPI markers. A linear sedimentation rate is estimated between the last RPI correlation tiepoint and the *Eucampia antarctica* deglaciation datum (green circle). The dark grey band indicates the high resolution window.

5.1.4.3. Age – Depth model evaluation

5.1.4.3.1. TPC063

The age-depth model for TPC063 is constructed through a novel combination of different techniques and we believe represents one of the most accurate chronologies for Southern Ocean glacial sediments. The most robust of these techniques is the RPI correlation, which between 677 cm and 427 cm identifies accurate ages through the correlation of globally synchronous geomagnetic variability. We are highly confident in the reliability of this portion of the record due to its correlation with the published SAPIS chronology. However, the rate of sedimentation implied by the RPI model beyond 427 cm cannot be sustained to the core top as it would result in negative sedimentation rates, indicating 30 cm of compaction (Figure 5.11), for which there is no evidence in the sediment or diatom record. This disparity indicates that sedimentation rate must have changed between the last known RPI age and the core top. The identification of the *Eucampia antarctica* datum further constrains this shift in sedimentation rate, indicating a change in rate somewhere between 427 cm and 90 cm. However, with no other constraining dates between these points, identification of the exact

point of rate change is difficult. Limited by our known ages and with no evidence to the contrary we have assumed an immediate, linear change in sedimentation between these points (Figure 5.11), a methodology often employed in palaeoclimate studies. In doing so we constrain this portion of the age model by providing an oldest possible age for the sediment. Based on a series of three radiocarbon dates, we have good reason to believe that we have identified the optimum sedimentation regime for TPC063 between 427 cm and 90 cm. Although these three dates cannot be used as absolute ages their stratigraphic correlation indicates an identical sedimentation rate to that inferred (Figure 5.11). However, ignoring the supporting radiocarbon dates, in the most extreme case scenario the RPI sedimentation rate could continue until 17.3 cal ka BP (which based on this rate would occur at ~357 cm) and be followed by either an instant sediment dumping of 267 cm or a hiatus in the sediment, for which there is no evidence in the sediment record. Although unlikely, if the sedimentation regime were to take this extreme path in preference to the one chosen here, or diverge from the RPI sedimentation rate at any point between 427 cm and 357 cm, the error would increase to a maximum of 6.3 kyrs at 357 cm, and decrease thereafter (Figure 5.11). Therefore, although we believe we have identified the most likely sedimentation regime and derived the most accurate chronology, the evaluation of absolute confidence in the age model would be:

- High confidence between 707 cm and 677 cm (Figure 5.11).
- Highest confidence between 677 cm and 427 cm (Figure 5.11).
- Decreasing confidence up to an error of 6.3 kyrs between 427 cm and 357 cm (Figure 5.11).
- Increasing confidence between 357 cm and 90 cm (Figure 5.11).

All interpretation and discussion in chapter 7 are based on the chosen age-model presented in Figure 5.10. However, although we consider it unlikely, it must be fore-stated that any interpretation of the timing of events between 427 cm and 90 cm could, potentially, be offset by a maximum error of 6.3 kyrs (at 357 cm).

5.1.4.3.2. TPC286

The age-depth model for TPC286 was derived in much the same way as TPC063, using the identical combination of RPI and biostratigraphic data and the same caveats apply. High confidence is placed in the age-depth model up to a depth of 324 cm based on RPI correlation with the published SAPIS chronology, however continuation of the RPI sedimentation rate would result in negative sedimentation rates, indicating 154 cm of compaction (Figure 5.11), for which there is no evidence in the sediment or diatom record. A further constraint, based

on the identification of the *E. antarctica* deglaciation datum (17.3 cal ka B.P.), indicates a change in the sedimentation regime between 324 cm and 50 cm. A linear rate of sedimentation between the two known ages is assumed, however, this represents the oldest possible age for sediments, which in the extreme scenario could differ by up to 6.3 kyrs at 270 cm (Figure 5.11). Therefore, although we believe we have identified the most likely sedimentation regime and derived the most accurate chronology, the evaluation of absolute confidence in the age model would be:

- High confidence between 929 cm and 324 cm (Figure 5.11).
- Highest confidence between 484 cm and 324 cm (Figure 5.11).
- Decreasing confidence up to an error of 6.3 kyrs between 324 cm and 270 cm (Figure 5.11).
- Increasing confidence between 270 cm and 50 cm (Figure 5.11).

All interpretation and discussion in chapter 7 are based on the chosen age-model presented in Figure 5.10. However, although we consider it unlikely, it must be fore-stated that any interpretation of the timing of events between 324 cm and 50 cm could, potentially, be offset by a maximum error of 6.3 kyrs (at 270 cm).

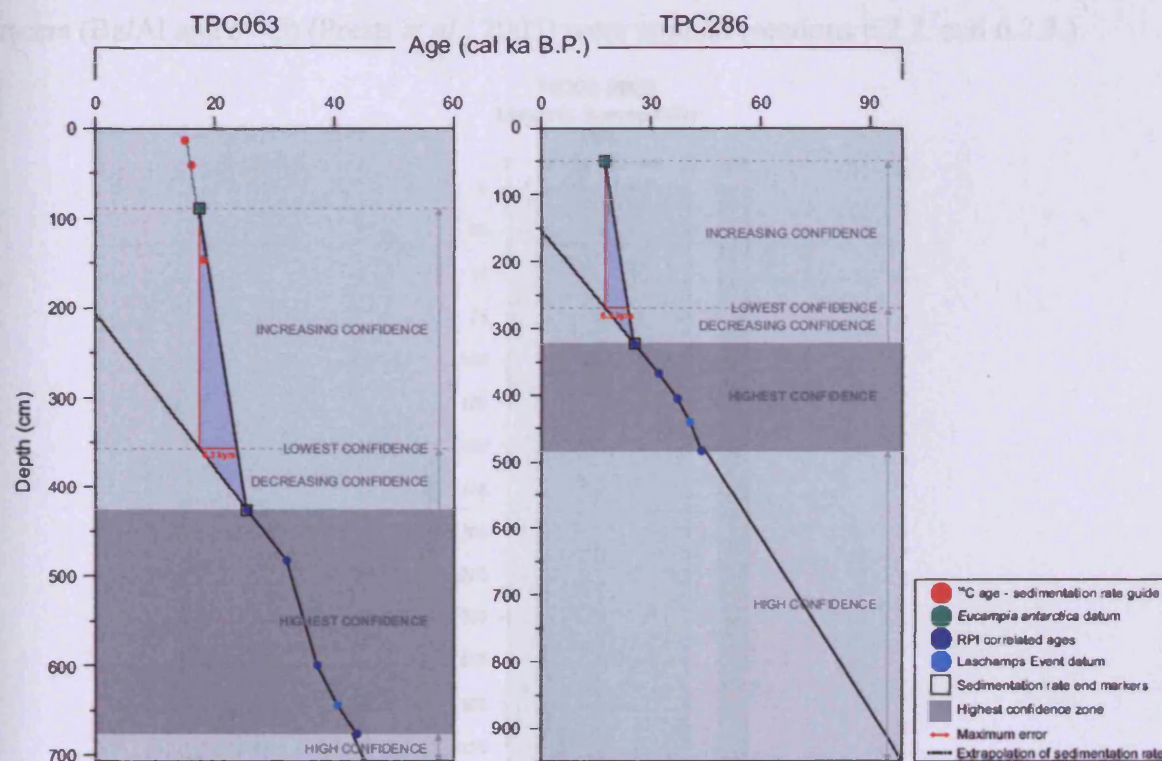


Figure 5.16. Evaluation of age-depth models for cores TPC063 and TPC286. The age-depth models are divided into areas of high and low confidence based on the uncertainty of the sedimentation regimes. Highest confidence is associated with the RPI correlations (dark grey band) with lower confidence associated with the linear sedimentation regime between the RPI model and the deglaciation datum. In the low confidence zone there is a maximum error of 6.3 kyrs.

5.2. Core MD03-2603

Core chronology for MD03-2603 was developed by M. Presti (2008), who defined a preliminary stratigraphy based on ^{230}Th Thorium-excess data (section 5.2.2) and later refined the age-model based on the correlation of the down core Aluminium/Barium ratio (section 5.2.3) with the LR04 oxygen isotope stratigraphy (6.2.4).

5.2.1. Magnetic Susceptibility

The MS trend in core MD03-2603 (Figure 5.12) is interpreted as spanning the last three marine isotope stages (MIS 1 – 3). Relatively low MS values between 380 cm and 310 cm are interpreted as representing a portion of MIS 3. The MS record shows a transition to higher values between 310 cm and 282 cm interpreted as indicating the transition to MIS 2, which extends between 282 cm and 104 cm. A second transition, to considerably lower MS values, between 104 cm and 86 cm is interpreted as representing the transition to the Holocene, which extends between 86 cm and the core top. Due to the proximity of the seasonal sea-ice zone, a degree of caution must be employed when interpreting these results, so previous independent analysis of thorium excess dating and geochemical and isotope tracers (Ba/Al and $\delta^{18}\text{O}$) (Presti *et al.*, 2005) were applied (sections 6.2.2. and 6.2.3.).

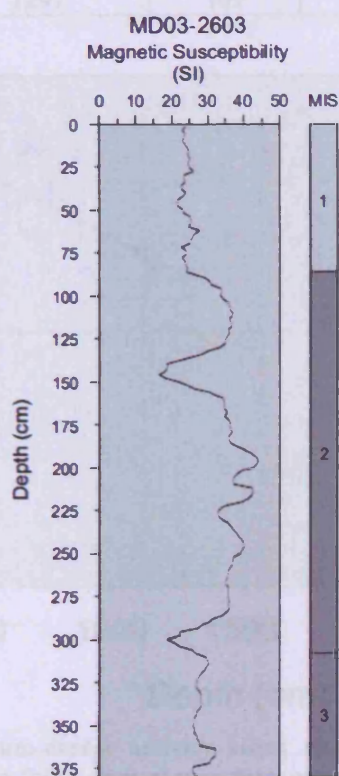


Figure 5.12. Core MD03-2603: Magnetic susceptibility curve and proposed MIS stratigraphy based on the relative contribution of terrigenous and biogenic derived material, which varies during warm and cold stages.

5.2.2. Thorium-excess Dating

Based on 20 samples taken from core MD03-2603, which were analysed for ^{232}Th and ^{238}U content using Alpha Spectrometry at EPOC - University of Bordeaux I by D. Denis, Presti *et al.* (2008) determined a mean sedimentation rate of 7.68 cm/kyr for the upper 13 meters of core MD03-2603 using $^{230}\text{Th}_{\text{excess}}$. Below 13 meters depth, the uncertainties related to the limited half-life of the ^{230}Th within the material make the technique unreliable (Figure 5.13). The sedimentation rate of 7.68 cm/kyr was used to generate an age-depth model for the upper ~1300 cm of the record (Table 5.3).

Table 5.3. Core MD03-2603: Thorium age- model.

Depth (cm)	Age (ka)	$\pm 1\sigma$ (ka)
6	0.8	0.02
75	10	0.4
145	19	0.5
283	37	1.3
349	45	1.5
485	63	2.3
691	90	4.6
759	99	3.8
897	117	3.1
1107	144	10.4
1157	151	10.2
1297	169	7

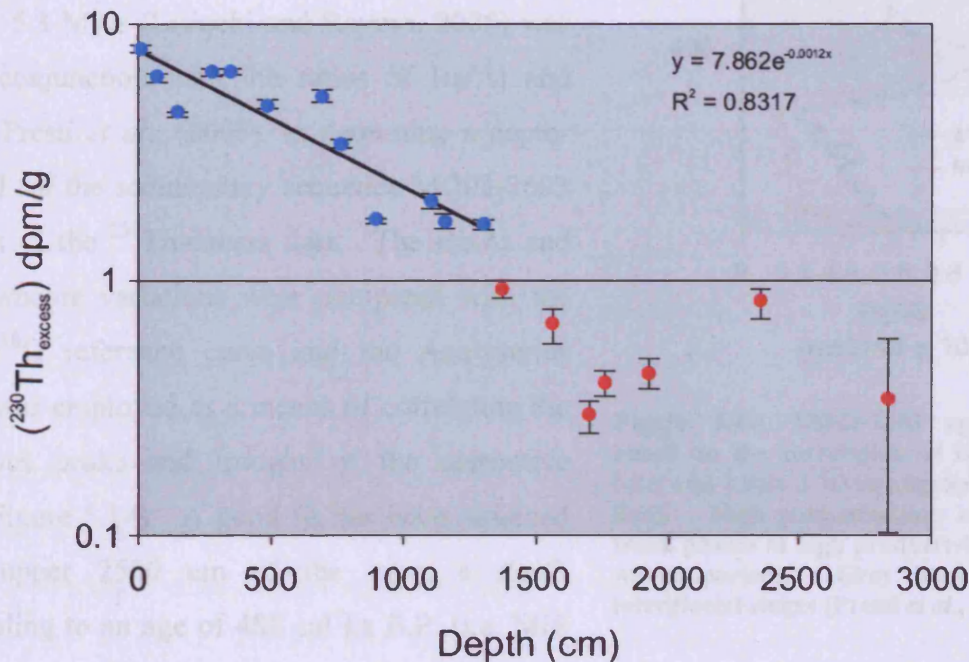


Figure 5.13. Decrease in ^{230}Th -excess activity along sediment core MD03-2603. The rate of sedimentation for the upper 1300 cm (blue circles) was determined based on variations in the activity of ^{230}Th -excess with depth. Error bars represent the standard error on the measurements at 1σ . Beyond 1300 cm (red circles) the uncertainties associated with the technique are too large and were not included in the regression (Data from Presti *et al.*, 2005).

5.2.3. Geochemical Tracers

The trace metals barium (Ba), aluminium (Al) and titanium (Ti), among others, were measured via mass spectrometry on 400 samples, primarily at a depth resolution of 8 cm at the OGS in Trieste by M. Presti, and analyses of the digested samples by ICP-AES at Chelab (chemical labs, Treviso), using a reading method EPA 6010 C/00 after having totally digested the samples by 2 ml HF ultrapure and 10 ml sol (3:1 HCl:HNO₃) (Presti *et al.*, 2008). The resulting down core variations in the both the ratios of Ba/Al and Ba/Ti clearly relate to glacial/interglacial stages, with the signal most pronounced in the Ba/Al record (Figure 5.14).

5.2.4. Oxygen Isotope Correlation

The oxygen isotope reference stack LR04, which is based on 57 globally distributed benthic $\delta^{18}\text{O}$ records and spans 5.3 Myrs (Lisiecki and Raymo, 2005) was used in, conjunction with the ratios of Ba/Al and Ba/Ti by Presti *et al.*, (2008), to determine a depth-age model for the sedimentary sequence MD03-2603 in support of the ^{230}Th -excess data. The Ba/Al and Ba/Ti downcore variations were compared with the benthic $\delta^{18}\text{O}$ reference curve and the Analyseries software was employed as a means of correlating the synchronous peaks and troughs of the respective records (Figure 5.14). A good fit has been obtained for the upper 2500 cm of the core, a depth corresponding to an age of 488 cal ka B.P. (i.e. MIS 13), and an age-depth conversion has been obtained for this whole period based on data presented in Figure 5.14. This accurate age model allows a close comparison of climate changes within records TPC063 and TPC286 (Figure 5.15).

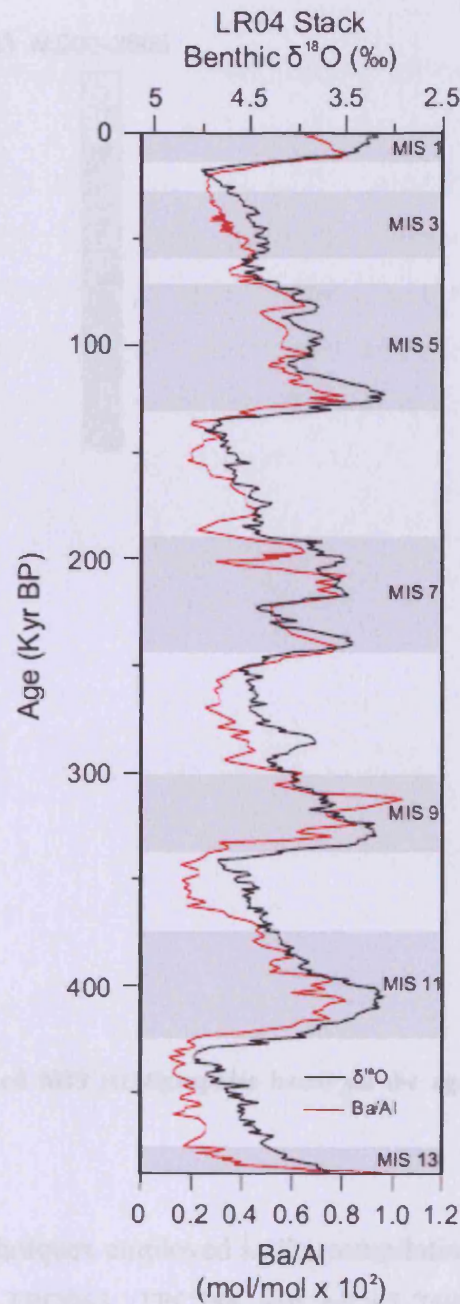


Figure 5.14. MD03-2603 age model based on the correlation of Ba/Al (red line) and LR04 $\delta^{18}\text{O}$ stratigraphy (black line). High concentrations of barium track phases of high productivity during warm periods. Grey bars indicate interglacial stages (Presti *et al.*, 2008).

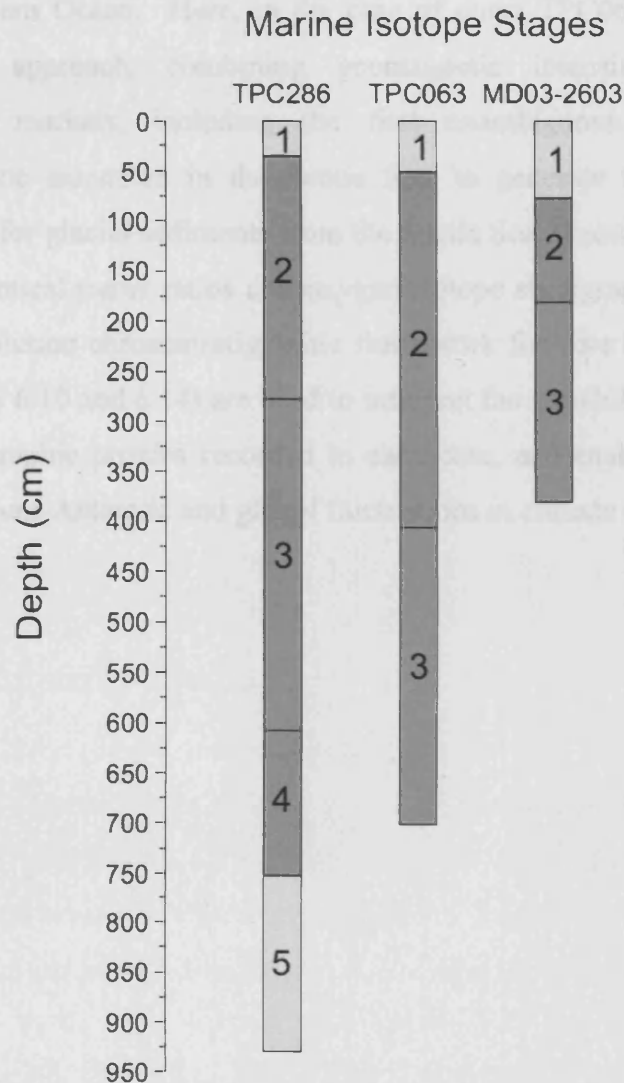


Figure 5.15. Cores TPC063, TPC286 and MD03-2603: Refined MIS stratigraphies based on the age-models constructed in the pervious sections.

5.3. Summary

The chapter has presented a detailed account of the techniques employed in the compilation of a chronostratigraphical structure for marine cores TPC063, TPC286 and MD03-2603 (Presti *et al.*, 2008). An accurate chronology is an essential facet of any palaeoclimate study as the objective comparison of palaeoclimatic records is necessary in order to decipher the complex mechanisms of global climate dynamics. However, attaining accurate chronologies for Late Pleistocene marine sediments in the Antarctic is notoriously problematic, and is the most influential factor in limiting the scope for interhemispheric and global comparison. Extensive dissolution of calcareous biota south of the Antarctic Polar Front prohibits the application of stable isotope techniques and radiocarbon dating, with the latter further complicated by uncertain reservoir effects, the magnitude of which vary dramatically

throughout the Southern Ocean. Here, in the case of cores TPC063 and TPC286, I have presented a novel approach, combining geomagnetic intensity data with several chronostratigraphical markers, including the first unambiguous identification of the Laschamp geomagnetic excursion in the Scotia Sea, to generate the first reliable, high-resolution age-model for glacial sediments from the Scotia Sea. Presti *et al.* (2008) employ a correlation of geochemical tracer ratios and oxygen isotope stratigraphy in the development of a robust, high-resolution chronostratigraphic framework for core MD03-2603. The age-depth models (Figures 6.10 and 6.14) are used to interpret the variability demonstrated by the climatic and oceanographic proxies recorded in each core, and enable the identification of contemporaneous circum-Antarctic and global fluctuations in climate during the LGC.

6. Interpretation and Discussion

In the following chapter I present palaeoceanographic reconstructions based on proxies analysed in sediment cores TPC063, TPC286 and MD03-2603. These palaeoceanographic reconstructions are based on the oceanographic settings and ecological associations detailed in Chapters 1 and 2. Cores TPC063 and TPC286 are used to reconstruct the Scotia Sea glacial environment and core MD03-2603 is used to represent the glacial environment adjacent to the Adélie Land Coast. Finally, a comparison of the two regional settings is presented.

6.1. TPC063

6.1.1. Summary of Interpretations

Core TPC063 represents a climate record spanning the last 44.7 kyrs (Chapter 5), covering the majority of marine isotope stages (MIS) 3 to 1, including the transition from the previous glacial to the current interglacial. Sedimentation rates are higher during the glacial in comparison to the interglacial and glacial conditions are dominant from the base of the core 44.7 cal ka B.P. to 17.3 cal ka B.P. (section 6.1.1.1.). The High Resolution Window (HRW) spans the mid-section of the core between 34.2 cal ka B.P. and 21.9 cal ka B.P. (section 6.1.4.), which includes the glacial maximum, and is the focus of this study (section 6.1.2.). During the HRW the oceanographic environment over core TPC063 (Figure 6.1) in the northern Scotia Sea was characterised by:

- The occurrence of an extensive peak in productivity at ~31 cal ka B.P.
- The deterioration of sea surface temperatures (SSTs), characterised by the influx of cold surface waters associated with the close proximity of the winter sea-ice (WSI) edge, beginning ~25 cal ka B.P.
- The gradual equatorward expansion of the WSI edge, several degrees of latitude further north than the modern day extent, reaching a maximum between 24.1 cal ka B.P. and 23.5 cal ka B.P. and followed by rapid retreat by 22.9 cal ka B.P.
- A muted signal of summer sea-ice (SSI) although no evidence that the SSI edge expanded as far north as the core site.

- A southern migration of the Antarctic Polar Front (APF) potentially associated with a southward migration or expansion of the southern hemisphere Westerly wind belt between 22.6 cal ka B.P. and 21.9 cal ka B.P.

The termination of the glacial regime is characterised by a period of deglaciation between 17.3 cal ka B.P. to 11.5 cal ka B.P. (section 6.1.1.2.), 11.5 kyrs of the core representing conditions characteristic of the Holocene interglacial (section 6.1.1.3.).

6.1.1.1. The Glacial, 44.7 cal ka B.P. to 17.3 cal ka B.P.

The portion of the record between 44.7 cal ka B.P. and 17.3 cal ka B.P. is characterised by glacial conditions, with the HRW between 34.2 cal ka B.P. and 21.9 cal ka B.P. encompassing the glacial maximum. Magnetic susceptibility (MS) (Chapter 4, Figure 4.1) is relatively high between 44.7 cal ka B.P. and 12 cal ka B.P. and peaks between 29.6 cal ka B.P. and 22.2 cal ka B.P.; the peak, interpreted as increased input of terrigenous material during the glacial, indicates glacial maximum. Total diatom concentrations are consistently low throughout the glacial period (apart from the unique peak in *Chaetoceros* sp. at 30.9 cal ka B.P.), with mean concentrations of 5.48×10^6 v/gds. In the build up to the glacial maximum, between 44.7 cal ka B.P. and 34.2 cal ka B.P., the diatom assemblage indicates a regime dominated by open ocean conditions of the Antarctic Circumpolar Current (ACC), with a strong influence of the APF. This regime is interrupted at 35.8 cal ka B.P. when the *Fragilariopsis* sea-ice group indicates the brief influence of the WSI edge over the core site and a return to open ocean conditions by 34.3 cal ka B.P.; hence this location was close to its maximum extent. The main part of the HRW is characterised by cooling surface waters and the encroachment of the WSI edge. Environmental change during the HRW is discussed in detail below (section 6.1.2.). Subsequent to the HRW, between 21.9 cal ka B.P. and 19.7 cal ka B.P., the end of the glacial is characterised by several occurrences of the WSI edge over the core site, indicated by relative abundance of the *Fragilariopsis* sea-ice group being in excess of 3%. These short-lived events occur at 22.4 cal ka B.P., 22.1 cal ka B.P., 21.1 cal ka B.P. and 19.7 cal ka B.P (Figure 4.2, Chapter 4).

Each event is succeeded by elevated concentrations of the open ocean indicator *T. lentiginosa* and the APF indicator *A. tabularis* (Figure 4.1, Chapter 4), indicating a return to full open water conditions and return of the APF between the events at 22.5 cal ka B.P., 22.3 cal ka B.P., 21.9 cal ka B.P., 20.4 cal ka B.P. and 19 cal ka B.P. and the retreat of the sea-ice edge to a more southerly location (Figure 6.1). A gradual reduction in seasonality is observed

between 19.7 cal ka B.P. and 17.8 cal ka B.P., when the diatom assemblage indicates a permanent retreat of the WSI edge to the south (Figure 6.2).

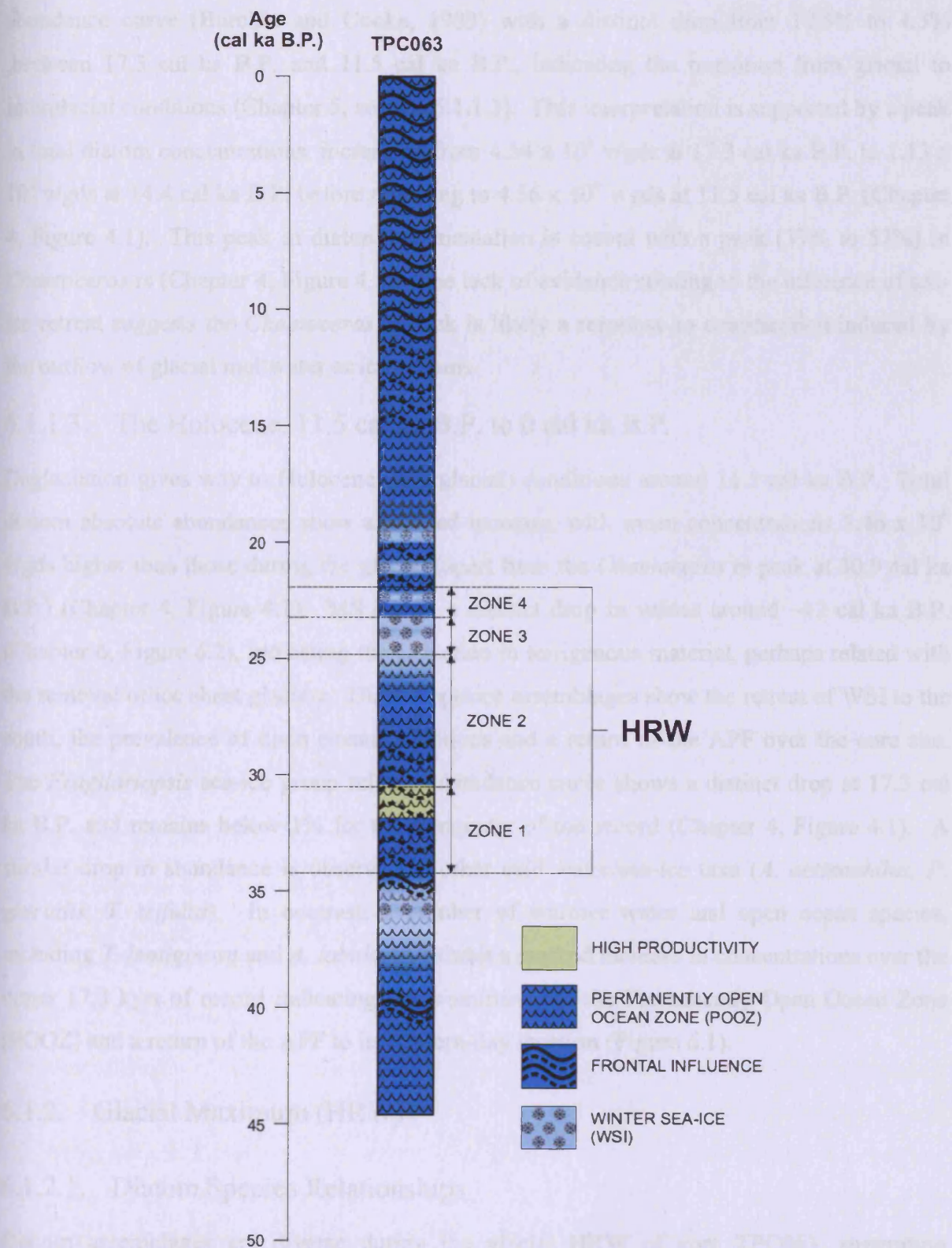


Figure 6.1. Core TPC063: Environmental log illustrating reconstructed oceanographic variability between 44.7 cal ka B.P. and the present day in the north Scotia Sea. Zonation is derived from PCA (Chapter 4). HRW = high resolution window.

6.1.1.2. Deglaciation, 17.3 cal ka B.P. to 11.5 cal ka B.P.

The timing of deglaciation in core TPC063 is based primarily on the *E. antarctica* relative abundance curve (Burckle and Cooke, 1983) with a distinct drop from 10.5% to 4.3% between 17.3 cal ka B.P. and 11.5 cal ka B.P., indicating the transition from glacial to interglacial conditions (Chapter 5, section 5.1.1.3). This interpretation is supported by a peak in total diatom concentrations, increasing from 4.54×10^6 v/gds at 17.3 cal ka B.P. to 1.13×10^7 v/gds at 14.4 cal ka B.P. before returning to 4.56×10^6 v/gds at 11.5 cal ka B.P. (Chapter 4, Figure 4.1). This peak in diatom sedimentation is coeval with a peak (37% to 57%) in *Chaetoceros* spp. (Chapter 4, Figure 4.1). The lack of evidence relating to the influence of sea-ice retreat suggests the *Chaetoceros* spp. peak is likely a response to stratification induced by the outflow of glacial meltwater or ice streams.

6.1.1.3. The Holocene, 11.5 cal ka B.P. to 0 cal ka B.P.

Deglaciation gives way to Holocene (interglacial) conditions around 11.5 cal ka B.P. Total diatom absolute abundances show a marked increase, with mean concentrations 5.46×10^6 v/gds higher than those during the glacial (apart from the *Chaetoceros* spp. peak at 30.9 cal ka B.P.) (Chapter 4, Figure 4.1). MS shows a distinct drop in values around ~12 cal ka B.P. (Chapter 6, Figure 6.2), indicating the reduction in terrigenous material, perhaps related with the removal of ice sheet glaciers. Diatom species assemblages show the retreat of WSI to the south, the prevalence of open ocean conditions and a return of the APF over the core site. The *Fragilariopsis* sea-ice group relative abundance curve shows a distinct drop at 17.3 cal ka B.P. and remains below 1% for the remainder of the record (Chapter 4, Figure 4.1). A similar drop in abundance is observed in other cold water/sea-ice taxa (*A. actinochilus*, *P. glacialis*, *T. trifurcata*). In contrast, a number of warmer water and open ocean species, including *T. lentiginosa* and *A. tabularis*, exhibit a marked increase in concentrations over the upper 17.3 kyrs of record indicating the prominence of the Permanently Open Ocean Zone (POOZ) and a return of the APF to its modern-day location (Figure 6.1).

6.1.2. Glacial Maximum (HRW)

6.1.2.1. Diatom Species Relationships

Diatom assemblages are diverse during the glacial HRW of core TPC063, suggesting complex and changing oceanographic conditions over the core site during sediment

deposition. Individual diatom assemblages derived from PCA and associated ecological interpretations are summarised below and illustrated in Figure 6.2.

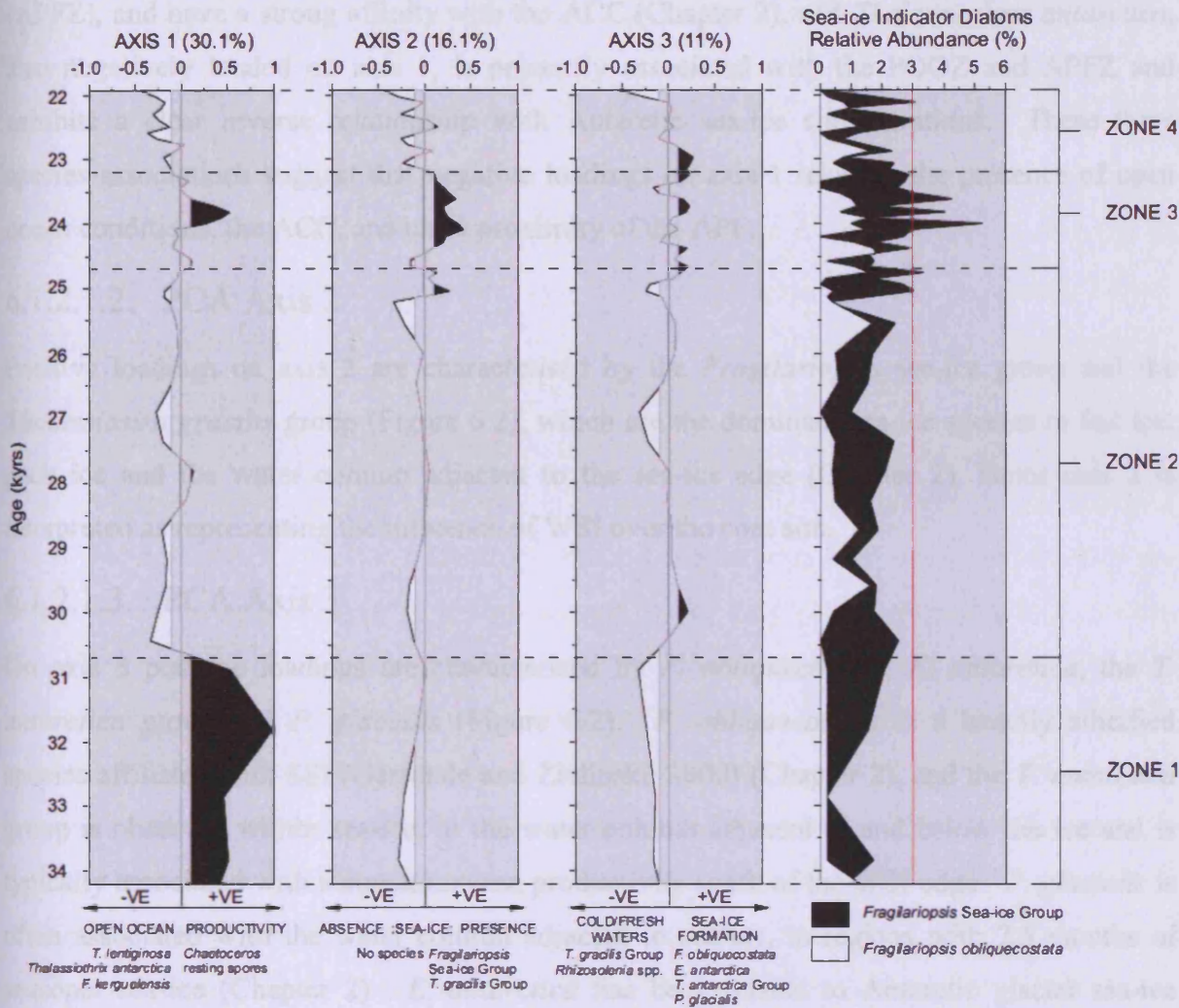


Figure 6.2. Core TPC063 (HRW): PCA component scores and environmental gradients associated with axes 1 to 3, compared with the relative abundance curves of the *Fragilariopsis* sea-ice group (black) and *Fragilariopsis obliquicostata* (white), plotted against age (kyrs). Shaded black and white polygons on axes 1 to 3 indicate significant positive and negative variability respectively (un-shaded areas indicate insignificant variability). Diatom indicator species associated with each axis are listed at the base of the figure. The red line on the sea-ice diatom plot indicates the 3% sea-ice threshold.

6.1.2.1.1. PCA Axis 1

Positive loadings on axis 1 relate to *Chaetoceros* rs, which have been associated with highly productive surface waters, Antarctic sea-ice environments and the stratified surface waters of the Marginal Ice Zone (MIZ) (Chapter 2) (Figure 6.2), often dominating spring blooms. They are rarely observed at high abundances in the POOZ of the northern Scotia Sea (Chapter 2). Positive loadings on axis 1 are therefore interpreted as high productivity, possibly related to the MIZ.

F. kerguelensis and *T. lentiginosa* characterise the negative end of axis 1 (Figure 6.2). These diatoms are common in surface sediments below the POOZ and Antarctic Polar Frontal Zone (APFZ), and have a strong affinity with the ACC (Chapter 2), and *Thalassiothrix antarctica*, also negatively loaded on axis 1, is primarily associated with the POOZ and APFZ and exhibits a clear inverse relationship with Antarctic sea-ice concentrations. These three species associations suggest that negative loadings on axis 1 relate to the presence of open ocean conditions, the ACC, and close proximity of the APF.

6.1.2.1.2. PCA Axis 2

Positive loadings on axis 2 are characterised by the *Fragilariopsis* sea-ice group and the *Thalassiosira gracilis* group (Figure 6.2), which are the dominant sea-ice species in fast ice, pack ice and the water column adjacent to the sea-ice edge (Chapter 2), hence axis 2 is interpreted as representing the influence of WSI over the core site.

6.1.2.1.3. PCA Axis 3

On axis 3 positive loadings are characterised by *F. obliquecostata*, *E. antarctica*, the *T. antarctica* group and *P. glacialis* (Figure 6.2). *F. obliquecostata* is a heavily silicified species affiliated with SSI (Gersonde and Zielinski, 2000) (Chapter 2), and the *T. antarctica* group is observed within sea-ice, in the water column adjacent to and below the ice and is typically associated with summer/autumn productivity south of the WSI edge. *P. glacialis* is often associated with the water column adjacent to sea-ice, in regions with 7.5 months of seasonal sea-ice (Chapter 2). *E. antarctica* has been related to Antarctic glacial sea-ice extent, however, there is no modern analogue at glacial abundance levels to support this hypothesis. *E. antarctica* has shown a strong response to iron enrichment (Blain *et al.*, 2007; Moore *et al.*, 2007; Pollard *et al.*, 2009) and has been associated with iceberg meltwater and sea-ice meltback (Burckle and Cooke, 1984; Smith *et al.*, 2007) (Chapter 2). Negative loadings on axis 3 are characterised by the *T. gracilis* group and *Rhizosolenia* spp. (Figure 6.2). The diatom group *Rhizosolenia* spp. includes a variety of species associated with oceanographic environments ranging from the WSI edge to the APF, however, common factors in their ecologies reflect frontal stability and freshwater intrusions. In each of the cases on axis 3 no single *Rhizosolenia* species dominates (Appendix 1), implying an environment capable of supporting a varied species assemblage (Chapter 2). Hence the environmental gradient of axis 3 is interpreted as sea-ice formation versus cold, fresh surface waters.

6.1.2.2. Palaeoenvironment Reconstruction Across the Glacial Maximum

Downcore environmental variability is defined by 4 HRW zones (Chapter 4) presented in Figures 6.1 and 6.2 and discussed below.

6.1.2.2.1. HRW Zone 1: Unique Productivity Event, 34.2 cal ka B.P. to 30.7 cal ka B.P.

Zone 1 is characterised by positive component scores on PCA axis 1, between 33.8 cal ka B.P. and 30.9 cal ka B.P., interpreted as representing highly productive surface waters, possibly relating to the proximity of the MIZ. However, significant but weak negative component scores on axis 2 indicate an absence of sea-ice. Axis 3 shows negative component scores, which suggests a nearby source of relatively cold, fresh, open waters.

Zone 1 is an unusually large productivity peak, dominated by *Chaetoceros* rs, between 33.8 cal ka B.P. to 30.9 cal ka B.P. *Chaetoceros* rs concentrations reach those observed in the Antarctic Peninsula (Crosta *et al.*, 1997, Armand *et al.*, 2005) and Falkland Trough (Allen, 2003; Allen *et al.*, 2005) but not found in the POOZ and atypical for core TPC063. One potential explanation is an advance (and retreat) of the WSI edge and dominance of a highly productive MIZ environment, however, this hypothesis is not supported by PCA axis 2, or the *Fragilariopsis* sea-ice group relative abundance curve (Figure 6.2). Such high *Chaetoceros* rs concentrations are unlikely to have been attained solely through advection from distal production sites because, at this point in time, the coastal Antarctic Peninsula sea was overlain by glacial ice and strong outflow of Scotia Sea waters was over the North Scotia Ridge (suggested by cold surface waters; axis 3), which lessens the likelihood of a transported signal from the Argentine Basin. In addition, the lack of similar concentrations of other heavily silicified taxa such as *F. kerguelensis* and *E. antarctica* make preferential preservation an unlikely factor. In summary, zone 1 appears to be related to a unique high productivity event, potentially triggered by a mechanism external to the local oceanographic regime (discussed further in section 6.3.2.3.).

6.1.2.2.2. HRW Zone 2: Cooling Open Ocean, 30.7 cal ka B.P. to 24.7 cal ka B.P.

In zone 2, axis 1 is characterised by negative component scores from 30.6 cal ka B.P., which indicates open ocean conditions associated with the ACC. Axis 2 negative component scores are weakly significant between 30.5 cal ka B.P. and 29.3 cal ka B.P., and 25.8 cal ka B.P. and

25.2 cal ka B.P., implying the absence of sea-ice and supporting the open ocean conditions inferred from axis 1. Axis 2 has 2 episodes of weakly significant positive component scores at 25.1 cal ka B.P. and 24.8 cal ka B.P., interpreted as increasing proximity of the WSI edge. Axis 3 shows a significant peak in positive component scores at 30 cal ka B.P., and two significant peaks in negative component scores at 26.9 cal ka B.P. and 25 cal ka B.P.. Negative component scores on axis 3 suggest the greater influence of colder, fresher waters over the core site, possibly related to sea-ice melt-back or frontal upwelling. The peak in positive component scores indicates the near-by formation, or possibly a transported signal, of sea-ice.

Zone 2 is characterised by open ocean conditions and the ACC. Although the diatoms present (*T. lentiginosa*, *Thalassiothrix antarctica* and *F. kerguelensis*) are robust and commonly associated with preferential dissolution, the presence of smaller, lightly silicified valves within the diatom assemblage suggests that dissolution, advection and winnowing are minimal. Cold, fresh surface waters characterise the environment overlying the core site between 27.7 cal ka B.P. and 26.5 cal ka B.P., interpreted as the influence of frontal conditions rather than sea-ice due to elevated relative abundances in the open ocean species *F. kerguelensis* and *T. lentiginosa*, the species group *Rhizosolenia* spp. and *Thalassiothrix antarctica*, which have each been associated with diatom blooms along the ocean fronts (Selph *et al.*, 2001; Smetacek *et al.*, 2002). However, during this period, the relative abundance of *A. tabularis*, the primary indicator of encroaching sub-Antarctic surface waters and thus related poleward shifts in the APF, remained relatively low. Hence the encroaching front could be a northward shift in the Southern Antarctic Circumpolar Current Front (SACCF) rather than a southern migration of the APF. Surface waters remain ice-free until 25 cal ka B.P. (Figure 6.1) when the WSI edge advanced toward the core site and the environment is characterised by the influx of associated cold, fresh surface waters.

6.1.2.2.3. HRW Zone 3: Glacial Sea-ice Maximum, 24.7 cal ka B.P. to 23.2 cal ka B.P.

In zone 3 positive component scores dominate axis 1 between 24 cal ka B.P. and 23.6 cal ka B.P., and are insignificant above and below this peak. This peak on axis 1 is interpreted as an increase in water column productivity, potentially related to water column stratification associated with the MIZ. Axis 2 is characterised by a weak significant peak in negative component scores between 24.7 cal ka B.P. and 24.5 cal ka B.P., highly significant positive scores dominate the remainder of zone 3, between 24.4 cal ka B.P. and 23.3 cal ka B.P..

Positive axis 2 component scores indicate the influence of sea-ice conditions over the site. Axis 3 is characterised by significant positive component scores for the majority of zone 3, with negative component scores becoming significant at ~24.3 cal ka B.P. and at ~23.4 cal ka B.P.. Positive axis 3 component scores are interpreted as increased summer/autumn production over, or close to, the core site associated with the formation of seasonal sea-ice. The short periods of significant component scores could be related to melt-out and/or the injection of colder, fresher waters.

Zone 3 is characterised by sea-ice diatoms and indicates the gradual extension and subsequent retreat of WSI over the core site. An episode of enhanced productivity occurred between 24 cal ka B.P. and 23.6 cal ka B.P., and is composed primarily of *Chaetoceros* spp. that reach relative abundances of >65% and valve concentrations of 5.49×10^6 v/gds, and is interpreted as the presence of the MIZ environment and the advance and retreat of WSI over the core site. This interpretation is supported by the *Fragilariopsis* sea-ice group (Figure 6.2), which reaches abundances greater than 3% (Gersonde and Zielinski, 2000). The *Fragilariopsis* sea-ice group exceeds the 3% threshold on several occasions indicating episodes of WSI advance and retreat over the core site, with maximum extent occurring between 24.1 cal ka B.P. and 23.5 cal ka B.P. This interpretation is further supported by HBI data, which parallels the trend shown by the *Fragilariopsis* sea-ice group, increasing to a robust peak in zone 3 (Chapter 4, Figure 4.6). WSI retreats by 22.9 cal ka B.P. at the onset of zone 4 (Figure 6.1). Although *F. obliquecostata* does not reach the critical threshold of 3% that is indicative of SSI presence (Gersonde and Zielinski, 2000), relative abundance does regularly exceed 1%, implying that winter sea-ice may have intermittently persisted throughout the spring and summer months (Allen *et al.*, 2005) between 24.8 cal ka B.P. and 24 cal ka B.P. (Figure 6.1).

6.1.2.2.4. HRW Zone 4: Enhanced Sea-ice Seasonality, 23.2 cal ka B.P. to 21.9 cal ka B.P.

In zone 4, PCA axis 1 is characterised by negative component scores above 23.3 cal ka B.P. This is interpreted as a gradual return of open ocean conditions over the core site. Axis 2 is also characterised by negative component scores, which are significant at ~23.1 cal ka B.P., ~22.7 cal ka B.P., ~22.3 cal ka B.P. and ~21.9 cal ka B.P., and are interpreted as the gradual retreat of the WSI edge away from the core site. Axis 3 is characterised by positive component scores between 23.3 cal ka B.P. and 22.8 cal ka B.P. followed by a peak in negative component scores at the top of zone 4 between 22.1 cal ka B.P. and 21.9 cal ka B.P..

This pattern is interpreted as the initial transition between WSI and open ocean conditions and the dominance of warmer waters, before the influx of cold, possibly freshwater at the top of zone 4.

HRW zone 4 is generally characterised by the continued retreat of WSI and a gradual return of POOZ conditions associated with the primary flow of the ACC. In the older portion of zone 4 there are periodic re-advances of the WSI edge into the northern Scotia Sea, supported by the *Fragilariopsis* sea-ice group relative abundance curve, which shows two excursions up to the 3% threshold at 22.4 cal ka B.P. and 22.1 cal ka B.P. The absence of a strong productivity signal indicates an unstable sea-ice edge unable to maintain bloom conditions, lack of water column stratification and a rapid return to POOZ conditions. This interpretation is based on enhanced relative abundance of the open ocean indicator *T. lentiginosa* and APF indicator *A. tabularis* before and after the occurrence of the sea-ice edge, indicating the rapid retreat of the sea-ice far to the south (Figure 6.1).

6.2. TPC286

6.2.1. Summary of Interpretations

Core TPC286 encompasses approximately 96 kyrs (Chapter 5), however, because TPC063 only covers the past 44.7 cal ka B.P., the following interpretation of TPC286 will mainly focus on the upper 47.9 cal ka B.P. (511 cm). The rate of sedimentation was much higher during the glacial and consequently glacial age sediments dominate the sequence (Chapter 5), extending from the base of the record at 96 cal ka B.P., to 17.3 cal ka B.P. (section 6.2.1.1.). The HRW extends between 34.3 cal ka B.P. and 22.2 cal ka B.P. (Chapter 5), includes the climax of the last glacial cycle (LGC) and represents the focus of this study (section 6.2.2.). During the HRW the oceanographic environment over core TPC286 (Figure 6.3), in the southern Scotia Sea, was characterised by:

- A northerly advance of the SSI edge by several degrees of latitude at least 13.3 kyrs before the EPILOG-LGM (~21 cal ka B.P.).
- The occurrence of an externally triggered productivity peak at ~31 cal ka B.P. synchronous with a near-identical event in core TPC063, from the northern Scotia Sea.
- Deterioration of SSTs and a second phase of extensive SSI advance into the southern Scotia Sea between ~29.8 cal ka B.P. and 22.9 cal ka B.P., which

represents the coldest period in the southern Scotia Sea during at least the past ~48 kyrs.

- The rapid retreat of the sea-ice edge across the entire Scotia Sea to a distal location in the Weddell Sea at 22.9 cal ka B.P.
- An expanded seasonal sea-ice zone, extending from the Weddell Sea to the northern Scotia Sea, beginning at 22.5 cal ka B.P. and extending to 17.7 cal ka B.P.

The termination of the glacial regime is characterised by a period of deglaciation between 17.3 cal ka B.P. and ~13 cal ka B.P. (section 6.2.1.2.), with conditions characteristic of the Holocene interglacial in the upper ~13 kyrs (section 6.2.1.3.).

6.2.1.1. The Glacial, 47.9 cal ka B.P. to 17.3 cal ka B.P.

Between 47.9 cal ka B.P. and 17.3 cal ka B.P. the core is characterised by glacial conditions, with the HRW between 34.3 cal ka B.P. and 22.2 cal ka B.P. representing the glacial maximum. Between 47.9 cal ka B.P. and 34.3 cal ka B.P., there are extremely low rates of diatom deposition, with total diatom concentrations of 2.16×10^5 v/gds (Chapter 4, Figure 4.7). Such low concentrations are indicative of perennial sea-ice cover over the core site, which is evident from 51.6 cal ka B.P. and was preceded by WSI cover from 59.1 cal ka B.P. Total diatom concentrations increase sharply to 1.11×10^7 v/gds at the base of the HRW (34.3 cal ka B.P.), interpreted as representing the retreat of perennial sea-ice cover.

The retreat of the perennial sea-ice edge over the core site is supported by the diatom assemblage, which shows relative abundances of *F. obliquecostata* of 6.2% at 34.3 cal ka B.P., immediately after perennial sea-ice retreat (Figure 6.4). Elevated relative abundances of cold water and sea-ice-related diatom species between 36.9 cal ka B.P. and 33.2 cal ka B.P. indicates continuing influence of WSI over the core site into the HRW. The HRW is characterised by cooling surface waters, a second advance of the SSI edge and a shift in seasonal dynamics. Environmental change associated with the HRW is discussed in detail below (section 6.2.2.). Following the HRW, between 22.2 cal ka B.P. and 17.8 cal ka B.P., the end of the glacial is characterised by a broad and rapidly fluctuating, seasonal sea-ice zone, extending from the Weddell Sea to the northern Scotia Sea. This interpretation is supported by the elevated relative abundance of *T. lentiginosa* and no evidence of a summer sea-ice edge signal over core site TPC286 (Chapter 4, Figure 4.7), while the WSI edge is observed on several occasions over core site TPC063 (section 6.1.). This period of enhanced seasonality ends at 17.8 cal ka B.P., when relative abundance of *T. lentiginosa* decreases and

high abundance of *F. obliquecostata* (5.5%) indicates the presence of the summer sea-ice edge over core site TPC286 (Figure 6.3).

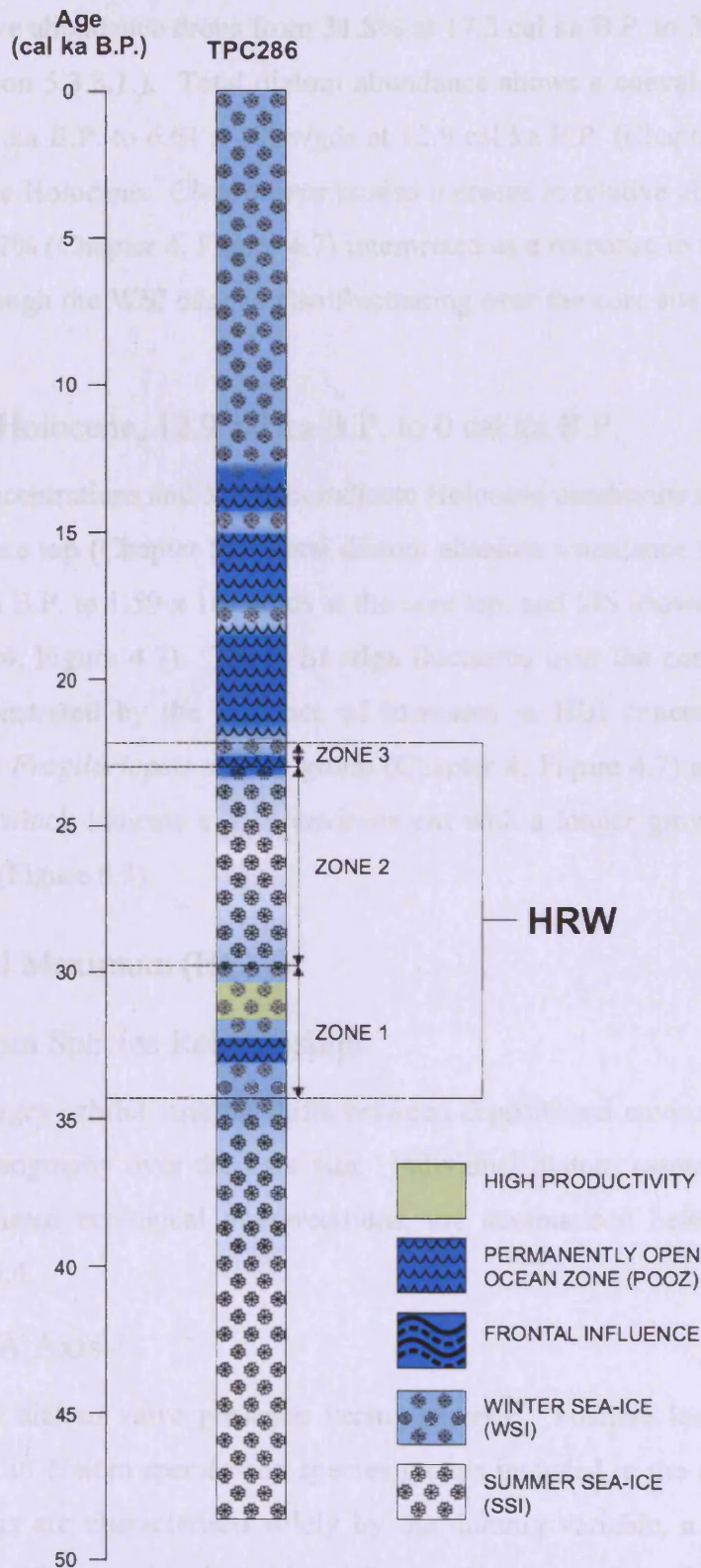


Figure 6.3. Core TPC286: Environmental log illustrating reconstructed oceanographic variability between 47.9 cal ka B.P. and the present day in the south Scotia Sea. Zonation is derived from PCA (Chapter 4). HRW = high resolution window.

6.2.1.2. Deglaciation, 17.3 cal ka B.P. to 12.9 cal ka B.P.

Based on the *E. antarctica* record, deglaciation at the core site begins at around 17.3 cal ka B.P. when relative abundance drops from 31.8% at 17.3 cal ka B.P. to 3% at 12.9 cal ka B.P. (Chapter 5, section 5.3.3.1.). Total diatom abundance shows a coeval rise from 3.24×10^6 v/gds at 17.3 cal ka B.P. to 6.61×10^6 v/gds at 12.9 cal ka B.P. (Chapter 4, Figure 4.7), and continues into the Holocene. *Chaetoceros* rs also increase in relative abundance at this time, from 16.8% to 77% (Chapter 4, Figure 4.7) interpreted as a response to the outflow of glacial meltwaters, although the WSI edge is also fluctuating over the core site at this time (Chapter 4, Figure 4.7).

6.2.1.3. The Holocene, 12.9 cal ka B.P. to 0 cal ka B.P.

Total diatom concentrations and MS data indicate Holocene conditions extend from 312.9 cal ka B.P. to the core top (Chapter 5). Total diatom absolute abundance rises from 6.61×10^6 v/gds 12.9 cal ka B.P. to 1.59×10^7 v/gds at the core top, and MS shows a coeval decrease in values (Chapter 4, Figure 4.7). The WSI edge fluctuates over the core site throughout the Holocene, demonstrated by the presence of increases in HBI concentrations (Chapter 4, Figure 4.13), the *Fragilariopsis* sea-ice group (Chapter 4, Figure 4.7) and elevated levels of *Chaetoceros* rs, which indicate a MIZ environment with a longer growth period during the summer months (Figure 6.3).

6.2.2. Glacial Maximum (HRW)

6.2.2.1. Diatom Species Relationships

Diatom assemblages exhibit striking shifts between depositional environments that relate to changes in oceanography over the core site. Individual diatom assemblages derived from PCA, and associated ecological interpretations, are summarised below and illustrated in Figures 6.3 and 6.4.

6.2.2.1.1. PCA Axis 1

Axis 1 indicates diatom valve presence versus absence. Positive loadings on axis 1 are characterised by all diatom species and species groups included in the analysis (Figure 6.4). Negative loadings are characterised solely by the dummy variable, a factor introduced to represent periods of low valve deposition (Chapter 3). Low rates of valve deposition can occur due to dissolution, advection, winnowing and the decline of export flux of terrestrial or

biologically derived materials (Chapter 2). Statistically, the significance of the *Chaetoceros* peak, identified in the diatom species assemblage around ~31 cal ka B.P., is diminished due to the overriding dominance of the downcore pattern of abundance.

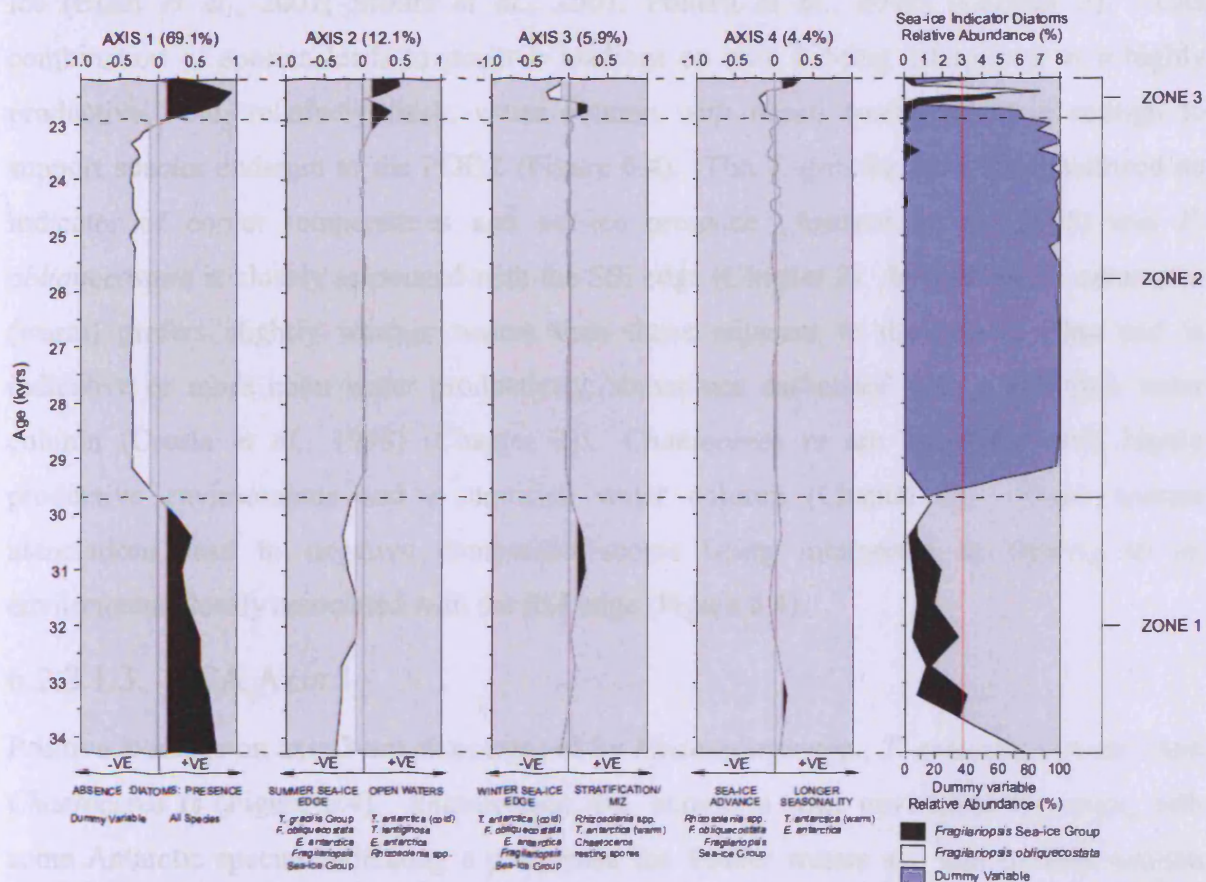


Figure 6.4. Core TPC286 (HRW): PCA component scores and environmental gradients associated with axes 1 to 4, compared with the relative abundance curves of the *Fragilariopsis* sea-ice group (black) and *Fragilariopsis obliquecostata* (white), plotted against age (kyrs). The relative abundance curve of the dummy variable (purple), is also included. Shaded black and white polygons on axes 1 to 4 indicate significant positive and negative variability respectively (un-shaded areas indicate insignificant variability). Diatom indicator species associated with each axis are listed at the base of the figure. The red line on the sea-ice diatom plot indicates the 3% sea-ice threshold.

6.2.2.1.2. PCA Axis 2

Positive loadings on axis 2 are characterised by *T. antarctica* (cold), *T. lentiginosa*, *E. antarctica* and, to a lesser extent, *Rhizosolenia* spp. Negative loadings are characterised by the *T. gracilis* group, *F. obliquecostata* and, to a lesser extent, *T. antarctica* (warm) and *Chaetoceros* (Figure 6.4). *T. antarctica* (cold) is related to cold water environments with a high influence of sea-ice and *T. lentiginosa* is associated with the POOZ (Chapter 2) although can occur as far south as the Weddell Sea (Gersonde and Zielinski, 2000). *Rhizosolenia* spp. occupy a wide environmental range, with some evidence indicating a preference for fresher waters and late summer/autumn conditions (Allen *et al.*, 2005) (Chapter 2). *E. antarctica* has

been linked to sea-ice (Burckle and Cooke, 1983), although there is no modern analogue at glacial abundance levels to support this hypothesis. More recently *E. antarctica* has been shown to respond to iron enrichment and has been associated with melting icebergs and sea-ice (Blain *et al.*, 2007; Moore *et al.*, 2007; Pollard *et al.*, 2009) (Chapter 2). This combination of species leads to positive loadings on axis 2 being interpreted as a highly productive, cold, relatively fresh, water column with ocean conditions open enough to support species endemic to the POOZ (Figure 6.4). The *T. gracilis* group is considered an indicator of cooler temperatures and sea-ice presence (Armand *et al.*, 2005) and *F. obliquecostata* is closely associated with the SSI edge (Chapter 2). In contrast, *T. antarctica* (warm) prefers slightly warmer waters than those adjacent to the sea-ice edge and is indicative of more open water productivity, sometimes associated with a stratified water column (Crosta *et al.*, 1998) (Chapter 2). *Chaetoceros* rs are associated with highly productive environments and a stratified water column (Chapter 2). These species associations lead to negative component scores being interpreted as relating to an environment closely associated with the SSI edge (Figure 6.4).

6.2.2.1.3. PCA Axis 3

Positive loadings on axis 3 are characterised by *Rhizosolenia* spp., *T. antarctica* (warm) and *Chaetoceros* rs (Figure 6.4). *Rhizosolenia* spp. occupy a wide environmental range, with some Antarctic species indicating a preference for fresher waters and late summer/autumn conditions (Allen *et al.*, 2005) (Chapter 2). *T. antarctica* (warm) has been observed in warm waters, north of the WSI edge (Chapter 2) and *Chaetoceros* rs are associated with highly productive environments and the MIZ, the combination of high abundances of these two diatoms is interpreted as reflecting a stratified water column (Crosta *et al.*, 1998). Hence, positive loadings are interpreted as an environment of cold, fresh, productive waters related to water column stratification and the MIZ (Figure 6.4). Negative loadings are characterised by the diatoms *T. antarctica* (cold), *F. obliquecostata* and *E. antarctica*. *T. antarctica* (cold) and *F. obliquecostata* are commonly observed within and adjacent to sea-ice, (association of *E. antarctica* with sea-ice is more tentative) (Chapter 2). Hence, negative loadings are interpreted as indicating colder waters, closely associated with sea-ice (Figure 6.4).

6.2.2.1.4. PCA Axis 4

The positive loadings on axis 4 are characterised by *T. antarctica* (warm) and *E. antarctica*. *T. antarctica* (warm) is generally observed in relatively warmer surface waters north of the

WSI edge and while *E. antarctica* has been associated with iceberg and sea-ice melt, it has also been shown to respond favourably to iron enrichment (Chapter 2). Both of these diatoms are also associated with late summer, autumn productivity and their presence here is interpreted as indicating increased growth seasons associated with winter sea-ice retreat. Negative loadings on axis 4 are characterised by *Rhizosolenia* spp., *F. obliquecostata* and the *Fragilariopsis* sea-ice group. Species within the *Rhizosolenia* spp. group have been closely associated with the WSI edge as well as open waters (Chapter 2) and *F. obliquecostata* and the *Fragilariopsis* sea-ice group are observed within and adjacent to the sea-ice environment (Chapter 2). Thus, the negative loadings are interpreted as indicating the close proximity of permanent sea-ice, or possibly summer/autumn productivity associated with new sea-ice growth (Figure 6.4).

6.2.2.2. Palaeoenvironment Reconstruction Across the Glacial Maximum

Downcore variability is divided into three zones based on the transitions between the positive and negative modes of variability on PCA axis 1 (Figure 6.4).

6.2.2.2.1. HRW Zone 1: Summer Sea-ice Retreat, 34.3 cal ka B.P. to 29.7 cal ka B.P.

Zone 1 is characterised by decreasing diatom abundance from its base at 34.3 cal ka B.P. to the top (29.7 cal ka B.P.). Negative component scores in axis 2 are interpreted as dominance of cold surface waters associated with close proximity to the SSI edge. Positive component scores on axis 3 occur between 31.4 cal ka B.P. and 30.2 cal ka B.P. and increase in significance as negative component scores on axis 2 decrease, at this point in time the *Rhizosolenia* spp. are characterised by a mixed assemblage of both pointed and rounded groups (Chapter 2), indicating water column stratification associated with the WSI edge as SSI retreats further south and the summer months are characterised by the MIZ. Positive component scores on axis 4 indicate retreat of the WSI edge, and a longer growing season at 33.2 cal ka B.P..

HRW zone 1 is characterised by diatom presence, and is further interpreted as a progression from permanent SSI cover to seasonal sea-ice with productivity associated with a stratified water column, followed by a re-advance of permanent sea-ice cover. At 34.3 cal ka B.P., the prevalence of cold surface waters and relative abundance of *F. obliquecostata* in excess of 3% (Figure 6.4), indicate the retreat of SSI and the near-by presence of the SSI edge. Retreat

of the WSI edge to the south of the core site at 33.2 cal ka B.P. is indicated by relative abundance of the *Fragilariopsis* sea-ice group being in excess of 3% and the prominence of diatoms associated with open ocean conditions and a longer growing season (Figure 6.4). Between 32.2 cal ka B.P. to 30.4 cal ka B.P. a re-advance of the WSI edge and its stabilization over/near the core site is indicated by a second peak in *Fragilariopsis* sea-ice group relative abundance in excess of 3% and the presence of diatoms associated with the MIZ (Figure 6.4) and independently supported by high concentrations of the HBI sea-ice biomarker (Chapter 4, Figure 4.13). Finally, between 30.4 cal ka B.P. and the top of the zone (29.7 cal ka B.P.), the re-advance of the SSI edge is indicated by the slightly elevated relative abundance of *F. obliquecostata* and the decline in MIZ species (Figure 6.4) and total diatom concentrations (Chapter 6, Figure 6.10). At 30.9 cal ka B.P., superimposed onto this regime of sea-ice variability, is a large peak in diatom concentration (102×10^6 v/gds), dominated by *Chaetoceros* sp. (~95%). This peak is unique in the record and is possibly related to a trigger external to the local oceanographic system (discussed further in section 6.3.2.3.) (Figure 6.3).

6.2.2.2.2. HRW Zone 2: Temperature Minima, 29.7 cal ka B.P. to 22.9 cal ka B.P.

HRW zone 2 is characterised by negative component scores on axis 1 related to low abundances of diatom valves and the presence of consolidated sea-ice cover over the core site and represents the coldest conditions in the Scotia Sea since at least ~48 cal ka B.P.

This zone is characterised by diatom valve absence and is interpreted as the result of permanent, SSI cover over the core site from 29.2 cal ka B.P. The sparse diatom assemblage supports this interpretation as prior to zone 2 the diatom assemblage shows relative abundances of *F. obliquecostata* (6.2%) and the *Fragilariopsis* sea-ice group (3.2%) levels indicative of the presence of SSI and WSI edges (Figure 6.4). This interpretation is independently supported by the absence of HBI biomarkers (Chapter 4, Figure 4.13).

Advection and winnowing are discounted as mechanisms producing valve absence because these processes would preferentially preserve heavily silicified valves, of which there are very few, and trace occurrences of those species that are susceptible to advection remain in the record. The influence of dissolution is likely because the presence of extensive, persistent consolidated sea-ice cover that acts to curtail primary production in the surface waters would result in low export rates of opal from the euphotic zone, reducing the silicate reservoir at depth (De La Rocha, 2005). Sediments almost barren of biogenic silica have also been reported from the Weddell Basin where the sediment/water interface is characterised by

strong dissolution (Abelmann and Gersonde, 1991) and the region is exposed to extensive multi-year ice (Zielinski and Gersonde, 1997) (Figure 6.3).

6.2.2.2.3. HRW Zone 3: Seasonal Shift in Sea-ice Dynamics, 22.9 cal ka B.P. to 22.2 cal ka B.P.

Axis 1 is characterised by positive component scores in zone 3 indicating diatom preservation related to the rapid retreat of consolidated sea-ice cover from over the site. Positive component scores on axis 2 are interpreted as an environment characterised by relatively cold and fresh open waters. Component scores on axis 3 are positive between 22.8 cal ka B.P. and 22.6 cal ka B.P. - characterised by a large pulse in the *Rhizosolenia* rounded group (Chapter 2) - before switching to being negative between 22.5 cal ka B.P. and 22.3 cal ka B.P. This pattern is interpreted as an initial period of highly productive, fresher, open surface waters, associated with close proximity of the sea-ice edge, which evolves into the presence of the WSI edge over the core site as sea-ice related diatoms increase in abundance. On axis 4, a small peak in negative component scores occurs at 22.5 cal ka B.P. and a peak in positive component scores between 22.4 cal ka B.P. and 22.2 cal ka B.P. The small negative peak relates to the lasting effects of the productivity pulse between 22.8 cal ka B.P. and 22.6 cal ka B.P. and indicates the presence of the WSI edge over the core site. Dominance of positive component scores at the top of the zone indicates a further retreat of WSI and the transition to a less cold, open water environment (Figure 6.3).

HRW zone 3 is characterised by an abrupt influx of diatoms to the sediment, signifying the rapid retreat of SSI and WSI between 23 cal ka B.P. and 22.9 cal ka B.P. to the south of the core site, into the Weddell Sea. This interpretation is supported by the lack of a sea-ice signal in the relative abundances of the *Fragilariopsis* sea-ice group and *F. obliquecostata* (Figure 6.4), which indicates that the respective sea-ice edges did not maintain stability over the core site during their rapid retreat. The onset of open water conditions, between 22.9 cal ka B.P. and 22.8 cal ka B.P., is supported by increases in *T. lentiginosa*, *F. kerguelensis*, *Rhizosolenia* spp. (rounded group) and species associated with summer/autumn growing seasons (*T. antarctica*, *E. antarctica*) (Figure 6.4). An increase in water column stratification, characterised by a MIZ assemblage and a decrease in the relative abundance of open water indicators *T. lentiginosa* and *F. kerguelensis* precedes the gradual re-advance of the WSI edge between 22.8 cal ka B.P. and 22.4 cal ka B.P. (Chapter 6, Figure 6.10). The re-advance of WSI into the Scotia Sea occurred between 22.5 cal ka B.P. and 22.4 cal ka B.P. and is characterised by relative abundance of *Fragilariopsis* sea-ice group and *F. obliquecostata* in

excess of 4% and 7%, respectively (Figure 6.4). The rapid retreat of the sea-ice edge to a distal location south of the core site and onset of open water conditions is repeated between 22.4 cal ka B.P. and 22.2 cal ka B.P., supported by the absence of a sea-ice edge signal in the relative abundance of the sea-ice diatoms and elevated concentrations of open ocean and summer/autumn growth season indicator species (Chapter 4, Figure 4.7).

6.3. Regional Reconstruction: The Scotia Sea

This section presents a reconstruction of the palaeoceanography and sea-ice regime of the Scotia Sea over the past ~60 kyrs, with a particular focus on the HRW period ~34 cal ka B.P. to 22 cal ka B.P., the culmination of the LGC. Portions of this reconstruction are limited by sampling resolution (Chapter 3) and potential errors associated with portions of the core chronology (Chapter 5). This is one of the very few reconstructions of palaeoceanographic and sea-ice variability in the glacial Southern Ocean (Shemesh *et al.*, 2002; Crosta *et al.*, 2004), and the first of its kind from the glacial Scotia Sea.

TPC286 and TPC063 are situated far to the north of the modern average SSI limit, which is presently confined to the Weddell Sea. In addition, core TPC063 is presently located marginally south of the APF. Hence, cores TPC286 and TPC063 can be employed to track oceanographic and sea-ice change across the Scotia Sea during the LGC. The environmental variability, determined from PCA and diatom abundance in sections 6.1. and 6.2., is summarized in a series of time-slice maps below (Figures 6.5 to 6.13) that relate to the primary changes in oceanography and sea-ice during the past ~50 kyrs. In addition to reconstructing the likely locations of the winter and summer sea-ice edges and the APF within the Scotia Sea, and the associated shift in oceanographic zones, during these time intervals I also discuss, in accordance with the literature, the wider implications that these shifts in palaeoceanography could have on regional components of the climate system, particularly sea surface temperatures (SSTs), deepwater formation, a strengthening/weakening of the polar vortex and the migration of the southern Westerly wind belt.

6.3.1. 48.6 cal ka B.P. to 34.4 cal ka B.P.

During this interval the WSI edge only approached core site TPC063 at 35.8 cal ka B.P., during which time the APF shifted closer to the North Scotia Ridge. The SSI edge was displaced significantly north of its modern-day location in the Weddell Sea, advancing into the southern confines of the Scotia Sea. In comparison to the modern-day a larger SIZ

prevailed across the Scotia Sea, which resulted in the northward migration of the POOZ and APFZ. This regime shift, albeit brief, indicates a drop in SSTs during this interval and enhanced surface water stratification due to an expanded area of sea-ice melt, which would restrict the ventilation of deepwaters. Expansion of the SIZ would have also intensified the polar vortex and could have possibly resulted in a brief northward migration of the southern Westerlies.

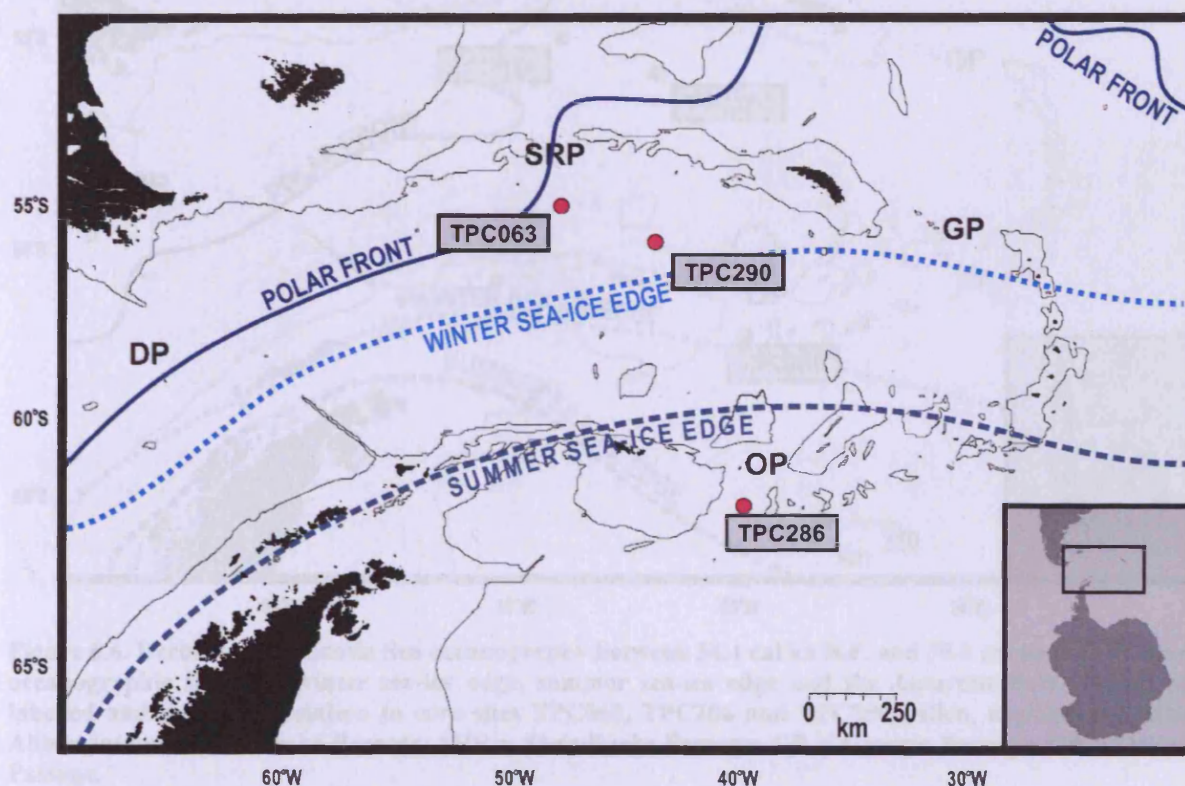


Figure 6.5. Reconstructed Scotia Sea oceanography between 48.6 cal ka B.P. and 34.4 cal ka B.P. Primary oceanographic features (winter sea-ice edge, summer sea-ice edge and the Antarctic Polar Front) are labelled and plotted in relation to core sites TPC063, TPC286 and TPC290 (Allen, unpublished data). Abbreviations: DP = Drake Passage; SRP = Shag Rocks Passage; GP = Georgia Passage; OP = Orkney Passage.

6.3.2. 34.4 cal ka B.P. to 30.4 cal ka B.P.

During this interval the WSI edge had retreated south of core site TPC286 by 33.2 cal ka B.P. and was frequently over the core site between 32.2 cal ka B.P. and 30.4 cal ka B.P. The SSI edge had retreated south of core site TPC286 at this time and was likely located in the Weddell Sea. These changes resulted in poleward shift, and shrinking of, the SIZ and the return of the APFZ and expansive POOZ to the Scotia Sea. The initial meltback would result in a large area of surface water stratification, the smaller SIZ and MIZ would reduce the area of future deepwater formation, the polar vortex would weaken and the southern Westerlies would return to a more southerly location, similar to the present. Such a scenario could

indicate SSTs warmer than today, or potentially reflect a weaker, less active Weddell Gyre and reduced northward export of sea-ice from the Weddell Sea. Additional core sites in the south Scotia Sea are needed to refine our understanding of this interval.

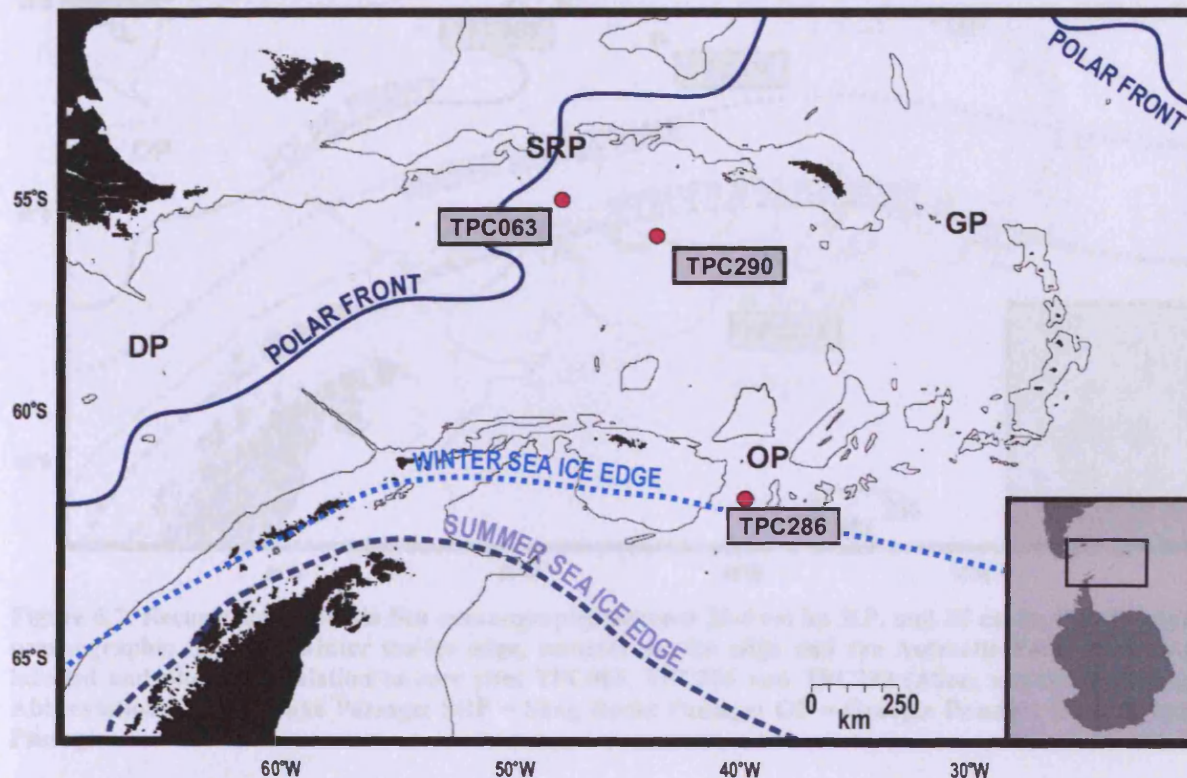


Figure 6.6. Reconstructed Scotia Sea oceanography between 34.4 cal ka B.P. and 30.4 cal ka B.P. Primary oceanographic features (winter sea-ice edge, summer sea-ice edge and the Antarctic Polar Front) are labelled and plotted in relation to core sites TPC063, TPC286 and TPC290 (Allen, unpublished data). Abbreviations: DP = Drake Passage; SRP = Shag Rocks Passage; GP = Georgia Passage; OP = Orkney Passage.

6.3.3. 30.4 cal ka B.P. to 25 cal ka B.P.

During this interval the WSI and SSI edges advanced into the Scotia Sea once more while the APF was still positioned over core site TPC063. The SIZ expanded, although the extent of the MIZ was probably similar to the previous interval. The continued presence of the APFZ suggests a much smaller POOZ. This regime shift indicates a reduction in SSTs, a more vigorous Weddell Gyre and a northward migration of the zone of deepwater formation. The continued presence of the APF over core site TPC063 suggest no significant strengthening of the polar vortex beyond that of the modern-day and no northward migration of the southern Westerlies.

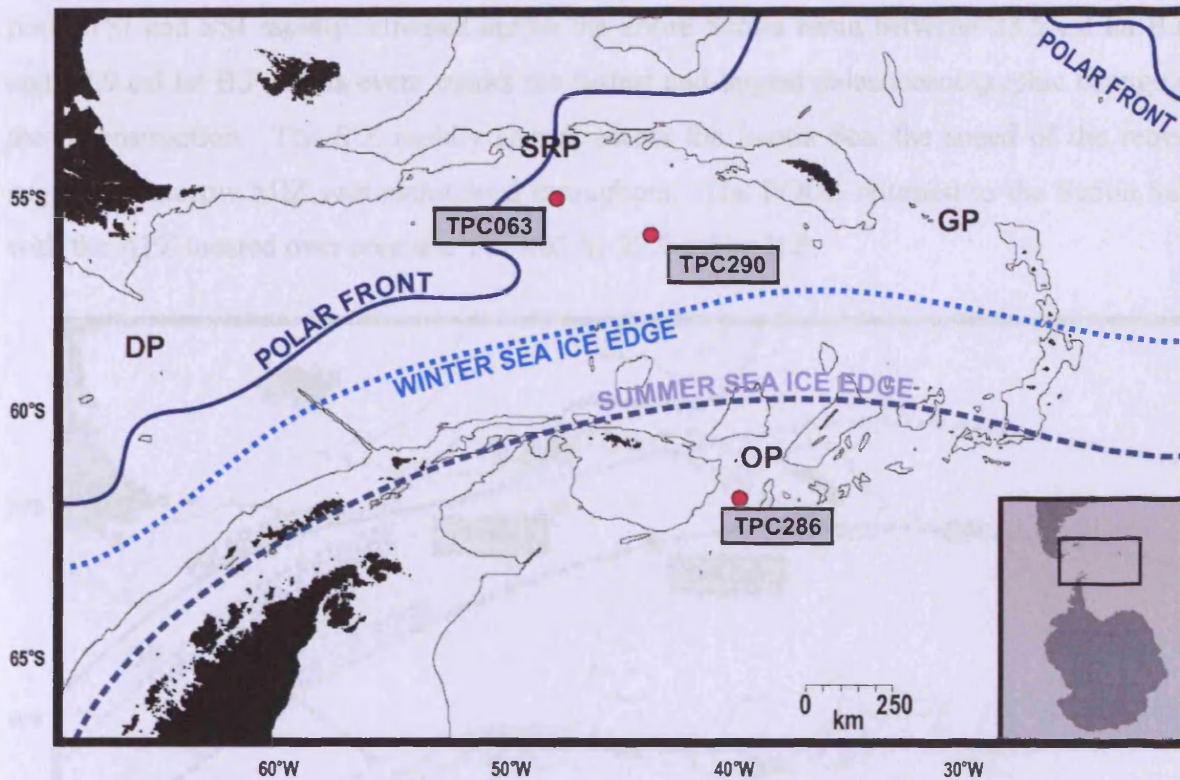


Figure 6.7. Reconstructed Scotia Sea oceanography between 30.4 cal ka B.P. and 25 cal ka B.P. Primary oceanographic features (winter sea-ice edge, summer sea-ice edge and the Antarctic Polar Front) are labelled and plotted in relation to core sites TPC063, TPC286 and TPC290 (Allen, unpublished data). Abbreviations: DP = Drake Passage; SRP = Shag Rocks Passage; GP = Georgia Passage; OP = Orkney Passage.

6.3.4. 25 cal ka B.P. to 23.5 cal ka B.P.

During this interval the glacial sea-ice maximum was reached in the Scotia Sea between 24.1 cal ka B.P. and 23.5 cal ka B.P. The WSI edge expanded north of core site TPC063 and the SSI edge was located within the northern Scotia Sea. The SIZ had expanded considerably, covering the majority of the Scotia basin. However, the MIZ was probably similar to the previous two intervals, indicating little change in seasonality. With no evidence of the APFZ or POOZ is assumed that these surface water regimes had migrated far to the north. However, confining sea-floor topography would have made it difficult for the APF to migrate north of the North Scotia Ridge. These oceanographic conditions indicate that SSTs had dropped to their lowest in ~60 kys and that deepwater formation associated with the MIZ was located within the northern Scotia Sea, with a much more expansive zone of deepwater formation associated with supercooling below permanent sea-ice. The maximum sea-ice extent indicates that the polar vortex was probably at its strongest intensification and that the southern Westerlies had migrated northward by several degrees of latitude (in comparison to the modern-day). The WSI edge fluctuated rapidly during these maximum conditions before

both WSI and SSI rapidly retreated across the entire Scotia basin between 23.5 cal ka B.P. and 22.9 cal ka B.P. This event marks the fastest and largest palaeoceanographic change in the reconstruction. The SIZ rapidly shrank across the Scotia Sea, the speed of the retreat suggests a narrow MIZ was maintained throughout. The POOZ returned to the Scotia Sea, with the APZ located over core site TPC063 by 22.9 cal ka B.P.

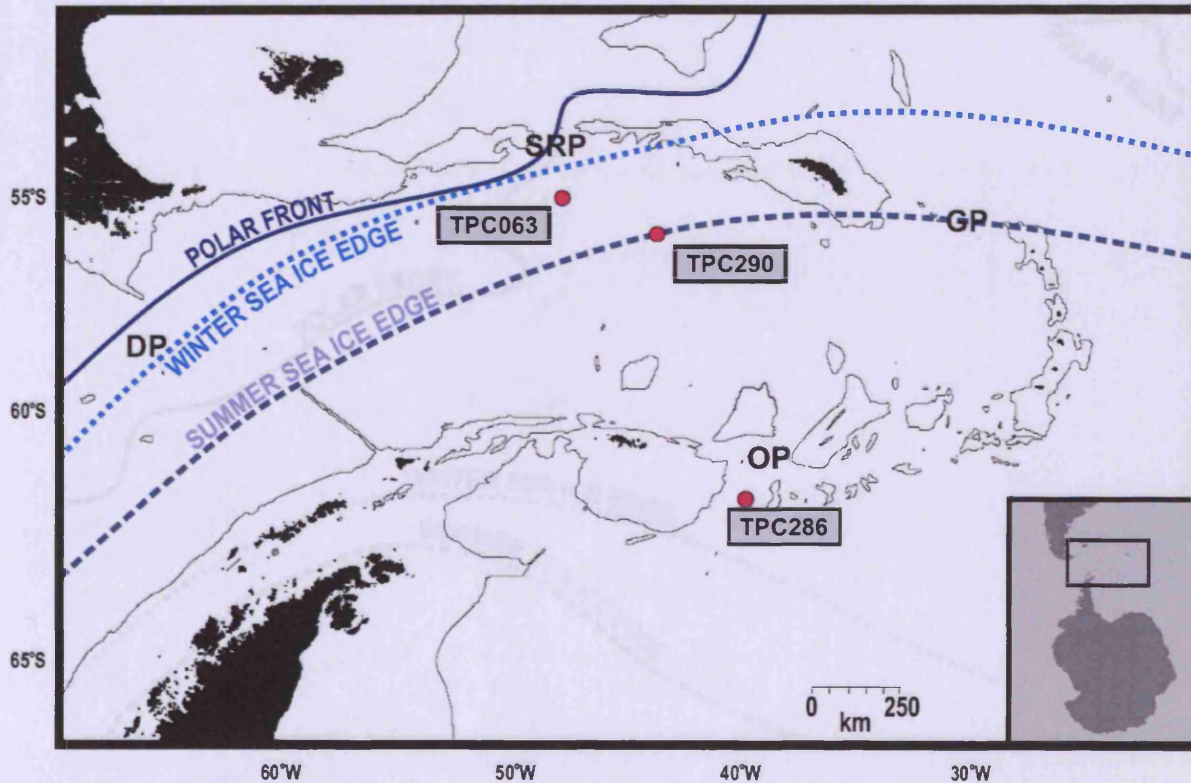


Figure 6.8. Reconstructed Scotia Sea oceanography between 25 cal ka B.P. and 23.5 cal ka B.P. Primary oceanographic features (winter sea-ice edge, summer sea-ice edge and the Antarctic Polar Front) are labelled and plotted in relation to core sites TPC063, TPC286 and TPC290 (Allen, unpublished data). Abbreviations: DP = Drake Passage; SRP = Shag Rocks Passage; GP = Georgia Passage; OP = Orkney Passage.

6.3.5. 22.9 cal ka B.P. to 22.8 cal ka B.P.

Following the rapid retreat between 23.5 cal ka B.P. and 22.9 cal ka B.P. the WSI and SSI edge had were briefly located in the northern Weddell Sea with open ocean conditions evident over core site TPC286. These conditions indicate a considerably smaller SIZ within the Weddell Sea and a return of the APFZ and POOZ to the entire Scotia Sea. Due to the location of both sea-ice edges to the south of core site TPC286 is it difficult to interpret the likely expanse of the MIZ. This shift indicates a rapid, yet brief, increase in SSTs. The rapid retreat of such an extensive area of sea-ice cover would lead to a substantial freshwater injection into the surface waters of the Scotia Sea and result in a wide area of stratification. The production of deep waters would be abruptly curtailed and confined to the Weddell

Basin, if only for a short period of time. If closely coupled to the sea-ice field, and capable of rapid variability, the polar vortex could have rapidly weakened and the southern Westerlies quickly migrated poleward by several degrees of latitude. As it is unlikely that the APF ever migrated further north than the North Scotia Ridge, its return to the northern Scotia Sea isn't necessarily indicative of a poleward Westerly migration.

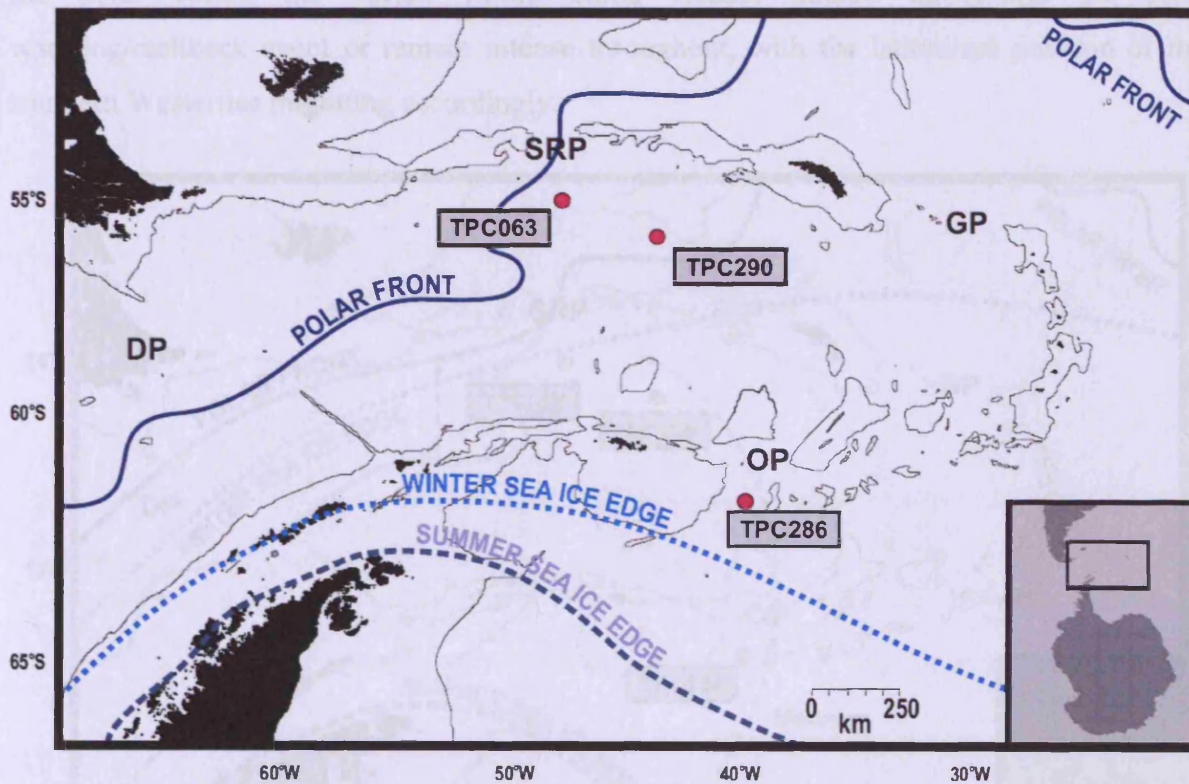


Figure 6.9. Reconstructed Scotia Sea oceanography between 22.9 cal ka B.P. and 22.8 cal ka B.P. Primary oceanographic features (winter sea-ice edge, summer sea-ice edge and the Antarctic Polar Front) are labelled and plotted in relation to core sites TPC063, TPC286 and TPC290 (Allen, unpublished data). Abbreviations: DP = Drake Passage; SRP = Shag Rocks Passage; GP = Georgia Passage; OP = Orkney Passage.

6.3.6. 22.8 cal ka B.P. to 19.7 cal ka B.P.

During this interval the WSI edge gradually returned to the north Scotia Sea, close to its previous maximum extent and became a seasonal feature by 22.4 cal ka B.P. The SSI remained located within the deep Weddell Basin, with no evidence of its proximity to core site TPC286. During this ~3kyr interval the seasonal locations of the winter and summer sea-ice edges were located at their maximum distance away from one another, resulting in the most extensive MIZ of the last ~60 kyrs, covering the entire Scotia Basin and extending into the Weddell Sea. The readvance of the WSI, following its rapid retreat, implies a drop in SSTs, although not to a level capable of supporting extensive sea-ice during the summer months. The expansive area of seasonal sea-ice formation and meltback has important

ramifications for the production and ventilation of deepwaters. During the formation of WSI brine injection into the surface waters would result in an expansive area of deepwater formation. The reverse is true during WSI meltback, when freshwater injections would produce a stratification cap across the entire Scotia Sea, restricting the ventilation of deepwaters. Depending on the complexities of the relationship between the sea-ice field and the polar vortex the vortex would either remain intense throughout the brief warming/meltback event or remain intense throughout, with the latitudinal position of the southern Westerlies migrating accordingly.

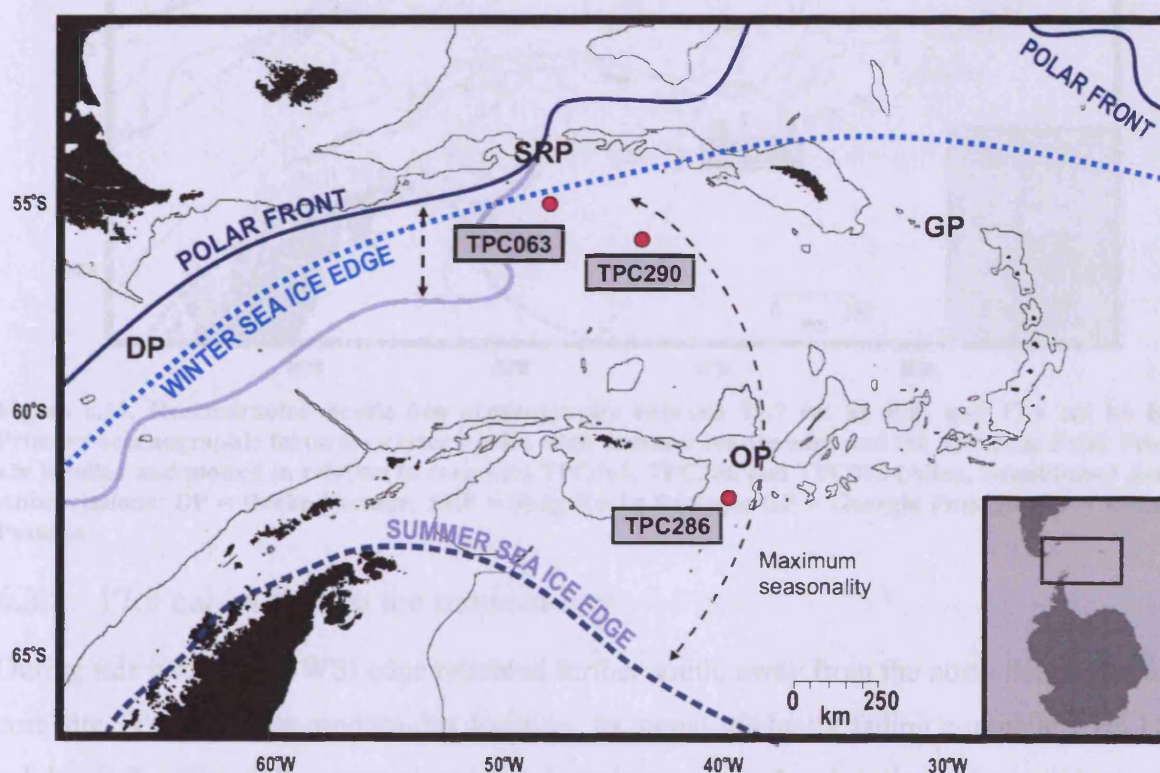


Figure 6.10. Reconstructed Scotia Sea oceanography between 22.4 cal ka B.P. and 19.7 cal ka B.P. Primary oceanographic features (winter sea-ice edge, summer sea-ice edge and the Antarctic Polar Front) are labelled and plotted in relation to core sites TPC063, TPC286 and TPC290 (Allen, unpublished data). Abbreviations: DP = Drake Passage; SRP = Shag Rocks Passage; GP = Georgia Passage; OP = Orkney Passage.

6.3.7. 19.7 cal ka B.P. to 17.8 cal ka B.P.

During this interval the WSI edge no longer extended as far north as core site TPC063 but was still relatively close. The SSI edge remained south of core site TPC286, located within the Weddell Sea, possibly shifting closer to a location similar to the present day. This oceanographic regime resulted in a gradual shrinking of the SIZ and MIZ and a southward migration of the POOZ and APFZ back into the northern Scotia Sea. This indicates a gradual increase in SSTs, and a reduction in the severity of the impact of sea-ice on the formation and

ventilation of deepwaters. The intense polar vortex would gradually weaken and the southern Westerlies would begin their poleward migration.

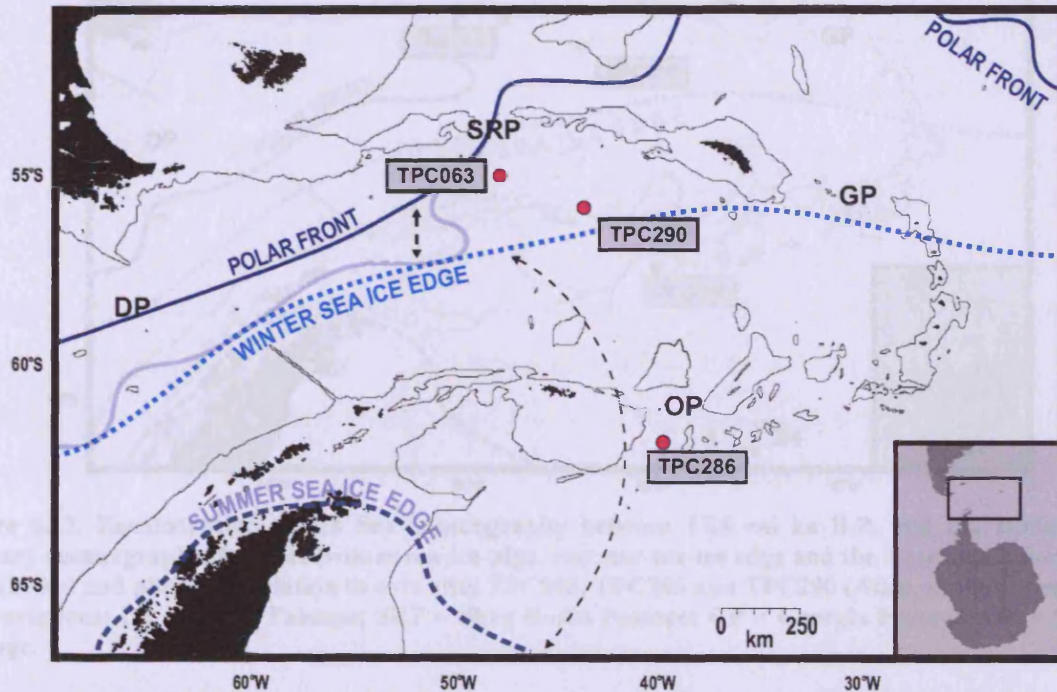


Figure 6.11. Reconstructed Scotia Sea oceanography between 19.7 cal ka B.P. and 17.8 cal ka B.P. Primary oceanographic features (winter sea-ice edge, summer sea-ice edge and the Antarctic Polar Front) are labelled and plotted in relation to core sites TPC063, TPC286 and TPC290 (Allen, unpublished data). Abbreviations: DP = Drake Passage; SRP = Shag Rocks Passage; GP = Georgia Passage; OP = Orkney Passage.

6.3.8. 17.8 cal ka B.P. to the modern-day

During this interval the WSI edge retreated further south, away from the north Scotia Sea and core site TPC063 to its modern-day location, its signal gradually fading completely by 11.5 cal ka B.P. The SSI retreated poleward to its modern-day location where it hugs the Antarctic Peninsula and extends into the deep confines of the Weddell Sea. The APF returned to its modern-day location, snaking across the northwest Scotia Sea from DP to SRP. This regime resulted in a slightly reduced SIJZ and MIZ and an expansive POOZ, with the APFZ dominant in the northern Scotia Sea. The return of the APFZ, indicates the continuing rise of SSTs and a poleward shift of the zone of deepwater formation toward its present location in the Weddell Sea. The polar vortex would continue its gradual weakening and the southern Westerlies would return south to their modern-day circumpolar location over the Southern Ocean.

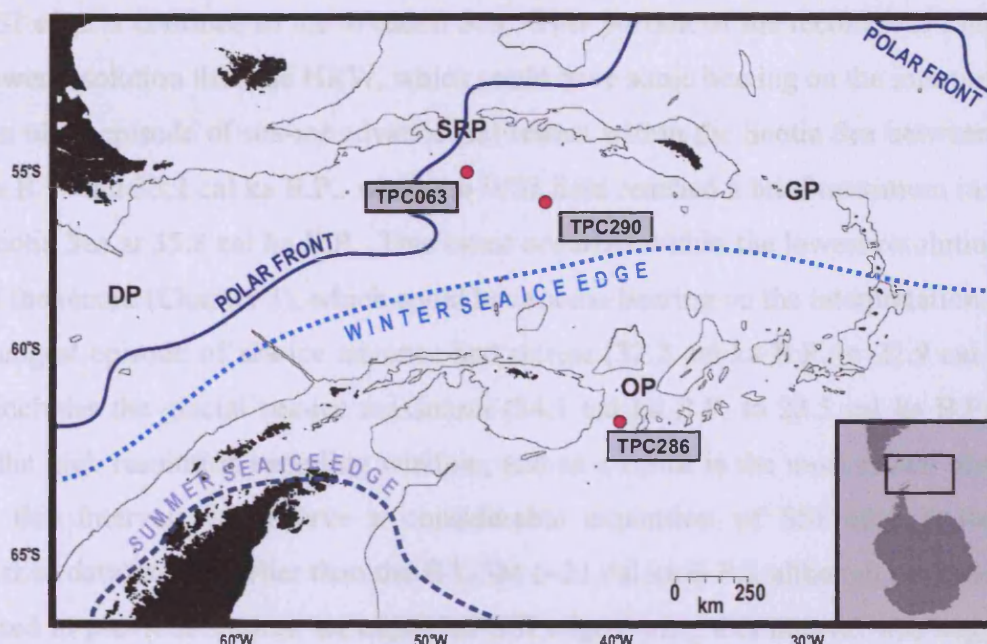


Figure 6.12. Reconstructed Scotia Sea oceanography between 17.8 cal ka B.P. and the modern-day. Primary oceanographic features (winter sea-ice edge, summer sea-ice edge and the Antarctic Polar Front) are labelled and plotted in relation to core sites TPC063, TPC286 and TPC290 (Allen, unpublished data). Abbreviations: DP = Drake Passage; SRP = Shag Rocks Passage; GP = Georgia Passage; OP = Orkney Passage.

6.3.9. Scotia Sea Reconstruction: Discussion

6.3.9.1. Sea-ice

A dynamic sea-ice regime existed across the Scotia Sea during the last ~60 kyrs, confirming its sensitivity during this period as suggested by models (Gildor and Tziperman, 2001; Knorr and Lohmann, 2003). Based on diatom assemblages and supported by HBI concentrations three primary observations have been made during this interval (see below). These events are compared with several regional records in an attempt to test their validity (Figure 6.13). However, due to differences between age models and sampling resolution only broad comparisons can be made at this time.

1. An extensive episode of sea-ice advance and retreat within the Scotia Sea between 32.2 cal ka B.P. and 22.9 cal ka B.P., which includes a glacial sea-ice maximum between 24.1 cal ka B.P. and 23.5 cal ka B.P. The sea-ice maximum is followed by a rapid retreat across the Scotia Sea between 23.5 cal ka B.P. and 22.9 cal ka B.P. These events occur within the high-resolution sampling window (HRW).
2. After 22.9 cal ka B.P. there is a marked shift to enhanced sea-ice seasonality within the Scotia Sea. Between 22.4 cal ka B.P. and 17.8 cal ka B.P., subsequent to the rapid sea-ice meltback, the WSI edge recovers and returns to the northern Scotia Sea, whereas the

SSI edge is confined to the Weddell Sea. This portion of the record was sampled at a lower resolution than the HRW, which could have some bearing on the interpretation

3. An older episode of sea-ice advance and retreat within the Scotia Sea between 59.1 cal ka B.P. and 33.2 cal ka B.P., when the WSI field reached a brief maximum in the north Scotia Sea at 35.8 cal ka B.P. This event occurred within the lowest resolution portion of the record (Chapter 3), which could have some bearing on the interpretation.

The youngest episode of sea-ice advance and retreat (32.2 cal ka B.P. to 22.9 cal ka B.P.), which includes the glacial sea-ice maximum (24.1 cal ka B.P. to 23.5 cal ka B.P.), occurs within the high resolution sampling window, and as a result is the most robust observation. During this interval we observe a considerable expansion of SSI edge (Allen, 2009, unpublished data) much earlier than the E-LGM (~21 cal ka B.P.), although not categorically recognised in previous studies, an expanded SSI edge during this interval was suggested by Gersonde *et al.* (2003), although they did not commit to a significantly expanded SSI field at glacial sea-ice maximum. The suggestion by Gersonde *et al.* (2003) is supported by the data presented in this thesis and indicates that the coldest period in the Scotia Sea, during the LGC, occurred between 32.2 cal ka B.P. and 24.1 cal ka B.P. This interval is also identified, in the high resolution $\delta^{18}\text{O}$ record from EDML, Antarctica (EPICA, 2006), as a decrease to the coldest period during the LGC (Figure 6.13). This pattern is replicated in SST records from the South Atlantic and SE Pacific Oceans (Charles *et al.*, 1996; Kaiser *et al.*, 2005), indicating a large regional shift to cooler temperatures at this time (Figure 6.13). These close comparisons between the data presented here and the regional temperature records indicates a good accuracy in our chronology, and certainly rules out the potential error of ~6 kyrs (Chapter 5). In comparison, the maximum extent achieved by the WSI field appears marginally north of 53° 56' S (core site TPC063) and is in close agreement with the Scotia Sea WSI limit of ~52° S estimated by the most recent EPILOG-LGM (E-LGM) sea-ice reconstruction (Gersonde *et al.*, 2005). However, the data presented in this thesis indicates that both the winter and summer sea-ice fields had achieved their maximum extents between 24.1 cal ka B.P. and 23.5 cal ka B.P., earlier than the ~21 cal ka B.P. LGM chronozone proposed by previous LGM time-slice reconstructions (Crosta *et al.*, 1998; Gersonde *et al.*, 2003; 2005). Having stated this, during their assignment of the optimum LGM window, the EPILOG authors (Mix *et al.*, 2001) did consider a 6 kyr E-LGM window spanning between 24 cal ka B.P. and 18 cal ka B.P. Such a window would almost envelop the glacial sea-ice maximum observed here. The maximum glacial sea-ice extent identified here coincides with

the culmination of the coldest interval in the EDML $\delta^{18}\text{O}$ record (when considering ocean-ice sheet signal transition errors) (Figure 6.13). A lower resolution sea-ice index from the South Atlantic (Stuut *et al.*, 2004) also agrees well with the timing of the onset and culmination of peak glacial sea-ice extent in the Scotia Sea, as do maximum glacier advances in the Strait of Magallen, Patagonia, dated at 24.6 ± 0.9 ka (Kaplan *et al.*, 2008) (Figure 6.13). Modeling and proxy studies indicate that an expansion of the Antarctic sea-ice field south of southern South America, i.e. in the Scotia Sea, could result in an intensification of the polar vortex and an equatorward shift of the circumpolar Westerly wind belt, cold, moisture-bearing air masses and the generation of a climatic regime, over Patagonia, capable of encouraging growth of the ice field (Simmonds, 1981; Stuut, 2001; Lamy 2001, 2002; Hulton *et al.*, 2002). The equatorward displacement of moisture-bearing air masses, as a result of an enhanced Antarctic sea-ice field, has also been linked with the strength of the mid-latitude trade winds off the Southeast African coast and the aridity budget of the Atacama desert, northern Chile (Stuut and Lamy, 2004). An increase in the strength of the trade winds off the Southeast African coast and a decrease in the aridity of northern Chile correlate well with the maximum sea-ice extent observed within the Scotia Sea (Figure 6.13). A record of ice rafted debris from the Southeast Atlantic (Kanfoush *et al.*, 2000) also shows an interesting correlation with the maximum sea-ice extent within the Scotia Sea, with Ice Rafted Debris concentrations peaking in time with maximum sea-ice extent (Figure 6.13). Keany *et al.* (1976) suggested that variations in the deposition of Ice Rafted Debris were related to the equatorward displacement of the APFZ and the zone of rapid melting of icebergs and that such a displacement would coincide with increasing sea-ice extent. Once again the close correlation between the sea-ice reconstructions presented here and several independently dated time-series validates our choice of chronology. The data presented here indicate that during the progression toward glacial sea-ice maximum (32.2 cal ka B.P. to ~23.5 cal ka B.P.) the SSI field expanded significantly compared the modern-day, whereas, in comparison, the WSI field expanded by a smaller amount. The data suggest that the two sea-ice fronts tracked each other closely throughout this interval, resulting in a narrower seasonal ice zone than that witnessed today. Due to the fact that a considerably expanded SSI field during glacial sea-ice maximum has not been committed to in previous studies the present consensus is that, during glacial sea-ice maximum, seasonality was much greater than the present day. Subsequent to the glacial sea-ice maximum, between 23.5 cal ka B.P. and 22.9 cal ka B.P., both the winter and summer sea-ice fronts rapidly (~600 years) withdrew from the Scotia

Sea, more than 5 kyrs prior to the estimated southern hemisphere age of deglaciation, around ~17.3 cal ka B.P. (Schaefer *et al.*, 2006). By 22.4 cal ka B.P. the WSI edge was once more a prominent feature in the north Scotia Sea. This rapid event indicates a sea-ice response to a brief but strong increase in oceanic or atmospheric temperatures. This rapid retreat event and subsequent readvance could coincide with the brief Antarctic isotope maxima 2, when considering offsets in age-models and sampling resolution, and return to low isotope values, observed in the EDML $\delta^{18}\text{O}$ record (EPICA, 2006) (Figure 6.13), indicating a potentially close relationship between the two, unfortunately the chronology presented in this thesis is not accurate enough to determine the phasing of these events. The results presented here, relating to the interval of time building up to the glacial sea-ice maximum in the Scotia Sea, further develop our understanding of glacial sea-ice extent and duration and its potential role in the climate regime gleaned from previous LGM-timeslice reconstructions and demonstrates the importance of longer records with a greater temporal resolution.

After 22.9 cal ka B.P. there is a marked shift to enhanced sea-ice seasonality within the Scotia Sea. Between 22.4 cal ka B.P. and 17.8 cal ka B.P., subsequent to the rapid sea-ice meltback, the WSI edge recovers and returns to the northern Scotia Sea, whereas the SSI edge is confined to the Weddell Sea. This portion of the record was sampled at a lower resolution than the HRW and so could have some bearing on the interpretation. Gersonde *et al.* (2005) also identified this enhanced seasonality and associated it with maximum sea-ice extent at ~21 cal ka B.P. The data presented in this thesis supports the conclusion regarding the persistence of enhanced sea-ice seasonality during the LGC but suggests a regime shift from reduced seasonality after maximum sea-ice conditions, which then remains a persistent feature of the Scotia Sea sea-ice field between 22.4 cal ka B.P. and deglaciation. This finding supports and builds on the studies by Crosta *et al.*, 1998 and Gersonde *et al.*, 2003; 2005. A reduction in both atmospheric and oceanic temperatures, coinciding with the readvance and presence of the WSI field in the north Scotia Sea, is reflected in the EDML $\delta^{18}\text{O}$ record from the Antarctic continent (EPICA, 2006) and SST records from the South Atlantic (Charles *et al.*, 1996) and Southeast Pacific (Kaiser *et al.*, 2005) Oceans (Figure 6.13), indicating a regional cooling of the climate. A possible reason for this shift in seasonality, manifest as a readvance of the WSI edge to the northern Scotia Sea and confinement of the SSI edge to the Weddell Sea, is the increasing values of southern hemisphere summer insolation at this time as a result of high obliquity (Berger and Loutre, 1991; Vandergoes *et al.*, 2005; Pena and Cacho, 2009).

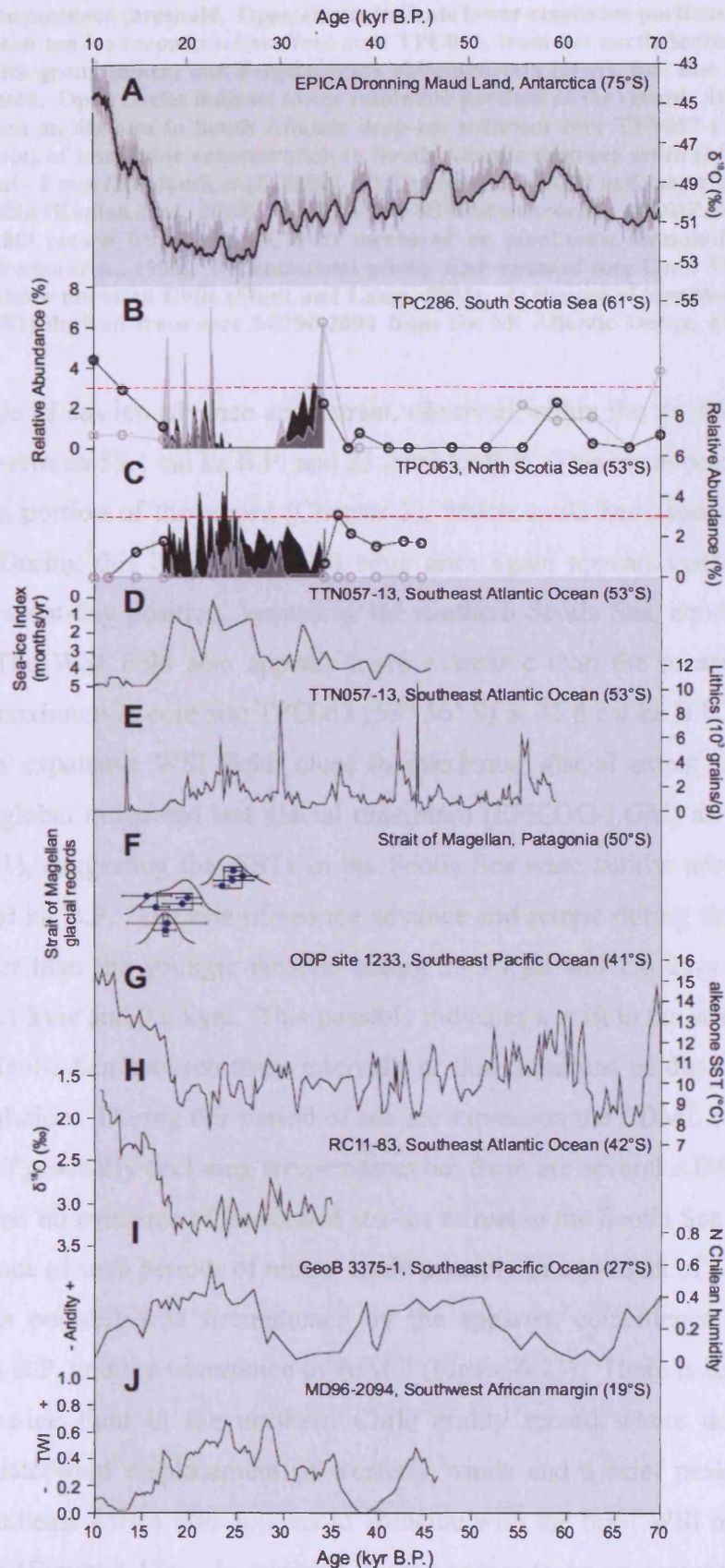


Figure 6.13. A) $\delta^{18}\text{O}$ record from the high resolution EPICA Dronning Maud Land ice core, Antarctica (EPICA, 2004). B) A diatom fossil-based sea-ice reconstruction from TPC286 from the southern Scotia Sea (this study). *Fragilariopsis* sea-ice group (black) and *Fragilariopsis obliquecostata* (gray). Red line

indicates 3% sea-ice presence threshold. Open circles indicate lower resolution portions of the record. C) A diatom fossil-based sea-ice reconstruction from core TPC063, from the north Scotia Sea (this study). *Fragilariopsis* sea-ice group (black) and *Fragilariopsis obliquecostata* (gray). Red line indicates 3% sea-ice presence threshold. Open circles indicate lower resolution portions of the record. D) Sea-ice presence reconstruction based on diatoms in South Atlantic deep-sea sediment core TTN057-13 (Shemesh *et al.*, 2002). E) Time series of total lithic concentration in South Atlantic deep-sea sediment core TTN057-13, size fraction 150 μm - 2 mm (Kanfoush *et al.*, 2000). F) Timing of the LGM and major glacial advances in the Strait of Magellan (Kaplan *et al.*, 2008). G) Alkenone SST reconstruction at ODP Site 1233 (Kaiser *et al.*, 2005). H) $\delta^{18}\text{O}$ record from core RC11-83 measured on planktonic foraminifera from the SE Atlantic Ocean (Charles *et al.*, 1996). I) Continental aridity time series of core GeoB 3375-1 from the SE Pacific Ocean, offshore northern Chile (Stuut and Lamy, 2004). J) Record of Southwest African trade-wind intensity (TWI) derived from core MD96-2094 from the SE Atlantic Ocean, offshore SE Africa (Stuut *et al.*, 2002).

The older episode of sea-ice advance and retreat, observed within the Scotia Sea during the LGC, occurred between 59.1 cal ka B.P. and 33.2 cal ka B.P. This event occurred within the lowest resolution portion of the record (Chapter 3), which could have some bearing on the interpretation. During this interval the SSI edge once again appears considerably further north than its present-day position, located in the southern Scotia Sea, equatorward of core site TPC286. The WSI field also appears more extensive than the present-day but only reaches a brief maximum at core site TPC063 (53° 56' S) at 35.8 cal ka B.P. None-the-less, this indicates an expansive WSI field, close to maximum glacial extent, some 14.8 kyrs earlier than the global integrated last glacial maximum (EPILOG-LGM) at ~21 cal ka B.P. (Mix *et al.*, 2001), suggesting that SSTs in the Scotia Sea were similar around 35.8 cal ka B.P. and 24.1 cal ka B.P. The rate of sea-ice advance and retreat during this older episode was much slower than the younger episode taking 23.3 kyrs and 2.6 kyrs respectively, in comparison to 8.1 kyrs and 0.6 kyrs. This possibly indicates a shift in the strength of climate forcings in the Scotia Sea between these intervals, or this could just be due to the difference in sampling resolution. During this period of sea-ice expansion the EDML $\delta^{18}\text{O}$ record does display a trend of gradually declining temperatures but there are several AIMs superimposed onto this trend and no evidence of associated sea-ice retreat in the Scotia Sea records (Figure 6.13). The absence of such periods of retreat could possibly be a product of a lower sampling resolution. This possibility is strengthened by the apparent coincidence of WSI retreat around 35 cal ka B.P. and the occurrence of AIM 7 (Figure 6.13). There is some evidence of an expanded sea-ice field in the northern Chile aridity record where decreased aridity indicates an equatorward displacement of westerly winds and a brief peak in trade wind intensity off Southeast Africa also appears to coincide with the brief WSI maximum in the north Scotia Sea (Figure 6.13). In addition, there appears to be an associated peak in Ice Rafted Debris in the Southeast Atlantic during the WSI maximum at 35.8 cal ka B.P., possibly indicating a northward displacement of surface ocean environmental conditions at

this time (Figure 6.13). Low sampling resolution prevents a closer correlation for this interval.

6.3.9.2. Antarctic Polar Front

The APF varies over the past 44.7 kyrs (Figure 6.5 to 6.13) and several migrations southeast toward, and northwest away from, core site TPC063 (53° 56' S) are interpreted as shifts in the surface water regime between Antarctic and sub-Antarctic surface waters, primarily in response to the fluctuating WSI edge. At no point during the past 44.7 kyrs did the deep water jet, associated with the APF migrate entirely poleward of 53° 56' S and the longest migration of the APF equatorward of 53° 56' S occurred during maximum sea-ice expansion between 24.1 cal ka B.P. and 23.5 cal ka B.P. Although the magnitude of this displacement cannot be determined by this work, it has been proposed that changes in Southern Ocean hydrography related to climate change may cause fronts to jump from one topographic feature to another, over more than 5° in latitude (Belkin and Gordon, 1996; Moore *et al.*, 1999; Gersonde *et al.*, 2005), however, with the exception of Shag Rocks Passage there are no other deep clefts in the North Scotia Ridge capable of accommodating the deep flow associated with the APF. Thus, a northward displacement of the APF in excess of ~3° is unlikely and would be entirely dependent on the decoupling of the surface signal of the APF from its associated deep-water flow. As previously mentioned, it is suggested that significant expansion of the Antarctic sea-ice field would result in a strengthening of the equator-pole thermal gradient, which in turn would intensify the polar vortex over Antarctica. Such intensification would force the circumpolar Westerly winds to migrate north and the effects of this northern displacement during times of sea-ice expansion during the LGC have been clearly demonstrated in a number of proxy records (Stuut, 2001; Lamy 2001, 2002; Stuut *et al.*, 2004, Stuut and Lamy, 2004). Although the overlying southern hemisphere Westerly winds primarily drive the ACC, the constraining bathymetry restricts large equatorward migrations of the ACC and its fronts during intervals of Westerly migration. As a consequence, during the LGC it is suggested that it was only the surface waters of the ACC that responded to the shift of the Westerly Winds (Keany *et al.*, 1976; Brathauer and Abelmann, 1999; Carter and Cortese, 2009). This study indicates that during intervals of sea-ice expansion within the Scotia Sea the APF migrated as far north as bathymetry would allow but only the surface water regime migrated beyond the North Scotia Ridge. Such migrations of the APF equatorward of 53° 56' S, and thus migrations of the surface water regime beyond the North Scotia Ridge, are observed between 37.2 cal ka B.P. and 35.8 cal ka B.P., 28.3 cal

ka B.P. and 24 cal ka B.P. and 22.3 cal ka B.P. and 17.9 cal ka B.P. and are associated with sea-ice migrations within the Scotia Sea. These surface water movements can be related to northward migrations of the Westerly winds and broadly coincide with intervals of intensified trade winds off Southeaster Africa and reduced aridity in the northern Chilean desert (Figure 6.13).

6.3.9.3. *Hyalochaete Chaetoceros* Resting Spore Peak (~30.9 cal ka B.P.)

A peak in *Chaetoceros* rs occurs in both the south (TPC286) and north Scotia Sea (TPC063) at ~30.9 cal ka B.P. These pulses in *Chaetoceros* rs could originate from the same source, however, the widely varying oceanographic regimes at each core site during the event – MIZ in the southern Scotia Sea and POOZ in the north Scotia Sea (section 6.3.1.2.) – suggest that a common casual mechanism is unlikely. In addition, the core sites are separated by the fast flowing frontal jets of the ACC, hence, the advection of equal quantities of diatoms to both core sites from a common distal source is also unlikely. One mechanism that could induce an intense bloom over a widespread area is surface ocean fertilization triggered by tephra outfall from a proximate volcanic eruption. Young (<3 Ma), active volcanoes (Smellie, 1999), stretch from the Andes Mountains, around the Scotia Arc to the South Sandwich Islands and down to the Antarctic Peninsula (Moreton, 1999). A number of these volcanoes have been active throughout the Quaternary (Smellie, 1999) and could have fertilized the surface waters of the Scotia Sea. However, due to the trajectory of the Westerly winds, volcanic sites to the east of the core sites are unlikely to exert a strong fertilization effect (J. Smellie, pers. comm. 25/08/2008), but instead, such an effect could originate in the Andes or along the Antarctic Peninsula. Deception Island is presently the most active volcano in the Antarctic Peninsula region (Smellie, 2001) and is known to be a major source of Quaternary tephra found in the sea-floor sediments of the Scotia Sea (Moreton & Smellie 1998, Smellie 1999a, Pallas *et al.* 2001). A tephra layer identified in Scotia Sea Quaternary sediments (Moreton *et al.*, 1999), dated 31.8 cal ka B.P., coincides with the *Chaetoceros* rs peaks (Figure 6.14) and could have had some fertilizing effect on the *Chaetoceros* rs productivity event in cores TPC063 and TPC286.

Chaetoceros rs blooms are widely associated with stable surface water stratification and as a result are often employed as a meltwater indicator (Leventer *et al.*, 1992; Crosta *et al.*, 1997; Bianchi and Gersonde, 2004). Although much more research has been conducted on meltwater pulses in the North Atlantic Ocean, which are associated with iceberg shedding (Heinrich Events) by the Laurentide Ice Sheet during the glacial, little had been done

concerning the West Antarctic Ice Sheet (WAIS), which is predominantly grounded below sea-level and is potentially susceptible to climate perturbations (Denton *et al.*, 1996; Kanfoush *et al.*, 2000). Based on records of Ice Rafted Debris concentrations in deep-sea sediment cores from the Southeast Atlantic, Kanfoush *et al.* (2000) proposed an interhemispheric coupling whereby changes in the North Atlantic Ocean result in iceberg discharge from the WAIS. This could be encouraged through an increase in the freshwater balance of the North Atlantic Ocean, through iceberg discharge during Heinrich Events, which act to curtail the formation of North Atlantic Deep Water (NADW) and, via the bipolar seesaw mechanism, traps heat in the Southern Ocean. This warming would destabilize the marine based WAIS and lead to the discharge of icebergs from the Weddell Sea resulting in the meltwater stratification of surrounding areas, i.e. the Scotia Sea. Heinrich Event 3 occurred ~31 ka, around the same time as the *Chaetoceros* rs peak identified in cores TPC063 and TPC286 (Figure 6.14). Kanfoush *et al.* (2000) show that this event is directly followed by an Ice Rafted Debris spike in the Southeast Atlantic Ocean at around 30 cal ka B.P. (Figure 6.14). The large *Chaetoceros* rs peaks identified in cores TPC063 and TPC286 could therefore be the result of widespread surface water stratification induced by largescale iceberg discharge from the Weddell Sea. Although a possibility, if this mechanism was in operation we would expect to observe similar *Chaetoceros* rs peaks during other Heinrich Events, which we do not.

A third potential mechanism that could have potentially induced the large spikes in *Chaetoceros* rs observed in the Scotia Sea is surface water fertilization as a result of wind blown dust from Patagonia. Dust has been shown to play an important role in the marine ecosystem (Hutchins and Brunland, 1998) providing limiting nutrients such as trace metals (Fung *et al.*, 2000). Due to climate changes in source regions and stronger winds dust transport increased significantly during the LGC and peaking during the LGM (Delmonte *et al.*, 2002), which are recorded in polar ice cores. A large peak in dust concentration is observed in the EDC at around ~31 cal ka B.P., coincident with the large *Chaetoceros* rs peaks identified in cores TPC063 and TPC286 (Figure 6.14). Although potentially a causal mechanism much larger peaks in dust concentration are observed during the subsequent LGM, for which we observe no *Chaetoceros* rs peak counterpart. The absence of any *Chaetoceros* rs peaks during this interval could be due to more expansive sea-ice cover preventing the deposition of dust into the surface waters. However, if this were the case we

would expect an exceptionally large productivity event during sea-ice retreat, which is not evident.

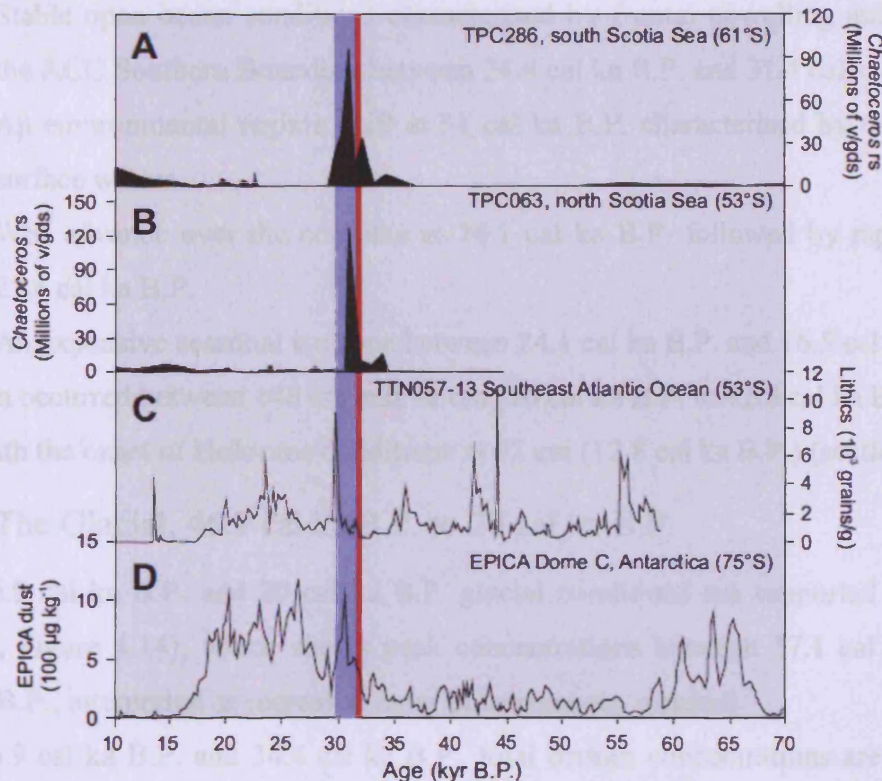


Figure 6.14. A) A relative abundance record of meltwater indicator diatom *Chaetoceros* resting spores (rs) from south Scotia Sea core TPC286 (this study). B) A relative abundance record of meltwater indicator diatom *Chaetoceros* resting spores (rs) from north Scotia Sea core TPC063 (this study). C) Time series of total lithic concentration in South Atlantic deep-sea sediment core TTN057-13, size fraction 150 μm - 2 mm (Kanfoush *et al.*, 2000). D) EPICA Dome C dust content (Delmonte *et al.*, 2002; EPICA, 2004). Red band: Ash layer identified in central Scotia Sea core TPC290 (sourced from Deception Island) (Moreton, 1999). Blue band: Heinrich Event 3.

6.4. MD03-2603

6.4.1. Summary of Interpretations

The upper 380 cm of core MD03-2603 spans the last 46.9 kyrs (Chapter 5), and is comparable with the time covered by cores TPC063 and TPC286 from the Scotia Sea. The sedimentation rate of ~ 7.7 cm/kyr has been relatively constant back to MIS 6 (Presti *et al.*, 2008) maintained by an increase in biogenic deposition during interglacials and an increase in terrigenous input during glacials. The glacial regime extends from 380 cm (46.9 cal ka B.P.) to 148 cm (20 cal ka B.P.) (section 6.4.1.1.), encompassing the majority of the HRW. The HRW, between 364 cm and 124 cm (34.4 cal ka B.P. to 16.47 cal ka B.P.), includes the intensification of glacial conditions, maximum global ice volumes (i.e. the glacial maximum)

and the onset of deglaciation. During the HRW the oceanographic environment over core site MD03-2603 (Figure 6.13) was characterised by:

- Stable open ocean conditions characterised by frontal upwelling associated with the ACC Southern Boundary between 34.4 cal ka B.P. and 31.4 cal ka B.P.
- An environmental regime shift at 31 cal ka B.P. characterised by the cooling of surface waters.
- WSI advance over the core site at 24.1 cal ka B.P. followed by rapid retreat at 23.6 cal ka B.P.
- An expansive seasonal ice zone between 24.1 cal ka B.P. and 16.5 cal ka B.P.

Deglaciation occurred between 148 cm and 92 cm (20 cal ka B.P. to 12.8 cal ka B.P.) (section 6.4.1.2.), with the onset of Holocene conditions at 92 cm (12.8 cal ka B.P.) (section 6.4.1.3.).

6.4.1.1. The Glacial, 46.9 cal ka B.P. to 20 cal ka B.P.

Between 46.9 cal ka B.P. and 20 cal ka B.P. glacial conditions are supported by MS data (Chapter 4., Figure 4.14), which shows peak concentrations between 37.1 cal ka B.P. and 21.8 cal ka B.P., interpreted as increased input of terrigenous material.

Between 46.9 cal ka B.P. and 34.4 cal ka B.P., total diatom concentrations are consistently low, with a mean of 7.69×10^6 v/gds, with the exception of a single peak of 16.7×10^6 v/gds at 45 cal ka B.P. (Chapter 4, Figure 4.14) indicating reduced biogenic sedimentation during the glacial. High relative abundances of sea-ice related species (*Fragilariopsis* sea-ice group, *A. actinochilus*) suggest proximity to the WSI edge between 46.9 cal ka B.P. and 41.9 cal ka B.P. A decrease in the relative abundance of these species between 41.9 cal ka B.P. and 34.4 cal ka B.P. is coeval with increased concentrations of species indicative of an increasing influence of an ACC regime (*A. tabularis*, *T. lentiginosa*, *Rhizosolenia* spp.) (Chapter 4, Figure 4.14). The Influence of the ACC continues until 34.4 cal ka B.P., after which the Southern Boundary also exerts a strong influence over the diatom assemblage (Figure 6.15). The glacial maximum occurs within the HRW (34.4 cal ka B.P. to 16.47 cal ka B.P.). In the HRW, between 34.4 cal ka B.P. to 20 cal ka B.P., the glacial maximum is characterised by a low total diatom concentration of 5.92×10^6 v/gds, gradually deteriorating environmental conditions, cooling surface waters and the encroachment of the WSI edge (Figure 6.15). The HRW is the focus of this study, with environmental change during this period discussed in detail below (section 6.4.2.).

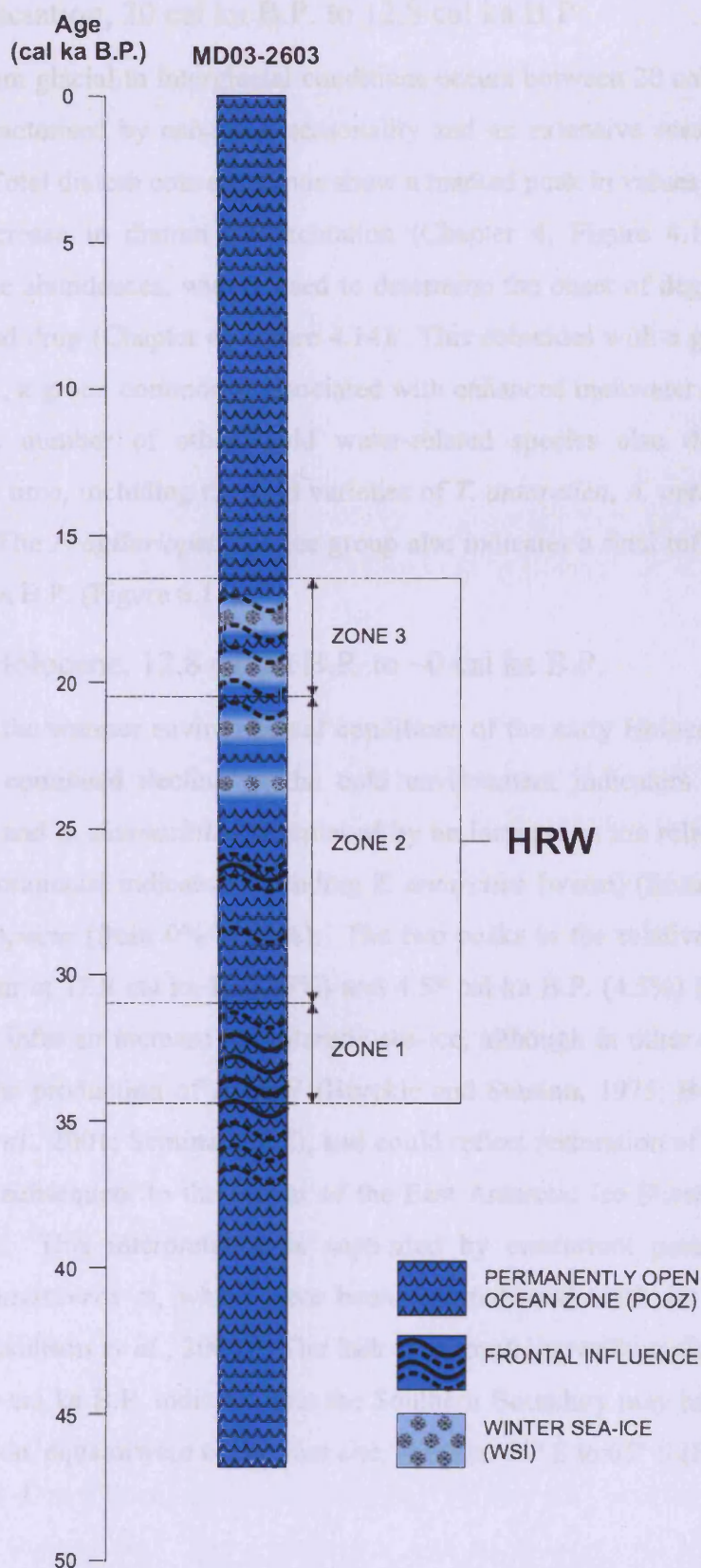


Figure 6.15. MD03-2603 downcore log illustrating reconstructed oceanographic variability between 46.9 cal ka B.P. and the present day along the Adélie Land Coast. Zonation derived from PCA (Chapter 4). HRW = high resolution window.

6.4.1.2. Deglaciation, 20 cal ka B.P. to 12.8 cal ka B.P.

The transition from glacial to interglacial conditions occurs between 20 cal ka B.P. and 12.8 cal ka B.P., characterised by enhanced seasonality and an extensive seasonal sea-ice zone (section 6.4.2). Total diatom concentrations show a marked peak in values (60.5×10^6 v/gds) indicating an increase in diatom sedimentation (Chapter 4, Figure 4.14), whilst the *E. antarctica* relative abundances, widely used to determine the onset of deglaciation (Chapter 5), show a marked drop (Chapter 4, Figure 4.14). This coincides with a gradual increase in *Rhizosolenia* spp., a group commonly associated with enhanced meltwater production during deglaciation. A number of other, cold water-related species also decline in relative abundance at this time, including the cold varieties of *T. antarctica*, *A. actinochilus* (Chapter 4, Figure 4.14). The *Fragilariopsis* sea-ice group also indicates a final influence of the WSI edge at 17.7 cal ka B.P. (Figure 6.15).

6.4.1.3. The Holocene, 12.8 cal ka B.P. to ~0 cal ka B.P.

The transition to the warmer environmental conditions of the early Holocene occurs at 12.8 cal ka B.P. A continued decline in the cold environment indicators *E. antarctica*, *T. antarctica* (cold) and *A. actinochilus* is replaced by an increase in the relative abundance of the warmer environmental indicators including *T. antarctica* (warm) (from 0% to 1.7%) and *T. gracilis* var. *expecta* (from 0% to 1.8%). The two peaks in the relative abundance of *F. ritscheri* that occur at 12.8 cal ka B.P. (5%) and 4.58 cal ka B.P. (4.5%) (Chapter 4, Figure 4.14) are used to infer an increase in Antarctic sea-ice, although in other studies it has also been related to the production of AABW (Burckle and Stanton, 1975; Booth and Burckle, 1976; Stickley *et al.*, 2001; Semina, 2003), and could reflect restoration of the Mertz Glacial Polynya (MGP), subsequent to the retreat of the East Antarctic Ice Sheet (EAIS) from the continental shelf. This interpretation is supported by concurrent peaks in the relative abundance of *Chaetoceros* spp., which have been reported to flourish in stratified polynya environments (Maddison *et al.*, 2006). The lack of a frontal upwelling signal between 12.8 cal ka B.P. and 0 cal ka B.P. indicates that the Southern Boundary may have returned to its present day location, equatorward of the core site, between 64° S to 65° S (Figure 6.15).

6.4.2. Glacial Maximum (HRW)

6.4.2.1. Diatom Species Relationships

Diatom assemblage data collected from core MD03-2603 during the glacial maximum show less variability than that seen in the Scotia Sea implying a more stable system, with a more gradual regime shift from an open ocean to a cold water sea-ice environment. Individual diatom assemblages and associated ecological interpretations are summarised below and illustrated in Figures 6.16 and 6.17.

6.4.2.1.1. PCA Axis 1

Positive loadings on axis 1 are characterised by *T. antarctica* (cold), *T. gracilis*, and *E. antarctica* and negative loadings characterised by *F. kerguelensis* and *A. tabularis* (Figure 6.16).

T. antarctica (cold) is closely affiliated with cold surface waters sea-ice with its distribution generally limited to the south of the WSI edge. Crosta *et al.* (2005) includes this species as a component of his water stratification group. *T. gracilis* is also an indicator of cooler surface waters and the near-by presence of sea-ice (Chapter 2). However, Gersonde and Zielinski (2000) claim this species has no ecological preference, whereas Crosta *et al.* (2005) include it in their POOZ group. Due to the association observed between *T. gracilis* and *T. antarctica* (cold) here, *T. gracilis* is considered an indicator of colder waters.

The precise ecological association of *E. antarctica* is debated, but it is thought to be an indicator of preferential preservation and nutrient-rich meltwater pools associated with iceberg pathways (Blain *et al.*, 2008) (Chapter 2). Collectively this diatom assemblage implies an environment characterised by cold, fresh, surface waters likely associated with seasonal sea-ice melt or frontal upwelling (Figure 6.16). The Southern Boundary frontal system is close to the core site and is characterised by the intense upwelling of cold, nutrient-rich Upper Circumpolar Deep Water (UCDW) into the surface mixed layer (Orsi *et al.*, 1995; Tynan, 1998).

F. kerguelensis is an indicator of open ocean conditions and maximum abundances between 70% and 80% are generally associated with the flow of the ACC, situated between the WSI edge and APF (Chapter 2). The species has also been employed as an indicator of Circumpolar Deep Water (CDW) upwelling, where it is found on the Antarctic continental shelf (Tanimura, 1992; Pike *et al.*, 2008). In the Weddell Sea similar *F. kerguelensis* concentrations have been associated with high rates of biogenic dissolution and strong

advection (Zielinski and Gersonde, 1997). However, the presence of smaller, less silicified valves and absence of other dissolution indicator taxa in the assemblage suggests that it is not a strong driver of the diatom assemblage at this location. *A. tabularis* only marginally exceeds the 0.5% relative abundance threshold required for its inclusion in the PCA. Hence, the negative mode of axis 1 is primarily driven by *F. kerguelensis* and implies a prevalence of permanently open ocean conditions (Figure 6.16).

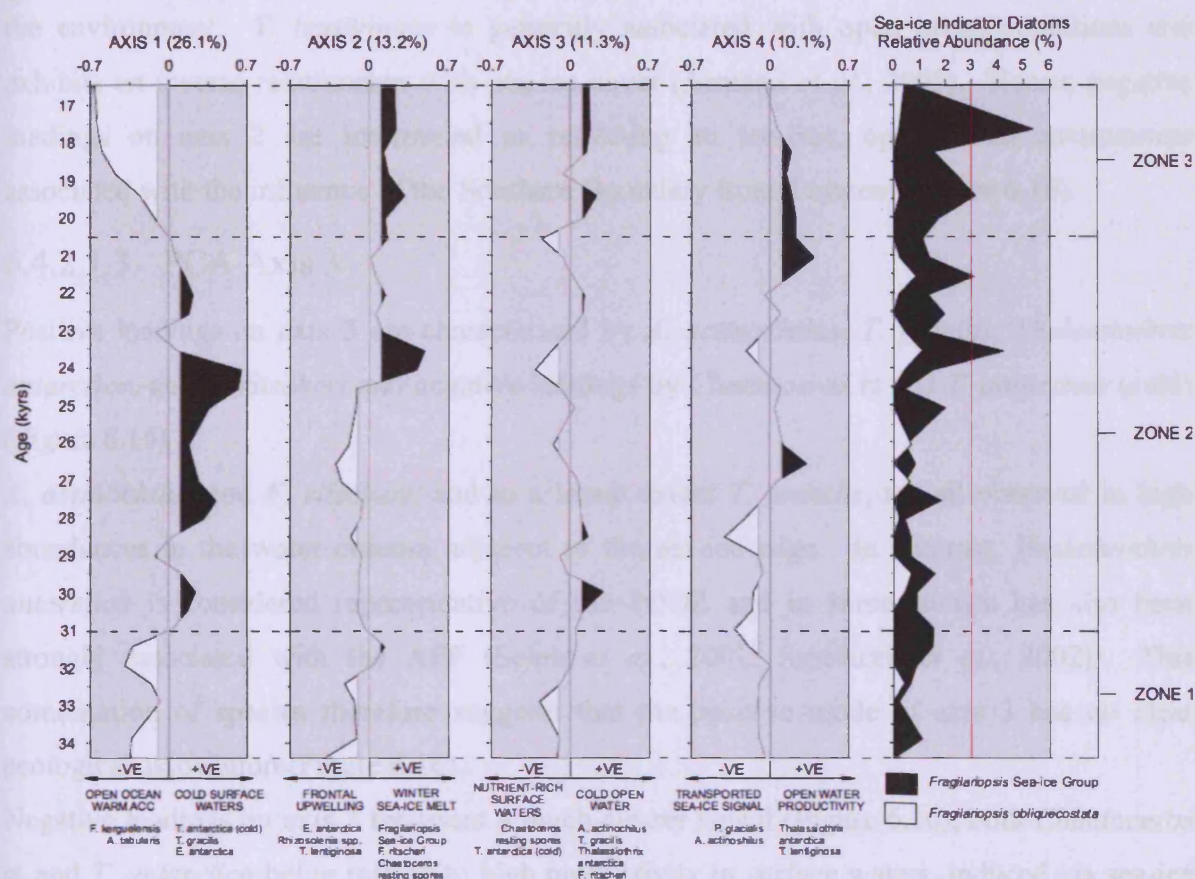


Figure 6.16. Core MD03-2603 (HRW): PCA component scores and environmental gradients associated with axes 1 to 3, compared with the relative abundance curves of the *Fragilariopsis* sea-ice group (black) and *Fragilariopsis obliquecostata* (white), plotted against age (kyrs). Shaded black and white polygons on axes 1 to 3 indicate significant positive and negative variability respectively (un-shaded areas indicate insignificant variability). Diatom indicator species associated with each axis are listed at the base of the figure. The red line on the sea-ice diatom plot indicates the 3% sea-ice threshold.

6.4.2.1.2. PCA Axis 2

Positive loadings on axis 2 are characterised by the *Fragilariopsis* sea-ice group and *F. ritscheri* and negative loadings by *E. antarctica*, *Rhizosolenia* spp., and *T. lentiginosa* (Figure 6.16).

The *Fragilariopsis* sea-ice group can be used to reconstruct the position of the average – maximum extent of the WSI edge (Gersonde and Zielinski, 2000). *F. ritscheri* is also associated with the WSI edge and meltwater conditions and has been employed as a tracer for

the transport of AABW (Chapter 2). Positive loadings on axis 2 are interpreted here as an increase in productivity related to melting sea-ice over, or near the core site (Figure 6.16).

E. antarctica has been associated with both iron fertilization and cold water environments. *Rhizosolenia* spp. span a wide ecological range, with some evidence of a preference for fresher waters, and frontal conditions (Pudsey *et al.*, 1992; Crosta *et al.*, 2005), however, the *Rhizosolenia* spp. counts are extremely low on axis 2 (<5 valves) and so not representative of the environment. *T. lentiginosa* is generally associated with open ocean conditions and exhibits an inverse relationship with sea-ice cover (Armand *et al.*, 2005). Hence, negative loadings on axis 2 are interpreted as reflecting an ice-free, open ocean environment associated with the influence of the Southern Boundary frontal system (Figure 6.16).

6.4.2.1.3. PCA Axis 3

Positive loadings on axis 3 are characterised by *A. actinochilus*, *T. gracilis*, *Thalassiothrix antarctica*, and *F. ritscheri* and negative loadings by *Chaetoceros* spp. and *T. antarctica* (cold) (Figure 6.16).

A. actinochilus and *F. ritscheri*, and to a lesser extent *T. gracilis*, are all observed in high abundances in the water column adjacent to the sea-ice edge. In contrast, *Thalassiothrix antarctica* is considered representative of the POOZ and in some studies has also been strongly associated with the APF (Selph *et al.*, 2001; Smetacek *et al.*, 2002). This combination of species therefore suggests that the positive mode of axis 3 has no clear ecological association (Figure 6.16).

Negative loadings on axis 3 represent a much clearer signal (Figure 6.16), both *Chaetoceros* spp. and *T. antarctica* being related to high productivity in surface waters, induced via sea-ice meltback or frontal upwelling, associated with spring and summer/autumn productivity respectively (Chapter 2).

6.4.2.1.4. PCA Axis 4

Positive loadings on axis 4 are characterised by *Thalassiothrix antarctica*, and *T. lentiginosa*, and negative loadings by *P. glacialis* and *A. actinochilus* (Figure 6.16). *Thalassiothrix antarctica* and *T. lentiginosa* have each been observed in high abundances in surface sediments below ACC frontal systems, therefore positive loadings on axis 4 are interpreted as representing a predominantly open water, possibly frontal signal (Figure 6.16). In contrast, *P. glacialis* and *A. actinochilus* are associated with consolidated sea-ice cover in excess of 7 months per year, although low concentrations observed here imply only the proximal or

intermittent exposure to this duration of sea-ice cover. Hence, negative loadings on axis 4 are interpreted as indicating an advected signal or the near-by persistence of sea-ice cover (Figure 6.16).

6.4.2.2. Palaeoenvironment Reconstruction Across the Glacial Maximum

Downcore variability is divided into three zones based on the transitions between the positive and negative modes of variability on PCA axis 1 (Figure 6.16)

6.4.2.2.1. HRW Zone 1: Open Water Frontal Upwelling, 34.4 cal ka B.P. to 31 cal ka B.P.

Zone 1 is characterised by negative component scores on axis 1. Two significant peaks are evident between 34.4 cal ka B.P. and 33 cal ka B.P., and between 32.7 cal ka B.P. and 31.1 cal ka B.P., indicating two episodes where open ocean conditions dominate. Axis 2 is characterised by significant negative component scores between 34.4 cal ka B.P. and 32.2. cal ka B.P., with two peaks at 34.4 cal ka B.P. and 32.4 cal ka B.P., supporting the interpretation of axis 1 and also indicating the close proximity of the Southern Boundary front. Positive component scores on axis 2 show a significant peak at 31.4 cal ka B.P., implying the close proximity of the WSI edge. Significant negative component scores dominate axis 3 between 34.4 cal ka B.P. and 32.5 cal ka B.P., peaking at 32.9 cal ka B.P. This peak is concurrent with an insignificant trough in negative component scores in axis 1 and indicates presence of cold, nutrient-rich waters, potentially related to frontal upwelling.

Zone 1 (34.4 cal ka B.P. to 31 cal ka B.P.), is characterised by open ocean conditions and a strong association with the ACC. This is supported by *F. kerguelensis* relative abundance of up to 74.3%, and partially supported by the abundance of *T. lentiginosa*, *E. antarctica* and *Rhizosolenia* spp., which suggest a stable, nutrient-rich, surface water environment generated through frontal upwelling, most prominent between 34.4 cal ka B.P. and 32.4 cal ka B.P. Further, due to close proximity of the ACC Southern Boundary to the Antarctic coast in this sector of the Southern Ocean (Orsi *et al.*, 1995; Tynan, 1998; Bindoff *et al.*, 2000; Sokolov and Rintoul, 2002) this variability might be a stratified system forced by the close proximity of the Southern Boundary. A transported signal of consolidated sea-ice cover from the south of the core site is observed at 31.4 cal ka B.P., signalling an environmental shift to colder surface waters (Figure 6.15).

6.4.2.2.2. HRW Zone 2: Cold Water Environment, 31 cal ka B.P. to 20.5 cal ka B.P.

Axis 1 is characterised by positive component scores, showing a pattern of peaks and troughs. There is a trend of increasing cold surface waters, which peaks at 24.1 cal ka B.P. Positive component scores on axis 1 decline at the top of zone 2 (20.5 cal ka B.P.) reflecting the removal of cold water conditions. Axis 2 shows a weak peak in negative component scores at 28.5 cal ka B.P. Above 27.4 cal ka B.P. negative component scores peak at 26.6 cal ka B.P., and then decline at 24.5 cal ka B.P. These peaks in negative component scores on axis 2 imply open ocean production associated with frontal upwelling. At 24.5 cal ka B.P., axis 2 is characterised by positive component scores for the remainder of zone 2, with the most significant peak at 24.6 cal ka B.P. The switch to positive component scores suggests an increasing influence of the WSI edge near-by, or possibly over, the core site. Axis 3 is characterised by positive component scores between 30.1 cal ka B.P. and 29.7 cal ka B.P., and between 28.6 cal ka B.P. and 28 cal ka B.P. Consideration of the primary and secondary axes, suggests that the older peak is related to an enhancement of cold surface waters, and that the younger peak is indicative of increasing frontal influence. Negative component scores peak on axis 3 at the top of zone 2 between 20.9 cal ka B.P. and 20.5 cal ka B.P., suggesting the returning influence of cold, nutrient-rich surface conditions over the core site. Zone 2 is characterised by an increasing influence of colder surface waters over the core site as the oceanographic regime shifts from open ocean and Southern Boundary frontal conditions to an increasing proximity of the WSI edge. A gradual intrusion of cold surface waters over the core site occurs between 31 cal ka B.P. and 24.1 cal ka B.P. and coincides with the waning influence of the Southern Boundary frontal upwelling (26.1 cal ka B.P. to 24.1 cal ka B.P.). This suggests a gradual advance of the WSI edge, acting to ‘cap’ the upwelling influence of the underlying Southern Boundary. Cold-water surface conditions peak at 24.1 cal ka B.P. coinciding with the first indication of WSI over, or close to, the core site (Figure 6.16). The remainder of zone 2, between 24.1 cal ka B.P. and 20.5 cal ka B.P., is strongly influenced by the *Fragilariopsis* sea-ice group, which – in accordance with Gersonde and Zielinski (2000) – signifies at least two phases of WSI edge advance and retreat over the core site during zone 2, at 23.6 cal ka B.P. (176 cm) and 21.6 cal ka B.P. (160 cm) (Figure 6.16). Periods of open ocean and at times upwelling conditions following sea-ice meltback imply an extensive seasonal ice zone, with the WSI edge retreating to a distal location and a removal of the sea-ice cap that prevents upwelling at the Southern Boundary

(Figure 6.15). Elevated relative abundances of the open ocean diatom *T. lentiginosa* at 23.1 cal ka B.P. (172 cm) and 21.1 cal ka B.P. (156 cm) support this interpretation (Chapter 4, Figure 4.14).

6.4.2.2.3. HRW Zone 3: Enhanced Sea-ice Seasonality, 20.5 cal ka B.P. to 16.5 cal ka B.P.

Axis 1 is characterised by negative component scores in zone 3, suggestive of open ocean conditions over the core site. Axis 2 is characterised by positive scores throughout zone 3, implying the continuation of fluctuations in WSI cover near-by or over the core site. Axis 3 is primarily characterised by positive component scores between 120 cal ka B.P. and 19.1 cal ka B.P., and between 18.4 cal ka B.P. and 16.5 cal ka B.P. Concurrence with axis 2 implies episodic fluctuations in the WSI edge.

Zone 3 is characterised by a strong ACC, open ocean signal together with a fluctuating WSI edge. A shift away from the cold surface water regime of zone 2 and a return to a typical open ocean ACC environment, with *F. kerguelensis* relative abundances increasing to 73.5%, occurs at the top of the zone at 16.5 cal ka B.P. In contrast, the WSI edge overlies the core site on several occasions, an interpretation supported fluctuations in the *Fragilariopsis* sea-ice group (Figure 6.16), at 19.4 cal ka B.P. and 17.7 cal ka B.P. These concurrent yet contrasting environmental signals are interpreted as representing extensive sea-ice seasonality and a continuation of the pattern observed at the top of zone 2 (23.6 cal ka B.P. to 21.1 cal ka B.P.) (Figure 6.15). Elevated relative abundance of the open water ACC indicator *T. lentiginosa* at 18.3 cal ka B.P. and 14.4 cal ka B.P support this interpretation (Chapter 4., Figure 4.14).

6.5. Regional Reconstruction: The Adélie Land Coast

This section discusses the glacial palaeoceanography of the Adélie Land Coast (Figure 6.17), including a reconstruction of the variability of glacial WSI and migratory pattern of the Southern Boundary, the southern-most frontier of the ACC.

6.5.1. Sea-ice

Analyses of MD03-2603 initially reveal a relatively stable regime that progressively deteriorated towards the climax of the LGC, including the gradual advance of the WSI edge over the core site and an extensive seasonal sea-ice zone.

The expansion of the WSI edge, adjacent to the Adélie Land Coast, between 24.1 cal ka B.P. and 17.7 cal ka B.P., extended to at least $64^{\circ} 17' 12''$ S (core site MD03-2603). However, the fluctuating nature of the WSI edge and the periodic open ocean conditions indicate that this latitude was close to the maximum extent of an expansive seasonal sea-ice zone. Presently, the WSI edge adjacent to the Adélie Land Coast extends as far north as $\sim 62^{\circ}$ S ($\sim 2^{\circ}$ north of core MD03-2603) (Comiso, 2003), it is therefore curious that core MD03-2603 does not show a greater sea-ice expansion over the core site prior to 24.1 cal ka B.P. The modern-day setting is such that the protruding Mertz Glacier Tongue (orientated southwest to northeast) channels strong katabatic winds towards the Adélie Land Coast, which forces coastal pack ice offshore. Geomorphological studies of the Adélie Land Coast continental shelf (Anderson, 2002) suggest that the EAIS extended to the mid-shelf during the glacial, changing the discharge path of the Mertz Glacier Tongue east-southeast to west-northwest (Presti *et al.*, 2005). If this was the case, the katabatic winds may have been directed elsewhere, and not able to force pack-ice, off shore, towards and over the core site. The *Fragilariopsis* sea-ice group shows concentrations in excess of 2% after 17.7 cal ka B.P., but less than the 3% threshold, indicating a relatively close WSI edge but at no time over the core site.

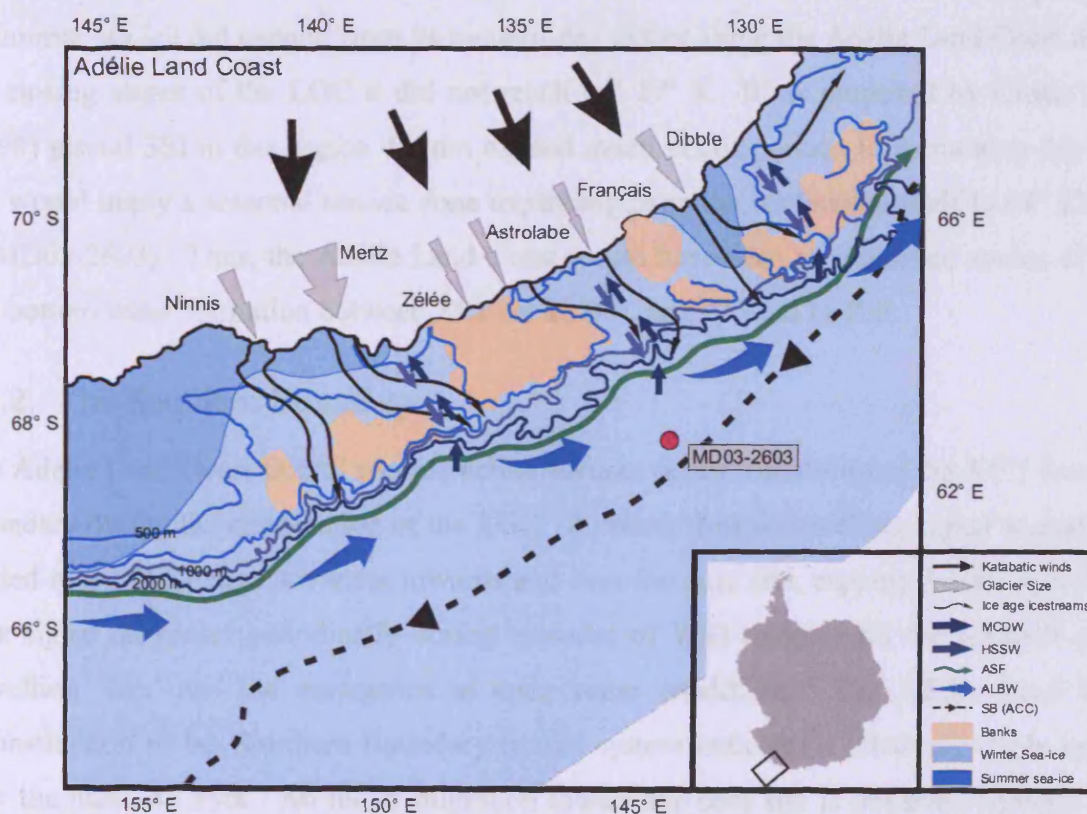


Figure 6.17. Map of the Adélie Land Coast, showing core location and primary oceanographic features mentioned in the text, the 500 m, 1000 m and 2000 m depth contours are also marked to give an impression of bathymetry. Abbreviations referred to in the legend are MCDW = Modified Circumpolar Deep Water; HSSW = High Salinity Surface Water; ASF = Antarctic Slope Front; ALBW = Adélie Land

Bottom Water and *Southern Boundary* = Southern Boundary. Primary glacier outflows, major sand banks, and average modern-day summer and winter sea ice extents are also marked. Map modified from Crosta *et al.*, (2007).

Gersonde *et al.* (2005) estimate a maximum glacial WSI limit, adjacent to the Adélie Land Coast, at $\sim 55^\circ$ S at the E-LGM (~ 21 cal ka B.P.). This estimate would place the WSI edge almost 10° north of core site MD03-2603. The data presented here indicates that the WSI edge fluctuated about its maximum extent between 24.1 cal ka B.P. and 17.7 cal ka B.P., a period of time that encompasses the E-LGM (~ 21 cal ka B.P.), implying an extensive LGM sea-ice expansion in the East Antarctic. However, in comparison with Gersonde *et al.* (2005) there is a clear disparity regarding the magnitude of sea-ice extent during this period. The Gersonde *et al.* (2005) E-LGM sea-ice estimate for this area is based on core MD88-787 ($56^\circ 22'$ S, $145^\circ 18'$ E), which shows a combined relative abundance of *F. curta* and *F. cylindrus* of 2.5%, interpreted by Gersonde *et al.* (2005) as being indicative of a close WSI edge. Instead, the data presented here suggests that the WSI edge was in fact located much further south.

There is no evidence for perennial sea-ice cover over core site MD03-2603 at any point in the record. *F. obliquecostata* shows maximum relative abundances of only 1.1%, suggesting that if summer sea-ice did expand from its modern-day extent along the Adélie Land Coast during the closing stages of the LGC it did not reach $64^\circ 17'$ S. If, as proposed by Crosta *et al.* (1998) glacial SSI in this region did not expand much in comparison to its modern-day limit this would imply a seasonal sea-ice zone expanding from the continental shelf to $64^\circ 17' 12''$ S (MD03-2603). Thus, the Adélie Land Coast would have been an important source of deep and bottom water formation between 24.1 cal ka B.P. and 17.7 cal ka B.P.

6.5.2. The Southern Boundary

The Adélie Land Coast frontal reconstruction focuses on the variability of the ACC Southern Boundary during the culmination of the LGC. A strong frontal upwelling signal is gradually eroded as the WSI edge advances towards and over the core site, capping frontal upwelling. This signal reappears periodically during episodes of WSI retreat with the removal of the upwelling 'cap' and the emergence of open water conditions. The Adélie Land Coast reconstruction of the Southern Boundary frontal system indicates a relatively stable regime over the past ~ 42 kyrs. An initial migration toward the core site is observed between 41.9 and 34.4 cal ka B.P.; it is positioned over, or close to $64^\circ 17' 12''$ S between 34.4 cal ka B.P. and 18.3 cal ka B.P., and finally migrates equatorward around 18.3 cal ka B.P. The Southern

Boundary is the only frontal system associated with the ACC that does not represent a segregation of surface water environments, and is instead representative of the southern extent and upwelling of UCDW (Orsi *et al.*, 1995; Tynan, 1998). Consequently, the Southern Boundary is detached from the surface waters and its location not strongly impacted by the expansion of cold surface waters or sea-ice. Therefore it is likely that the Southern Boundary is constantly present over or near the core site.

6.5.3. Influence of the Australia – Antarctic Basin Gyre

F. kerguelensis is commonly the primary contributor to the circum-Antarctic opal belt that underlies the main flowpath of the ACC, with maximum abundances of 70% to 80% observed in sediments between the WSI edge and the APF (Burckle and Cirilli, 1987). Although *F. kerguelensis* has also been observed in areas with consolidated sea-ice cover it is more common in the open ocean, with abundances sharply falling in waters with SSTs of 0° C (Crosta *et al.*, 2005). Kozlova (1962) observed a modern maximum *F. kerguelensis* relative abundance of 60% in the Indian sector of the Southern Ocean between 45° S and 60° S and Crosta *et al.*'s (2004) 220,000 year long record from 56° 40' S shows a maximum relative abundance in *F. kerguelensis* of 75% (during interglacial regimes). Considering its more southerly latitude (64° 17' 12" S), it is therefore surprising to find similarly high relative abundances of *F. kerguelensis* throughout core MD03-2603, varying between 51.2% and 74.2% relative abundance, with a mean of 69%, and at times coexisting with WSI cover. These elevated concentrations of *F. kerguelensis* occur right up onto the continental shelf, where relative abundances >30% have been observed (Leventer *et al.*, 1992; Tanimura *et al.*, 1992; Crosta *et al.*, 2008).

A possible explanation for the unusually strong *F. kerguelensis* ACC signal at the core site relates to the gyre circulation proposed by McCartney and Donohue (2007). Based on World Ocean Circulation Hydrographic Program sections I8S and I9S, McCartney and Donohue (2007) propose the existence of a strong (76 ± 26 Sv) cyclonic gyre in the AAB. This is partially forced by the primary flow of the ACC (APF) and entrains surface waters from this portion of the current, which it then recirculates in a westward flow along the Antarctic continental slope (Figure 6.18). The circulation of this gyre has also been cited by other authors (Bindoff *et al.*, 2000; Sokolov and Rintoul, 2002; Reid, 2005) and could transport or displace live phytoplankton cells, typical of the primary ACC flow, to more southerly latitudes. In addition, the northern extent of the coastline along this margin of Antarctica

encourages the upwelling of MCDW onto the continental shelf (Chapter 1). This, combined with the enhanced ACC phytoplankton assemblage entrained by the cyclonic gyre, could explain the high relative abundances of *F. kerguelensis* observed over the continental shelf.

The cyclonic gyre could also help explain the presence of *A. tabularis* in MD03-2603; typically cited as a subtropical diatom, with maximal growth in SSTs between 13° C and 11° C. It is often observed in the Sub-Antarctic Zone (SAZ) and occasionally the Antarctic Zone (AZ), but has only ever been documented at trace levels along the Antarctic coast (Romero *et al.*, 2005). In core MD03-2603 *A. tabularis* occurs in relative abundances in excess of 2% on more than one occasion, and could be linked to the strength or propagation of the cyclonic gyre circulation proposed by McCartney and Donohue (2007). Its presence before (36.8 cal ka B.P.) and after (16.5 cal ka B.P.) the cold-water/sea-ice regime could be associated with a stronger ACC circulation, or gyre strength.

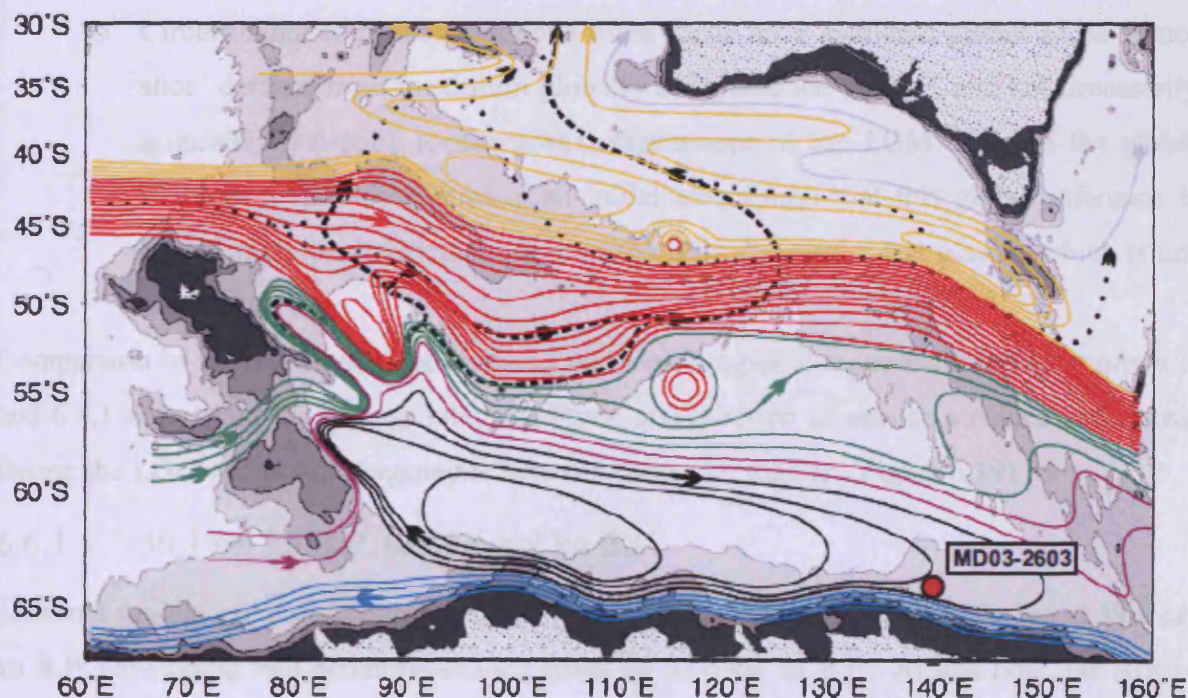


Figure 6.18. Schematic of the primary circulation features of the Australia – Antarctic Basin. Basin-scale total transport field, with 10 Sv contour intervals is indicated (McCartney and Donohue, 2007). Core site MD03-2603 (64° 17, 139° 22) indicated by red circle.

6.6. Circum-Antarctic Comparison

The palaeoceanographic reconstruction of the Scotia Sea (TPC286 and TPC063), West Antarctica, is now directly compared with that of the Adélie Land Coast (MD03-2603), East Antarctica. This comparison focuses on glacial sea-ice and frontal dynamics between ~60 cal. ka B.P. and ~17 cal. ka B.P. (Figure 6.19).

6.6.1. Circum-Antarctic Sea-ice

The most recent circum-Antarctic palaeo-sea-ice reconstructions suggest that the Antarctic WSI field expanded 100% relative to its modern-day extent at the E-LGM, between 23 cal ka B.P. and 19 cal ka B.P. (CLIMAP, 1981; Gersonde *et al.*, 2005). Estimates of SSI expansion however, remain severely constrained by a lack of direct evidence, in particular:

- Data coverage is very sparse in places, with the Scotia Sea and Adélie Land Coast particularly underrepresented in most recent circum-Antarctic sea-ice reconstruction (Gersonde *et al.*, 2005).
- A lot of focus has been placed on reconstructing SST using transfer functions and from this inferring of sea-ice presence, rather than the direct identification of sea-ice diatoms/proxies (Crosta *et al.*, 1998; Gersonde *et al.*, 2003; Bianchi and Gersonde, 2004; Gersonde *et al.*, 2005).
- Circum-Antarctic reconstructions often focus on a synthetic global LGM ‘time-slice’ derived from maximum globally integrated ice volume, and not necessarily accurately depicting local/regional expressions of the LGM. Use of the global LGM as a time-slice implies an initial assumption that this global reference is coeval with local maximal sea-ice expansion during the last glacial, which is not necessarily true.

Comparison of the Scotia Sea and Adélie Land Coast regional reconstructions (sections 6.3. and 6.4.) shows that the timing, rate, amplitude and duration of sea-ice advance and retreat during the LGC was not homogeneous between these two regions (Figure 6.19).

6.6.1.1. 59.1 cal ka B.P. to 31.6 cal ka B.P.

Seasonal sea-ice expanded equatorward of 61° 47' 3" S in the southern Scotia Sea at 59.1 cal ka B.P. developing into perennial sea-ice cover by 51.6 cal ka B.P. At this time, the Adélie Land Coast at 64° 17' 12" S was characterized by relatively stable permanently open ocean conditions, and shows no evidence of sea-ice influence.

WSI continued to expand into the northern Scotia Sea to its maximum extent at ~53° 56' S at 35.8 cal ka B.P. Adjacent to the Adélie Land Coast, open ocean conditions continued to prevail, with a strong ACC signal. Conditions in the Scotia Sea began to improve and SSTs increased between 35.8 cal ka B.P. and 33.2 cal ka B.P. This is marked by a retreat of perennial and seasonal sea-ice cover across the Scotia Sea, and the establishment of permanently open ocean conditions at both 53° 56' S and 61° 47' 3" S by 34.4 cal ka B.P.

and 33.2 cal ka B.P. respectively. During this period of sea-ice retreat from the Scotia Sea, the Adélie Land Coast experienced relatively stable, permanently open conditions in the strong presence of the ACC (Figure 6.19).

6.6.1.2. 32.2 cal ka B.P. to 17.7 cal ka B.P.

The second episode of WSI expansion into the southern Scotia Sea, occurred at 32.2 cal ka B.P. with development of perennial sea-ice cover by 29.2 cal ka B.P. This coincided with the introduction of distinctly colder surface waters at 64° 17' 12" S adjacent to the Adélie Land Coast from 31 cal ka B.P. A continued expansion of this WSI is indicated by the influx of cold surface waters at 53° 56' S at the northern Scotia Sea site at 25 cal ka B.P. and at the Adélie Land Coast site at 25.1 cal ka B.P. WSI expanded further equatorward in both the northern Scotia Sea and adjacent to the Adélie Land Coast at 24.1 cal ka B.P., but sea-ice proxies indicate that in each case the maximum sea-ice edge is only marginally north of the core site latitudes. By 22.9 cal ka B.P. there was a poleward retreat of the WSI and SSI edge is poleward of 61° 47' 3" S into the Weddell Sea. Adjacent to the Adélie Land Coast, the WSI edge also shows its first retreat south of the core site between 23.6 cal ka B.P. and 23.1 cal ka B.P., beginning a 5.9 kyr period (23.6 cal ka B.P. to 17.7 cal ka B.P.) of expansive seasonal sea-ice conditions, probably extending from the continental margin to 64° 17' 12" S. This seasonal regime is similar in the Scotia Sea, where, between 22.4 cal ka B.P. and 17.8 cal ka B.P., the WSI edge rapidly expands and retreats in the region between the Weddell Sea and northern Scotia Sea (Figure 6.19).

6.6.1.3. Circum-Antarctic Sea-ice: Discussion

This circum-Antarctic comparison represents an important advance in understanding Antarctic sea-ice variability during the LGC. It shows that sea-ice advance and retreat has been far from synchronous around the Antarctic coast over the past ~47 kyrs. In particular, the WSI field showed considerable expansion between 59.1 cal ka B.P. and 35.8 cal ka B.P., extending to around 53° 56' S in the Scotia Sea and occupying the modern-day POOZ, just poleward of the APF. This implies an equatorward displacement of more than 3° in latitude from its modern-day extent.

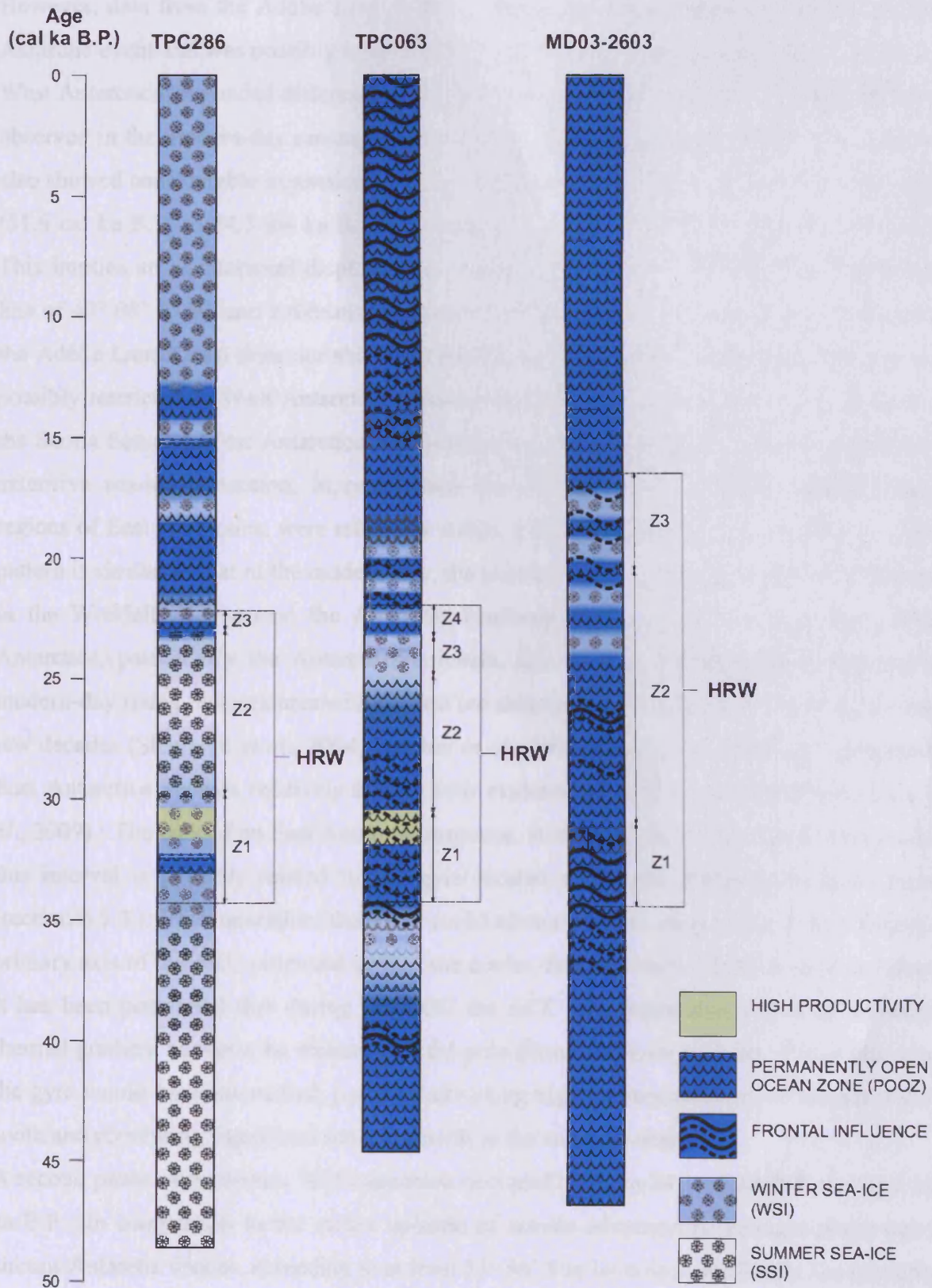


Figure 6.19. Downcore environmental logs for Southern Ocean cores TPC063, TPC286 and MD03-2603, showing contemporaneous nature of high-resolution windows (HRW) and related palaeoenvironmental zones (Z).

However, data from the Adélie Land Coast indicates that this expansion was not a circum-Antarctic event and was possibly restricted to West Antarctica, this suggests that the East and West Antarctica responded differently to climate forcing during the LGC. This has also been observed in the modern-day circum-Antarctic sea-ice field (Parkinson, 2004). The SSI field also showed considerable expansion in comparison to the modern-day limit during this period (51.6 cal ka B.P. to 34.3 cal ka B.P.), extending to at least $61^{\circ} 47' 3''$ S in the Scotia Sea. This implies an equatorward displacement of at least $\sim 6^{\circ}$ in latitude along the longitudinal line of $40^{\circ} 08' 3''$ W, and a diminished sea-ice seasonality compared to present. Once again the Adélie Land Coast does not show this feature at this time and so the SSI expansion was possibly restricted to West Antarctica. Hence, between 59.1 cal ka B.P. to 35.8 cal ka B.P. the Scotia Sea and West Antarctica were sensitive to climate changes, which is manifest in extensive sea-ice expansion, in comparison the Adélie Land Coast, and possibly larger regions of East Antarctica, were relatively stable, with no evidence of sea-ice advance. This pattern is similar to that of the modern-day, the primary sea-ice production centres are located in the Weddell Sea, around the Antarctic Peninsula and down to the Ross Sea. West Antarctica, particularly the Antarctic Peninsula, has recently demonstrated a response to modern-day rising temperatures with several ice sheet collapses and glacier retreat in the past few decades (Shepherd *et al.*, 2004; Bamber *et al.*, 2007, Steig *et al.*, 2009). In comparison East Antarctica appears relatively stable, with evidence of declining temperatures (Steig *et al.*, 2009). The lack of an East Antarctic response, at least off the Adélie Land Coast during this interval is possibly related to the gyre located within the Antarctic-Australia Basin (section 6.5.3.). If in operation, the gyre would advect warmer, more saline waters from the primary axis of the ACC poleward toward the cooler, fresher waters off the continental slope. It has been postulated that during the LGC the ACC was intensified due to an enhanced thermal gradient between the equator and the pole (Stuut and Lamy, 2004). If this did occur the gyre would have intensified, possibly advecting higher concentrations of warmer waters south and preventing significant sea-ice growth in the surface waters.

A second phase of maximum WSI expansion occurred between 24.1 cal ka B.P. and 23.5 cal ka B.P. In comparison to the earlier episode of sea-ice advance this younger phase was a circum-Antarctic feature, extending to at least $53^{\circ} 56'$ S in latitude in the Scotia Sea (possibly into the modern-day APFZ) and to at least $64^{\circ} 17' 12''$ S along the Adélie Land Coast. This indicates an equatorward displacement of 3° to 4° in latitude in the Scotia Sea, but a similar position to the present along the Adélie Land Coast. The rapid retreat of both WSI and SSI

from the Scotia Sea and into the Weddell Sea between 23.5 cal ka B.P. and 22.9 cal ka B.P. indicate that the Scotia Sea (West Antarctica) was sensitive to perturbations in climate. WSI also showed a relatively rapid retreat around 23 cal ka B.P. along the Adélie Land Coast (East Antarctica), indicating a circum-Antarctic response to this period of warming (Figure 6.20).

The SSI field in the Scotia Sea also showed considerable expansion at this time, extending to at least 55° 33' S (TPC290) between 29.2 cal ka B.P. and ~23 cal ka B.P.; an equatorward displacement of ~12° in latitude, which would have resulted in a reduced seasonality compared to the present. In comparison, there is no evidence of SSI edge advance along the Adélie Land Coast, agreeing with Crosta *et al.* (1998) that the SSI edge in this region of the Antarctic during the glacial was probably similar to its modern position. The restriction of SSI expansion to West Antarctica again implies that West Antarctica was much more sensitive to perturbations in climate than East Antarctica (Between 51.6 cal ka B.P. and 23.5 cal ka B.P.).

Gersonde *et al.* (2005) proposed that WSI reached a maximum extent of ~52° S in the Scotia Sea and ~54° S along the Adélie Land Coast, between 23 cal ka B.P. and 19 cal ka B.P. (Figure 6.20.). The data presented here agrees with this extent, but due to the benefit of a longer time-series these new core data build on this suggestion and indicate that maximum WSI expansion actually occurred a little earlier than the E-LGM (Mix *et al.*, 2001), between 24.1 cal ka B.P. and 23.5 cal ka B.P., and was less extensive along the Adélie Land Coast (Figure 6.20). Based on the Scotia Sea reconstruction of SSI this study also suggests that Southern Ocean temperatures, within the Atlantic sector of the Southern Ocean at least, were coldest during the period 29.2 cal ka B.P. to 22.9 cal ka B.P., rather than during the E-LGM (~21 cal ka B.P.), supporting the suggestion by Gersonde *et al.* (2003), and that this period was followed by an interval of strong warming around ~23 cal ka B.P., which is supported by ice-core (EPICA, 2006) and SST records (Kaiser *et al.*, 2005). Strong cooling between ~30 cal ka B.P. and 25 cal ka B.P. is supported by SST and sea-ice records from the East Atlantic and East Indian sectors of the Southern Ocean (Gersonde *et al.*, 2003; Armand and Leventer, 2003; Crosta *et al.*, 2004). My data also allows a more extensive assessment of SSI variability during the LGC. The data indicates that the majority of LGM time-slice studies underestimate the expansion of SSI (in the Atlantic sector of the Southern Ocean), although a greater extent during the cold interval highlighted above is alluded to by Gersonde *et al.* (2003). The data presented here also indicates that the majority of LGM time-slice studies also overestimate the circum-Antarctic expansion and permanence of WSI (Figure 6.20).

The relative variability of SSI and WSI has important implications for the dynamics of the seasonal sea-ice zone, which can exert a significant impact on global climate dynamics. My data indicates that during the glacial, between 59.1 cal ka B.P. and 23.5 cal ka B.P., sea-ice seasonality in the Scotia Sea was considerably reduced in comparison to the present, a conclusion that disagrees with the majority of circum-Antarctic sea-ice reconstructions, which propose enhanced seasonality during maximum sea-ice extent (Gersonde *et al.*, 2005). A reduction in the seasonality of Antarctic sea-ice would result in an increase in the Southern Ocean's efficiency as an albedo surface due to an expanded permanent sea-ice surface. Such a change would increase the thermal gradient between the pole and equator, resulting in a less stable atmospheric circulation and increased storminess. This extensive covering of sea-ice would also act to reduce sea-air gas/heat exchange, and limit the ventilation of gases such as CO₂. This effect would be compounded by more stable MIZ conditions during WSI retreat, which have the capability of supporting more intense diatom blooms, increasing CO₂ drawdown. The decrease in the seasonal production of WSI would also result in a reduction in deep-water formation, slowing the global propagation of heat within the global ocean conveyor (THC).

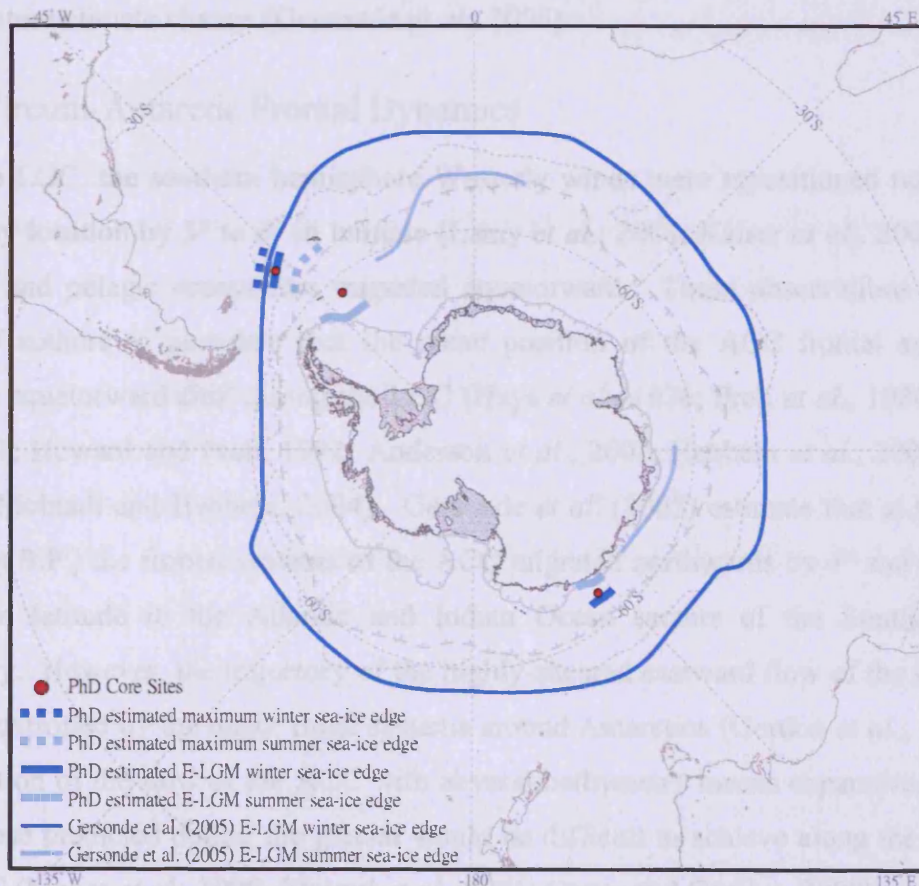


Figure 6.20. PhD estimated winter and summer sea-ice edges at their maximum extent during the last glacial cycle and at the E-LGM, compared to Gersonde *et al.* (2005) E-LGM sea-ice reconstruction.

The lack of evidence regarding SSI expansion along the Adélie Land Coast however, indicates that a reduction in glacial sea-ice seasonality during maximum sea-ice extent was not a circum-Antarctic feature. However, there was a marked regime shift in sea-ice seasonality in the Scotia Sea between 22.4 cal ka B.P. and 17.8 cal ka B.P. when the SSI edge was confined to the Weddell Sea, whereas the WSI edge expanded to the northern Scotia Sea. This period of enhanced seasonality coincides with similar seasonal dynamics along the Adélie Land Coast between 23.6 cal ka B.P. and 17.7 cal ka B.P. This indicates that between 22.4 cal ka B.P. and 17.8 cal ka B.P. enhanced sea-ice seasonality was possibly a circum-Antarctic feature related to increasing levels of southern hemisphere summer insolation (Beger and Loutre, 1991) that would have important implications for the climate system; decreasing albedo efficiency and the strength of equator – pole thermal gradients, increasing sea-air gas/heat exchange and the ventilation of gases such as CO₂. It would induce a less stable water column, decreasing surface water productivity and associated CO₂ drawdown and result in a large increase in the production of deep and bottom waters, increasing the velocity of the ACC and thus the global transport of heat within the global ocean conveyor (THC). These data will help test climate models and increase their ability to accurately simulate future climate change (Gersonde *et al.*, 2005).

6.6.2. Circum-Antarctic Frontal Dynamics

During the LGC, the southern hemisphere Westerly winds were repositioned north of their modern-day location by 5° to 6° in latitude (Lamy *et al.*, 2004; Kaiser *et al.*, 2005; Ledru *et al.*, 2006) and pelagic ecosystems migrated equatorward. These observations have led a number of authors to postulate that the mean position of the ACC frontal systems also showed an equatorward shift during the LGC (Hays *et al.*, 1976; Prell *et al.*, 1980; Mortlock *et al.*, 1991; Howard and Prell, 1992; Anderson *et al.*, 2002; Hebbeln *et al.*, 2002; Lamy *et al.*, 2004; Mohtadi and Hebbeln, 2004). Gersonde *et al.* (2005) estimate that at the E-LGM (~21 cal ka B.P.) the frontal systems of the ACC migrated northwards by 4° and between 5° and 10° in latitude in the Atlantic and Indian Ocean sectors of the Southern Ocean, respectively. However, the trajectory of the highly-sheared eastward flow of the ACC fronts is firmly controlled by the major ridge systems around Antarctica (Gordon *et al.*, 1978), thus the interaction of the flow of the ACC with abyssal bathymetry means expansive migrations such as those predicted during the glacial would be difficult to achieve along the full length of the ACC (Moore *et al.*, 1999; Rintoul *et al.*, 2001; Carter and Cortese, 2009).

Comparison of the reconstructions of the APF and Southern Boundary shows that the timing, amplitude and duration of variability associated with these fronts, during the LGC, was not homogeneous between the two regions.

6.6.2.1. 44.7 cal ka B.P. to 34.3 cal ka B.P.

Between 44.7 cal ka B.P. and 34.3 cal ka B.P. the position of the APF, in the northern Scotia Sea, co-varies with fluctuations in WSI; migrating toward, away from and toward 53° 56' S between 44.7 cal ka B.P. and 37.2 cal ka B.P., 37.2 cal ka B.P. and 35.8 cal ka B.P. and 35.8 cal ka B.P. and 34.3 cal ka B.P. respectively. Subsequent to the third migration the APF remains close to 53° 56' S until 28.3 cal ka B.P. At a similar time (41.9 cal ka B.P. and 32.2 cal ka B.P.), adjacent to the Adélie Land Coast, the signature of the Southern Boundary grows in influence, gradually becoming a permanent feature at 64° 17' 12" S.

6.6.2.2. 32.2 cal ka B.P. to 24 cal ka B.P.

Between 28.3 cal ka B.P. and 24 cal ka B.P. the APF in the northern Scotia Sea migrates away from 53° 56' S, coinciding with the influx of cold surface waters and expansion of WSI. A similar phenomenon is observed adjacent to the Adélie Land Coast, where between 32.2 cal ka B.P. and 24.6 the signature of the Southern Boundary weakens as cold surface waters and WSI expand over 64° 17' 12" S.

6.6.2.3. 24 cal ka B.P. to 17.8 cal ka B.P.

In the northern Scotia Sea, the APF returns to 53° 56' S between 24 cal ka B.P. and 22.3 cal ka B.P. as WSI cover retreats from its peak extent. Between 22.3 cal ka and 17.9 cal ka B.P. the influence of the APF at 53° 56' S migrates away from and toward the core site in relation to fluctuations in the seasonal sea-ice zone. Adjacent to the Adélie Land Coast the signature of the Southern Boundary at 64° 17' 12" S occurs repeatedly between 22.6 cal ka B.P. and 17.8 cal ka B.P, coinciding with the fluctuating WSI edge. The signature of the Southern Boundary over 64° 17' 12" S disappears once more at 17.8 cal ka B.P., coeval with the final WSI meltback associated with deglaciation.

6.6.2.4. Circum-Antarctic Fronts: Discussion

These migrations of the frontal systems of the ACC would have important oceanographic and climatic implications, effecting intermediate water formation, deep ocean ventilation, rates of air-sea gas and heat exchange as well as ecosystem shifts effecting the efficiency of the Southern Ocean biological pump and associated CO₂ drawdown (Anderson, 2002). The APF

is an important boundary in terms of air-sea fluxes and the heat and salt budgets of the Southern Ocean (Moore and Abbott, 2002) and the Southern Boundary represents an extensive source of nutrients to support primary production. Phytoplankton blooms along frontal boundaries play an important role in the sequestration of CO₂ (Tynan, 1998).

Direct comparison of the reconstructions of the APF and Southern Boundary from cores TPC063 and MD03-2603 respectively, is difficult, as each record is recovered from a different environment that represents a different component of the ACC zonal flow. The Scotia Sea is one of the most constrictive portions of the ACC where the ACC and its associated frontal systems are forced through the relatively narrow Drake Passage and exit the Scotia Sea via a restricted number of deep ocean clefts in the Scotia Arc. The associated deep-water flow of the primary ACC front, the APF, reconstructed here, is presently constrained at two locations, entering the Scotia Sea via Drake Passage, and exiting via Shag Rocks Passage. In comparison, core MD03-2603 is located at the poleward extent of the ACC in the southeast Indian Ocean sector of the Southern Ocean, one of the most expansive regions of ACC flow (Orsi *et al.*, 1995). The frontal systems of the ACC are physically segregated as they enter the Australia-Antarctica Basin via topographic lows in the Kerguelen Plateau and subsequently navigate the southeast Indian Ocean Ridge (Orsi *et al.*, 1995; Rintoul *et al.*, 2001; Reid, 2003; McCartney and Donohue, 2007) and the Southern Boundary flows especially close to the Antarctic continent in this ocean basin. However, if, as predicted by several authors (Hebbeln *et al.*, 2002; Lamy *et al.*, 2004; Mohtadi and Hebbeln, 2004; Kaiser *et al.*, 2005), the entire ACC system makes latitudinal shifts in response to the strengthening/weakening of the southern hemisphere Westerly winds, it is reasonable to assume that near synchronous frontal migrations should be apparent in both the APF in the Scotia Sea and the Southern Boundary adjacent to the Adélie Land Coast.

This reconstruction of the APF in the Scotia Sea shows a high degree of variability over the past 44.7 cal ka B.P., with migrations away from and toward the core site associated with changes in the surface water regime. In comparison, the Southern Boundary reconstruction implies a much more stable system, generally showing a constant presence over or near the core site, despite the prevalence of WSI. These differences in behaviour of the frontal systems could potentially relate to the complex relationships between the frontal systems and the surface water regime. For example, the frequent and fast response of the APF in the Scotia Sea could be a consequence of pinning points at Drake Passage and Shag Rocks Passage where only a relatively short section of the APF (the 'S-shaped' meander) has to

react in order to record variability in the diatom assemblage. In contrast, the broader, more expansive characteristics of the ACC in the southeast Indian Ocean results in a larger system to shift, leading to a slower, more sluggish response of the Southern Boundary. In addition, the APFZ represents a clear surface water boundary between the cold, nutrient-rich surface waters of the AZ and the relatively warm, nutrient-poor waters of the SAZ. As such, its reconstruction is primarily based on shifts in relative positioning of surface waters relating to the AZ and SAZ. Surface water regimes are easily influenced by the WSI edge, which could explain the apparent high variability of the APF in conjunction with WSI fluctuations. In comparison, the Southern Boundary delineates the poleward extent of UCDW and does not directly relate to a surface water boundary. As such, although the influence of the Southern Boundary is ‘capped’ by the presence of seasonal sea-ice and MIZ conditions, the position of the front is not ‘forced’ to migrate in any way. This distinction could explain the relative stability of the Southern Boundary in comparison to the APF.

Although constricted by the bathymetry of the Scotia Sea, the shifts shown by the APF and associated surface waters during the glacial could relate to large-scale circum-polar shifts in the ACC, possibly triggered by displacement of the southern hemisphere Westerly winds. If this is indeed the case it is not unreasonable to assume that the Southern Boundary adjacent to the Adélie Land Coast should record shifts at a similar time. However, the low variability shown by the Southern Boundary at no point appears synchronous with that of the APF, implying that synchronous circum-Antarctic migrations of the frontal systems of the ACC were not a feature of the LGC.

6.7. Summary

In this chapter I have discussed and compared the reconstructed environmental variability of the Scotia Sea and Adélie Land Coast during the LGC. Based on a robust relative palaeointensity chronology (Chapter 5), independently verified by the first identification of the Laschamps Event in the Scotia Sea, I show that between at least 46.9 cal ka B.P. and ~25 cal ka B.P., the environmental response to climate was divergent between the Scotia Sea and the Adélie Land Coast, the Scotia Sea being dynamic and sensitive to perturbations in climate, and the Adélie Land Coast relatively stable. Between ~25 cal ka B.P. and 17.3 cal ka B.P. the chronology is less robust but is supported by several independently dated regional records of palaeo-climate. Both environmental settings show regional differences in terms of the rate, duration and magnitude of palaeoceanographic change. Between ~25 cal ka B.P.

Chapter 6. Interpretation and Discussion

and 17.7 cal ka B.P., the environmental response to climate was similar in the Scotia Sea and Adélie Land Coast and included maximum glacial sea-ice extents between 24.1 cal ka B.P. and 23.5 cal ka B.P.

7. Addressing the Aims

In this section I address the 4 aims outlined in Chapter 1:

- Was West Antarctica as sensitive to perturbations in climate during the last glacial cycle (LGC) as it is today?
- Was East Antarctica as stable in comparison to West Antarctica during the LGC as it appears today?
- When was the last glacial maximum (LGM)?
- How important were changes in the Southern Ocean to global climate during marine isotope stages (MIS) 2 and 3?

7.1. Was West Antarctica as sensitive to perturbations in climate during the LGC as it is today?

West Antarctica is today dominated by a marine based ice sheet, grounded at over 2 km below sea-level in places, which holds the equivalent of 6 m of global sea-level rise (Anderson, 1999). The West Antarctic Ice Sheet (WAIS) drains into and is potentially buttressed by extensive ‘continent-sized’ ($>530 \times 10^3 \text{ km}^2$) ice shelves that extend hundreds of kilometres off shore and are grounded at water depths of up to 1300 m (Anderson, 1999), making them, along with the WAIS, highly susceptible to perturbations in climate. The WAIS has been shown to be one of the most rapidly warming regions on the planet, with temperatures rising more than 0.1°C per decade for the past 50 years (Steig *et al.*, 2009) and in response a number of glaciers and ice shelves that litter the West Antarctic coast have recently shown signs of retreat, thinning and collapse. The Pine Island, Thwaites and Smith glaciers and related ice shelves in the Amundsen Sea region have sped up and progressively thinned during at least the last 15 years (Shepherd *et al.*, 2004; Bamber *et al.*, 2007). In addition, the Larsen A ice shelf collapsed in 1995 followed by Larsen B in 2002 and most recently the Wilkins ice shelf in 2008. In order to help understand the modern-day response of West Antarctica to the changing climate it is important to determine how West Antarctica has responded during past interval of rapid climate changes, for example during the last glacial cycle when rapid millennial-scale change was a standard feature of the climate system. A key question for palaeoclimate studies is: was West Antarctica as sensitive to perturbations in climate during the last glacial cycle as it is today?

Here I focus on the marine realm of West Antarctica, more precisely the sediment archives of the Scotia Sea, which can provide valuable insight into the past dynamics of climatic change in West Antarctica. The Scotia Sea, is located in the South Atlantic sector of the Southern Ocean, sandwiched between the ‘Antarctic’ Weddell Sea and the ‘Atlantic’ Argentine Basin and thus between Antarctic and Atlantic climatic signals. The marine based WAIS is thought to respond primarily to changes in the surrounding ocean, including increasing SSTs and sea-level rise (Kanfoush *et al.*, 2000; Huybrechts *et al.*, 2002). Due to repeated episodes of glacial advance and retreat since the onset of Antarctic glaciation geomorphological evidence from the continental shelf cannot be used to accurately determine the behaviour of the WAIS during the LGC. As a sensitive indicator of oceanographic change, sea-ice reconstructions should provide a useful gauge for WAIS sensitivity.

The sea-ice reconstructions from cores TPC286 and TPC063 (Chapter 6, sections 6.1, 6.2 and 6.3), indicate that the Scotia Sea was a highly dynamic environment during the last ~60 kyrs, with a high degree of sensitivity and responsiveness to oceanographic and climate forcings. This sensitivity is manifest as two episodes of sea-ice advance and retreat across the entire Scotia basin (Section 6.3.). These episodes are characterised by extensive summer sea-ice (SSI) and winter sea-ice (WSI) expansion, a gradual advance across the Scotia basin, brief maxima and a rapid retreat. The first episode occurred between 59.1 cal ka B.P. and 33.2 cal ka B.P. with the SSI and WSI advancing gradually across the Scotia Sea (23.3 kyrs), culminating in a maximum WSI extent (~53° 56' S) at 35.8 cal ka B.P. Duration of the maxima was extremely brief, with the WSI edge having retreated entirely from the basin by 33.2 cal ka B.P. The second episode is observed between 32.2 cal ka B.P. and 22.9 cal ka B.P., with SSI and WSI showing a relatively gradual advance across the basin (8.1 kyrs), with the WSI edge reaching its maximum extent (53° 56' S) by 24.1 cal ka B.P. Maximum conditions persisted for 600 years, until 23.5 cal ka B.P. and were followed by rapid retreat (600 years) across the basin, with the WSI edge having retreated from the basin entirely by 22.9 cal ka B.P.

These episodes show that sea-ice responses in this region of the West Antarctic, comparable to the scale of those at glacial maxima, were also occurring during the preceding ~30 kyrs. Such large-scale changes in the Scotia Sea sea-ice field can be related to larger regional changes in oceanic and atmospheric temperatures (Chapter 6, Figure 6.14) and could indicate that West Antarctica responded to millennial-scale climate changes during the LGC in a similar fashion as it is to the rapidly rising temperatures of the present-day. More regional

studies from the West Antarctic are needed in order to determine the robustness of this finding.

7.2. Was East Antarctica's climate stable in comparison to West Antarctica during the LGC as it appears today?

East Antarctica is today dominated by the East Antarctic Ice Sheet (EAIS), a huge ice mass, grounded predominantly above sea-level, averaging 3 km in thickness and representing the equivalent of 66 m of global sea-level rise. The EAIS drains into outlet glaciers that protrude from the towering ice cliffs that characterise much of the East Antarctic coast, which for the most part lacks the extensive ice shelves characteristic of West Antarctica (Anderson, 1999). In contrast to the rapidly warming West, East Antarctica is shown to exhibit slight cooling over the past 50 years (Steig *et al.*, 2009) and the large-scale collapses witnessed in West Antarctica have thus far been absent in the East. Although a number of East Antarctic glaciers in the sector ~100 - 160° E do appear to be thinning slightly near their grounding lines (Bamber *et al.*, 2007). Due to its sheer size, being grounded mainly above sea-level and the lack of sensitive ice shelves, the EAIS is thought to have been relatively stable for the past 14 million years (Denton *et al.*, 1993; Sugden *et al.*, 1993; Ingólfsson, 2005) and recent satellite altimetry data indicates that the EAIS is presently gaining mass in relation to elevated precipitation (Davis *et al.*, 2005). Due to the severe implications for global climate that a melting of the EAIS would have, it is important to determine whether the present changes occurring in West Antarctica are a precursor for future change in the East, or whether the stability of the East will prevail over modern climate changes. In order to determine this it is key to understand the variability of the EAIS during the last glacial cycle, the most recent period of rapid millennial scale climate change. One of the most pressing questions confronting today's palaeoclimate studies is: was East Antarctica as stable in comparison to West Antarctica during the last glacial cycle as it appears today?

Here I focus on the marine realm of East Antarctica, more precisely a sediment archive from the Adélie Land Coast, which can provide valuable insight into the past dynamics of climatic change in East Antarctica. The Adélie Land Coast is located on the Wilkes Land Margin of East Antarctica, a primary drainage basin of the EAIS. This region is characterised by a number of outlet glaciers, the most impressive of which are the Ninnis and Mertz Glacier Tongues. Today, the coastline supports several polynya systems and is thought to produce up to 25% of all Antarctic Bottom Waters (AABW). The sediment core from the Adélie Land

Coast provides valuable insight into the past dynamics of climatic change in this region of East Antarctica. The reconstruction of sea-ice variability adjacent to the Adélie Land Coast during the glacial indicates that this sector of the East Antarctic coast remained relatively stable during the period 46.9 cal ka B.P. to 25 cal ka B.P., in contrast to the dynamic nature of the Scotia Sea in the west, but between 25 cal ka B.P. and 17.8 cal ka B.P. the sea-ice behaviour of the two regions was similar, increasing to maximum conditions and maintaining an expanded WSI field until deglaciation.

The reconstructed palaeoceanography shows a relatively stable system between 46.9 cal ka B.P. and 31 cal ka B.P., with the local environment dominated by permanently open ocean conditions and frontal upwelling, in contrast to the Scotia Sea, which was characterised by the first of two expansive episodes of sea-ice advance, this is potentially the result of warmer waters being advected south by an invigorated gyre circulation in the Australia-Antarctic Basin as a result of the strengthening of the southern Westerly wind belt or possibly due to the absence of a sea-ice factory such as the Weddell Sea south of the Scotia Sea. A gradual change in the palaeoceanography at the Adélie Land Coast is observed around 31 cal ka B.P. when the local environment is characterised by the gradual influx of colder surface waters becoming most prominent at 24.5 cal ka B.P., when temperatures capable of supporting the growth of WSI are established. An influx of cold surface waters is also noted in the northern Scotia Sea, later, at around 25 cal ka B.P. At the Adélie Land Coast the WSI edge appears to reach a maximum extent close to the core site (64° 17' 12" S) between 24.1 cal ka B.P. and 23.6 cal ka B.P. and WSI in the Scotia Sea also reaches a near synchronous maximum extent at 24.1 cal ka B.P., and also retreats around 23.5 cal ka B.P. Further, between 22.4 cal ka B.P. and 17.8 cal ka B.P., both the Adélie Land Coast and Scotia Sea are the sites of an expansive seasonal sea-ice zone. These findings indicate the relative stability of the Adélie Land Coast, in comparison with the Scotia Sea, was a feature of the LGC between 46.9 cal ka B.P. and ~25 cal ka B.P. However, the WSI of both regions appear to show a coincident expansion between ~25 cal ka B.P. and 23.5 cal ka B.P., with a regime shift in the Scotia Sea around 22.4 cal ka B.P. resulting in synchronous expansive seasonal sea-ice zones between 22.4 cal ka B.P. and 17.8 cal ka B.P. in both the Scotia Sea and along the Adélie Land Coast, this regime shift is potentially in response to changes in the southern hemisphere insolation budget (Berger and Loutre, 1991). More regional studies are required in order to determine whether these environmental patterns are indeed characteristic of the entirety of East Antarctica and West Antarctica and whether maximum WSI expansion and seasonal sea-ice zone dynamics were indeed synchronous around the Antarctic during the LGC.

7.3. When was the last glacial maximum?

High-resolution sea-ice reconstructions from East Antarctica (Adélie Land Coast) and West Antarctica (Scotia Sea) presented in this study suggest a circum-Antarctic sea-ice maximum between 24.1 cal ka B.P. and 23.5 cal ka B.P. This indicates a sea-ice maximum earlier than the globally recognised LGM (~21 cal ka B.P.) and enables better temporal placement of previous LGM time-slice sea-ice reconstructions.

Although sea-ice is not a significant component of integrated global maximum ice volume, it is an important component of climate change via a series of positive feedback mechanisms. The most recent and most cited reconstruction of circum-Antarctic sea-ice extent during the LGC is the EPILOG LGM (E-LGM) time-slice reconstruction (Gersonde *et al.*, 2005). Gersonde *et al.* (2005) propose that at the E-LGM (23 cal ka B.P. to 19 cal ka B.P.) the Antarctic WSI field showed a circum-Antarctic expansion of 100% relative to the modern-day extent. Whether sea-ice maxima coincide with local LGM conditions, or represent a sensitive precursor to local terrestrial glacial maxima, accurate identification of this interval will provide a constraint for the onset of any local LGM and provide valuable boundary conditions for climate models. The regional sea-ice reconstructions that I present in this study offer the opportunity to determine the earliest possible onset of a local LGM and to validate some of the results of Gersonde *et al.* (2005).

The high-resolution sea-ice records from the Scotia Sea and Adélie Land Coast presented in this thesis show sea-ice expansion episodes between 32.2 cal ka B.P. and 17.8 cal ka B.P. in the Scotia Sea and between ~25 cal ka B.P. and 17.7 cal ka B.P. along the Adélie Land Coast, and indicate a circum-Antarctic WSI maxima between 24.1 cal ka B.P. and 23.5 cal ka B.P., earlier than the E-LGM (Mix *et al.*, 2001) (Figure 7.1). Based on the Scotia Sea SSI reconstruction I also propose that Southern Ocean temperatures, within the Atlantic sector at least, were coldest during the period 29.2 cal ka B.P. to 23.5 cal ka B.P., rather than during the E-LGM and were quickly followed by a period of strong warming around 23 cal ka. Together this data implies synchronous sea-ice maxima in both the West Antarctic and East Antarctic between 24.1 cal ka B.P. and 23.5 cal ka B.P. These findings indicate a constraint of 24.1 cal ka B.P. should be considered as an earliest possible onset for the local LGM in the Scotia Sea and along the Adélie Land Coast, and a larger window of 29.2 cal ka B.P. to 17.8 cal ka B.P. indicating the coldest conditions in the Southern Ocean during the LGC. The latter window, indicating coldest conditions in the Southern Ocean isn't too dissimilar to the LGM window 27 cal ka B.P. to 20 cal ka B.P. proposed by Suggate and Almond (2005).

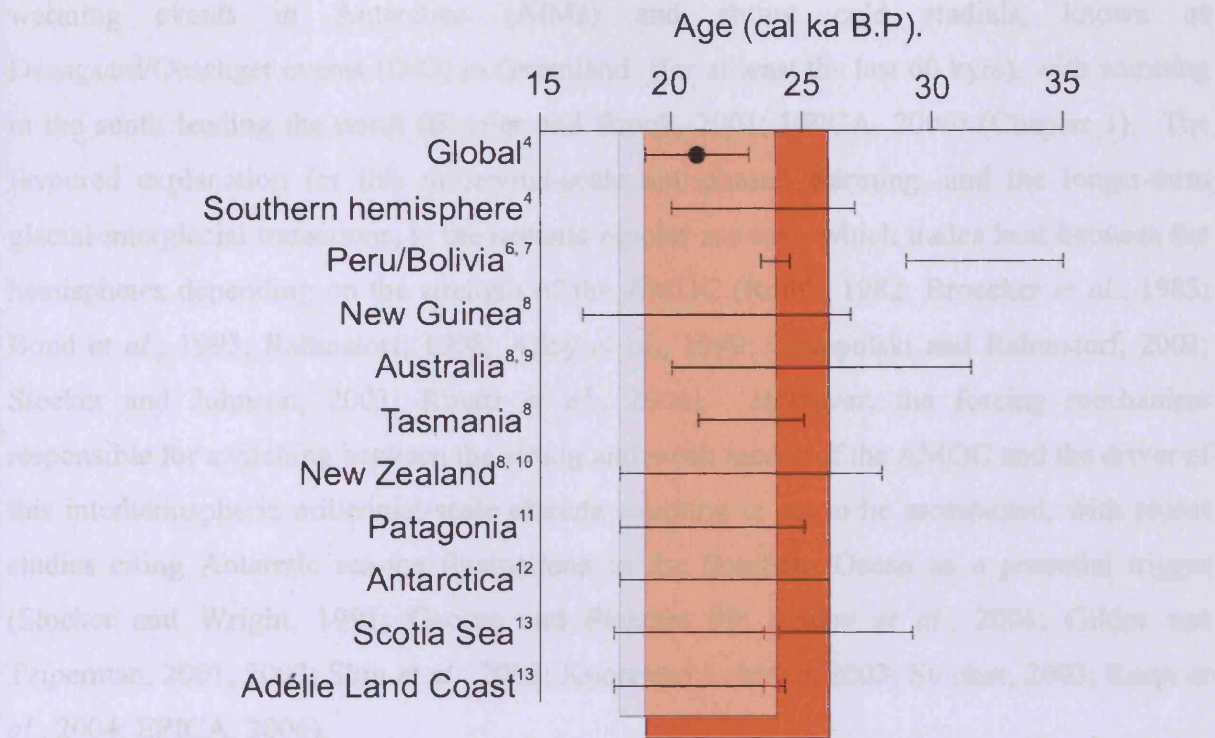


Figure 7.1. Demonstration of the large variation in the timings of local LGMs in comparison to global and hemispheric LGM windows. Dark band indicates the LGM as derived from sea-level lowstands. Light band indicates the duration of Marine Isotope Stage 2, as derived from oxygen isotopes. References: 1. Peltier and Fairbanks (2006), 2. Hanebuth *et al.* (2009), 3. Martinson *et al.* (1987), 4. Mix *et al.* (2001), 5. Suggate and Almond (2005), 6. Bromley *et al.* (2009), 7. Smith *et al.* (2005), 8. Barrows *et al.* (2002), 9. Petherick *et al.* (2008), 10. Denton *et al.* (1999b), 11. Kaplan *et al.* (2008), 12. Petit *et al.* (1999), 13. This study, red bar indicates maximum sea-ice conditions.

7.4. What was the role of the Southern Ocean in global forcings and feedbacks during MIS 2 and 3?

The Antarctic sea-ice reconstructions presented in this study indicate that, within the constraints of our age-model, Antarctic sea-ice retreat may have closely coincided with Antarctic Isotope Maxima (AIM), as shown in Antarctic ice cores, and possibly preceded increased concentrations of North Atlantic Deep Water (NADW) in the South Atlantic, implying a trigger for Atlantic Meridional Overturning Circulation (AMOC) resumption and potentially explaining interhemispheric climate coupling shown in Antarctic and Greenland ice core records as suggested in previous studies (Knorr and Lohmann, 2003; Shin *et al.*, 2003; EPICA, 2006).

The geologic record provides abundant evidence that abrupt climatic change was a fundamental characteristic of global climate during the LGC (110 ka to 10 ka). The global nature of this climatic variability is shown most emphatically in the high-resolution ice core records from Greenland and Antarctica, which show a one-to-one coupling of gradual

warming events in Antarctica (AIMs) and abrupt cold stadials, known as Dansgaard/Oeschger events (D/O) in Greenland (for at least the last 60 kyrs), with warming in the south leading the north (Blunier and Brook, 2001; EPICA, 2006) (Chapter 1). The favoured explanation for this millennial-scale anti-phased warming, and the longer-term glacial-interglacial transitions, is the oceanic bipolar sea-saw, which trades heat between the hemispheres depending on the strength of the AMOC (Rooth, 1982; Broecker *et al.*, 1985; Bond *et al.*, 1993; Rahmstorf, 1998; Alley *et al.*, 1999; Ganopolski and Rahmstorf, 2001; Stocker and Johnson, 2003; Knutti *et al.*, 2004). However, the forcing mechanism responsible for switching between the strong and weak modes of the AMOC and the driver of this interhemispheric millennial-scale climate coupling is yet to be ascertained, with recent studies citing Antarctic sea-ice fluctuations in the Southern Ocean as a potential trigger (Stocker and Wright, 1991; Goosse and Fichefet 99; Seidov *et al.*, 2001; Gildor and Tziperman, 2001, 2003; Shin *et al.*, 2003; Knorr and Lohman, 2003; Stocker, 2003; Kaspi *et al.*, 2004; EPICA, 2006).

Sea-ice is a sensitive, fast reacting amplifier, capable of causing enhanced glacial climate variability through complex positive feedbacks related to albedo budgets and heat, moisture and salinity transfers, and has important ramifications for deep ocean circulation, atmospheric circulation and CO₂ budgets (Stephens and Keeling, 2001; Thomas & Dieckmann, 2003; Gildor and Tziperman, 2001, 2003; Crosta *et al.*, 2004; Kaspi *et al.*, 2004; Stuut and Lamy, 2004). A sensitive temperature threshold for formation and decay and rapid advance and retreat, possibly due to albedo related feedbacks, not only makes this critical climatic parameter an important amplifier of glacial climate, but also affords the potential for an abrupt forcing mechanism responsible for millennial-scale climate change. Expanded Antarctic sea-ice fields in the Southern Ocean during the LGC could impact the global climate through several mechanisms. For example, an expanded sea-ice field will reduce surface temperatures due to enhanced albedo, i.e. the reflection of solar energy. This will increase the equator-pole thermal gradient and could potentially intensify the polar vortex. This could in turn force an equatorward migration of the southern hemisphere Westerly wind belt, shifting moisture-bearing air masses northward (Stuut and Lamy, 2004). Secondly, an expanded Antarctic sea-ice field in the Southern Ocean would cause an expansion of the sea-ice zone and result in an equatorward shift of the Permanently Open Ocean Zone (POOZ) and Antarctic Polar Front Zone (APFZ). Even if the large, latitudinal movements of the geostrophic deep water jets of the ACC are restricted by sea-floor topography, surface water environments would shift northward (Kanfoush, 2000; Carter and Cortese, 2009). The APFZ

is the optimal area of primary productivity in the Southern Ocean, recorded in the sediments as a circumpolar opal belt. Sea-ice cover over this normally highly productive region would reduce CO₂ drawdown during photosynthesis (Sigman and Boyle, 2001). It is further suggested that an expanded Antarctic winter sea-ice field in the Southern Ocean would have a strong impact on the ventilation of CO₂ and other gases from the deep ocean. It is proposed that either year round sea-ice cover, or winter sea-ice cover combined with strong ice-induced summer stratification, would severely curtail upwelling and thus deep water ventilation and air-sea gas exchange (Stephens and Keeling, 2000; Sigman and Boyle, 2000). Sea-ice can also exert a strong impact on the formation of deep waters. The formation of sea-ice results in brine rejection from the ice crystal lattice, leading to a brine injection into surrounding surface waters. This significantly increases the salinity and thus density of surrounding waters and induces convection and the formation of deep waters. The overall balance of deepwater formation is dependent upon sea-ice seasonality and the size of the seasonal ice zone, i.e. the area of ocean only covered during the winter months. An increase in this area, i.e. a greater expansion of the WSI field relative to the SSI, will result in a greater production of deep and bottom waters and enhance the velocity of the ACC and impact the intensity of the AMOC (Crosta *et al.*, 1998; Gersonde *et al.*, 2003, 2005). Modelling results also indicate that mass sea-ice retreat in the Southern Ocean has the ability to enhance the flow regime of the AMOC through increased transport of warm, saline surface waters into the North Atlantic via the Indian Ocean (Knorr and Lohmann, 2003). Through these mechanisms Antarctic sea-ice fluctuations in the Southern Ocean can play a pivotal role in millennial-scale climate changes, on a regional, hemispheric and potentially global scale during the LGC.

The high-resolution Antarctic sea-ice reconstructions, spanning the late glacial and termination 1, presented in this study, provide an opportunity to investigate the potential relationships required to validate the recent EPICA community suggestion that the intrinsic feedbacks of a reduced sea-ice cover in the Southern Ocean during AIMs, followed by a delayed onset of deep-water formation in the north, could potentially explain the interhemispheric climate coupling seen in our records during MIS 3. The validation of this statement could also have important ramifications for the proposed impact of Southern Ocean sea-ice cover on the ventilation of CO₂ (Stephens and Keeling, 2001). Unfortunately the age-model presented in this study, although one of the better chronologies from the Southern Ocean, is not accurate enough to determine precise peak-to-peak phasing between these climate components (Chapter 5). Inherent differences between age-models and sampling resolution may also cause slight offsets between different climate records. However, close

correlations with independently dated regional records (Chapter 6) gives us confidence to assess the likelihood of the EPICA (2006) implied relationships between Southern Ocean sea-ice extent and other key components of the climate system during the LGC.

I investigate the validity of the EPICA statement through the comparison of three new, high-resolution Southern Ocean glacial sea-ice reconstructions from the Scotia Sea (TPC286, TPC063) and Adélie Land Coast (MD03-2603) with several key proxy records detailing the primary climate dynamics during the LGC (Figure 8.1). These records include the high-resolution ice core temperature records from EPICA Dronning Maud Land (EDML) and the North Greenland Ice-core Project (NGRIP) employed by EPICA community members to demonstrate the one-to-one interhemispheric climate coupling during MIS3 (EPICA, 2006), a composite CO₂ curve from the EPICA Dome C and Byrd ice cores (Monnin *et al.*, 2001; Ahn and Brook, 2008), and a record of neodymium isotope ratios from the South Atlantic, which are used as a proxy of the balance between NADW and AABW (Piotrowski *et al.*, 2008). The comparison of my sea-ice reconstruction high-resolution windows (HRWs) with these data (Figure 7.2) identify several interesting features:

- Expanded SSI in the Scotia Sea is evident during the HRW between 29.2 cal ka B.P. and 22.9 cal ka B.P. This phase of perennial sea-ice cover appears to coincide with the coldest phase of the EDML temperature record, between AIM 4 and AIM 2 (Figure 7.2), indicating regionally low temperatures. Secondly the onset of SSI advance is appear to be lagged slightly by a marked drop in CO₂ concentrations as recorded in the Byrd ice core, and appears to coincide with an interval of reduced AABW production in favour of increased NADW production (Figure 7.2). An expanded SSI field would reduce upwelling and deep water ventilation, preventing sea-air gas exchange and reduce the size of the seasonal ice zone, the site of deep water formation.
- According to the sea-ice reconstructions presented in this thesis maximum WSI extent is a synchronous circum-Antarctic feature occurring in both the Scotia Sea and along the Adélie Land Coast between 24.1 and ~23.5 cal ka B.P. When considering the inherent differences between age models and sampling resolution, and potential error in our chronology, this peak could potentially occur at the culmination of the low in temperatures between AIM 4 and AIM 2 recorded in the EDML ice core and the end of the longest cold period in the NGRIP temperature record (Figure 7.2).

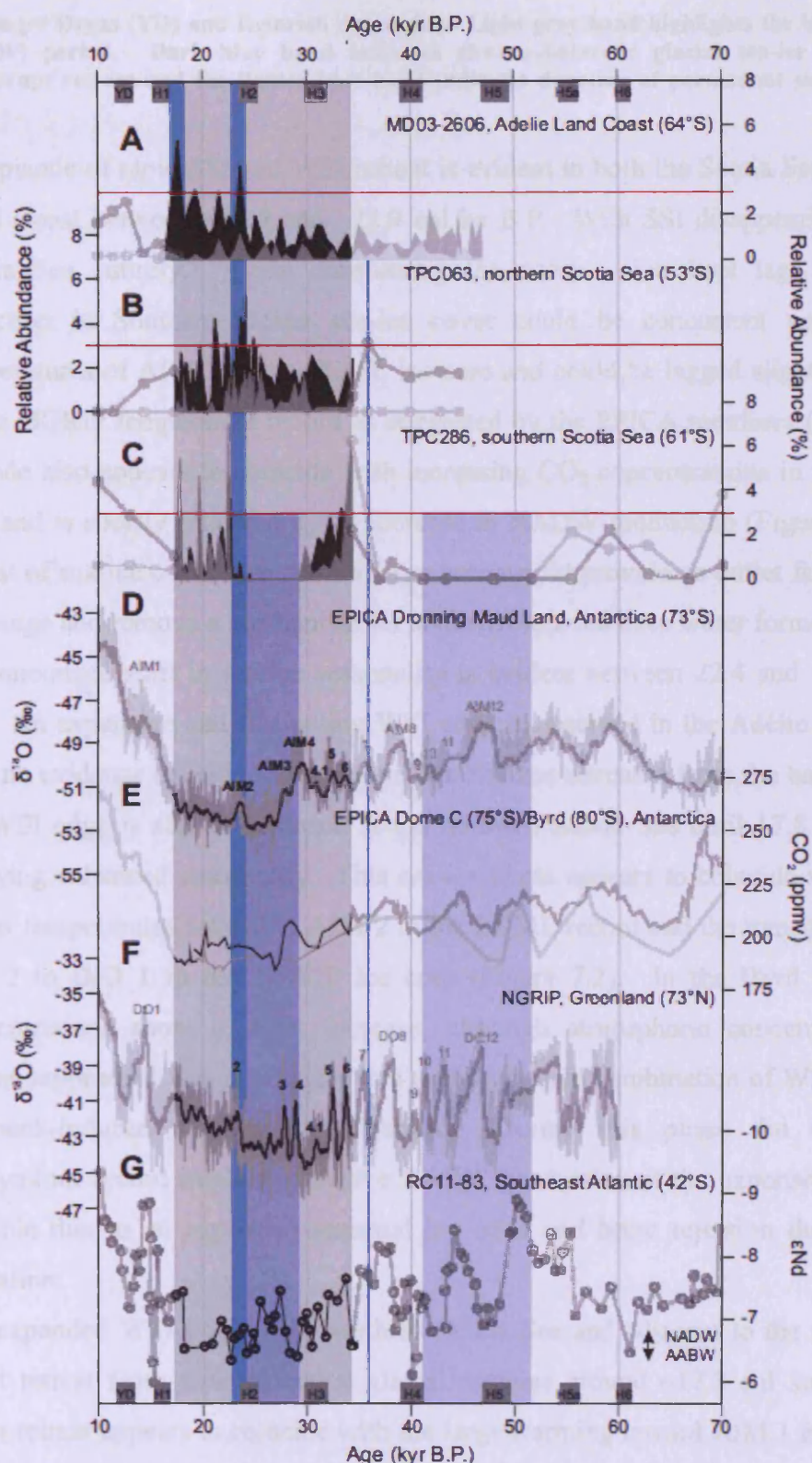


Figure 7.2. Comparison of Antarctic sea-ice dynamics with global records of millennial scale climate change during the LGC. A-C) Diatom fossil-based sea-ice reconstructions from cores MD03-2603, TPC063 and TPC286, *Fragilariopsis* sea-ice group (black) and *Fragilariopsis obliquecostata* (gray). Open circles indicate low-resolution data and red line show the 3% sea-ice presence threshold (this study). D) Oxygen isotope record from EDML ice core, Antarctica (EPICA, 2006). E) Carbon dioxide records from EDC and Byrd ice cores, Antarctica Monnin *et al.*, 2001; Ahn and Brook, 2008. F) Oxygen isotope record from NGRIP ice core, Greenland EPICA, 2006. G) Neodymium record as a measure of bottom water formation from the Cape Basin, South Atlantic (Piotrowski *et al.*, 2008). Small dark gray blocks indicate

timing of Younger Dryas (YD) and Heinrich events (H). Light gray band highlights the high-resolution window (HRW) period. Dark blue band indicates circum-Antarctic glacial sea-ice maxima and subsequent abrupt retreat and the lighter blue band indicates duration of permanent sea-ice cover in Scotia Sea.

- An episode of rapid SSI and WSI retreat is evident in both the Scotia Sea and Adélie Land Coast between ~23.5 and ~22.9 cal ka B.P. With SSI disappearing from the Scotia Sea entirely. Again considering the ocean – ice-sheet lag, this marked reduction in Southern Ocean sea-ice cover could be concurrent with the high temperatures of AIM 2 in the EDML ice core and could be lagged slightly by D/O 2 in the NGRIP temperature record as suggested by the EPICA members (2006). This episode also appears to coincide with increasing CO₂ concentrations in the Byrd ice core and is shortly followed by an increase in NADW production (Figure 7.2). The retreat of sea-ice cover over such a large area would provide an outlet for sea-air gas exchange and remove a mechanism for southern sourced deep water formation.
- A pronounced shift in sea-ice seasonality is evident between 22.4 and ~17.8 cal ka B.P. An expansive and fluctuating WSI edge is observed in the Adélie Land Coast, with no evidence of SSI. In the Scotia Sea SSI has retreated from the basin, whereas the WSI edge is still in evidence at the northern Scotia Sea until 17.8 cal ka B.P., implying enhanced seasonality. This sea-ice phase appears to coincide with a return to low temperatures following AIM 2 in the EDML record and the transition between D/O 2 to D/O 1 in the NGRIP ice core (Figure 7.2). In the Byrd CO₂ record, concentrations show a slight increase, although atmospheric concentrations still appear suppressed, this is possibly due to the seasonal combination of WSI cover and meltback-induced summer stratification. During this phase the Cape Basin neodymium record implies extensive AABW production at the expense of NADW, possible due to an expanded seasonal ice zone and brine rejection during sea-ice formation.
- The expanded WSI field in the northern Scotia Sea and adjacent to the Adélie Land Coast retreat from their extended glacial margins around ~17.8 cal ka B.P. This major retreat appears to coincide with the large warming toward AIM 1 in the EDML ice core and toward D/O 1 in the NGRIP ice core (Figure 7.2). A marked increase in CO₂ concentrations in Byrd are also evident at this point, possibly due to a reduced zone of ice cover and stratification, and is followed by a large peak in NADW potentially due to diminished AABW production through reduced brine injection and enhanced transport of warm, saline surface waters into the North Atlantic via the

Indian Ocean (Figure 7.2). This supports the mechanism for AMOC resumption suggested by Knorr and Lohmann (2003).

Although our chronology is not accurate enough to determine phasing between these climate components the records do indicate a good relationship between sea-ice fluctuations, Antarctic and Greenland temperature records, deep water formation budgets and atmospheric CO₂ concentrations. Sea-ice advance and retreat appears to coincide with variations in Antarctic temperatures, possibly responding to this temperature change through variations in Southern Ocean heat accumulation due to intensity changes within the AMOC or possibly forcing the change through hemispheric cooling in response to obliquity led changes in high-latitude summer insolation (Vandergoes *et al.*, 2005). Sea-ice retreat could be forced once heat accumulation builds to a maximum (i.e. AIM 2) and a new equilibrium must be reached. The resulting sea-ice meltback could potentially significantly reduce or shutdown AABW production and result in a delayed resumption of the AMOC in the North Atlantic through the mechanism proposed by Knorr and Lohmann (2003). The transfer of heat from the Southern Ocean to the North Atlantic would result in a further reduction in Antarctic temperatures. Changes in atmospheric CO₂ concentrations potentially lag changes in Southern Ocean sea-ice cover and seasonal regime, which in turn appear to respond to Southern Ocean heat accumulation and changes in summer insolation budgets. Expansion of the SSI field and reduced seasonality restricts ocean upwelling and air-sea gas exchange resulting in reduced atmospheric CO₂ concentrations. The retreat of the SSI field combined with a shift to enhanced seasonality lessens the restriction on ocean ventilation but maintains some degree of control through WSI cover and summer stratification. Gradual retreat of the WSI field in addition to SSI results in steadily rising atmospheric CO₂ concentrations.

The relationships between Southern Ocean sea-ice variability, Antarctic Isotope Maxima, deep-water formation and CO₂ variability identified in this section confirms that Southern Ocean sea-ice potentially plays an important role in global millennial-scale climate change during the LGC, as suggested by EPICA community members (2006), but can not yet determine its role as a potential driver of this system. This study offers much needed insight into glacial Southern Ocean sea-ice dynamics in a location and at a resolution that, for the first time, allows comparison with glacial climate dynamics and validation of model-based hypotheses. Further high-resolution regional reconstructions of glacial Southern Ocean sea-ice dynamics are urgently required in order to further develop our understanding of this critically important component of millennial-scale climate change and its phasing with other climate components.

7.5. Future Work

7.5.1. Scotia Sea Low-Resolution Sections

I recommend additional high-resolution analysis of the low-resolution sections of Scotia Sea cores TPC063 and TPC286 in order to investigate implied synchronicity with the palaeoclimate records illustrated in Figure 8.1. The sections of cores TPC063 and TPC286 sampled at a lower resolution (open circles Figure 8.1.) indicate the continuation of the dynamics observed during the HRW (dark grey band Figure 8.1.) throughout MIS 3. Several consistent features are indicated in Figure 8.1:

- A potential episode of winter sea-ice retreat in core TPC286 appears to coincide with Antarctic warming event AIM 14.
- SSI expansion into the Scotia Sea (TPC286) between 51.6 cal ka B.P. and 36.9 cal ka B.P. appears to coincide with phases of cooling in the EDML temperature record between AIM 13 and AIM 8 and is also lagged by associated drops in CO₂ concentrations in the Byrd core. Although warming event AIM 12 occurs in the middle of this period of SSI expansion, possibly calling into question the above interpretation, the event occurs at a point outside of the sampling resolution and re-sampling this portion of the record at a higher resolution could improve the fit.
- WSI maxima in the northern Scotia Sea (TPC063) appears to occur at the end of these cooling episodes (AIM 13 to AIM 8) with retreat phases possibly concurrent with AIM 8 and AIM 7.
- Variability within the neodymium isotope ratios also indicates a degree of consistency between deep-water formation and the sea-ice record.

Additional sampling of these core sections would enable the validation of these potentially vital relationships.

7.5.2. Additional Core Sites

Additional core sites would help confirm the primary oceanographic features evident in the regional reconstructions presented here, specifically:

- Recovery of a high-resolution sediment core along the Adélie Land Coast, from a latitude between core MD03-2603 (64° 17' 12" S, 139° 22' 51" E) (this study) and MD88-787 (56° 22' 48" S, 145° 18' E) (Gersonde *et al.*, 2005), would prove valuable in further constraining the extent of glacial sea-ice between 24.1 cal ka B.P. and 17.8 cal ka B.P.

- Further, the recovery of a high-resolution sediment core from a latitude between MD03-2603 (64° 17' 12" S, 139° 22' 51" E) (this study) and the Adélie Land Coast continental margin would prove valuable in determining whether there was any expansion of SSI along this margin of the continent during the last ~60 kyrs.
- A core site northwest of TPC063, along the North Scotia Ridge (NSR) could further constrain fluctuations of the APF, and potentially determine whether the frontal jet did in fact deviate from its deep-water pathway through Shag Rocks Passage. A potential coring site was identified during British Antarctic Survey cruise JR179 in the form of a drift deposit located poleward of Burdwood Bank.
- A high-resolution core recovered from the central Scotia Sea, north of core TPC290 and south of TPC063, would further constrain the extent of SSI during between 29.2 cal ka B.P. and 22.9 cal ka B.P.
- And finally, a core site recovered south of TPC286, from the Weddell Sea, could further constrain the poleward limit of the expansive seasonal ice zone identified here between 22.4 cal ka B.P. and 17.8 cal ka B.P.

7.5.3. Highly Branched Isoprenoids

All indications from the present work regarding highly branched isoprenoids (HBIs) are that these biochemical fingerprints have great potential as a proxy for sea-ice. Studies comparing modern marine sediments (<20 years), characterised by extremely high, seasonal sedimentation rates, with satellite chlorophyll data are slowly revealing the intricacies and seasonal dynamics of the relationship between HBI production and sea-ice (G. Massé, pers. Com.). The pilot study conducted here, showing the potential of HBIs in Quaternary sediments, has uncovered similar relationships to those identified in the studies of modern sediments and indicates that HBIs will also be a very useful proxy for palaeosea-ice reconstructions. I recommend further high-resolution work on this proxy in the cores presented in this study and in other high-resolution Quaternary sediments.

7.5.4. *Hyalochaete Chaetoceros* Resting Spore Productivity Peak

Low preservation potential of calcareous sediments and the dilution effect of 'old carbon' inhibit the application of conventional Quaternary dating techniques on Southern Ocean sediments. The identification of a unique productivity event at 30.9 cal ka B.P. in sediment

cores TPC063 and TPC286, possibly generated through volcanic/dust fertilization or meltwater stratification, assisted in the development of a robust age model in this study. A clearly defined association between productivity events and accurately dated volcanic eruptions or meltwater pulses could provide a useful chronological marker for Late Quaternary sediments recovered from the Scotia Sea. I recommend further investigation into this potential relationship, which could prove invaluable considering the difficulties associated with many Antarctic marine sediments.

7.5.5. Relative Palaeointensity versus Beryllium-10

The generation of a robust age model and the first categorical identification of the Laschamps Event in the Scotia Sea, and possibly Antarctic sediments, support the application of relative palaeointensity (RPI) as an accurate dating tool. This technique could prove very important for the notoriously ‘difficult to date’ Southern Ocean sediments south of the APF and I recommend further application on other Scotia Sea and Southern Ocean sediments to improve the reliability and accuracy of the regional and global comparisons of palaeoclimate records. I further recommend the comparison of the RPI records generated in this study with Beryllium-10 (^{10}Be) records from high-resolution Antarctic ice cores, possibly the Berkner or EDML cores. Like RPI records, fluctuating concentration of ^{10}Be are a direct result of changes in the dynamics of the Earth’s magnetic field. Accurate correlations between these two archives, especially in the South Atlantic sector of the Southern Ocean (i.e. Scotia Sea) are urgently required in order to validate the proposed role of the bi-polar seesaw mechanism in the propagation of millennial-scale climate change.

A means of accurately comparing these two climate archives was recently proposed by Pugh *et al.* (2009), who suggest the correlation of Scotia Sea and Southern Ocean magnetic susceptibility records with Antarctic ice core dust records. The authors suggest that the magnetic susceptibility signal in Southern Ocean sediments is controlled by the input of the same fine-grained atmospheric dust that is deposited over the Antarctic Ice Sheet and show a strong correlation between the two. However, as demonstrated in this study, important sediments exposed to perennial sea-ice cover do not have reliable magnetic susceptibility records, thus invalidating this relationship. RPI/ ^{10}Be correlations could provide a viable alternative.

References

- Abbott, M. R., J. G. Richman, R. M. Letelier and J. S. Bartlett (2000). "The spring bloom in the Antarctic Polar Frontal Zone as observed from a mesoscale array of bio-optical sensors." *Deep Sea Research Part I: Oceanographic Research Papers* **47**(15-16): 3285-3314.
- Abbott, M. R., J. G. Richman, J. S. Nahorniak and B. S. Barksdale (2001). "Meanders in the Antarctic Polar Frontal Zone and their impact on phytoplankton." *Deep Sea Research Part II: Topical Studies in Oceanography* **48**(19-20): 3891-3912.
- Abbott, W. H. (1974). "Temporal and spatial distribution of Pleistocene diatoms from the southeast Indian Ocean." *Nova Hedwigia Beiheft* **25**: 291-346.
- Abelmann, A. and R. Gersonde (1991). "Biosiliceous particle-flux in the Southern Ocean." *Marine Chemistry* **35**(1-4): 503-536.
- Abelmann, A., R. Gersonde and V. Spiess (1990). "Pliocene - Plietocene palaeoceanography in the Weddell Sea - siliceous microfossil evidence." *Book: Geological History of the Polar Oceans: Arctic Versus Antarctic*: 729-759.
- Ahn, J. and E. J. Brook (2008) "Atmospheric CO₂ and climate on millennial time scales during the last glacial period." *Science* **322**: 83-85
- Allredge, A. L. and C. C. Gotschalk (1989). "Direct observations of the mass flocculation of diatom blooms: characteristics, settling velocities and formation of diatom aggregates." *Deep Sea Research Part I: Oceanographic Research Papers* **36**: 159-171.
- Allen, C. S. (2003). Late Quaternary palaeoceanography of the Scotia Sea, Southwest Atlantic: Evidence from the Diatom Record. *School of Earth, Ocean and Planetary Science*. Cardiff, Cardiff University, Ph.D: 218.
- Allen, C. S., J. Pike, C. J. Pudsey and A. Leventer (2005). "Submillennial variations in ocean conditions during deglaciation based on diatom assemblages from the southwest Atlantic." *Paleoceanography* **20**(2): doi:10.1029/2004PA001055.
- Alley, R. B., J. Marotzke, W. D. Nordhaus, J. T. Overpeck, D. M. Peteet, R. A. Pielke, R. T. Pierrehumbert, P. B. Rhines, T. F. Stocker, L. D. Talley and J. M. Wallace (2003). "Abrupt climate change." *Science* **299**(5615): 2005-2010.
- Anderson, J. B. (1999). *Antarctic Marine Geology*. Cambridge, Cambridge University Press.
- Anderson, J. B., S. S. Shipp, A. L. Lowe, J. S. Wellner and A. B. Mosola (2002). "The Antarctic Ice Sheet during the Last Glacial Maximum and its subsequent retreat history: a review." *Quaternary Science Reviews* **21**(1-3): 49-70.
- Anderson, R. F., Z. Chase, M. Q. Fleisher and J. Sachs (2002). "The Southern Ocean's biological pump during the Last Glacial Maximum." *Deep Sea Research Part II: Topical Studies in Oceanography* **49**(9-10): 1909-1938.
- Andreoli, C., C. Tolomio, I. Moror, M. Radice, E. Moschin and S. Bellato (1995). "Diatoms and dinoflagellates in Terra Nova Bay (Ross Sea-Antarctica) during austral summer 1990." *Polar Biology* **15**: 465-475.
- Arhan, M., A. C. N. Garabato, K. J. Heywood and D. P. Stevens (2002). "The Antarctic Circumpolar Current between the Falkland Islands and South Georgia." *Journal of Physical Oceanography* **32**(6): 1914-1931.
- Armand, L. (1997). The use of diatom transfer functions in estimating sea-surface temperature and sea-ice in cores from the southeast Indian Ocean. *Geology*, Australian National University.
- Armand, L. (2000). An ocean of ice - Advance in the estimation of past sea ice in the Southern Ocean. *GSA Today*. **10**: 1-7.
- Armand, L. K., X. Crosta, O. Romero and J.-J. Pichon (2005). "The biogeography of major diatom taxa in Southern Ocean sediments: 1. Sea ice related species." *Palaeogeography, Palaeoclimatology, Palaeoecology* **223**(1-2): 93-126.
- Armand, L. K. and A. Leventer (2003). Palaeo sea ice distribution, reconstruction and palaeoclimatic

- significance. Sea Ice – An Introduction to its Physics, Chemistry, Biology and Geology. Thomas, D.N. and Dieckmann, G. S. Oxford, Blackwell Science Ltd: 333-372.
- Arrigo, K. (2003). Primary production in sea ice. Sea Ice – An Introduction to its Physics, Chemistry, Biology and Geology. Thomas, D.N. and Dieckmann, G. S. Oxford, Blackwell Science Ltd: 143-183.
- Arrigo, K. and D. N. Thomas (2004). "Large scale importance of sea ice biology in the Southern Ocean." *Antarctic Science* 16(04): 471-486.
- Arrigo, K., D. L. Worthen, P. Dixon and M. P. Lizotte (1998). Primary productivity of near surface communities within Antarctic pack ice. Antarctic Sea Ice: biological processes, interactions and variability; Antarctic Research Series. B. o. A. Editors. Washington DC, American Geophysical Union. 73: 198.
- Arrigo, K. A., M. P. Lizotte, D. L. Worthen, P. Dixon and G. Dieckmann (1997). "Primary production in Antarctic sea ice." *Science* 276: 394-397.
- Arrigo, K. R., D. H. Robinson, R. B. Dunbar, A. R. Leventer and M. P. Lizotte (2003). "Physical control of chlorophyll a, POC, and TPN distributions in the pack ice of the Ross Sea, Antarctica." *Journal of Geophysical Research - Oceans* 108(C10): art. no.-3316.
- Arrigo, K. R. and C. W. Sullivan (1992). "The influence of salinity and temperature covariation on the photophysiological characteristics of Antarctic sea ice microalgae." *Journal of Phycology* 28(6): 746-756.
- Bak, Y.-S., K.-C. Yoo, H. I. Yoon, J.-D. Lee and H. Yun (2007). "Diatom evidence for Holocene paleoclimatic change in the South Scotia Sea, West Antarctica." *The Association of Korean Geoscience Societies* 11(1): 1-92.
- Bamber, J. L., R. B. Alley and I. Joughin (2007). "Rapid response of modern day ice sheets to external forcing." *Earth and Planetary Science Letters* 257(1-2): 1-13.
- Bao, R., V. M. and R. Prego (1997). "Mesoscale distribution patterns of diatoms in surface sediments as tracers of coastal upwelling of the Galician shelf (NW Iberian Peninsula)." *Marine Geology* 144: 117-130.
- Barker, P. F., & Burrell, J. (1977). "The opening of Drake Passage." *Marine Geology* 25: 15-34.
- Barker, P. F. (2001). "Scotia Sea regional tectonic evolution: implications for mantle flow and palaeocirculation." *Earth Science Reviews* 55(1-2): 1-39.
- Barker, P. F., & Thomas, E. (2004). "Origin, signature and palaeoclimatic influence of the Antarctic Circumpolar Current." *Earth Science Reviews* 66: 143-162.
- Barker, P. F. and J. Burrell (1977). "The opening of Drake Passage." *Marine Geology* 25: 15-34.
- Barker, P. F., J. A. Dalziel and B. C. Storey (1991). Tectonic development of the Scotia Arc region. The Geology of Antarctica. R. J. Tingey. Oxford, Clarendon Press: 215-248.
- Barker, P. F., B. Diekmann and C. Escutia (2007). "Onset of Cenozoic Antarctic glaciation." *Deep Sea Research Part II: Topical Studies in Oceanography* 54(21-22): 2293-2307.
- Barker, P. F., G. M. Filippelli, F. Florindo, E. E. Martin and H. D. Scher (2007). "Onset and role of the Antarctic Circumpolar Current." *Deep Sea Research Part II: Topical Studies in Oceanography* 54(21-22): 2388-2398.
- Barker, S., P. Diz, M. J. Vautravers, J. Pike, G. Knorr, I. R. Hall and W. S. Broecker (2009). "Interhemispheric Atlantic seesaw response during the last deglaciation." *Nature* 457: 1097-1103.
- Barrows, T. T., J. O. Stone, L. K. Fifield and R. G. Cresswell (2001). "Late Pleistocene Glaciation of the Kosciuszko Massif, Snowy Mountains, Australia." *Quaternary Research* 55(2): 179-189.
- Barrows, T. T., J. O. Stone, L. K. Fifield and R. G. Cresswell (2002). "The timing of the Last Glacial Maximum in Australia." *Quaternary Science Reviews* 21(1-3): 159-173.
- Bart, P. J. and J. B. Anderson (2000). "Relative temporal stability of the Antarctic ice sheets during the late Neogene based on the minimum frequency of outer shelf grounding events." *Earth and Planetary Science Letters* 182(3-4): 259-272.
- Barth, C., G. H. Krause and K. Winter (2001). "Responses of photosystem I compared with photosystem II to high-light stress in tropical shade and sun leaves." *Plant, Cell and Environment* 24: 163-176.
- Basile, I., F. E. Grousset, M. Revel, P. E. Biscaye, J. R. Petit and N. I. Barkov (1997). "Patagonian origin of glacial dust deposited in East Antarctica Vostok, Dome C during stages 2, 4 and 6." *Earth and Planetary Science Letters* 146: 573-589.

- Bathmann, U., J. Priddle, P. Treguer, M. Lucas, Hall, J. and J. Parslow (2000). Plankton ecology and biogeochemistry in the Southern Ocean: a review of the Southern Ocean JGOFS. The Dynamic Ocean Carbon Cycle: A Midterm Synthesis of the Joint Global Ocean Flux Study. R. B. Hansen, Ducklow, H.W. and Field, J.G. **International Geosphere-Biosphere Programme Book**: 300-337.
- Bathmann, U. V., R. Scharek, C. Klaas, C. D. Dubischar and V. Smetacek (1997). "Spring development of phytoplankton biomass and composition in major water masses of the Atlantic sector of the Southern Ocean." *Deep Sea Research Part II: Topical Studies in Oceanography* **44**(1-2): 51-67.
- Baumgartner, S., Beer, J., Masarik, J., Wagner, G., Meynadier, L. and Synal, H.A. (1998). "Geomagnetic modulation of ^{36}Cl flux in the GRIP ice core Greenland." *Science* **279**: 1330-1332.
- Baumgartner, S., J. Beer, M. Suter, B. Dittich-Hannen, H.-A. Synal, P. W. Kubik, C. Hammer and S. Johnsen (1997). " ^{36}Cl fallout in the summit Greenland Ice Core Project ice core." *Journal of Geophysical Research* **102**: 26659-26662.
- Belkin, I. M. and A. L. Gordon (1996). "Southern Ocean fronts from the Greenwich meridian to Tasmania." *Journal of Geophysical Research - Oceans* **101**(C2): 3675-3696.
- Belt, S. T., G. Massé, S. J. Rowland, M. Poulin, C. Michel and B. LeBlanc (2007). "A novel chemical fossil of palaeo sea ice: IP25." *Organic Geochemistry* **38**(1): 16-27.
- Belt, S. T., G. Massé, S. J. Rowland and M. Rohmer (2006). "Highly branched isoprenoid alcohols and epoxides in the diatom *Haslea ostrearia* Simonsen." *Organic Geochemistry* **37**(2): 133-145.
- Bender, M., T. Sowers and L. Labeyrie (1994). "The Dole Effect and Its Variations During the Last 130,000 Years as Measured in the Vostok Ice Core." *Global Biogeochemical Cycles* **8**(3): 363-376.
- Berger, A. and M. F. Loutre (1991). "Insolation values for the climate of the last 10 million years." *Quaternary Science Reviews* **10**: 297-318.
- Bianchi, C and R. Gersonde (2004). "Climate evolution at the last deglaciation: the role of the Southern Ocean." *Earth and Science Planetary Letters* **228**: 407-424.
- Bianchi, G. G. and I. N. McCave (1999). "Holocene periodicity in North Atlantic climate and deep-ocean flow south of Iceland." *Nature* **397**(6719): 515-517.
- Bindoff, N. L., M. A. Rosenberg and M. J. Warner (2000). "On the circulation and water masses over the Antarctic continental slope and rise between 80 and 150 degrees E." *Deep Sea Research Part II: Topical Studies in Oceanography* **47**(12-13): 2299-2326.
- Bindoff, N. L., G. D. Williams and I. Allison (2001). Sea-ice growth and water-mass modification in the Mertz Glacier polynya, East Antarctica, during winter. *Annals of Glaciology*. Cambridge, International Glaciological Society. **33**: 399-406.
- Blain, S., B. Queguiner, L. Armand, S. Belviso, B. Bombled, L. Bopp, A. Bowie, C. Brunet, C. Brussaard, F. Carlotti, U. Christaki, A. Corbiere, I. Durand, F. Ebersbach, J. L. Fuda, N. Garcia, L. Gerringa, B. Griffiths, C. Guigue, C. Guillemin, S. Jacquet, C. Jeandel, P. Laan, D. Lefevre, C. Lo Monaco, A. Malits, J. Mosseri, I. Obernosterer, Y. H. Park, M. Picheral, P. Pondaven, T. Remenyi, V. Sandroni, G. Sarthou, N. Savoye, L. Scouarnec, M. Souhaut, D. Thuiller, K. Timmermans, T. Trull, J. Uitz, P. van Beek, M. Veldhuis, D. Vincent, E. Viollier, L. Vong and T. Wagener (2007). "Effect of natural iron fertilization on carbon sequestration in the Southern Ocean." *Nature* **446**(7139): 1070-U1.
- Blunier, T. and E. J. Brook (2001). "Timing of millennial-scale climate change in Antarctica and Greenland during the last glacial period." *Science* **291**(5501): 109-112.
- Bond, G., W. Broecker, S. Johnsen, J. McManus, L. Labeyrie, J. Jouzel and G. Bonani (1993). "Correlation between climate records from north-Atlantic sediments and Greenland ice." *Nature* **365**(6442): 143-147.
- Bond, G., H. Heinrich, W. Broecker, L. Labeyrie, J. McManus, J. Andrews, S. Huon, R. Jantschik, S. Clasen, C. Simet, K. Tedesco, M. Klas, G. Bonani and S. Ivy (1992). "Evidence for massive discharges of icebergs into the north-Atlantic Ocean during the last glacial period." *Nature* **360**(6401): 245-249.
- Bond, G. C. and R. Lotti (1995). "Iceberg discharges into the north-Atlantic on millennial time scales during the last glaciation." *Science* **267**(5200): 1005-1010.
- Bonhommet, N. and J. Babkine (1967). "Sur la presence d'aimantation inverses dans la Chaîne des Puys." *Compte Rendu Academy Science Series B* **264**: 92-94.
- Bonhommet, N. and J. Zähringer (1969). "Paleomagnetism and potassium-argon age determinations of the Laschamp geomagnetic polarity event." *Earth and Planetary Science Letters* **6**: 43-46.

- Booth, J. D. and L. H. Burckle (1976). "Displaced Antarctic diatoms in the southwestern and central Pacific." *Pacific Geology* 11: 99-108.
- Bowen, D. Q., F. M. Phillips, A. M. McCabe, P. C. Knutz and G. A. Sykes (2002). "New data for the Last Glacial Maximum in Great Britain and Ireland." *Quaternary Science Reviews* 21(1-3): 89-101.
- Boyd, P. W. (2004). "Ironing out algal issues in the Southern Ocean." *Science* 304: 396-397.
- Boyd, P. W., T. Jickells, C. S. Law, S. Blain, E. A. Boyle, K. O. Buesseler, K. H. Coale, J. J. Cullen, H. J. W. de Baar, M. Follows, M. Harvey, C. Lancelot, M. Levasseur, N. P. J. Owens, R. Pollard, R. B. Rivkin, J. Sarmiento, V. Schoemann, V. Smetacek, S. Takeda, A. Tsuda, S. Turner and A. J. Watson (2007). "Mesoscale Iron Enrichment Experiments 1993-2005: Synthesis and Future Directions." 315(5812): 612-617.
- Boyd, P. W., A. J. Watson, C. S. Law, E. R. Abraham, T. Trull, R. Murdoch, D. C. E. Bakker, A. R. Bowie, K. O. Buesseler, H. Chang, M. Charette, P. Croot, K. Downing, R. Frew, M. Gall, M. Hadfield, J. Hall, M. Harvey, G. Jameson, J. LaRoche, M. Liddicoat, R. Ling, M. T. Maldonado, R. M. McKay, S. Nodder, S. Pickmere, R. Pridmore, S. Rintoul, K. Safi, P. Sutton, R. Strzepek, K. Tanneberger, S. Turner, A. Waite and J. Zeldis (2000). "A mesoscale phytoplankton bloom in the polar Southern Ocean stimulated by iron fertilization." *Nature* 407(6805): 695-702.
- Brachfeld, S. A. and S. K. Banerjee (2000). "Rock-magnetic carriers of century-scale susceptibility cycles in glacial-marine sediments from the Palmer Deep, Antarctic Peninsula." *Earth and Planetary Science Letters* 176(3-4): 443-455.
- Bradley, R. S. (1999). *Palaeoclimatology: Reconstructing Quaternary Environments*, Academic Press.
- Brathauer, U., and A. Abelmann (1999) "Late Quaternary variation in sea surface temperatures and their relationship to orbital forcing recorded in the Southern Ocean." *Paleoceanography* 14(2): 135-138.
- Brierley, A. S. and D. N. Thomas (2002). "Ecology of Southern Ocean pack ice." *Advances in Marine Biology* 43: 171-276.
- Broecker, W. (1991). "The great ocean conveyor." *Oceanography* 4: 79-89.
- Broecker, W. (2001). The Big Climate Amplifier Ocean Circulation-Sea Ice-Storminess-Dustiness-Albedo. *The Oceans and Rapid Climate Change: Past, Present and Future*. D. Seidov, B. J. Haupt and M. Maslin. Washington, AGU. 126: 53-56.
- Broecker, W. S. (1994). "Massive iceberg discharges as triggers for global climate change." *Nature* 372(6505): 421-424.
- Broecker, W. S. (1994). "Ocean circulation - an unstable superconveyor." *Nature* 367(6462): 414-415.
- Broecker, W. S., G. C. Bond, M. Klas, E. Clark and J. F. McManus (1992). "Origin of the northern Atlantic's Heinrich events." *Climate Dynamics* 6: 265-273.
- Broecker, W. S. and S. Hemming (2001). PALEOCLIMATE: Climate Swings Come into Focus. 294: 2308-2309.
- Bromley, G. R. M., J. M. Schaefer, G. Winckler, B. L. Hall, C. E. Todd and K. M. Rademaker (2009). "Relative timing of last glacial maximum and late-glacial events in the central tropical Andes." *Quaternary Science Reviews* In Press, Corrected Proof.
- Brook, E. J., J. W. C. White, A. S. M. Schilla, M. L. Bender, B. Barnett, J. P. Severinghaus, K. C. Taylor, R. B. Alley and E. J. Steig (2005). "Timing of millennial-scale climate change at Siple Dome, West Antarctica, during the last glacial period." *Quaternary Science Reviews* 24(12-13): 1333-1343.
- Brown, B., C. Gaina and R. D. Müller (2006). "Circum-Antarctic palaeobathymetry: Illustrated examples from Cenozoic to recent times." *Palaeogeography, Palaeoclimatology, Palaeoecology* 231(1-2): 158-168.
- Brown, J., A. Colling, D. Park, J. Phillips, D. Rothery and J. Wright (1989). *Ocean Circulation*. Oxford, Pergamon Press plc.
- Brzezinski, M. A., M.-L. Dickson, D. M. Nelson and R. Sambrotto (2003). "Ratios of Si, C and N uptake by microplankton in the Southern Ocean." *Deep Sea Research Part II: Topical Studies in Oceanography* 50: 619-613
- Brzezinski, M. A., J. L. Jones and M. S. Demarest (2005). "Control of silica production by iron and silicic acid during the Southern Ocean Iron Experiment (SOFEX)." *Limnology and Oceanography* 50(3): 810-824.
- Brzezinski, M. A., D. M. Nelson, V. M. Franck and D. E. Sigmon (2001). "Silicon dynamics within an

- intense open-ocean diatom bloom in the Pacific sector of the Southern Ocean." *Deep Sea Research Part II: Topical Studies in Oceanography* 48(19-20): 3997-4018.
- Budillon, G., S. G. Cordero and E. Salusti (2002). "On the dense water spreading off the Ross Sea shelf (Southern Ocean)." *Journal of Marine Systems* 35(3-4): 207-227.
- Buesseler, K. O., R. T. Barber, M. L. Dickson, M. R. Hiscock, J. K. Moore and R. Sambrotto (2003). "The effect of marginal ice-edge dynamics on production and export in the Southern Ocean along 170 degrees W." *Deep Sea Research Part II: Topical Studies in Oceanography* 50(3-4): 579-603.
- Buffen, A., A. Leventer, A. Rubin and T. Hutchins (2007). "Diatom assemblages in surface sediments of the northwestern Weddell Sea, Antarctic Peninsula." *Marine Micropaleontology* 62(1): 7-30.
- Burckle, L. H. (1978). Early Miocene to Pliocene diatom datum levels for the equatorial Pacific. Proceedings Second Working Group Mtg. Biostratigraphic Datum Planes, Pacific Neogene, IGCP Proj. 114, Special Publication, Geological Research Development Center.
- Burckle, L. H. (1984). "Diatom distribution and paleoceanographic reconstruction in the Southern Ocean – Present and last glacial maximum." *Marine Micropaleontology* 9(3): 241-261.
- Burckle, L. H. (1987). "Diatom distribution in the Weddell Gyre region during late winter." *Micropaleontology* 33(2): 177-184.
- Burckle, L. H. and J. Cirilli (1987). "Origin of diatom ooze belt in the Southern Ocean - Implications for Late Quaternary paleoceanography." *Micropaleontology* 33(1): 82-86.
- Burckle, L. H. and D. W. Cooke (1983). "Late Pleistocene *Eucampia antarctica* abundance stratigraphy in the Atlantic sector of the Southern Ocean." *Micropaleontology* 29(1): 6-10.
- Burckle, L. H., D. E. Kellogg, T. B. Kellogg and J. L. Fastook (1997). "A mechanism for emplacement and concentration of diatoms in glaciogenic deposits." *Boreas* 26(1): 55-60.
- Burckle, L. H., D. Robinson and D. Cooke (1982). "Reappraisal of sea-ice distribution in Atlantic and Pacific sectors of the Southern Ocean at 18,000 yr BP." *Nature* 299(5882): 435-437.
- Burckle, L. H. and D. Stanton (1975). Distribution of displaced Antarctic diatoms in the Argentine Basin. Third Symposium on Recent and Fossil Marine Diatoms, Germany.
- Caburlotto, A., L. De Santis, C. Zanolla, A. Camerlenghi and J. K. Dix (2006). "New insights into Quaternary glacial dynamic changes on the George V Land continental margin (East Antarctica)." *Quaternary Science Reviews* 25(21-22): 3029-3049.
- Carcaillet, J., D. L. Bourlès, T. N. and M. Arnold (2004). "A high resolution authigenic $^{10}\text{Be}/^{9}\text{Be}$ record of geomagnetic moment variations over the last 300 ka from sedimentary cores of the Portuguese margin." *Earth and Planetary Science Letters* 219: 397-412.
- Carmack, E. C. and T. D. Foster (1975). "On the flow of water out of the Weddell Sea." *Deep Sea Research* 22: 711-724.
- Carter, L. and G. Cortese (2009). "Change in the Southern Ocean: Responding to Antarctica." *PAGES news* 17(1): 30-32.
- Cassata, W. S., B. S. Singer and J. Cassidy (2008). "Laschamp and Mono Lake geomagnetic excursions recorded in New Zealand." *Earth and Planetary Science Letters* 268(1-2): 76-88.
- Cassie, V. (1963). "Distribution of surface phytoplankton between New Zealand and Antarctica December 1957." *Trans-Antarctic Expedition 1955-1958 Scientific Reports* 7.
- Cavalieri, D. J. and S. Martin (1985). A passive microwave study of polynyas along the Antarctic Wilkes Land coast. Oceanology of the Antarctic Continental Shelf (AGU Antarctic Research Series No. 43). S. S. Jacobs. Washington D.C., American Geophysical Union: 227-252.
- Channell, J. E. T., D. A. Hodell, C. Xuan, A. Mazaud and J. S. Stoner (2008). "Age calibrated relative paleointensity for the last 1.5 Myr at IODP Site U1308 (North Atlantic)." *Earth and Planetary Science Letters* 274(1-2): 59-71.
- Channell, J. E. T., A. Mazaud, P. Sullivan, S. Turner and M. E. Raymo (2002). "Geomagnetic excursions and paleointensities in the Matuyama Chron at Ocean Drilling Program Sites 983 and 984 (Iceland Basin)." *Journal of Geophysical Research* 107.
- Channell, J. E. T., J. S. Stoner, D. A. Hodell and C. D. Charles (2000). "Geomagnetic paleointensity for the last 100 kyr from the sub-antarctic South Atlantic: a tool for inter-hemispheric correlation." *Earth and Planetary Science Letters* 175(1-2): 145-160.
- Chapman, M. R., N. J. Shackleton and J.-C. Duplessy (2000). "Sea surface temperature variability during the

- last glacial-interglacial cycle: assessing the magnitude and pattern of climate change in the North Atlantic." *Palaeogeography, Palaeoclimatology, Palaeoecology* 157(1-2): 1-25.
- Chappell, J. and N. J. Shackleton (1986). "Oxygen isotopes and sea level." *Nature* 324: 137-140.
- Charles, C.D., J. Lynch-Stieglitz, U. S. Ninnemann and R. G. Fairbanks (1996) "Climate connections between the hemispheres revealed by deep sea sediment core/ice core correlations." *Earth and Planetary Science Letters* 142: 19-27.
- Cisewski, B., V. H. Strass and H. Prandke (2005). "Upper-ocean vertical mixing in the Antarctic Polar Front Zone." *Deep Sea Research Part II: Topical Studies in Oceanography* 52(9-10): 1087-1108.
- Clement, A. C. and L. C. Peterson (2008). "Mechanisms of abrupt climate change of the last glacial period." *Reviews of Geophysics* 46.
- CLIMAP (1976). "The surface of the Ice-age Earth." *Science* 191: 1131-1137.
- CLIMAP (1981). "Seasonal Reconstruction of the Earth's surface at the last glacial maximum." *Geological Society of America Map Chart Series* 36.
- Coale, K. H., K. S. Johnson, S. E. Fitzwater, R. M. Gordon, S. Tanner, F. P. Chavez, L. Ferioli, C. Sakamoto, P. Rogers, F. Millero, P. Steinberg, P. Nightingale, D. Cooper, W. P. Cochlan, M. R. Landry, J. Constantinou, G. Rollwagen, A. Trasvina and R. Kudela (1996). "A massive phytoplankton bloom induced by an ecosystem-scale iron fertilization experiment in the equatorial Pacific Ocean." *Nature* 383(6600): 495-501.
- Comiso, J. C. (2003). Large-scale characteristics and variability of the global sea ice cover. *Sea Ice – An Introduction to its Physics, Chemistry, Biology and Geology*. Thomas, D.N. and Dieckmann, G. S. Oxford, Blackwell Science: 112-142.
- Cooke, D. W. a. H., J.D. (1982). Estimates of Antarctic ocean seasonal ice-cover during glacial intervals. *Antarctic Geoscience*. C. Craddock, IUGS. 4: 1017-1025.
- Coolen, M. J. L., J. K. Volkman, B. Abbas, G. Muyzer, S. Schouten and J. S. S. Damste (2007). "Identification of organic matter sources in sulfidic late Holocene Antarctic fjord sediments from fossil rDNA sequence analysis." *Paleoceanography* 22(2): 11.
- Crosta, X., D. Denis and O. Ther (2008). "Sea ice seasonality during the Holocene, Adélie Land, East Antarctica." *Marine Micropaleontology* 66(3-4): 222-232.
- Crosta, X., J. Pichon and M. Labracherie (1997). "Distribution of *Chaetoceros* resting spores in modern peri-Antarctic sediments." *Marine Micropaleontology* 29: 283-299.
- Crosta, X., J. J. Pichon and L. H. Burckle (1998). "Application of modern analog technique to marine Antarctic diatoms: Reconstruction of maximum sea-ice extent at the Last Glacial Maximum." *Paleoceanography* 13(3): 284-297.
- Crosta, X., J. J. Pichon and L. H. Burckle (1998). "Reappraisal of Antarctic seasonal sea-ice at the Last Glacial Maximum." *Geophysical Research Letters* 25(14): 2703-2706.
- Crosta, X., O. Romero, L. K. Armand and J.-J. Pichon (2005). "The biogeography of major diatom taxa in Southern Ocean sediments: 2. Open ocean related species." *Palaeogeography, Palaeoclimatology, Palaeoecology* 223(1-2): 66-92.
- Crowley, T. J. (1992). "North Atlantic Deep Water cools the southern hemisphere." *Paleoceanography* 7: 489-497.
- Cunningham, W. L. and A. Leventer (1998). "Diatom assemblages in surface sediments of the Ross Sea: relationship to present oceanographic conditions." *Antarctic Science* 10(2): 134-146.
- Cunningham, W. L., A. Leventer, J. T. Andrews, A. E. Jennings and K. J. Licht (1999). "Late Pleistocene-Holocene marine conditions in the Ross Sea, Antarctica: evidence from the diatom record." *Holocene* 9(2): 129-139.
- Dansgaard, W., S. J. Johnsen, H. B. Clausen, D. Dahljensen, N. S. Gundestrup, C. U. Hammer, C. S. Hvidberg, J. P. Steffensen, A. E. Sveinbjornsdottir, J. Jouzel and G. Bond (1993). "Evidence for general instability of past climate from a 250Kyr ice core record." *Nature* 364(6434): 218-220.
- Davis, C. H., Y. Li, J. R. McConnell, M. M. Frey and E. Hanna (2005). "Snowfall-driven growth in East Antarctic Ice Sheet mitigates recent sea-level rise." *Science* 308(5730): 1898-1901.
- de Baar, H. J. W., P. W. Boyd, K. H. Coale, M. R. Landry, A. Tsuda, P. Assmy, D. C. E. Bakker, Y. Bozec, R. T. Barber, M. A. Brzezinski, K. O. Buesseler, M. Boye, P. L. Croot, F. Gervais, M. Y. Gorbunov, P. J. Harrison, W. T. Hiscock, P. Laan, C. Lancelot, C. S. Law, M. Levasseur, A. Marchetti, F. J. Millero,

- J. Nishioka, Y. Nojiri, T. van Oijen, U. Riebesell, M. J. A. Rijkenberg, H. Saito, S. Takeda, K. R. Timmermans, M. J. W. Veldhuis, A. M. Waite and C. S. Wong (2005). "Synthesis of iron fertilization experiments: From the iron age in the age of enlightenment." *Journal of Geophysical Research - Oceans* 110(C9): 24.
- De La Rocha, C. L. and M. J. Bickle (2005). "Sensitivity of silicon isotopes to whole-ocean changes in the silica cycle." *Marine Geology* 217(3-4): 267-282.
- Deacon, G. E. R. (1937). "The hydrology of the Southern Ocean." *Discovery Reports XV*: 1-124.
- Dearing, J. (1994). "Environmental magnetic susceptibility: Using the Bartington MS2 system." *Chi, Kentworth, UK. Technical Report*. 49.
- DeConto, R. M. and D. Pollard (2003). "Rapid Cenozoic glaciation of Antarctica induced by declining atmospheric CO₂." *Nature* 421(6920): 245-249.
- Defelice, D. R. and J. Wise, Sherwood W. (1981). "Surface lithofacies, biofacies, and diatom diversity patterns as models for delineation of climatic change in the southeast Atlantic Ocean." *Marine Micropaleontology* 6(1): 29-70.
- Delmonte, B., J. R. Petit, and V. Maggi (2002) "Glacial to Holocene implications of the new 27,000-year dust record from the EPICA Dome C (East Antarctica) ice core." *Clim.ate Dynamics* 18(8): 647- 660.
- Delmonte, B., J. R. Petit, K. K. Andersen, I. Basile-Doelseh, V. Maggi and V. Y. Lipenkov (2004). "Dust size evidence for opposite regional atmospheric circulation changes over east Antarctica during the last climatic transition." *Climate Dynamics* 23(3-4): 427-438.
- Demaster, D. J. (1981). "The supply and accumulation of silica in the marine environment." *Geochemica et Cosmochimica Acta* 45: 1715-1732.
- DeMaster, D. J., O. Ragueneau and C. A. Nittrouer (1996). "Preservation efficiencies and accumulation rates for biogenic silica and organic C, N and P in high-latitude sediments: the Ross Sea." *Journal of Geophysical Research* 101(18): 501-518.
- Denton, G. H., Sugden, D.R., Marchant, D.R., Hall, B.L. and Wilch, T.I. (1993). "East Antarctic Ice Sheet sensitivity to Pliocene climate change from a Dry Valleys perspective." *Geografiska Annaler* 75A: 155-204.
- Denton, G. H., Heusser, C.J., Lowell, T.V., Moreno, P.I., Andersen, and H. B.G., L.E., Schlacter, C. and Marchant, D.R. (1999). "Interhemispheric linkage of paleoclimate during the last glaciation." *Geografiska Annaler* 81A: 107-153.
- Denton, G. H., M. L. Prentice and L. H. Burckle (1991). Cainozoic history of the Antarctic Ice Sheet. *The Geology of Antarctica*. R. J. Tingey. Oxford, Clarndon Press: 365-433.
- Dezileau, L., G. Bareille, J. L. Reyss and F. Lemoine (2000). "Evidence for strong sediment redistribution by bottom currents along the southeast Indian ridge." *Deep Sea Research Part I: Oceanographic Research Papers* 47(10): 1899-1936.
- Diekmann, B., G. Kuhn, R. Gersonde and A. Mackensen (2004). "Middle Eocene to early Miocene environmental changes in the sub-Antarctic Southern Ocean: evidence from biogenic and terrigenous depositional patterns at ODP Site 1090." *Global and Planetary Change* 40(3-4): 295-313.
- Diester-Haass, L., C. Robert and H. Chamley (1996). "The Eocene-oligocene preglacial-glacial transition in the Atlantic sector of the Southern Ocean (ODP site 690)." *Marine Geology* 131(3-4): 123-149.
- Divenere, V., D. V. Kent and I. W. D. Dalziel (1996). Summary of paleomagnetic results from West Antarctica: implications for the tectonic evolution of the Pacific margin of Gondwana during the Mesozoic. *Weddell Sea Tectonics and Gondwana Break-up*. B. C. Storey, King, E.C. and Livermore, R.A. London, Special Publication Geological Society. 108: 31-43.
- Donahue, J. G. (1973). Distribution of planktonic diatoms in surface sediments of the Southern South Pacific. *Marine Sediments of the Southern Oceans, Antarctic Map Folio Series*. H. G. Goodel, et al., American Geophysical Society. 17: 18.
- Donda, F., G. Brancolini, L. D. Santis and F. Trincardi (2003). "Seismic facies and sedimentary processes on the continental rise off Wilkes Land (East Antarctica): evidence of bottom current activity." *Deep Sea Research Part II: Topical Studies in Oceanography* 50(8-9): 1509-1527.
- Dornbusch, U. (2002). "Pleistocene and present day snowlines rise in the Cordillera Ampato, Western Cordillera, southern Peru (15°15'-15°45' S and 77°30'-77°15' W)." *Neues Jahrbuch für Geologie und*

- Paläeontologie Abhandlungen* 225: 103-126.
- Dowsett, H. J. and T. M. Cronin (1990). "High eustatic sea level during the middle Pliocene: evidence from southeastern U.S. Atlantic coastal plain." *Geology* 18: 435-438.
- Driscoll, N. W. and G. H. Haug (1998). "A short circuit in thermohaline circulation: A cause for northern hemisphere glaciation?" *Science* 282(5388): 436-438.
- Dugdale, R. C., F. P. Wilkerson and H. J. Minas (1995). "The role of a silicate pump in driving new production." *Deep Sea Research Part I: Oceanographic Research Papers* 42: 697-719.
- Dunbar, R. B., J. B. Anderson, E. W. Domack and S. S. Jacobs (1985). Oceanographic influences on sedimentation along the Antarctic continental shelf. *Antarctic Research Series*, American Geophysical Union. 43: 291-312.
- Dyke, A. S., J. T. Andrews, P. U. Clark, J. H. England, G. H. Miller, J. Shaw and J. J. Veillette (2002). "The Laurentide and Innuitian ice sheets during the Last Glacial Maximum." *Quaternary Science Reviews* 21(1-3): 9-31.
- Eagles, G., R. A. Livermore, D. Fairhead and P. Morris (2005). "Tectonic evolution of the west Scotia Sea." *Journal of Geophysical Research* 110(B02401).
- Eicken, H. (2003). From the microscopic, to the macroscopic, to the regional scale: Growth, microstructure and the properties of sea ice. *Sea Ice – An Introduction to its Physics, Chemistry, Biology and Geology*. Thomas, D.N. and Dieckmann, G. S. Oxford, Blackwell Science: 22-81.
- Eittrheim, S. L., A. K. Cooper and J. Wanner (1995). "Seismic stratigraphic evidence of ice-sheet advances on the Wilkes Land margin of Antarctica." *Sedimentary Geology* 96: 131-156.
- El-Sayed, S. Z. (1971). "Observations on phytoplankton bloom in the Weddell Sea." *Antarctic Research Series* 17: 301-312.
- El-Sayed, S. Z. (2005). "History and evolution of primary productivity studies of the Southern Ocean." *Polar Biology* 28(6): 423-438.
- Emery, W. J. (1977). "Antarctic Polar Front Zone from Australia to the Drake Passage." *Journal of Physical Oceanography* 7: 811-822.
- Emiliani, C. (1955). "Pleistocene temperatures." *Journal of Geology* 63: 538-578.
- England, M. H. and S. Rahmstorf (1999). "Sensitivity of ventilation rates and radiocarbon uptake to subgrid-scale mixing in ocean models." *Journal of Physical Oceanography* 29(11): 2802-2828.
- EPICA (2004). "Eight glacial cycles from an Antarctic ice core." *Nature* 429(6992): 623-628.
- EPICA (2006). "One-to-one coupling of glacial climate variability in Greenland and Antarctica." *Nature* 444(7116): 195-198.
- Escutia, C., Eittrheim, S.L., Cooper, A.K. and Nelson, C.H. (2000). "Morphology and acoustic character of the Antarctic Wilkes Land turbidite systems: ice-sheet sourced vs. river-sourced fans." *Journal of Sedimentary Research* 70(1): 84-93.
- Escutia, C., L. De Santis, F. Donda, R. B. Dunbar, A. K. Cooper, G. Brancolini and S. L. Eittrheim (2005). "Cenozoic ice sheet history from East Antarctic Wilkes Land continental margin sediments." *Global and Planetary Change* 45(1-3): 51-81.
- Escutia, C., S. L. Eittrheim and A. K. Cooper (1997). "Cenozoic glaciomarine sequences on the Wilkes Land continental rise, Antarctica." *Proceedings Volume-VII International Symposium on Antarctic Earth Sciences* 791-795.
- Ettwein, V. J., C. E. Stickley, E. R. Laurie, A. Rosell-Melé, L. Vidal and M. Brownless (2001). "Fluctuations in productivity and upwelling intensity at site 1083 during the intensification of Northern Hemisphere Glaciation (2.40-2.65 Ma)." *Proceedings of the Ocean Drilling Program. Scientific Results* 175: 1-24.
- Exon, N. F. (2002). Paleogene tectonics and the sediments deposited as Australia and Antarctica separated: ODP Leg 189. *American Geophysical Union, Fall Meeting 2002*.
- Exon, N. F., J. P. Kennett and M. J. Malone (2001). "Shipboard Scientific Party 2001 Proceedings of ODP Initial Reports. 189 [CD-ROM]. Available from: Ocean Drilling Program, College Station, TX 77845-9547, USA."
- Eynaud, F., J. Giraudeau, J. J. Pichon and C. J. Pudsey (1999). "Sea-surface distribution of coccolithophores, diatoms, silicoflagellates and dinoflagellates in the South Atlantic Ocean during the late austral summer 1995." *Deep Sea Research Part I: Oceanographic Research Papers* 46(3): 451-482.

- Fahrbach, E., G. Rohardt, N. Scheele, M. Schröder, V. H. Strass and A. Wisotzki (1995). "Formation and discharge of deep and bottom water in the northwestern Weddell Sea." *Journal of Marine Research* **53**: 515-538.
- Falkowski, P. G., R. T. Barber and V. Smetacek (1998). "Biogeochemical controls and feedbacks on ocean primary production." *Science* **281**(5374): 200-206.
- Fenner, J., H. J. Schrader and G. Wienigk (1976). "Diatom phytoplankton studies in the Southern Pacific Ocean, composition and correlation to the Antarctic convergence and its paleoecological significance." *Deep Sea Drilling Programme* **25**(initial reports): 757-813.
- Fischer, G., R. Gersonde and G. Wefer (2002). "Organic carbon, biogenic silica and diatom fluxes in the marginal winter sea-ice zone and in the Polar Front Region: interannual variations and differences in composition." *Deep Sea Research Part II: Topical Studies in Oceanography* **49**(9-10): 1721-1745.
- Fischer, H., F. Fundel, U. Ruth, B. Twarloh, A. Wegner, R. Udisti, S. Becagli, E. Castellano, A. Morganti, M. Severi, E. Wolff, G. Littot, R. Rothlisberger, R. Mulvaney, M. A. Hutterli, P. Kaufmann, U. Federer, F. Lambert, M. Bigler, M. Hansson, U. Jonsell, M. de Angelis, C. Boutron, M.-L. Siggaard-Andersen, J. P. Steffensen, C. Barbante, V. Gaspari, P. Gabrielli and D. Wagenbach (2007). "Reconstruction of millennial changes in dust emission, transport and regional sea ice coverage using the deep EPICA ice cores from the Atlantic and Indian Ocean sector of Antarctica." *Earth and Planetary Science Letters* **260**(1-2): 340-354.
- Fitzgerald (2002). "Tectonics and landscape evolution of Antarctica." *Royal society of New Zealand bulletin* **35**: 453-469.
- Florindo, F., A. K. Cooper and P. E. O'Brien (2003). "Introduction to 'Antarctic Cenozoic palaeoenvironments: geologic record and models'." *Palaeogeography, Palaeoclimatology, Palaeoecology* **198**(1-2): 1-9.
- Flower, B. P. (1999). "Cenozoic deep-sea temperatures and polar glaciation: the oxygen isotope record." *Terra Antarctica Reports* **3**: 27-42.
- Foldvik, A., T. Gammelsrød, S. Åsterhus, E. Fahrbach, G. Rohardt, M. Schröder, K. W. Nicholls, L. Padman and R. A. Woodgate (2004). "Ice shelf water overflow and bottom water formation in the southern Weddell Sea." *Journal of Geophysical Research* **109**.
- Foldvik, A., T. Gammelsrød, E. Nygaard and S. Åsterhus (2001). "Current measurements near Ronne Ice Shelf: Implications for circulation and melting." *Journal of Geophysical Research* **106**.
- Fortin, M.-J. and M. R. T. Dale (2008). *Spatial analysis: A guide for ecologists*. Cambridge, Cambridge University Press.
- Francis, J. E. and I. Poole (2002). "Cretaceous and early Tertiary climates of Antarctica: evidence from fossil wood." *Palaeogeography, Palaeoclimatology, Palaeoecology* **182**(1-2): 47-64.
- Franck, V. M., K. W. Bruland, D. A. Hutchins and M. A. Brzezinski (2003). "Iron and zinc effects on silicic acid and nitrate uptake kinetics in three high-nutrient, low-chlorophyll (HNLC) regions." *Marine Ecology Progress Series* **252**: 15-33.
- Franck, V. M., M. A. Brzezinski, K. H. Coale and D. M. Nelson (2000). "Iron and silicic acid concentrations regulate Si uptake north and south of the Polar Frontal Zone in the Pacific Sector of the Southern Ocean." *Deep Sea Research Part II: Topical Studies in Oceanography* **47**(15-16): 3315-3338.
- Frank, M., B. Schwarz, S. Baumann, P. W. Kubik, M. Suter and A. Mangini (1997). "A 200 kyr record of cosmogenic radionuclide production rate and geomagnetic field intensity from ¹⁰Be in globally stacked deep-sea sediments." *Earth and Planetary Science Letters* **149**: 121-129.
- Froneman, P. W., C. D. McQuaid and R. Perissinotto (1995). "Biogeographic Structure of the Microphytoplankton Assemblages of the South Atlantic and Southern Ocean During Austral Summer." *Journal of Plankton Research* **17**(9): 1791-1802.
- Fryxell, G. A. (1989). "Marine phytoplankton at the Weddell Sea ice edge: seasonal changes at the specific level." *Polar Biology* **10**(1): 1-18.
- Fryxell, G. A. (1994). *Planktonic Marine Diatom Winter Stages: Antarctic Alternatives to Resting Stages*. 11th Diatom Symposium, California Academy of Sciences.
- Fryxell, G. A., A. K. S. K. Prasad and P. A. Fryxell (1989). "*Eucampia antarctica* (Castracane) Mangin (Bacillariophyta): Complex nomenclatural & taxonomic history." *Taxon* **38**: 638-640.
- Fung, I., S. Meyn, I. Tegen, S. C. Doney, J. John, and J. K. E. Bishop (2000) "Iron supply and demand in the

- upper ocean." *Global Biogeochemical Cycles* **14**: 281–296.
- Ganopolski, A. and S. Rahmstorf (2001). Stability and variability of the thermohaline circulation in the past and future: A study with a coupled model of intermediate complexity. *The Oceans and Rapid Climate Change: Past, Present and Future*. D. Seidov, B. J. Haupt and M. Maslin. Washington, AGU. **126**: 261–276.
- Garabato, A. C. N., K. J. Heywood and D. P. Stevens (2002). "Modification and pathways of Southern Ocean Deep Waters in the Scotia Sea." *Deep Sea Research I* **49**(4): 681–705.
- Garabato, A. C. N., E. L. McDonagh, D. P. Stevens, K. J. Heywood and R. J. Sanders (2002). "On the export of Antarctic Bottom Water from the Weddell Sea." *Deep Sea Research Part II: Topical Studies in Oceanography* **49**(21): 4715–4742.
- Garrison, D. L., Buck, K.R. and Fryxell, G.A. (1987). "Algal assemblages in Antarctic pack ice and in ice-edge plankton." *Journal of Phycology* **23**: 564–572.
- Garrison, D. L. (1991). "Antarctic Sea Ice Biota." *American Zoologist* **31**(1): 17–33.
- Garrison, D. L., S. F. Ackley and K. R. Buck (1983). "A physical mechanism for establishing algal populations in frazil ice." *Nature* **306**: 363–365.
- Garrison, D. L. and K. R. Buck (1986). "Organism losses during ice melting - a serious bias in sea ice community studies." *Polar Biology* **6**(4): 237–239.
- Garrison, D. L. and K. R. Buck (1989). "The biota of Antarctic pack ice in the Weddell Sea and Antarctic Peninsula regions." *Polar Biology* **10**: 211–219.
- Garrison, D. L. and A. R. Close (1993). "Winter ecology of the sea-ice biota in Weddell Sea pack ice." *Marine Ecology Progress Series* **96**(1): 17–31.
- Gersonde, R. (1984). Siliceous microorganisms in sea-ice and their record in the sediments in the southern Weddell Sea (Antarctica). Proceedings 8th Diatom Symposium Paris, Koenigstein.
- Gersonde, R. (1986). "Biogenic siliceous particle-flux in Antarctic Waters and its Paleocological significance." *South African Journal of Science* **82**(9): 500–501.
- Gersonde, R., A. Abelmann, U. Brathauer, S. Becquey, C. Bianchi, G. Cortese, H. Grobe, G. Kuhn, H. S. Niebler, M. Segl, R. Sieger, U. Zielinski and D. K. Futterer (2003). "Last glacial sea surface temperatures and sea-ice extent in the Southern Ocean (Atlantic-Indian sector): A multiproxy approach." *Paleoceanography* **18**(3): art. no.-1061.
- Gersonde, R., X. Crosta, A. Abelmann and L. Armand (2005). "Sea-surface temperature and sea ice distribution of the Southern Ocean at the EPILOG Last Glacial Maximum – a circum-Antarctic view based on siliceous microfossil records." *Quaternary Science Reviews: Multiproxy Approach for the Reconstruction of the Glacial Ocean surface* **24**(7–9): 869–896.
- Gersonde, R. and D. A. Hodell (2002). "Southern Ocean paleoceanography - Insights from Ocean Drilling Program Leg 177." *Palaeogeography Palaeoclimatology Palaeoecology* **182**(3–4): 145–149.
- Gersonde, R. and G. Wefer (1987). "Sedimentation of biogenic siliceous particles in Antarctic waters from the Atlantic sector." *Marine Micropaleontology* **11**(4): 311–332.
- Gersonde, R. and U. Zielinski (2000). "The reconstruction of late Quaternary Antarctic sea-ice distribution - the use of diatoms as a proxy for sea-ice." *Palaeogeography, Palaeoclimatology, Palaeoecology* **162**: 263–286.
- Gildor, H. and E. Tziperman (2001). Sea ice, as the glacial cycles' climate switch, and interhemispheric thermohaline teleconnections. *Annals of Glaciology, Vol 33*. Cambridge, International Glaciological Society. **33**: 501–506.
- Gildor, H., E. Tziperman and J. R. Toggweiler (2002). "Sea ice switch mechanism and glacial-interglacial CO₂ variations." *Global Biogeochemical Cycles* **16**(3): art. no.-1032.
- Gillot, P. Y., J. Labeyrie, C. Laj, G. Valladas, G. Guerin, G. Poupeau and G. Delibrias (1979). "Age of the Laschamp paleomagnetic excursion revisited." *Earth and Planetary Science Letters* **42**: 444–450.
- Giunta, S., A. Negri, P. Maffioli, F. Sangiorgi, L. Capotondi, C. Morigi, M. S. Principato and C. Corselli (2006). "Phytoplankton dynamics in the eastern Mediterranean sea during marine isotopic stage 5e." *Palaeogeography Palaeoclimatology Palaeoecology* **235**(1–3): 28–47.
- Gleitz, M., A. Bartsch, G. S. Dieckmann and H. Eicken (1998). Composition and succession of sea-ice diatom assemblages in the eastern and southern Weddell Sea, Antarctica. Antarctic Sea Ice: biological processes, interactions and variability; Antarctic Research Series. B. o. A. editors.

- Washington, American Geophysical Union. 73: 107-120.
- Gleitz, M., S. Grossmann, R. Scharek and V. Smetacek (1996). "Ecology of diatom and bacterial assemblages in water associated with melting summer sea ice in the Weddell Sea, Antarctica." *Antarctic Science* 8(2): 135-146.
- Goosse, H. and T. Fichefet (1999). "Importance of ice-ocean interactions for the global ocean circulation: A model study." *Journal of Geophysical Research - Oceans* 104(C10): 23337-23355.
- Gordon, A. L. (1966). "Potential temperature, oxygen and circulation of bottom water in the Southern Ocean." *Deep Sea Research* 13: 1125-1138.
- Gordon, A. L., Molinelli, E.J. and Baker, T. (1978). "Large-scale relative dynamic topography of the Southern Ocean." *Journal of Geophysical Research* 83: 3023-3032.
- Gordon, A. L. (1998). "Coelacanth populations may go with the flow." *Nature* 395(6703): 634-634.
- Gordon, A. L. (2001). Interocean Exchange. *Ocean Circulation and Climate*. G. Siedler, J. Church and J. Gould. London, Academic Press: 303-316.
- Gordon, A. L. and P. T. Tchernia (1972). Waters of the continental margin off Adélie Coast, Antarctica. *Antarctic Oceanography II: The Australian-New Zealand sector*. D. E. Hayes. Washington DC, AGU. 9: 59-69.
- Green, S. E. and R. N. Sambrotto (2006). "Plankton community structure and export of C, N, P and Si in the Antarctic Circumpolar Current." *Deep Sea Research Part II: Topical Studies in Oceanography* 53(5-7): 620-643.
- Grigorov, I., R. B. Pearce and A. E. S. Kemp (2002). "Southern Ocean laminated diatom ooze: mat deposits and potential for palaeo-flux studies, ODP leg 177, Site 1093." *Deep Sea Research Part II: Topical Studies in Oceanography. The Southern Ocean II: Climatic Changes and the Cycle of Carbon* 49(16): 3391-3407.
- Grousset, F. E., P. E. Biscaye, M. Revel, J. R. Petit, K. Pye, S. Joussaume and J. Jouzel (1992). "Antarctic ice core dusts at 18 kyr B.P.: isotopic constraints on origin and atmospheric circulation." *Earth and Planetary Science Letters* 111: 175-182.
- Guillou, H., B. S. Singer, C. Laj, C. Kissel, S. Scaillet and B. R. Jicha (2004). "On the age of the Laschamp geomagnetic excursion." *Earth and Planetary Science Letters* 227(3-4): 331-343.
- Guyodo, Y. and J.-P. Valet (1996). "Relative variations in geomagnetic intensity from sedimentary records: the past 200 thousand years." *Earth and Planetary Science Letters* 143: 23-36.
- Guyodo, Y. and J.-P. Valet (1999). "Global changes in intensity of the earth's magnetic field during the past 800 kyr." *Nature* 399: 249-252.
- Hanebuth, T. J. J., K. Stattegger and A. Bojanowski (2009). "Termination of the Last Glacial Maximum sea-level lowstand: The Sunda-Shelf data revisited." *Global and Planetary Change* 66(1-2): 76-84.
- Hare, C. E., G. R. DiTullio, S. F. Riseman, A. C. Crossley and L. C. Popels (2007). "Effects of changing continuous iron input rates on a Southern Ocean algal assemblage." *Deep Sea Research I* 54: 732-746.
- Hare, C. E., G. R. DiTullio, C. G. Trick, S. W. Wilhelm, K. W. Bruland, E. L. Rue and D. A. Hutchins (2005). "Phytoplankton community structure changes following simulated upwelled iron inputs in the Peru upwelling region." *Aquatic Microbial Ecology* 38: 269-282.
- Hargraves, P. E. (1979). "Studies on marine plankton diatoms: IV. Morphology of *Chaetoceros* resting spores." *Nova Hedwigia Beiheft* 64: 99-120.
- Hargraves, P. E. and F. W. French (1983). Diatom resting spores: significance and strategies. *Survival strategies of the algae*. G. A. Fryxell. Cambridge, Cambridge University Press: 49-68.
- Harris, J. R., L. Wilkonson and E. C. Grunsky (1999). "Techniques for analysis and visualization of lithogeochemical data with applications to the Swayze greenstone belt, Ontario." *Journal of Geochemical Exploration* 67: 301-334.
- Hasle, G. R. (1976). "The biogeography of some marine diatoms." *Deep Sea Research I* 23: 319-338.
- Hasle, G. R. and E. E. Syvertsen (1996). Marine diatoms. *Identifying Marine Diatoms and Dinoflagellates*. C. R. Tomas. San Diego, Academic Press: 5-385.
- Hays, J. D., J. A. Lozano, N. J. Shackleton and G. Irving (1976). Reconstruction of the Atlantic and western Indian Ocean sectors of the 18,000 BP Antarctic Ocean. *Investigation of Late Quaternary Paleoceanography and Paleoclimatology*. R. M. Cline and J. D. Hays. Boulder, Colorado, Geological

- Society of America. *Memoir* 145: 337-372.
- Hebbeln, D., M. Marchant and G. Wefer (2002). "Paleoproductivity in the southern Peru-Chile Current through the last 33000 yr." *Marine Geology* 186: 487-504.
- Heine, K. (1996). "The extent of the last glaciation in the Bolivian Andes (Cordillera Real) and paleoclimatic implications." *Zeitschrift für Geomorphologie N.F., Suppl. Bd.* 104: 187-202.
- Heinrich, H. (1988). "Origin and consequences of cyclic ice-rafting in the Northeast Atlantic Ocean during the past 130,000 yrs." *Quaternary Research* 29: 142-152.
- Hellmer, H. H. and A. Beckmann (2001). "The Southern Ocean: A ventilation contributor with multiple sources." *Geophysical Research Letters* 28(15): 2927-2930.
- Hemming, S. R. (2004). "Heinrich Events: Massive Late Pleistocene detritus layers of the North Atlantic and their global climate imprint." *Reviews of Geophysics* 42: RG1005.
- Hense, I., R. Timmermann, A. Beckmann and U. V. Bathmann (2003). "Regional ecosystem dynamics in the ACC: simulations with a three-dimensional ocean-plankton model." *Journal of Marine Systems* 42(1-2): 31-51.
- Heusser, C.J. (1989) "Polar perspective of Late-Quaternary climates in the Southern Hemisphere." *Quaternary Research* 32: 60-71.
- Heusser, C.J. (2003) *Ice Age Southern Andes: A Chronicle of Palaeoecological Events*. Elsevier, Netherlands.
- Heywood, K. J., A. C. Naveira Garabato, D. P. Stevens and R. D. Muench (2004). "On the fate of the Antarctic Slope Front and the origin of the Weddell Front." *Journal of Geophysical Research* 109.
- Hofmann, A. (1999). "Kurzfristige Klimaschwankungen im Scotiameer und Ergebnisse zur Kalbungsgeschichte der Antarktis während der letzten 200.000 Jahre. Ph.D thesis." *Institut für Polar und Meeresforschung, Bremerhaven, Berichte zu Polarforschung* 345: 1-162.
- Hofmann, D. I., K. Fabian, F. Schmieder, B. Donner and U. Bleil (2005). "A stratigraphic network across the Subtropical Front in the central South Atlantic: Multi-parameter correlation of magnetic susceptibility, density, X-ray fluorescence and $\delta^{18}\text{O}$ records." *Earth and Planetary Science Letters* 240: 649-709.
- Hooker, J. D. (1847). The Botany of the Antarctic Voyage of H.M. Discovery Ships Erebus and Terror in the Years 1839-1843. . I. *Flora Antarctica*. Weinheim, Cramer, J.: 503-519.
- Horner, R. A. (1985). Ecology of sea-ice microalgae. *Sea-ice biota*. R. A. Horner. Boca Raton, CRC Press: 83-103.
- Howard, W. R. and W. L. Prell (1992). "Late Quaternary surface circulation of the southern Indian Ocean and its relationship to orbital variations." *Paleoceanography* 7: 79-117.
- Howe, J. A. and C. J. Pudsey (1999). "Antarctic Circumpolar Deep Water; a Quaternary paleoflow record from the northern Scotia Sea, South Atlantic Ocean " *Journal of Sedimentary Research* 69(4): 847-861.
- Huber, M., H. Brinkhuis, C. E. Stickley, K. Doos, A. Sluijs, J. Warnaar, S. A. Schellenberg and G. L. Williams (2004). "Eocene circulation of the Southern Ocean: Was Antarctica kept warm by subtropical waters?" *Paleoceanography* 19: art no.-PA4026.
- Hughen, K. A. (2007). Radiocarbon dating of deep-sea sediments. *Proxies in Late Cenozoic Paleoceanography*. De Vernal, A., Hillaire-Marcel, C. Amsterdam, Elsevier: 185-206.
- Hulton, N.R.J., T. S. Purves, R. D. McCulloch, D. E. Sugden and M. J. Bentley (2002) "The Last Glacial maximum and deglaciation in southern South America." *Quaternary Science Reviews* 21: 233-241.
- Hutchins, D.A., and K. W. Brunland (1998) "Iron-limited diatom growth and Si:N uptake ratios in a coastal upwelling regime." *Nature* 393: 561- 564.
- Hutchins, D. A., P. N. Sedwick, G. R. DiTullio, P. W. Boyd, B. Que ´guiner, F. B. Griffiths and C. Crossley (2001). "Control of phytoplankton growth by iron and silicic acid availability in the subantarctic Southern Ocean: Experimental results from the SAZ project." *Journal of Geophysical Research* 106: 31559-31572.
- Huybrechts, P. (2002). "Sea-level changes at the LGM from ice-dynamic reconstructions of the Greenland and Antarctic ice sheets during the glacial cycles." *Quaternary Science Reviews* 21(1-3): 203-231.
- Imbrie, J., J. D. Hays, D. G. Martinson, A. McIntyre, A. C. Mix, J. J. Morley, N. G. Paces, W. L. Prell and N. J. Shackleton (1984). The orbital theory of Pleistocene climate: Support from a revised chronology of the marine $\delta^{18}\text{O}$ record. *Milankovitch and Climate*. A. Berger. Norwell, D. Reidel: 269-305.

- Ingolfsson, O. and C. Hjort (2002). "Glacial history of the Antarctic Peninsula since the Last Glacial Maximum - a synthesis." *Polar Research* 21(2): 227-234.
- Jacobs, S. S. (1991). "On the nature and significance of the Antarctic Slope Front." *Marine Chemistry* 35: 9-24.
- Jacobs, S. S. (2004). "Bottom water production and its links with the thermohaline circulation." *Antarctic Science* 16(4): 427-437.
- Jacobs, S. S., A. F. Amos and P. M. Bruchhausen (1970). "Ross Sea oceanography and Antarctic Bottom Water formation." *Deep Sea Research* 17: 935-962.
- Jacques, G. and M. Panouse (1991). "Biomass and composition of size fractionated phytoplankton in the Weddell-Scotia Confluence area." *Polar Biology* 11(5): 315-328.
- Johns, L., E. J. Wraige, S. T. Belt, C. A. Lewis, G. Massé, J. M. Robert and S. J. Rowland (1999). "Identification of a C₂₅ highly branched isoprenoid (HBI) diene in Antarctic sediments, Antarctic sea-ice diatoms and cultured diatoms." *Organic Geochemistry* 30(11): 1471-1475.
- Jokat, W., T. Boebel, M. Koenig and U. Meyer (2003). "Timing and geometry of early Gondwana breakup." *Journal of Geophysical Research - Solid Earth* 108.
- Jouse', A. P., G. S. Koroleva and G. A. Nagaeva (1962). "Diatoms in the surface layer of sediment in the Indian sector of the Antarctic." *Trudy Instituta Okeanologii Akademii Nauk SSSR* 61: 20-91.
- Jouzel, J., C. Lorius, J. R. Petit, C. Genthon, N. Barkov, V. M. Kotlyakov and V. M. Petrov (1987). "Vostok ice core: a continuous isotope temperature record over the last climatic cycle (160,000 years)." *Nature* 329: 403-8.
- Kaiser, J., F. Lamy and D. Hebbeln (2005). "A 70-kyr sea surface temperature record off southern Chile (Ocean Drilling Programme Site 1233)." *Paleoceanography* 20: PA4009.
- Kanfoush, S. L., D. A. Hodell, C. D. Charles, T. P. Guilderson, P. G. Mortyn and U. S. Ninnemann (2000). "Millennial-Scale Instability of the Antarctic Ice Sheet During the Last Glaciation." *Science* 288: 1815-1818.
- Kang, S. H. and G. A. Fryxell (1991). "Most abundant diatom species in water column assemblages from five Leg 119 drill sites in Prydz Bay, Antarctica: Distributional Patterns." *Proceedings of the Ocean Drilling Programme Scientific Results Leg 119*: 645-666.
- Kang, S. H. and G. A. Fryxell (1992). "*Fragilariopsis cylindrus* (Grunow) Krieger - the most abundance diatom in water column assemblages of Antarctic marginal ice-edge zones." *Polar Biology* 12(6-7): 609-627.
- Kang, S. H. and G. A. Fryxell (1993). "Phytoplankton in the Weddell Sea, Antarctica - composition, abundance and distribution in water-column assemblages of the marginal ice-edge zone during austral autumn." *Marine Biology* 116(2): 335-348.
- Kang, S. H., J. S. Kang, S. Lee, K. H. Chung, D. Kim and M. G. Park (2001). "Antarctic phytoplankton assemblages in the marginal ice zone of the northwestern Weddell Sea." *Journal of Plankton Research* 23(4): 333-352.
- Kaplan, M. R., C. J. Fogwill, D. E. Sugden, N. R. J. Hulton, P. W. Kubik and S. P. H. T. Freeman (2008). "Southern Patagonian glacial chronology for the Last Glacial period and implications for Southern Ocean climate." *Quaternary Science Reviews* 27(3-4): 284-294.
- Karpuz, N. K. and E. Jansen (1992). "A high-resolution diatom record of the last deglaciation from the SE Norwegian Sea: documentation of rapid climatic changes." *Paleoceanography* 7(4): 499-520.
- Kaspi, Y., R. Sayag and E. Tziperman (2004). "A 'triple sea-ice state' mechanism for the abrupt warming and synchronous ice sheet collapses during Heinrich events." *Paleoceanography* 19(3).
- Keany, J., M. Ledbetter, N. Watkins, T.-C. Huang (1976) "Diachronous deposition of ice-rafted debris in sub-Antarctic deep-sea sediments." *Geological Society of America Bulletin* 87: 873-882.
- Kemp, A. E. S. (1995). Laminated sediments from coastal and open ocean upwelling systems: what variability do they record? Upwelling in the Ocean: Modern Processes and Ancient Records. Dahlem Workshop Report. C. P. Summerhayes, Emeis, K.-C., Angel, M.V., Smith, R.L. and Zeitzschel, B. Chichester, Wiley: 239-257.
- Kemp, A. E. S., R. B. Pearce, I. Koizumi, J. Pike and S. J. Rance (1999). "The role of mat-forming diatoms in the formation of Mediterranean sapropels." *Nature* 398(6722): 57-61.
- Kemp, A. E. S., J. Pike, R. B. Pearce and C. B. Lange (2000). "The 'Fall dump' - a new perspective on the

- role of a "shade flora" in the annual cycle of diatom production and export flux." *Deep Sea Research Part II: Topical Studies in Oceanography* 47(9-11): 2129-2154.
- Kennett, J. P. (1977). "Cenozoic Evolution of Antarctic Glaciation, the Circumpolar Antarctic Ocean, and their Impact on Global Palaeoceanography." *Journal of Geophysical Research* 82(C27): 3843 - 3860.
- Kennett, J. P. (1978). "The development of planktonic biogeography in the Southern Ocean during the Cenozoic." *Marine Micropaleontology* 3(4): 301-345.
- Kennett, J. P. and R. C. Thunell (1975). "Global Increase in Quaternary Explosive Volcanism." *Science* 187(4176): 497-502.
- Kennett, J. P. and R. C. Thunell (1977). "On explosive Cenozoic volcanism and climatic implications." *Science* 196: 1231-1234.
- Kim, J.-H., X. Crosta, E. Michel, S. Schouten, J. Duprat and J. S. Sinninghe Damsté (2009). "Impact of lateral transport on organic proxies in the Southern Ocean." *Quaternary Research* 71(2): 246-250.
- King, E. C. (1996). Weddell Sea tectonics and Gondwana breakup: an introduction. Weddell Sea tectonics and Gondwana breakup. B. C. Storey, King, E.C., & Livermore, R.A. London, Geological Society.
- Knorr, G. and G. Lohmann (2003). "Southern Ocean origin for the resumption of Atlantic thermohaline circulation during deglaciation." *Nature* 424(6948): 532-536.
- Knutti, R., J. Fluckiger, T. F. Stocker and A. Timmermann (2004). "Strong hemispheric coupling of glacial climate through freshwater discharge and ocean circulation." *Nature* 430(7002): 851-856.
- Kovach, W. L. (1999). MVSP - A Multivariate Statistical Package for Windows, ver 3.1. Pentraeth, Wales, Kovach Computing Services.
- Kozlova, O. G. (1966). Diatoms of the Indian and Pacific sectors of the Antarctic. Isreal Program for Scientific Translations. N. S. Foundation. Washington DC: 185.
- Kozlova, O. G. and V. V. Muchina (1967). "Diatoms and silicoflagellates in suspension and floor sediments of the Pacific Ocean." *International Geology Review (translated from Geokhimiya Kremnezema, N.K.65-12(51), 192-218, 1967)* 9: 1322-1342.
- Krebs, W. N., J. H. Lipps and L. H. Burckle (1987). "Ice diatom floras, Arthur Harbor, Antarctica." *Polar Biology* 7(3): 163-171.
- Kristjansson, L. and A. Gudmundsson (1980). "Geomagnetic excursion in late glacial basalt outcrops in southwestern Iceland." *Geophysical Research Letters* 7: 337-340.
- Labeyrie, L., M. Labracherie, N. Gorfti, J. J. Pichon, M. Vautravers, M. Arnold, J. C. Duplessy, M. Paterne, E. Michel, J. Duprat, M. Caralp and J. L. Turon (1996). "Hydrographic changes of the Southern Ocean (southeast Indian sector) over the last 230 kyr." *Paleoceanography* 11(1): 57-76.
- Labeyrie, L. D., J. C. Duplessy and P. L. Blanc (1987). "Variations in Mode of Formation and Temperature of Oceanic Deep Waters over the Past 125,000 Years." *Nature* 327(6122): 477-482.
- Laj, C., J. E. T. Channell and S. Gerald (2007). Geomagnetic Excursions. Treatise on Geophysics. Amsterdam, Elsevier: 373-416.
- Laj, C., C. Kissel, A. Mazaud, J. E. T. Channell and J. Beer (2000). "North Atlantic palaeointensity stack since 75 ka (NAPIS-75) and the duration of the Laschamp event." *Philosophical Transactions of the Royal Society of London Series a-Mathematical Physical and Engineering Sciences* 358(1768): 1009-1025.
- Lambeck, K., T. M. Esat and E.-K. Potter (2002). "Links between climate and sea levels for the past three million years." *Nature* 419(6903): 199-206.
- Lamy, F., J. Klump, D. Hebbeln and G. Wefer (2000) "Late Quaternary rapid climate change in northern Chile." *Terra Nova* 12: 8-13.
- Lamy, F., D. Hebbeln, U. Rfhl and G. Wefer (2001) "Holocene rainfall variability in southern Chile: a marine record of latitudinal shifts of the Southern Westerlies." *Earth and Planetary Science Letters* 185: 369- 382.
- Lamy, F., C. Rqhlemann, D. Hebbeln and G. Wefer (2002) "High- and low-latitude climate control on the position of the southern Peru-Chile current during the Holocene." *Paleoceanography* 17: 1601-1610.
- Lamy, F., J. Kaiser, U. Ninnemann, D. Hebbeln, H. W. Arz and J. Stoner (2004). "Antarctic Timing of Surface Water Changes off Chile and Patagonian Ice Sheet Response." *Science* 304(5679): 1959-1962.

- Lance, V. P., M. R. Hiscock, A. K. Hilding, D. A. Stuebe, R. R. Bidigare, J. W. O. Smith and R. T. Barber (2007). "Primary productivity, differential size fraction and pigment composition responses in two Southern Ocean in situ iron enrichments." *Deep Sea Research Part I: Oceanographic Research Papers* 54(5): 747-773.
- Lancelot, C., E. Hannon, S. Becquevort, C. Veth and H. J. W. De Baar (2000). "Modeling phytoplankton blooms and carbon export production in the Southern Ocean: dominant controls by light and iron in the Atlantic sector in Austral spring 1992." *Deep Sea Research Part I: Oceanographic Research Papers* 47(9): 1621-1662.
- Lancelot, C., S. Mathot, C. Veth and H. W. J. de Baar (1993). "Factors controlling phytoplankton ice-edge blooms in the marginal ice-zone of the north western Weddell Sea during sea ice retreat 1988: Field observations and mathematical modelling." *Polar Biology* 13: 337-387.
- Lawver, L. A. and L. M. Gahagan (2003). "Evolution of Cenozoic seaways in the circum-Antarctic region." *Palaeogeography Palaeoclimatology Palaeoecology* 198(1-2): 11-37.
- Lawver, L. A., L. M. Gahagan and M. F. Coffin (1992). The Development of Palaeoseaways Around Antarctica. *The Antarctic Palaeoenvironment: A Perspective on Global Change*. J. P. Kennett and D. A. Warnke. Washington, DC, American Geophysical Union. 56: 7-30.
- Leblanc, K., C. E. Hare, P. W. Boyd, K. W. Bruland, B. Sohst, S. Pickmere, M. C. Lohan, K. Buck, M. Ellwood and D. A. Hutchins (2005). "Fe and Zn effects on the Si cycle and diatom community structure in two contrasting high and low-silicate HNLC areas." *Deep Sea Research Part I: Oceanographic Research Papers* 52(10): 1842-1864.
- Ledru, M.-P., G. Ceccantini, S. E. M. Gouveia, J. A. López-Sáez, L. C. R. Pessenda and A. S. Ribeiro (2006). "Millenial-scale climatic and vegetation changes in a northern Cerrado (Northeast, Brazil) since the Last Glacial Maximum." *Quaternary Science Reviews* 25(9-10): 1110-1126.
- Legendre, L., S. F. Ackley, G. S. Dieckmann, B. Gulliksen, R. Horner, T. Hoshiai, I. A. Melnikov, W. S. Reeburgh, M. Spindler and C. W. Sullivan (1992). "Ecology of Sea Ice Biota .2. Global Significance." *Polar Biology* 12(3-4): 429-444.
- Legendre, L. and P. Legendre (1983). *Numerical ecology. Developments in environmental modeling*. Amsterdam, Elsevier Scientific Publishing Company.
- Leventer, A. (1992). "Modern distribution of diatoms in sediments from the George V Coast, Antarctica." *Marine Micropaleontology* 19(4): 315-332.
- Leventer, A. (1998). The fate of Antarctic "sea ice diatoms" and their use as paleoenvironmental indicators. *Antarctic Sea Ice: biological processes, interactions and variability; Antarctic Research Series*. Board of Associate Editors. Washington, American Geophysical Union. 73: 121-137.
- Leventer, A. (2003). Particulate flux from sea ice in polar waters. *Sea Ice – An Introduction to its Physics, Chemistry, Biology and Geology*. Thomas, D.N. and Dieckmann, G. S. Oxford, Blackwell Science Ltd: 303-332.
- Leventer, A., E. Domack, A. Barkoukis, B. McAndrews and J. Murray (2002). "Laminations from the Palmer Deep: A diatom-based interpretation." *Paleoceanography* 17(2): art. no.-1027.
- Leventer, A., E. W. Domack, S. E. Ishman, S. Brachfeld, C. E. McClennen and P. Manley (1996). "Productivity cycles of 200-300 years in the Antarctic Peninsula region: Understanding linkages among the sun, atmosphere, oceans, sea ice, and biota." *Geological Society of America Bulletin* 108(12): 1626-1644.
- Leventer, A. and R. B. Dunbar (1996). "Factors influencing the distribution of diatoms and other algae in the Ross Sea." *Journal of Geophysical Research - Oceans* 101(C8): 18489-18500.
- Leventer, A., R. B. Dunbar and D. J. Demaster (1993). "Diatom evidence for late Holocene climatic events in Granite Harbour, Antarctica." *Paleoceanography* 8(3): 373-386.
- Levi, S., H. Audunson, R. A. Duncan, L. Kristjansson, P. Y. Gillot and S. P. Jakobsson (1990). "Late Pleistocene geomagnetic excursion in Icelandic lavas: confirmation of the Laschamp excursion." *Earth and Planetary Science Letters* 96: 443-457.
- Ligowski, R. (1993). Marine Diatoms (Bacillariophyceae) in the Antarctic Ecosystem and Their Importance as An Indicator of Food Source of Krill (*Euphasia Superba* Dana). Lodz, Wydawnictwo Uniwersytetu Łódzkiego. PhD: 242.
- Lisiecki, L. E. and M. E. Raymo (2005). "A Pliocene-Pleistocene stack of 57 globally distributed benthic $\delta^{18}\text{O}$

- records." *Paleoceanography* 20(1).
- Livermore, R., G. Eagles, P. Morris and A. Maldonado (2004). "Shackleton Fracture Zone: No barrier to early circumpolar ocean circulation." *Geology* 32(9): 797 - 800.
- Livermore, R., C. Hillenbrand, M. Meredith and G. Eagles (2005). Drake Passage and Cenozoic climate: an open and shut case? *American Geophysical Union, Fall Meeting 2005*.
- Livermore, R., A. Nankivell, G. Eagles and P. Morris (2005). "Paleogene opening of Drake Passage." *Earth and Planetary Science Letters* 236(1-2): 459-470.
- Lizotte, M. P. (2001). "The contributions of sea ice algae to Antarctic marine primary production." *American Zoologist* 41(1): 57-73.
- Lizotte, M. P. (2003). Microbiology of sea-ice. *Sea Ice – An Introduction to its Physics, Chemistry, Biology and Geology*. Thomas, D.N. and Dieckmann, G. S. Oxford, Blackwell Science: 184-210.
- Locarnini, R. A., T. Whitworth and W. D. Nowlin (1993). "The Importance of the Scotia Sea on the Outflow of Weddell Sea Deep-Water." *Journal of Marine Research* 51(1): 135-153.
- Lucchi, R. G., M. Rebesco, A. Camerlenghi, M. Buseti, L. Tomadin, G. Villa, D. Persico, C. Morigi, M. C. Bonci and G. Giorgetti (2002). "Mid-late Pleistocene glaciomarine sedimentary processes of a high-latitude, deep-sea sediment drift (Antarctic Peninsula Pacific margin)." *Marine Geology* 189(3-4): 343-370.
- Lund, S., J. S. Stoner, J. E. T. Channell and G. Acton (2006). "A summary of Brunhes paleomagnetic field variability recorded in Ocean Drilling Program cores." *Physics of the Earth and Planetary Interiors* 156(3-4): 194-204.
- Mackensen, A. and W. U. Ehrmann (1992). "Middle Eocene through Early Oligocene climate history and paleoceanography in the Southern Ocean: Stable oxygen and carbon isotopes from ODP Sites on Maud Rise and Kerguelen Plateau." *Marine Geology* 108(1): 1-27.
- Macri, P., L. Sagnotti, J. Dinares-Turell and A. Caburlotto (2005). "A composite record of Late Pleistocene relative geomagnetic paleointensity from the Wilkes Land Basin (Antarctica)." *Physics of the Earth and Planetary Interiors* 151(3-4): 223-242.
- Macri, P., L. Sagnotti, R. G. Lucchi and M. Rebesco (2006). "A stacked record of relative geomagnetic paleointensity for the past 270 kyr from the western continental rise of the Antarctic Peninsula." *Earth and Planetary Science Letters* 252(1-2): 162-179.
- Maddison, E. J., J. Pike, A. Leventer, R. Dunbar, S. Brachfeld, E. W. Domack, P. Manley and C. McClennen (2006). "Post-glacial seasonal diatom record of the Mertz Glacier Polynya, East Antarctica." *Marine Micropaleontology* 60(1): 66-88.
- Malej, A., P. Mozetic, V. Malacic, S. Terzic and M. Ahel (1995). "Phytoplankton Responses to Fresh-Water Inputs in a Small Semienclosed Gulf (Gulf of Trieste, Adriatic Sea)." *Marine Ecology Progress Series* 120(1-3): 111-121.
- Mann, D. G. (1999). "Phycological Reviews 18: The species concept in diatoms." *Phycologia* 38(6): 437-495.
- Markgraf, V. (1989) "Reply to C.J. Heusser's "Southern Westerlies during Last Glacial Maximum." *Quaternary Research* 31: 426-432.
- Markgraf, V., J. R. Dodson, A. P. Kershaw, M. S. McGlone, and N. Nicholls (1992) "Evolution of late Pleistocene and Holocene climates in the circum-South Pacific land areas." *Climate Dynamics* 6: 193-211.
- Marks, L. (2002). "Last Glacial Maximum in Poland." *Quaternary Science Reviews* 21(1-3): 103-110.
- Martin, J. H., R. M. Gordon and S. E. Fitzwater (1990). "Iron in Antarctic Waters." *Nature* 345(6271): 156-158.
- Martinson, D. G., N. G. Pisias, J. D. Hays, J. Imbrie, Moore and N. J. Shackleton (1987). "Age dating and the orbital theory of the ice ages: Development of a high-resolution 0 to 300,000-year chronostratigraphy." *Quaternary Research* 27(1): 1-29.
- Masse, G., S. T. Belt, S. J. Rowland and M. Rohmer (2004). "Isoprenoid biosynthesis in the diatoms *Rhizosolenia setigera* (Brightwell) and *Haslea ostrearia* (Simonsen)." *Proceedings of the National Academy of Sciences of the United States of America* 101(13): 4413-4418.
- Massé, G., S. J. Rowland, M.-A. Sicre, J. Jacob, E. Jansen and S. T. Belt (2008). "Abrupt climate changes for Iceland during the last millennium: Evidence from high resolution sea ice reconstructions." *Earth and Planetary Science Letters* 269(3-4): 565-569.

- Massom, R. A., P. T. Harris, K. J. Michael and M. J. Potter (1998). "The distribution and formative processes of latent-heat polynyas in East Antarctica." *Annals of Glaciology* 27: 420-426.
- Matano, R. P., A. L. Gordon, R. D. Muench and E. D. Palma (2002). "A numerical study of the circulation in the northwestern Weddell Sea." *Deep Sea Research Part II: Topical Studies in Oceanography* 49(21): 4827-4841.
- Mazaud, A., M. A. Sicre, U. Ezat, J. J. Pichon, J. Duprat, C. Laj, C. Kissel, L. Beaufort, E. Michel and J. L. Turon (2002). "Geomagnetic-assisted stratigraphy and sea surface temperature changes in core MD94-103 (Southern Indian Ocean): possible implications for North-South climatic relationships around H4." *Earth and Planetary Science Letters* 201(1): 159-170.
- McCartney, M. S. and K. A. Donohue (2007). "A deep cyclonic gyre in the Australian-Antarctic Basin." *Progress In Oceanography* 75(4): 675-750.
- McGowran, B. (2005). *Biostratigraphy Microfossils and Geological Time*. Cambridge, Cambridge University Press.
- Measures, C. I. and S. Vink (2001). "Dissolved Fe in the upper waters of the Pacific sector of the Southern Ocean." *Deep Sea Research Part II: Topical Studies in Oceanography* 48(19-20): 3913-3941.
- Meguro, H. (1962). "Plankton ice in the Antarctic Ocean." *Nankyoku Shiryo (Antarct. Rec.)* 14: 72-79.
- Mengelt, C., M. R. Abbott, J. A. Barth, R. M. Letelier, C. I. Measures and S. Vink (2001). "Phytoplankton pigment distribution in relation to silicic acid, iron and the physical structure across the Antarctic Polar Front, 170 degrees W, during austral summer." *Deep Sea Research Part II: Topical Studies in Oceanography* 48(19-20): 4081-4100.
- Merrill, R. T. and P. L. McFadden (2005). "The use of magnetic field excursions in stratigraphy." *Quaternary Research* 63(3): 232-237.
- Mix, A. C., E. Bard and R. Schneider (2001). "Environmental processes of the ice age: land, oceans, glaciers (EPILOG)." *Quaternary Science Reviews* 20(4): 627-657.
- Mohtadi, M. and D. Hebbeln (2004). "Mechanisms and variations of the paleoproductivity off northern Chile (24 degrees S-33 degrees S) during the last 40,000 years." *Paleoceanography* 19(2): art. no.-PA2023.
- Monnin, E., A. Indermühle, A. Dällenbach, J. Flückiger, B. Stauffer, T. F. Stocker, D. Raynaud, J.-M. Barnola (2001) "Atmospheric CO₂ Concentrations over the Last Glacial Termination." *Science* 291:112-114.
- Moore, C. M., A. E. Hickman, A. J. Poulton, S. Seeyave and M. I. Lucas (2007). "Iron-light interactions during the CROZet natural iron bloom and EXport experiment (CROZEX) II: Taxonomic responses and elemental stoichiometry." *Deep Sea Research Part II: Topical Studies in Oceanography* 54(18-20): 2066-2084.
- Moore, J. K. and M. R. Abbott (2000). "Phytoplankton chlorophyll distributions and primary production in the Southern Ocean." *Journal of Geophysical Research - Oceans* 105(C12): 28709-28722.
- Moore, J. K. and M. R. Abbott (2002). "Surface chlorophyll concentrations in relation to the Antarctic Polar Front: seasonal and spatial patterns from satellite observations." *Journal of Marine Systems* 37(1-3): 69-86.
- Moore, J. K., M. R. Abbott and J. G. Richman (1999). "Location and dynamics of the Antarctic Polar Front from satellite sea surface temperature data." *Journal of Geophysical Research - Oceans* 104(C2): 3059-3073.
- Moore, J. K., M. R. Abbott, J. G. Richman, W. O. Smith, T. J. Cowles, K. H. Coale, W. D. Gardner and R. T. Barber (1999). "SeaWiFS satellite ocean color data from the Southern Ocean." *Geophysical Research Letters* 26(10): 1465-1468.
- Morales Maqueda, M. A. and S. Rahmstorf (2002). "Did Antarctic sea-ice expansion cause glacial CO₂ decline?" *Geophysical Research Letters* 29(0).
- Moreton, S. G. (1999). Tephrochronology of the Scotia Sea and Bellingshausen Sea, Antarctica. Cheltenham, Cheltenham and Gloucester College of Higher Education. Ph.D.: 192.
- Moreton, S. G. and J. L. Smellie (1998). "Identification and correlation of distal tephra layers in deep-sea sediment cores, Scotia Sea, Antarctica." *Annals of Glaciology* 27: 285-289.
- Mortlock, R. A., C. D. Charles, P. N. Froelich, M. A. Zibello, J. Saltzman, J. D. Hays and L. H. Burckle (1991). "Evidence for lower productivity in the Antarctic Ocean during the last glaciation." *Nature*

- 351(6323): 220-223.
- Mosseri, J., B. Quéguiner, L. Armand and V. Cornet-Barthaux (2008). "Impact of iron on silicon utilization by diatoms in the Southern Ocean: A case study of Si/N cycle decoupling in a naturally iron-enriched area." *Deep Sea Research Part II: Topical Studies in Oceanography* 55(5-7): 801-819.
- Nelson, A. R., B. F. Atwater, P. T. Bobrowsky, L. A. Bradley, J. J. Clague, G. A. Carver, M. E. Darienzo, W. C. Grant, H. W. Krueger, R. Sparks, T. W. Stafford and M. Stuiver (1995). "Radiocarbon Evidence for Extensive Plate-Boundary Rupture About 300 Years Ago at the Cascadia Subduction Zone." *Nature* 378(6555): 371-374.
- Nelson, D. M., D. J. DeMaster, R. B. Dunbar and W. O. Smith (1996). "Cycling of organic carbon and biogenic silica in the Southern Ocean: Estimates of water-column and sedimentary fluxes on the Ross Sea continental shelf." *Journal of Geophysical Research - Oceans* 101(C8): 18519-18532.
- Nelson, D. M. and L. I. Gordon (1982). "Production and pelagic dissolution of biogenic silica in the Southern Ocean." *Geochemica et Cosmochimica Acta* 46: 491-501.
- Nicholls, K. W., K. Makinson and S. Osterhus (2004). "Circulation and water masses beneath the northern Ronne Ice Shelf, Antarctica." *Journal of Geophysical Research* 109: art no.-C12017.
- Nichols, D. S., P. D. Nichols and C. W. Sullivan (1993). "Fatty-Acid, Sterol and Hydrocarbon Composition of Antarctic Sea-Ice Diatom Communities During the Spring Bloom in Mcmurdo Sound." *Antarctic Science* 5(3): 271-278.
- Nowlin, W. D. and J. M. Klinck (1986). "The Physics of the Antarctic Circumpolar Current." *Reviews of Geophysics* 24(3): 469-491.
- Ó Cofaigh, C., J. A. Dowdeswell and C. J. Pudsey (2001). "Late Quaternary Iceberg Rafting along the Antarctic Peninsula Continental Rise and in the Weddell and Scotia Seas." *Quaternary Research* 56(3): 308-321.
- O'Brien, P. (1989). The Magnetostratigraphy of marine sediments from Jane Basin, Southeast of the South Orkney Microcontinent, Antarctica. *Department of Geology*. Southampton, University of Southampton. PhD: 221.
- Opdyke, N. D. (1972). "Paleomagnetism of deep-sea cores." *Review of Geophysics* 10: 213-249.
- Orsi, A. H., G. C. Johnson and J. L. Bullister (1999). "Circulation, mixing, and production of Antarctic Bottom Water." *Progress in Oceanography* 43(1): 55-109.
- Orsi, A. H., W. D. Nowlin Jr. and T. Whitworth III (1993). "On the circulation and stratification of the Weddell Gyre." *Deep Sea Research I* 40: 169-203.
- Orsi, A. H., I. Whitworth, Thomas and J. Nowlin, Worth D. (1995). "On the meridional extent and fronts of the Antarctic Circumpolar Current." *Deep Sea Research Part I: Oceanographic Research Papers* 42(5): 641-673.
- Pahlow, M., U. Riebesell and D. A. Wolf-Gladrow (1997). "Impact of cell shape and chain formation on nutrient acquisition by marine diatoms." *Limnology and Oceanography* 42: 1660-1672.
- Pallas, R., J. L. Smellie, J. M. Casas and J. Calvet (2001). "Using tephrochronology to date temperate ice: correlation between ice tephra on Livingston Island and eruptive units on Deception Island volcano (South Shetland Islands, Antarctica)." *Holocene* 11(2): 149-160.
- Park, M. K., S. R. Yang, S. H. Kang, K. H. Chung and J. H. Shim (1999). "Phytoplankton biomass and primary production in the marginal ice zone of the northwestern Weddell Sea during austral summer." *Polar Biology* 21: 251-261.
- Patil, G. P. (2002). Environmental and ecological statistics. *Encyclopedia of Environmetrics*. A. H. a. P. El-Shaarawi, W.W. Chichester, John Wiley and Sons. 2: 672-674.
- Peltier, W. R. and R. G. Fairbanks (2006). "Global glacial ice volume and Last Glacial Maximum duration from an extended Barbados sea level record." *Quaternary Science Reviews* 25(23-24): 3322-3337.
- Pena, L. D. and I. Cacho (2009). "High- to low-latitude teleconnections during glacial terminations associated with ENSO-like variability." *PAGES News* 17(1): 5-7.
- Peterson, R. G. and T. Whitworth (1989). "The Subantarctic and Polar Fronts in relation to deep water masses through the Southwestern Atlantic." *Journal of Geophysical Research* 94((C8)): 10,817-10,838.
- Petherick, L., H. McGowan and P. Moss (2008). "Climate variability during the Last Glacial Maximum in eastern Australia: evidence of two stadials?" *Journal of Quaternary Science* 23(8): 787-802.

- Petit, J. R., J. Jouzel, D. Raynaud, N. I. Barkov, J. M. Barnola, I. Basile, M. Bender, J. Chappellaz, M. Davis, G. Delaygue, M. Delmotte, V. M. Kotlyakov, M. Legrand, V. Y. Lipenkov, C. Lorius, L. Pepin, C. Ritz, E. Saltzman and M. Stievenard (1999). "Climate and atmospheric history of the past 420,000 years from the Vostok ice core, Antarctica." *Nature* **399**(6735): 429-436.
- Pfuhl, H. A. and I. N. McCave (2005). "Evidence for late Oligocene establishment of the Antarctic Circumpolar Current." *Earth and Planetary Science Letters* **235**(3-4): 715-728.
- Pichon, J. J., G. Bareille, M. Labracherie, L. D. Labeyrie, A. Baudrimont and J. L. Turon (1992). "Quantification of the Biogenic Silica Dissolution in Southern- Ocean Sediments." *Quaternary Research* **37**(3): 361-378.
- Pichon, J. J., M. Labracherie, L. D. Labeyrie and J. Duprat (1987). "Transfer-function between diatom assemblages and surface hydrology in the Southern Ocean." *Palaeogeography Palaeoclimatology Palaeoecology* **61**(1-2): 79-95.
- Pickard, G. L. and W. J. Emery (1990). *Descriptive physical oceanography: an introduction*. - 5th ed. Oxford, Butterworth-Heinemann.
- Pike, J., C. S. Allen, A. Leventer, C. E. Stickley and C. J. Pudsey (2008). "Comparison of contemporary and fossil diatom assemblages from the western Antarctic Peninsula shelf." *Marine Micropaleontology* **67**: 274-287.
- Piotrowski, A.M., S. L. Goldstein, S. R. and Hemming, R. G. Fairbanks and D. R. Zylberberg (2008). "Oscillating glacial northern and southern deep water formation from combined neodymium and carbon isotopes." *Earth and Planetary Science Letters* **272**: 394-405.
- Pirrung, M., C. D. Hillenbrand, B. Diekmann, D. Futterer, H. Grobe and G. Kuhn (2002). "Magnetic susceptibility and ice-rafted debris in surface sediments of the Atlantic sector of the Southern Ocean." *Geo-Marine Letters* **22**(3): 170-180.
- Plenier, G., J.-P. Valet, G. Guérin, J.-C. Lefèvre, M. LeGoff and B. Carter-Stiglitz (2007). "Origin and age of the directions recorded during the Laschamp event in the Chaîne des Puys (France)." *Earth and Planetary Science Letters* **259**(3-4): 414-431.
- Pollard, R. T., I. Salter, R. J. Sanders, M. I. Lucas, C. M. Moore, R. A. Mills, P. J. Statham, J. T. Allen, A. R. Baker, D. C. E. Bakker, M. A. Charette, S. Fielding, G. R. Fones, M. French, A. E. Hickman, R. J. Holland, J. A. Hughes, T. D. Jickells, R. S. Lampitt, P. J. Morris, F. H. Nedelec, M. Nielsdottir, H. Planquette, E. E. Popova, A. J. Poulton, J. F. Read, S. Seeyave, T. Smith, M. Stinchcombe, S. Taylor, S. Thomalla, H. J. Venables, R. Williamson and M. V. Zubkov (2009). "Southern Ocean deep-water carbon export enhanced by natural iron fertilization." *Nature* **457**(7229): 577-580.
- Prasad, A. K. S. K. and J. A. Nienow (1986). "Marine diatoms of sediments from Croft Bay, Antarctica." *Antarctic Journal of the United States* **21**: 157-159.
- Prell, W. L., W. H. Hutson, D. F. Williams, A. W. H. Be, K. Geitzenauer and B. Molino (1980). "Surface circulation of the Indian-Ocean during the Last Glacial Maximum, approximately 18,000 yr BP." *Quaternary Research* **14**: 309-336.
- Presti, M., L. Barbara, D. Denis, X. Crosta, C. Kissel and L. De Santis (2008). Late Pliocene glacial/interglacial changes recorded by sediments of the Adélie Land Margin (East Antarctica). *EPICA Open science conference*. Venice, Italy.
- Presti, M., L. De Santis, G. Brancolini and P. T. Harris (2005). "Continental shelf record of the East Antarctic Ice Sheet evolution: seismo-stratigraphic evidence from the George V Basin." *Quaternary Science Reviews* **24**(10-11): 1223-1241.
- Priddle, J., D. B. Nedwell, M. J. Whitehouse, D. S. Reay, Safidge, L. C. Gilpin, E. J. Murphy and C. Ellis-Evans (1998). "Re-examining the Antarctic Paradox: speculation on the Southern Ocean as a nutrient-limited system." *Annals of Glaciology* **27**: 661-668.
- Pudsey, C. J. (1992). "Late Quaternary changes in Antarctic bottom water velocity inferred from sediment grain-size in the Northern Weddell Sea." *Marine Geology* **107**(1-2): 9-33.
- Pudsey, C. J. (2000). "Sedimentation on the continental rise west of the Antarctic Peninsula over the last three glacial cycles." *Marine Geology* **167**(3-4): 313-338.
- Pudsey, C. J. and J. A. Howe (1998). "Quaternary history of the Antarctic Circumpolar Current: evidence from the Scotia Sea." *Marine Geology* **148**(1-2): 83-112.
- Pugh, R. S., I. N. McCave, C. D. Hillenbrand and G. Kuhn (2009). "Circum-Antarctic age modelling of

- Quaternary marine cores under the Antarctic Circumpolar Current: Ice-core dust-magnetic correlation." *Earth and Planetary Science Letters* **284**: 113-223.
- Rahmstorf, S. (2002). "Ocean circulation and climate during the past 120,000 years." *Nature* **419**(6903): 207-214.
- Rahmstorf, S., M. Crucifix, A. Ganopolski, H. Goosse, I. Kamenkovich, R. Knutti, G. Lohmann, R. Marsh, L. A. Mysak, Z. Wang and A. J. Weaver (2005). "Thermohaline circulation hysteresis: A model intercomparison." *Geophysical Research Letters* **32**: L23605.
- Raymo, M. E., K. Ganley, S. Carter, D. W. Oppo and J. McManus (1998). "Millennial-scale climate instability during the early Pleistocene epoch (vol 392, pg 699, 1998)." *Nature* **394**(6695): 809.
- Raymo, M. E. and W. F. Ruddiman (1992). "Tectonic forcing of Late Cenozoic Climate." *Nature* **359**(6391): 117-122.
- Reid, J. L. (2003). "On the total geostrophic circulation of the Indian Ocean: flow patterns, tracers, and transports." *Progress In Oceanography* **56**(1): 137-186.
- Reid, J. L. (2005). "On the world-wide circulation of the deep water from the North Atlantic Ocean." *Journal of Marine Research* **63**(1): 187-201.
- Renfrew, I. A., J. C. King and T. Markus (2002). "Coastal polynyas in the southern Weddell Sea: Variability of the surface energy budget." *Journal of Geophysical Research* **107**.
- Riebesell, U., Schloss, I. and Smetacek, V. (1991). "Aggregation of algae released from melting sea-ice: implications for seeding and sedimentation." *Polar Biology* **11**(4): 239-248.
- Rintoul, S. R. (1998). On the Origin and Influence of Adélie Land Bottom Water. *Ocean, Ice, and Atmosphere: Interactions at the Antarctic Continental Margin*. S. S. Jacobs and R. Weiss. Washington, American Geophysical Union. **75**: 151-172.
- Rintoul, S. R., C. H. Hughes and D. Olbers (2001). The Antarctic Circumpolar Current System. *Ocean Circulation and Climate*. G. Siedler, J. Church and J. Gould. London, Academic Press: 271-302.
- Robinson, L. F. and T. van de Flierdt (2009). "Southern Ocean evidence for reduced export of North Atlantic Deep Water during Heinrich 1." *Geology* **36**: 991-994.
- Rodbell, D. T. (1991). Late Quaternary glaciation and climatic change in the northern Peruvian Andes. Boulder, University of Colorado. Ph.D.: 216.
- Romero, O. E., L. K. Armand, X. Crosta and J. J. Pichon (2005). "The biogeography of major diatom taxa in Southern Ocean surface sediments: 3. Tropical/Subtropical species." *Palaeogeography, Palaeoclimatology, Palaeoecology* **223**(1-2): 49-65.
- Romero, O. E., G. Fischer, C. B. Lange and G. Wefer (2000). "Siliceous phytoplankton of the western equatorial Atlantic: sediment traps and surface sediments." *Deep Sea Research Part II: Topical Studies in Oceanography* **47**(9-11): 1939-1959.
- Rowland, S. J., S. T. Belt, E. J. Wraige, G. Massé, C. Roussakis and J. M. Robert (2001). "Effects of temperature on polyunsaturation in cytotstatic lipids of *Haslea ostrearia*." *Phytochemistry* **56**(6): 597-602.
- Ruddiman, W. F. (1999). *Earth's Climate: Past and Future*. New York, W.H. Freeman.
- Sagnotti, L., P. Macri, A. Camerlenghi and M. Rebesco (2001). "Environmental magnetism of Antarctic Late Pleistocene sediments and interhemispheric correlation of climatic events." *Earth and Planetary Science Letters* **192**(1): 65-80.
- Sancetta, C., L. Heusser and M. A. Hall (1992). "Late Pliocene Climate in the Southeast Atlantic - Preliminary- Results from a Multidisciplinary Study of DSDP Site 532." *Marine Micropaleontology* **20**(1): 59-75.
- Santis, L. D., G. Brancolini and F. Donda (2003). "Seismo-stratigraphic analysis of the Wilkes Land continental margin (East Antarctica): influence of glacially driven processes on the Cenozoic deposition." *Deep Sea Research Part II: Topical Studies in Oceanography* **50**(8-9): 1563-1594.
- Sarthou, G., K. R. Timmermans, S. Blain and P. Treguer (2005). "Growth physiology and fate of diatoms in the ocean: a review." *Journal of Sea Research* **53**(1-2): 25-42.
- Schaefer, J. M., G. H. Denton, D. J. A. Barrell, S. Ivy-Ochs, P. W. Kubik, B. G. Andersen, F. M. Phillips, T. V. Lowell and C. Schluchter (2006). "Near-synchronous interhemispheric termination of the last glacial maximum in mid-latitudes." *Science* **312**(5779): 1510-1513.
- Scher, H. D., & Martin, E. E. (2006). "Timing and Climatic Consequences of the Opening of Drake Passage."

- Science* 312(5772): 428-430.
- Scherer, R. P. (1994). "A new method for the determination of absolute abundance of diatoms and other silt-sized sedimentary particles." *Journal of Paleolimnology* 12: 171-179.
- Schmittner, A., O. A. Saenko and A. J. Weaver (2003). "Coupling of the hemispheres in observations and simulations of glacial climate change." *Quaternary Science Reviews* 22(5-7): 659-671.
- Schnack-Schiel, S. B. (2003). The macrobiology of sea ice. *Sea Ice – An Introduction to its Physics, Chemistry, Biology and Geology*. Thomas, D.N. and Dieckmann, G. S. Oxford, Blackwell Science: 211-239.
- Schodlok, M. P., H. H. Hellmer and A. Beckmann (2002). "On the transport, variability and origin of dense water masses crossing the South Scotia Ridge." *Deep Sea Research Part II: Topical Studies in Oceanography* 49(21): 4807-4825.
- Schuette, G. and H. Schrader (1981). "Diatom taphocoenoses in the coastal upwelling area off south west Africa." *Marine Micropaleontology* 6: 133-155.
- Scott, P., A. McMinn and G. Hosie (1994). "Physical Parameters Influencing Diatom Community Structure in Eastern Antarctic Sea-Ice." *Polar Biology* 14(8): 507-517.
- Sedwick, P. N., S. Blain, B. Queguiner, F. B. Griffiths, M. Fiala, E. Bucciarelli and M. Denis (2002). "Resource limitation of phytoplankton growth in the Crozet Basin, Subantarctic Southern Ocean." *Deep Sea Research Part II: Topical Studies in Oceanography* 49(16): 3327-3349.
- Sedwick, P. N. and G. R. DiTullio (1997). "Regulation of algal blooms in Antarctic shelf waters by the release of iron from melting sea ice." *Geophysical Research Letters* 24(20): 2515-2518.
- Seidov, D., E. Barron and B. J. Haupt (2001). "Meltwater and the global ocean conveyor: northern versus southern connections." *Global and Planetary Change* 30(3-4): 257-270.
- Selph, K. E., M. R. Landry, C. B. Allen, A. Calbet, S. Christensen and R. R. Bidigare (2001). "Microbial community composition and growth dynamics in the Antarctic Polar Front and seasonal ice zone during late spring 1997." *Deep Sea Research Part II: Topical Studies in Oceanography* 48(19-20): 4059-4080.
- Semina, H. J. (1979). "The geography of plankton diatoms of the Southern Ocean." *Nova Hedwigia Beihefte* 64: 341-358.
- Semina, H. J. (2003). "SEM-studied diatoms of different regions of the World Ocean." *Iconographia Diatomologica* 10: 1-362.
- Shackleton, N. J. (1967). "Oxygen isotope analysis and Pleistocene temperature reassessed." *Nature* 215: 15-17.
- Shackleton, N. J., M. A. Hall and E. Vincent (2000). "Phase relationships between millennial-scale events 64,000- 24,000 years ago." *Paleoceanography* 15(6): 565-569.
- Shepherd, A., D. J. Wingham and E. Rignot (2004). "Warm ocean is eroding West Antarctic Ice Sheet." *Geophysical Research Letters* 31: L23402.
- Shemesh, A., D. A. Hodell, X. Crosta, S. L. Kanfoush, C. D. Charles and T. P. Guilderson (2002) "Sequence of events during the last deglaciation in Southern Ocean sediments and Antarctic ice cores." *Paleoceanography* 17: 1056- 1062.
- Shin, S. I., Z. G. Liu, B. L. Otto-Bliesner, J. E. Kutzbach and S. J. Vavrus (2003). "Southern Ocean sea-ice control of the glacial North Atlantic thermohaline circulation." *Geophysical Research Letters* 30(2): art. no.-1096.
- Sigman and Boyle (2001) Reply to Keeling, R. F. and M. Visbeck's "Antarctic stratification and glacial CO₂." *Nature* 412: 605-606.
- Simmonds, I. (1981) "The effect of sea ice on a general circulation model of the Southern Hemisphere." *International Association of Hydrological Sciences Special Publication* 131: 193- 206.
- Singer, B. S. (2007). Polarity transitions: radioisotopic dating. *Encyclopedia of Geomagnetism and Paleomagnetism*. D. a. H.-B. Gubbins, E., Springer: 834 - 839.
- Singer, B. S., K. A. Hoffman, E. Schnepf and H. Guillou (2008). "Multiple Brunhes Chron excursions recorded in the West Eifel (Germany) volcanics: Support for long-held mantle control over the non-axial dipole field." *Physics of the Earth and Planetary Interiors* 169(1-4): 28-40.
- Sinninghe Damsté, J. S., W. I. C. Rijpstra, M. J. L. Coolen, S. Schouten and J. K. Volkman (2007). "Rapid sulfurisation of highly branched isoprenoid (HBI) alkenes in sulfidic Holocene sediments from Ellis

- Fjord, Antarctica." *Organic Geochemistry* **38**(1): 128-139.
- Sjunneskog, C. and F. Taylor (2002). "Postglacial marine diatom record of the Palmer Deep, Antarctic Peninsula (ODP Leg 178, Site 1098) 1. Total diatom abundance." *Paleoceanography* **17**(3): 10.1029/2000PA000563.
- Smellie, J. L. (1999). "Lithostratigraphy of Miocene - Recent, alkaline volcanic fields in the Antarctic Peninsula and eastern Ellsworth Land." *Antarctic Science* **11**(3): 362-378.
- Smellie, J. L. (1999). "The upper Cenozoic tephra record in the south polar region: a review." *Global and Planetary Change* **21**(1-3): 51-70.
- Smetacek, V. (1999). "Diatoms and the Ocean Carbon Cycle." *Protist* **150**(1): 25-32.
- Smetacek, V., C. Klaas, S. Menden-deuer and T. Rynearson (2002). "Mesoscale distribution of dominant diatom species relative to the hydrological field along the Antarctic Polar Front." *Deep Sea Research Part II: Topical Studies in Oceanography* **49**: 3835-3848.
- Smith, J., K.L., B. H. Robison, J. J. Helly, R. S. Kaufmann, H. A. Ruhl, T. J. Shaw, B. S. Twining and M. Vernet (2007). "Free-drifting icebergs: hotspots of Chemical and Biological Enrichment in the Weddell Sea." *Science* **317**(5837): 478 - 482.
- Smith, J. A., Mark, B.G. and Rodbell, D.T. (2008). "The timing and magnitude of mountain glaciation in the tropical Andes." *Journal of Quaternary Science* **23**(6-7): 609-634.
- Smith, J. A., G. O. Seltzer, D. L. Farber, D. T. Rodbell and R. C. Finkel (2005). "Early Local Last Glacial Maximum in the Tropical Andes." *Science* **308**(5722): 678-681.
- Smith, J. A., G. O. Seltzer, D. T. Rodbell, R. C. Finkel and D. L. Farber (2001). "Cosmogenic dating of glaciation in the Peruvian Andes: >400 ¹⁰Be ka to last glacial maximum " *Geological Society of America Abstracts with Programs* **33**(6): 441.
- Smith, W. O. and D. Nelson (1985). "Phytoplankton bloom produced by a receding ice edge in the Ross Sea: spatial coherence with the density field." *Science* **227**: 163-166.
- Sokolov, S. and S. R. Rintoul (2002). "Structure of Southern Ocean fronts at 140°E." *Journal of Marine Systems* **37**(1-3): 151-184.
- Spall, S. A. and K. J. Richards (2000). "A numerical model of mesoscale frontal instabilities and plankton dynamics -- I. Model formulation and initial experiments." *Deep Sea Research Part I: Oceanographic Research Papers* **47**(7): 1261-1301.
- Steig, E. J., D. P. Schneider, S. D. Rutherford, M. E. Mann, J. C. Comiso and D. T. Shindell (2009). "Warming of the Antarctic ice-sheet surface since the 1957 International Geophysical Year." *Nature* **460**(7256): 766-766.
- Stickley, C. E., H. Brinkhuis, S. A. Schellenberg, A. Sluijs, U. Rohl, M. Fuller, M. Grauert, M. Huber, J. Warnaar and G. L. Williams (2004). "Timing and nature of the deepening of the Tasmanian Gateway." *Paleoceanography* **19**(4): art. no.-PA4027.
- Stickley, C. E., L. Carter, I. N. McCave and P. P. E. Weaver (2001). Lower circumpolar deep water flow through the SW Pacific gateway for the last 190 kyr: evidence from Antarctic diatoms. The Oceans and rapid climate change: past, present and future (AGU Geophysical Monograph). D. Seidov, Haupt, B.J. and Maslin, M. Washington DC, USA, American Geophysical Union. 126: 101-116.
- Stocker, T. F. and S. J. Johnsen (2003). "A minimum thermodynamic model for the bipolar seesaw." *Paleoceanography* **18**(4): art. no.-1087.
- Stocker, T. F. and O. Marchal (2000). "Abrupt climate change in the computer: Is it real?" *Proceedings of the National Academy of Sciences* **97**(4): 1362-1365.
- Stocker, T. F., D. G. Wright and L. A. Mysak (1992). "A zonally averaged, coupled ocean-atmosphere model for paleoclimate studies." *Journal of Climate* **5**: 773-797.
- Stockwell, D. A. (1991). "Distribution of Chaetoceros resting spores in the Quaternary sediments from Leg 119." *Proceedings of the Ocean Drilling Programme Scientific Results Leg 119*: 599-610.
- Stockwell, D. A. and P. E. Hargraves (1984). Morphological variability within resting spores of the marine diatom genus Chaetoceros Ehrenberg. Proceedings of the 8th Symposium on Living and Fossil Diatoms. M. Ricard. Koenigstein, S. Koeltz: 81-95.
- Stoner, J. S., J. E. T. Channell and C. Hillaire-Marcel (1998). "A 200 ka geomagnetic chronostratigraphy for the Labrador Sea: Indirect correlation of the sediment record to SPECMAP." *Earth and Planetary Science Letters* **159**: 165-181.

- Stoner, J. S., C. Laj, J. E. T. Channell and C. Kissel (2002). "South Atlantic and North Atlantic geomagnetic paleointensity stacks (0-80 ka): implications for inter-hemispheric correlation." *Quaternary Science Reviews* 21(10): 1141-1151.
- Storey, B. C., A. P. M. Vaughan and I. L. Millar (1996). Geodynamic evolution of the Antarctic Peninsula during Mesozoic times and its bearing on Weddell Sea history. *Weddell Sea Tectonics and Gondwana Break-up*. B. C. Storey, King, E.C. and Livermore, R.A. London, Special Publication Geological Society. 108: 87-104.
- Stramski, D., R. A. Reynolds, M. Kahru and B. G. Mitchell (1999). "Estimation of particulate organic carbon in the ocean from satellite remote sensing." *Science* 285: 239-241.
- Strass, V. H., U. V. Bathmann, M. M. Rutgers van den Loeff, V. Smetacek and A. Wegener (2002). "Mesoscale physics, biogeochemistry and ecology of the Antarctic Polar Front, Atlantic sector: an introduction to and summary of cruise ANT XIII/2 of R.V. Polarstern." *Deep Sea Research Part II: Topical Studies in Oceanography* 49(18): 3707-3711.
- Strass, V. H., A. C. Naveira Garabato, R. T. Pollard, H. I. Fischer, I. Hense, J. T. Allen, J. F. Read, H. Leach and V. Smetacek (2002). "Mesoscale frontal dynamics: shaping the environment of primary production in the Antarctic Circumpolar Current." *Deep Sea Research Part II: Topical Studies in Oceanography* 49(18): 3735-3769.
- Stuut, J.-B.W. (2001). Late Quaternary southwestern African terrestrial climate signals in the marine record of Walvis Ridge, SE Atlantic Ocean. *Geologica Ultraiectiona* No. 212, Utrecht University, Ph.D.
- Stuut, J.-B. W. and F. Lamy (2004) "Climate variability at the southern boundaries of the Namib (southwestern Africa) and Atacama (northern Chile) coastal deserts during the last 120,000 yrs." *Quaternary Research* 62: 301– 309.
- Stuut, J.-B. W., M. A. Prins, R. R. Schneider, G. J. Weltje, J. H. F. Jansen and G. Postma (2002) "A 300-kyr record of aridity and wind strength in southwestern Africa: inferences from grain-size distributions of sediments on Walvis Ridge, SE Atlantic Ocean." *Marine Geology* 190: 563– 571.
- Stuut, J.-B.W., X. Crosta, K. van der Borg and R. Schneider, R (2004) "Relationship between Antarctic sea ice and southwest African climate during the Late Quaternary." *Geology* 32: 909–912.
- Sugden, D. E., D. R. Marchant and G. H. Denton (1993). "The case for a stable East Antarctic ice Sheet." *Geografiska Annaler* 75A: 351.
- Suggate, R. P. and P. C. Almond (2005). "The Last Glacial Maximum (LGM) in western South Island, New Zealand: implications for the global LGM and MIS 2." *Quaternary Science Reviews* 24(16-17): 1923-1940.
- Tanimura, Y. (1992). Distribution of diatom species in the surface sediments of Lqtzow–Holm Bay, Antarctica. *Centenary of the Japanese Micropaleontology*. K. a. S. Ishizaki, T. Tokyo, Terra Scientific Publishing Company: 399-411.
- Tanimura, Y., M. Fukuchi, K. Watanabe and K. Moriwaki (1990). "Diatoms in water column and sea-ice in Lutzow-Holm Bay, Antarctica, and their preservation in preservation in the underlying sediments." *Bulletin of the National Science Museum, Tokyo, Series C* 18(1): 15-39.
- Taylor, F. and A. Leventer (2003). "Late quaternary palaeoenvironments in Prydz Bay, East Antarctica: interpretations from marine diatoms." *Antarctic Science* 15(4): 512-521.
- Taylor, F. and A. McMinn (2001). "Evidence from diatoms for Holocene climate fluctuation along the East Antarctic margin." *Holocene* 11(4): 455-466.
- Taylor, F., A. McMinn and D. Franklin (1997). "Distribution of diatoms in surface sediments of Prydz Bay, Antarctica." *Marine Micropaleontology* 32(3-4): 209-229.
- Thamban, M., S. S. Naik, R. Mohan, A. Rajakumar, N. Basavaiah, W. D'Souza, A. Kerkar, M. M. Subramaniam, M. Sudhakar and P. C. Pandey (2005). "Changes in the source and transport mechanism of terrigenous input to the Indian sector of Southern Ocean during the late Quaternary and its Palaeoceanographic implications." *Journal of Earth System Science* 114(5): 443-452.
- Thomas, D. and G. Dieckmann (2003). *Sea Ice – An Introduction to its Physics, Chemistry, Biology and Geology*. Thomas, D.N. and Dieckmann, G. S. Oxford, Blackwell Science Ltd.
- Thomas, E. (2003). Onset and Development of the Antarctic Circumpolar Current. *Seattle Annual Meeting*. Seattle.
- Thomson, M. R. A. (2004). "Geological and palaeoenvironmental history of the Scotia Sea region as a basis

- for biological interpretation." *Deep Sea Research Part II: Topical Studies in Oceanography* 51(14-16): 1467-1487.
- Thornton, D. C. O. (2002). "Diatom aggregation in the sea: mechanisms and ecological implications." *European Journal of Phycology* 37(2): 149-161.
- Tingey, R. J. (1991). The regional geology of Archaean and Proterozoic rocks in Antarctica. *The Geology of Antarctica*. R. J. Tingey. Oxford, Oxford University Press: 1-73.
- Tomas, C. R. (1997). *Identifying Marine Diatoms and Dinoflagellates*. New York, Academic Press Inc.
- Treguer, P., D. M. Nelson, A. J. Vanbennekorn, D. J. Demaster, A. Leynaert and B. Queguiner (1995). "The Silica Balance in the World Ocean - a Re-estimate." *Science* 268(5209): 375-379.
- Tremblay, J. E., M. I. Lucas, G. Kattner, R. Pollard, V. H. Strass, U. Bathmann and A. Bracher (2002). "Significance of the Polar Frontal Zone for large-sized diatoms and new production during summer in the Atlantic sector of the Southern Ocean." *Deep Sea Research Part II: Topical Studies in Oceanography* 49: 3793-3811.
- Truesdale, R. S. and T. B. Kellogg (1979). "Ross Sea diatoms: Modern assemblage distributions and their relationship to ecologic, oceanographic, and sedimentary conditions." *Marine Micropaleontology* 4: 13-31.
- Tynan, C. T. (1998). "Ecological importance of the Southern Boundary of the Antarctic Circumpolar Current." *Nature* 392(6677): 708-710.
- van der Loeff, M. M. R., K. Buesseler, U. Bathmann, I. Hense and J. Andrews (2002). "Comparison of carbon and opal export rates between summer and spring bloom periods in the region of the Antarctic Polar Front, SE Atlantic." *Deep Sea Research Part II: Topical Studies in Oceanography* 49(18): 3849-3869.
- van Iperen, J. M., T. C. E. V. Weering, J. H. F. Jansen and A. J. van Bennekom (1987). "Diatoms in surface sediments of the Zaire deep-sea fan (SE Atlantic Ocean) and their relation to overlying water masses." *Netherlands Journal of Sea Research* 21(3): 203-217.
- Vandergoes, M. J., R. M. Newnham, F. Preusser, C. H. Hendy, T. V. Lowell, S. J. Fitzsimons, A. G. Hogg, H. U. Kasper and C. Schlüchter (2005) "Regional insolation forcing of late Quaternary climate change in the Southern Hemisphere." *Nature* 436: 242-245.
- Vaughan, D. G. (2000). "Bedmap subglacial and seabed topography for Antarctica." from www.antarctica.ac.uk/BAS_Science/Highlights/2000/bedmap.html.
- Vellinga, M. a. W., R.A. (2002). "Global climatic impacts of a collapse of the Atlantic thermohaline circulation." *Climate Change* 54: 251-267.
- Venkatesan, M. I. (1988). "Organic geochemistry of marine sediments in Antarctic region: marine lipids in McMurdo Sound." *Organic Geochemistry* 12: 13-27.
- Villareal, T. A. and G. A. Fryxell (1983). "Temperature Effects on the Valve Structure of the Bipolar Diatoms *Thalassiosira antarctica* and *Porosira glacialis*." *Polar Biology* 2(3): 163-169.
- Visbeck, M. (2007). "Oceanography: Power of pull." *Nature* 447(7143): 383-383.
- Voelker, A. H. L. (2002). "Global distribution of centennial-scale records for Marine Isotope Stage (MIS) 3: a database." *Quaternary Science Reviews* 21(10): 1185-1212.
- Volkman, J. K., S. M. Barrett and G. A. Dunstan (1994). "C₂₅ and C₃₀ highly branched isoprenoid alkenes in laboratory cultures of two marine diatoms." *Organic Geochemistry* 21: 407-413.
- Wagner, G., J. Beer, C. Laj, C. Kissel, R. Muscheler, J. Masarik, M. R. and H.-A. Synal (2000). "Chlorine-36 evidence for Mono Lake event in the Summit GRIP ice core." *Earth and Planetary Science Letters* 181: 1-6.
- Walker, M. (2005). *Quaternary Dating Methods*. Chichester, John Wiley and Sons.
- Warr, K. and S. Smith (2001). *Science Matters: Changing Climate*. Cambridge, The Burlington Press (Cambridge) Ltd.
- Weppernig, R., P. Schlosser, S. Khaliwala and R. G. Fairbanks (1996). "Isotope data from Ice Station Weddell: Implications for deep water formation in the Weddell Sea." *Journal of Geophysical Research - Oceans* 101(C11): 25723-25739.
- Whitney, J., H. P. Johnson, S. Levi and B. Evans (1971). "Investigations of some magnetic and mineralogical properties of the Laschamp and Olby flows, France." *Quaternary Research* 1: 511-522.
- Willmott, V., E. W. Domack, M. Canals and S. Brachfeld (2006). "A high resolution relative paleointensity

- record from the Gerlache-Boyd paleo-ice stream region, northern Antarctic Peninsula." *Quaternary Research* **66**(1): 1-11.
- Worby, A. P., C. A. Geiger, M. J. Paget, M. L. Van Woert, S. F. Ackley and T. L. DeLiberty (2008). "Thickness and distribution of Antarctic sea-ice." *Journal of Geophysical Research* **113**.
- Yoder, J. A., S. Ackleson, R. T. Barber, P. Flamant and W. A. Balch (1994). "A line in the sea." *Nature* **371**: 689-692.
- Yoon, H. I., B. K. Khim, K. C. Yoo, Y. S. Bak and J. I. Lee (2007). "Late glacial to Holocene climatic and oceanographic record of sediment facies from the South Scotia Sea off the northern Antarctic Peninsula." *Deep Sea Research Part II: Topical Studies in Oceanography* **54**(21-22): 2367-2387.
- You, Y. (2002). "Quantitative estimate of Antarctic Intermediate Water contributions from the Drake Passage and the southwest Indian Ocean to the South Atlantic." *Journal of Geophysical Research* **107**(C4): 6:1-6:20.
- Zachos, J., M. Pagani, L. Sloan, E. Thomas and K. Billups (2001). "Trends, rhythms, and aberrations in global climate 65 Ma to present." *Science* **292**(5517): 686-693.
- Zachos, J. C., T. M. Quinn and K. A. Salamy (1996). "High-resolution (10(4) years) deep-sea foraminiferal stable isotope records of the Eocene-Oligocene climate transition." *Paleoceanography* **11**(3): 251-266.
- Zielinski, U. (1993). "Quantitative Bestimmung von Palaouweltparametern des Antarktischen Oberflächenwassers im Spätquater anhand von Transferfunktionen mit Diatomeen." *Ber. Polarforsch* **126**.
- Zielinski, U. (1997). "Parnales species (siliceous marine nanoplankton) in surface sediments of the Weddell Sea, Southern Ocean: indicators for sea ice environment?" *Marine Micropaleontology* **32**(3-4): 387-395.
- Zielinski, U., C. Bianchi, R. Gersonde and M. Kunz-Pirrung (2002). "Last occurrence datums of the diatoms *Rouxia leventerae* and *Rouxia constricta*: indicators for marine isotope stages 6 and 8 in Southern Ocean sediments." *Marine Micropaleontology* **46**(1-2): 127-137.
- Zielinski, U. and R. Gersonde (1997). "Diatom distribution in Southern Ocean surface sediments (Atlantic sector): Implications for paleoenvironmental reconstructions." *Palaeogeography Palaeoclimatology Palaeoecology* **129**(3-4): 213-250.
- Zielinski, U., R. Gersonde, R. Sieger and D. Futterer (1998). "Quaternary surface water temperature estimations: Calibration of a diatom transfer function for the Southern Ocean." *Paleoceanography* **13**(4): 365-383.
- Zwally, H. J., J. C. Comiso and A. L. Gordon (1985). Antarctic offshore leads and polynyas and oceanographic effects. *Oceanology of the Antarctic Continental Shelf*. S. S. Jacobs. Washington DC, agu: 203-226.

Appendix 1: Diatom Count Data – Core TPC063

Depth (cm)	4	24	38	54	74	82	90	99	107	115	123
<i>Actinocyclus actinochilus</i>	2	0	4	1	5	0	5	7	5	7	1
<i>Actinocyclus ingens</i>	0	0	0	0	0	0	0	1	1	0	0
<i>Asteromphalus hookeri</i>	2	0	0	2	0	0	0	0	0	3	0
<i>Asteromphalus hyalinus</i>	0	0	0	0	0	0	0	0	0	0	0
<i>Asteromphalus parvulus</i>	0	0	0	0	0	0	1	0	0	0	0
<i>Azpeitia tabularis</i>	8	8	9	10	10	3	4	5	2	1	7
<i>Cocceneis</i> spp.	0	0	1	0	1	1	1	0	0	0	0
<i>Corethron</i> spp.	4	0	0	0	1	1	1	0	0	0	0
<i>Coscinodiscus bouvet</i>	0	0	0	0	0	0	1	1	0	0	0
<i>Dactyliosolen</i> girdle bands	7	2	2	0	0	0	4	0	0	0	1
<i>Denticulopsis</i> sp.	2	0	0	0	4	1	0	2	1	0	2
<i>Eucampia antarctica</i>	23	12	16	20	19	17	46	32	40	42	44
<i>Fragilariopsis curta</i>	4	2	1	0	0	5	8	6	2	11	8
<i>Fragilariopsis cylindrus</i>	0	0	0	0	0	1	0	0	1	1	0
<i>Fragilariopsis kerguelensis</i>	274	258	143	240	117	125	117	213	180	158	181
<i>Fragilariopsis obliquecostata</i>	0	0	1	0	0	0	0	2	1	1	0
<i>Fragilariopsis rhombica</i>	0	0	0	0	0	0	2	0	0	0	0
<i>Fragilariopsis ritscheri</i>	0	0	0	0	0	0	0	0	0	0	0
<i>Fragilariopsis separanda</i>	15	19	3	14	2	2	3	4	5	2	2
<i>Fragilariopsis vanheurckii</i>	0	0	0	0	0	0	0	1	1	0	1
<i>Hyalochaete Chaetoceros</i> resting spores	84	198	172	145	211	268	166	121	149	144	163
<i>Odontella weissflogii</i>	0	0	4	0	1	0	0	0	0	0	0
<i>Paralia</i> spp.	0	1	0	0	0	0	0	0	0	0	0
<i>Porosira glacialis</i>	0	0	0	0	0	0	0	1	0	2	0
<i>Rhizosolenia antennata antennata</i>	0	0	0	1	0	1	0	0	0	0	0
<i>Rhizosolenia antennata semispina</i>	1	1	0	1	1	0	0	0	0	2	0
<i>Rhizosolenia crassa</i>	1	0	0	0	0	0	0	0	0	0	0
<i>Rhizosolenia polydactyla polydactyla</i>	15	4	3	1	0	1	2	1	1	0	1
<i>Rhizosolenia polydactyla squamosa</i>	1	0	0	0	1	0	1	0	0	0	0
<i>Rhizosolenia simplex</i>	0	0	0	1	0	0	0	1	0	1	0
<i>Rhizosolenia styliiformis</i>	0	0	0	0	0	0	0	0	0	0	0
<i>Rhizosolenia</i> spp. total	24	5	3	4	2	2	3	2	1	3	1
<i>Stellarima microtrias</i> rs	0	0	0	0	0	0	0	0	0	1	0
<i>Stephanopyxis</i>	0	0	0	0	0	0	0	0	1	0	0
<i>Thalassionema</i> spp.	3.5	0	1	0	0.5	0.5	0.5	1.5	0.5	0.5	0.5
<i>Thalassiosira antarctica</i> rs	6	4	3	1	1	1	6	3	3	6	3
<i>Thalassiosira eccentrica</i>	0	1	0	0	0	1	0	0	3	0	2
<i>Thalassiosira gracilis</i> var. <i>expecta</i>	1	1	1	1	1	1	0	1	2	3	4
<i>Thalassiosira gracilis</i> var. <i>gracilis</i>	8	5	7	5	1	2	2	4	4	4	4
<i>Thalassiosira lentiginosa</i>	91	32	56	30	41	18	43	28	38	37	30
<i>Thalassiosira oestrupii</i>	0	0	0	0	0	0	0	0	0	0	0
<i>Thalassiosira oliverana</i>	6	2	3	3	4	3	2	3	1	4	0
<i>Thalassiosira perpusilla</i>	0	1	0	0	0	0	0	0	0	0	1
<i>Thalassiosira trifulta</i>	5	0	5	1	7	8	7	13	12	6	5
<i>Thalassiosira tumida</i>	0	0	2	0	0	0	0	0	0	0	0
<i>Thalassiothrix</i> spp.	4.5	4.5	8.5	3.5	13	9	14.5	8.5	9.5	12	15
<i>Trichotoxen</i>	0.5	0	0	0	0	0	0	0	2	1	0
Unidentified centrics	4	0	5	0	2	0	0	0	0	0	0
Unidentified pennates	2	0	1	0	0	0	0	0	0	0	0
Total diatoms	580.5	555.5	451.5	480.5	443.5	469.5	437	460	465	449.5	475.5

Weight (g)	0.037	0.049	0.034	0.05	0.045	0.05	0.035	0.05	0.05	0.051	0.051
Area Counted (mm ²)	10.3	5.333	20.59	4.444	17.16	6.504	21.84	14.04	17.78	16.73	17.78
Beaker Area (mm ²)	7854	7854	7854	7854	7854	7854	7854	7854	7854	7854	7854

Appendix 1: Diatom Count Data

126	131	139	143	147	155	162	169	177	190	205	222	237	250	286
7	9	5	3	1	1	8	2	4	7	7	6	6	6	8
0	0	0	1	0	0	0	1	0	0	0	0	0	0	0
2	1	0	0	0	0	1	0	0	1	0	0	1	1	0
0	1	0	0	0	0	0	0	0	1	0	0	0	0	0
0	0	0	0	0	0	0	0	0	0	0	0	0	0	0
4	8	5	5	1	7	10	5	9	3	4	13	6	6	3
0	3	0	1	0	0	0	1	0	1	0	1	0	4	0
0	0	0	0	0	0	0	0	0	0	0	0	0	0	0
1	0	1	1	0	0	0	0	0	0	0	1	0	0	2
2	1	2	0	2	0	1	1	0	4	1	0	0	2	6
1	1	3	1	2	3	0	1	1	1	0	2	0	1	2
18	42	55	59	63	37	58	33	75	31	36	33	50	35	35
3	8	6	8	6	4	9	4	4	10	6	0	3	17	1
0	3	3	2	1	0	0	1	1	3	0	0	0	0	0
132	174	173	118	181	203	143	202	156	143	124	194	230	149	201
5	1	0	0	0	0	1	0	0	0	0	0	2	0	0
0	0	0	0	0	0	0	0	0	0	0	0	0	0	0
0	0	0	0	0	0	0	0	1	0	0	0	0	0	0
1	0	1	1	2	4	4	0	2	2	5	3	2	3	0
0	2	0	0	0	0	0	0	1	0	0	0	1	0	0
176	148	154	195	117	125	145	143	137	164	250	72	95	106	35
0	0	0	0	0	0	0	0	0	0	0	0	0	0	0
0	0	0	0	0	0	0	0	0	0	0	0	0	0	0
6	0	2	0	1	3	2	1	0	0	1	0	0	3	0
0	0	0	0	0	0	0	0	0	0	0	0	0	0	0
2	0	0	0	0	0	0	0	0	0	0	0	0	0	2
0	0	0	0	0	0	0	0	0	0	0	0	0	0	0
2	0	3	1	0	0	1	0	2	0	0	1	0	1	3
0	0	0	0	0	0	0	0	0	1	0	1	0	0	2
0	0	0	1	2	1	0	0	0	0	1	0	1	1	0
0	0	0	0	0	0	1	0	0	0	0	0	0	2	0
3	0	3	2	2	1	2	0	2	1	1	2	1	4	7
0	0	0	1	0	0	0	0	0	0	0	0	0	0	0
0	0	1	0	0	1	0	0	0	0	0	0	1	0	0
5	0.5	0	0	0	0	1.5	0	0	1	0.5	2	0.5	3.5	2.5
1	5	1	1	0	2	1	1	2	2	5	0	2	4	2
0	0	1	4	2	1	1	1	0	3	2	0	0	0	0
2	5	6	1	3	2	2	1	2	6	4	0	7	0	0
3	3	4	4	7	6	3	8	10	0	4	9	6	5	6
32	51	25	33	40	32	38	23	20	31	20	46	27	33	64
0	0	1	1	0	0	0	2	1	1	0	4	1	0	0
1	1	0	1	1	2	0	1	0	0	0	0	0	1	2
0	0	2	0	0	1	0	0	1	0	0	0	2	0	0
6	13	5	4	15	9	11	3	5	2	8	4	2	7	7
0	0	0	0	0	0	0	0	0	0	0	2	0	0	0
16.5	9.5	14.5	10.5	8.5	7	12.5	11.5	12.5	11.5	7.5	11.5	13.5	10.5	21
0	0	0.5	0	0	0	0	0	0	0	0	1.5	0	0	0.5
3	0	0	1	0	0	6	1	1	2	0	0	0	2	0
1	0	0	0	0	0	0	0	0	0	0	0	0	0	0
431.5	490	474	458.5	455.5	451	460	447.5	447.5	431.5	486	407	459	403	405

0.035	0.05	0.05	0.05	0.05	0.049	0.037	0.05	0.05	0.035	0.05	0.015	0.051	0.016	0.016
27.46	17.15	17.25	13.33	11.57	10.97	24.02	13.09	15.25	20.59	12.93	71.5	17.78	66	77
7854	7854	7854	7854	7854	7854	7854	7854	7854	7854	7854	7854	7854	7854	7854

Appendix 1: Diatom Count Data

290	294	298	302	306	310	314	318	322	326	330	334	338	342	346
4	10	9	4	5	5	17	7	6	9	8	10	10	11	8
0	0	0	0	0	0	0	0	0	0	0	0	0	0	0
0	1	1	1	0	5	0	0	1	0	4	1	1	0	1
1	0	0	0	0	0	0	0	0	0	0	0	0	0	0
0	0	0	0	0	0	0	0	0	0	2	0	0	0	0
7	6	9	19	8	8	11	3	6	9	7	8	12	11	4
1	5	1	1	1	0	0	1	0	0	3	0	0	0	1
0	0	0	0	0	0	0	0	0	0	0	0	0	0	0
0	0	0	0	0	0	1	1	0	0	0	2	0	1	0
2	3	2	0	1	4	4	1	1	3	1	1	0	0	1
0	2	1	2	0	4	2	2	3	4	2	3	4	1	2
24	43	36	42	34	28	28	39	25	34	41	33	44	22	21
7	14	3	9	12	9	5	3	4	8	3	11	10	11	9
0	2	0	0	2	1	0	0	2	2	0	0	1	2	5
182	217	178	156	217	172	198	216	246	147	197	177	204	224	214
1	4	4	1	4	5	0	1	4	7	3	2	4	5	0
2	2	1	0	0	0	0	0	0	0	0	0	0	0	4
0	0	0	0	0	0	0	0	0	0	0	0	0	0	0
4	2	5	1	1	6	3	0	2	6	1	0	2	8	2
0	0	0	0	0	0	0	0	0	0	0	0	0	0	0
102	93	92	91	104	67	34	86	68	99	42	106	115	88	167
0	1	6	0	0	0	0	0	0	2	6	3	0	0	0
0	0	0	0	0	0	0	0	0	0	0	0	0	0	0
1	1	0	1	0	2	0	4	1	13	5	12	4	2	6
0	0	1	1	0	0	0	0	0	1	0	0	0	0	0
0	0	0	0	0	0	2	0	0	0	0	0	0	0	1
0	0	0	0	0	0	0	0	0	0	0	0	0	0	0
1	1	0	1	1	0	2	0	1	0	0	0	0	0	1
0	0	0	0	0	0	1	0	0	0	0	0	0	0	0
0	1	1	0	0	2	0	0	0	1	0	0	0	1	1
0	0	0	0	0	0	0	0	1	0	0	0	0	0	0
1	5	2	2	2	2	5	0	2	2	0	0	0	1	3
0	0	0	0	0	0	0	0	0	0	0	0	0	0	0
0	0	0	0	0	0	0	0	0	0	0	0	0	0	0
1.5	2.5	2.5	3.5	1	2.5	5	2.5	0	1	0.5	2	0.5	0.5	1.5
7	3	6	1	5	0	0	5	3	4	2	6	6	6	2
0	0	0	1	0	0	0	0	0	0	0	1	0	0	0
0	0	0	0	0	0	0	0	0	0	0	1	1	1	2
3	6	2	3	8	2	3	3	4	4	1	3	5	3	2
34	65	34	54	29	55	53	34	33	48	46	58	40	40	38
1	2	1	0	2	5	0	0	0	0	0	0	0	2	2
1	0	0	0	2	2	0	3	0	1	2	0	3	0	0
0	0	0	0	0	0	0	0	0	0	0	0	0	0	0
6	8	5	8	6	5	8	4	2	7	4	7	4	2	6
0	2	0	0	0	1	0	2	0	2	1	2	4	1	0
18	19	18.5	23	14.5	10.5	18	7	6	13	9.5	9	15	7.5	7.5
2	0.5	1	0.5	0	0	0	1	0	0	0	0	1	0	0
0	2	0	2	0	1	0	0	0	4	0	2	0	1	1
0	0	0	0	0	0	0	0	0	0	0	1	0	1	0
412.5	521	420	426	458.5	402	395	425.5	419	429	391	461	490.5	452	510

0.051	0.05	0.049	0.05	0.05	0.054	0.018	0.052	0.053	0.05	0.051	0.05	0.059	0.05	0.049
19.53	13.73	17.16	27.9	17.16	11.17	104.5	22	10.3	13.73	10.3	10.3	13.73	13.73	12.11
7854	7854	7854	7854	7854	7854	7854	7854	7854	7854	7854	7854	7854	7854	7854

Appendix 1: Diatom Count Data

350	354	358	362	366	370	374	378	382	386	390	394	398	402	406
4	2	10	6	10	3	9	9	9	8	11	2	8	7	6
0	0	0	0	0	0	0	0	0	0	0	0	0	0	0
2	0	0	0	1	0	0	1	0	0	1	0	1	0	1
0	0	0	0	0	1	0	0	0	0	0	0	0	0	0
0	0	0	0	1	0	0	1	0	0	0	1	0	0	0
5	6	10	3	7	6	9	1	1	10	3	2	7	6	5
0	2	2	0	1	0	1	1	0	3	1	0	1	0	1
0	0	0	0	0	0	0	0	0	0	0	0	0	0	0
0	0	0	0	0	0	0	0	1	0	0	1	1	0	0
3	1	2	0	4	1	2	1	3	0	1	2	0	0	2
1	0	1	0	1	0	0	0	2	1	0	1	1	0	0
19	33	24	12	31	14	29	50	15	39	36	27	28	33	33
10	13	16	6	14	3	16	11	9	6	10	6	6	5	14
0	1	5	2	5	4	5	1	2	2	2	1	2	2	1
192	208	223	91	138	87	171	188	193	244	173	213	183	221	221
0	3	5	5	3	8	4	6	0	5	7	8	1	5	7
0	0	0	2	0	0	0	0	0	0	0	1	0	0	1
0	0	0	0	0	0	0	0	0	0	0	0	0	0	0
3	2	4	0	2	1	4	5	5	3	2	1	1	2	6
0	0	0	0	0	0	0	0	0	0	0	0	0	0	0
71	133	92	252	154	332	83	80	94	74	83	103	158	89	74
0	0	0	0	0	2	0	0	0	0	0	1	0	1	0
0	0	0	0	0	0	0	0	0	0	0	0	0	0	0
13	6	11	4	7	5	6	0	5	5	3	0	1	4	2
0	0	1	1	0	0	0	0	0	0	0	0	0	0	0
0	0	0	0	1	0	0	0	0	0	0	0	0	0	0
1	0	0	0	0	0	0	0	0	0	1	1	0	0	0
0	0	0	1	2	1	2	0	0	1	2	1	0	1	1
0	0	0	0	0	0	0	0	2	0	0	0	0	0	0
0	3	2	2	0	2	2	0	0	1	3	2	1	3	2
0	0	0	0	1	0	0	0	0	0	0	0	0	0	1
1	3	3	4	4	3	4	0	1	3	6	4	1	4	4
0	0	0	0	0	0	0	0	0	0	0	0	0	0	0
0	0	0	0	0	0	0	0	0	0	0	0	0	0	0
2.5	0.5	3.5	0	2	1	4	0.5	5	0	1	0.5	0	1	1.5
0	6	3	7	5	6	1	3	0	0	3	4	5	5	1
0	0	0	0	1	0	0	0	1	0	0	0	0	0	0
0	0	0	1	5	3	1	0	0	1	0	1	2	0	3
11	6	7	1	5	5	9	5	6	4	1	4	0	2	5
43	23	45	16	53	9	23	27	42	29	53	49	37	42	39
0	0	0	0	3	0	0	1	0	0	0	0	3	0	1
1	0	0	1	0	1	1	0	0	1	0	1	0	2	0
0	0	0	0	0	0	0	0	0	0	0	0	0	0	0
11	1	11	2	0	1	2	3	2	6	3	2	4	2	2
0	0	2	1	1	0	1	1	0	0	2	4	0	1	0
9.5	6	7	0	3.5	8	11.5	8.5	10.5	8	8.5	14	7	6.5	13.5
0	0.5	0.5	1.5	0	0	0	0	0	1.5	0	0	0	0	0
0	1	4	1	4	0	2	0	0	0	0	0	1	0	2
0	0	0	0	2	0	1	0	0	0	0	0	0	0	0
402	457	491	418.5	467.5	504	399.5	404	406.5	453.5	410.5	453.5	459	440.5	446

0.018	0.05	0.052	0.05	0.051	0.046	0.05	0.05	0.019	0.05	0.054	0.05	0.052	0.051	0.053
44	13.73	13.73	6.864	13.73	10.3	17.16	15.6	66	13.73	13.73	13.73	10.3	7.738	13.73
7854	7854	7854	7854	7854	7854	7854	7854	7854	7854	7854	7854	7854	7854	7854

Appendix 1: Diatom Count Data

410	414	418	422	426	430	434	438	442	446	450	454	458	462	466
6	9	6	11	7	5	1	16	8	5	6	9	4	5	10
0	0	0	0	0	0	0	0	0	0	0	0	0	0	0
0	0	0	2	2	0	2	2	0	1	0	2	1	1	1
0	0	0	0	0	0	0	0	0	0	0	0	0	0	0
1	0	0	0	0	0	0	0	0	1	0	2	0	0	0
9	6	5	5	5	7	7	9	5	6	3	9	13	10	4
0	0	1	0	0	0	0	0	0	0	0	1	1	1	0
0	0	0	0	0	0	0	0	0	0	0	0	0	0	0
0	0	1	2	0	0	0	1	0	1	0	0	0	0	0
0	5	0	2	0	0	3	3	1	3	0	0	1	3	1
2	0	1	0	3	1	2	2	0	1	1	2	1	0	1
29	21	37	38	46	35	28	34	11	31	35	35	42	27	43
9	8	13	5	0	8	7	7	3	9	9	7	8	5	9
0	3	1	2	1	5	0	1	1	1	2	0	1	0	0
253	218	241	202	238	239	203	286	226	215	98	195	224	203	255
1	0	2	1	2	9	2	3	0	2	2	2	6	2	8
0	0	2	1	0	0	1	0	0	0	1	0	0	0	1
0	0	0	0	0	0	0	0	0	0	0	0	0	0	0
0	2	1	0	1	11	3	0	2	3	7	4	7	7	6
0	0	0	0	0	0	0	0	0	0	0	0	0	0	0
134	53	68	77	116	112	91	48	32	65	302	64	69	112	72
1	0	0	1	0	0	2	0	0	2	1	1	5	3	1
0	0	0	0	0	0	0	0	0	0	0	0	0	0	0
4	1	0	1	1	0	0	0	0	1	1	2	1	3	3
0	0	0	0	0	0	0	0	0	0	0	0	0	0	0
0	1	1	0	0	1	0	0	1	0	1	0	0	0	1
0	0	0	0	0	0	0	0	0	0	0	0	0	0	0
0	1	2	0	0	0	0	0	1	2	1	0	4	5	0
0	1	0	0	0	0	0	0	3	0	0	0	0	0	0
2	0	1	3	0	0	0	0	0	3	2	2	4	0	2
0	0	0	1	0	0	0	3	0	0	0	2	0	1	0
2	3	4	4	0	1	0	3	5	5	4	4	8	6	3
0	0	0	0	0	0	0	0	0	0	0	0	0	0	0
0	0	0	0	0	0	0	0	0	0	0	0	0	0	0
2	1.5	1.5	2.5	1	2.5	1.5	2	3.5	0.5	0	0.5	3	1	1
7	0	7	2	9	5	4	3	1	8	5	6	14	5	8
0	1	0	0	0	0	0	0	1	0	0	2	0	0	0
2	0	1	2	0	1	0	0	0	1	1	1	0	0	0
1	14	4	2	3	4	5	6	7	2	6	3	8	2	4
36	50	46	60	48	61	37	67	78	37	29	56	44	59	38
0	0	1	3	0	0	2	1	1	0	0	3	0	1	2
4	1	0	4	4	1	2	3	0	1	0	3	4	2	1
0	0	0	0	0	0	0	0	0	0	0	0	0	0	0
7	2	4	3	2	4	4	4	1	1	4	6	3	10	6
0	0	1	1	0	2	0	2	0	0	0	1	0	0	0
11.5	12.5	14	22.5	12	20.5	6.5	15	17	17.5	7	15.5	16	18.5	17.5
0	0	0	0.5	0.5	0	0	0.5	0	0.5	0.5	0	1	0.5	0
0	0	0	2	0	0	2	4	0	1	0	0	0	1	1
0	0	0	0	0	4	0	0	0	0	0	0	0	0	1
521.5	411	462.5	458.5	501.5	538	416	522.5	403.5	421.5	524.5	436	485	488	497.5

0.052	0.017	0.052	0.053	0.051	0.05	0.052	0.06	0.018	0.05	0.048	0.056	0.052	0.05	0.051
13.73	44	13.73	10.3	13.73	10.3	10.3	10.3	38.5	10.3	10.3	10.3	10.3	10.3	13.73
7854	7854	7854	7854	7854	7854	7854	7854	7854	7854	7854	7854	7854	7854	7854

Appendix 1: Diatom Count Data

470	474	478	482	486	490	494	510	542	574	606	638	670	702
8	11	0	1	2	4	5	5	7	6	6	8	7	9
0	0	0	0	0	0	0	0	0	0	0	0	0	0
0	2	0	0	0	0	0	0	1	1	1	1	2	1
0	0	0	0	0	0	0	0	0	0	0	0	0	0
0	0	0	0	1	0	1	0	0	0	0	0	0	0
13	10	0	3	3	4	5	17	6	5	7	11	1	6
0	2	0	0	0	0	1	1	0	0	0	0	0	0
0	0	0	0	0	0	0	0	0	0	0	0	0	0
0	1	0	1	1	1	0	0	0	0	0	0	0	1
2	4	4	1	2	0	0	0	5	0	1	3	8	3
0	0	0	0	0	0	0	2	1	1	2	0	0	0
43	29	0	17	15	5	17	17	17	10	21	29	12	16
8	11	10	7	0	8	3	9	2	11	9	6	8	7
0	0	0	0	1	0	1	1	1	2	0	0	0	0
237	216	5	124	157	77	193	206	203	255	214	220	251	246
2	0	1	1	1	1	6	0	0	0	0	0	0	0
0	0	0	0	0	0	0	0	0	0	0	0	0	0
0	0	0	0	0	0	0	0	0	0	0	0	0	0
5	1	1	3	4	1	2	1	2	2	1	0	1	4
0	0	0	0	0	0	0	0	0	0	0	0	0	0
51	62	443	261	213	339	153	38	64	41	50	24	52	33
0	0	1	0	1	1	1	0	1	0	2	0	0	0
0	0	0	0	0	0	0	0	0	0	0	0	0	0
1	0	0	1	4	0	2	0	1	0	0	2	0	0
0	0	3	0	0	0	0	0	0	0	0	0	0	0
0	0	1	0	0	0	0	0	0	0	1	1	1	3
0	0	0	1	0	0	0	0	0	0	0	1	0	0
0	2	1	1	0	5	0	1	3	2	4	1	9	0
0	2	0	0	0	0	0	2	6	3	0	0	0	0
1	0	1	0	1	0	1	0	0	1	0	0	0	0
0	0	0	1	0	0	1	0	0	1	0	0	0	0
1	4	6	3	1	5	2	3	9	6	5	4	10	3
0	0	0	0	0	0	0	0	0	0	0	0	0	0
0	0	0	0	0	0	0	0	0	0	0	0	0	0
1	1.5	0	0.5	0	0	0	2.5	5	4.5	9.5	6	3.5	3
1	1	4	6	4	1	6	0	2	0	1	0	1	0
0	0	0	0	0	0	0	0	0	1	0	0	0	0
1	0	1	0	1	0	0	0	0	0	0	0	0	0
0	7	3	4	4	1	6	3	10	6	5	9	4	7
58	54	2	12	21	10	27	78	64	50	53	44	70	57
1	0	0	0	1	2	0	0	0	0	0	0	0	1
3	0	0	1	1	1	3	3	0	0	1	0	0	0
0	0	0	0	0	0	0	0	0	0	0	0	0	0
10	6	0	1	4	1	2	5	8	7	3	7	6	7
2	0	0	1	0	0	0	0	0	0	0	0	0	0
14.5	15	0.5	4	8	4.5	13	21	18	11.5	20	15.5	10	5
1	0	0	0	0	0	0	0	0	0	0	0	0	0
0	0	0	0	0	0	1	0	0	0	3	1	0	2
0	0	0	0	0	0	2	0	2	0	0	1	0	0
463.5	437.5	481.5	452.5	450	466.5	452	412.5	429	420	414.5	391.5	446.5	411

0.05	0.016	0.046	0.044	0.051	0.045	0.045	0.017	0.017	0.017	0.017	0.017	0.016	0.017
13.73	44	0.593	4.477	5.163	3.728	8.939	27.5	38.5	38.5	38.5	38.5	27.5	38.5
7854	7854	7854	7854	7854	7854	7854	7854	7854	7854	7854	7854	7854	7854

Appendix 1: Diatom Count Data – TPC286

Depth (cm)	0	16	32	36	50	66	74	82	90	98	110
<i>Actinocyclus actinochilus</i>	8	7	4	7	15	18	15	20	9	5	13
<i>Actinocyclus ingens</i>	0	0	0	0	1	0	0	0	1	0	0
<i>Asteromphalus hookeri</i>	0	0	0	0	0	0	0	0	0	0	0
<i>Asteromphalus hyalinus</i>	0	0	0	1	0	0	0	0	0	0	0
<i>Azpeitia tabularis</i>	0	0	0	0	1	0	0	0	0	0	0
<i>Cocceneis</i> spp.	1	1	0	0	0	0	0	0	0	0	2
<i>Corethron</i> spp.	0	0	0	0	0	0	0	0	2	0	0
<i>Coscinodiscus bouvet</i>	1	0	0	0	0	0	0	2	0	0	0
<i>Cyclotella</i> sp.	0	2	0	0	2	0	0	0	0	0	0
<i>Dactylosolen</i> girdle bands	2	2	2	0	1	0	1	0	1	1	0
<i>Denticulopsis</i> sp.	1	1	0	0	0	0	1	1	1	0	2
<i>Eucampia antarctica</i>	7	21	5	13	146	100	129	110	124	36	91
<i>Fragilariopsis curta</i>	20	4	16	8	5	7	1	2	1	4	3
<i>Fragilariopsis cylindrus</i>	4	1	7	5	0	0	0	1	0	1	0
<i>Fragilariopsis kerguelensis</i>	21	24	16	14	111	111	73	75	52	43	55
<i>Fragilariopsis obliquecostata</i>	6	0	3	3	2	30	0	2	0	3	3
<i>Fragilariopsis rhombica</i>	0	0	0	0	0	0	0	0	0	0	0
<i>Fragilariopsis ritscheri</i>	0	0	0	0	3	0	0	0	0	0	0
<i>Fragilariopsis separanda</i>	1	3	0	0	4	0	2	0	2	3	3
<i>Fragilariopsis sublinearis</i>	0	0	0	0	0	0	0	0	0	0	0
<i>Fragilariopsis vanheurckii</i>	0	2	0	0	0	0	0	0	0	0	0
<i>Hyalochaete Chaetoceros</i> resting spores	402	323	360	345	77	200	115	101	127	158	94
<i>Melosira</i> spp.	0	0	0	0	0	0	0	0	0	0	0
<i>Odontella weissflogii</i>	5	1	0	2	6	14	1	5	6	4	5
<i>Paralia</i> spp.	0	0	0	0	0	0	0	0	0	1	0
<i>Porosira glacialis</i>	2	0	1	1	4	10	4	6	2	5	3
<i>Porosira pseudodenticulata</i>	0	0	0	0	0	0	0	0	0	0	0
<i>Rhizosolenia antennata semispina</i>	7	1	0	3	2	0	3	2	1	0	2
<i>Rhizosolenia crassa</i>	0	0	0	0	1	0	0	0	0	0	0
<i>Rhizosolenia polydactyla polydactyla</i>	2	13	0	1	2	2	2	2	0	5	3
<i>Rhizosolenia polydactyla squamosa</i>	0	0	0	0	0	0	0	0	0	0	0
<i>Rhizosolenia sima sima</i>	0	0	0	0	0	0	0	0	0	0	0
<i>Rhizosolenia simplex</i>	10	3	4	4	1	3	1	0	2	1	1
<i>Rhizosolenia styliformis</i>	8	0	6	5	0	0	0	0	0	0	1
<i>Rhizosolenia</i> spp. total	27	17	10	13	6	5	6	4	3	6	7
<i>Stellarima microtrias</i> rs	1	2	0	0	1	4	6	7	8	4	1
<i>Stephanopyxis</i>	0	0	0	0	1	0	0	0	2	0	0
<i>Thalassionema</i> spp.	0	0	0	0	0	0	0	0	0	0	0.5
<i>Thalassiosira antarctica</i> rs (cold)	3	0	1	1	0	0	2	7	5	4	3
<i>Thalassiosira antarctica</i> rs (warm)	16	16	14	18	12	15	28	60	51	32	41
<i>Thalassiosira eccentrica</i>	0	0	0	0	1	0	3	0	1	0	0
<i>Thalassiosira gracilis</i> var. <i>expecta</i>	3	2	1	3	0	0	3	1	2	0	0
<i>Thalassiosira gracilis</i> var. <i>gracilis</i>	5	4	7	6	13	2	4	7	3	4	5
<i>Thalassiosira lentiginosa</i>	15	13	5	3	36	23	40	29	45	21	59
<i>Thalassiosira oestrupii</i>	0	0	0	0	0	0	0	0	0	1	0
<i>Thalassiosira oliverana</i>	1	1	0	0	0	3	6	2	2	0	2
<i>Thalassiosira perpusilla</i>	0	0	0	0	0	0	0	0	0	0	0
<i>Thalassiosira trifulta</i>	0	0	0	1	8	4	3	2	4	3	1
<i>Thalassiosira tumida</i>	0	0	0	0	0	0	0	0	0	1	0
<i>Thalassiothrix</i> spp.	1.5	0.5	2.5	2.5	2.5	0.5	1	2	1	0	1
<i>Trichotoxen</i>	0	0	0	0	1	0	0	0	0	0	0
Extinct reworked	0	0	0	0	0	0	0	0	0	0	0
Unidentified centrics	1	0	0	0	0	0	0	2	0	1	0
Unidentified pennates	0	0	0	1	0	0	0	0	0	1	0

Appendix 1: Diatom Count Data

Total diatoms	554.5	447.5	454.5	447.5	459.5	546.5	444	448	455	342	394.5
Dummy variable (DV)	0	0	0	0	0	0	0	0	0	0	0
Valve total (inc. DV)	554.5	447.5	454.5	447.5	459.5	546.5	444	448	455	342	394.5

Weight (g)	0.04	0.046	0.05	0.07	0.045	0.05	0.05	0.071	0.07	0.051	0.04
Area Counted (mm2)	6.864	8.12	3.432	7.55	24.74	10.3	43.67	17.16	40	33.57	21.84
Beaker Area (mm2)	7854	7854	7854	7854	7854	7854	7854	7854	7854	7854	7854

118	126	130	138	146	154	162	182	194	206	218	222	226	230	234
12	14	10	15	19	28	4	18	5	15	7	20	17	11	17
0	1	0	1	1	1	0	0	0	0	0	0	0	0	0
0	0	0	0	0	0	0	0	0	0	0	0	0	0	0
0	0	0	0	0	0	0	0	0	1	0	0	0	1	0
0	0	0	0	1	1	0	2	0	0	0	0	0	0	0
0	0	0	0	1	0	0	0	0	0	0	0	0	0	0
0	0	0	0	0	0	0	0	2	142	0	0	0	1	0
0	0	0	0	0	0	0	0	0	0	0	0	1	0	0
0	0	0	0	0	0	0	0	0	0	0	0	0	0	0
0	0	0	0	0	0	2	1	6	4	0	0	0	0	0
2	0	0	0	0	0	1	0	1	0	3	1	0	0	0
129	95	101	145	138	91	59	54	17	9	75	127	52	27	33
0	1	1	2	0	2	8	1	6	11	2	3	20	16	4
0	0	0	2	0	0	1	0	0	0	0	0	0	7	0
73	63	100	92	102	41	32	109	25	26	15	41	72	41	83
0	0	21	1	0	1	7	0	8	6	0	2	34	4	0
0	0	0	0	0	0	0	0	0	0	0	0	0	0	1
0	1	0	1	0	0	0	0	0	0	0	2	0	4	0
2	3	2	3	4	2	0	5	1	1	0	0	2	1	0
0	0	0	0	0	0	0	0	0	0	1	5	0	2	0
0	0	0	0	0	1	0	0	0	2	0	0	0	5	0
98	137	110	102	137	138	210	95	279	168	57	179	228	343	206
0	0	0	0	0	0	0	0	0	0	0	0	0	0	0
5	2	3	2	2	3	7	5	1	0	3	3	6	2	1
0	0	0	0	0	0	0	0	0	0	0	0	0	0	0
1	3	3	0	1	3	0	0	2	0	2	5	5	2	1
0	0	2	0	0	0	0	0	0	0	0	0	0	0	0
0	0	1	0	0	0	0	0	0	7	0	0	2	0	0
0	0	0	0	0	0	1	0	0	0	0	0	0	0	0
2	1	1	1	2	6	7	31	2	2	2	5	0	1	77
0	0	0	0	0	0	17	0	0	0	0	0	0	0	0
0	0	0	0	0	0	0	0	0	0	0	0	0	1	1
1	1	2	1	0	3	12	6	0	0	0	4	0	0	2
0	0	0	0	0	0	0	0	0	0	0	0	6	0	0
3	2	4	2	2	9	37	37	2	9	2	9	8	2	80
1	0	2	1	1	1	0	0	1	0	0	3	0	0	0
0	0	0	0	0	0	0	0	0	0	0	0	0	0	0
0	0	0	0.5	0	0	1	0	0	0.5	0	0	0	0	0
3	8	1	1	3	7	5	15	0	0	8	23	15	4	1
77	90	51	27	19	11	17	7	3	3	3	3	0	3	1
0	0	0	0	0	2	0	0	0	0	0	0	0	0	0
1	1	0	2	1	2	0	0	0	12	0	0	0	0	0
4	1	8	1	2	3	2	1	4	4	1	1	7	3	2
40	14	29	54	63	115	27	96	48	49	25	26	14	11	30
0	0	0	0	0	0	1	0	0	0	0	0	0	0	0
3	3	1	0	0	1	0	0	0	0	0	2	1	0	1
0	0	0	0	0	0	0	0	1	0	0	0	0	0	0
4	2	1	13	1	3	1	1	0	0	0	0	0	1	0

Appendix 1: Diatom Count Data

0	0	0	1	0	0	0	0	1	0	1	2	1	0	0
0	0.5	0	1	1.5	2.5	2.5	8	6.5	4	0	2.5	1	0	1
0.5	0.5	0	0.5	0	0.5	0	0	1	0.5	0	0	1.5	0	0
0	0	0	0	0	0	0	0	0	0	1	0	0	0	0
0	0	0	2	0	0	1	0	0	0	0	0	1	0	1
0	0	0	0	0	0	1	0	0	0	0	0	0	0	0
458.5	442	450	472	499.5	469	426.5	455	420.5	467	206	459.5	486.5	491	463
0	0	0	0	0	0	0	0	0	0	194	0	0	0	0
458.5	442	450	472	499.5	469	426.5	455	420.5	467	400	459.5	486.5	491	463

0.051	0.051	0.05	0.051	0.059	0.069	0.051	0.07	0.073	0.081	0.069	0.07	0.07	0.069	0.07
13.33	4.444	3.791	5.737	7.171	19.8	34.63	39.27	6.864	5.232	34.66	14.73	6.864	4.134	10.59
7854	7854	7854	7854	7854	7854	7854	7854	7854	7854	7854	7854	7854	7854	7854

238	242	246	250	254	258	262	266	270	274	278	282	286	290	294
3	5	0	1	0	0	0	0	0	0	0	0	0	0	0
0	0	0	0	0	0	0	0	0	0	0	0	0	0	0
0	0	0	0	0	0	0	0	0	0	0	0	0	0	0
0	0	0	0	0	0	0	0	0	0	0	0	0	0	0
0	0	0	0	0	0	0	0	0	0	0	0	0	0	0
0	0	0	0	0	0	0	0	0	0	0	0	0	0	0
0	0	0	0	0	0	0	0	0	0	0	0	0	0	0
0	0	0	0	0	0	0	0	0	0	0	0	0	0	0
0	0	0	0	0	0	0	0	0	0	0	0	0	0	0
0	0	0	0	0	0	0	0	0	0	0	0	0	0	0
0	0	0	0	0	0	0	0	0	0	0	0	0	0	0
0	2	1	1	0	0	0	0	0	0	0	0	0	0	0
18	10	7	10	1	0	0	0	0	0	0	0	0	0	0
1	1	0	1	0	0	3	1	0	0	0	0	0	0	1
0	0	0	0	0	0	0	0	0	0	0	0	0	0	0
5	11	1	1	0	0	1	0	0	0	0	0	0	0	1
0	0	0	0	0	0	0	0	0	0	0	0	0	0	0
0	0	0	0	0	0	0	0	0	0	0	0	0	0	0
0	0	0	0	0	0	0	0	0	0	0	0	0	0	0
0	0	0	0	0	0	0	0	0	0	0	0	0	0	0
1	1	0	0	0	0	0	0	0	0	0	0	0	0	0
0	0	0	0	0	0	0	0	0	0	0	0	0	0	0
0	0	0	0	0	0	0	0	0	0	0	0	0	0	0
59	45	13	32	12	0	47	9	0	21	1	11	7	4	5
0	0	0	0	0	0	0	0	0	0	0	0	0	0	0
1	2	0	0	0	0	0	0	0	0	0	0	0	0	0
0	0	1	0	0	0	0	0	0	0	0	0	0	0	0
2	0	0	0	0	0	0	0	0	0	0	0	0	0	0
0	0	0	0	0	0	0	0	0	0	0	0	0	0	0
0	0	0	0	0	0	0	0	0	0	0	0	0	0	0
0	0	0	0	0	0	0	0	0	0	0	0	0	0	0
0	0	1	0	0	0	1	0	0	0	0	0	0	0	0
1	2	1	1	0	0	0	0	0	0	0	0	0	0	0
0	0	0	0	0	0	0	0	0	0	0	0	0	0	0
0	0	0	0	0	0	0	0	0	0	0	0	0	0	0
0	0	0	0	0	0	0	0	0	0	0	0	0	0	0
0	0	0	0	0	0	0	0	0	0	0	0	0	0	0
0	0	0	0	0	0	0	0	0	0	0	0	0	0	0
1	2	2	1	0	0	1	0	0	0	0	0	0	0	0
0	0	0	0	0	0	0	0	0	0	0	0	0	0	0
1	0	0	3	1	0	0	0	0	0	0	0	0	0	0
0.5	0	0	0	0	0	0	0	0	0	0	0	0	0	0
3	1	0	0	0	0	0	0	0	0	0	0	0	0	0
0	2	0	0	0	0	0	0	1	0	0	0	2	0	0
0	0	0	0	0	0	0	0	0	0	0	0	0	0	0
1	0	0	0	0	0	1	0	0	0	0	0	0	0	0

Appendix 1: Diatom Count Data

0	0	0	0	0	0	0	0	0	0	0	0	0	0	0
6	8	0	0	0	0	0	0	0	0	0	0	0	0	0
0	0	0	0	0	0	0	0	0	0	0	0	0	0	0
0	0	0	0	0	0	0	0	0	0	0	0	0	0	0
0	0	0	0	0	0	0	0	0	0	0	0	0	0	0
0	0	0	3	0	0	0	0	0	0	0	0	0	0	0
0	0	0	0	0	0	0	0	0	0	0	0	0	0	0
0	0.5	0	0	0	0	0	0	0	0	0	0	0	0	0
0	0.5	0	0	0	0	0	0	0	0	0	0	0	0	0
0	0	0	4	0	0	0	0	0	0	0	0	0	0	0
0	0	0	0	0	0	0	0	0	0	0	0	0	0	0
0	1	0	0	0	0	0	0	0	0	0	0	0	0	0
102.5	92	25	57	14	0	53	10	1	21	1	11	9	4	7
297.5	308	375	343	386	400	347	390	399	379	399	389	391	396	393
400	400	400	400	400	400	400	400	400	400	400	400	400	400	400

0.694	0.069	0.071	0.069	0.07	0.071	0.069	0.07	0.07	0.07	0.07	0.07	0.07	0.073	0.069
30.53	34.32	30.39	31.76	31.59	34.32	30.97	31.82	32.51	44.44	44.44	44.44	43.15	34.32	44.44
7854	7854	7854	7854	7854	7854	7854	7854	7854	7854	7854	7854	7854	7854	7854

298	302	306	310	314	318	322	326	330	334	338	342	346	350	354
0	5	0	0	0	0	1	0	0	0	0	0	0	0	0
0	0	2	0	0	0	0	0	0	0	0	0	0	0	0
0	0	0	0	0	0	0	0	0	0	0	0	0	0	0
0	0	0	0	0	0	0	0	0	0	0	0	0	0	0
0	0	0	0	0	0	0	0	0	0	0	0	0	0	0
0	0	0	0	0	0	1	0	0	0	0	0	0	0	1
0	0	0	0	0	0	0	0	0	0	0	0	0	0	0
0	0	0	0	0	0	0	0	0	0	0	0	0	0	0
0	0	0	0	0	0	0	0	0	1	1	0	1	0	0
0	0	1	0	0	0	2	0	0	0	0	0	1	0	0
0	0	0	0	0	0	0	0	0	0	0	0	0	0	1
0	0	0	0	0	0	0	0	0	0	0	0	1	1	17
0	0	0	0	0	0	0	0	0	0	0	0	0	0	3
0	0	0	0	0	0	0	0	0	0	0	0	0	0	0
0	0	1	0	0	0	1	1	0	0	0	0	0	0	13
0	0	0	0	0	0	0	0	0	0	0	0	0	0	7
0	0	0	0	1	0	0	0	0	0	0	0	0	0	0
0	0	0	0	0	0	0	0	0	0	0	0	0	0	0
0	0	0	0	0	0	0	0	0	0	0	0	0	1	0
0	0	0	0	0	0	0	0	0	0	0	0	0	0	0
0	0	0	0	0	0	0	0	0	0	0	0	0	0	0
5	4	7	2	4	2	23	3	7	2	2	1	0	9	429
0	0	0	0	0	0	0	0	0	0	0	0	0	0	0
0	0	0	0	0	0	0	0	0	0	0	0	0	0	2
0	0	0	0	0	0	0	0	0	0	0	0	0	0	0
0	0	0	0	0	0	0	0	0	0	0	0	0	0	0
0	0	0	0	0	0	0	0	0	0	0	0	0	0	0
0	0	0	0	0	0	0	0	0	0	0	0	0	0	0
0	0	0	0	0	0	0	0	0	0	0	0	0	0	0
0	0	0	0	0	0	0	0	0	0	0	0	0	0	2
0	0	0	0	0	0	0	0	0	0	0	0	0	0	0
0	0	1	0	0	0	0	0	0	0	0	0	0	0	0
0	0	0	0	0	0	0	0	0	0	0	0	0	0	0
0	0	1	0	0	0	0	0	0	0	0	0	0	0	2
0	0	0	0	0	0	0	0	0	0	0	0	0	0	0

Appendix 1: Diatom Count Data

0	1	0	0	0	0	0	0	0	0	0	0	0	0	0
0	0	0	0	0	0	0	0	0	0	0	0	0	0	0
0	0	0	0	0	0	0	0	0	0	0	0	0	0	0
0	1	1	0	0	0	0	0	1	0	0	0	0	0	7
0	0	0	0	0	0	0	0	0	0	0	0	0	0	0
0	0	0	0	0	1	0	0	0	0	0	1	0	0	2
0	0	0	0	0	0	0	0	0	0	0	0	0	0	7
0	0	0	0	0	0	0	0	0	0	0	1	0	0	5
0	0	0	0	0	0	0	0	0	0	0	0	0	0	0
0	0	0	0	0	0	0	0	0	0	0	0	0	0	0
0	0	0	0	0	0	0	0	0	0	0	0	0	0	0
0	0	0	0	0	0	0	0	0	0	0	0	0	0	0
0	0	0	0	0	0	0	0	0	0	0	0	0	0	0
0	0	0	0	0	0	0	0	0	0	0	0	0	0	0
0	0	0	0	0	0	0	0	0	0	0	0	0	0	1.5
0	0	0	0	0	0	0	0	0	0	0	0	0	0	0
0	0	0	0	0	0	0	0	0	0	0	0	0	0	0
0	0	6	0	0	0	0	0	0	0	0	0	0	0	1
0	0	0	0	0	0	0	0	0	0	0	0	0	0	0
5	11	19	2	5	3	28	4	8	3	3	3	3	11	498.5
395	389	381	398	395	397	372	396	392	397	397	397	397	389	0
400	400	400	400	400	400	400	400	400	400	400	400	400	400	498.5

0.069	0.07	0.071	0.071	0.07	0.071	0.071	0.07	0.069	0.07	0.071	0.07	0.07	0.07	0.058
44.44	41.73	43.27	44.24	44.44	44.44	34.32	43.71	44.44	42.38	43.43	42.42	30.93	44.44	2.246
7854	7854	7854	7854	7854	7854	7854	7854	7854	7854	7854	7854	7854	7854	7854

358	362	366	370	374	378	386	406	418	450	479	511	543	576	608
4	1	11	3	7	13	13	0	0	0	0	0	0	13	19
0	0	0	0	0	1	0	0	0	0	0	0	0	0	0
0	0	0	0	0	0	0	0	0	0	0	0	0	0	0
0	0	0	0	0	0	0	0	0	0	0	0	0	0	0
0	0	0	0	0	0	0	0	0	0	0	0	0	0	0
0	0	0	0	0	0	0	0	0	0	0	0	0	1	2
0	0	0	1	0	0	0	0	0	0	0	0	0	0	0
0	0	0	0	0	0	0	0	0	0	0	0	0	0	0
0	0	0	0	0	1	0	0	0	0	0	0	0	0	0
4	1	4	0	4	1	0	0	0	0	0	0	0	0	1
0	1	0	0	1	0	1	0	0	0	0	0	1	2	2
3	0	6	6	10	34	21	3	0	0	0	0	0	153	102
3	9	7	12	6	15	11	0	3	0	0	0	0	0	5
0	0	0	2	0	0	0	0	0	0	0	0	0	0	5
3	2	20	8	6	36	23	0	2	0	0	1	0	46	68
1	2	3	2	5	3	31	0	0	0	0	0	0	10	6
0	0	0	0	0	0	0	0	0	0	0	0	0	0	0
0	0	0	0	0	0	0	0	0	0	0	0	0	0	0
2	2	1	5	1	1	4	0	0	0	0	0	0	0	0
0	1	1	0	0	0	0	0	0	0	0	0	0	0	0
0	0	0	1	0	0	0	0	0	0	0	0	0	0	0
436	452	383	432	377	324	355	56	68	17	82	43	16	184	180
0	0	0	0	0	0	0	0	0	0	0	0	0	0	0
1	0	0	1	0	3	9	0	0	0	0	0	0	11	4
0	0	0	0	0	0	0	0	0	0	0	0	0	0	0
0	0	0	0	1	0	0	0	0	0	0	0	0	6	7
0	0	0	0	0	0	0	0	0	0	0	0	0	2	0
0	0	0	2	0	1	0	0	0	1	0	0	0	1	1
0	0	0	0	0	0	0	0	0	0	0	0	0	0	0
3	2	3	2	1	0	1	3	0	0	0	0	0	3	0

Appendix 1: Diatom Count Data

0	0	0	0	0	0	0	0	0	0	0	0	0	0	0
0	0	0	0	0	0	0	0	0	0	0	0	0	0	0
1	0	0	1	2	0	1	0	0	0	0	0	0	0	2
0	0	0	0	0	0	0	0	0	0	0	0	0	0	1
6	2	3	5	3	1	2	3	0	1	0	0	0	4	4
0	1	0	1	0	0	0	1	0	0	0	0	0	1	3
0	0	0	0	0	1	0	0	0	0	0	0	0	0	0
0	0	0	0	0	0.5	0	0	0	0	0	0.5	0.5	0	0.5
0	0	4	4	0	2	0	0	0	0	0	0	0	0	4
4	1	2	4	8	9	7	0	0	0	0	0	0	21	8
0	0	0	0	0	0	0	0	0	0	0	0	0	0	0
0	0	0	3	2	4	0	0	0	0	0	0	0	0	1
3	0	0	7	4	8	16	0	0	0	0	2	0	0	6
11	2	12	2	4	4	1	1	1	0	0	0	0	15	17
0	0	0	0	0	0	0	0	0	0	0	0	0	0	0
0	0	1	3	0	2	0	1	0	0	0	0	0	0	0
0	0	0	0	0	0	0	0	0	0	0	0	0	0	0
0	0	1	0	0	0	0	0	0	0	0	0	0	0	1
0	0	1	0	0	0	1	0	0	0	0	0	0	0	0
0	0	0.5	0.5	0	0	0.5	0	0	0	0	0	0	0	0
0	0	0	0.5	0	0.5	0	0	0	0	0	0	0	0	0
0	0	0	0	0	0	0	0	0	0	0	0	0	0	0
0	0	0	0	1	2	1	0	0	0	0	0	0	4	1
0	0	0	0	0	0	0	0	0	0	0	0	0	0	0
481	477	460.5	503	440	466	496.5	65	74	18	82	46.5	17.5	473	446.5
0	0	0	0	0	0	0	335	326	382	318	353.5	382.5	0	0
481	477	460.5	503	440	466	496.5	400	400	400	400	400	400	473	446.5

0.06	0.049	0.051	0.049	0.041	0.062	0.051	0.085	0.071	0.056	0.05	0.053	0.06	0.06	0.06
1.576	0.747	4.181	2.02	4.586	21.09	6.864	34.32	32.17	34.32	34.32	34.32	34.32	13.73	24.02
7854	7854	7854	7854	7854	7854	7854	7854	7854	7854	7854	7854	7854	7854	7854

640	673	705	721	737	769	801	833	849	865	897	929
15	0	3	16	10	16	17	0	6	18	6	5
0	0	0	0	0	0	0	0	0	0	0	0
1	0	0	0	0	0	0	0	0	0	0	1
0	0	0	0	0	0	0	0	0	0	0	0
0	0	0	0	0	0	0	0	0	0	0	0
0	0	0	0	0	2	0	0	0	0	0	0
0	0	0	0	0	0	0	0	0	0	33	19
0	0	0	1	0	0	0	0	0	0	0	0
0	0	0	0	0	0	0	0	0	0	0	0
0	0	0	1	1	5	4	0	2	0	8	15
0	0	0	0	0	1	0	2	1	1	0	0
72	1	110	230	124	119	38	6	76	41	12	9
1	0	3	3	7	12	6	0	0	9	8	15
0	0	0	1	9	5	1	0	0	2	0	2
23	0	13	32	59	58	48	3	58	139	23	46
7	0	18	4	9	15	13	1	2	12	44	54
0	0	0	0	0	0	0	0	0	0	0	0
0	0	0	0	0	0	0	0	0	0	0	0
0	0	2	0	0	0	0	0	1	0	2	22
0	0	0	0	0	0	0	0	0	0	0	0
0	0	0	0	0	0	0	0	0	0	0	0
269	3	195	84	168	124	235	22	136	155	254	195
1	0	0	0	0	0	0	0	1	0	0	0
4	0	12	10	8	9	2	0	8	8	1	1

Appendix 1: Diatom Count Data

0	0	0	0	0	0	0	0	0	0	0	0
2	0	7	7	2	15	6	0	6	7	1	1
0	0	0	0	0	1	1	0	0	0	1	0
0	0	0	0	0	1	0	0	0	3	0	20
0	0	0	0	0	0	0	0	0	0	0	0
1	0	1	1	3	0	5	1	1	1	1	6
0	0	0	0	0	0	0	0	0	0	0	0
0	0	0	0	0	0	0	0	0	0	0	0
2	0	2	4	5	0	0	1	4	0	2	0
0	0	0	0	3	0	3	0	0	3	0	0
3	0	3	5	11	1	8	2	5	6	3	26
2	0	1	3	2	1	3	0	3	1	0	1
0	0	0	0	0	1	0	0	0	0	0	0
0	0	0	0	0	0	0.5	0	1	0	1.5	0
0	0	1	2	3	1	7	0	10	1	4	4
14	0	47	54	24	61	20	2	27	27	1	0
0	0	0	0	0	0	0	0	0	0	0	0
0	0	0	0	0	3	3	0	0	2	12	4
3	0	1	2	0	1	5	0	3	1	5	14
34	1	18	40	34	22	34	5	30	20	12	8
0	0	0	0	0	0	0	0	0	0	0	0
0	0	0	1	3	0	5	0	1	0	0	0
0	0	0	0	0	1	1	0	0	1	0	0
0	0	0	0	0	0	0	0	1	0	0	1
0	0	0	0	0	2	2	0	0	0	0	0
0.5	0	1	3	4.5	0.5	5	0.5	1	3.5	8	1.5
0	0	1	0	0	0	0	0	0	1	0	0.5
2	0	0	0	0	0	0	0	0	0	0	0
4	0	1	2	0	3	0	1	1	2	1	1
0	0	0	0	1	0	2	0	0	1	6	2
457.5	5	437	501	479.5	479.5	466.5	44.5	380	458.5	446.5	448
0	395	0	0	0	0	0	355.5	0	0	0	0
457.5	400	437	501	479.5	479.5	466.5	400	380	458.5	446.5	448

0.051	0.061	0.06	0.07	0.06	0.052	0.051	0.045	0.07	0.06	0.017	0.02
27.46	34.32	17.16	13.73	3.432	6.864	13.73	34.01	34.32	3.432	5.32	386.9
7854	7854	7854	7854	7854	7854	7854	7854	7854	7854	7854	7854

Appendix 1: Diatom Count Data – MD03-2603

Depth (cm)	4	16.5	32	48	60	76	92	108	120	124	128
<i>Actinocyclus actinocyclus</i>	1	0	1	0	0	0	0	1	2	1	2
<i>Actinocyclus curvatus</i>	0	0	0	0	0	0	0	0	0	0	0
<i>Asteromphalus hookeri</i>	1	0	0	0	0	0	0	0	0	0	0
<i>Asteromphalus hyalinus</i>	0	1	0	0	0	0	1	0	0	0	0
<i>Asteromphalus parvulus</i>	0	1	0	1	1	0	0	2	0	0	0
<i>Azpeitia tabularis</i>	3	2	0	2	1	1	1	4	3	8	4
<i>Cocceneis</i> spp.	0	0	0	0	0	0	0	0	0	0	0
<i>Corethron</i> spp.	0	0	0	0	0	0	0	0	0	0	0
<i>Coscinodiscus bouvet</i>	0	0	0	0	0	0	0	0	0	1	0
<i>Coscinodiscus</i> spp.	0	0	0	0	0	0	0	0	0	0	0
<i>Dactyliosolen</i> girdle bands	25	21	8	44	15	9	2	28	0	0	0
<i>Denticulopsis</i> sp.	0	0	1	0	0	0	0.5	1	0	1	0
<i>Eucampia antarctica</i>	11	1	2	0	2	5	1	7	3	9	7
<i>Fragilariopsis curta</i>	5	7	6.5	6	3.5	7.5	7.5	1	3	3	3
<i>Fragilariopsis cylindrus</i>	0.5	0.5	0	1.5	0	0	1	0.5	0	0	0
<i>Fragilariopsis kerguelensis</i>	219	245	184.5	198.5	224	213	213.5	198.5	332	338	140
<i>Fragilariopsis obliquecostata</i>	1	0.5	2.5	2	3	0.5	0.5	1	0	2	1
<i>Fragilariopsis pseudonana</i>	0	0	0	1	1	0	0	0	0	0	0
<i>Fragilariopsis rhombica</i>	6	8	7.5	3	8	6.5	15	4	0	1	3
<i>Fragilariopsis ritscheri</i>	2.5	2.5	4.5	1	1	1	5	0.5	2	4	3
<i>Fragilariopsis separanda</i>	15	5	3.5	6.5	8.5	6.5	4	7	12	13	6
<i>Fragilariopsis sublinearis</i>	0	1	0	0	0	0	0	0	0	0	1
<i>Fragilariopsis vanheurckii</i>	0	1.5	2	0.5	0	2	1.5	0.5	0	0	0
<i>Hyalochaete Chaetoceros</i> resting spores	34	24	48	40	25	42	42	30	54	43	22
<i>Chaetoceros</i> sp. Veg. <i>Hyalochaete</i>	1	2	6	2	1	3	2	3	0	0	0
<i>Odontella litigiosa</i>	1	0	0	0	0	0	0	0	0	0	0
<i>Odontella weisflogii</i>	0	0	0	0	0	0	0	0	0	0	0
<i>Paralia</i> spp.	0	0	0	0	0	0	0	0	0	0	0
<i>Porosira glacialis</i>	0	0	0	0	0	0	0	2	0	0	0
<i>Porosira pseudodenticulata</i>	0	0	0	0	0	1	0	0	0	1	0
<i>Pseudonitzschia</i> sp.	0	0	0	0	0	0	0.5	0	0	0	0
<i>Rhizosolenia antennata antennata</i>	0	0	0	0	0	0	0	0	0	0	0
<i>Rhizosolenia antennata semispina</i>	2	0	0	3	2	0	1	2	0	0	0
<i>Rhizosolenia crassa</i>	0	0	0	0	0	0	0	0	0	0	0
<i>Rhizosolenia polydactyla polydactyla</i>	0	0	0	0	0	0	0	0	0	0	0
<i>Rhizosolenia simplex</i>	0	0	0	0	0	0	0	0	0	1	0
<i>Rhizosolenia styliiformis</i>	0	1	0	0	0	0	0	0	0	0	0
<i>Rhizosolenia</i> spp. total	3	2	2	3	6	4	1	4	0	1	0
<i>Stellarima microtrias</i> rs	0	0	0	0	0	0	0	1	0	1	1
<i>Stephanopyxis</i>	0	0	0	0	0	0	0	0	0	0	0
<i>Thalassionema</i> spp.	1.5	2	1	0.5	0.5	2	1.5	1	1	0.5	0
<i>Thalassiosira antarctica</i> rs (cold)	0	0	0	0	1	0	0	0	0	0	0
<i>Thalassiosira antarctica</i> rs (warm)	4	1	1	2	3	6	1	0	0	0	0
<i>Thalassiosira eccentrica</i>	0	0	0	0	0	0	0	0	1	0	0
<i>Thalassiosira gracilis</i> var. <i>expecta</i>	7	8	3	3	0	2	1	2	3	0	0
<i>Thalassiosira gracilis</i> var. <i>gracilis</i>	7	8	10	7	4	6	1	2	6	2	8
<i>Thalassiosira lentiginosa</i>	31	23	13	23	13	18	13	30	23	25	54
<i>Thalassiosira oestrupii</i>	0	0	0	0	0	0	0	0	0	0	0
<i>Thalassiosira oliverana</i>	0	1	0	2	1	0	0	0	0	0	0
<i>Thalassiosira perpusilla</i>	0	0	0	0	0	0	0	0	0	0	0
<i>Thalassiosira trifluta</i>	0	0	0	0	1	1	0	0	1	1	0
<i>Thalassiosira tumida</i>	0	0	0	0	0	0	0	1	0	0	0
<i>Thalassiothrix</i> spp.	5	3.5	3.5	5	4	5.5	8.5	1	1	4.5	0
<i>Trichotoxen</i>	0	0	0	0	0	0	0	0	0.5	0	0

Appendix 1: Diatom Count Data

Extinct reworked	0	0	0	0	0	0	0	0	0	0	0
Unidentified centrics	2	3	4	3	2	1	2	2	0	0	0
Unidentified pennates	1	1.5	1.5	1.5	1	3	1.5	0.5	0	0	0
Total diatoms	389.5	377	316	362	332.5	346.5	329.5	337.5	447.5	460	255

Weight (mg)	0.051	0.05	0.03	0.051	0.027	0.05	0.045	0.05	0.055	0.054	
Area Counted (mm2)	0.367	0.648	0.605	3.24	0.562	5.184	5.832	7.992	1.061	2.215	
Beaker Area (mm2)	7854	7854	7854	7854	7855	7854	7854	7854	7854	7854	7854

132	136	140	144	148	152	156	160	164	168	172	176	180	184	188
1	1	0	2	0	0	0	2	6	2	2	4	3	6	4
0	0	0	0	0	0	0	0	0	0	0	0	0	0	0
0	1	0	0	0	1	1	1	0	0	0	0	0	0	0
0	0	0	1	0	0	0	0	0	0	0	0	0	0	0
0	0	0	0	0	0	0	0	0	0	0	0	0	0	0
3	8	4	2	1	0	3	1	2	1	1	0	1	3	2
0	0	0	0	0	0	0	0	0	0	0	0	0	0	0
0	0	0	0	0	0	0	0	0	0	0	0	0	0	0
0	0	0	0	0	0	0	0	0	0	0	0	0	0	0
0	0	0	0	0	0	0	0	0	1	0	0	0	0	0
0	0	1	3	0	2	1	0	2	0	1	0	1	2	1
0	0	0	1	0	2	0	5	2	1	1	0	1	4	1
2	5	1	6	18	9	16	13	21	18	12	16	25	32	26
22	7	11	11	6	4	6	11	4	8	6	15	6	2	9
3	0	0	3	2	1	0	3	3	1	0	4	1	0	0
316	324	318	287	302	280	265	290	338	289	309	234	236	261	268
1	0	0	1	0	0	1	4	1	0	2	5	2	0	0
0	0	0	0	0	0	0	0	0	0	0	0	0	0	0
0	0	0	0	0	0	0	1	0	0	0	0	0	0	0
2	1	1	8	1	4	3	3	2	5	1	15	0	8	0
1	5	16	9	6	10	10	11	12	8	12	14	12	15	10
0	0	0	0	1	0	0	0	0	0	0	2	0	0	0
0	0	0	0	0	0	0	0	0	0	0	0	0	0	0
66	46	77	51	88	89	58	64	80	85	58	111	115	79	90
0	0	0	0	0	0	0	0	0	0	0	0	0	0	0
0	0	0	0	0	0	0	0	0	0	0	0	0	0	0
0	0	0	0	0	0	0	0	0	0	0	0	0	0	0
0	0	0	0	0	0	1	0	0	0	0	0	0	1	0
0	0	0	0	0	0	0	1	0	0	2	1	0	0	1
0	1	0	0	0	1	0	0	0	0	0	0	1	2	0
0	0	0	0	0	0	0	0	0	0	0	0	0	0	0
0	0	0	0	0	0	0	0	0	0	0	0	1	0	0
1	0	1	1	0	0	1	1	0	0	0	0	0	0	0
0	0	0	1	0	0	0	0	0	0	0	0	0	0	0
1	0	0	6	1	0	0	0	1	2	1	0	1	3	2
0	2	0	0	0	2	2	0	2	1	2	0	3	3	1
0	0	0	0	0	0	0	0	0	0	0	0	0	0	0
2	2	1	8	1	2	3	1	3	3	3	0	5	6	3
0	0	0	1	0	0	0	0	0	0	0	0	0	0	0
0	0	0	0	0	0	0	0	1	0	1	2	2	0	0
0	0	1	0	0	0	2	0.5	0.5	0.5	0	0.5	1	1	0.5
0	1	1	0	4	1	4	5	3	3	0	5	10	4	3
0	1	0	0	0	2	1	2	0	1	0	0	1	2	0
0	0	0	0	0	1	0	0	0	0	0	0	0	1	0
4	1	1	0	0	2	1	0	1	2	1	1	3	4	0
1	2	3	8	2	6	3	7	6	6	1	4	5	8	4
31	36	18	29	22	23	45	20	30	20	35	13	26	24	25

Appendix 1: Diatom Count Data

0	0	0	0	0	0	0	0	0	0	0	0	0	1	0
2	2	1	1	1	0	1	1	1	0	1	0	0	1	1
0	1	1	2	0	1	1	0	0	1	0	0	0	0	0
4	2	0	1	1	1	0	2	0	0	0	0	2	0	0
0	0	0	0	0	0	0	0	0	1	0	0	0	0	0
4.5	5	2	7.5	4	6	8	5.5	8	5	3	2	2	5	6.5
0	1	0	0	0	0.5	0	0	0	0	0	0	0	0	0
0	0	0	0	0	0	0	0	0	0	0	0	0	0	0
0	0	0	1	0	0	0	0	0	0	0	0	0	0	0
0	0	0	2	0	0	0	0	0	0	0	0	0	0	0
465.5	453	458	445.5	460	448.5	434	454	526.5	461.5	452	448.5	461	472	455

0.052	0.054	0.038	0.035	0.038	0.043	0.046	0.022	0.057	0.05	0.054	0.055	0.058	0.055	0.055
2.262	5.663	11.12	12.25	15.13	9.251	10.3	22.48	13.71	13.73	6.853	13.73	11.31	10.3	11.92
7854	7854	7854	7854	7854	7854	7854	7854	7854	7854	7854	7854	7854	7854	7854

192	196	200	204	208	212	216	220	224	228	232	236	240	244	248
3	0	4	4	3	4	3	1	7	6	3	5	5	3	3
0	0	0	0	0	0	0	0	0	0	0	0	1	0	0
0	0	0	0	1	0	0	0	0	0	0	0	0	0	0
0	0	0	0	0	0	1	0	0	0	0	0	0	0	0
0	0	0	0	0	0	0	0	0	0	0	0	0	0	0
0	3	1	1	0	4	1	1	4	1	0	2	2	4	0
0	0	0	0	0	0	0	0	0	0	0	0	1	0	0
0	0	0	0	0	0	0	0	0	0	0	0	0	0	0
0	0	0	0	0	0	0	0	0	0	0	0	0	0	0
0	0	0	0	0	0	0	0	0	0	0	0	0	0	0
0	2	0	2	2	4	0	2	0	3	1	1	0	1	3
0	2	0	0	0	1	1	3	2	0	1	0	1	0	0
4	25	15	25	25	28	16	17	29	19	20	19	11	15	24
1	2	4	2	7	2	3	3	7	4	4	7	7	4	3
0	0	0	0	1	0	0	0	0	0	0	0	0	0	0
42	268	287	333	255	320	320	310	270	309	295	306	322	335	295
0	3	0	3	0	1	0	0	3	2	0	0	0	0	2
0	0	0	0	0	0	0	0	0	0	0	0	0	0	0
1	0	0	0	0	0	0	0	0	0	0	0	1	0	0
1	1	3	3	4	1	4	0	2	1	1	0	9	0	0
1	14	5	9	13	3	9	10	10	8	6	8	8	8	5
1	0	0	0	1	0	1	1	0	0	0	0	1	0	0
0	0	0	0	0	0	0	0	0	0	0	0	0	0	0
2	67	80	47	73	54	51	75	53	48	68	63	57	47	61
0	0	0	0	0	0	0	0	0	0	0	0	0	0	0
0	0	0	0	0	0	0	0	0	0	0	0	0	0	0
0	0	0	0	3	0	0	0	0	0	0	0	0	0	1
0	2	1	1	1	0	0	0	0	0	0	1	0	0	0
0	0	0	0	0	2	1	0	0	0	1	1	0	0	0
0	0	1	0	0	0	0	0	0	0	0	0	0	0	0
0	0	0	0	0	0	0	0	0	0	0	0	0	0	0
0	0	0	0	1	0	0	0	0	0	0	0	0	0	0
0	0	0	0	0	0	0	0	0	0	1	0	0	0	0
0	0	0	1	0	0	0	0	0	0	0	0	0	0	0
0	2	2	2	1	2	3	2	3	1	1	0	1	1	1
0	3	5	0	0	1	2	1	0	0	2	0	0	0	3
0	0	0	0	0	0	0	0	0	0	0	0	0	0	0
0	5	7	3	2	3	5	3	3	1	4	0	1	1	4
0	0	0	0	0	0	0	0	0	0	0	0	0	0	0
0	0	0	0	0	0	0	0	0	0	0	0	0	1	0

Appendix 1: Diatom Count Data

0	0.5	0	1.5	1	1	0	1	0	0	0	0	0	0	0.5
0	5	7	8	5	3	1	1	5	2	5	0	1	2	3
0	0	0	0	0	0	1	3	1	1	0	0	0	0	0
0	0	0	0	0	0	0	1	0	0	0	0	0	0	1
0	0	1	2	0	1	0	0	4	0	0	2	0	1	1
1	5	5	7	9	7	7	1	9	5	8	6	1	2	4
13	36	38	26	19	19	20	16	22	19	23	29	26	19	39
0	0	0	1	0	1	0	0	0	0	0	0	0	0	0
1	1	2	0	3	2	1	2	2	1	1	0	0	1	7
0	0	2	0	1	0	0	0	1	0	0	0	0	0	0
0	0	0	0	1	0	1	0	1	1	0	0	0	0	2
0	0	0	0	0	0	0	0	0	0	0	0	0	0	0
0	4.5	9.5	1.5	8	1.5	5	3.5	5.5	7	5	2.5	6	6.5	2
0	0	0.5	0	0	0.5	1.5	1	1	0.5	0	0	0.5	0.5	1
0	0	0	0	0	0	0	0	0	0	0	0	0	0	0
0	0	0	0	0	0	0	0	0	0	0	0	0	0	2
0	0	0	0	0	0	0	0	0	0	0	0	0	0	0
71	446	473	480	438	463	453.5	455.5	441.5	438.5	446	452.5	461.5	451	463.5

	0.062	0.06	0.061	0.062	0.057	0.06	0.062	0.025	0.053	0.051	0.055	0.064	0.059	0.065
	11.59	20.25	13.73	10.3	14.65	6.552	10.3	20.59	15.76	14.91	11.56	4.337	14.82	15.02
7854	7854	7854	7854	7854	7854	7854	7854	7854	7854	7854	7854	7854	7854	7854

252	256	260	264	268	272	276	280	284	288	292	296	300	304	308
0	3	3	0	2	2	2	0	5	8	4	1	4	7	0
0	0	0	0	0	0	0	0	0	0	0	0	0	0	0
0	0	0	1	0	1	0	0	0	0	0	0	0	0	0
0	0	0	0	0	0	1	0	0	0	0	0	0	0	2
0	0	0	0	0	0	0	0	0	0	0	0	0	0	0
1	0	3	3	6	1	2	10	1	6	1	2	0	1	1
0	0	0	0	0	0	0	0	0	1	0	1	0	0	0
0	0	0	0	0	0	0	0	0	0	0	0	0	0	0
0	0	0	0	0	0	0	0	0	0	0	0	0	0	0
0	0	0	0	0	0	0	0	0	0	0	0	0	0	0
2	0	2	0	0	0	0	0	0	0	0	0	1	0	1
0	0	0	0	0	2	1	0	0	0	1	0	0	0	0
18	4	26	30	27	39	34	3	33	24	27	25	33	15	25
1	1	5	0	6	5	2	4	2	3	3	2	2	5	3
0	0	0	0	1	0	0	0	1	0	0	0	0	0	0
328	38	319	290	318	302	332	323	282	281	311	331	311	297	334
0	0	0	0	2	0	1	0	1	3	0	0	0	2	3
0	0	0	0	0	0	0	0	0	0	0	0	0	0	0
0	1	0	0	0	0	0	9	0	0	0	0	0	0	0
2	1	0	0	0	5	6	1	0	0	0	0	2	3	3
12	1	11	5	6	9	7	0	8	7	6	6	9	2	9
0	1	0	0	0	0	0	0	1	0	0	0	1	0	0
0	0	0	0	0	0	0	0	0	0	0	0	0	0	0
57	2	40	72	45	48	25	10	61	54	50	62	29	66	30
0	0	0	0	0	0	0	0	0	0	0	0	0	0	0
0	0	0	0	0	0	0	0	0	0	0	0	0	0	0
0	0	0	0	0	0	0	0	0	0	0	0	0	0	0
2	0	0	0	1	0	0	0	1	0	0	0	0	0	0
0	0	0	1	0	0	0	48	0	1	0	0	1	0	0
0	0	0	0	0	0	0	0	0	0	1	0	0	0	0
0	0	0	0	0	0	0	0	0	0	0	0	0	0	0
0	0	0	0	0	0	0	0	0	0	0	0	0	0	0
0	0	0	0	1	0	0	0	1	1	0	0	0	1	1

Appendix 1: Diatom Count Data

0	0	0	0	0	0	0	0	0	0	0	0	0	0	0
0	0	3	1	0	2	2	1	1	2	1	1	1	3	1
0	0	1	2	0	1	1	4	1	2	1	0	1	2	0
0	0	0	0	0	0	0	0	0	0	0	0	0	0	0
0	0	4	3	1	3	3	0	3	5	2	1	2	7	2
0	0	0	0	0	0	0	0	1	1	0	0	0	0	0
0	0	0	1	0	0	1	1	0	0	0	0	0	0	0
0	0	0	0	0	0.5	0.5	2.5	0	1	0.5	1.5	1	0	0
3	0	0	2	5	4	1	0	3	6	5	5	2	1	5
0	0	0	0	1	1	0	0	1	3	0	0	0	0	1
0	0	0	0	0	0	0	0	0	0	0	0	0	0	0
2	0	1	0	1	0	0	1	1	1	0	2	4	0	0
2	1	3	2	4	0	5	9	3	7	3	4	2	6	2
21	12	27	42	35	22	49	28	25	28	28	25	49	27	29
0	0	0	1	0	0	1	0	0	0	0	0	0	0	0
0	1	0	1	2	0	1	1	2	0	1	1	0	3	2
0	0	0	0	0	1	0	2	0	1	0	0	0	0	0
0	0	0	1	0	0	0	0	1	2	0	0	1	4	1
0	0	0	0	0	0	0	0	0	0	0	0	0	0	0
3	0	5.5	4.5	6	7.5	7	0	6.5	2	3.5	7	4.5	5	6.5
0.5	0	0.5	0	0.5	0	0.5	0	0	0.5	0	0	0	0	0
0	0	0	0	0	0	0	0	0	0	0	0	0	0	0
0	0	0	0	0	0	0	0	0	0	0	0	0	0	0
0	0	0	0	0	0	0	0	0	0	0	0	0	0	0
454.5	66	450	459.5	469.5	453	482	452.5	442.5	446.5	447	476.5	458.5	451	459.5

0.06		0.056	0.056	0.054	0.056	0.054	0.056	0.055	0.034	0.06	0.045	0.04	0.04	0.04
10.3		15.04	12.85	16.66	11.68	17.16	7.145	15.66	14.57	9.688	13.51	13.73	11.2	15.38
7854	7854	7854	7854	7854	7854	7854	7854	7854	7854	7854	7854	7854	7854	7854

312	316	320	328	344	348	352	356	360	364	368	372	380
6	10	7	6	4	2	0	5	0	5	3	2	4
0	0	0	0	0	0	0	0	0	0	0	0	0
0	0	0	0	1	2	0	1	4	1	3	0	0
0	1	0	0	0	0	1	0	0	0	0	0	0
0	0	0	0	0	0	0	0	0	0	0	0	0
1	3	0	1	2	2	9	2	1	1	4	2	2
0	0	0	0	0	0	0	0	0	0	0	0	0
0	0	0	0	0	0	4	0	0	0	0	0	0
0	0	0	0	0	0	0	0	0	0	0	0	0
	0	0			0	0	0		0		0	0
0	0	0	1	0	1	0	0	1	1	0	1	1
0	0	0	0	0	0	0	0	0	0	0	0	0
12	40	13	14	9	11	2	25	16	16	24	16	19
4	11	1	4	6	3	8	1	0	1	7	4	7
0	0	0	0	0	0	0	0	0	0	0	0	0
308	330	97	351	312	350	306	324	324	338	280	365	327
1	1	1	1	0	0	2	0	2	1	0	0	0
0	0	0	0	0	0	0	0	0	0	0	0	0
1	0	0	0	2	0	0	3	0	1	0	0	3
2	4	9	1	3	1	5	6	5	1	10	5	1
7	9	1	6	4	9	11	6	5	6	9	2	5
0	0	1	0	0	0	0	0	2	0	0	0	0
0	0	0	0	0	0	0	0	0	0	0	0	0
57	24	4	45	42	43	10	32	49	50	56	35	36
0	0	0	0	0	0	0	0	0	0	0	0	0
0	0	0	0	0	0	0	0	0	0	0	0	0

Appendix 1: Diatom Count Data

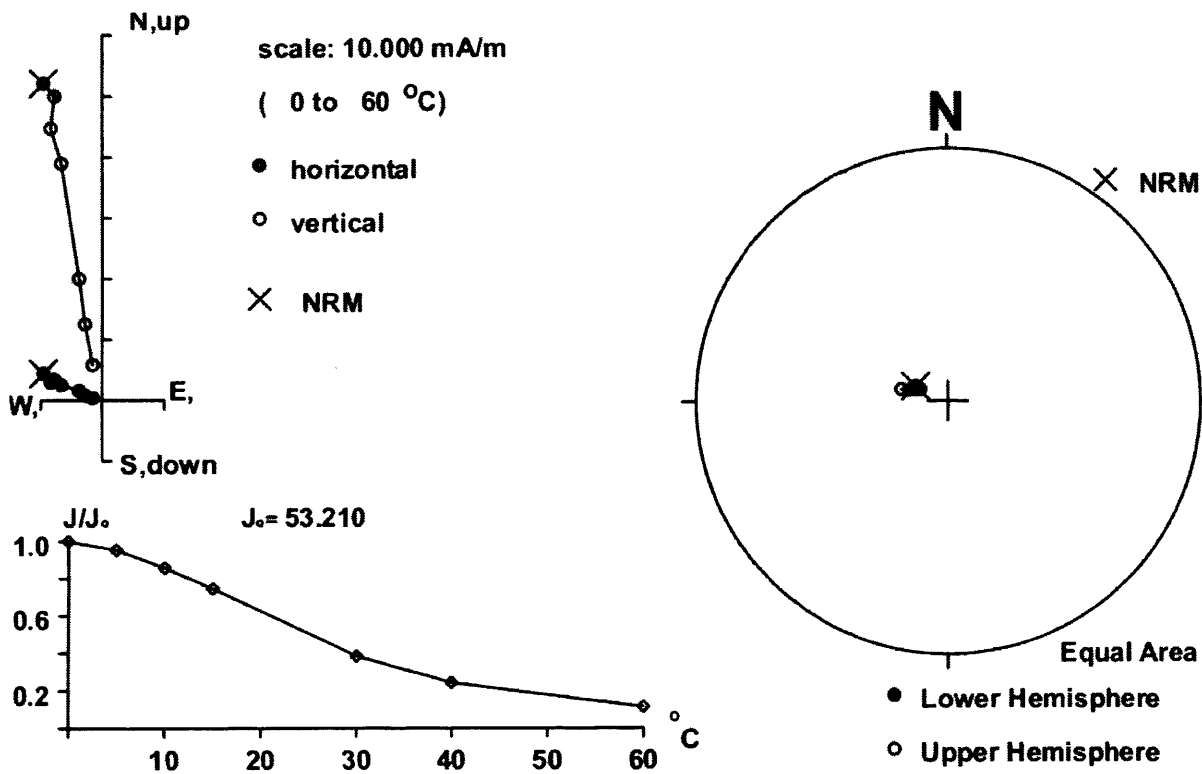
0	0	0	0	0	0	0	0	1	0	0	0	0
1	0	0	0	1	0	0	0	0	0	2	0	0
1	0	1	0	0	3	45	0	0	1	0	0	0
0	0	0	0	0	0	0	0	0	0	0	0	0
0	0	0	0	0	0	0	0	0	0	0	0	0
0	0	0	0	0	0	0	0	0	0	0	0	0
0	1	0	1	0	0	0	1	0	1	0	0	0
0	0	0	0	0	0	0	0	0	0	0	0	0
0	0	0	0	4	2	0	3	5	4	1	3	2
2	2	0	4	3	0	0	2	2	2	4	2	2
0	0	0	0	0	0	0	0	0	0	0	0	0
2	3	0	5	7	2	0	6	7	7	5	5	4
0	1	1	0	0	0	0	0	0	0	0	0	0
0	1	0	0	0	0	0	1	0	0	0	0	0
0	0.5	0	1	0	0	0	1.5	0.5	0.5	0	1	0.5
2	4	0	4	3	2	0	1	0	0	0	1	1
1	1	0	0	0	0	3	0	0	0	1	0	0
0	0	0	0	0	0	0	0	0	0	0	0	0
1	0	0	0	0	0	2	2	0	0	0	1	2
5	4	5	7	6	4	2	7	6	4	6	5	3
33	53	23	29	36	27	34	38	20	27	22	27	21
0	0	0	0	0	0	0	0	0	2	0	0	0
0	3	3	4	1	2	0	2	1	1	7	1	5
0	0	0	0	0	0	1	0	0	0	0	0	1
1	0	0	0	0	0	1	1	0	0	0	0	0
0	0	1	0	0	0	2	0	0	0	0	0	0
4.5	5	0	6	4.5	5	1	2.5	3	3	4	6.5	5
0	0	0	0	0	0	0	0.5	1	0	0.5	0.5	1
0	0	0	0	0	0	0	0	0	0	0	0	0
0	0	0	0	0	0	0	0	0	0	0	0	0
0	0	0	0	0	1	0	0	0	0	0	0	0
450.5	508.5	168	486	443.5	470	449	467.5	448.5	467.5	443.5	480	448.5

0.046	0.05		0.046	0.046	0.046	0.043	0.046	0.045	0.046	0.044	0.05	0.045
10.58	10.3		12.67	9.797	13.29	5.6	4.727	5.554	7.784	11.26	15.8	10.17
7854	7854	7854	7854	7854	7854	7854	7854	7854	7854	7854	7854	7854

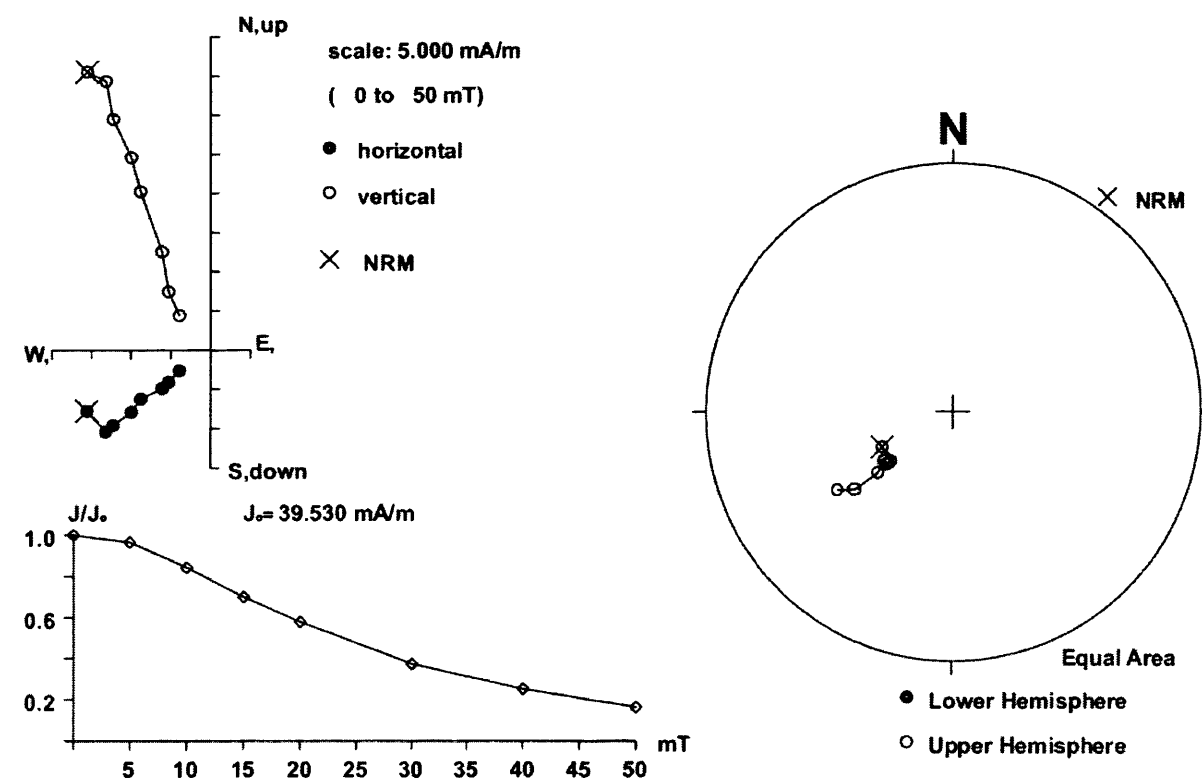
Counts by X. Crosta

Appendix 2: RPI Demagnetisation Plots - TPC063

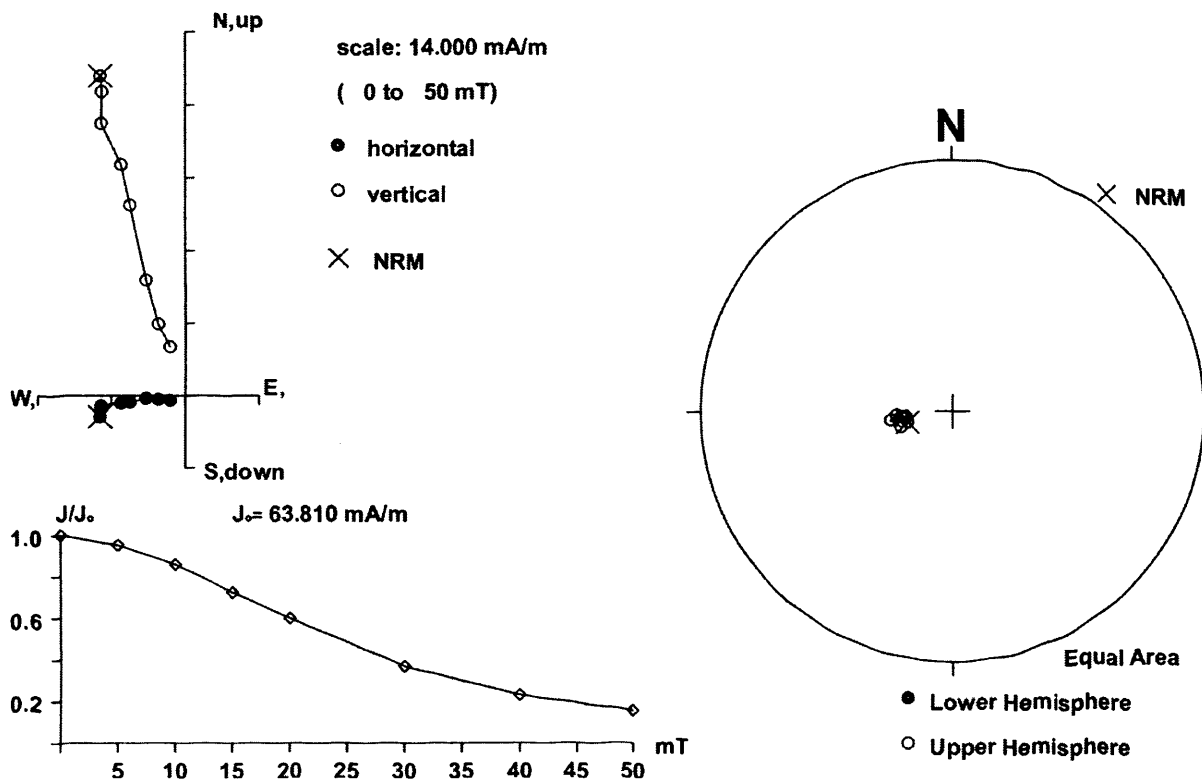
261 cm



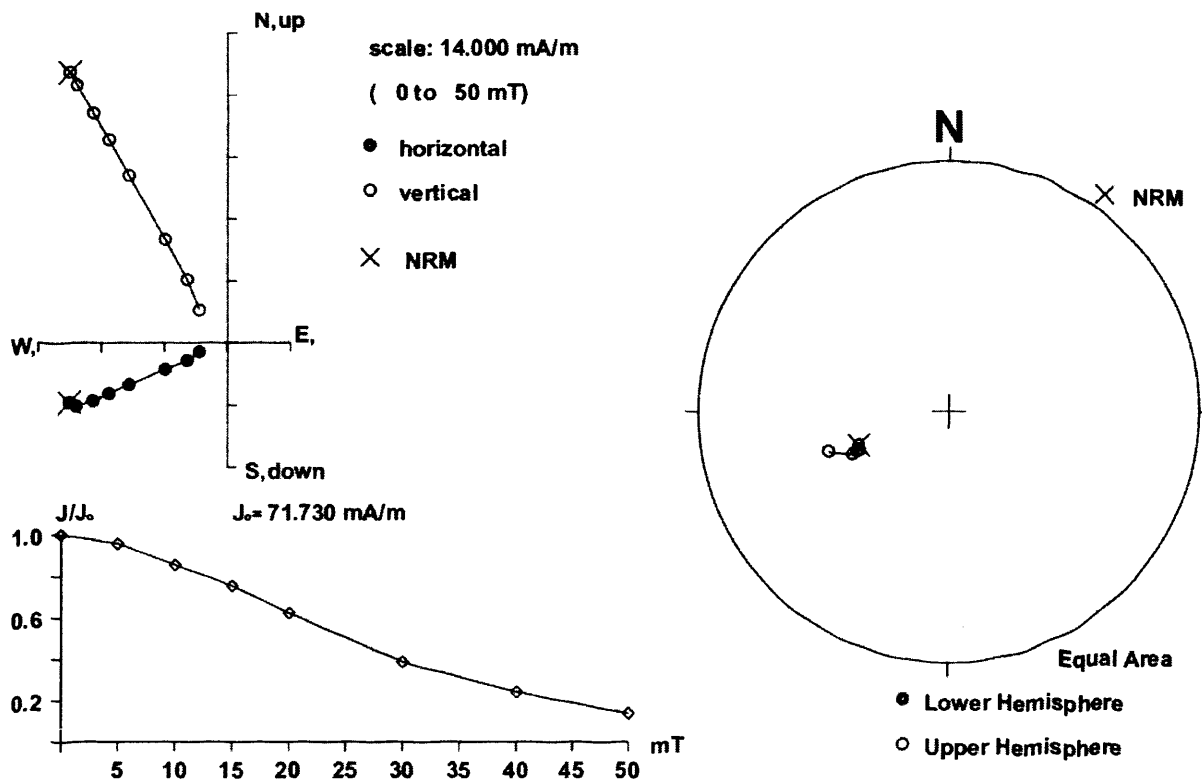
285 cm



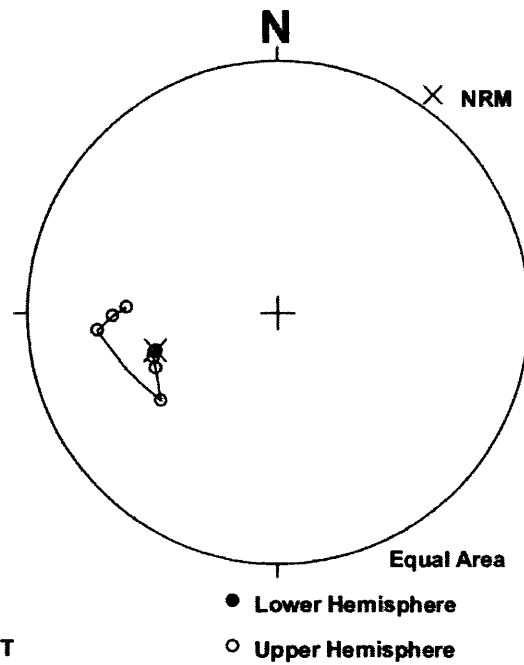
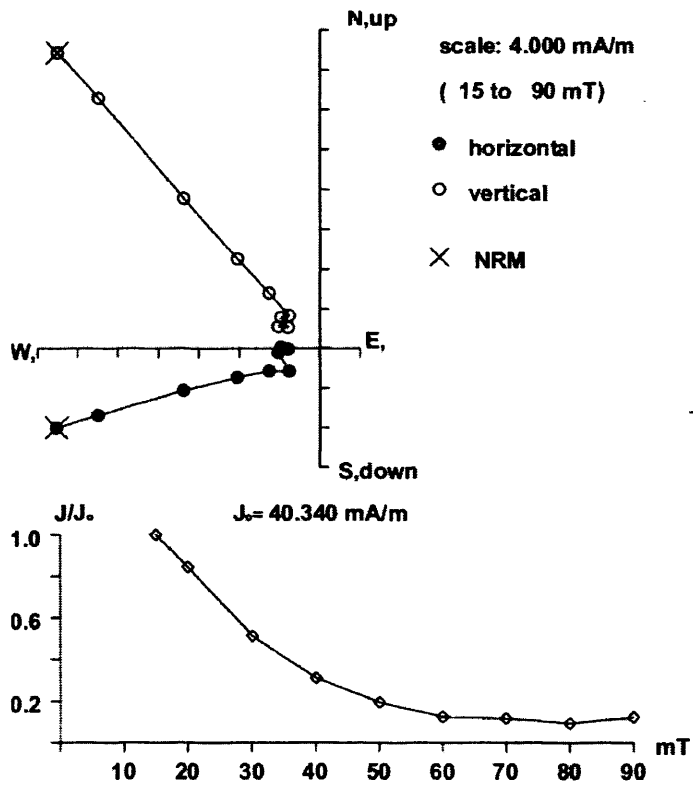
309 cm



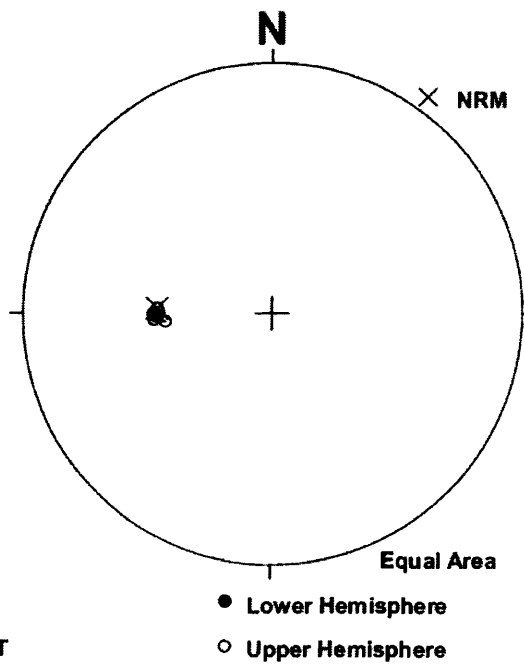
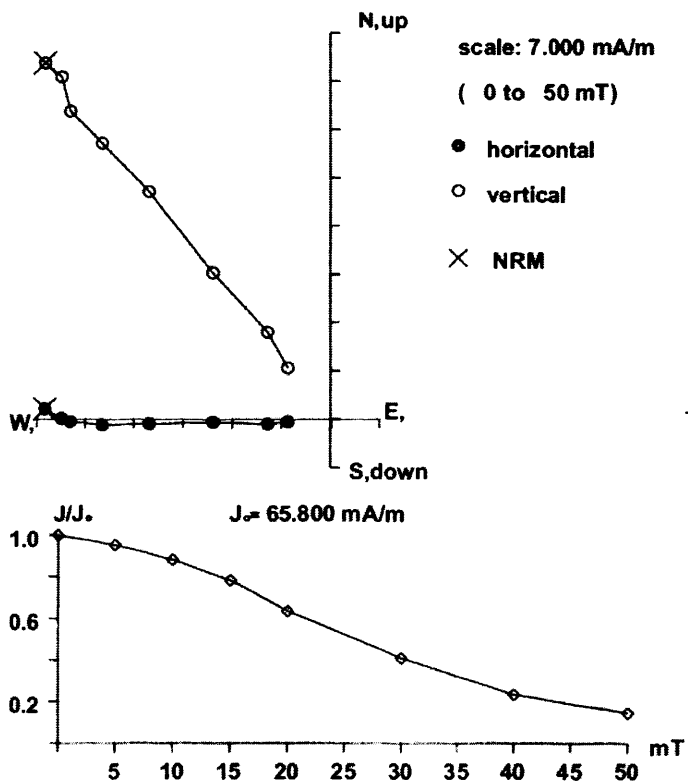
333 cm



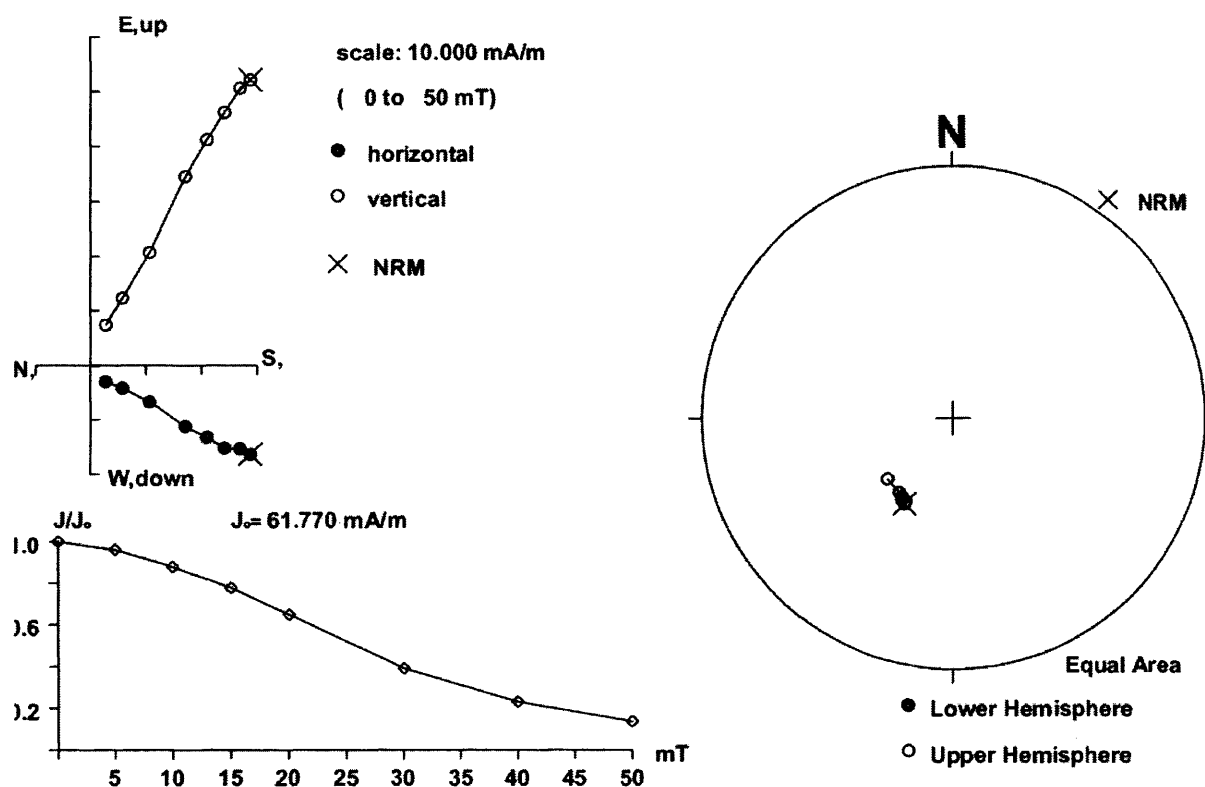
349 cm



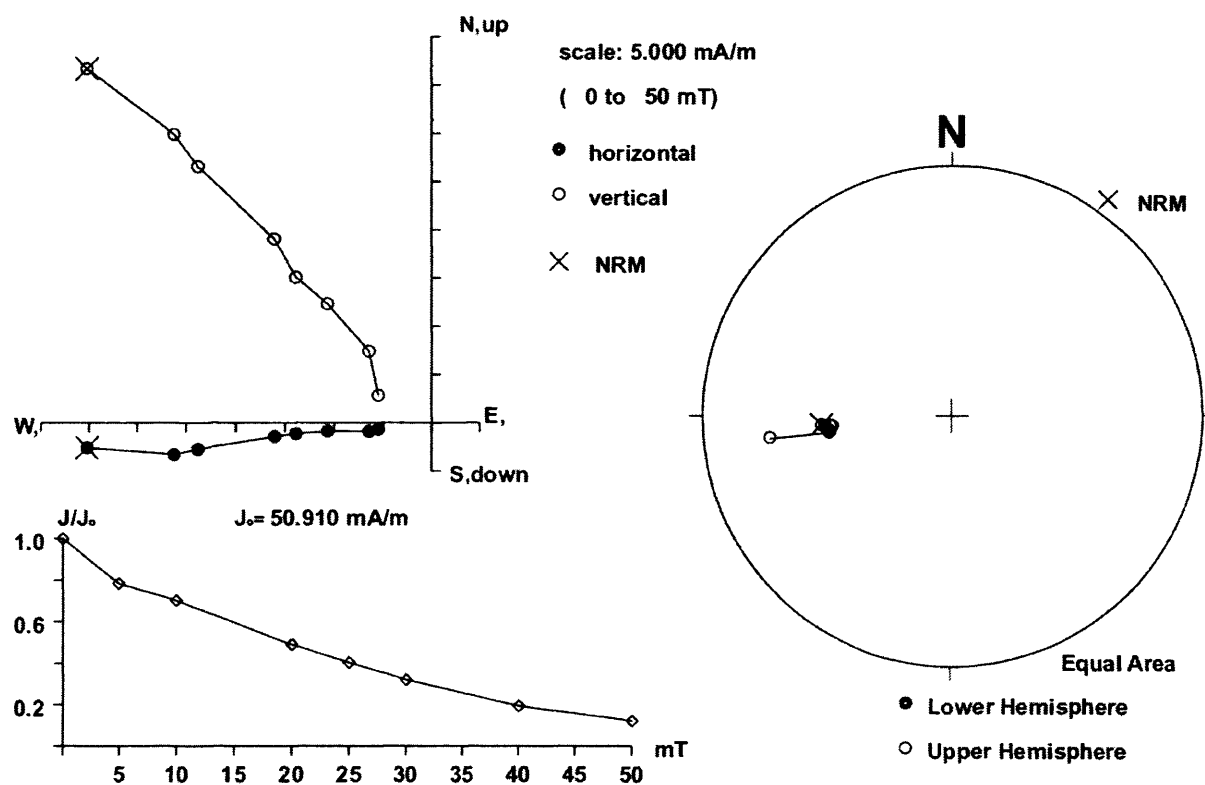
357 cm



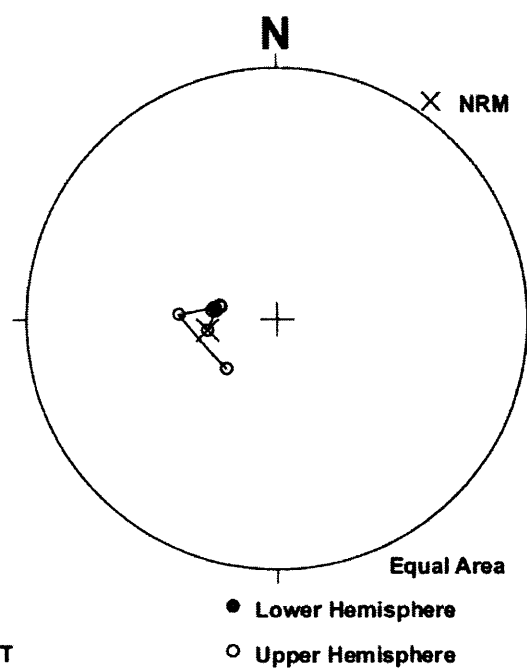
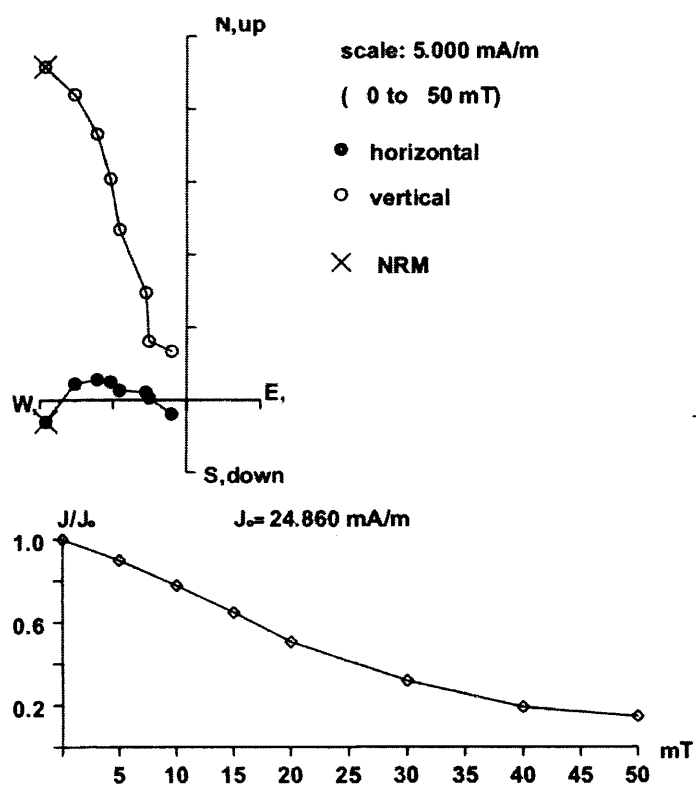
381 cm



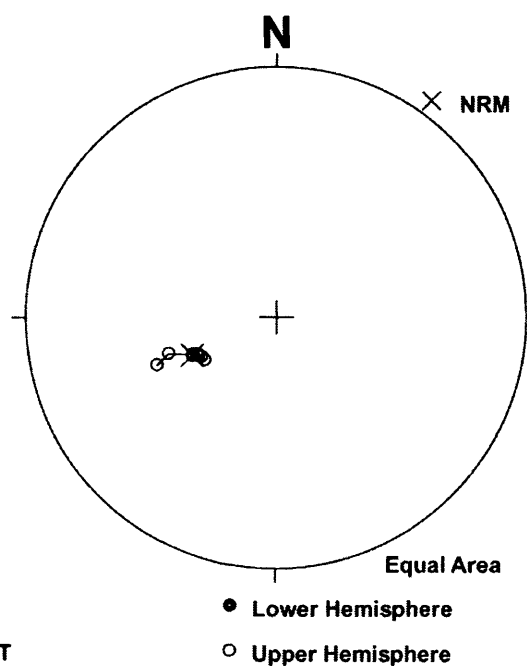
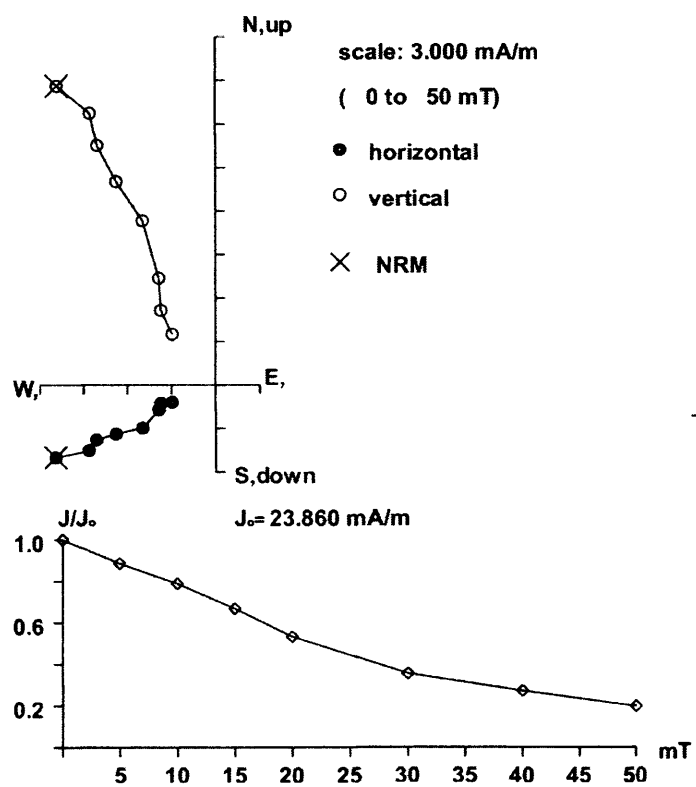
405 cm



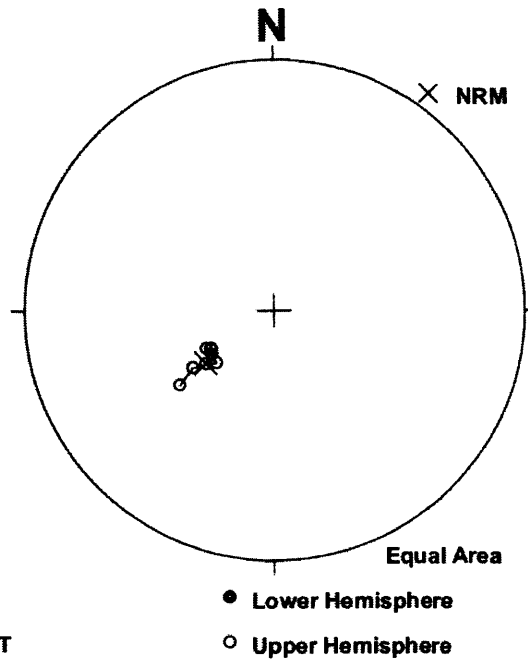
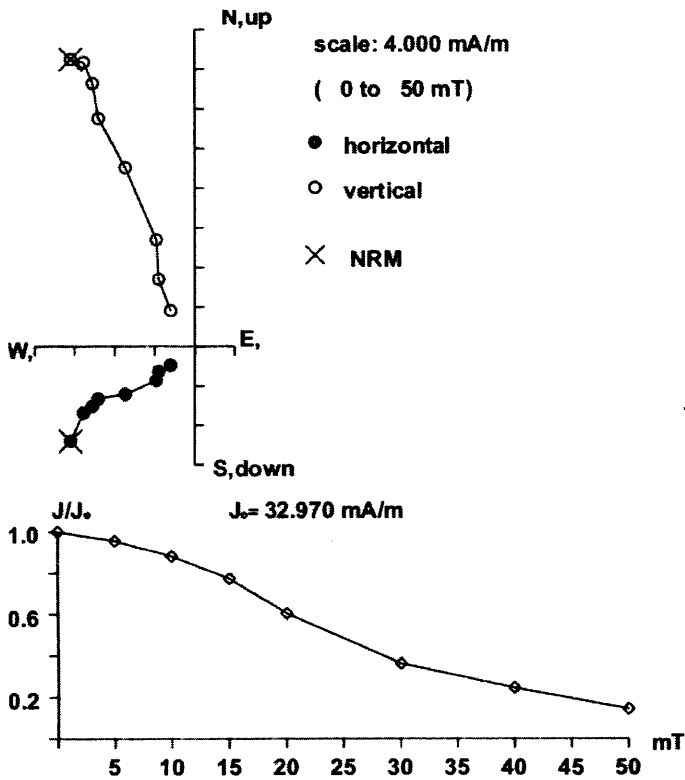
429 cm



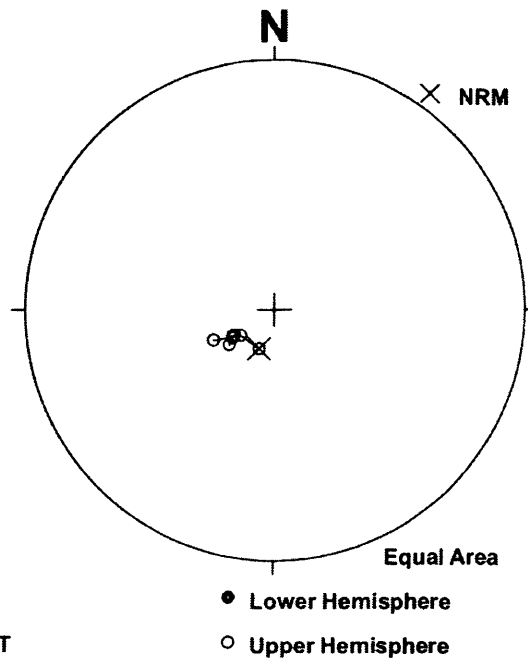
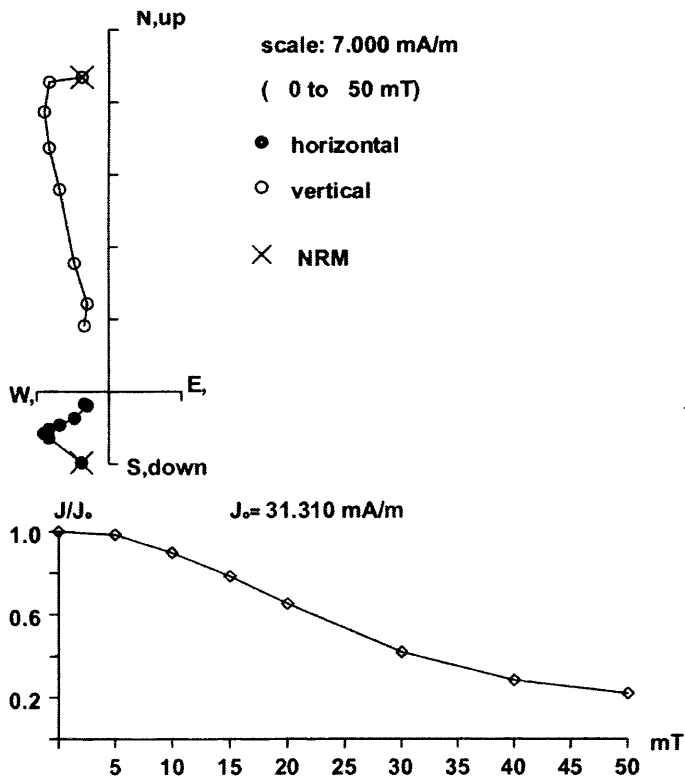
453 cm



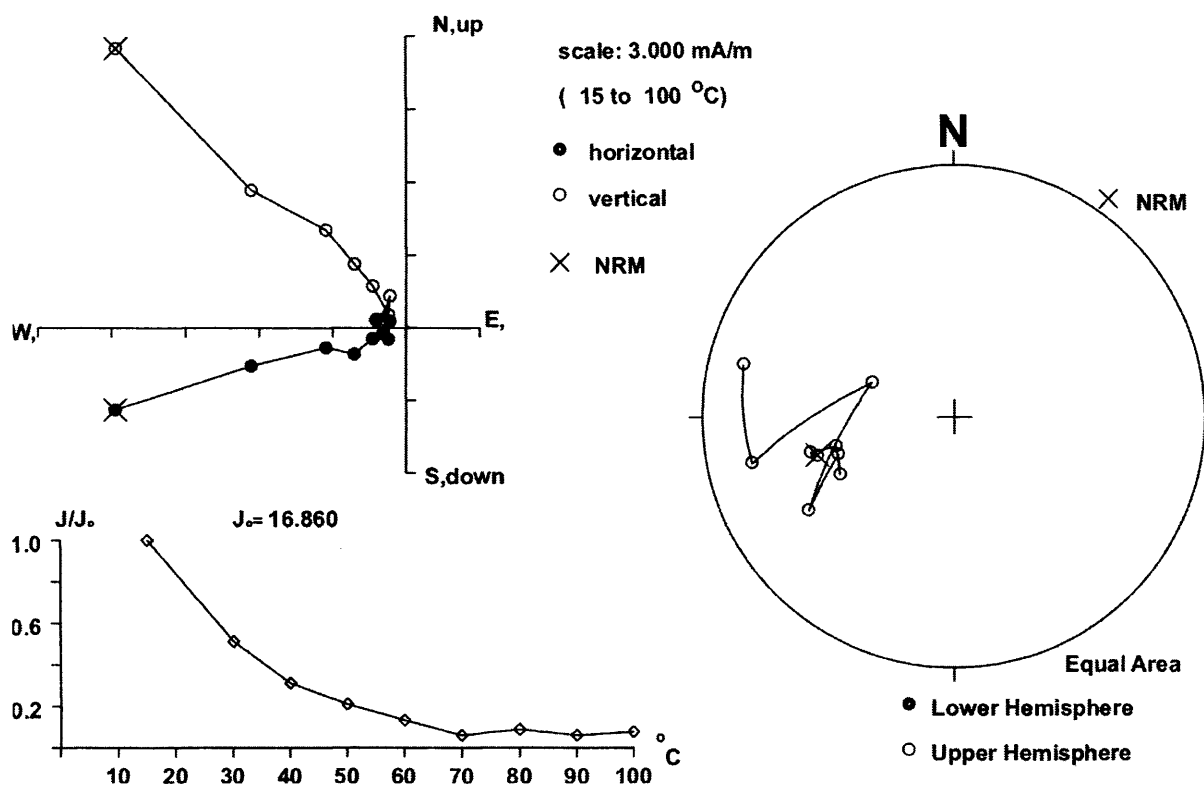
477 cm



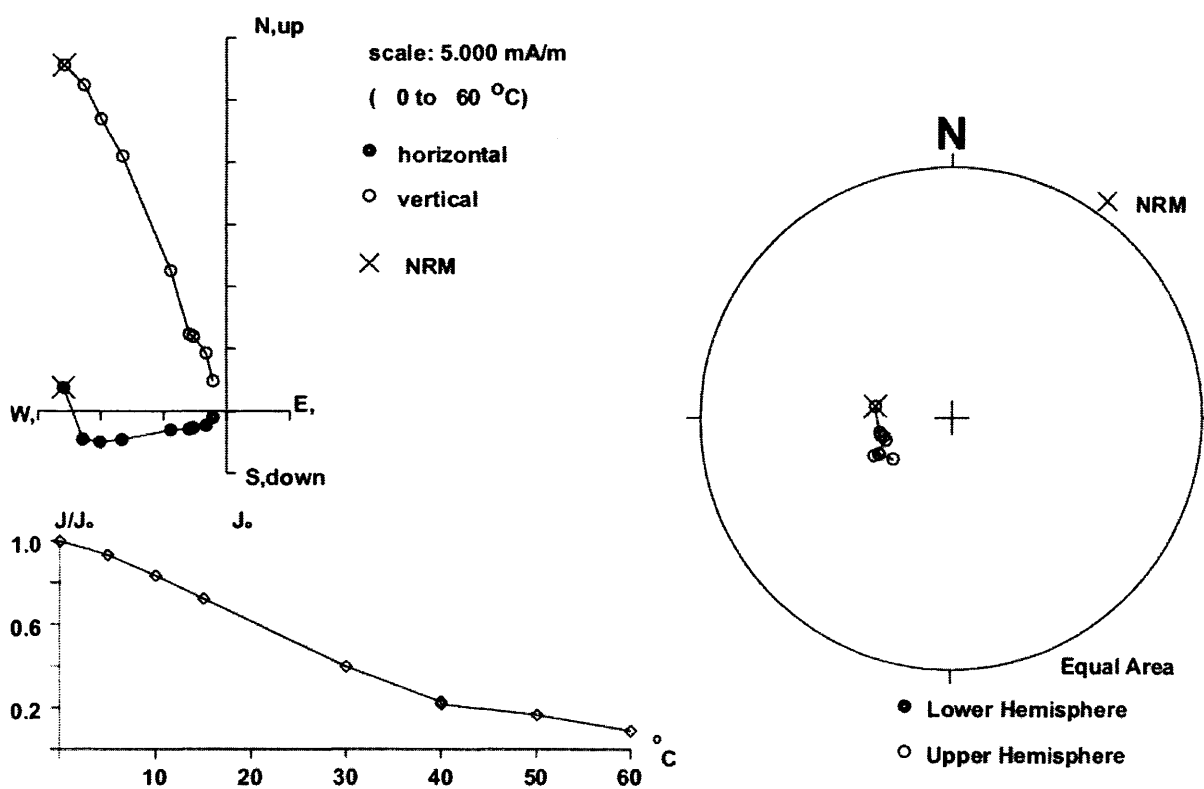
501 cm



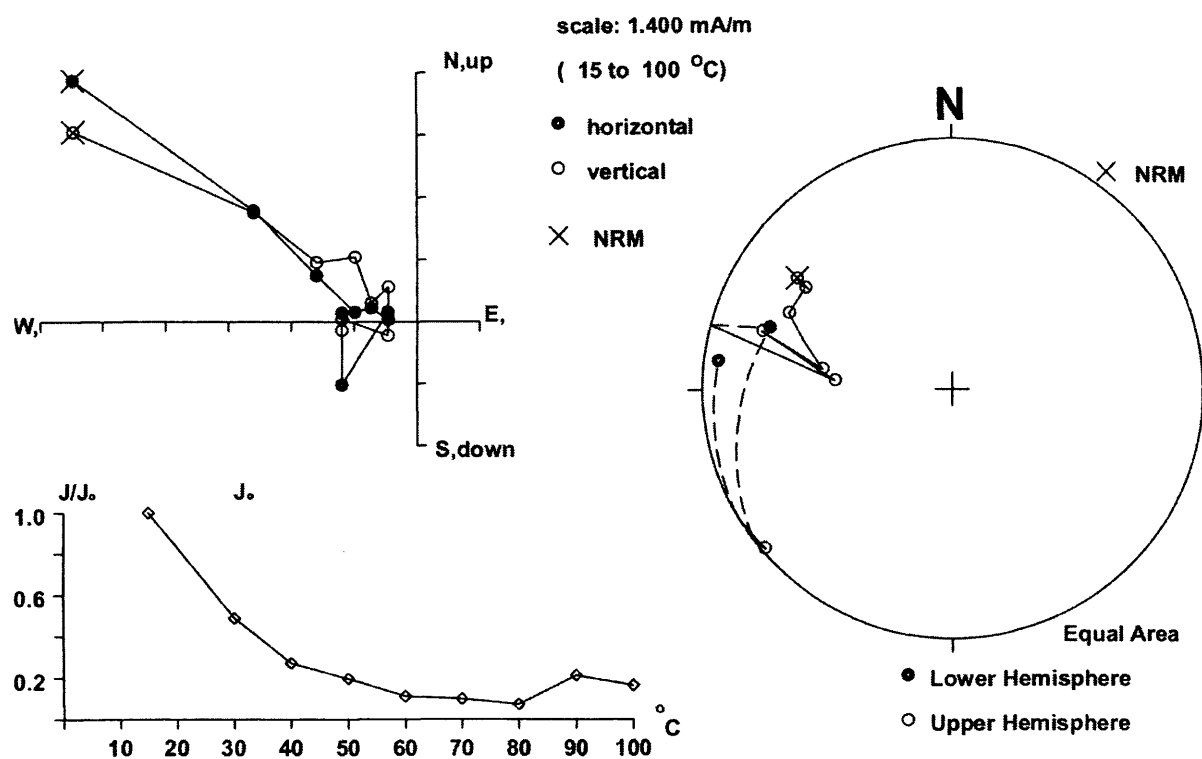
519 cm



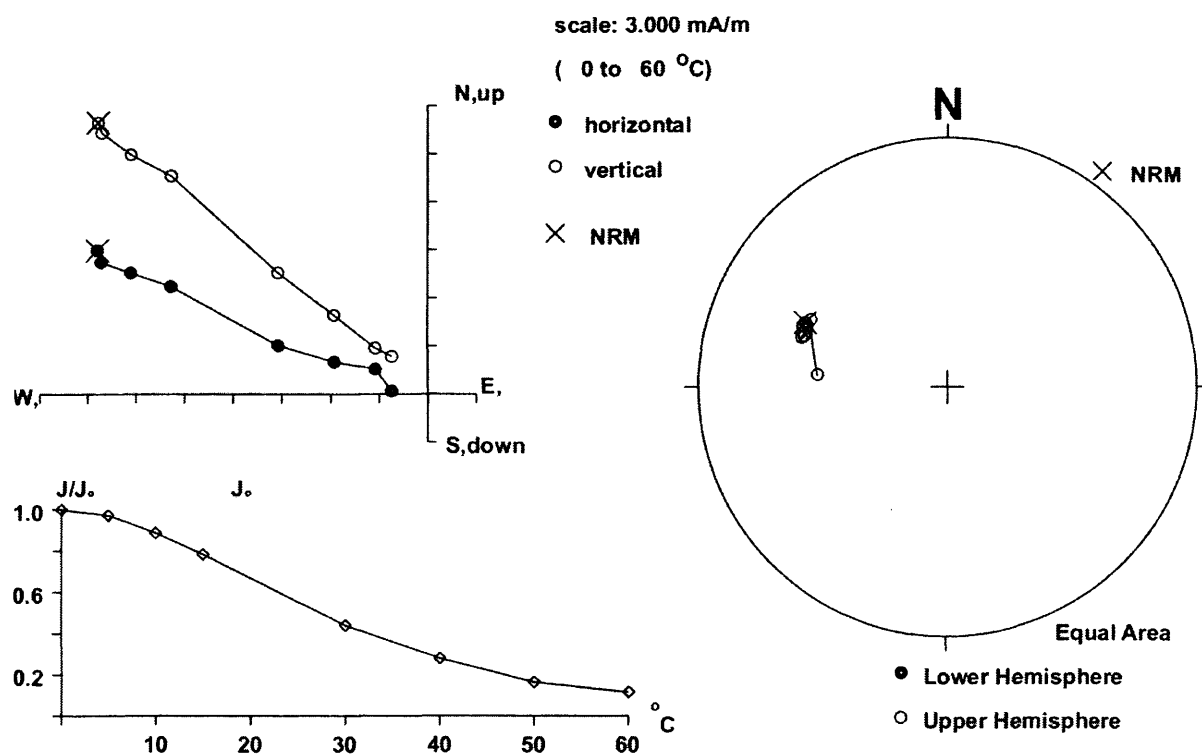
523 cm



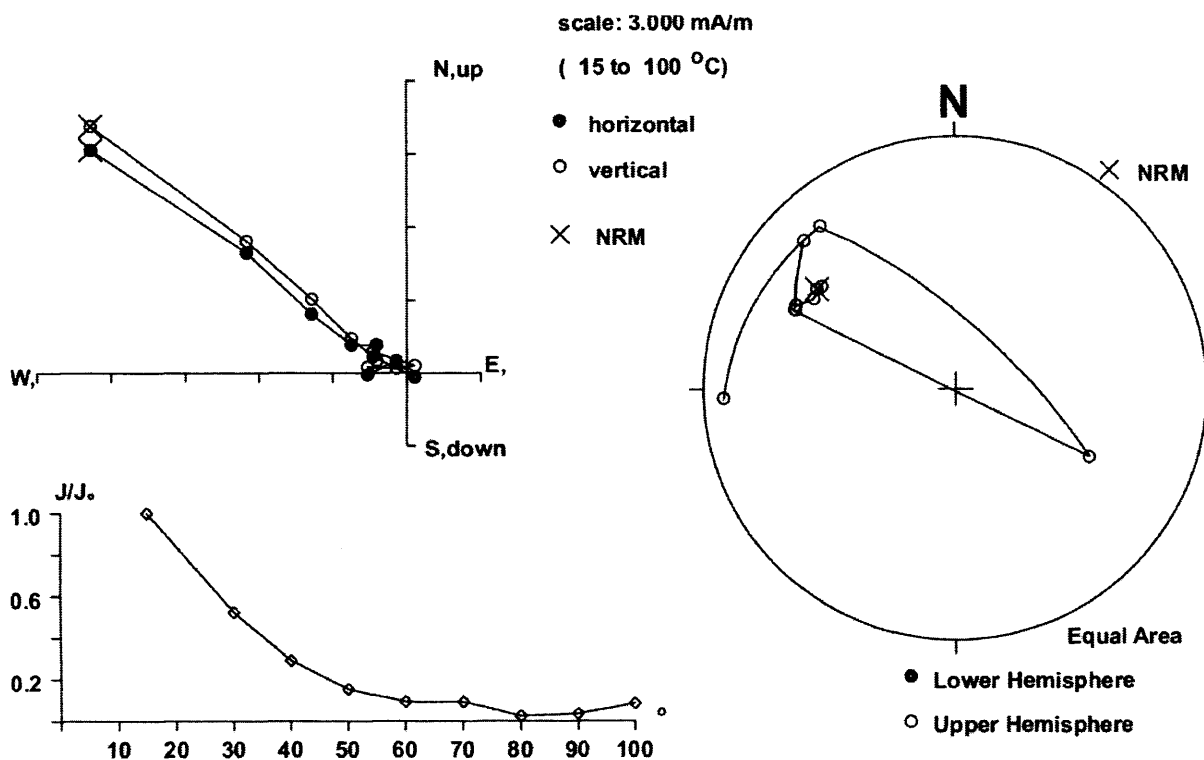
543 cm



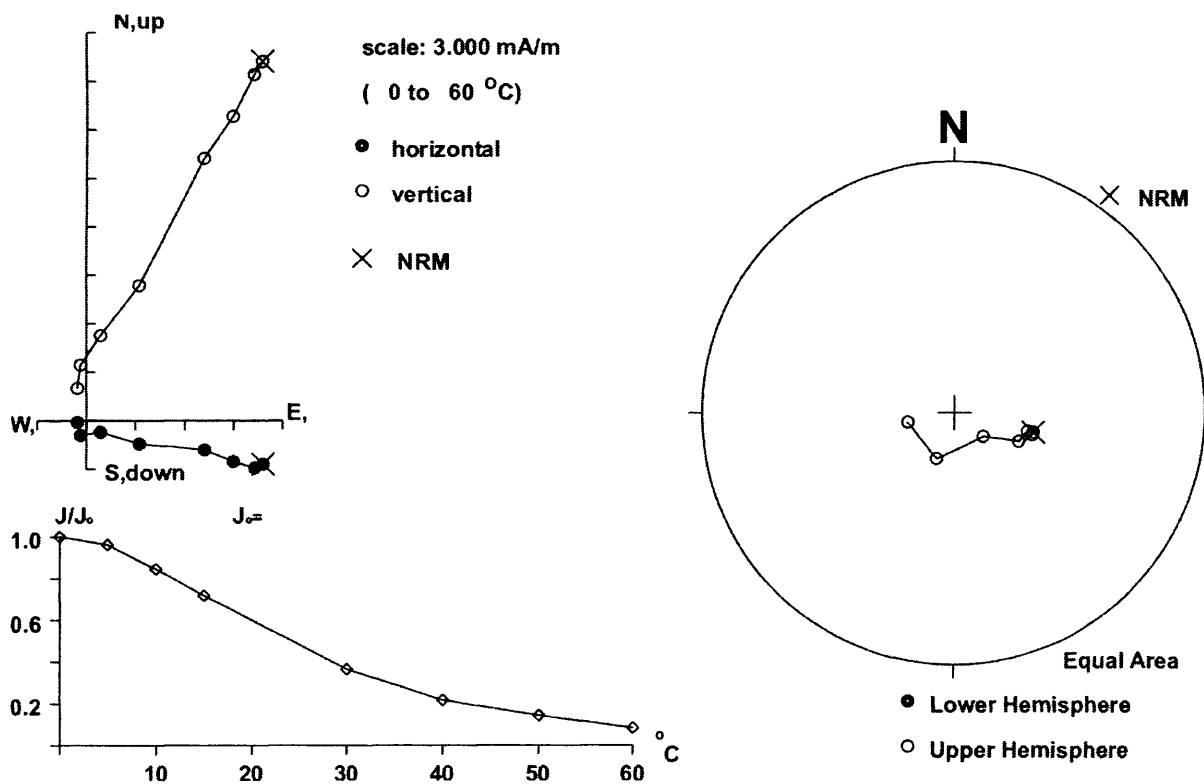
547 cm



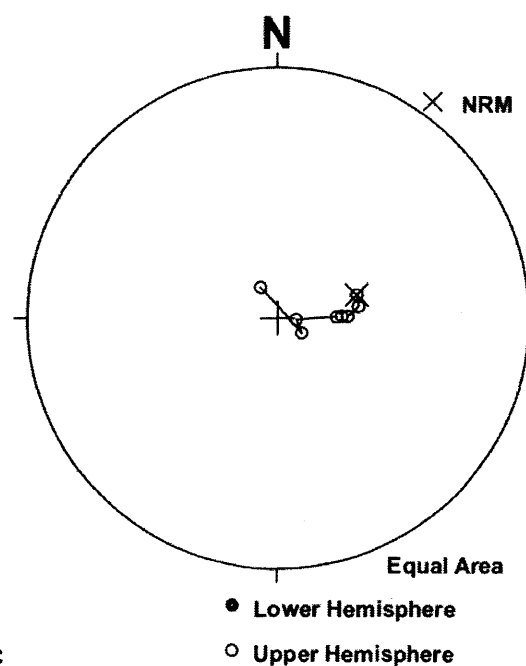
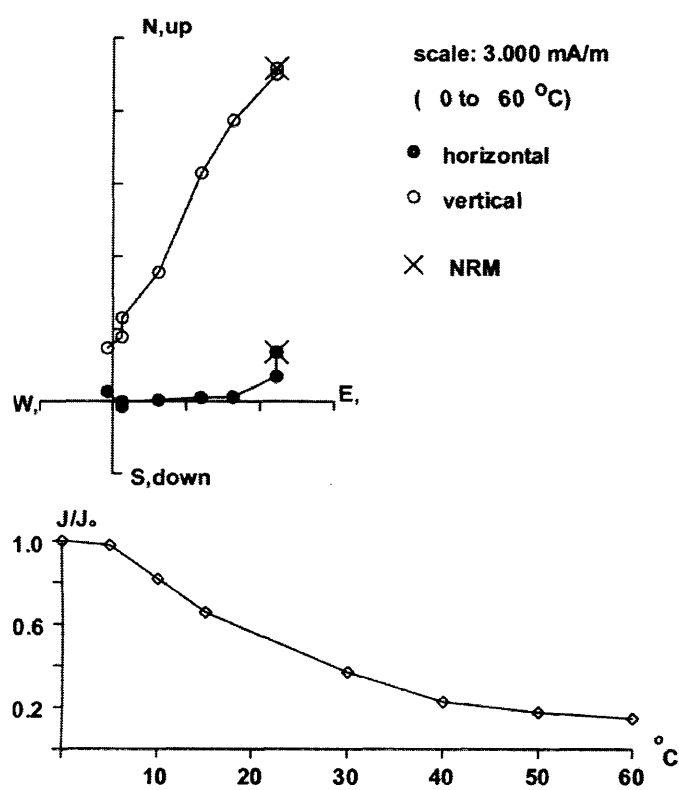
551 cm



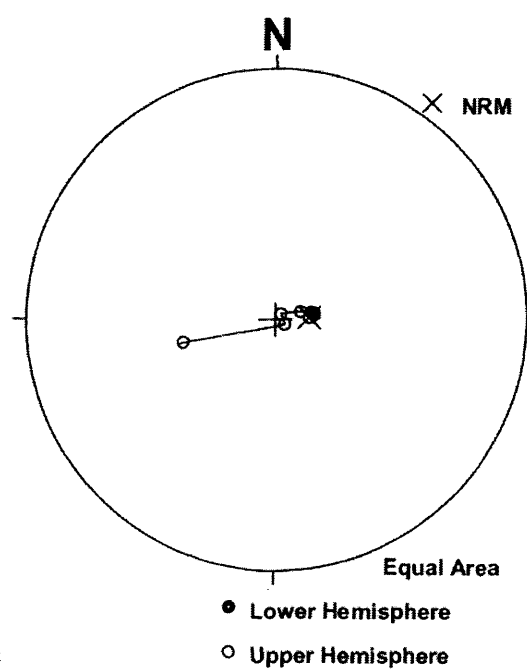
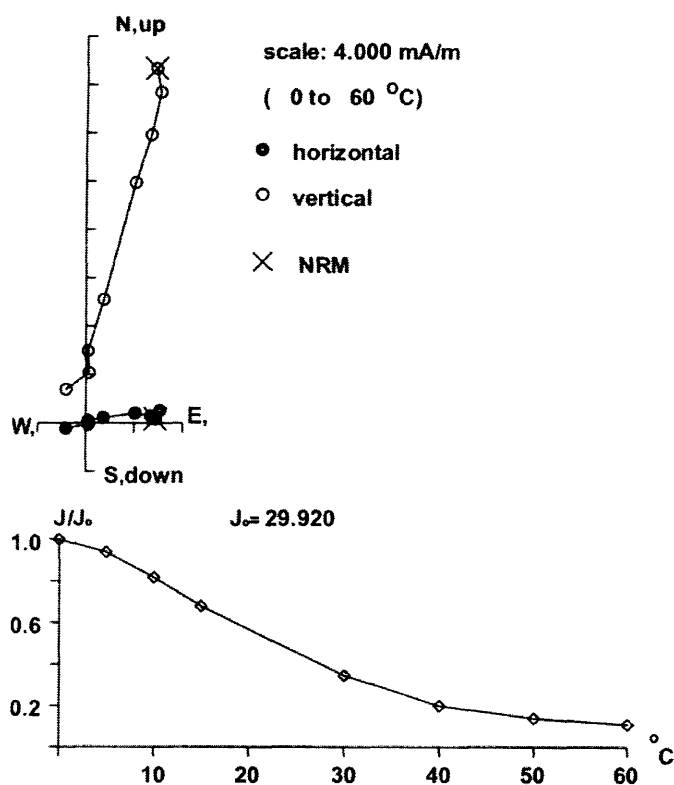
570 cm



594 cm

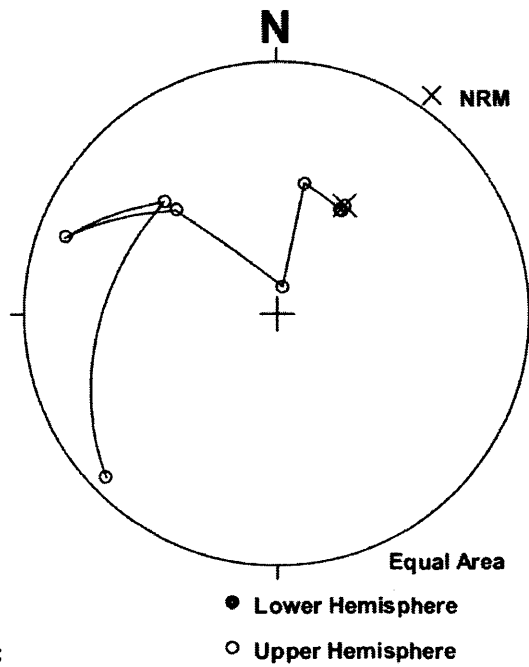
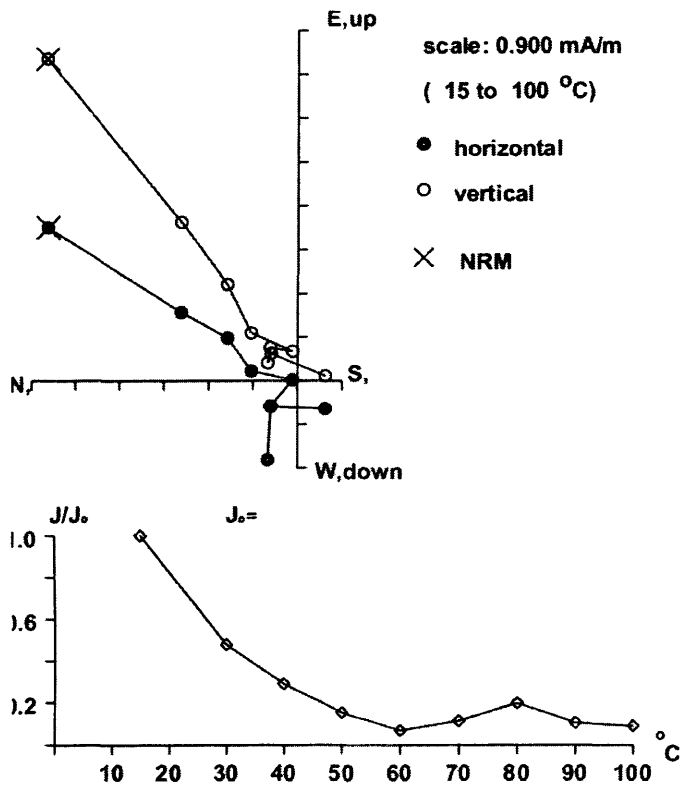


618 cm

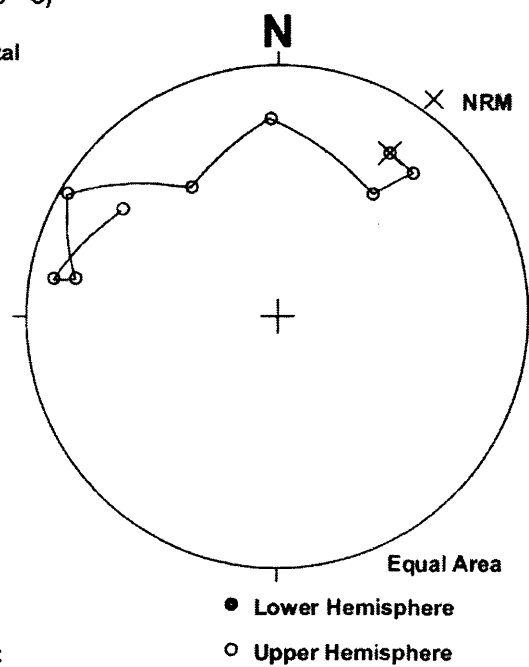
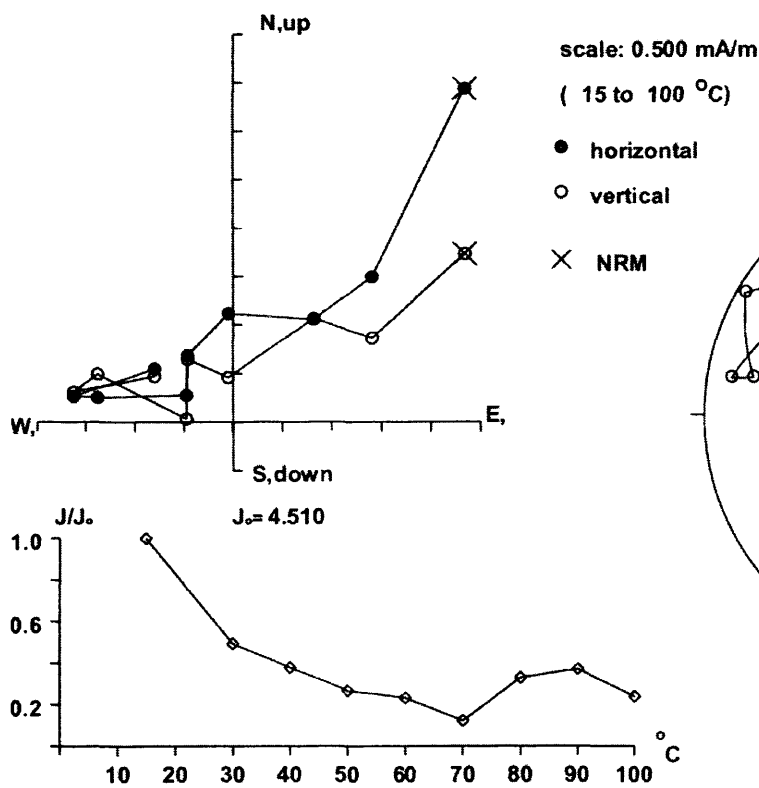


Appendix 2: Demagnetisation Plots

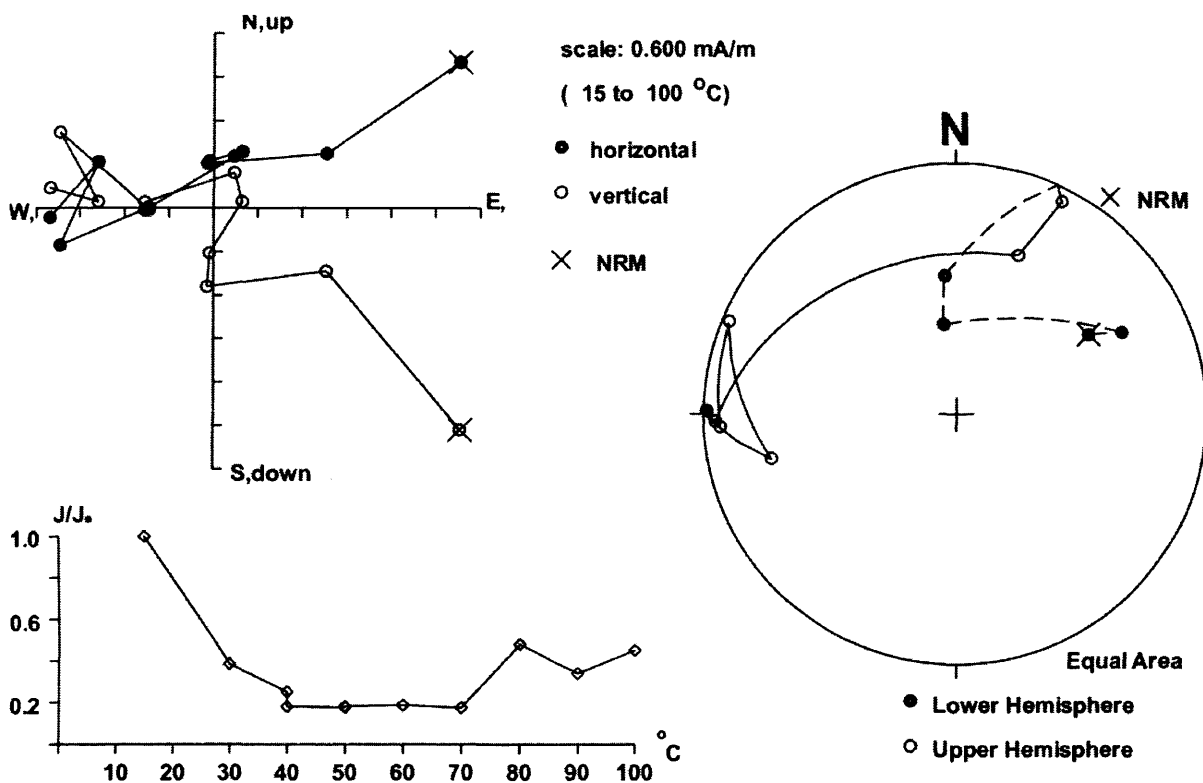
626 cm



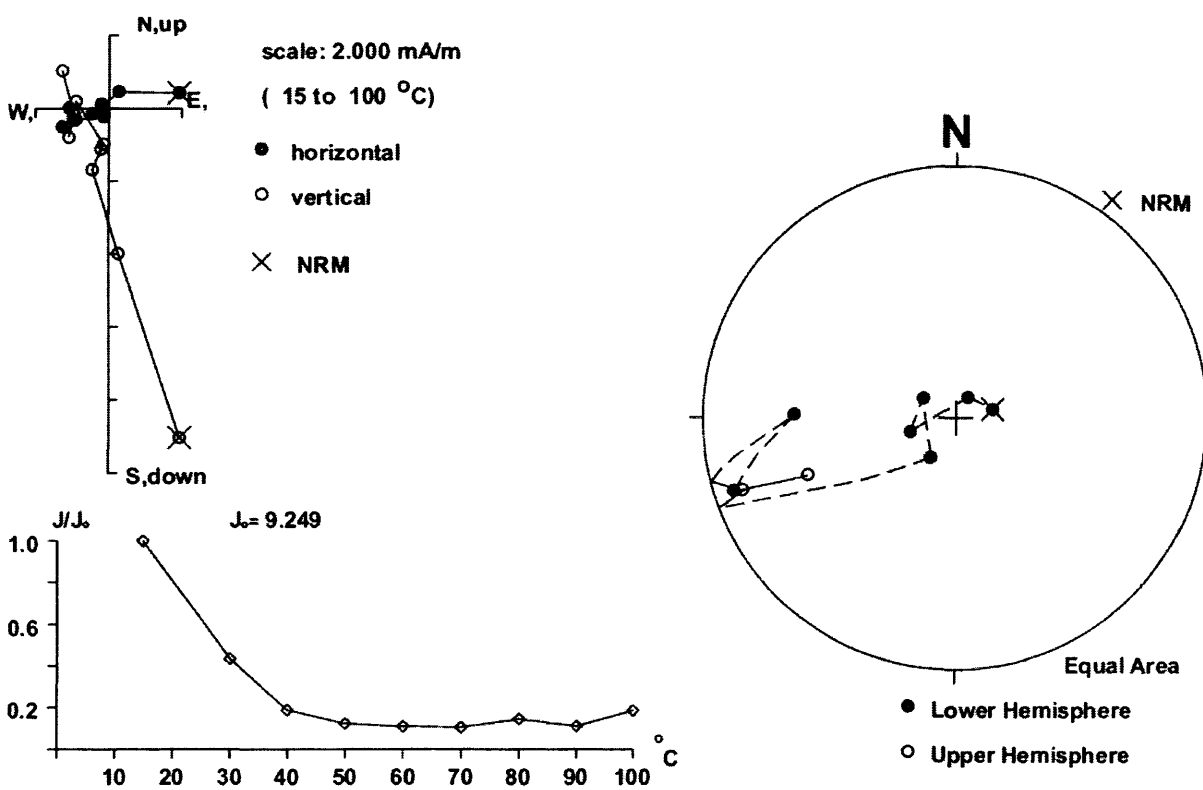
630 cm



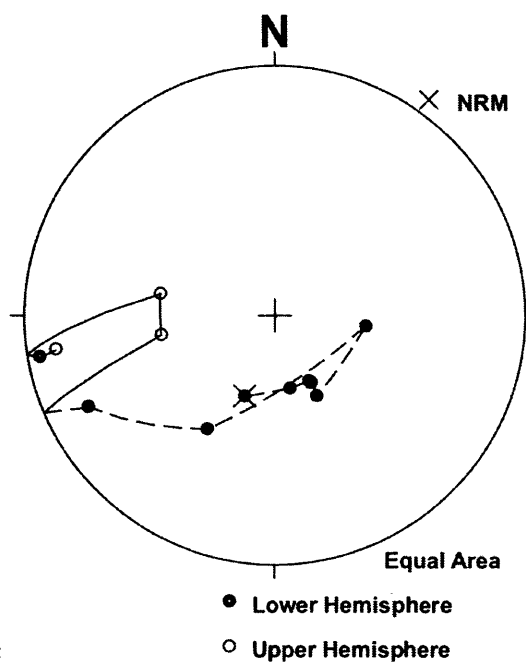
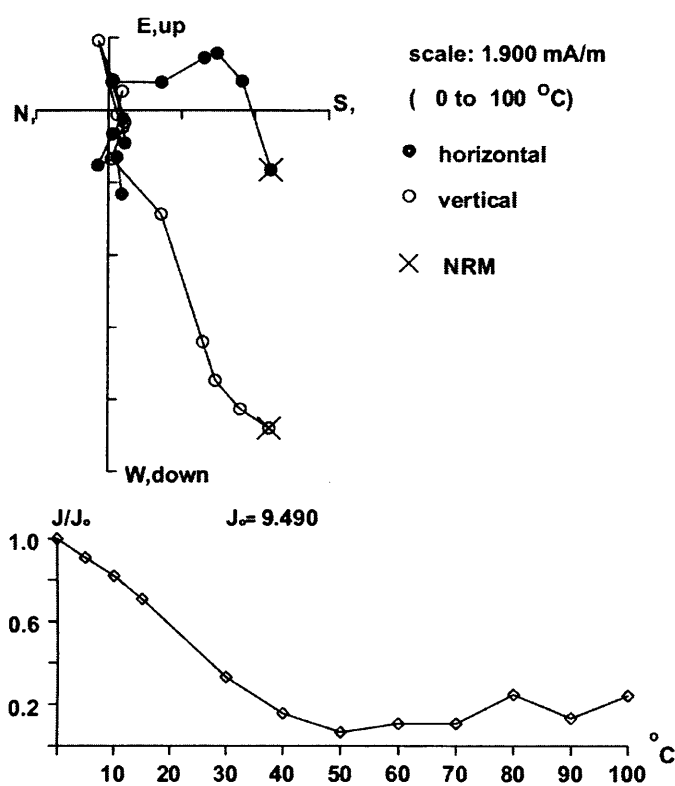
634 cm



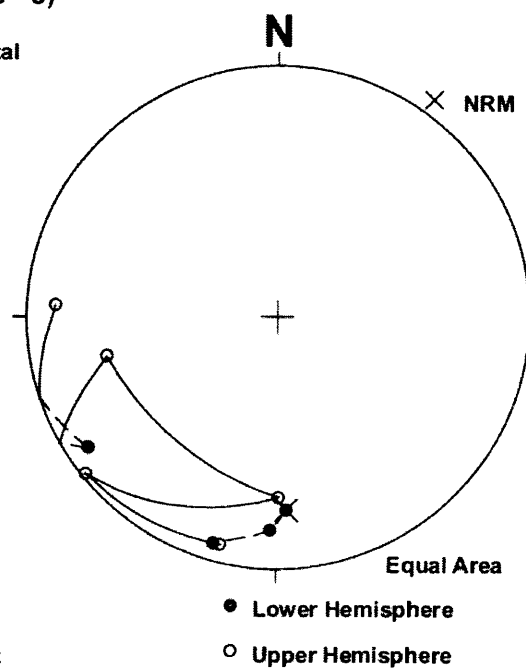
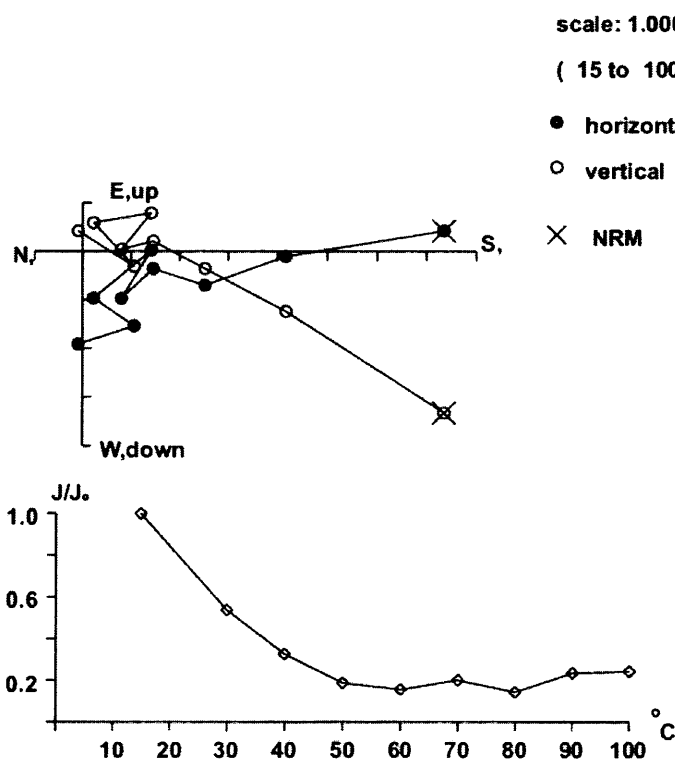
638 cm



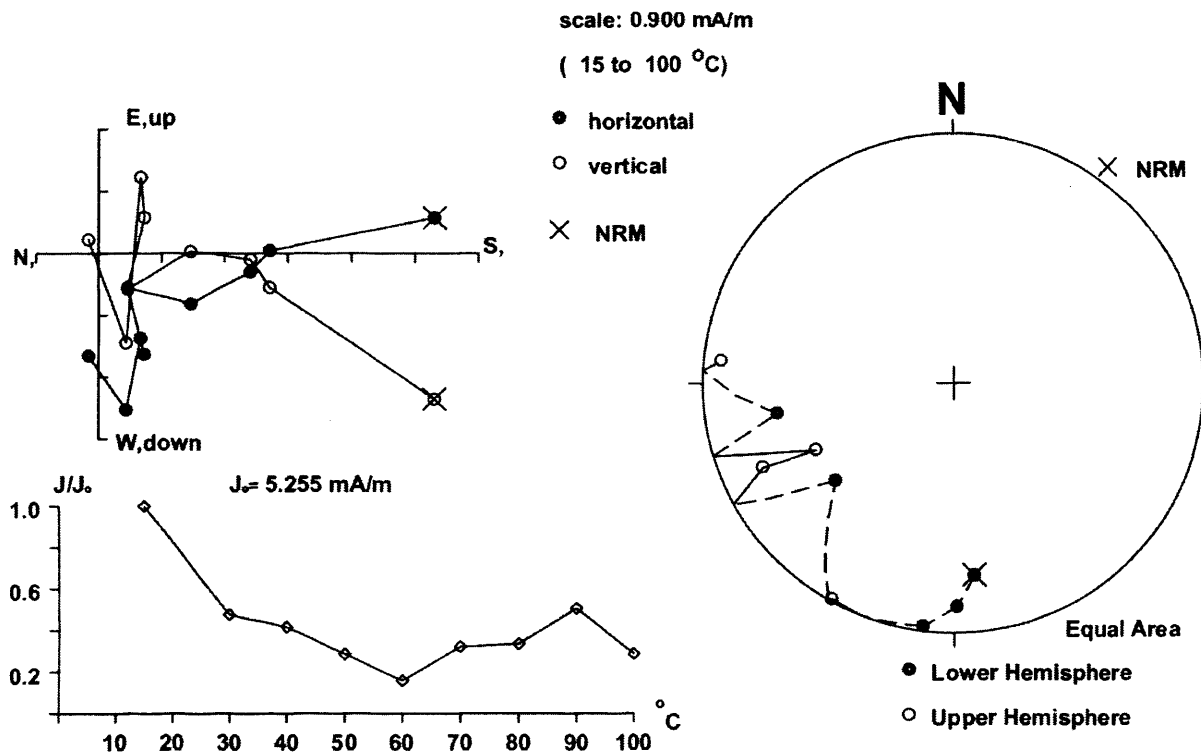
642 cm



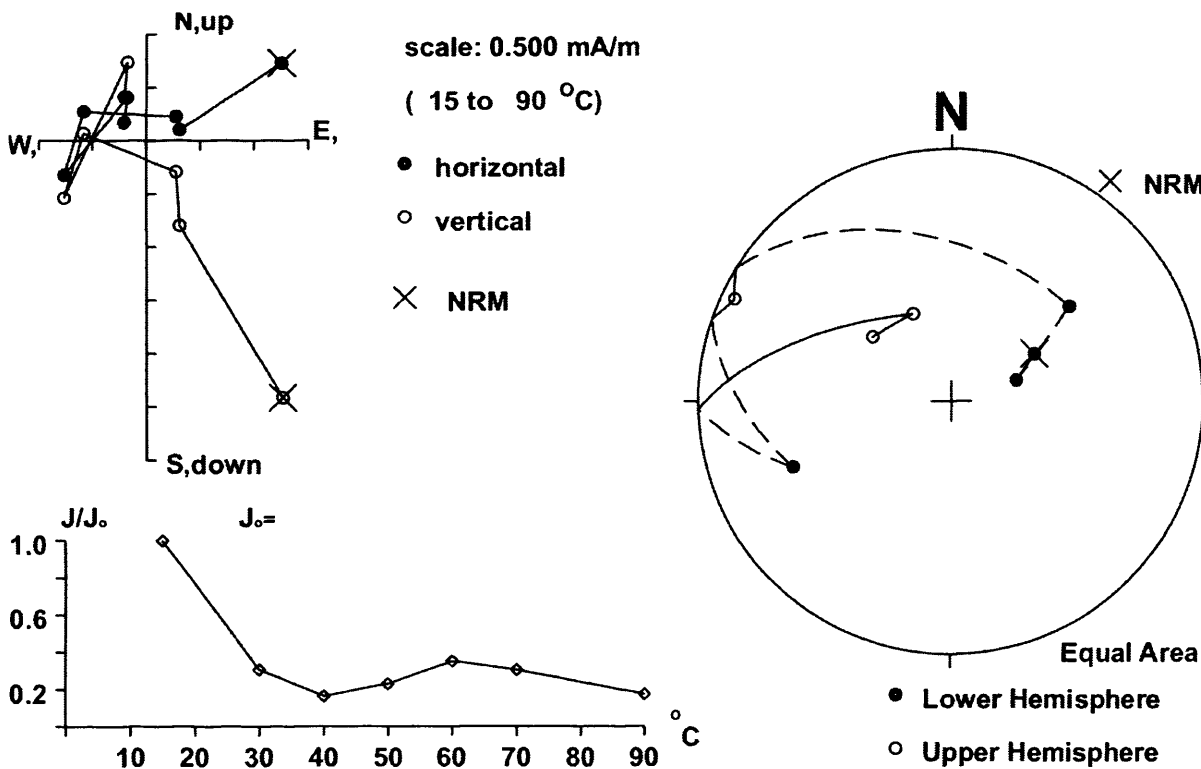
646 cm



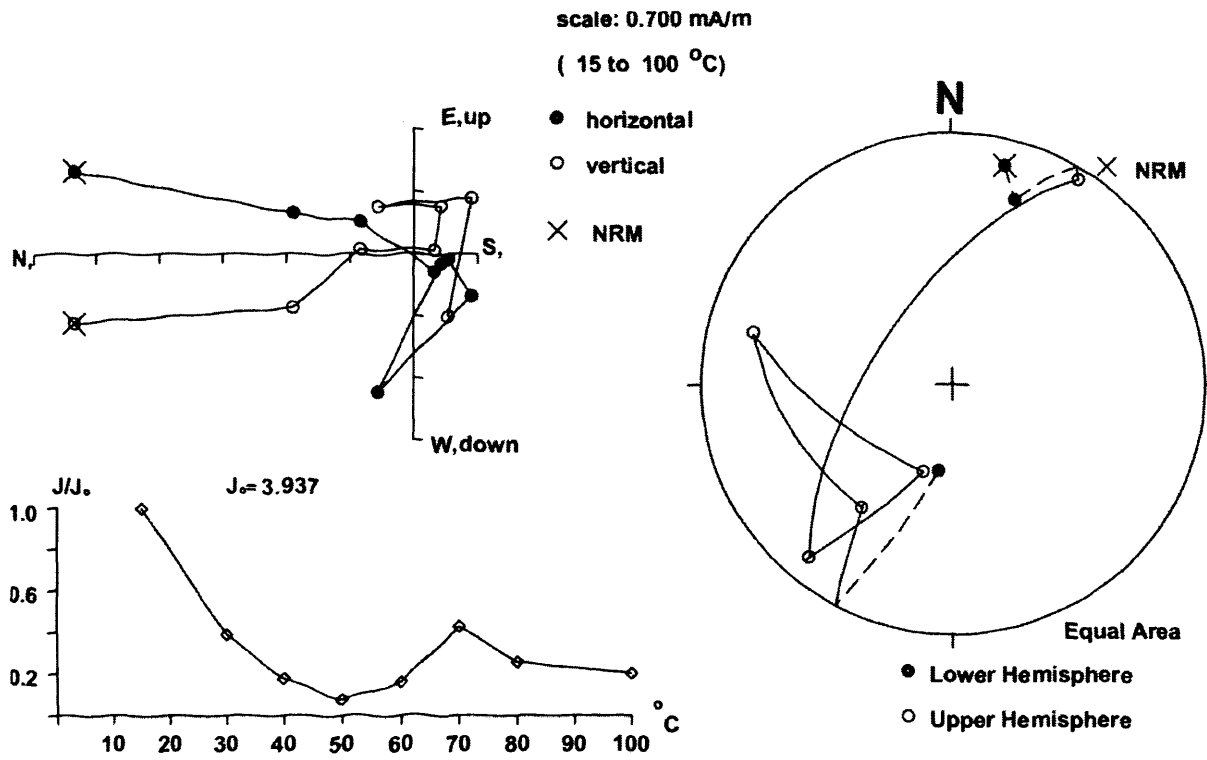
650 cm



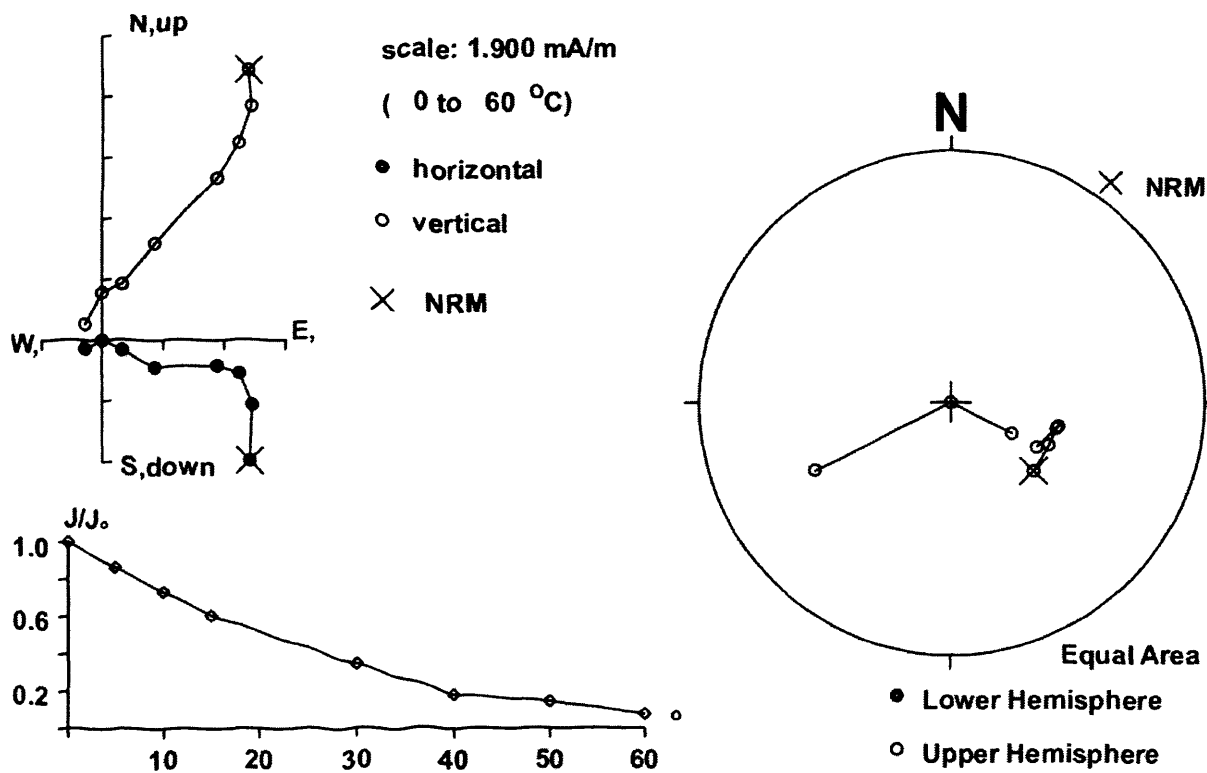
654 cm



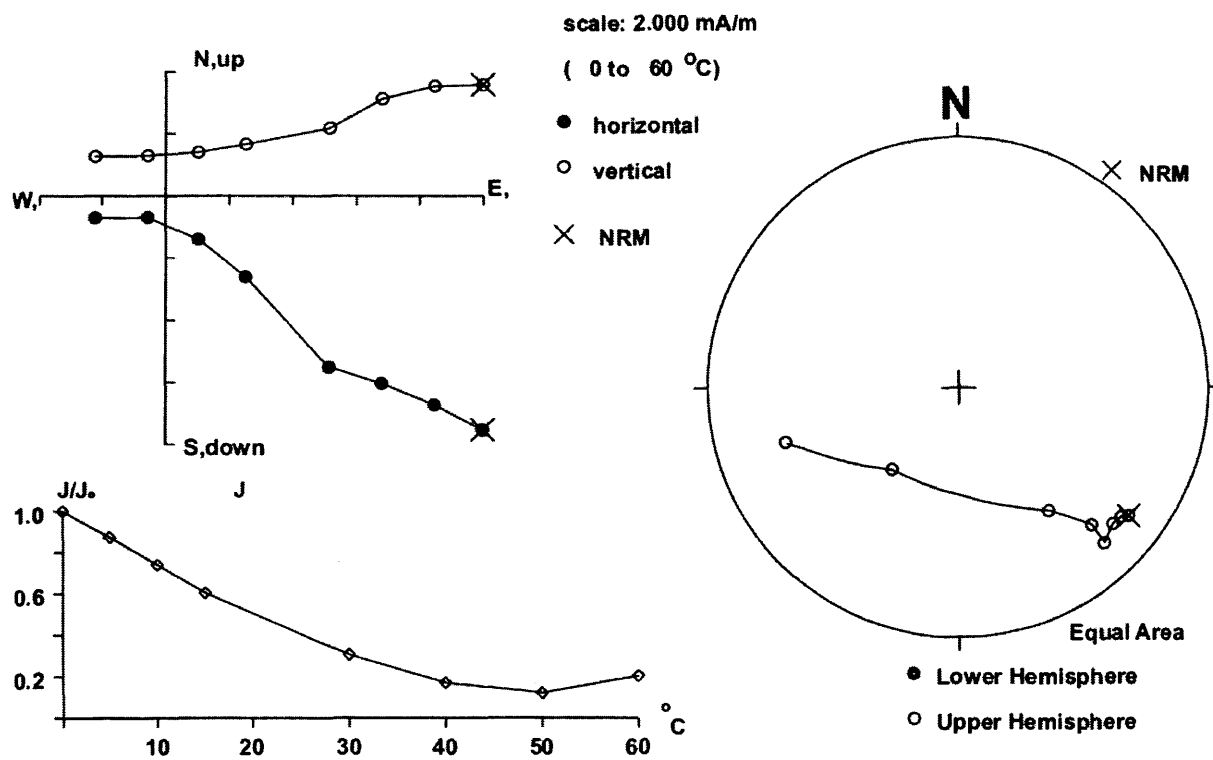
658 cm



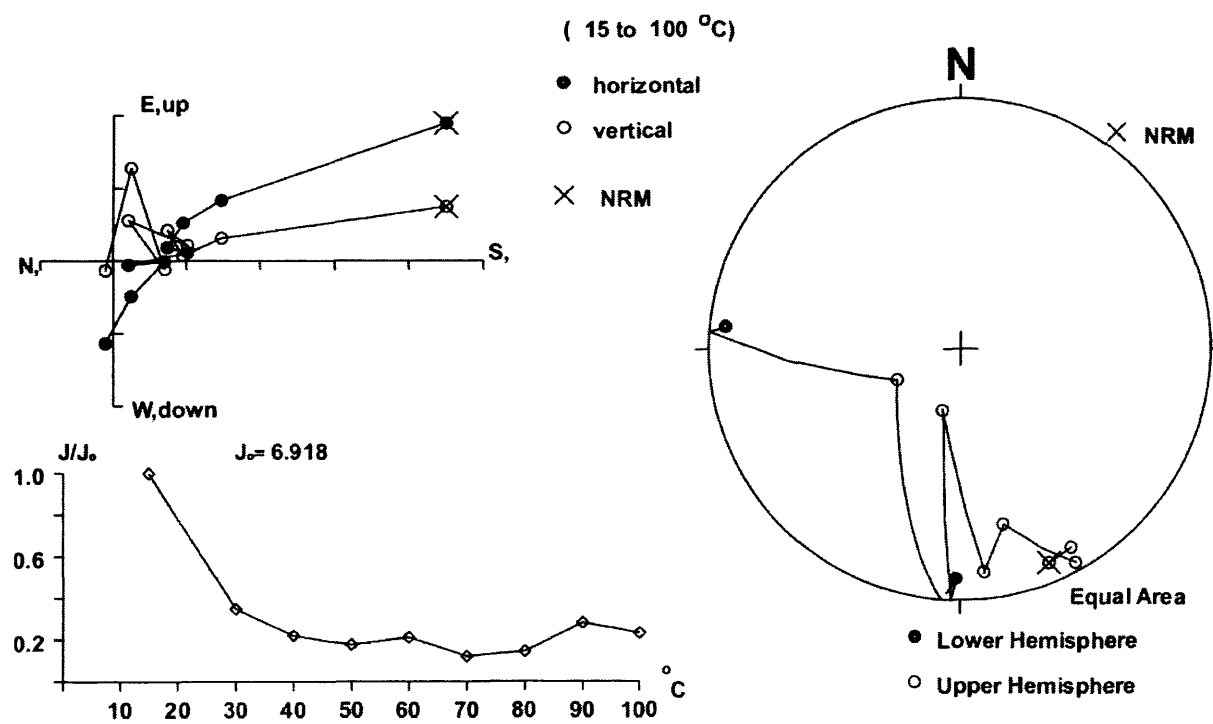
666 cm



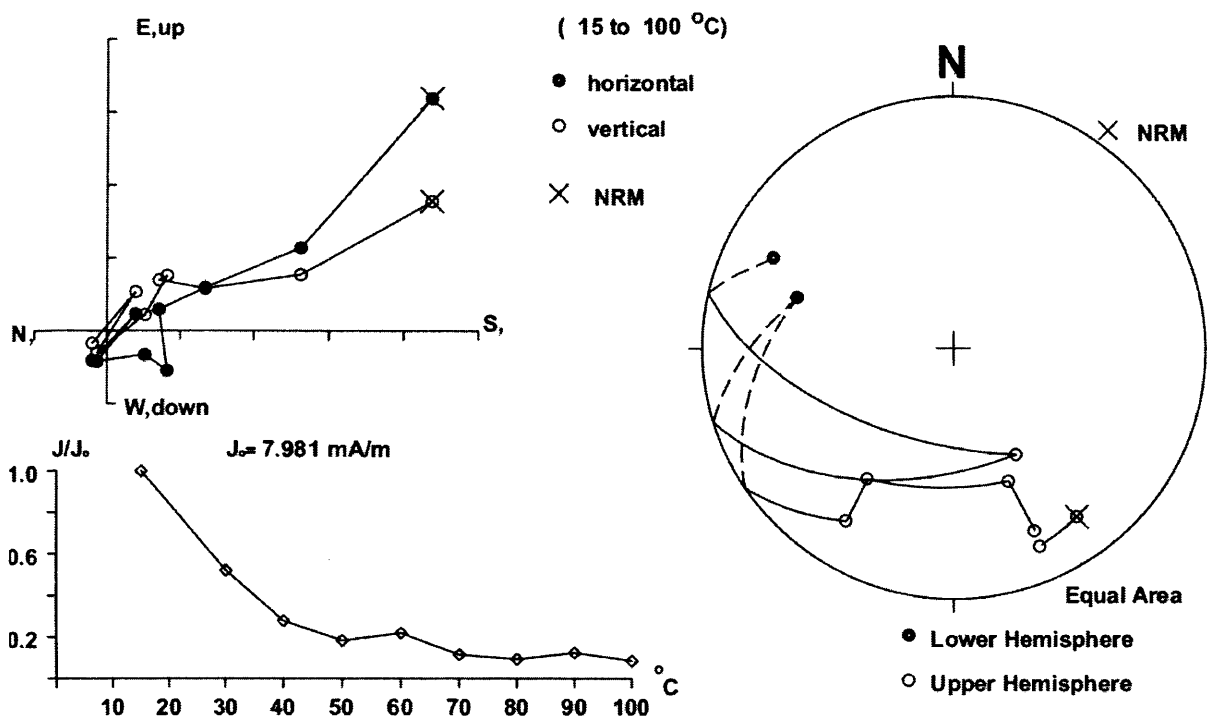
690 cm



694 cm

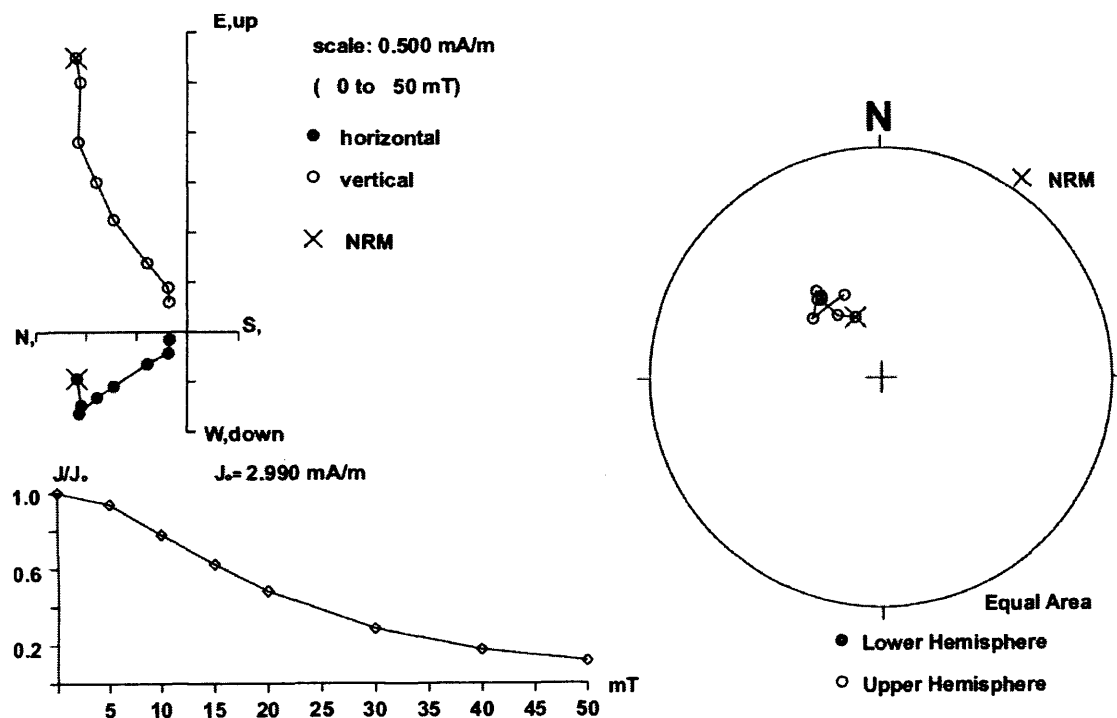


698 cm

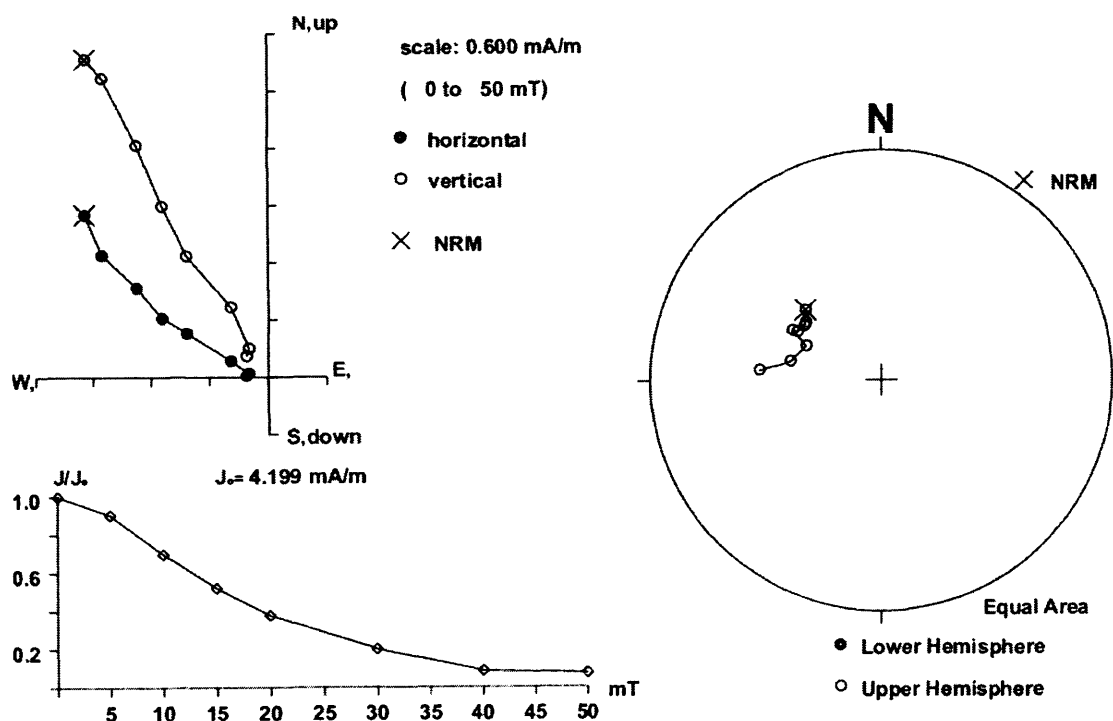


Appendix 2: RPI Demagnetization Plots - TPC286

144 cm

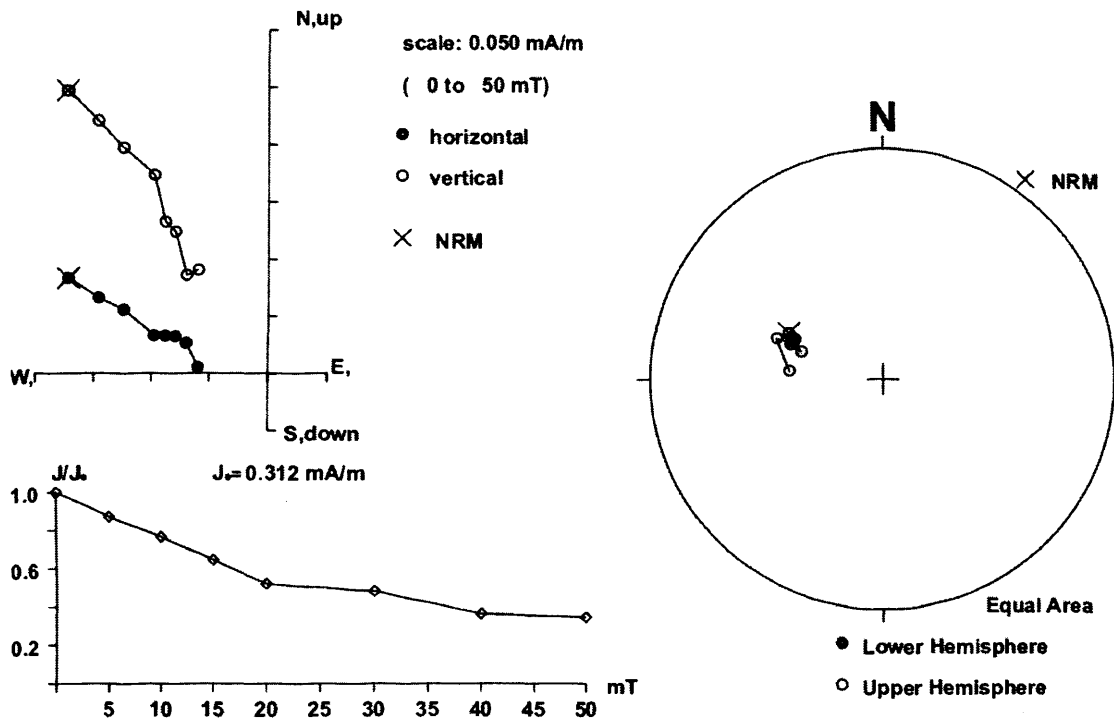


168 cm

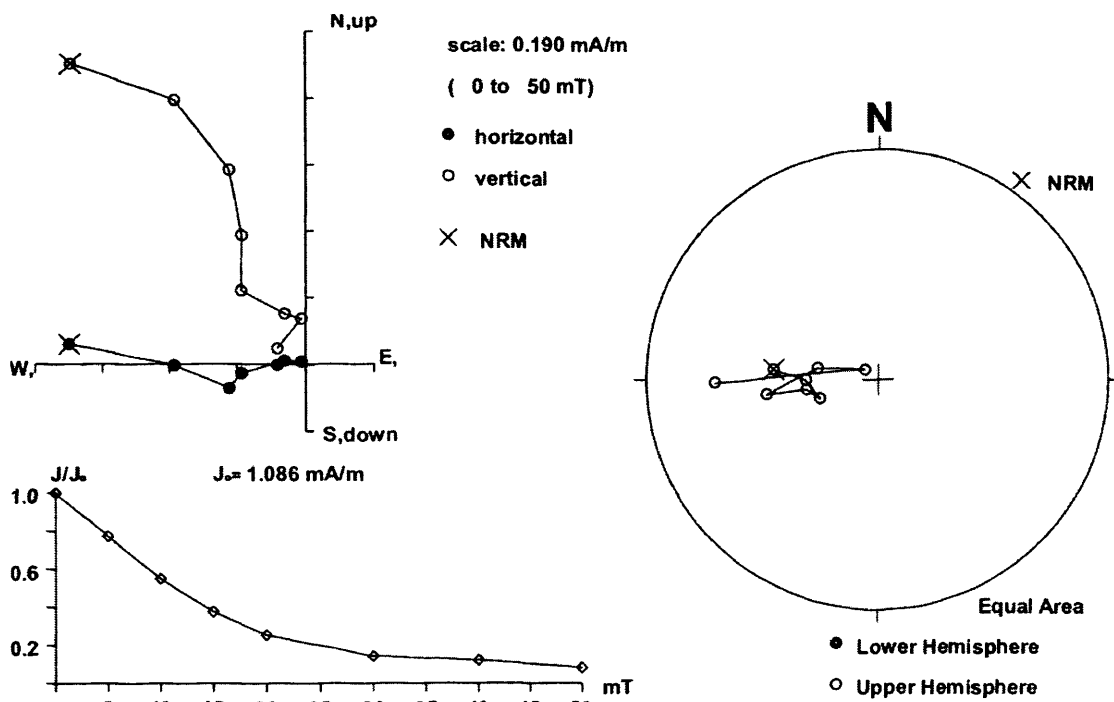


Appendix 2: Demagnetisation Plots

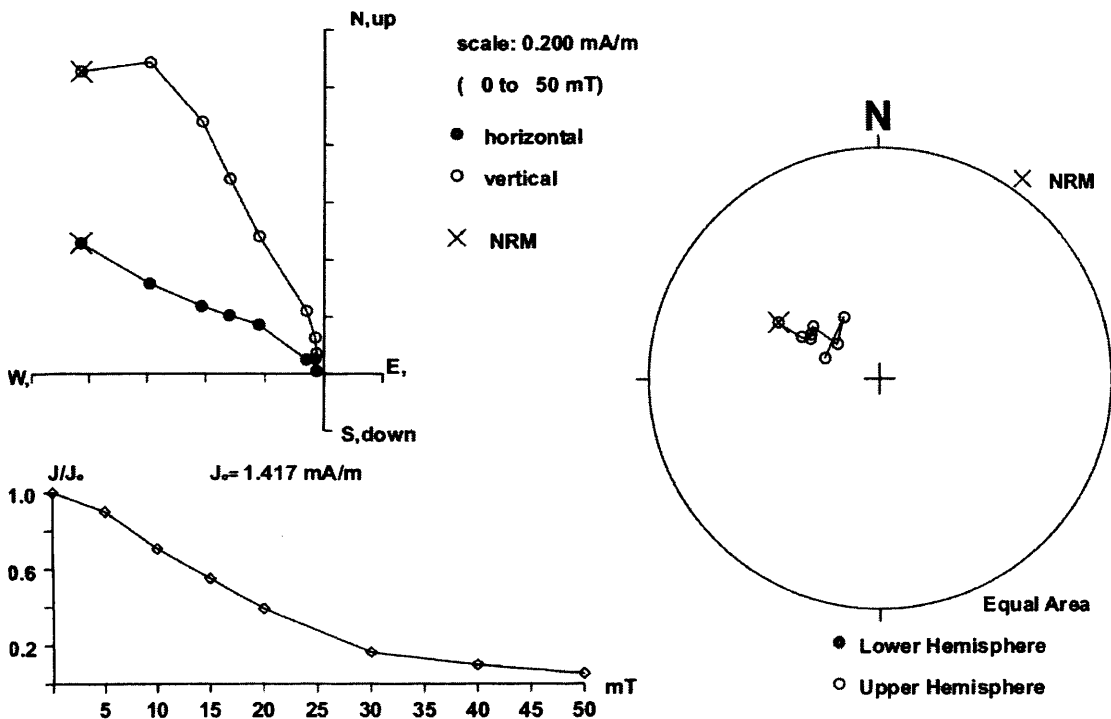
192 cm



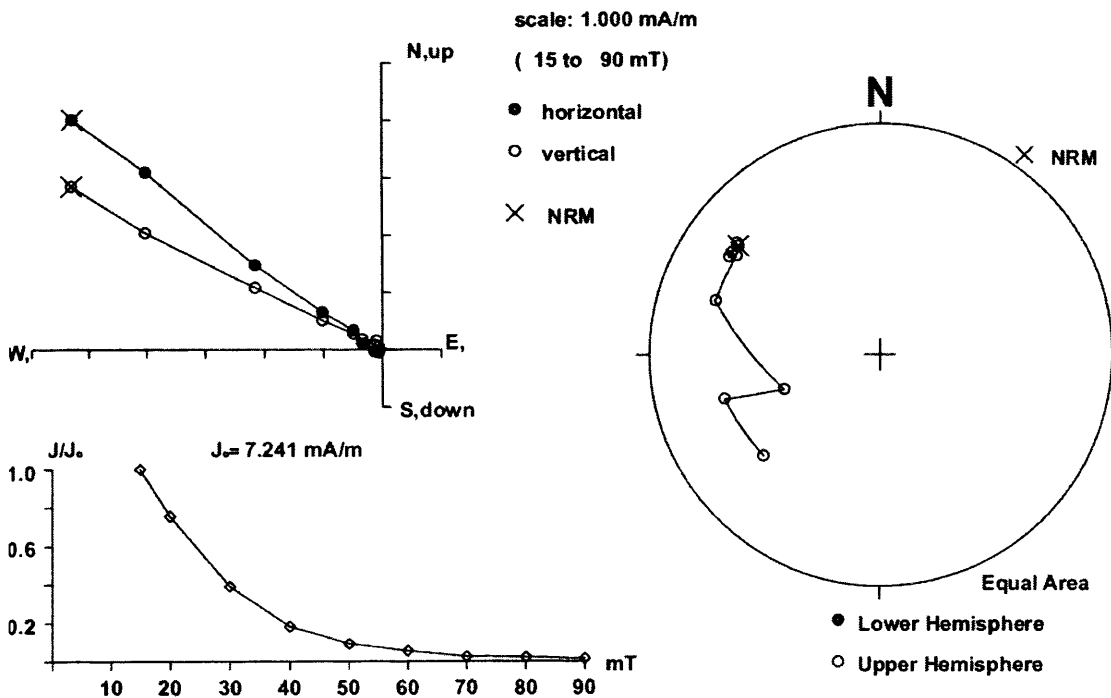
216 cm



240 cm

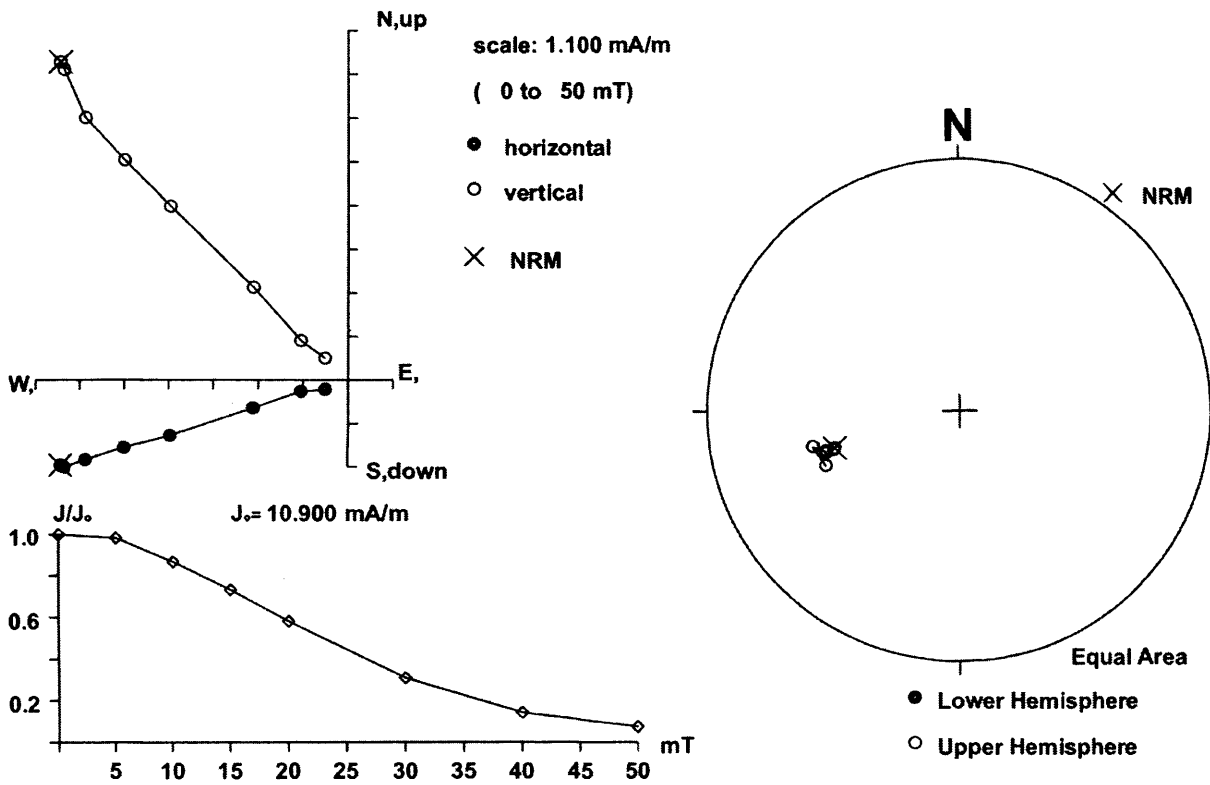


256 cm

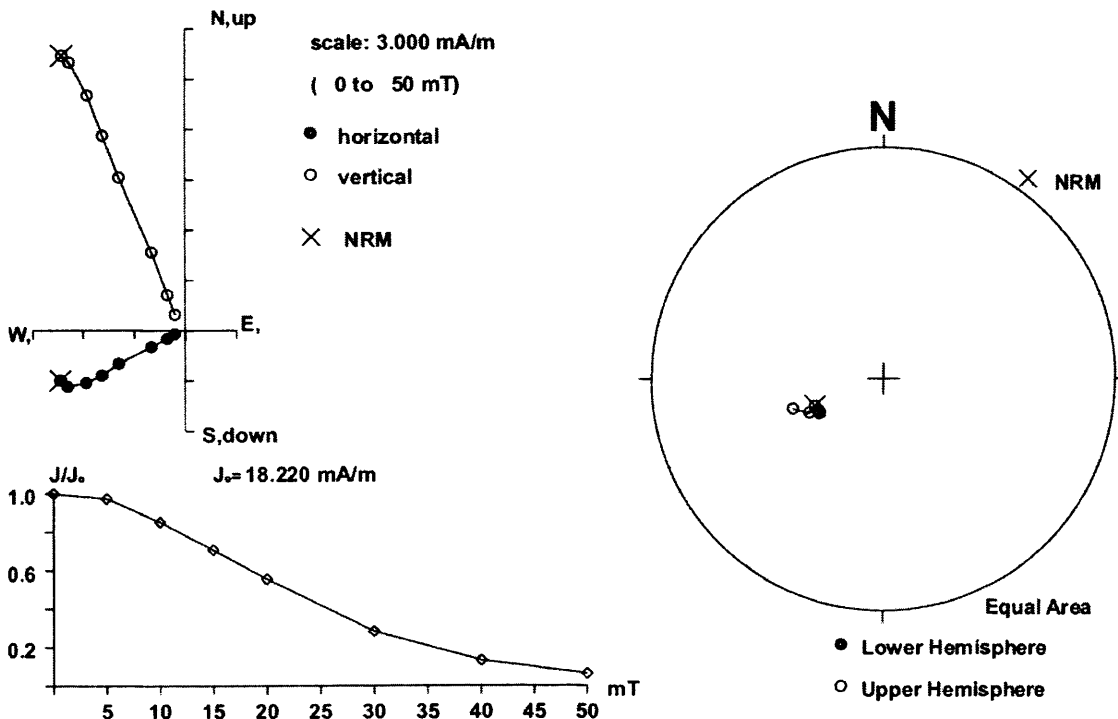


Appendix 2: Demagnetisation Plots

264 cm

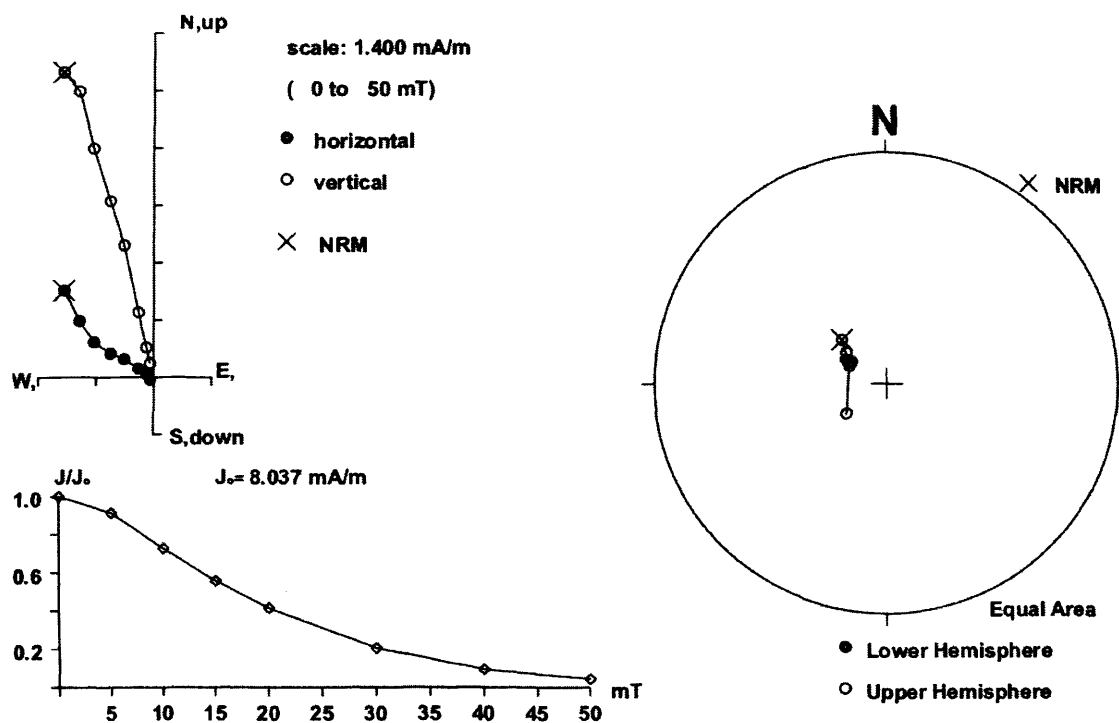


288 cm

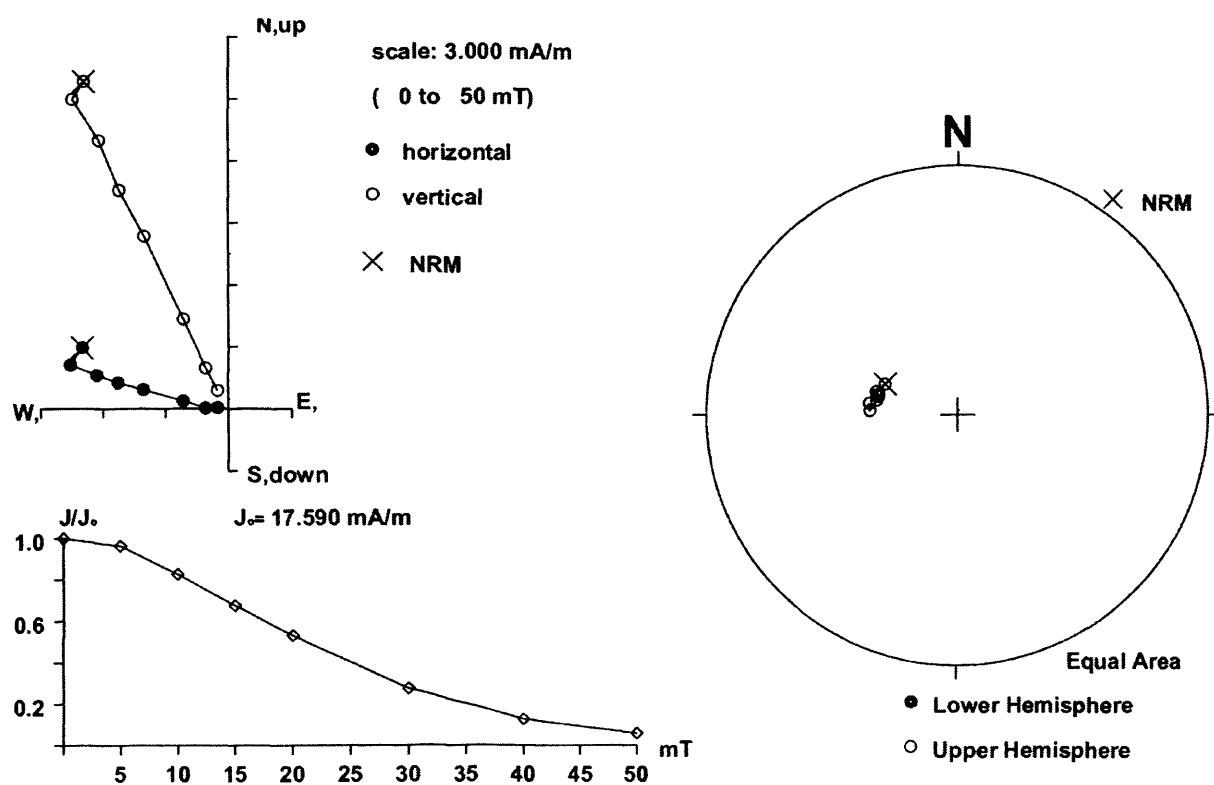


Appendix 2: Demagnetisation Plots

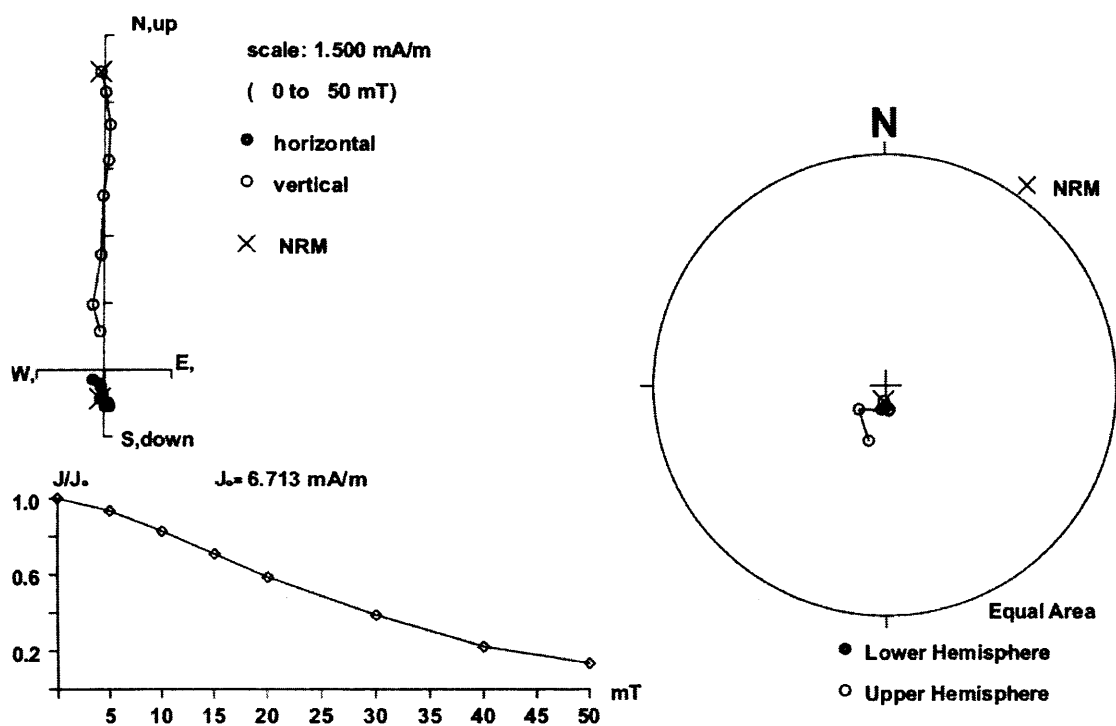
312 cm



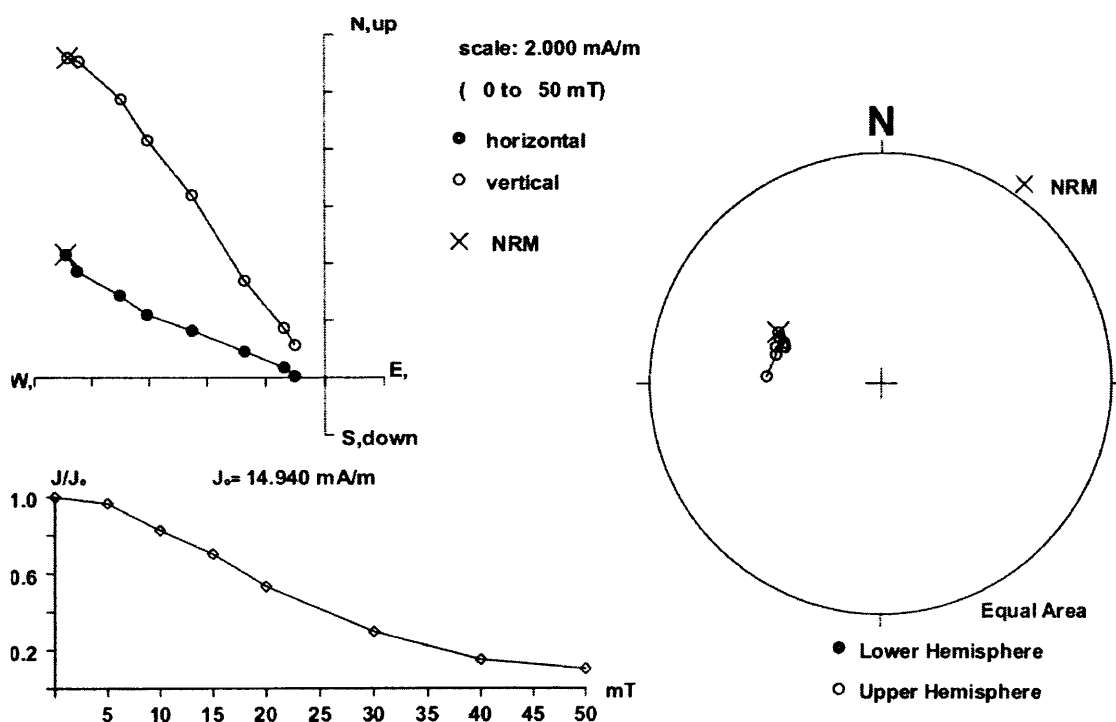
336 cm



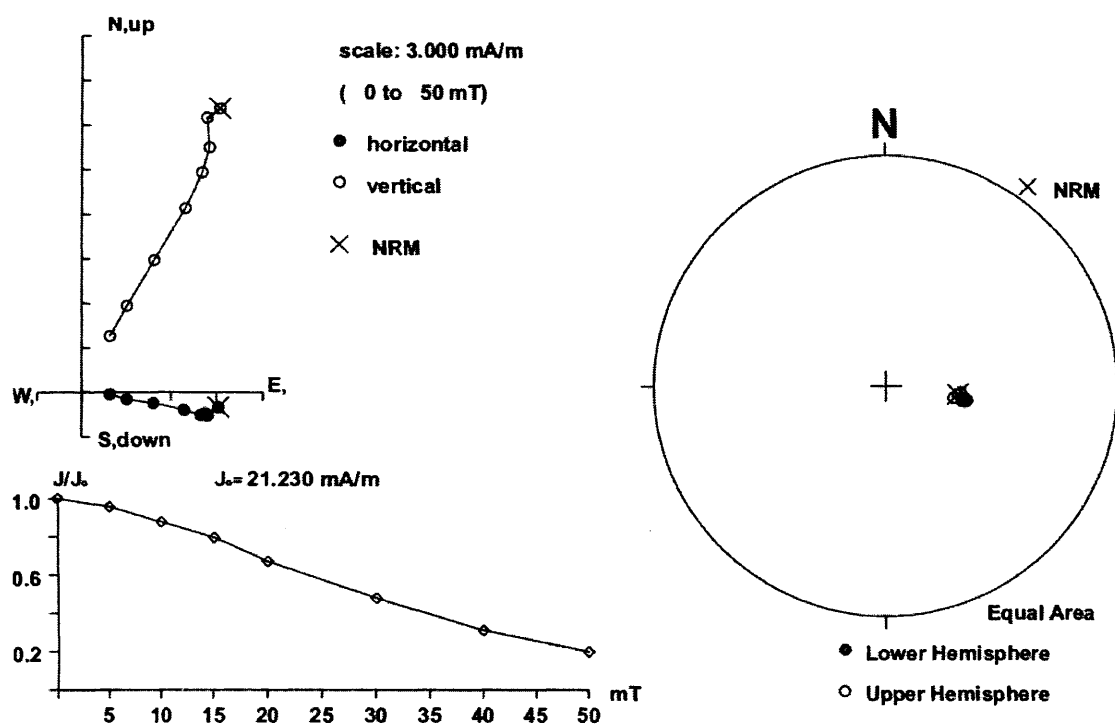
360 cm



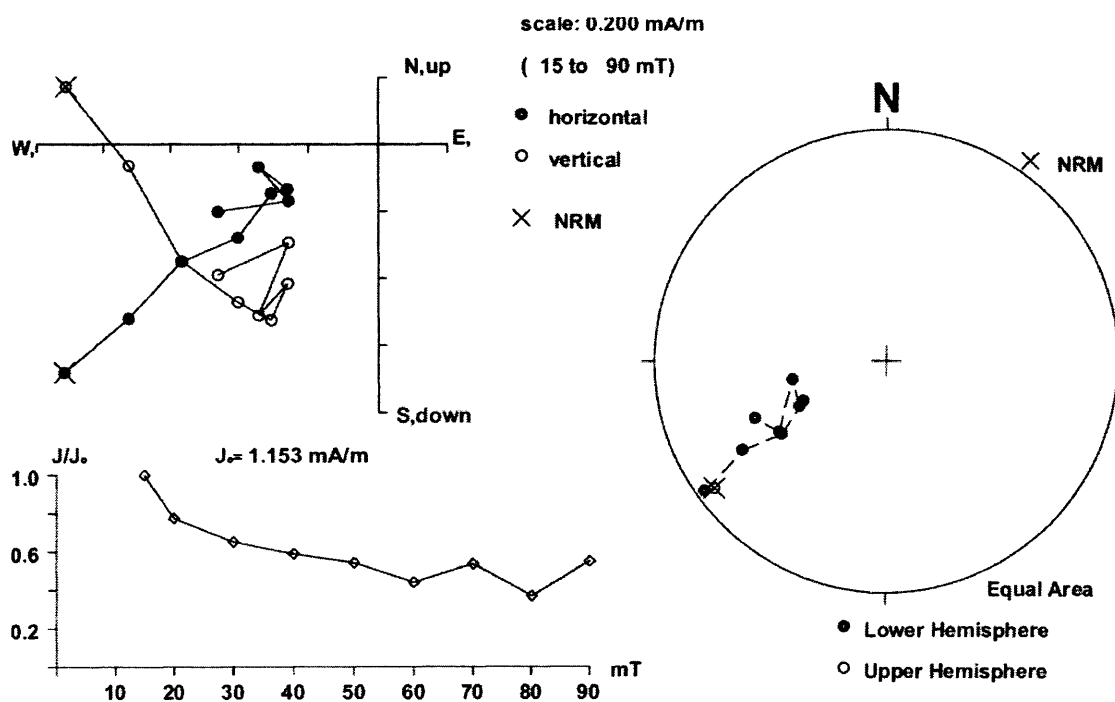
384 cm



408 cm

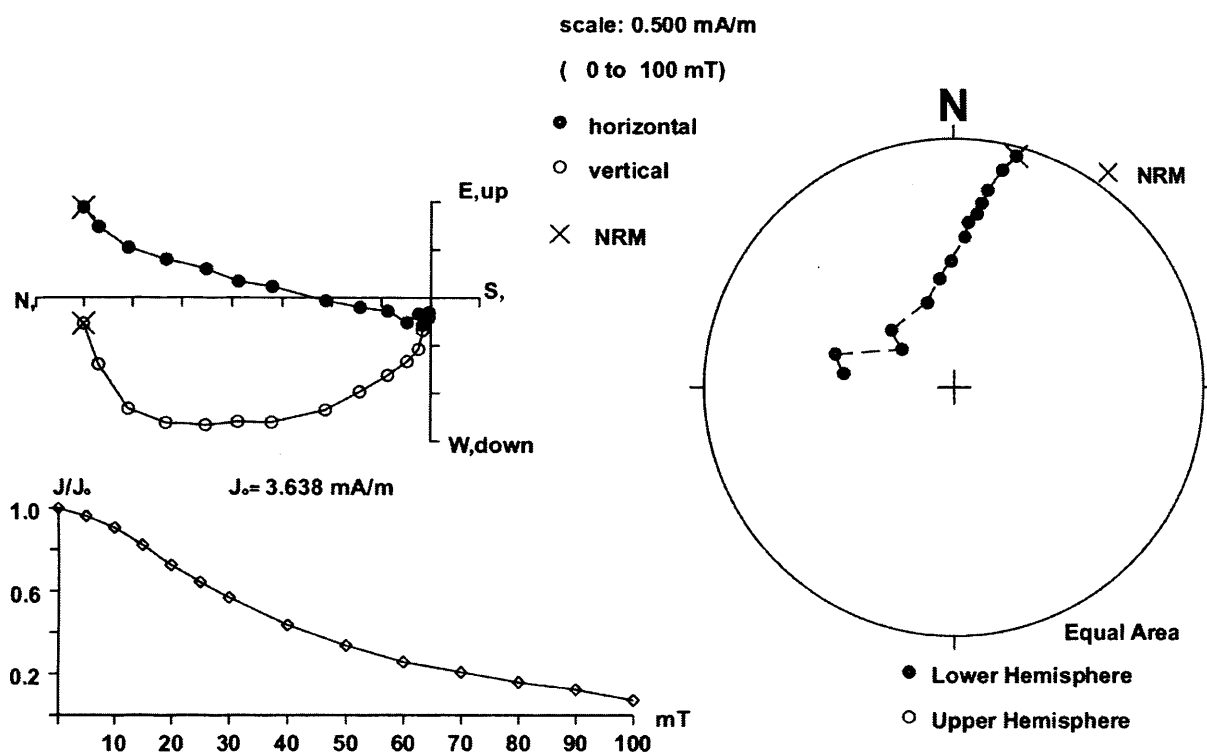


420 cm

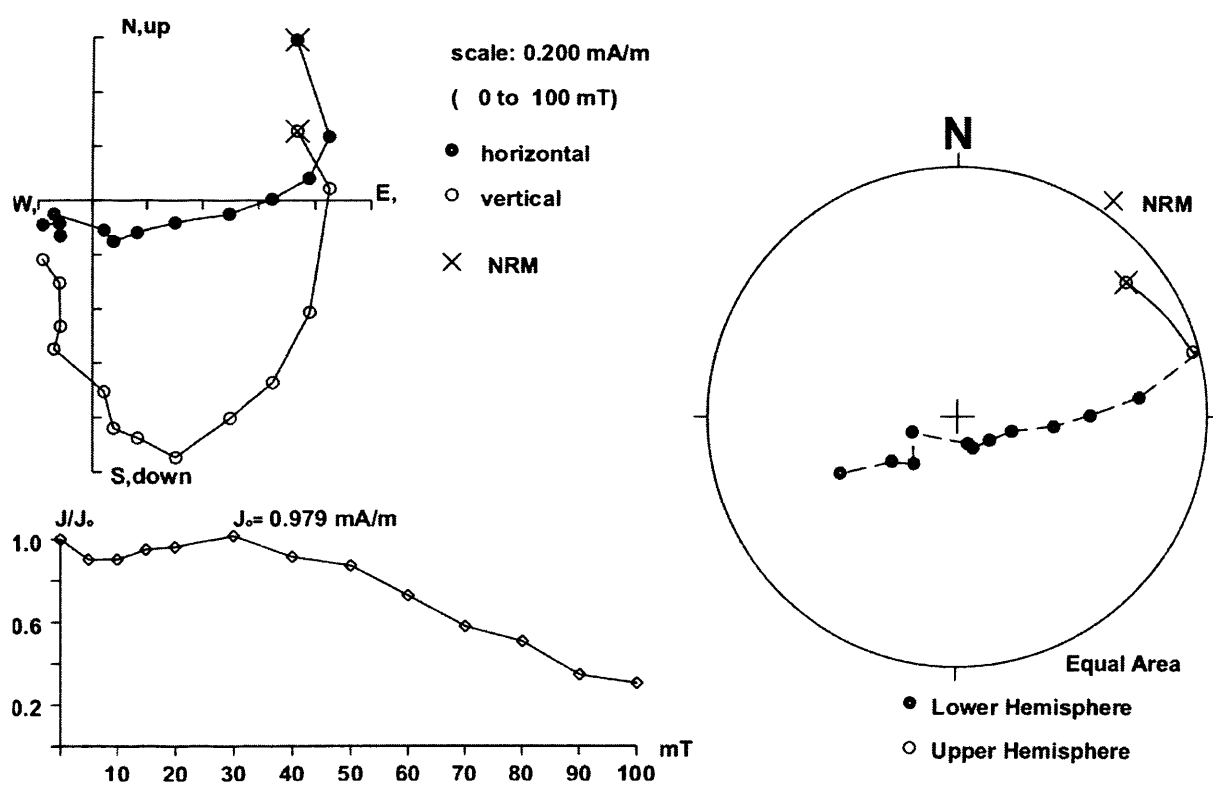


Appendix 2: Demagnetisation Plots

428 cm

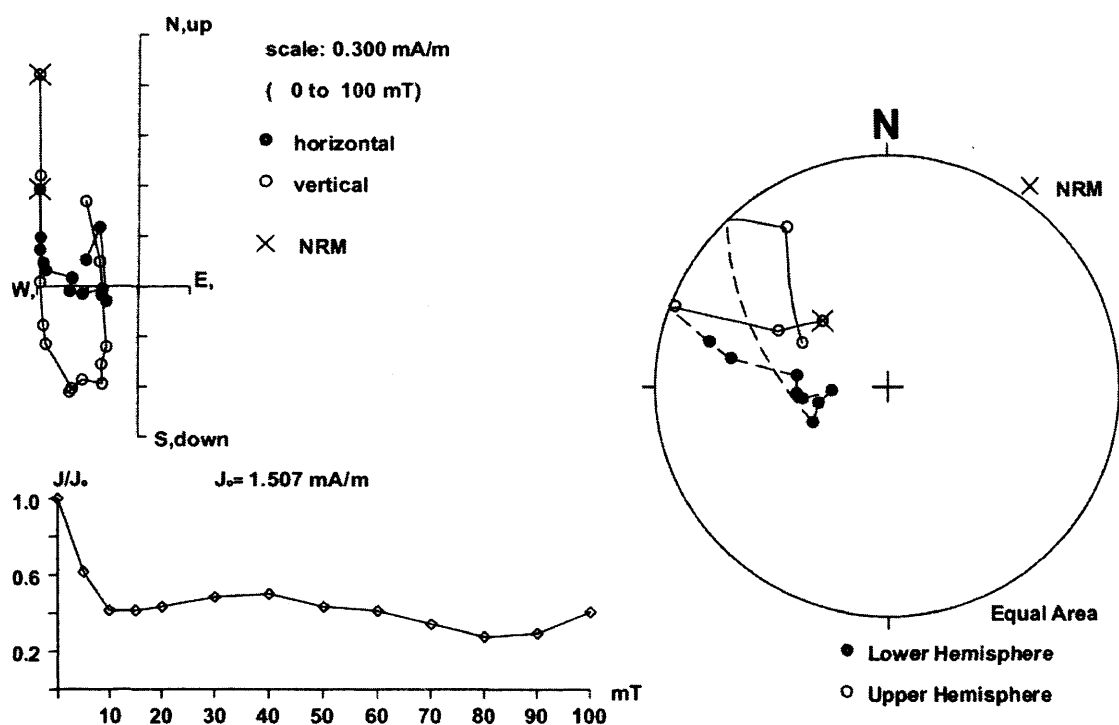


432 cm

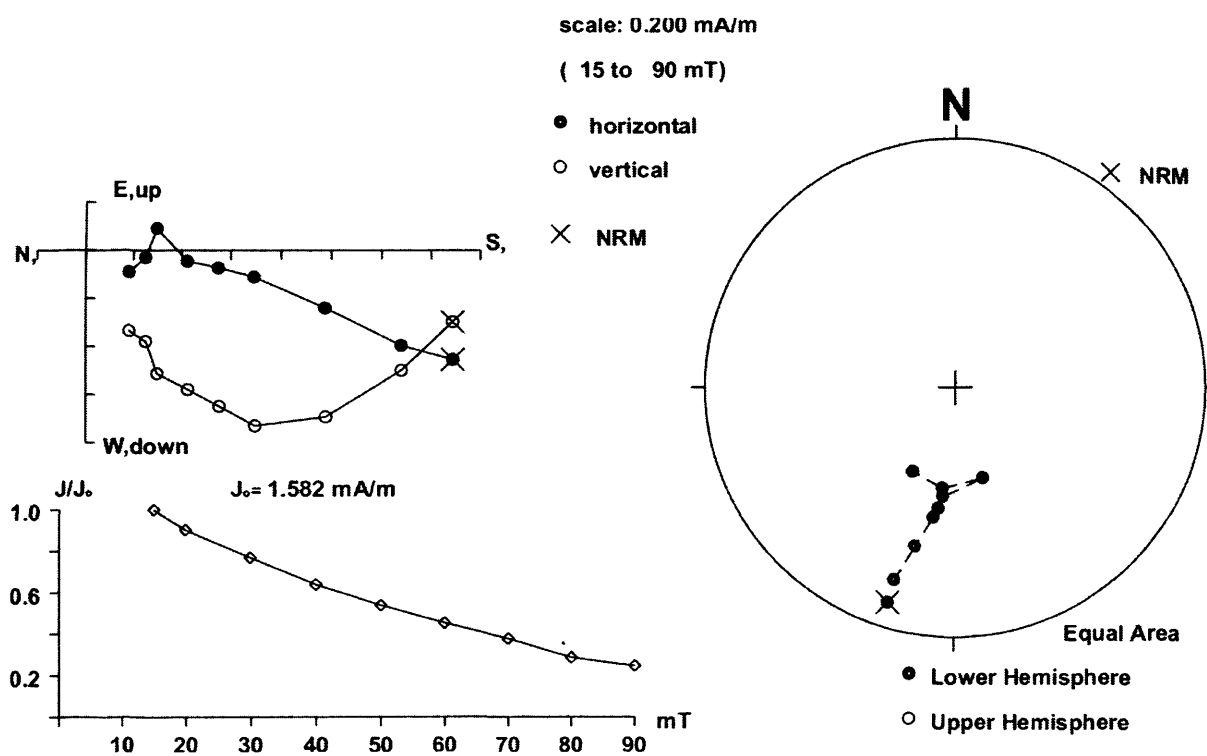


Appendix 2: Demagnetisation Plots

436 cm

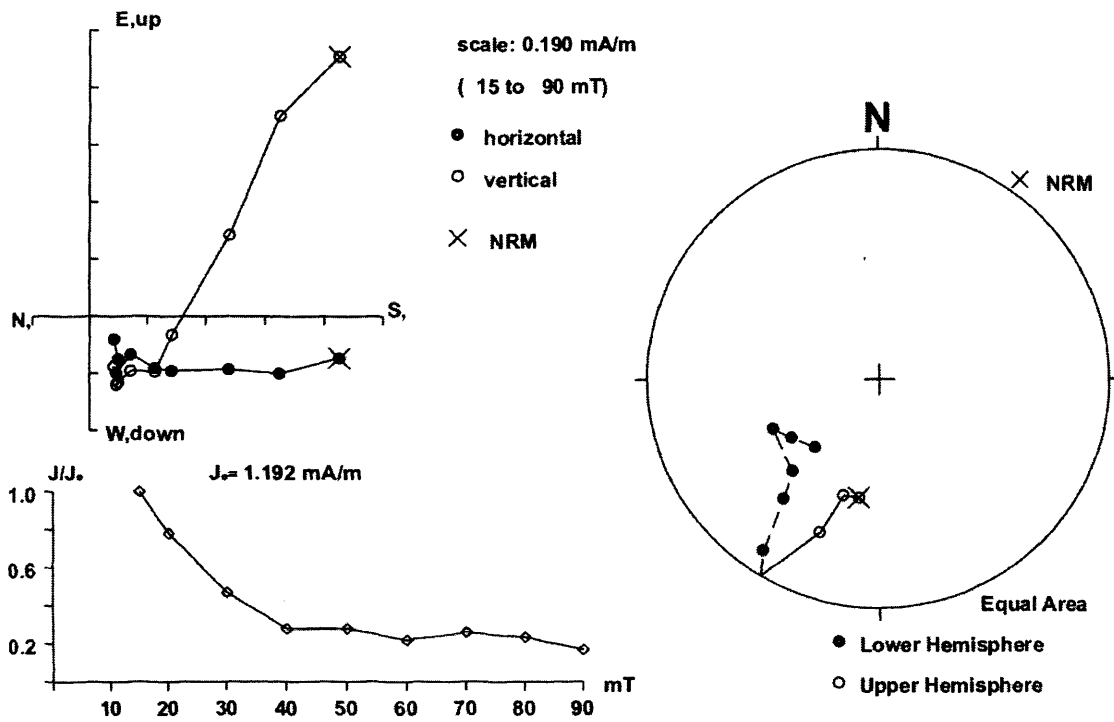


448 cm

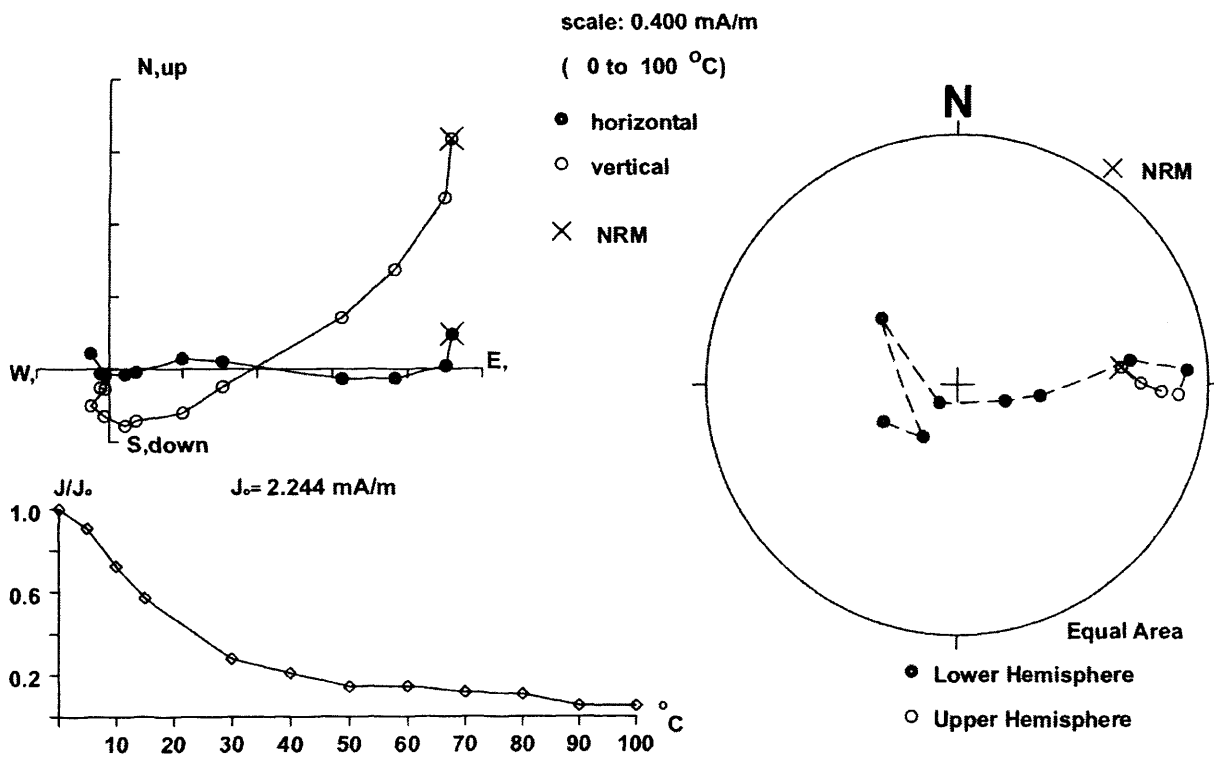


Appendix 2: Demagnetisation Plots

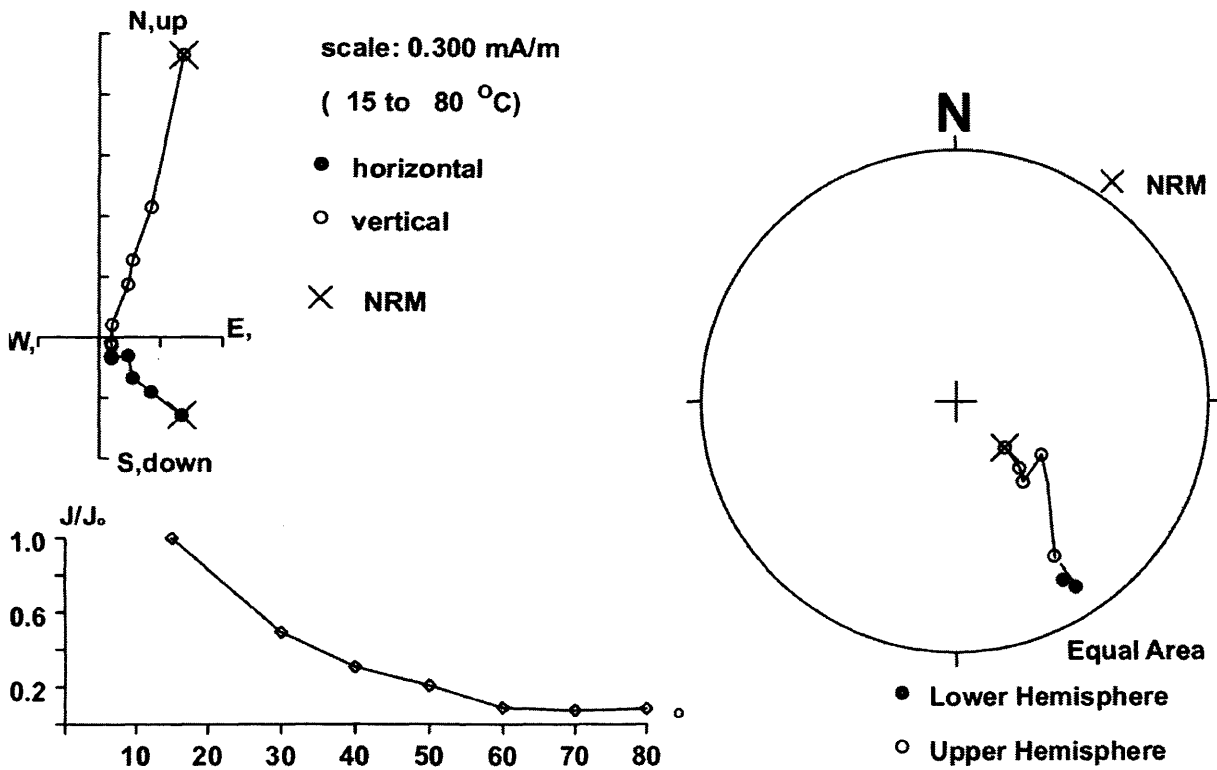
452 cm



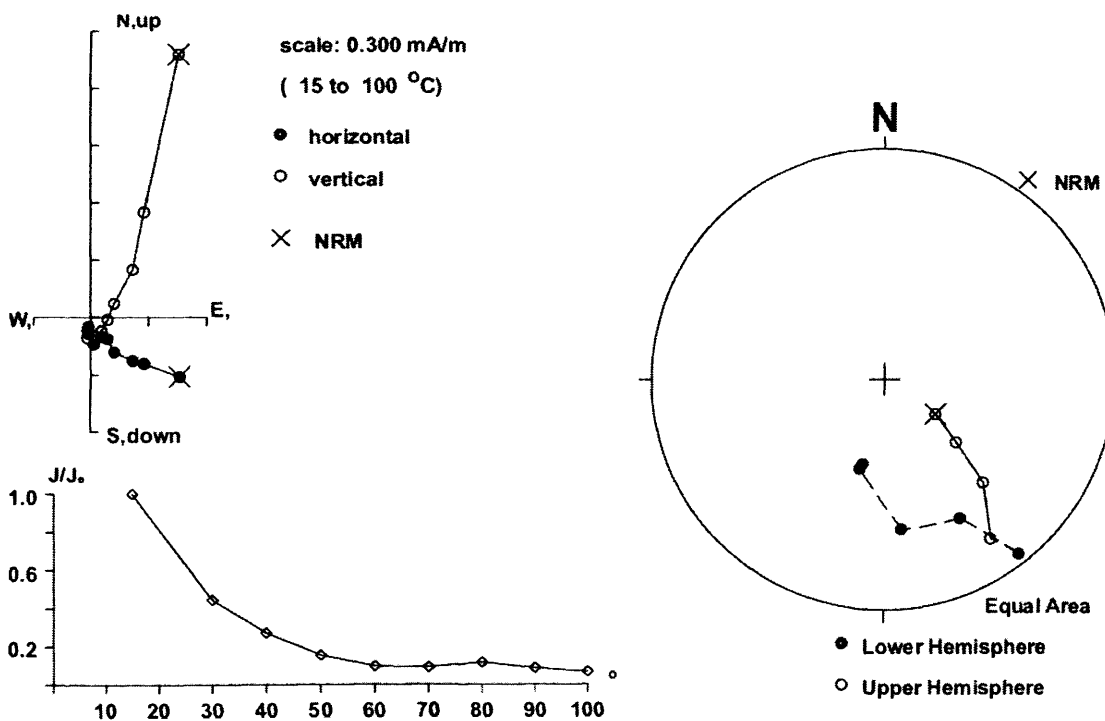
456 cm



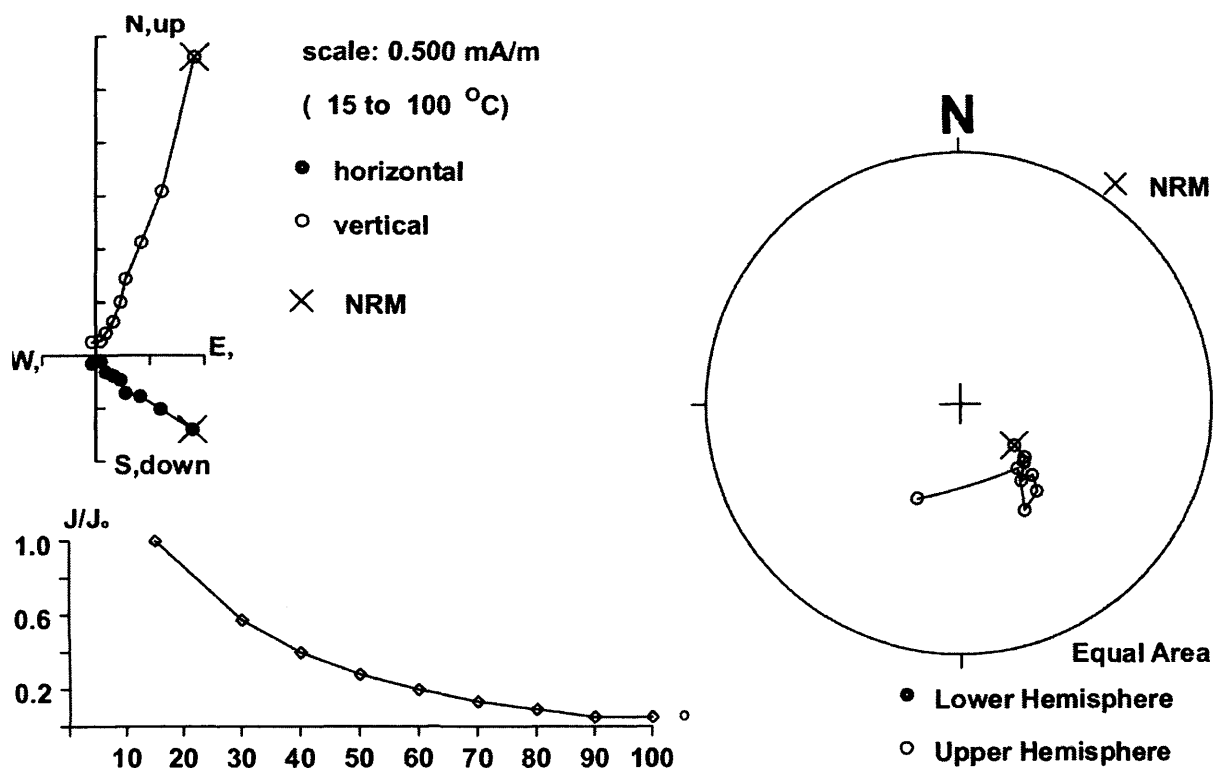
460 cm



464 cm



468 cm



480 cm

